List of Contributors

T. M. Alam, *Department of Organic Materials, Sandia National Laboratories, Albuquerque, NM 87008-0888 USA*

M. K. Alam, *Department of Chemical and Biological Sensing, Imaging and Analysis, Sandia National Laboratories, Albuquerque, NM 87008-0886, USA*

P. Bernatowicz, *Institute of Organic Chemistry, Polish Academy of Sciences, Kasprzaka 44, 01-224, Warszawa, Poland*

M. Bjerring, *Interdisciplinary Nanoscience Center (iNANO) and Laboratory for Biomolecular NMR Spectroscopy, Department of Chemistry, University of Aarhus, DK-8000 Aarhus C, Denmark*

A. Goldbourt, *Department of Chemical Physics, Weizmann Institute of Science, Rehovot 76100, Israel*

C. T. Kehlet, *Institut für Organische Chemie und Biochemie, Technische Universität München, D-85747 Garching, Germany and Interdisciplinary Nanoscience Center (iNANO) and Laboratory for Biomolecular NMR Spectroscopy, Department of Chemistry, University of Aarhus, DK-8000 Aarhus C, Denmark*

P. K. Madhu, *Department of Chemical Sciences, Tata Institute of Fundamental Research, Homi Bhabha Road, Colaba, Mumbai 400 005, India*

R. Marek, *National Center for Biomolecular Research, Faculty of Science, Masaryk University, Kotlářská 2, CZ-61137 Brno, Czech Republic*

N. Chr. Nielsen, *Interdisciplinary Nanoscience Center (iNANO) and Laboratory for Biomolecular NMR Spectroscopy, Department of Chemistry, University of Aarhus, DK-8000 Aarhus C, Denmark*

A. C. Sivertsen, *Interdisciplinary Nanoscience Center (iNANO) and Laboratory for Biomolecular NMR Spectroscopy, Department of Chemistry, University of Aarhus, DK-8000 Aarhus C, Denmark*

V. Sklenář, *National Center for Biomolecular Research, Faculty of Science, Masaryk University, Kotlářská 2, CZ-61137 Brno, Czech Republic*

S. Szymański, *Institute of Organic Chemistry, Polish Academy of Sciences, Kasprzaka 44, 01-224, Warszawa, Poland*

T. Takayama, *Department of Applied Chemistry, Faculty of Engineering, Kanagawa University, 3-27-1 Rokkakubashi, Yokohama 221-8686, Japan*

Y. Takeuchi, *Department of Chemistry, Faculty of Science, Kanagawa University, 2946 Tsuchiya, Hiratuka 259-1293, Japan*

T. Vosegaard, *Interdisciplinary Nanoscience Center (iNANO) and Laboratory for Biomolecular NMR Spectroscopy, Department of Chemistry, University of Aarhus, DK-8000 Aarhus C, Denmark*

Preface

It is a pleasure for me to introduce Volume 54 of Annual Reports on NMR. As is customary with this series the present volume reflects the protean nature of NMR by including reviews from six rather disparate scientific areas of activity.

S. Szymański and P. Bernatowicz commence the volume with an account of The Symmetrization Postulate of Quantum Mechanics in NMR Spectra; this is followed by a review of Chemometric Analysis of NMR Spectroscopy Data by T.M. Alam and M.K. Alam; Multiple Quantum Magic Angle Spinning: High Resolution Solid State NMR of Half-Integer Spin Quadrupolar Nuclei is covered by A. Goldbourt and P.K. Madhu; Y. Takeuchi and T. Takayama report on ^{73}Ge NMR Spectroscopy of Organogermanium Compounds; NMR Studies of Purines are surveyed by R. Marek and V. Sklenar; finally Numerical Simulations in Biological Solid-State NMR Spectroscopy is reviewed by A.C. Sivertsen, M. Bjerring, C.T. Kehlet, T. Vosegaard and N.C. Nielsen.

My sincere thanks goes to all of these reporters for their dedication to the task and for their support of Annual Reports on NMR.

Royal Society of Chemistry
Burlington House
Piccadilly
London, W1J OBA
UK

G. A. WEBB
June 2004

Contents

^{73}Ge NMR Spectroscopy of Organogermanium Compounds
YOSHITO TAKEUCHI AND TOSHIO TAKAYAMA

NMR Studies of Purines
RADEK MAREK AND VLADIMÍR SKLENÁŘ

Numerical Simulations in Biological Solid-State NMR Spectroscopy
ASTRID C. SIVERTSEN, MORTEN BJERRING, CINDIE T. KEHLET, THOMAS VOSEGAARD AND NIELS CHR. NIELSEN

The Symmetrization Postulate of Quantum Mechanics in NMR Spectra

S. SZYMAŃSKI AND P. BERNATOWICZ

Institute of Organic Chemistry, Polish Academy of Sciences, Kasprzaka 44, 01-224, Warszawa, Poland

In NMR spectroscopy, consequences of the symmetrization postulate of quantum mechanics for groupings of identical atomic nuclei are usually ignored. A common view is that only in rare instances this general practice must be suspended. However, according to recent experimental and theoretical findings, such instances are not so exotic as it is generally believed. Occurrence of the so-called quantum exchange couplings, stemming from the spin-space correlations imposed by the symmetrization postulate, is now routinely oberved in liquid-phase NMR of some transition metal tri- and dihydrides. Moreover, most recent studies on the dynamics of methyl-type molecular rotors reveal that even stochastic motions of such nuclear systems, generally treated as classical par excellence*, can in fact be shaped up by the symmetrization postulate. Interestingly, the quantum nature of such motions can be visible not only at cryogenic but also at ambient temperatures.*

The main issues that are addressed in the present review include manifestations of the symmetrization postulate in NMR spectra of the metal hydrides and methyl-type rotors. Emphasis is laid on the new developments in the field as well as on the relevant problems that await further analysis.

ANNUAL REPORTS ON NMR SPECTROSCOPY
VOLUME 54 ISSN 0066 4103
DOI 10.1016/S0066-4103(04)54001-2

1. INTRODUCTION

In NMR spectroscopy, the implicit picture of the molecules under study comprises a sort of quantum–classical eclecticism: (i) the atomic nuclei are localized at definite sites in the molecule; (ii) nuclides of the same type are differentiable; (iii) only the nuclear spins need to be treated quantum mechanically. Until the late 1980s, there had been no necessity to go beyond that picture, unless at liquid helium temperatures if the so-called quantum rotation, involving methyl groups and ammonium ions, was the focus. In 1989, the occurrence of phenomena similar to the quantum rotation was for the first time spotted in liquid-phase NMR, in the spectra of the hydride protons in some transition metal polyhydrides.[1,2] The anomalously large couplings between the hydride protons were shown to be the quantum mechanical exchange couplings (QECs)[3] arising from the symmetrization postulate of quantum mechanics (the Pauli exclusion principle). Since the latter reflects the presupposed non-differentiability of like particles, legitimacy of the simplification described under points (i) and (ii) above was challenged also for ambient temperatures. Since 1989, numerous examples of the quantum exchange couplings in the spectra of the metal hydrides have been reported. A survey of the relevant literature up to the first half of 1997 was published in the 1998 issue of this series.[4] In the present contribution, that survey is updated. Moreover, a new subject is added, involving the most recent advances in the studies on the quantum rotation. A comprehensive review on the latter topic, covering the literature up to the first half of 1999, was reported by Horsewill.[5] In the present contribution, the pre-1999 papers on the quantum rotation are only selectively referenced. The focus is on the most recent results involving hindered rotation of the methyl group at cryogenic temperatures as well as in liquids at ambient temperatures. These results shed new light onto the so-called quantum to classical transition in the behaviour of quantum objects composed of like particles, embedded in condensed environment. They show that for such objects, the spin–space correlations can be relevant not only to the coherent but to the stochastic dynamics as well. Even in liquid phase NMR spectra, consequences of the Pauli principle can be recognized in the stochastic behaviour of strongly hindered methyl groups. The standard semiclassical Alexander–Binsch (AB) theory[6,7] of NMR line shape must in such instances be replaced by a consistently quantum mechanical description.[8]

The recent research on the methyl group dynamics was inspired in part by the past developments in the studies on the metal hydrides. This is reflected in the arrangement of the present review. It is not intended to be exhaustive, but rather to highlight new advances in the field and to bring out the aspects that still await a deeper analysis.

2. BASIC PRINCIPLES OF QUANTUM EXCHANGE COUPLING

Below, the basic principles of the QEC effect observed in NMR spectroscopy are outlined. Sufficient conditions are specified under which the spin–space Hamiltonian of a set of N-like nuclei in a molecule can be converted into an effective NMR Hamiltonian. The reasoning that follows is a reproduction of long-known ideas, which, however, are sometimes misinterpreted. It is essentially an adaptation of the pertinent formalism

by Herring[9] who once addressed many-electron systems in insulators. The concept of space-fixed spin basis, introduced *ad hoc* to simplify derivation of the effective Hamiltonian,[10,11] will not be used.

According to the symmetrization postulate of quantum mechanics, the spin–space state function of a system of N nondifferentiable nuclei must be invariant under any of the $N!/2$ even permutations $\hat{W}^R\hat{W}^S$ performed simultaneously on the space (R) and spin (S) particles' coordinates. Under odd permutations, the state function of N fermions changes sign while that of N bosons remains invariant.

In general, the vibrational energy levels of a molecule containing N-like nuclei come in (nearly) degenerate clusters and the corresponding, spin–space correlated eigenfunctions are delocalized over all of the $N!$ equivalent potential energy minima each of which represents a definite distribution of the N nuclear tags over the N nuclear sites. The concept of the effective NMR Hamiltonian can be useful in the instances where permutational tunnelling of such nuclei through the energy barriers separating the equivalent potential energy minima is feasible. The quantum mechanical description to be of interest in such a case is based on the rather obvious assumption that the relevant vibrational eigenstates can be represented in terms of suitably chosen, mutually orthogonal one-particle basis functions $\psi_{\mathrm{A}}(r), \psi'_{\mathrm{A}}(r), \ldots, \psi_{\mathrm{B}}(r), \psi'_{\mathrm{B}}(r), \ldots, \psi_{\mathrm{F}}(r), \psi'_{\mathrm{F}}(r), \ldots$ localized at the individual nuclear sites $\mathrm{A}, \mathrm{B}, \ldots, \mathrm{F}$. The condition of orthogonality for the functions localized at the same site is rigorous while for those at the different sites it need not be such. In the latter case, it only states that the possible residual overlaps between the functions are practically negligible: as long as the vibrating molecule retains a definite structure, the overlaps between the nuclei vibrating at the neighbouring sites are vanishingly small. An explicit knowledge of the basis functions is not needed for the validity of the following argument. The product $\psi_{\mathrm{A}}(r_1)\psi_{\mathrm{B}}(r_2)\cdots\psi_{\mathrm{F}}(r_N)$, where the individual functions ψ have the norm of 1, will further be denoted by Ψ. In general, Ψ can be taken as a linear combination of such products including one basis function for each site. The detailed derivation to be presented below involves the effective Hamiltonian of the ground torsional level in which instance taking only one such product should be sufficient.

In order to avoid a possible confusion with the approaches invoking space-fixed spin bases,[10,11] for the purposes of the present derivation formal definition of the familiar z-component spin functions must be reminded. Thus, for nucleus n of spin I, the symbols $\chi_M(\sigma_{\mathrm{n}})$, where $M = -I, -I+1, \ldots, I$, and $\sigma_{\mathrm{n}} \epsilon \{-I, -I+1, \ldots, I\}$ is the spin coordinate of nucleus n, denote mappings of the set of spin coordinates onto the set $\{0, 1\}$ such that $\chi_M(\sigma_{\mathrm{n}}) = 1$ when $\sigma_{\mathrm{n}} = M$ and 0 otherwise. The products of N spin functions $\chi_M(\sigma_1)\chi_M{}'(\sigma_2)\cdots\chi_M{}''(\sigma_N)$ will be denoted by X_s, with $s = 1, 2, \ldots, (2I+1)^N$, where $(2I+1)^N \equiv N_I$ is the total number of functions X_s, or the dimension of the spin–space concerned.

Now, the set of N_I spin–space states spanning the interesting vibrational manifold will include the Slater determinants (or, for bosons, permanents) $|\Phi_s\rangle$ defined according to

$$|\Phi_s\rangle = (N!)^{1/2}\hat{A}|\Psi\rangle|X_s\rangle, \tag{1}$$

where

$$\hat{A} = \frac{1}{N!} \sum_{k=1}^{N!} z_k^{2I} \hat{W}_k^R \hat{W}_k^S, \tag{2}$$

with z_k being 1 (-1) if the kth permutation is even (odd). By construction, all these states fulfil the requirements of the symmetrization postulate. Their mutual orthonormality is exact to terms of the order of the nucleus–nucleus overlaps, which are vanishingly small in ordinary matter. Moreover, they form a complete set in the space of the (spin–space correlated) sublevels of the ground vibrational level. (If the set is incomplete, it can in principle be rendered to be complete by including in Ψ further products of site-centred basis functions, with the respective contributions calculated according to an equivalent of the Configuration Interaction scheme of the quantum theory of many-electron systems; the question of an implementation of such a scheme in practice is of no concern here). Therefore, the matrix representation of the relevant vibrational Hamiltonian $\hat{H}'$ in the basis $\{|\Phi_s\rangle, s = 1, 2, \ldots, N_I\}$ is virtually exact. The same holds true for the complete Hamiltonian $\hat{H} = \hat{H}' + \hat{H}''$ (from here on formulated in angular frequency units) of the system placed in an external magnetic field, where the second term describes the relevant spin-dependent interactions, because perturbations of the vibrational motions by the field can safely be neglected in the present context.

In the calculations of the matrix elements concerned, three points are to be taken into account: (i) the operator (projector) $\hat{A}$ is idempotent; (ii) the Hamiltonian $\hat{H}$ is formulated according to the principles of quantum mechanics and as such it commutes with $\hat{A}$ as well as with the individual spin–space permutations $\hat{W}_k^R \hat{W}_k^S$; (iii) the spin-dependent interactions across the barriers separating the individual energy minima are negligible. Point (iii) is commented exhaustively in, e.g., Ref. 11.

When points (i) and (ii) are taken into account, the matrix elements will be given by

$$\langle \Phi_s | \hat{H} | \Phi_{s'} \rangle = N! \langle X_s | (\langle \Psi | \hat{A} \hat{H} | \Psi \rangle) | X_{s'} \rangle. \tag{3}$$

Because $\hat{H}$ is dynamically dependent on spin and space variables, the expression in parentheses in the r.h.s. of Eq. (3) involving integration over the latter defines a spin operator. This is just the effective Hamiltonian of interest to us. By virtue of point (iii), when the integrations are to be performed for the $\hat{H}''$ term in the Hamiltonian, only the unit operator in $\hat{A}$ need to be retained. The resulting expression will thus have the form $\langle \Psi | \hat{H}'' | \Psi \rangle$. If one takes into account that the space state $|\Psi\rangle$ is a product (or a combination of products, see above) of localized, one-particle states, one can immediately see that upon integrating over the spatial variables r_n, $n = 1, 2, \ldots, N$, the spatial parts of the individual spin-dependent terms will be replaced by the corresponding quantum mechanical averages. Thus, for $\hat{H}''$, the entire expression in Eq. (3) is none other than one of the matrix element of the standard NMR Hamiltonian, $\hat{H}_{\mathrm{NMR}}$, between two spin-product basis states, $\langle X_s | \hat{H}_{\mathrm{NMR}} | X_{s'} \rangle$.

As far as the remaining, spin-independent part $\hat{H}'$ is concerned, the integration over space variables prescribed in Eq. (3) gives the expression $\langle X_s | \sum_k z_k^{2I} 2\pi\Pi_k \hat{W}_k^S | X_{s'} \rangle$, where $2\pi\Pi_k = \langle \Psi | \hat{W}_k^R \hat{H}' | \Psi \rangle$ is a numerical parameter.

Summarizing, when the matrix elements of the correct quantum mechanical Hamiltonian of the system in question are calculated in a special basis conforming to the symmetrization postulate then, upon integrating over the spatial variables, the following effective spin Hamiltonian is obtained

$$\hat{H}_{\text{eff}} = H_{\text{NMR}} + \sum_k z_k^{2I} 2\pi\Pi_k \hat{W}_k, \tag{4}$$

where the superscript S at the operator symbols has been dropped, which will not lead to ambiguities. In Eq. (4), the summation over k can be confined to a subgroup of the full permutation group of N objects. Such subgroup, sometimes called the feasible group,[12] describes the smallest closed set of the equivalent potential minima connectible by facile tunnelling routes. The individual sublevels of the cluster can be labelled by the irreducible representations of the feasible group. In the case where the feasible group is isomorphic with C_2, the (only) quantity Π measuring the feasibility of permutational tunnelling of a pair of nuclei equals half of the tunnelling splitting between the vibrational sublevels A and B. For the feasible group isomorphic with C_3, the corresponding relationship is also simple (see Section 4.1). For more complicated tunnelling systems, closed-form expressions of the quantities Π in terms of the splittings within the vibrational clusters may be non-existent.

In what follows, the permutation operators $\hat{W}_k$ describing pair permutations and cyclic permutations of three objects will be denoted by $\hat{P}$ and $\hat{Q}$, respectively. For spin-1/2 nuclei (and only for such nuclei) the terms $\hat{P}$ and the sums $\hat{Q} + \hat{Q}^{-1}$ can be expressed as J-couplings between (pairs) of the corresponding nuclei.[13] These apparent J-couplings add up to the usual, magnetic J-couplings entering the $\hat{H}_{\text{NMR}}$ term.

Actually, the above formalism can also be applied to excited vibrational states. For this purpose, it would be essential to take function Ψ in Eq. (1) as a combination of products of various site-localized functions ψ [see the parenthetical comment following Eq. (2)]. The effective Hamiltonians obtained in this way for the excited states will still have the same form as that in Eq. (4) but, obviously, the numerical values of the relevant parameters will be different. Therefore, one might consider the actual effective Hamiltonian controlling the NMR experiments as Boltzmann average of the effective Hamiltonians for the sequential vibrational levels, 'produced' by fast vibrational relaxation processes. In two specific instances where such processes were addressed explicitly in a consistently quantum mechanical way,[8,14] the above intuitive picture could essentially be confirmed (if the term 'Boltzmann averaging' is not taken too literally). However, as far as the stochastic spin dynamics that evolve with increasing temperature are concerned, a description thereof invoking the notion of the effective Hamiltonian just from the beginning may be inadequate. The correct effective description can be obtained when a complete spin–space picture conforming with the symmetrization postulate is used at the start. However, this non-trivial problem has as yet been resolved for two relatively simple systems. They will be addressed in detail in the two sections that follow.

3. QUANTUM EXCHANGE COUPLINGS IN METAL HYDRIDE NMR

In 1998, apart from the already quoted review,[4] concentrated on the relevant NMR theories, a review focused on the electronic structure and chemistry of the metal hydrides exhibiting the QEC effect was published.[15] Developments in modelling of the effect by quantum chemical calculations were also reviewed.[16] In the present survey, only the aspects directly related to manifestations of the QEC effect in NMR spectra are covered. A review of the recent results will be preceded by a brief recapitulation of the main developments in the past research on the metal hydrides.

The basic structures which can be of interest in the discussion of the QEC effect are shown in Fig. 1. In the trihydrides, the hydride nuclei are positioned at the vertices of an isosceles triangle; the distance between the central and sideward positions are about 1.7 A; the distance between the latter generally exceeds 2 A.[17] In the *cis*-dihydrides, the H–H distance can range from 1.7 to the values about 1.5 A; the species with the H–H distance between 1.5 and 1 A are called nonclassical dihydrides or enlongated dihydrogen complexes[18] and those with the distance still shorter are called dihydrogen complexes. The hydrido dihydrogen complexes which are of interest in the present review contain a dihydrogen ligand and a single hydride situated *cis* to the latter.[19] The fact that the anomalously large hydride–hydride couplings are manifestations of the QEC effect was for the first time reported in 1989 by Zilm *et al.*[1] and, simultaneously, by Weitekamp *et al.*[2] The experimental data addressed by those authors involved the trihydride complexes in which, generally, the quantum exchange engages pairs comprising the hydride in the symmetry plane and one of the out-of-plane hydrides. It is now well documented that the QEC can also be observed for *cis*-dihydrides.[20–22] In the dihydrogen complexes, the QECs are generally very large and have not so far been

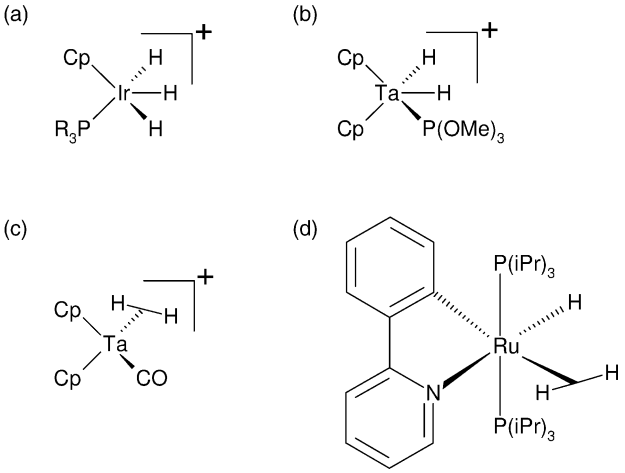

Fig. 1. Basic structures of the metal hydride complexes exhibiting the QEC effect. (a) Trihydride, (b) *cis*-dihydride, (c) dihydrogen, and (d) hydrido dihydrogen complexes. The symbol Cp denotes variously substituted cyclopentadiene anions.

detected in solution-state NMR. In a two-spin system, if the QEC greatly exceeds the Larmor frequency difference, it effects a collapse of the spectral pattern to a singlet; in such an instance there is practically no way to discriminate between the coherent and a rapid stochastic spin exchange as the possible causes of the collapse.

In the dihydride and dihydrogen complexes, the relevant quantum motion is confined to a two-well potential in configuration space (see Fig. 2). The vibrational levels are therefore split into doublets whose components transform as the irreps A and B of C_2. In the trihydrides, cyclic permutations of all three hydrides as well as pair permutation involving the sideward hydrides are unfeasible.[17] Nevertheless, all of the six equivalent minima at the potential energy surface are connectible by routes of facile tunnelling between the central and either of the sideward positions. Thus, the feasible permutation group is the same as the complete permutation group of three objects and is isomorphic with C_{3v}. Accordingly, the rovibrational levels come in six-membered clusters which are further grouped into two Kramers doublets and two singlets. Under permutations from the feasible group, the latter transform as the one-dimensional irreducible representations A and B, and the former as the two-dimensional irrep E of C_{3v}.[10] In the perprotio species, sublevels A are unoccupied because spin states of the complementary symmetry B, required by the symmetrization postulate, are non-existent for three spin-1/2 particles. The same level structure is in the hydrido dihydrogen complexes.

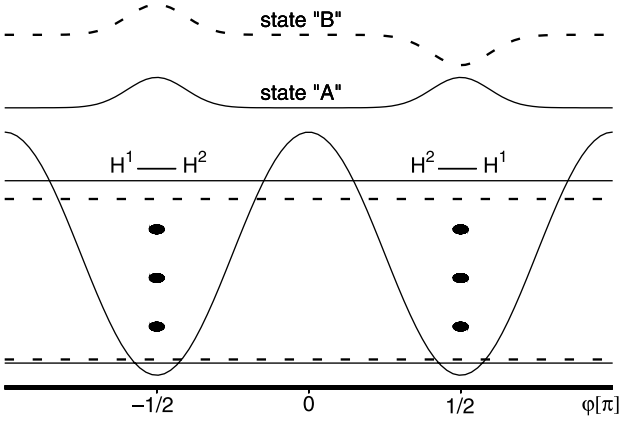

Fig. 2. The potential energy surface for exchange of hydrides 1 and 2 at two (inequivalent) sites in a dihydride metal complex. The single periodic coordinate φ describes schematically multidimensional motions effecting permutation of hydrides 1 and 2. The vibrational energy eigenstates concerned come in tunnelling doublets with closely spaced energies $E_n^{A,B}$, where A and B denote the components that are even and odd, respectively, under the particle permutation. The eigenstates are delocalized over both of the potential energy minima. Schematic representations of the eigenfuctions of the ground level are shown. For a pair of fermions (protons), the spin–space correlations are $A \leftrightarrow B$ and $B \leftrightarrow A$; for bosons (deuterons) the correlations are $A \leftrightarrow A$ and $B \leftrightarrow B$. The tunnelling splittings $\Delta_n = E_n^A - E_n^B$ increase with increasing level energy. Because of a multidimensional character of the tunnelling motion in the hydrides, alternation of the sign of Δ_n for the sequential levels need not occur; such an effect would be observed for strictly one-dimensional (rotational) motion of the hydride pair.

At temperatures where the stochastic dynamics are frozen, the spectra of the hydrides can be interpreted in terms of the effective Hamiltonian in Eq. (4). For the perprotio species, the QEC terms (pair permutation terms) add up to the proton–proton *J*-couplings. The resulting, apparent *J*-couplings generally increase strongly with temperature. This effect can be interpreted in terms of growing, with increasing temperature, contribution to the average Hamiltonian of the vibrationally excited states for which the tunnelling splittings are much greater than for the ground state. The averaging is effected by a rapid, steady-state flow of the population between the energy levels, occurring at the rates in the picosecond range typical of vibrational relaxation in liquids. In NMR spectra of the hydrides, the increase of temperature leads not only to changes of the exchange couplings but to a gradual acceleration of the stochastic dynamics as well. The latter cause broadenings, coalescences and motional narrowing of the hydride patterns, leading eventually to a collapse of the fine structure. Like in the systems showing no exchange couplings, these stochastic effects are generally interpreted in terms of the classical, random jump model assumed in the well-known AB NMR line shape theory.[6,7] Even though such an approach should afford a correct theoretical reproduction of the observed spectra, it would create a fundamental conceptual difficulty in setting together two disparate concepts: from one side the tunnelling of like nuclei assisted by the Pauli principle, and a classical motion implying differentiability of the same nuclei from the other.

For the simplest but still non-trivial system of two hydrides (or deuterides) in a two-well potential, this difficulty was already resolved.[14] When the relevant vibrational relaxation processes involving spin–space correlated states are addressed in a consistent way, the following picture is obtained. Nearly all of the possible quantum coherences in the hydride system are damped so rapidly that they escape detection in NMR experiments. There is only one coherence that is spared by the rapid vibrational relaxation processes. It comprises a weighted average of the coherences between sublevels A and B at the sequential vibrational levels; each such particular coherence comes with a temperature-dependent weight of the magnitude close to the Boltzmann factor involved. This specific, long-lived coherence evolves with the oscillation frequency Δ and is damped with rate constant k, which is generally much smaller than the vibrational relaxation constants; to a crude approximation, Δ is a Boltzmann average of the tunnelling splittings (expressed in Hz) at the sequential levels. The system's dynamics that are observable in NMR experiments can be shown to be fully describable in terms of the spin variables only. The final equation for the system's spin density matrix $\hat{\rho}$ obtained in this way is a close analog of the AB equation, thus:

$$\mathrm{d}\hat{\rho}/\mathrm{d}t = -i[-\omega_{\mathrm{A}}\hat{I}_{z1} - \omega_{\mathrm{B}}\hat{I}_{z2} - \pi\Delta\hat{P}, \hat{\rho}] - (k/2)[\hat{\rho} - \hat{P}\hat{\rho}\hat{P}]. \tag{5}$$

As was already mentioned, for a proton pair the term $\pi\Delta\hat{P}$ can be replaced with the *J*-coupling term $2\pi\Delta\hat{I}_1\hat{I}_2$; for a pair of deuterons (spin-1), that term (no longer expressible as *J*-coupling) would come with the 'plus' sign. Note also that in the AB equation for a *J*-coupled pair of protons undergoing 'classical' mutual exchange with rate constant k_{class}, the factor of 1/2 in front of the last term in Eq. (5) would be absent. In other words,

the quantity interpreted as rate constant of the 'site exchange' equals half of the damping-rate constant k.

The observed behaviour of a system of two exchange-coupled nuclei can, therefore, be described consistently in terms of a single quantum process: the damped (with rate constant k) oscillation (with angular frequency $2\pi\Delta$) of a quantum coherence involving spin and space variables of the nuclear pair. Despite the fact that for pair exchange the approach quoted essentially reproduces the known line shape equation, it sheds new light onto the molecular rate processes involving permutations of like particles. In Section 4, a more recent theory which addresses systems with cyclic exchange of three particles (e.g., the hindered methyl group) is summarized.

For an iridium trihydride, the temperature behaviour of the long-lived quantum coherence described above was modelled theoretically under the simplifying assumption that the relevant dynamics of either of the two exchanging hydride pairs can be described in terms of a periodic two-well potential.[23] Excellent agreement with the experimental $k(T)$ and $\Delta(T)$ curves was obtained.

3.1. Developments in theory

During the recent period, the theoretical research on the hydride dynamics was pursued essentially in the traditional (eclectical) spirit.

In 1998, Limbach *et al.*[24] reported a refinement of their earlier model of QEC in the metal hydrides[25] invoking a dynamic equilibrium between the dihydride and dihydrogen structures. The latter are supposed to exhibit extremely large QECs. In the approach quoted, the symmetrization postulate is abandoned from the start and a dynamic equilibrium between four localized quasi-species X, X′, Y, and Y′ is considered. In Fig. 2, the species X and X′ are represented by the low-lying states localized in the individual potential wells while those Y and Y′ are represented by the respective, highly excited localized states. The essential idea of the approach considered is that interconversions of these four species can be described by 'rate constants' having also imaginary components. The imaginary rate constants iJ_X and iJ_Y measure interconversions within degenerate pairs of the quasi-species (X, X′) and (Y, Y′), respectively, occurring via the coherent tunnelling. The real rate constants $k_{XX'}$, $k_{YY'}$, k_{XY}, etc., describe the corresponding incoherent interconversions. The set of four coupled differential equations for the time-dependent molar fractions is solved under assumption of the steady-state condition for the low-abundance species Y and Y′. The solutions for the fractions of X and X′ contain components which exhibit damped oscillatory behaviour. Working equations describing the NMR line shape of an exchanging proton pair are obtained under the assumption that in addition to Larmor precession in an external magnetic field, the relevant quantum coherences in the spin manifold suffer the same dynamics as do the molar fractions of the quasi-species. The derivation goes along the way once initiated by Johnson[26] and further refined by Binsch,[7] employing the concept of composite Liouville space to the description of the individual interconverting (quasi) species. The line shape equation obtained in this way, formulated finally in the 'primitive' Liouville space[7] is again the AB equation with the QEC term expressed as J-coupling. In the above approach, the parameters Δ and k

entering the AB equation can in an explicit way be related to the imaginary and real rate constants describing the hypothetical dynamic equilibrium between the four quasi-species. This affords a qualitative interpretation of the effects involved in terms of formal kinetics. In particular, a comparison of the dynamics observed for the perprotio and the corresponding selectively deuterated species can be made. An example of application to a practical problem of the approach by Limbach *et al.*[24] will be given in Section 3.3.

The concept of composite Liouville space was also employed to derive the line shape equation for a pair of deuterons exhibiting the QEC and stochastic exchange effects in ^{2}H NMR solid-state spectra.[27] The derivation goes along the standard way;[7,26] the stochastic dynamics are described in terms of interconversion with real rate constant of two quasi-species, corresponding to the two arrangements of the hydrides (and, in fact, deuterides) at the respective binding sites. The spin Hamiltonian of either of the quasi-species is the effective Hamiltonian in the sense of Eq. (4) since it includes the QEC term represented by the pair permutation operator. (As was already mentioned in the comment to Eq. (5), for spin-1 particles it is no longer equivalent to the *J*-coupling). It also contains the secular parts (ones invariant under rotations about the direction of the external magnetic field) of the relevant anisotropic interactions involving the nuclear spins. In the case considered, the most significant are the interactions between the quadrupole moments of the deuterons and the electric field gradients at the nuclear sites involved as well as the dipole–dipole interactions. Again, the NMR line shape equation, formulated finally in the 'primitive' Liouville space,[7] is strictly analogous to the AB equation. Authors' interest in the solid-state NMR was motivated by the fact that for certain orientations of the molecule with respect to the external magnetic field, differences between the quadrupolar interactions at the individual deuteride sites can be three- to four-orders of magnitude larger than the corresponding Larmor frequency differences. In solid-state NMR, the limiting magnitudes of QEC between deuterons that can still be measured can, therefore, be much greater than in (isotropic) liquids. Moreover, the temperature range can be explored down to the liquid helium temperatures. One such solid-state study will be described in some detail in the following subsection.

3.2. The dihydrides and dihydrogen complexes

First direct evidence was reported[28] of QEC between two deuterons in a selectively deuterated dihydrogen ruthenium complex **1** (Fig. 3). It was obtained from solid-state ^{2}H NMR spectra measured for a polycrystalline sample of **1** in the temperature range 5.4–320 K. At temperatures below 20 K, the spectra show features characteristic of the QEC effect. A fair reproduction of the observed spectra was achieved in line shape simulations employing the AB equation with the QEC and stochastic exchange terms as in Eq. (5), augmented with the corresponding quadrupolar terms (see Fig. 4). It was found that the QEC constant Δ increases slightly with temperature, from the value 19.7 kHz at 5.4 K to 22.4 kHz at 8.8 K. On the other hand, the incoherent exchange rate constant $k_{\mathrm{class}}/2\pi$ grows strongly from 5 kHz at 5.4 K to about 2.5 MHz at 103 K. The narrow peak emerging gradually in the centre was attributed to the natural abundance deuterons from the phenyl rings, which can become highly mobile at elevated temperatures.

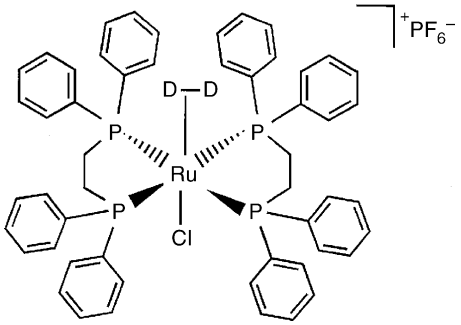

Fig. 3. Structure of the *trans*-$[Ru(D_2)PPh_2CH_2CH_2PPh_2]^+PF_6^-$ complex, **1**.

The large values of the QEC constant for the D_2 moiety confirm that **1** is a dihydrogen rather than *cis*-dihydride complex.

While the QEC patterns of three-fold quantum rotors are almost routinely observed in the powder as well as single-crystal H^2 NMR spectra of deuterated methyl groups and ND_4 ions (see Sections 4 and 5), the patterns of a genuine two-fold D-D rotor, shown in Fig. 4, were reported for the first time.

As far as liquid-phase NMR is concerned, no resolved QECs between deuterons have so far been detected. However, indirect evidence has been mounting that in some deuterated dihydrogen complexes the lack of observable splittings of the ^2H resonance signal is due to the occurrence of a large QEC between the deuterons rather than rapid stochastic exchange

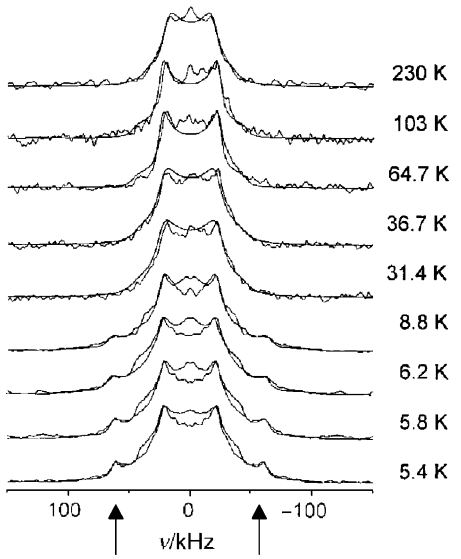

Fig. 4. Experimental and simulated ^2H NMR spectra of the $Ru-D_2$ complex **1** at the indicated temperatures. The peaks marked with arrows originate from the QEC between the deuterons. (Reproduced with permission from Ref. 28. Copyright by The PCCP Owner Societies, 1999).

of the latter. For a dihydrogen complex of tantalum, $[Cp_2Ta(H_2)(CO)]^+$, $Cp = (C_5H_5)^-$, it was once found that the deuteron resonance in the HD isotopomer decoalesces into a pair of signals differing by about 40 Hz in their Larmor frequencies while no decoalescence was observed for the HH and DD isotopomers.[21] The deceptive simplicity of the resonance patterns in the latter isotopomers at temperatures where the stochastic exchange in the HD species is frozen was attributed to the occurrence of large QEC effects. Specifically, for the DD isotopomer it was assessed that the QEC constant must exceed 250 Hz for the fine structure to be collapsed.[21] A similar situation was also observed for dihydrogen isocyanine niobocene, $[Cp_2'Nb(H_2)(CNR)]^+$, $Cp' = (C_5H_4SiMe_3)^-$.[29]

In summary, for the perprotio dihydrogen complexes no resolved structures of the dihydrogen resonances have been observed. It must be added that for some dihydrogen compounds, the dihydrogen signals are anomalously broadened. Their widths-at-half-height are incompatible with those calculated from the nuclear spin-lattice relaxation rates and are dependent on the magnetic field strength.[30] These features have not been explained yet.

As far as the dihydride complexes are concerned, earlier observations of the proton–proton QEC in a *cis*-dihydride complex of tantalum in solution[20,21] were recently presented in a wider context.[22] The observations for the dihydrides provide an indirect corroboration of the pairwise character of the QEC effects observed typically in symmetric trihydride complexes.

3.3. Trihydride complexes

Like in the past, most of the data on the QEC effect involve this class of the metal hydrides. The NMR formalism used in the description of the coherent and stochastic dynamics in the trihydrides is a phenomenological generalization of that describing the two-particle case. In consistence with the spirit of the semiclassical AB theory, the dynamics in the two two-particle subsystems (of which either engages the nucleus in the centre) are assumed to be independent. In the trihydrides, the central hydride atom lies in the molecular symmetry plane such that the three hydride nuclei form an A_2B system. Therefore, the pertinent line shape equation has the form

$$\begin{aligned} d\hat{\rho}/dt = &- i[-\omega_A(\hat{I}_{z1} + \hat{I}_{z3}) - \omega_B\hat{I}_{z2} - \pi\Delta(\hat{P} + \hat{P}'), \hat{\rho}] \\ &- k_{class}[2\hat{\rho} - \hat{P}\hat{\rho}\hat{P} - \hat{P}'\hat{\rho}\hat{P}'], \end{aligned} \tag{6}$$

where $\hat{P}$ and $\hat{P}'$ represent pair permutations (12) and (23), respectively. For three-particle systems in which cyclic exchanges of all three particles are unfeasible, Eq. (6) can be obtained in a consistently quantum mechanical approach,[31] which involves a generalization of the earlier theory addressing two-particle systems.[14] However, the assumption that the system has symmetry plane on the NMR time scale is essential for the derivation. For unsymmetrical three-particle systems, the corresponding theoretical argument is still lacking.

There are several experimental studies of the trihydrides confirming that use of the AB equation affords correct theoretical reproduction of the observed spectra, including

unsymmetrical systems. In the thorough study by Limbach *et al.*[24] on a ruthenium trihydride $(C_5Me_5)RuH_3PCy_3$ (Cy = cyclohexyl) **2**, Eq. (6) has proven adequate in the description of the hydride spectra measured over a broad temperature range 167–297 K. In that range, the values of $|J|$ grow monotonically from 40 Hz at 167 K up to about 320 Hz at 297 K. Above 200 K, impact of the incoherent exchange becomes more and more pronounced; at 297 K, $k_{\text{class}} \approx 90,000s^{-1}$. Interestingly, from the data obtained for isotopomers d_1, d_2, and d_3 of **2** it follows that within the margin of error there is no kinetic isotope effects on the stochastic dynamics. No resolved QEC patterns could be observed for **2**-d_3. These findings were interpreted in terms of authors' own theory of QEC associated with the stochastic dynamics, addressed in Section 3.1.

Eq. (6) was also used for theoretical reproduction of the experimental spectra of several osmium trihydrides exhibiting the QEC and the stochastic exchange effects.[32] Some visible discrepancies between the theoretical and experimental spectra, observed for a ruthenium trihydride,[33] are probably due to a process of reversible H_2 loss occurring at elevated temperatures.

A careful study of the QEC and stochastic exchange effects in a broad temperature range, exploiting the EXSY technique[34] in the slow exchange limit, was reported for the niobocene trihydride $[C_5H_3(SiMe_3)_2]_2NbH_3$.[35] However, no examples of fits between the experimental and theoretical spectra were shown.

As is well known,[36] the trihydrides can form adducts with coinage metal cations. Such cations, acting as a Lewis acid, are coordinated to two hydride pairs from two trihydride moieties. Each pair includes the central and one of the sideward hydrides. In consequence, the symmetry of the hydride patterns is reduced to ABC (no couplings between the hydrides from the different trihydride moieties engaged in the adduct can be observed). In the adducts, the QEC effects can still occur and, at elevated temperatures, the stochastic exchange of the hydride protons becomes operative. An extensive study was reported involving temperature effects in the spectra of the adducts of a ruthenium trihydride with Cu, Ag, and Au.[37] Again, excellent agreement was obtained between the experimental and theoretical spectra calculated using the AB line shape equation adapted to the unsymmetrical ABC system. As was mentioned in the foregoing, theoretical confirmation of the validity of the AB theory for unsymmetrical systems is still lacking.

At the end, two cases where the exchange couplings are extremely large will be discussed in some detail. The coherent and stochastic exchange was observed for $(C_5Me_5)RuH_3PPy_3$ (Py = pyrolyl) **3**, for which the values of $|J|$ increase monotonically from 950 Hz at 140 K up to about 5300 Hz at 210 K.[38] Here, too, the AB theory affords a fair description of the observed line shapes of the hydride protons (see Fig. 5). For values of $|J|$ greatly exceeding the chemical shift difference $|\nu_A - \nu_B|$ the limiting A_2B spectral pattern is a symmetric 1:10:1 triplet with the splittings equal to $2|\nu_A - \nu_B|/3$.[40] This is the situation occurring in the spectra of **3**, but in this compound the limiting pattern is modified by *J*-couplings between the ^{31}P nucleus and the hydride protons A.

From numerical line shape simulations employing Eq. (6) it follows that in general, the central signal (signals) in the spectra having such a limiting structure is (are) relatively insensitive to the stochastic exchange. Indeed, in the spectra of **3** shown in Fig. 5 the occurrence of the rate processes described by k_{class} is manifested as a broadening and then coalescence of the sidebands, with only little impact on the line shape of the signals in

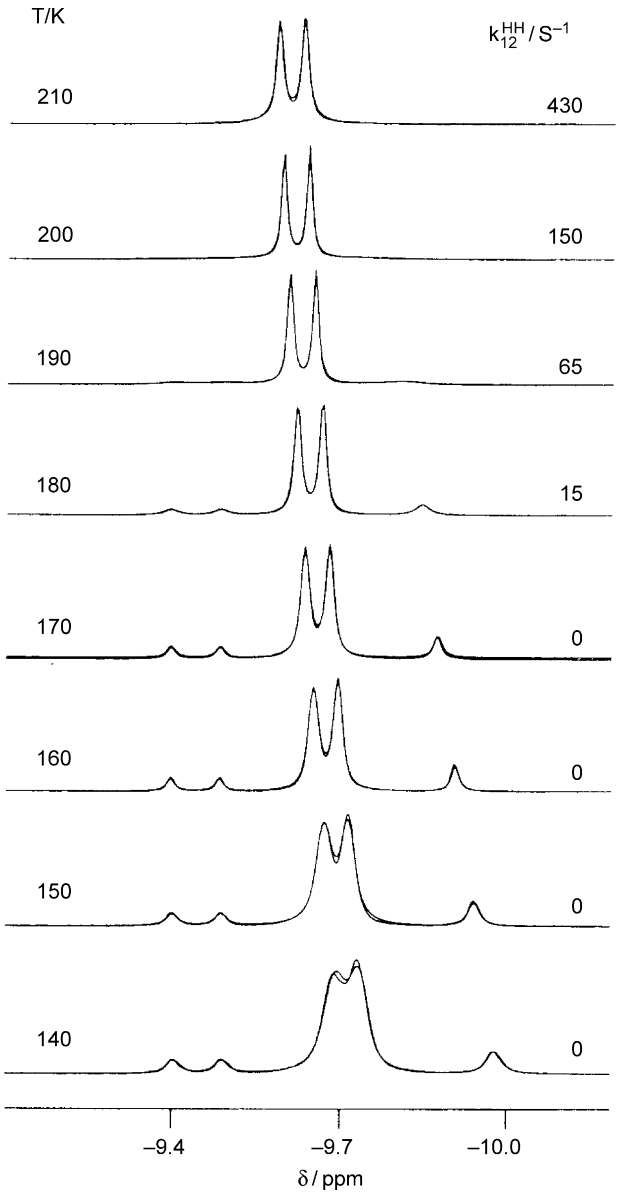

Fig. 5. Superimposed temperature dependent and calculated 500 MHz ^{1}H NMR hydride spectra of $(C_5Me_5)RuH_3PPy_3$ **3**. The *J*-coupling constants between ^{31}P and protons A and B are 31 and 0 Hz, respectively. (Reproduced with permission from Ref. 38. Copyright by Wiley-VCH Verlag GmbH, 1998).

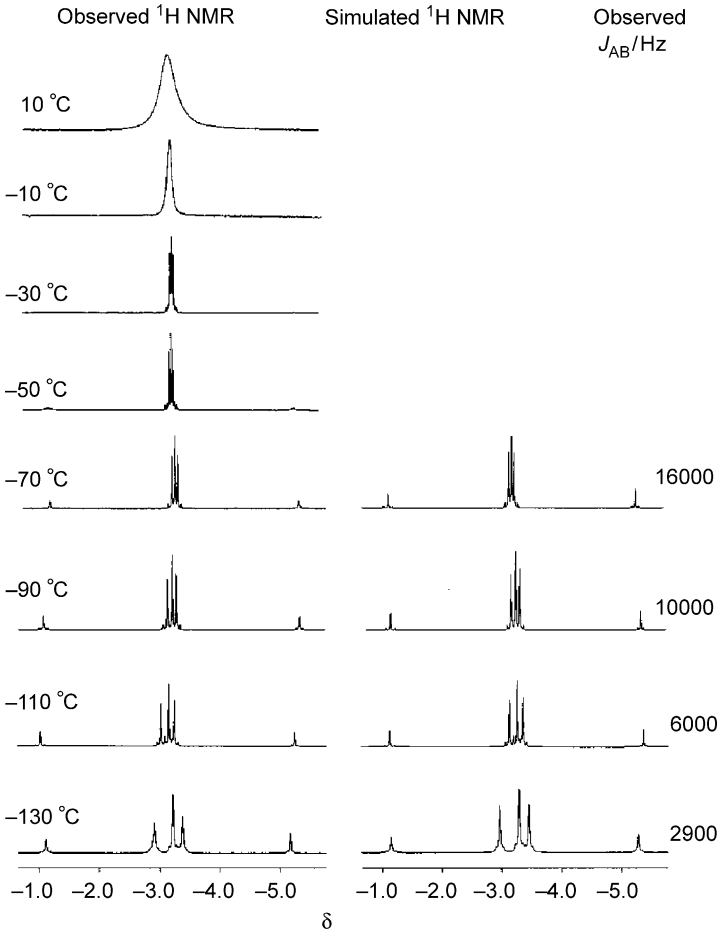

Fig. 6. Variable-temperature ^{1}H (500 MHz) spectra of $[W(\eta\text{-}C_5H_4)CMe_2(\eta\text{-}C_5H_4)H_3]^+PF_6^-$ **4** and the simulated spectra in the hydride region. (Reproduced with permission from Ref. 39. Copyright by The Royal Society of Chemistry, 1997).

the centre. In view of the foregoing, the strong broadenings of the central resonances in the spectra of a tungsten trihydride cation $[W(\eta\text{-}C_5H_4)CMe_2(\eta\text{-}C_5H_4)H_3]^+$, **4**[39] appears as a puzzling effect. The spectra of the hydride proton A_2B system in **4** are shown in Fig. 6. In the range -130 to -70°C, J_{AB} increases from about 3000 to 16,000 Hz. The latter value is probably the highest unambiguously determined exchange coupling reported so far for liquid phase. In the spectra of **4**, the splittings of the central signal are due to the fact that the values of the ratio $(\nu_A - \nu_B)^2/J_{AB}$ remain still finite; these residual splittings are proportional to that ratio.[40] In the spectrum at -30°C these splittings are about twice smaller than those in the spectrum at -70°C. One can, therefore, guess that the magnitude of J_{AB} increases further by about a factor of 2 on passing from -70 to -30°C. Accordingly, if there had been no stochastic exchange

above −30°C, the limiting 1:10:1 triplet with no resolved structure of the central signal would have been observed at these temperatures. Instead, one can see an unstructured, substantially broadened resonance, which undergoes further, strong broadening with increasing temperature. Such a behaviour cannot be explained in terms of temperature-accelerated stochastic exchange described by Eq. (6) unless one assumes that above −30°C there occurs a rapid collapse of the exchange coupling, from about 30,000 Hz at −30°C down to about 0 Hz at 10°C. The typical temperature behaviour of QEC in the metal hydrides is a rapid increase of its magnitude with temperature. The reverse trend was observed only for a series of osmium trihydrides L_2OsH_3X ($L = P^iPr_3$, X = Cl, Br, I), although in the latter compounds the variations of QEC with temperature are rather mild.[41] Thus, further studies are needed to understand the temperature effects observed in the spectra of **4**.

3.4. The hydrido dihydrogen complexes

For the first time, QEC was detected between the hydride and dihydrogen ligands in a series of hydrido dihydrogen complexes of ruthenium, $RuH(H_2)XP^iPr_3$, X = 2-phenylpyridine (**5**), benzoquinoline (**6**), and phenylpyrazole (**7**).[19,42] The spectra modified by the concomitant stochastic spin exchange between the hydrogen ligands were interpreted in terms of the AB theory. The nuclei concerned were treated as an A_2B system where A_2 denotes the dihydrogen moiety. In the low-temperature spectra of **5** reported in Ref. 19 it can be seen that the natural broadening (i.e., one resulting from processes other than the stochastic exchange) of the dihydrogen resonances greatly exceeds the natural broadening of the signal of the hydride ligand (see Fig. 7). A proper account of these differences may pose an extra difficulty in the line shape fits. For **5**–**7**,

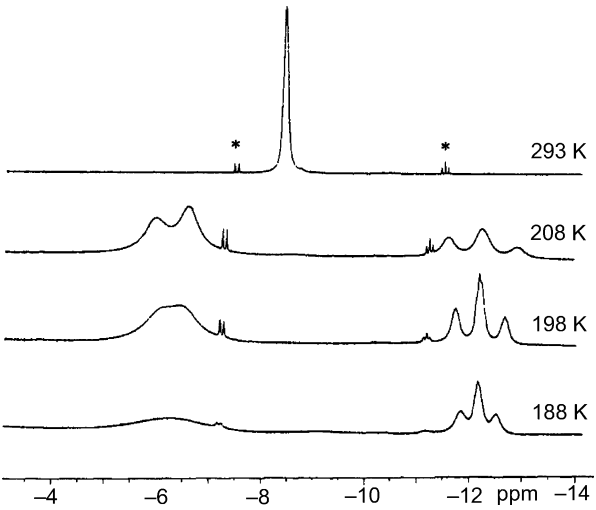

Fig. 7. The ^1H NMR spectra (500 MHz) of the hydrogen ligands in **5** at various temperatures. (Reproduced with permission from Ref. 19. Copyright by The American Chemical Society, 1998).

the values of J at 213 K are in the range 300–400 Hz. At room temperature, the resonances of the hydride ligands in **5**–**7** in phosphorus-decoupled ^{1}H spectra appear as broadened singlets.

The observations of QEC between the hydride and dihydrogen moieties have fundamental significance for the understanding of the microscopic mechanism of the effect. They point to the lack of substance to the claim, frequently formulated in the literature that the occurrence of a rapid dynamic equilibrium between an abundant *cis*-dihydride and residual dihydrogen forms is a necessary condition for the QEC to be observed. While it is quite probable that in the systems discussed above the three hydrogen ligands can undergo recombination in such a way that the enantiomeric hydrido dihydrogen structure is obtained, a postulate of a similar recombination yielding still another hydrido dihydrogen form, a metastable one, does not seem realistic. On the other hand, the mechanism where an averaging over the vibrational ladder is postulated does seem to be capable of explaining the QEC effect in the hydrido dihydrogen complexes.

4. THE DYNAMICS OF METHYL-LIKE QUANTUM ROTORS IN NMR SPECTRA

NMR investigations of quantum rotors have long tradition. In the early 1960s, in wide-line spectra of molecular solids containing methyl groups, measured at liquid helium temperatures, some specific features were noticed which could not be explained at that time.[43] In the same period, puzzling effects of a similar nature were observed in electron spin resonance (ESR) spectra of unpaired electrons in molecules containing methyl groups.[44] In the context of ESR spectroscopy, the fact that these offending effects can be explained in terms of the coherent tunnelling of the methyl group, assisted by the Pauli principle, was soon recognized by Freed.[45] In NMR, the analogous theory was presented by Apaydin and Clough in 1968.[13] The term 'quantum exchange coupling', although fully appropriate here, is virtually of no use in the literature on the quantum rotation. In the sequel, that practice will not be continued. Despite differences in the corresponding microscopic mechanisms, the nature of the effect in the metal hydrides and in the quantum rotors is essentially the same.

Unlike for the metal hydrides, for methyl-like quantum rotors the pairwise exchanges are unfeasible. On the other hand, cyclic permutations of the three like particles constituting the rotor are relevant. Thus, the feasible group of interest is C_3. Basic concepts used in the NMR theories of the methyl-type rotors are described in the caption to Fig. 8.

Until recently, the quantum nature of the problem was being taken into account only in NMR studies at cryogenic temperatures. At such temperatures, the coherent behaviour is prevalent. The formalism affording theoretical description of the observed spectra involves augmentation of the standard solid-state NMR Hamiltonian with the corresponding tunnelling term [*c.f.* Eq. (4)],

$$\frac{2\pi\Delta}{3}(\hat{Q}+\hat{Q}^{-1}), \tag{7}$$

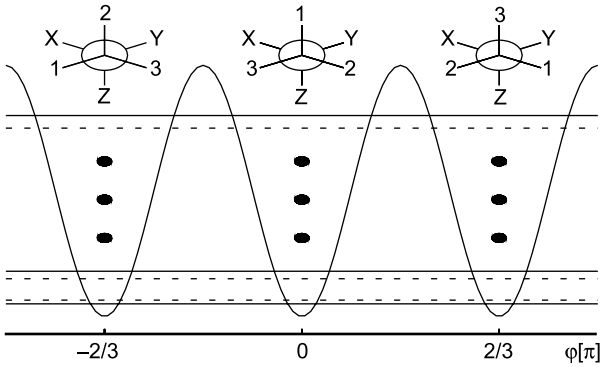

Fig. 8. The torsional potential and energy levels of a methyl-like rotor. The feasible group is isomorphic with C_3. The three minima of the potential correspond to the three equilibrium orientations of the rotor in its molecular/crystal surrounding. The torsional levels come in triplets whose individual components transform according to the irreps A, E_a, and E_b of C_3. The E sublevels come in perfectly degenerate Kramers pairs; those of A symmetry are shifted in energy from the Kramers sublevels by the tunnelling quanta $E_A - E_E$ the magnitudes of which rapidly grow with growing torsional energy while their signs alternate. The energy eigenfunctions are delocalized over all three minima of the potential. Since pair permutations do not enter the feasible group, the spin–space correlations are the same for fermions (e.g., CH_3 groups) and bosons (e.g., CD_3 groups): $A \leftrightarrow A$, $E_a \leftrightarrow E_b$, and $E_b \leftrightarrow E_a$.

where $\hat{Q}$ represents cyclic permutation of the three like particles constituting the rotor and Δ measures the tunnelling frequency. Unlike in the metal hydrides, in the methyl rotors studied at liquid helium temperatures the tunnelling frequency Δ decreases with temperature; its maximum value in the low-temperature limit equals the tunnelling splitting of the ground torsional level, $E_A^0 - E_E^0$. In 1999, an extensive review of the sometimes very sophisticated experimental techniques to study the temperature dependence of Δ for methyl-like rotors was reported.[5] In the period covered in that review, little attention was devoted to the incoherent processes that evolve with increasing temperature. For a long time, the research was confined to multicrystalline (powder) samples the spectral patterns of which are ill structured. In such a context, there was practically no way to discriminate between various phenomenological theories formulated *ad hoc* to describe the stochastic dynamics of the quantum rotors (see, for example, Ref. 46). In the 1990s, essential improvements in the experimental techniques to study the quantum rotation in oriented single crystals were implemented by Haeberlen.[47,48] In single-crystal ^2H spectra of selectively deuterated species, the relative resolution (measured as a ratio of the typical line width to the typical signal separation) is not much worse than in liquid-phase ^1H spectra (see Fig. 9). Effects of the stochastic dynamics on the spectral patterns could, therefore be monitored with the accuracy similar as in liquid phase proton spectra. These developments have created demand for an adequate line shape theory. Actually, the first consistent quantum mechanical treatment, addressing an idealized instance of the CD_3 rotor in the limit of infinitely large tunnelling frequency Δ (as compared to the quadrupolar splittings) was

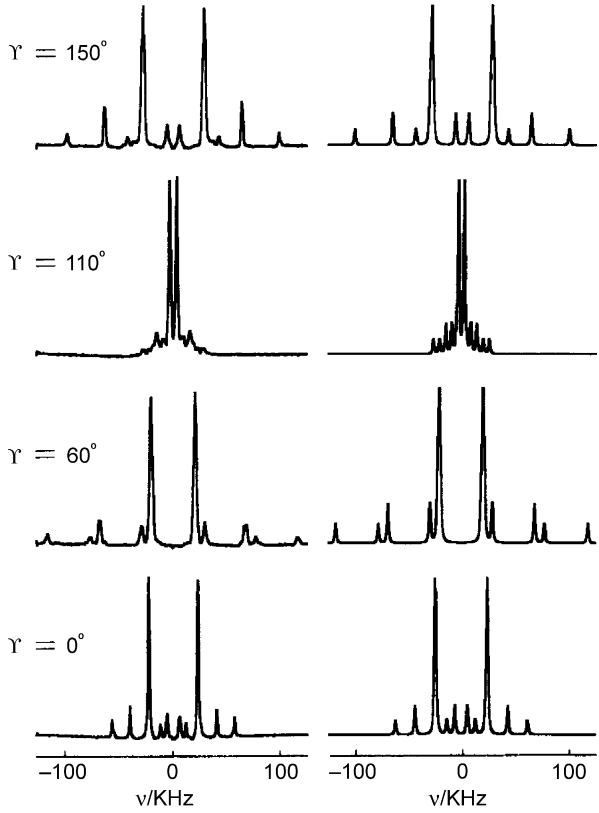

Fig. 9. Experimental (left panel) and theoretical (right panel) ^{2}H spectra of the methyl deuterons in an oriented single crystal of acetylsalicylic acid-d_3 selectively deuterated in the methyl group. The spectra were measured at 12.5 K for four orientations (measured by angle ϒ) such that the magnetic field remains parallel to the monoclinic plane of the crystal. At 12.5 K, the tunnelling frequency Δ is about 2.70 MHz and is much greater than the quadrupolar coupling constants q_D (about 170 kHz) at the individual methyl deuteron sites. The spectral patterns shown in the figure are the limiting patterns; upon further increase of the magnitude of Δ they would remain virtually unchanged. Each such pattern includes five doublets centred at the same frequency; the components of the most intense doublet and those of the remaining four, low intensity doublets are called β and α lines, respectively. (Reproduced with permission from Ref. 48. Copyright by Verlag der Zeitschrift für Naturforschung, 1995).

reported from Haeberlen's laboratory by Heuer in 1992.[49] Because of its intrinsic limitations, that approach has not attracted a wider attention. Until the late 1990s, the phenomenological AB theory adapted once by Clough[50] to the general case of quantum rotation was also ignored in the pertinent literature. Nevertheless, in accord with the assumptions of the latter theory and, in fact, with the spirit of the Correspondence Principle of quantum mechanics, the impact of the stochastic dynamics, growing with temperature, was (and still is) generally interpreted as a transition to the so-called classical limit. In that limit, the Pauli principle is tacitly abandoned and the dynamics

are pictured as a process of random, thermally activated jumps of the rotor between its three equilibrium orientations.

The above interpretation has recently been challenged; the recent results for a CD_3 rotor at cryogenic temperatures (to be described in the sequel) show for the first time that consequences of the symmetrization postulate involve the stochastic dynamics as well.[51]

4.1. Developments in theory: the damped quantum rotor model

The damped quantum rotor (DQR) description of NMR line shapes of methyl-like moieties undergoing the coherent and stochastic dynamics was reported in 1999[8] as a generalization of the already quoted theory involving the pairwise exchange in the metal hydrides.[14] In the generalized approach, the reduced density matrix (RDM) theory[52] is applied to the rotor embedded in a thermal bath, which is modelled by a large set of harmonic oscillators representing vibrations of the rigid lattice (phonons). The assumption that the rotor-bath (spin-independent) couplings leading to dissipation (relaxation) in the rotor subsystem are linear in the bath coordinates affords a straightforward modelling of the relevant temperature dependences but is not critical for the validity of the final results. The same involves the assumption about the particular form of the thermal bath. Like in the case of pairwise exchange, analysis of the RDM equation for the perturbed rotor reveals that only selected coherences between the quantum states of the rotor are sufficiently long lived to be relevant to the NMR experiments. Because in a three-well potential the torsional sublevels come in triplets (see Fig. 8), in place of a single such coherence occurring in the two-well system there appear now two different long-lived coherences. One of them, dubbed the overall Kramers coherence, involves the Kramers pairs (E_a, E_b) at the sequential torsional levels. It is damped with rate constant k_K and, because the pairs (E_a, E_b) are perfectly degenerate, it has zero oscillation frequency. The other one, the overall tunnelling coherence, comprises the corresponding pairs (A, E_b) (or (A, E_a)); it evolves as damped oscillation with frequency Δ and damping-rate constant k_t, where Δ is a thermal average of the individual tunnelling splittings (see caption to Fig. 8). The prototypes of Δ, k_t, and k_K appear in the description of inelastic neutron scattering patterns of weakly hindered CH_3 rotors. Specifically, Δ and k_t correspond to the position and width of the inelastic peak[53,54] while k_K corresponds to the width of the quasielastic peak.[49,55,56]

In an external magnetic field, the dynamics of these long-lived coherences are superposed with those generated by the spin-dependent interactions. In the context of NMR line shape experiments, the overall evolution of the relevant spin–space coherences can be described in the sole spin manifold; the final DQR equation for the effective spin density matrix of a methyl-like rotor reads:[8]

$$\begin{aligned} \mathrm{d}\hat{\rho}/\mathrm{d}t = &- \mathrm{i}\left[\hat{H}_{\mathrm{NMR}} + \frac{2\pi}{3}\Delta(\hat{Q} + \hat{Q}^{-1}), \hat{\rho}\right] - \frac{k_K}{3}[2\hat{\rho} - \hat{Q}\hat{\rho}\hat{Q}^{-1} - \hat{Q}^{-1}\hat{\rho}\hat{Q}] \\ &- \frac{k_t - k_K}{2}[\hat{\rho} - \hat{U}\hat{\rho}\hat{U}], \end{aligned} \tag{8}$$

where $\hat{H}_{\mathrm{NMR}}$ is the standard NMR Hamiltonian (in angular frequency units) appropriate to the experimental conditions (solid- or liquid-phase NMR) and $\hat{U}$ is a unitary, self-inverse operator defined according to

$$\hat{U} = \frac{1}{3}[2(\hat{Q} + \hat{Q}^{-1}) - \hat{1}]. \tag{9}$$

Obviously, for spin-1/2 nuclei, the QEC term in Eq. (8) can be expressed in terms of J-couplings.

When k_t and k_K happen to be equal, Eq. (8) becomes formally identical with the AB equation. However, the stochastic dynamics of the methyl rotor can then be regarded as 'classical' in an operational sense only, because the two underlying quantum rate processes never merge into a single process. When $k_t \neq k_K$, a superficial look at Eq. (8) might suggest that the dynamics concerned are a combination of the classical jump process characterized by rate constant $k_K/3$ and a quantum rate process occurring with rate constant $(k_t - k_K)/2$. However, in view of the fact that the sign of the latter quantity can be negative,[51] such an interpretation must be rejected. By and large, the DQR approach leading to Eq. (8) seems to open new perspectives in our understanding of molecular rate processes involving exchange of like nuclei. While for the two-fold rotor described in Eq. (5) it merely gives a re-interpretation of the semiclassical AB theory, in the case of a three-fold rotor a novel picture is obtained. In a recent work, the stochastic terms in Eq. (8) are reformulated in such a way that the similarity to the AB equation is no longer apparent:[57]

$$\begin{aligned} \mathrm{d}\hat{\rho}/\mathrm{d}t = &- \mathrm{i}\left[\hat{H}_{\mathrm{NMR}} + \frac{2\pi}{3}\Delta(\hat{Q} + \hat{Q}^{-1}), \hat{\rho}\right] - \frac{k_K}{4}[\hat{\rho} + \hat{U}\hat{\rho}\hat{U} - \hat{V}\hat{\rho}\hat{V} - \hat{V}^*\hat{\rho}\hat{V}^*] \\ &- \frac{k_t}{2}[\hat{\rho} - \hat{U}\hat{\rho}\hat{U}], \end{aligned} \tag{10}$$

where $\hat{V}$ is a unitary self-inverse operator defined according to

$$\hat{V} = \frac{1}{3}[2(\varepsilon\hat{Q} + \varepsilon^*\hat{Q}^{-1}) - \hat{1}], \tag{11}$$

with $\varepsilon = \exp(2\pi i/3)$. The operators $\hat{1}$, $\hat{U}$, $\hat{V}$, and $\hat{V}^*$ form four-element group isomorphic with C_{2v}.[57] Because the QEC term $\hat{Q} + \hat{Q}^{-1}$ can alternatively be expressed as $\frac{3}{2}\hat{U} - 2\hat{1}$, the three-fold symmetry of the rotor is no longer referred to in the description of its dynamical behaviour and, accordingly, there are no intrusive associations with a mechanical motion. A heuristic picture behind that equation is that the stochastic dynamics accelerated by temperature effect a progressive symmetrization of the spin density matrix. Curiously, the symmetry species engaged in the symmetrization process belong to the C_{2v} rather than C_3 symmetry.[57] Of course, the significance of such an interpretation should not be overestimated since it involves an effective equation of motion. In the complete DQR equation including also the spatial degrees of freedom (which are redundant in the context of NMR experiments), the true

physical processes referred to are the dissipative dynamics of the overall Kramers and tunnelling coherences.[8]

Preliminary applications of the DQR equation to practical problems are reviewed in the two subsections that follow.

4.2. The DQR model at cryogenic temperatures

As yet, there has been only one example of application of the DQR equation to low-temperature NMR spectra of a methyl rotor.[51] To this purpose, a novel methodology was elaborated. It was applied to the ^{2}H spectra of a single crystal of acetylsalicylic acid-d_3 selectively deuterated in the methyl group, **8**. The novel methodology is based on a multiparameter, least-squares fits of theoretical line shapes to sets of spectra measured at the same temperature setting. Each such set includes the standard spectrum and a series of solid echo spectra[58] measured for suitable echo times. In the studies of the coherent tunnelling of CD_3 rotors, advantages of the solid echo technique were recognized earlier.[59] Another new aspect of the methodology is that effects due to a finite duration of the stimulating radiofrequency pulses are taken into account in the line shape calculations. Such an exact modelling of the NMR experiment allows even subtle misfits to the experimental data to be identified clearly.

In an earlier study on **8**,[60] on basis of a visual comparison of the experimental and theoretical spectra it was concluded that the AB approach (to which there was virtually no alternative at that time) is basically correct. A series of studies initiated by the latter work is addressed in Section 4.4. The novel methodology affords a revision of the above conclusion. Moreover, the (deceptive) success of the AB approach to the interpretation of the spectra of **8** could later on be rationalized from the perspective of the DQR theory.[51] The relevant argument is briefly summarized below.

In **8**, the magnitude of Δ, although decreasing with temperature, does remain substantially greater than the quadrupolar coupling constants concerned, q_D, even at temperatures where the stochastic dynamics become relevant. Thus, in the temperature range of interest, the structure of the underlying spectral pattern closely resembles its limiting form which would be attained for $|q_D/\Delta| \ll 1$[47,48] (such limiting patterns are trivial only for two-particle systems). For a general orientation of the crystal, the limiting pattern consists of five doublets centred at the same frequency; the lines of the most intense doublet and the remaining lines are called β and α lines, respectively[48] (*c.f.* the spectra shown in Fig. 9). Along with decrease of $|\Delta|$ with increasing temperature, a fine structure of the individual lines is being gradually revealed; the β lines are being affected first. From considerations of Eq. (8) it follows that as long as this emerging fine structure remains hidden under the 'natural' line broadening, the impact of the stochastic dynamics will be observable only for the α lines. These line shape effects will be described by the first dissipative term in the r.h.s. of that equation, formally identical with the AB term; the second dissipative term will remain irrelevant. Only with the onset of the splittings of the β lines, the latter term may gain significance. However, the most prominent line shape features will still be described by the AB term. This is why in the application[60] of

the AB theory to the spectra of **8** (deceptively) fair fits could be obtained. However, as was noticed recently,[51] the temperature dependence of k_{class} determined in those fits bears some characteristic flaws whose origin can be attributed to the inadequacy of the AB approach to the spectra of **8**. Because the problem of such seemingly fair fits is essential for NMR studies on the quantum rotation, it will also be discussed further in Subsection 4.4. The main advantage of the solid echo technique (which was first employed in Ref. 51 to the studies on the stochastic dynamics) stems from the fact that the emerging fine structure of the β lines is much better exposed in the echo spectra than in the standard spectra. On the other hand, strongly broadened α resonances can in general be better represented in the standard spectra (the accuracy is, however, limited by the length of the 'death time' of the receiver). Thus, a combined use of the standard and echo spectra does offer a possibility to detect the effects described by both the first and the second dissipative term in Eq. (8).

In Ref. 51, this task was attained. For one orientation of the crystal of **8** for which the signals of interest and those of the impurities (originating mainly from incompletely deuterated methyl groups) do not overlap a clear discrimination between the DQR and AB models could be made. Examples of the DQR fits are shown in Fig. 10. For two temperatures, a comparison of the AB and DQR fits for selected echo spectra is shown in Figs. 11 and 12.

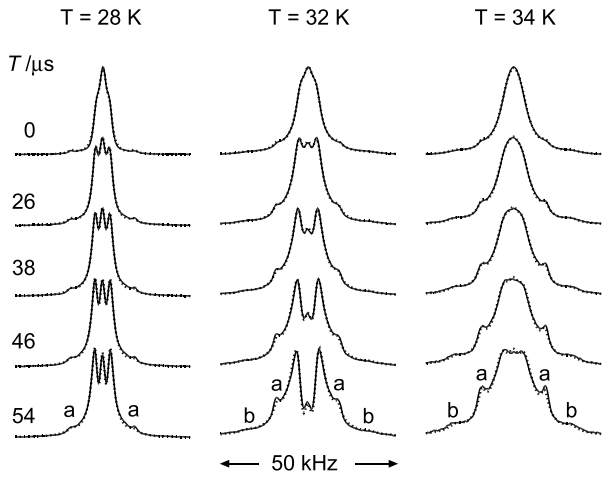

Fig. 10. Selected experimental standard ($\tau = 0$) and solid echo ($\tau > 0$) spectra of **8** (solid lines) with superimposed theoretical 'best fit' spectra (dotted lines) obtained using the DQR model. The rotation axis of the crystal relative to the external magnetic field is the same as for the spectra shown in Fig. 9; the actual orientation corresponds to $Y = 30.0°$. For this special orientation, there occurs a degeneracy of the β doublet and the two pairs of the α doublets merge into two doublets. At the indicated temperatures, the α signals on the wings (not shown) are strongly broadened. The impurity signals denoted with a and b were included in the fits, each with an assumed structure of a static quadrupolar doublet. (Reproduced with permission from Ref. 51. Copyright, 2001, with permission from Elsevier).

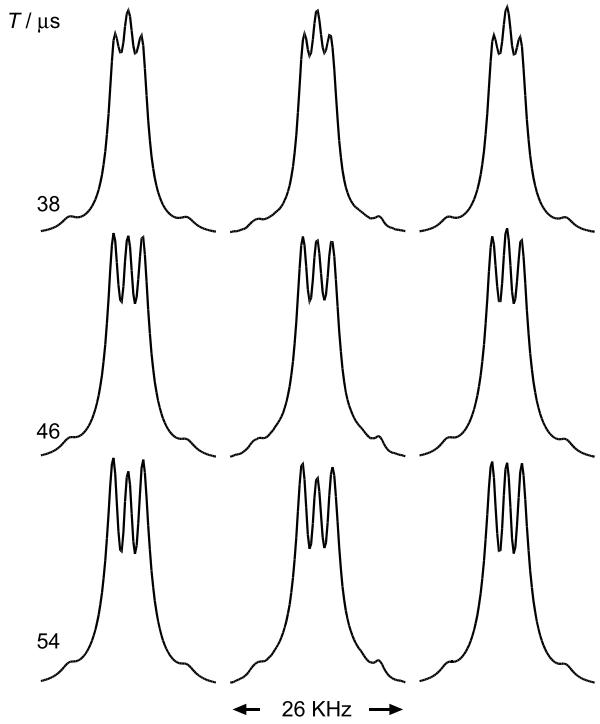

Fig. 11. A comparison of selected experimental solid echo spectra of **8** at 28 K (middle column) with the 'best fit' theoretical spectra obtained using the DQR (left column) and AB model (right column). In the AB fits, the amplitudes of the peak in the centre are systematically overestimated. At this temperature, the value of $k_t/k_K \equiv c = 1.95$ was obtained in the DQR fit. (Reproduced from Ref. 51. Copyright, 2001, with permission from Elsevier).

For **8**, the values of Δ, k_K, and k_t could be determined over the range 28–34 K. The corresponding Arrhenius plots will be commented upon further in Section 4.4. The observed temperature trend of the ratio $c = k_t/k_K$ shows a monotonical decrease from the value of 1.95 at 28 K to 0.70 at 34 K. Therefore, there is no good reason to expect that with further temperature increase the trend will be changed such that eventually, the value of 1 be approached and, accordingly, the regime of validity of the AB theory be entered. In other words, the common belief that at elevated temperatures the dynamics of quantum rotors enter the classical regime was for the first time challenged: even under conditions where the rotor experiences intense perturbations by its condensed environment (generally considered as a generator of classicality[61]), the spin–space correlated states involved preserve some of their quantum properties. It must also be emphasized that even for such methyl-like rotors for which the values of c happen to be close to 1, the relevant stochastic dynamics can hardly be regarded as classical; the damping processes described by k_K and k_t will still be prevented by the symmetrization postulate from merging into a single, classical process.

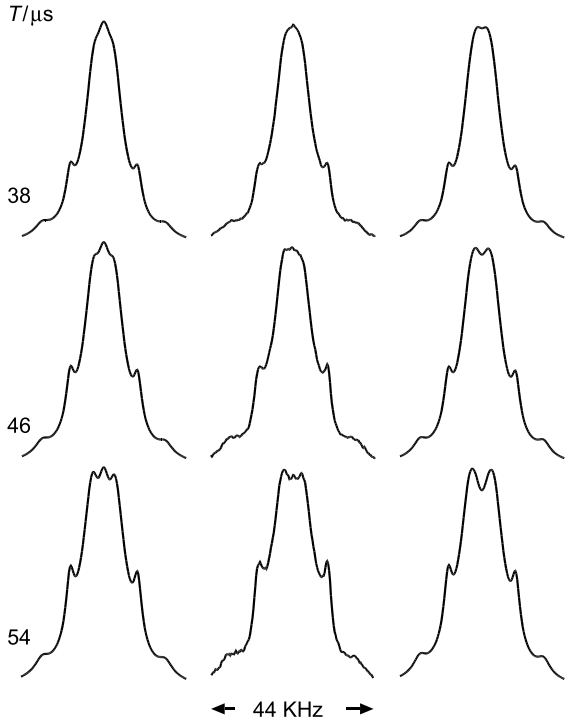

Fig. 12. A comparison of selected experimental solid echo spectra of **8** at 34 K (middle column) with the 'best fit' theoretical spectra obtained using the DQR (left column) and AB model (right column). In the AB fits, the amplitudes of the peak in the center are systematically underestimated. At this temperature, the value of $k_t/k_K \equiv c = 0.70$ was obtained in the DQR fit. (Reproduced from Ref. 51. Copyright, 2001, with permission from Elsevier).

4.3. The DQR model at ambient temperatures

At ambient temperatures, the stochastic motions of methyl groups are generally fast on the NMR time scale. The only exceptions reported so far involve the methyl group in 9-methyltriptycene derivatives (see Fig. 13) in which the torsional energy barriers concerned can be very high;[62] they can exceed 40 kJ/mol.[63] In the latter compounds, the stochastic dynamics of the methyl rotor can be frozen out on the time-scale of NMR experiments in liquids. The liquid-phase NMR investigations on a number of 9-methyltriptycene derivatives, performed in the period up to the early 1990s, were reviewed by Oki.[64] The experimental spectra of the methyl protons were interpreted in terms of the AB theory; there were no mentions to the possible inadequacies of the AB model in the description of the observed line shapes.

Recently, some of the methyltriptycene derivatives were re-investigated with use of the methodology of Ref. 51 (Section 4.2) to line shape analysis. In these liquid-phase studies, instead of the solid echo spectra, the Carr–Purcell (CP)[65] echo spectra were

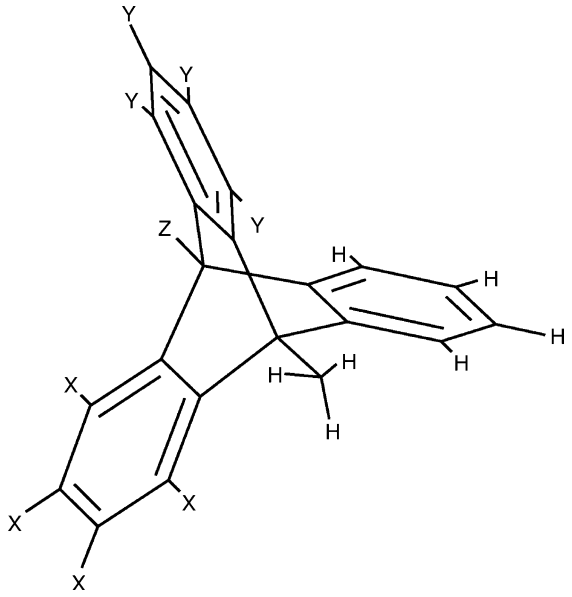

Fig. 13. The structure of 9-methyltriptycene derivatives with high torsional barriers for the methyl group re-orientation. The symbol X denotes halogen atoms, Y stands for either a halogen or hydrogen substituent, and Z denotes either H or CH_3.

measured. Moreover, the fits were performed separately to the standard spectra and to sets (of at least two) echo spectra. For two of the compounds, 1,2,3,4-tetrabromo-9-methyltriptycene **9**, and 1,2,3,4-tetrachloro-9-methyltriptycene **10**, visible deviations from the experimental spectra of the 'best fit' theoretical spectra, calculated using the AB equation, were observed.[66,67] In the fits to the DQR model, where only one more parameter is added to the set of the parameters optimized in the AB model, there were practically no observable misfits.

In **9** and **10**, the methyl protons form an A_2B system. The standard and CP echo spectra of the methyl protons in **10** in the slow exchange limit are displayed in Fig. 14. The AB and DQR fits to the standard spectra of the methyl group in **10** are shown in Fig. 15 for the resonances of proton B. It can be seen in Fig. 15 that the quality of the AB fits is apparently improving along with increasing signal broadening. The improvement is accompanied by a progressive, steep decrease of the values of J_{AB} obtained from these fits. The values of J_{AB} obtained in the DQR fits show an analogous but much milder trend. In the fits to the CP echo spectra, the perfection of the DQR model is more strongly contrasted with the evident inadequacy of the AB model (see Fig. 16). The estimates of the relevant parameters, obtained from the fits to the standard and echo spectra, were consistent. In particular, virtually the same temperature dependences of J_{AB} were obtained from both series of fits. The steep decrease of J_{AB} with temperature, observed in the AB fits, was interpreted to be an artefact produced by the minimization routine employed for which an underestimation of the latter parameter

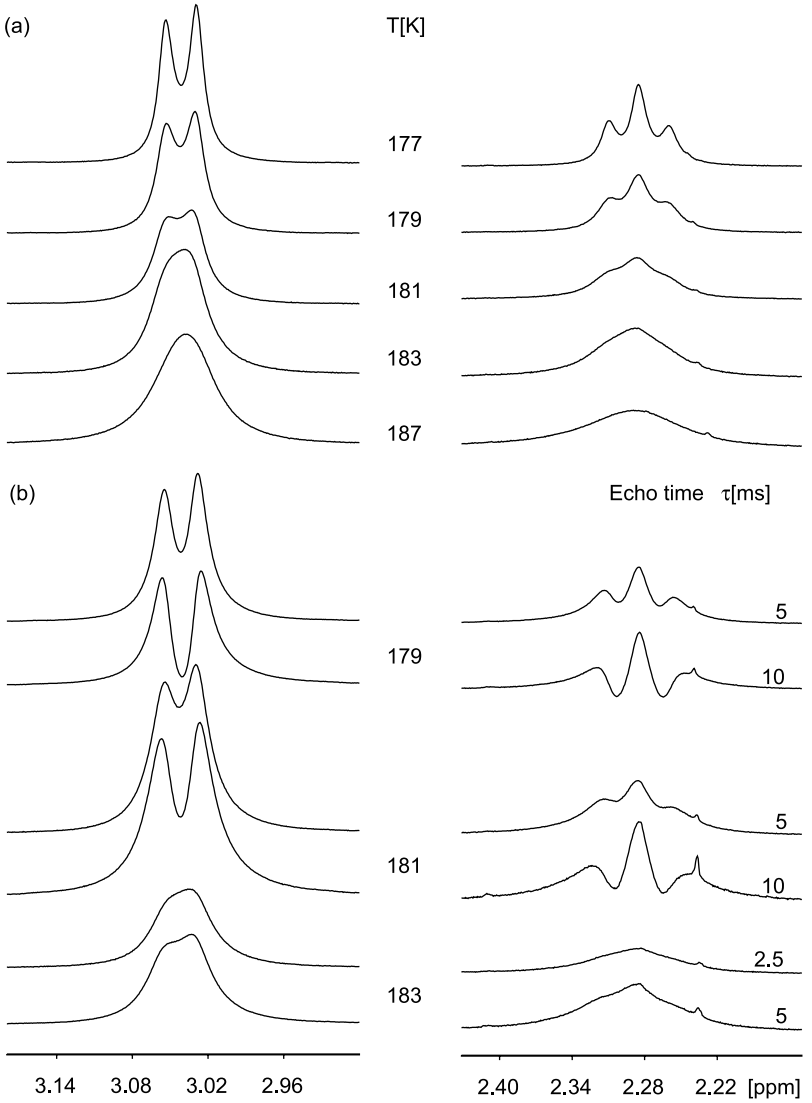

Fig. 14. (a) Temperature-dependent, standard NMR spectra (500 MHz) of the methyl protons in 1,2,3,4-tetrachloro-9-methyltriptycene **10**. (b) Examples of Carr–Purcell echo spectra measured for two echo times τ at the indicated temperatures. The narrow signals at 2.24 and 2.40 ppm come from traces of impurities. (Reproduced with permission from Ref. 67. Copyright by the American Institute of Physics 2003).

is presumably the easiest way to make up for the inadequacy of the AB model. On the other hand, the corresponding (but milder) trend observed for the estimates of J_{AB} obtained in the DQR fits was attributed to a physical effect, a temperature-dependent contribution of QEC to the apparent *J*-coupling. Similar effect is also reported for **9**.[66,67]

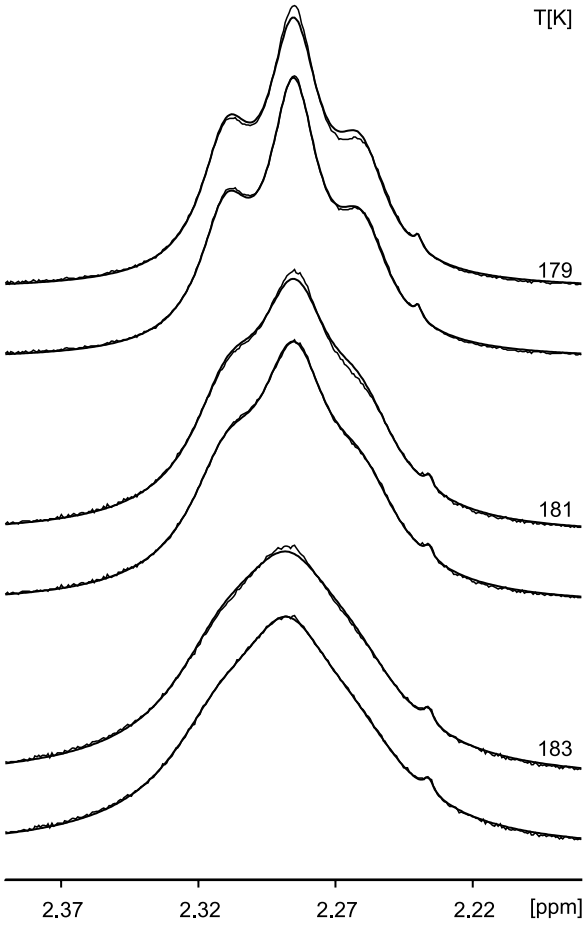

Fig. 15. The standard experimental spectra of 1,2,3,4-tetrachloro-9-methyltriptycene **10**, for the methyl proton B, superposed with the corresponding 'best-fit' theoretical AB (top) and DQR (bottom) spectra. The impurity signal at 2.24 ppm was included in the fits, with assumed Lorentzian lineshape. (Reproduced with permission from Ref. 67. Copyright by the American Institute of Physics 2003).

The magnitude of the effect is very small, of the order of a hertz. Nevertheless, this would be the first observation of QEC for methyl groups in liquid-phase NMR.

For **9** and **10**, the values of J_{AB}, k_K, and $c = k_t/k_K$ could be determined over relatively narrow temperature ranges of about 10 K. The results obtained from fits to the standard spectra are consistent with those extracted from the CP echo spectra. For both of the compounds, the values of c appear to be independent of temperature, although this need not be so over a wider temperature span. In the ranges actually investigated, the average values of c for **9** and **10** are 1.18 and 1.19, respectively.[66,67] For 1,2,3,4-tetrachloro-9,10-dimethyltriptycene **11** in which the two methyl groups are equivalent, the average value of

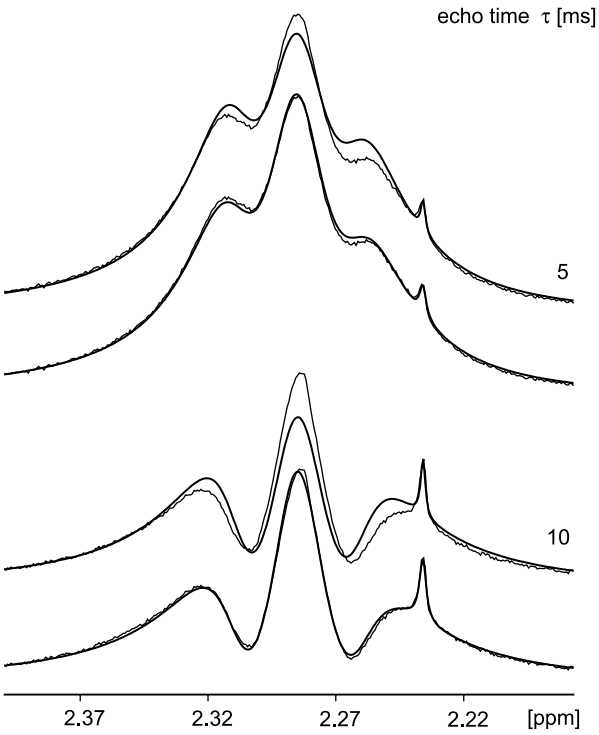

Fig. 16. Two Carr–Purcell echo spectra of 1,2,3,4-tetrachloro-9-methyltriptycene **10** at 181 K, for the methyl proton B, superposed with the corresponding 'best-fit' theoretical AB (top) and DQR (bottom) spectra. The impurity signal at 2.24 ppm was included in the fits, with assumed Lorentzian lineshape. (Reproduced with permission from Ref. 67. Copyright by the American Institute of Physics 2003).

c is 1.10.[68] For the latter compound, such a significant departure from the regime of validity of the AB theory can be observed at temperature as high as 200 K. In **11**, there is no observable contribution of QEC to the J-coupling. The same is true for 1,2,3,4,5,6,7,8-octachloro-9-methyltriptycene **12** for which the values of c fall close to 1.[67]

The observations for **9**–**11** described in the foregoing confirm that the validity of the DQR approach[8] is not restricted to the cryogenic range. For the first time, wave-like properties of such a massive object as the methyl group were detected in its environment-induced dynamics at ambient temperatures. For the objects subject to the Pauli principle, the common practice to use the term 'stochastic dynamics' as a synonym for 'classical dynamics' need not be valid even when the relevant behaviour under ambient conditions is referred to.

4.4. The Alexander–Binsch model at cryogenic temperatures

The observations reviewed in Section 4.2 illustrate typical obstacles to successful applications of the DQR model to the solid-state spectra of quantum rotors. One of the

most serious difficulties is the occurrence of impurity signals under the signals of interest. When the experimental data of the required quality are not available, use of the AB model can be a reasonable alternative. However, in some instances a seemingly fair reproduction of the experimental spectra can be associated with severe bias on the optimized values of k_{class}. A survey of experimental studies utilizing the AB approach will therefore be preceded by a discussion of its intrinsic limitations. For sake of brevity, the discussion will be confined to deuterated rotors although the relevant conclusions are generally valid.

According to Ref. 51, the status of the AB approach in the low-temperature studies can be described as follows. Beyond the obvious instance where (i) $c = k_t/k_K$ approaches 1, use of the AB model is fully legitimate in the case where (ii) $\Delta \rightarrow \infty$ (it is the latter instance that is addressed in the already mentioned line shape theory by Heuer[49]).

If condition (ii) is rigorously fulfilled for a CD_3 rotor in the whole temperature range, only the α resonances (defined in the caption to Fig. 9) will be affected by the underlying stochastic dynamics; the β lines will remain unchanged. With increasing temperature, the α lines will broaden and then coalesce to one broad doublet whose components, coinciding with the β lines, will eventually undergo motional narrowing such that in the high temperature limit only one doublet or, for some specific orientations of the rotor, one singlet (*c.f.* Section 4.2) will be obtained. These lineshape effects can be exactly reproduced using the AB line shape equation with $k_{\text{class}} = k_K/3$.

For CD_3 rotors, condition (ii) usually undergoes a progressive 'softening' with temperature increase for $|\Delta|$ decreases with temperature. This is manifested in a gradual emergence of fine structure of the β lines (with the splittings proportional to q_D^2/Δ[48]). The emerging β multiplets gradually gain sensitivity to the stochastic dynamics, including those described by the second dissipative term in Eq. (8). However, an inference from numerical simulations is that the line shapes of such β multiplets can still be reproduced by the AB equation, but now with rate constant k_{class} put equal to $k_t/3$.[51] It is the latter feature that renders the spectra concerned prone to a misinterpretation when the AB approach is applied. For the reason to be exposed below, even when the actual ratio $c = k_t/k_K$ is significantly different from 1, use of the AB model can afford a satisfactory reproduction of the experimental spectra in a broad temperature range. Fortunately, instances of c departing strongly from 1 can in principle be identified by inspection of the $k_{\text{class}}(T)$ curve determined from such seemingly good fits: A characteristic 'tooth' will generally occur on such a curve near the critical temperature at which the α lines attain maximum broadening (before entering the phase of motional narrowing). The mechanism by which such tooth is produced is as follows.

Below the critical temperature, the fits are aimed at a perfect reproduction of the most prominent features of the spectra, the broadenings of the α resonances; to achieve this goal, one can easily sacrifice some misfits left for the β lines, the more so as the latter are much less sensitive to the stochastic effect than the α lines. Accordingly, the values of k_{class} extracted from the spectra will follow the temperature dependence of k_K. At the critical temperature and in some range above it, the fits are aimed at a possibly perfect reproduction of the β multiplets since the (very broad and unstructured) α resonances become then practically invisible. According to what was mentioned in the foregoing, the β pattern can still be reproduced by the AB equation when k_{class} is put equal to $k_t/3$.

Hence, at the critical temperature and just above it, attempts at reproducing the shape of the β pattern will generally deliver values of k_{class} close to $k_t/3$. The tooth on the $k_{class}(T)$ curve determined in this way will occur when k_K and k_t happen to be substantially different at the critical temperature.

Such a singularity is clearly visible on the Arrhenius curve of k_{class} determined for a crystal of acetylsalicylic acid-d_3 **8**.[60] In Fig. 17 this curve is compared with those for the values of k_K and k_t determined recently for the same system[51] (*cf.* Subsection 4.2).

In the remaining part of this subsection, examples of legitimate use of the AB model are presented. An example where condition (i) does appear to be valid is an inclusion compound, hydroquinone/acetonitrile-d_3.[69] In the latter system, the torsional barriers for all three magnetically inequivalent CD_3 groups in the unit cell are relatively high. The limiting, low-temperature values of Δ for two of the groups were found to be about 29 kHz; for the third group, the corresponding value is 59 kHz. In the single-crystal ^2H spectra of the compound, the stochastic dynamics become relevant in the range 40–60 K; above 60 K, a motionally averaged spectrum is observed. The values of k_{class}, determined

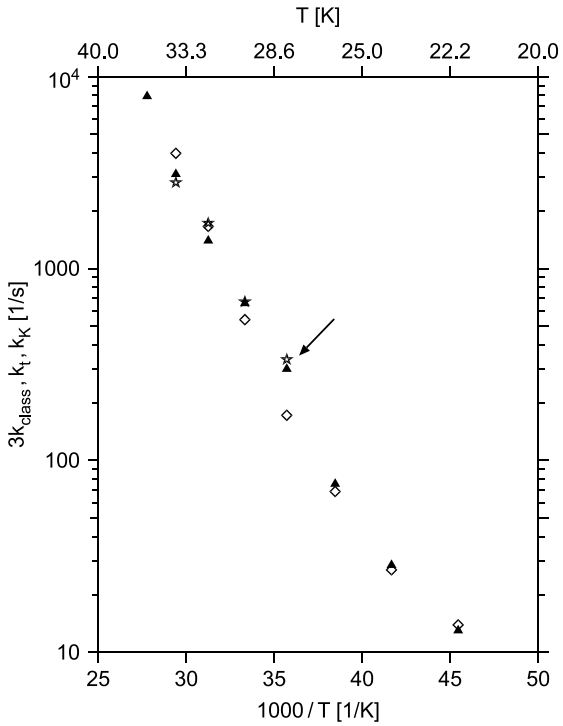

Fig. 17. The Arrhenius plots for the rate constants k_K (diamonds), $k_t/3$ (stars), and $3k_{class}$ (full triangles) for **8**, reported in Ref. 51. The arrow marks the singularity on the k_{class} (T) curve the occurrence of which is an indirect indication of the inadequacy of the AB model to the system investigated. On the other hand, the $k_k(T)$ and $k_t(T)$ curves are smooth. A non-Arrhenius behaviour of $k_k(T)$ is remarkable.

by a visual comparison of the theoretical and experimental spectra, show a smooth, linear alignment on the Arrhenius plot. This is an indirect corroboration of the validity of the AB model to that particular system.

The applicability of condition (ii) above is not restricted to ^{2}H spectra. In particular, it should also be valid to ^{13}C spectra of protonated methyl groups in the instances where Δ is much greater than the relevant dipolar coupling constants, $|d(^{1}H-^{1}H)| \approx 24$ kHz and $|d(^{13}C-^{1}H)| \approx 23$ kHz. An example where such a situation does take place is the hydroquinone/acetonitrile clathrate mentioned above in which instead of acetonitrile-d_3 its perprotio isotopomer occurs as the host. Condition (ii) ought to be valid for this system since the tunnelling frequencies of protonated methyl groups are typically at least two orders of magnitude greater than the corresponding frequencies of their deuterated counterparts. The ^{13}C spectra of the latter material, ^{13}C-enriched in the methyl group, were interpreted in terms of the AB model by Detken *et al.*.[70] The temperature-dependent values of k_{class} extracted from these spectra obey the Arrhenius law rather closely; they represent the temperature behaviour of k_K.

In the latter paper, a throughout ^{13}C NMR study on a single crystal of acetylsalicylic acid selectively ^{13}C-labelled in the methyl group is also reported. Despite the fact that in the temperature range investigated condition (ii) is perfectly fulfilled for the above material (at that range, the values of Δ approach 300 MHz), the observed ^{13}C spectra cannot be interpreted in terms of the AB model unless one admits that below 25 K the values of k_{class} *increase* with further decrease of temperature.[70] It must be stressed that use of the DQR instead of the AB model would offer no help to rationalize that strange behaviour: in the limit of $|d/\Delta| \ll 1$, where $d = \max[|d(^{1}H-^{1}H)|, |d(^{13}C-^{1}H)|]$, the calculated spectra are insensitive to the second dissipative term in Eq. (8). The spectra exhibiting these intriguing effects are shown in Fig. 18. In ^{13}C relaxation studies on the same material no anomalies in the relevant dynamic behaviour were found (however, the temerature region below 25 K was not explored).[71,72]

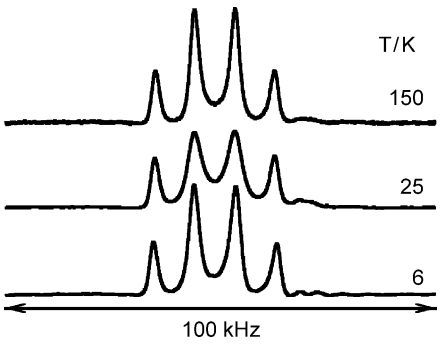

Fig. 18. Experimental ^{13}C NMR spectra of a single crystal of acetylsalicylic acid selectively ^{13}C-labelled in the methyl group. At 25 K, the stochastic dynamics are slowed down such that features characteristic of the ^{13}C pattern in the limit of $|d/\Delta| \ll 1$ start to emerge. At 6 K, the spectrum is again identical to that at 150 K, as if there were a renewed acceleration of the stochastic dynamics below 25 K. (Reproduced with permission from Ref. 70. Copyright by Taylor & Francis Ltd; Internet address: http://www.tandf.co.uk/journals).

5. THE DYNAMICS OF AMMONIUM IONS IN NMR SPECTRA

The isotopically homogeneous NX_4^+ ions, where X stands for H or D, embedded in a solid lattice, are quantum rotors whose dynamic behaviour can in principle be much more complicated than that of the methyl-like rotors. However, pairwise exchanges as well as cyclic permutation of all of the four X nuclei are generally unfeasible for NX_4 rotors. The facile permutations normally involve re-orientations about the four three-fold axes coincident with the individual NX bonds. It is also conceivable that re-orientations about the three two-fold axes bisecting the individual XNX angles can be relevant.[73] In summary, the feasible group of practical interest is isomorphic with T rather than T_d and, accordingly, the relevant potential energy surface comprises 12 equivalent minima.

The general form of the effective spin Hamiltonian, shown in Eq. (4), is valid also for NX_4 rotors. Therefore, in an unsymmetrical environment, the corresponding QEC term can be formulated as follows:

$$\sum_{k=1,2,3,4} 2\pi\Pi_{(k)}(\hat{Q}_{(k)} + \hat{Q}_{(k)}^{-1}) + \sum_{l=1,2,3} 2\pi\Pi'_{(l)}\hat{R}_{(l)}, \tag{12}$$

where k and l enumerate the three- and two-fold axes, respectively, $\hat{Q}_{(k)}$ represents cyclic permutation of the three nuclei out of axis k, $\hat{R}_{(l)}$ represents the product of two pair permutations effected by rotation around axis l; $\Pi_{(k)}$ and $\Pi'_{(l)}$ are the corresponding tunnelling frequencies which are combinations of the tunnelling splittings of the torsional states restricted by the 12-well potential.[74–76]

A consistently quantum mechanical theory describing the coherent and stochastic dynamics of tetrahedral rotors has not been reported yet. Nevertheless, in the extreme situations where the facile re-orientations involve only one axis, the DQR theory will be rigorously valid also for such rotors. Specifically, if the unique axis is a three-fold axis, the stochastic term will have the same form as in Eq. (8) [or the equivalent form in Eq. (10)]. In the case of a two-fold axis, the AB term such as that in Eq. (5) will be obtained, but with the pair-permutation operator $\hat{P}$ replaced by the operator $\hat{R}$ defined above. One can thus reasonably expect that even in the cases where there are more than one facile re-orientation axes, applicability of the phenomenological AB approach will suffer similar restrictions as those specified in Subsection 4.4 for methyl-like rotors.

As far as experimental investigations of the ammonium ion dynamics are concerned, the present authors are aware of only two reports where both the coherent and stochastic effects are taken into account in the interpretation of the observed spectra.[76,77] Both the reports involve ^2H spectra of a single crystal of variously deuterated ammonium persulfate. For this material it was found that at temperatures below 40 K, the relevant dynamics are dominated by re-orientations about one of the possible re-orientation axes of the ND_4^+ ions. Since it is a three-fold axis, the picture seen in the spectra is essentially similar to that for a deuterated methyl group. The experimental ^2H spectra concerned could be fairly reproduced in terms of the AB model (see Fig. 19).

However, when the values of k_{class} obtained in this way (fits based on visual similarity criteria) are displayed in an Arrhenius plot, a characteristic tooth can be seen at 28 K (see Fig. 20). In view of the discussion of Subsection 4.4, its occurrence may reflect a basic

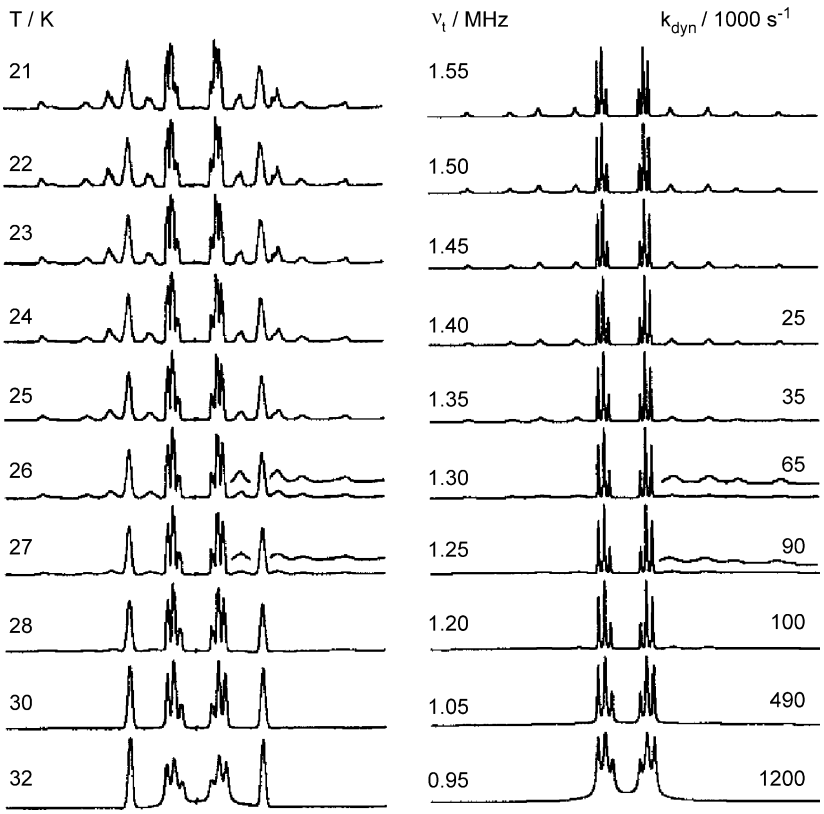

Fig. 19. Experimental variable-temperature ^{2}H spectra of a single crystal of ammonium persulfate-d_4. The outermost doublet in the spectrum at 32 K which appears practically unchanged in the spectra at the remaining temperatures comes from the 'static' deuteron situated at the re-orientation axis. The intense multiplet in the centre is the resolved β doublet. The remaining, weak lines that disappear above 28 K are the α lines. Right column: Theoretical spectra simulated using the AB line shape equation [i.e., Eq. (8) in which the second dissipative term is dropped]. The presence of the 'static' deuteron was disregarded in the calculations. The quantities ν_t and k_{dyn} are equivalents of Δ and k_{class}, respectively. (Reproduced with permission from Ref. 77. Copyright by the American Institute of Physics, 2002).

inadequacy of the AB model to the system investigated, the more so as the tooth appears at the temperature where the α lines attain such a large broadening that they practically disappear from the spectrum.

This is, however, a provisional interpretation. Apart from the 'primary' re-orientation mentioned above, the authors quoted managed to identify another facile re-orientation route in the system, which involves one of the remaining three three-fold axes. The secondary coherent tunnelling, whose maximum low-temperature frequency was estimated at 4.5 kHz, produces additional tiny splittings that affect the β multiplet. With increasing temperature, the frequency of the secondary tunnelling decreases to zero and, in the temperature range of interest in the present discussion (above 23 K, see

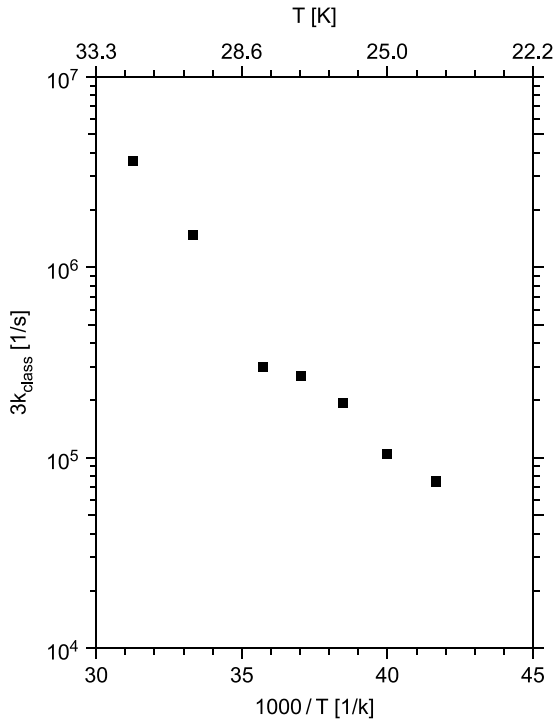

Fig. 20. The Arrhenius plot of the values of $3k_{\text{class}}$ obtained from the AB fits to the spectra of ammonium persulfate-d_4 shown in Fig. 19.

Fig. 19), these additional splittings gradually disappear. In the line shape simulations, this secondary process was neglected, which could impose some extra bias on the estimated values of k_{class} and contribute to the above artefact. Moreover, the dipolar ND interactions producing resolved splittings of some of the α lines were also neglected. Nevertheless, because observable departures from the jump model are now well documented also for ambient-temperature dynamics of quantum rotors, it would be unreasonable to exclude *a priori* the possibility of such a behaviour of the system discussed presently, investigated at cryogenic temperatures.

The character of the singularity on the $k_{\text{class}}(T)$ curve in Fig. 20 is different than for acetylsalicylic acid-d_3 **8** (see Fig. 17). For **8**, it happens that k_t is about twice as large as k_K at the critical temperature (28 K); the ratio $c = k_t/k_K$ drops below 1 only above 32 K. In the crystalline ammonium persulfate, at the corresponding critical temperature (again 28 K) one would see c having already dropped below 1. If the temperature trends of k_t and k_K were similar as in the case of **8**, ammonium persulfate would be the second ever observed example of a system whose stochastic dynamics do not approach any 'classical limit' with increasing temperature. (For the methyltriptycene derivatives discussed in Section 4.3, the question regarding their limiting behaviour is open because the relevant temperature trends could not be determined over sufficiently wide temperature ranges).

In the period reviewed, there has been a number of reports focussed on the coherent exchange of deuterated ammonium ions in both powder and single-crystal materials. Thus, the QEC effects involved were used as sensitive probes of the domain structure in diammonium hexachlorotellurate[78] and of a mobility of the domain walls in diammonium tetrachloroplatinate[73] and diammonium hexachloroplumbate.[79]

6. MISCELLANEOUS RESULTS

One of the most spectacular consequences of the Pauli principle for nuclear systems is the existence of ortho- and parahydrogen as separate chemical species. In 1987, Bowers and Weitekamp[80] reported on the theoretical background to and practical methods of use of the internal nuclear polarization existing in parahydrogen to monitor hydrogenation reactions in NMR spectroscopy. In the experimental variant called ALTADENA, the reaction is performed outside the magnet prior to the insertion of the sample tube into the NMR probe; in the PASADENA technique, the hydrogenation is carried out *in situ*.[81] In both the variants, an enormous, transient polarization enhancement (exceeding the thermal equilibrium polarization of the Zeeman levels by orders of magnitude) can be achieved for the products obtained from hydrogenation with parahydrogen. A prerequisite for such an effect to occur is that the two protons of parahydrogen are transferred pairwise to the reactant and, moreover, the symmetry of the proton pair is broken in the product molecule. From a chemical perspective, the pre-1999 NMR studies on systems with the parahydrogen-induced polarization (PHIP) were reviewed by Duckett and Sleight.[82] Earlier, a review involving also theoretical aspects of the effect was reported by Natterer and Bargon.[83] In recent years, there appear 5–10 papers a year involving applications of PHIP to the studies on hydrogenation reaction in liquid samples. Account of applications of the PHIP effect to individual chemical problems is out of scope of the present review. On the other hand, a recent theory of polarization transfer from the hyperpolarized proton subsystem to the heteronuclei present in the molecule, illustrated with the relevant experimental data, should be mentioned in the present context.[84]

In solid-state NMR, a somewhat similar technique of polarization transfer to hetronuclei was elaborated for systems containing weakly hindered methyl rotors.[85] If the tunnelling splitting of the ground torsional state of such a rotor is several times greater than the proton Zeeman energy in the applied magnetic field, at temperatures at which only the ground level is populated the thermal polarization of the tunnelling-split sublevels will correspondingly exceed that of the Zeeman levels. If such a sample is equilibrated for some time at low temperature (about 5 K) and then its temperature is abruptly increased, the polarization of the A and E sublevels, acquired at low temperature, can be transferred to the spin degrees of freedom that are directly observable in NMR experiments; the transfer will be effected via the dipolar spin–spin interactions. This is known as the Haupt effect;[86,87] like that PHIP, the Haupt effect is ultimately caused by the spin statistics of non-differentiable proton particles. Again, by making use of an appropriate pulse technique, the hyperpolarized proton subsystem can be contacted with that of a heteronucleus and, eventually, an enhancement of the resonance signal of

the latter will be achieved. Such an enhancement was demonstrated for the natural-abundance ^{13}C nuclei in γ -picoline and the ^{15}N nuclei in the guest molecules of acetonitrile-^{15}N isolated in the γ-picoline matrix.[85]

There has been a growing recognition of the significance of the symmetrization postulate for nuclear spin relaxation of quantum rotors in the solid state. However, even the conventional theories of the latter phenomenon, based on the classical jump model, are specialized to such an extent that for a proper presentation of the problem a separate review should be provided. Therefore, only a brief reference will be made here to a recent paper where a consistently quantum description of the relaxation behaviour of weakly hindered CD_3 rotors is reported.[88] The relevance of the latter work to the content of the present review stems from the fact that the relaxation processes are described therein in terms of essentially the same quantum coherences as those entering the DQR theory of NMR line shapes addressed in Section 4.1. This points to a relative generality of the DQR theory.

REFERENCES

1. K. W. Zilm, D. M. Heinekey, D. M. Millar, N. G. Payne and P. Demou, *J. Am. Chem. Soc.*, 1989, **111**, 3089.
2. D. H. Jones, J. A. Labinger and D. P. Weitekamp, *J. Am. Chem. Soc.*, 1989, **111**, 3087.
3. (a) W. Heisenberg, *Z. Phys.*, 1926, **38**, 411; (b) W. Heisenberg, *Z. Phys.*, 1926, **39**, 499; (c) W. Heisenberg, *Z. Phys.*, 1927, **41**, 239.
4. S. Szymański, *Annu. Rep. NMR Spectrosc.*, 1998, **25**, 1.
5. A. J. Horsewill, *Prog. NMR Spectrosc.*, 1999, **35**, 359.
6. S. Alexander, *J. Chem. Phys.*, 1962, **37**, 974.
7. (a) G. Binsch, *J. Am. Chem. Soc.*, 1969, **91**, 1304; (b) D. A. Kleier and G. Binsch, *J. Magn. Reson.*, 1970, **3**, 146.
8. S. Szymanski, *J. Chem. Phys.*, 1999, **111**, 288.
9. C. Herring, *Magnetism*, Vol. IIB, G. T. Rado and H. Suhl, eds., Academic Press, New York, 1966, 2.
10. S. J. Inati and K. W. Zilm, *Phys. Rev. Lett.*, 1992, **68**, 3273.
11. S. Szymański, *J. Mol. Struct.*, 1994, **321**, 115.
12. G. S. Ezra, *Lect. Notes Chem.*, Vol. 28, G. Berthier, M. J. S. Dewar, H. Fischer, K. Fukui, G. G. Hall, H. Hartmann, H. H. Jaffé, J. Jortner, W. Kutzelnigg, K. Ruedenberg and E. Scrocco, eds., Springer, Berlin, 1982.
13. F. Apaydin and S. Clough, *J. Phys. C*, 1968, **2** (**1**), 932.
14. (a) S. Szymański, *J. Chem. Phys.*, 1996, **104**, 8216; (b) S. Szymański, *J. Chem. Phys.*, 1997, **106**, 3430.
15. S. Sabo-Etienne and B. Chaudret, *Chem. Rev.*, 1998, **98**, 2077.
16. F. Maseras, A. Lledós, E. Clot and O. Eisenstein, *Chem. Rev.*, 2000, **100**, 601.
17. D. M. Heinekey, J. M. Millar, T. F. Koetzle, N. G. Payne and K. W. Zilm, *J. Am. Chem. Soc.*, 1990, **112**, 909.
18. J. K. Law, H. Mellows and D. M. Heinekey, *J. Am. Chem. Soc.*, 2002, **124**, 1024.
19. Y. Guari, S. Sabo-Etienne and B. Chaudret, *J. Am. Chem. Soc.*, 1998, **120**, 4228.
20. B. Chaudret, H.-H. Limbach and C. Moise, *CRC Acad. Sci.*, 1992, **2** (**315**), 533.
21. S. Sabo-Etienne, B. Chaudret, H. Abou el Makarim, J. C. Barthelat, J. P. Daudey, S. Ulrich, H.-H. Limbach and C. Moïse, *J. Am. Chem. Soc.*, 1995, **117**, 11602.
22. S. Sabo-Etienne, V. Rodriguez, B. Donnadieu, B. Chaudret, H. Abou el Makarim, J.-C. Barthelat, S. Ulrich, H.-H. Limbach and C. Moïse, *New J. Chem.*, 2001, **25**, 55.
23. C. Scheurer, R. Wiedenbruch, R. Meyer, R. R. Ernst and D. M. Heinekey, *J. Chem. Phys.*, 1997, **106**, 1.
24. H. H. Limbach, S. Ulrich, S. Gründemann, G. Buntkowsky, S. Sabo-Etienne, B. Chaudret, G. J. Kubas and J. Eckert, *J. Am. Chem. Soc.*, 1998, **120**, 7929.

25. H. H. Limbach, G. Scherer, M. Maurer and B. Chanudret, *Angew. Chem. Int. Edit.*, 1992, **31**, 1369.
26. C. S. Johnson, *J. Chem. Phys.*, 1964, **41**, 3277.
27. G. Buntkowsky, H.-H. Limbach, F. Wehrmann, I. Sack, H. H. Vieth and R. H. Morris, *J. Phys. Chem. A*, 1997, **101**, 4679.
28. F. Wehrmann, T. P. Fong, R. H. Morris, H.-H. Limbach and G. Buntkowsky, *Phys. Chem. Chem. Phys.*, 1999, **1**, 4033.
29. A. Antiñolo, F. CarrilloHermosilla, M. Fajardo, S. GarciaYuste, A. Otero, S. Camanyes, F. Maseras, M. Moreno, A. Lledos and J. M. Lluch, *J. Am. Chem. Soc.*, 1997, **119**, 6107.
30. W. B. Yao, J. W. Faller and R. H. Crabtree, *Inorg. Chim. Acta*, 1997, **259**, 71.
31. S. Szymanski, to be published.
32. A. Castillo, M. A. Esteruelas, E. Oñate and N. Ruiz, *J. Am. Chem. Soc.*, 1997, **119**, 9691.
33. D. V. Yandulov, D. Huang, J. C. Huffman and K. G. Caulton, *Inorg. Chem.*, 2000, **39**, 1919.
34. J. Jeener, B. H. Meier, P. Bachmann and R. R. Ernst, *J. Chem. Phys.*, 1979, **71**, 4546.
35. U. Drexler, R. Wiedenbruch, C. Scheurer, R. Meyer, R. R. Ernst, S. Chaloupka and L. M. Venanzi, *Mol. Phys.*, 1998, **93**, 471.
36. A. Antiñolo, F. Carillo, J. Fernández-Baeza, A. Otero and B. Chaudret, *Inorg. Chem.*, 1992, **31**, 5156.
37. B. Manzano, F. Jalon, S. Sabo-Etienne, B. Chaudret, S. Ulrich and H.-H. Limbach, *J. Chem. Soc., Dalton Trans.*, 1997, 3153.
38. S. Gründemann, H.-H. Limbach, V. Rodriguez, B. Donnadieu, S. Sabo-Etienne and B. Chaudret, *Ber. Bunsenges. Phys. Chem.*, 1998, **102**, 344.
39. A. Chernega, J. Cook, M. L. H. Green, L. Labella, S. J. Simpson, J. Souter and A. H. H. Stephens, *J. Chem. Soc., Dalton Trans.*, 1997, 3225.
40. P. L. Corio, *Structure of High-Resolution NMR Spectra*, Academic Press, New York, 1966.
41. R. Kuhlman, E. Clot, C. Leforestier, W. E. Streib, O. Eisenstein and K. G. Caulton, *J. Am. Chem. Soc.*, 1997, **119**, 10153.
42. J. Matthes, S. Gründemann, A. Toner, Y. Guari, B. Donnadieu, J. Spandl, S. Sabo-Etienne, E. Clot, H.-H. Limbach and B. Chaudret, *Organometallics*, 2004, **23**, 1424.
43. E. R. Andrew, R. G. Eades, Z. M. Elsaffar and J. P. Llewellyn, *Bull. Ampere*, 1960, **9**, 379.
44. I. Miyagawa and K. Itoh, *J. Chem. Phys.*, 1962, **36**, 2157.
45. J. H. Freed, *J. Chem. Phys.*, 1965, **43**, 1710.
46. U. Werner and W. Müller-Warmuth, *Z. Phys B*, 1993, **91**, 65.
47. T. Bernhard and U. Haeberlen, *Chem. Phys. Lett.*, 1991, **186**, 307.
48. A. Detken, P. Focke, H. Zimmermann, U. Haeberlen, Z. Olejniczak and Z. T. Lalowicz, *Z. Naturforsch.*, 1995, **50A**, 95.
49. A. Heuer, *Z. Phys. B Condens. Matter*, 1992, **88**, 39.
50. S. Clough, *NMR Basic Principles and Progress*, Vol. 13, P. Diehl, E. Fluck and R. Kosfeld, eds., Springer, Berlin, 1976, 113.
51. S. Szymanski, Z. Olejniczak, A. Detken and U. Haeberlen, *J. Magn. Reson.*, 2001, **148**, 277.
52. K. Blum, *Density Matrix. Theory and Applications*, Plenum Press, New York, 1981, Chapter 7.
53. (a) A. Hewson, *J. Phys. C*, 1982, **15**, 3841; (b) A. Hewson, *J. Phys. C*, 1982, **15**, 3855.
54. A. Würger, *Z Phys. B: Condens. Matter*, 1989, **76**, 65.
55. A. Würger, *J. Phys. B: Condens. Matter*, 1989, **1**, 6901.
56. A. Würger and A. Heidemann, *Z. Phys. B: Condens. Matter*, 1990, **80**, 113.
57. P. Bernatowicz and S. Szymański, *J. Magn. Reson.*, 2003, **164**, 60.
58. I. Solomon, *Phys. Rev.*, 1958, **110**, 61.
59. Z. Olejniczak, A. Detken, B. Manz and U. Haeberlen, *J. Magn. Reson. A*, 1996, **118**, 55.
60. S. Szymański, Z. Olejniczak and U. Haeberlen, *Physica B*, 1996, **226**, 161.
61. D. Giulini, E. Joos, C. Kiefer, J. Kupsch, I. O. Stamatescu and H. D. Zeh, *Decoherence and the Appearance of a Classical World in Quantum Mechanics*, Springer, Berlin, 1996.
62. J. E. Anderson and D. I. Rawson, *J. Chem. Soc., Chem. Commun.*, 1973, 830.
63. M. Nakamura, M. Oki, H. Nakanishi and O. Yamamoto, *Bull. Soc. Chem. Jpn*, 1974, **47**, 2415.
64. M. Oki, *Reactiviy and Structure Concepts in Organic Chemistry*, Vol. 30, K. Hafner, J. M. Lehn, C. W. Rees, P. von Rague Schleyer, B. M. Trost and R. Zahradnik, eds., Springer, Berlin, 1993, 84.

65. H. Y. Carr and E. M. Purcell, *Phys. Rev.*, 1954, **94**, 630.
66. P. Beranatowicz and S. Szymanski, *Phys. Rev. Lett.*, 2002, **89**, art. no. 023004.
67. I. Czerski, P. Bernatowicz, J. Jazwinski and S. Szymański, *J. Chem. Phys.*, 2003, **118**, 7157.
68. P. Bernatowicz, I. Czerski, J. Jazwinski and S. Szymanski, *J. Magn. Reson.*, 2004, **169**, 284.
69. A. Detken, P. Schiebel, M. R. Johnson, H. Zimmermann and U. Haeberlen, *Chem. Phys.*, 1998, **238**, 301.
70. A. Detken, H. Zimmermann and U. Haeberlen, *Mol. Phys.*, 1999, **96**, 927.
71. M. Kankaanpaa, M. Punkkinen and E. Ylinen, *Mol. Phys.*, 2002, **100**, 2877.
72. M. Kankaanpaa, E. E. Ylinen and M. Punkkinen, *Solid State NMR*, 2003, **23**, 224.
73. Z. T. Lalowicz, M. Punkkinen, Z. Olejniczak, A. Birczyński and U. Haeberlen, *Solid State NMR*, 2002, **22**, 373.
74. Z. T. Lalowicz, C. A. McDowell and P. Raghunathan, *J. Chem. Phys.*, 1979, **70**, 4819.
75. Z. T. Lalowicz, U. Werner and W. Müller-Warmuth, *Z. Naturforsch. A*, 1988, **43**, 219.
76. Z. Olejniczak, Z. T. Lalowicz, T. Schmidt, H. Zimmermann, U. Haeberlen and H. Schmitt, *J. Chem. Phys.*, 2002, **116**, 10343.
77. T. Schmidt, H. Schmitt, U. Haeberlen, Z. Olejniczak and Z. T. Lalowicz, *J. Chem. Phys.*, 2002, **117**, 9818.
78. A. Birczynski, Z. T. Lalowicz, Z. Olejniczak, G. Stoch and B. Petelenz, *Chem. Phys. Lett.*, 2001, **339**, 229.
79. P. Filipek, Z. T. Lalowicz, Z. Olejniczak and A. Birczyński, *Chem. Phys. Lett.*, 2003, **367**, 55.
80. C. R. Bowers and D. P. Weitekamp, *J. Am. Chem. Soc.*, 1987, **109**, 5543.
81. C. R. Bowers, D. H. Jones, N. D. Kurur, J. A. Labinger, M. G. Pravica and D. P. Weitekamp, *Adv. Magn. Opt. Reson.*, 1990, **14**, 269.
82. S. B. Duckett and J. C. Sleight, *Progr. NMR Spectrosc.*, 1999, **34**, 71.
83. J. Natterer and J. Bargon, *Progr. NMR Spectrosc.*, 1997, **31**, 293.
84. S. Aime, R. Gobetto, F. Reineri and D. Canet, *J. Chem. Phys.*, 2003, **119**, 8890.
85. M. Tomaselli, C. Degen and B. H. Meier, *J. Chem. Phys.*, 2003, **118**, 8559.
86. J. Haupt, *Phys. Lett.*, 1972, **38A**, 389.
87. J. Haupt, *Z. Naturfosch*, 1973, **28A**, 98.
88. G. Diezemann, *Appl. Magn. Reson.*, 1999, **17**, 345.

Chemometric Analysis of NMR Spectroscopy Data: A Review

TODD M. ALAM[1] AND M. KATHLEEN ALAM[2]

[1]*Department of Organic Materials, Sandia National Laboratories, Albuquerque, NM 87008-0888 USA*
[2]*Department of Chemical and Biological Sensing, Imaging and Analysis, Sandia National Laboratories, Albuquerque, NM 87008-0886, USA*

The application of chemometric or multivariate analysis techniques to nuclear magnetic resonance (NMR) spectroscopic data is reviewed. Descriptions of the different processing and data manipulation procedures being utilized to produce reproducible input data sets for chemometric analysis are discussed. A brief review of

ANNUAL REPORTS ON NMR SPECTROSCOPY
VOLUME 54 ISSN 0066 4103
DOI 10.1016/S0066-4103(04)54002-4

some of the standard supervised and unsupervised chemometric classification methods as applied to NMR data is presented. The application of spectral resolution algorithms in the decomposition of NMR data to obtain pure component spectra and concentrations is also described. Specific examples of the use of chemometrics in NMR for a wide range of different fields are presented. The limitations, advantages and future directions of chemometric analysis in NMR are also discussed.

1. INTRODUCTION

Nuclear magnetic resonance (NMR) spectroscopy continues to be one of the more powerful spectroscopic tools for the investigation of the chemistry and physical properties in complex mixtures. The use of NMR is becoming universal for a wide range of fields including biochemical, agricultural, medical, materials, chemical, industrial, environmental, and pharmaceutical. One of the benefits of NMR spectroscopy is the ability to probe complex systems without necessarily requiring a separation of individual components prior to analysis. With the continued development of NMR spectroscopy as an analysis tool, the size and complexity of NMR data sets make them more difficult to analyze simply through operator interaction. The introduction of NMR into the process and clinical environment, along with automatic sample changers, robotics, flow-probes, cryogenically cooled-probes, parallel-detection coils, flow injection analysis (FIA) and direct injection (DI) techniques, has led to the collection of enormous amounts of NMR spectral data that needs to be quickly analyzed in an automated manner. For example, using flow-NMR, FIA–NMR and DI–NMR it is possible to routinely obtain hundreds of high-resolution ^{1}H NMR samples a day, per NMR instrument.[1–3] Combine this number of spectra with a high degree of spectral complexity, for example, a high resolution ^{1}H NMR spectrum (at 900 MHz) of urine has about 9000 discernable resonances,[4] and the effectiveness of manual interpretation quickly diminishes. In addition, conjugated NMR techniques incorporating liquid chromatography (LC), high pressure liquid chromatography (HPLC), mass spectroscopy (MS), gel-permeation chromatography (GPC), super critical fluid chromatography (SCF), and solid phase extraction (SPE) via LC–NMR, LC–MS–NMR, HPLC–NMR, HPLC–NMR–MS, GPC–NMR, SCF–NMR and SPE–NMR, have also become more common, and only adds to the increased dimensionality and complexity of the data set size.[5] Couple high throughput and increasing spectral complexity, together with conjugated plus automated NMR capabilities, and it is easy to become overwhelmed with data. Chemometric analysis often allows the researcher to reduce a large amount of data to a more readily interpretable view, focusing on the important variances within the data.

Chemometric or multivariate methods are routinely utilized in other forms of spectroscopy for the analysis of complex mixtures.[6] The use of chemometrics in NMR is more limited, but has quickly become an important tool for the NMR spectroscopist.[7–11] For this review, we define chemometrics as the application of statistical and mathematical methods to extract chemically relevant information produced in NMR

experiments. There are a number of excellent and detailed books describing chemometrics and multivariate analysis methods.[12–14]

The emerging fields of metabonomics and metabolomics have brought the use of chemometrics to the forefront of the NMR field. Metabonomics analyzes biofluids and tissues to quantitatively determine the dynamic biochemical profiles and regulation of function in whole organisms.[15,16] The related concept of metabolomics investigates the metabolic regulation and functions in individual cells.[16] The majority of metabonomics or metabolomics investigations have focused on the use of high-resolution solution ^{1}H NMR spectra to investigate a wide variety of biological fluids and tissues, but there have been some examples utilizing solution ^{31}P and ^{13}C NMR, as well as ^{1}H magic angle spinning (MAS) NMR studies of tissues. The major advances in the use of chemometrics on NMR have truly been driven by developments in the metabonomic and metabolomic fields. While many examples from the bionomic fields are referenced in different sections of this review, a thorough discussion of the large and rapidly developing metabonomics/metabolomics fields is beyond the scope of this review. Other areas within NMR that have seen a surge in the use of chemometric techniques include magnetic resonance (MR) imaging and clinical magnetic resonance spectroscopy for image analysis and classification schemes. These areas of study are also quite large and specialized and cannot be adequately covered within this chapter. Interested readers are strongly encouraged to read several excellent reviews on the use of chemometrics in metabonomics,[7,8,17,18] MRI,[19] and clinical spectroscopy.[20]

In this review, we will instead focus on the use of chemometrics as applied to NMR spectroscopy in other scientific fields, primarily chemistry, food science and materials. In each section, specific literature examples will be provided to illustrate the general concepts along with the robustness of the technique. Figure 1 provides a flow chart showing the different steps and pathways that may be employed during chemometric analysis of NMR spectroscopic data. This figure also provides an outline of the review including data representation, preprocessing, binning, and instrumental transfer of NMR data sets (Section 2), non-supervised chemometric classification methods (Section 3), supervised classification methods (Section 4), and spectral resolution methods (Section 6). As this review focuses on the chemometric methods, it will not include a discussion of experimental design. The amount of information that can be obtained from the presented chemometric methods can significantly increase if a good experimental design is used. The reader is encouraged to consult several excellent references on the subject.[21,22]

2. NMR DATA

This section presents the mathematical description of the NMR data sets and reviews some of the preprocessing and data manipulations that are employed to improve the performance of the subsequent chemometric analysis. Descriptions of the different chemometric methods involve the use of matrices, vectors and scalars, such that a brief note on the notation used in the subsequent sections is warranted. Throughout this

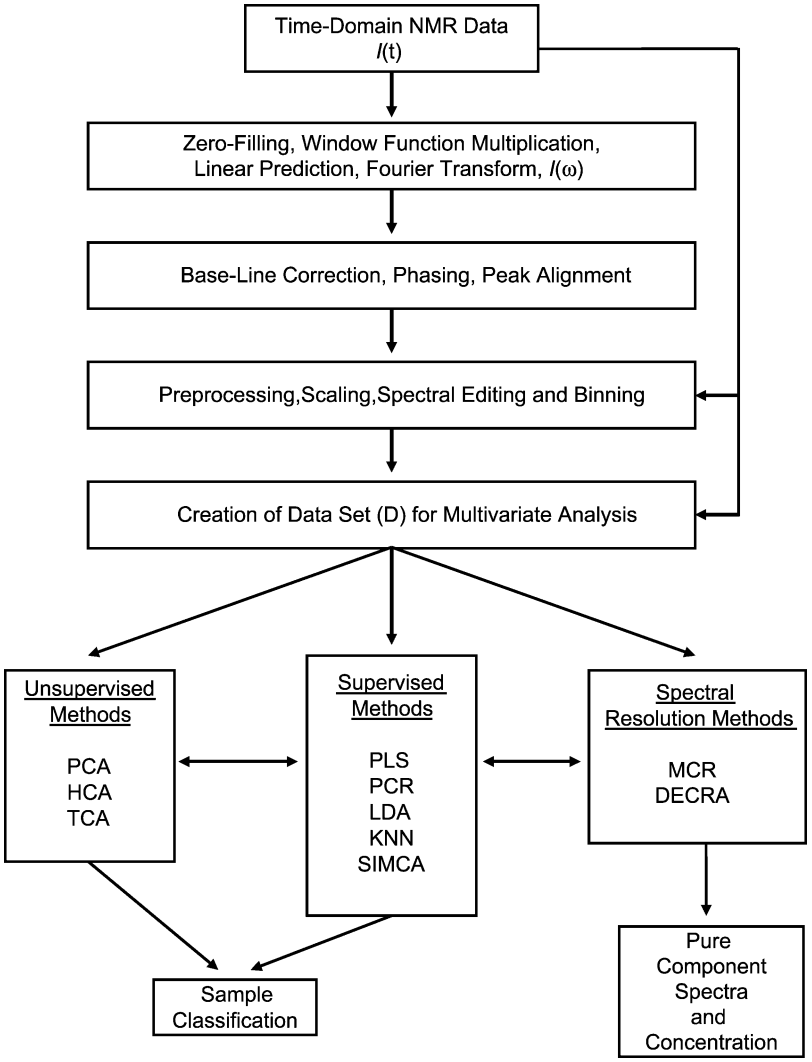

Fig. 1. A flow chart of the different steps and chemometric methods that can be utilized during the analysis of NMR spectral data.

review we will denote matrices as bold upper case letters ($\mathbf{D}$) while individual scalar elements of that matrix are denoted as $(D_{i,j})$. Vectors (or one-dimensional (1D) arrays extracted from matrices) will be given by uppercase, italicized letters (D_i), while simple scalars will be given by lowercase italicized letters (c). Throughout the review the transpose of a matrix is given by ($\mathbf{D}^{\mathrm{T}}$), the pseudoinverse by ($\mathbf{D}^{+}$), the inverse by ($\mathbf{D}^{-1}$), estimated or calculated matrices by ($\hat{\mathbf{D}}$), the norm is given by ($\|\mathbf{D}\|$), while derivatives will be denoted by primes (D_i', D_i'').

2.1. Representation of NMR data sets

For the chemometric analysis of NMR spectral data it is generally assumed that the observed NMR data matrix is composed of spectra, $I_j(\omega)$, where each different jth spectrum covers a frequency range ω, and is composed of n_{freq} real or complex intensities for the frequencies within the observable window (spectral window). It is also possible to perform chemometric analysis on the complex time domain signal, $I_j(t)$, which is the original form of the NMR data following quadrature detection. The time-domain signal and the frequency spectrum are related through a Fourier transformation[23]

$$I_j(\omega) = \int_0^{\infty} I_j(t) \mathrm{e}^{(-\mathrm{i}\omega t)} \mathrm{d}t \tag{1}$$

While there many examples of multivariate analysis involving NMR time domain data,[24–36] it will be assumed in this review that the data matrix of interest is (or is derived from) the frequency domain data $I_j(\omega)$, unless otherwise specified. In most situations the NMR spectrum of the jth sample (different mixture, time, etc.) can be described as the linear combination of n_{comp} pure component spectrum, $S_k(\omega)$, each with a concentration or intensity C_{jk}

$$I_j(\omega) = \sum_{k=1}^{n_{\text{comp}}} C_{jk} S_k(\omega) \tag{2}$$

A data set (**D**) comprised of n_{samp} different NMR samples (spectra) can be constructed from these individual $I_j(\omega)$ spectrum

$$\mathbf{D} = \{I_j(\omega)\}, \qquad j = 1, 2, 3, \ldots, n_{\text{samp}} \tag{3}$$

The linear decomposition of the data set **D** into a matrix containing the concentration profiles (**C**) and a matrix of individual pure component spectra (**S**) can be expressed as

$$\mathbf{D} = \mathbf{CS} \tag{4}$$

A graphical representation of the data matrix (**D**) is shown in Fig. 2. As an example, consider an NMR data matrix containing individual spectra from 24 sample or mixtures ($n_{\text{samp}} = 24$), where each NMR spectra is composed of 32,768 complex points or frequencies ($n_{\text{freq}} = 32\text{K}$) that result from the linear spectral combination of 16 different chemical species or pure components ($n_{\text{comp}} = 16$) within the mixtures. The dimensions of the various matrices in Eqs. (2)–(4) would be $24 \times 32\text{K}$ ($n_{\text{samp}} \times n_{\text{freq}}$) for **D**, 24×16 ($n_{\text{samp}} \times n_{\text{comp}}$) for **C**, and $16 \times 32\text{K}$ ($n_{\text{comp}} \times n_{\text{freq}}$) for **S**. Note that in some instances researchers create the data matrix with the descriptors (i.e., frequencies) as the first row or dimension to give a matrix with $n_{\text{freq}} \times n_{\text{samp}}$ dimensions. The $n_{\text{freq}} \times n_{\text{samp}}$ definition of the data matrix is the transpose ($\mathbf{D}^{\mathrm{T}}$) of the **D** defined in Eq. (3). This nomenclature difference should be kept in mind when comparing descriptions from literature. In Fig. 2 the data matrix (**D**) was created from the association of individual 1D NMR spectra to create the final two-dimensional (2D) data set. Higher and more

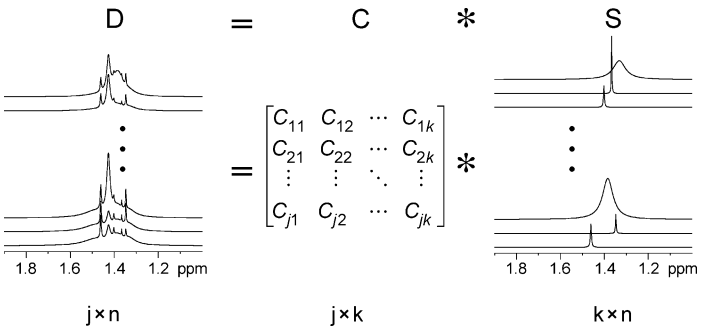

Fig. 2. Schematic representation of a frequency domain NMR data set (**D**), which is a linear combination of individual pure component spectra (**S**), described by the concentration profile matrix (**C**). The data matrix has $(j \times n)$ dimensions composed of $j = 1$ through n_{samp} samples, by $n = 1$ through n_{freq} frequency points, while **C** has $(j \times k)$ dimensions with $k = 1$ through n_{comp} pure components. Finally, the pure component spectra matrix **S** has $(k \times n)$ dimensions. Figure adapted from Ref. 9 and reproduced with permission of Advanstar Communications, Inc.

complex dimensionalities are easily envisioned. Joining of individual 2D matrices for different n_{samp} mixtures (for example 2D heteronuclear multiple-bond correlation (HMBC) NMR spectra) would result in a three-dimensional (3D) data matrix (**D**) for chemometric analysis. Now, imagine following the evolution of this sample set as a function of time, where at each time you obtain the 3D data matrix **D** for your mixtures, combining them to form a four-dimensional (4D) data set, which can be continued infinitely.

For the example in Fig. 2, the Fourier transformed NMR spectra (variables or descriptors being intensity as a function of frequency) were utilized for the creation of the data matrix **D**. It should be noted that many different descriptors can be used to create **D**, with the descriptor selection depending on the analysis method and the information to be extracted. For example, in the spectral resolution methods (Section 6), the desired end result is the determination of the 'true' or pure component spectra and relative concentrations present within the samples or mixtures [Eq. (4)]. For this case, the unmodified real spectra $I_j(\omega)$ are commonly used for the chemometric analysis. In contrast, for the non-supervised and supervised methods described in Sections 3 and 4, the classification of a sample into different categories is the desired outcome. For these types of non-supervised and supervised methods the original NMR spectrum $I_j(\omega)$ can manipulated or transformed to produce new descriptors including:[37]

- The peak intensity for individual frequency regions or specific resonances.
- The number of resolvable resonances in defined spectral regions.
- The total area integral for a defined spectral region.
- The multiplicity and/or line width of specific resonances.
- The variation of chemical shift of individual resonances.
- Select chemical shift values and spin–spin J coupling values.

Many of these descriptor transformations reduce the size of $I_j(\omega)$, thereby decreasing the dimensionality of the input data matrix **D**. These reductions in size can increase

the computational speed of the chemometric analysis, as well as the data storage requirements. In addition, the size of the input NMR data set undergoing analysis can be further reduced by removal of unused or undesired spectral regions, through the use of binning or smoothing functions. These different types of data manipulations are described below. For the experimental examples discussed in this review, we will note the form of the NMR input data and specific/unique data manipulations employed prior to chemometric analysis.

2.2. Baseline, phase correction, and frequency shifts

Experimental variation of individual spectra within large data sets can lead to difficulties in accurately determining peak areas (quantification) as well as problems in classification using principal component analysis (PCA) or partial least squares (PLS) methods (see Sections 3 and 4). Changes include inconsistencies in the NMR spectral phases, undesired changes in the line position, plus variations in line width and line shape. These variations in the line position, peak phase and baseline can result from chemically induced changes and/or instrumental and temperature instability, field inhomogeneities, and sample susceptibility effects. Chemical shift variations may also be due to changes in concentration, solvent, metal binding, and pH between samples. Even the window weighting functions applied to time domain data prior to the Fourier transform can impact the analysis, but these typically produce minor changes in the line width and shape.[37] In the past, many of these spectral variations were manually corrected, but this proves very time-intensive for large spectral data sets. Standard commercial and public domain NMR software programs now include multiple methods to automatically correct baseline offset and baseline roll. The simplest routines utilize regions of the spectra containing no analyte signal to define a flat baseline across the desire spectral window. In addition, many of the NMR software packages now contain methods for automated phase adjustment, although the performance of these varies greatly between software programs. Well-defined numerical methods have now been reported for the rapid and automatic adjustment of both the phase and frequency variations present within large NMR data sets.[38–40] Brown and Stoyanova[38,40] presented a PCA method for correcting phase and frequency shifts. The experimentally observed complex NMR spectrum is described as containing a frequency and/or phase shift described by

$$I_j(\omega) = A_j e^{i\phi_j} f(\omega + \Delta\omega_j) \tag{5}$$

where $I_j(\omega)$ is the jth spectrum at the ω th frequency point, with an amplitude A_j, a phase offset of ϕ_j, described by the complex line shape function $f(\omega)$ along with the frequency offset $\Delta\omega_j$. Brown and Stoyanova demonstrated that while the first loading (P_1) of the data matrix **D** provided a good estimate of the true, correctly phased spectrum $I_j(\omega)$, at least two additional loadings (P_2 and P_3) were needed to describe the variance due to frequency and phase shifts. (Additional discussion and details about loadings and scores is given in Section 3.) A transformation of the orthonormal principal component set (P_1, P_2, P_3) to a new coordinate system defined by P_1, P_1', and P_1^i is then performed.

In this new basis, P'_1 is the derivative of P_1 (obtained via numerical differentiation) and P^{i}_1 is the imaginary part of P_1 from the Hilbert transform of P_1. The transformation matrix **J** is defined by

$$\mathbf{J} = \frac{1}{P}\begin{pmatrix} P'_1 \cdot P_2 & P'_1 \cdot P_3 \\ P^{\mathrm{i}}_1 \cdot P_2 & P^{\mathrm{i}}_1 \cdot P_3 \end{pmatrix} \tag{6}$$

where the normalization factor P results in the determinant of **J** being 1. The original scores of the jth spectrum for the second and third loading, $T_2(j)$ and $T_3(j)$, are subsequently projected onto the new basis set utilizing **J**, to give the new scores, $T'_1(j)$ and $T^{\mathrm{i}}_1(j)$. An estimate of the jth reconstructed experimental spectrum is then given by

$$\hat{I}_j(\omega) = T_1(j)P_1(\omega) + T'_1(j)P'_1(\omega) + T^{\mathrm{i}}_1(j)P^{\mathrm{i}}_1(\omega) \tag{7}$$

where $\hat{I}_j(\omega)$ denotes a reconstructed spectra. An estimate of the phase and frequency offset can be obtained from these transformed scores via,

$$\tan\phi_j = \frac{-T^{\mathrm{i}}_1(j)}{T_1(j)} \tag{8}$$

$$\Delta\omega_j = \frac{T'_1(j)}{T_1(j)} \tag{9}$$

The phase correction for spectrum j can be directly applied by multiplication of the phase factor $\exp(-\mathrm{i}\phi_j)$. The calculated frequency shift can be applied to the time domain signal $I_j(t)$ (via the inverse Fourier transform relationship given in Eq. (1)), through the multiplication by the frequency shift term $\exp(-\mathrm{i}\Delta\omega_j t)$, then transforming this result back to the frequency domain spectrum $I_j(\omega)$. The transformation into the time domain allows a frequency shift smaller than the actual spectral resolution to be employed. These PCA steps can be repeated until a minimized solution is obtained, where convergence results in P_2 and P_3 containing nothing but noise. In this manner, phase and frequency corrections can be applied across the entire NMR data set simultaneously. This method appears to work very well for phasing and frequency shifting of spectral regions that contain well-resolved resonances that do not include the overlap of multiple chemical species.

Witjes and co-workers[39] extended this automatic correction to the phase and frequency shifts to also include distortions to the line shape. In their improved method, the original spectra are approximated by combinations of P_1 (the major loading), the imaginary component and its derivatives, where linear regression is used to estimate the expansion coefficients $(b_{i,j})$[39]

$$\hat{I}_j(\omega) = b_{1,j}P_1(\omega) + b_{2,j}P^{\mathrm{i}}_1(\omega_n) + b_{3,j}P'_1(\omega_n) + b_{4,j}P^{i\,\prime}_1 + b_{5,j}P''_1 + \cdots \tag{10}$$

The calculation of the coefficients for this expansion onto higher order derivatives is obtained in a single step using simple fitting procedures, versus the method of Brown and Stoyanova where a transformation of basis sets is required. It was also noted that by using Eq. (10), higher order terms in the Taylor expansion can be included to reconstruct spectra with larger phase and frequency variations. Similar to Eqs. (8) and (9), the phase and frequency shift for each spectrum j is given by these fit coefficients[39]

$$\tan\phi_j = \frac{-b_{2,j}}{b_{1,j}} \tag{11}$$

$$\Delta\omega_j = \frac{b_{3,j}}{b_{1,j}} \tag{12}$$

Figure 3 shows an example of automated phase correction for a ^{1}H NMR data set using this polynomial method, along with the loadings determined in the initial step. This procedure was easily implemented in MATLAB (The MathWorks Inc., Natick MA). In Fig. 3a, there are small errors in the phasing for individual spectrum within the data set. Note particularly the center spectrum in Fig. 3a. Following two to three iterations of the procedure described above these errors or variations in the spectrum phase are removed (Fig. 3b). Note that the first principal component P_1 nicely describes the desired spectral line shape, while higher order P_i components contain the phase and frequency shift variations (Fig. 3c). Again this method appears to work well for spectral regions with limited overlap between multiple chemical species.

In addition to these methods, Vogels and co-workers[41] presented a preprocessing tool that uses a partial linear fit (PLF) algorithm to correct for small variations in the chemical shift within NMR data sets, without reduction of resolution and loss of spectral fine structure. Recently, a method using a combination of rapid search techniques and sparse mapping has also been proposed for the peak alignment of NMR data.[42]

2.3. Scaling, spectral editing, and binning

Other preprocessing steps that are commonly applied to the NMR spectral data include scaling, spectral editing, and binning. Scaling and spectral editing can significantly improve the rate of identification and separation of groups during classification. If spectral line shape resolution and concentration determination is the final objective, no scaling of the NMR data should be done, since the relative intensities of the NMR resonances are proportional to the concentration of the observe nuclei. On the other hand, the dominant resonances within the NMR spectra may not necessarily be the spectral features that reveal systematic variations occurring within the analyzed samples. Mean centered scaling (removal of the mean spectrum) or similarly the subtraction of the first principal component (a type of spectral editing) has also been used to emphasize weaker spectral components. This produces an NMR data set that contains both positive and negative intensities, which is not usable with some

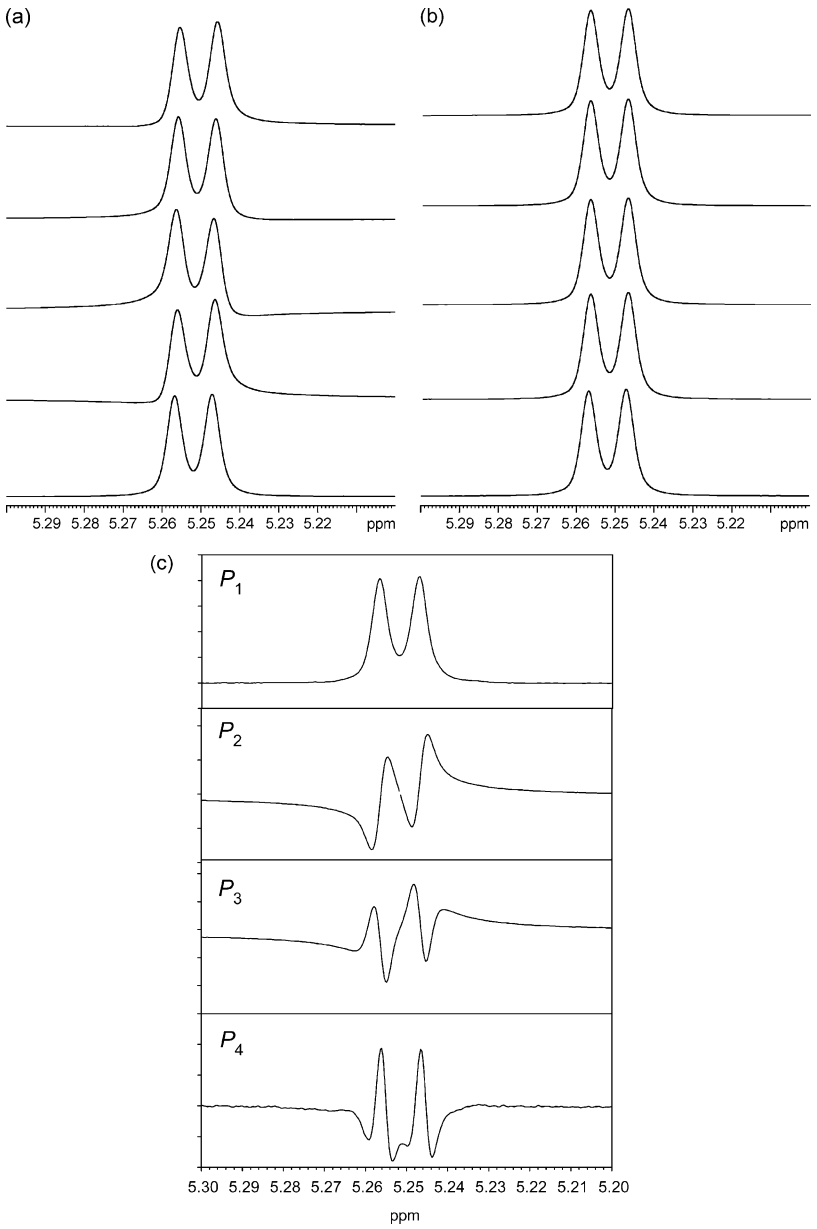

Fig. 3. An example of the automatic phase correction method as described by Witjes and co-workers.[39] In (a) are five representative spectra for a small expanded region in a ^{1}H NMR spectra data set containing 15 total spectra. Note the small differences in phase shift between the spectra, most notable in the central spectrum. In (b) the same NMR spectra are shown following three iterations of the phase and frequency correction. The (c) first five initial loadings (P_i) for the NMR data set reveal that the first loading (P_1) is a good descriptor of the desired spectral line shape, while higher loadings (P_2 and P_3) contain the majority of the information concerning phase shifts and frequency shifts between spectra in the data set.

techniques such as multivariate curve resolution (MCR) methods utilizing positive intensity constraints. For these situations construction and removal of a least common spectrum (the minimum intensity for each frequency) can be used. In some examples, the NMR data is scaled such that the resonance from a major constituent has the same intensity in all the spectra within **D**, while in other NMR studies (i.e., metabonomics) the total NMR spectra integral is scaled to unity (assuring equivalence in concentration of the observed nuclei) for each spectra within **D**. These differences in the observed signal intensity might arise from variations in sample osmolity, sample concentration, or changes in sample density, which are not important to the goal of analysis. Scaling to unit variance (autoscaling) has also been employed, where each variable (typically the spectral intensity at a given frequency) is weighted by the reciprocal of the standard deviation $(1/\sigma)$, where σ is defined as[12]

$$\sigma_n = \sqrt{\frac{\sum_j (D_{j,n} - \bar{D}_n)^2}{n_{\text{samp}} - 1}} \tag{13}$$

where $D_{j,n}$ are the matrix elements of the data matrix **D** (see Fig. 2), n is the index over input descriptor or variable (frequency), j the index over the sample (spectrum) number, and n_{samp} is the total number of samples. This unit variance scaling causes the variables to have equal probability of influencing the model. Intermediate between no scaling and unit variance scaling are studies that use the factor $1/\sqrt{\sigma}$. Other types of weighting functions have also been proposed.

More recent developments in NMR data scaling use methods that incorporate prior knowledge of the importance of specific spectral variables into determining the scaling weight. Variable stability scaling (VAST) has been described, and involves reducing the weighting of variables that are the least stable with respect to the ability to distinguish between different classes.[43] Another method that has seen recent success in metabonomics NMR data analysis is the orthogonal signal correction (OSC) method.[44] During OSC the spectral variations that are orthogonal to the identity of the class (those spectral components that do not correlate with spectral features that give rise to classification) are removed, such that subsequent analysis of the reduced data sets is completely associated with separation of the different classification groups. In the original indirect OSC method this is accomplished by the creation of an orthogonal score vector T_{osc} defined by

$$T_{\text{osc}} = (1 - Y(Y^{\text{T}}Y)^{-1}Y^{\text{T}})T_1 \tag{14}$$

where Y is the classification vector, for example the concentration vector (Refer to Section 4 for a more complete description of the PCA and PLS method), Y^{T} is the transpose, and T_1 is the score vector of the first principal component describing the data matrix **D**. The product of the orthogonal score vector and loading vector (P_1^{T}) can be removed from the original data set, to give the filtered data matrix $\mathbf{D}_{\text{OSC}}$. There are now several different OSC methods and approaches which are described in a series of

papers.[44–48] The OSC method has been used for ^{1}H NMR of biofluids,[49,50] and ^{13}C MAS NMR analysis of softwood pulps.[26] By inspection of these non-correlated components using OSC it has been possible to identify spectral changes that were interfering with the classification analysis. For example, OSC has been used to identify the effects of instrumental drift within NMR spectral data sets,[7] and intra- and inter-instrumental variations,[49] as well as physiological diurnal variations in animal populations.[50]

In many situations, it may also be important to remove or edit certain spectral regions (another form of spectral editing) that contain resonances that are not of interest, but may strongly bias or skew the subsequent chemometric analysis. A primary example is the removal of the intense water resonance and surrounding region ($\delta \sim +6.0$ to $+4.5$ ppm) as commonly done in the majority of ^{1}H NMR metabonomic studies. The different water suppression techniques employed in these NMR studies dramatically attenuate the resonances within this spectral region, plus produce highly variable line shapes for the residual water signal. Other molecular species (e.g., urea) that cross saturate with the water resonance due to exchange may also be attenuated. In studies of complex mixtures, it may also be important to remove spectral signatures of additives or other chemical species. Examples also exist where NMR spectral regions that contain only noise, or signals below a given threshold were removed. A good example of this is in the analysis of LC–NMR and HPLC–NMR data sets, where the signal-to-noise (S/N) levels can be low for systems operating in an on-flow configuration, impacting the performance of the chemometric analysis. Brereton and co-workers[51] have utilized the standard deviation at each observe frequency, σ_n [Eq. (13)] to select only those frequencies (variables) that have $\sigma_n > 10\%$ of the maximum standard deviation. The spectral frequencies that do not meet these criteria can be removed from the data matrix prior to analysis. While removing portions of the data set can greatly reduce the size of the input data matrix **D** and improve the speed of analysis, the researcher should keep in mind that for future classification schemes, these removed NMR spectral region may contain signals for species that are important markers for classification or outlier detection. The impact of scaling and spectral editing on the resulting chemometric analysis is an area requiring additional research.

As mentioned in Section 2.1, the input variables need not simply be the NMR spectral intensity at each frequency, but could represent the number of peaks in a region, the spectral intensity in a given region, a *J* coupling, etc. Binning is an example of a preprocessing tool that modifies the input variable, and has seen considerable use for NMR data. During binning the integral of signal intensity for a defined frequency width (bin width) becomes the input variable, instead of the actual NMR spectra. Binning effectively reduces the spectral resolution, but has the advantage of successfully eliminating the impact of small chemical shift variations between different samples (due to concentration, temperature, pH, and metal binding effects) on the subsequent chemometric analysis. In the metabonomics literature binning on the order of $\Delta\delta \sim 0.04$ ppm appears to be the common bin sized used prior to either PCA or PLS analysis methods (see Sections 3 and 4 for a discussion of these methods). The impact of different bin sizes on the chemometric analyses is not commonly reported. The use of 'smart binning' or masking, where the bin size can vary with spectral region, is one area of active research being pursued in a number of research groups. Figure 4 shows an

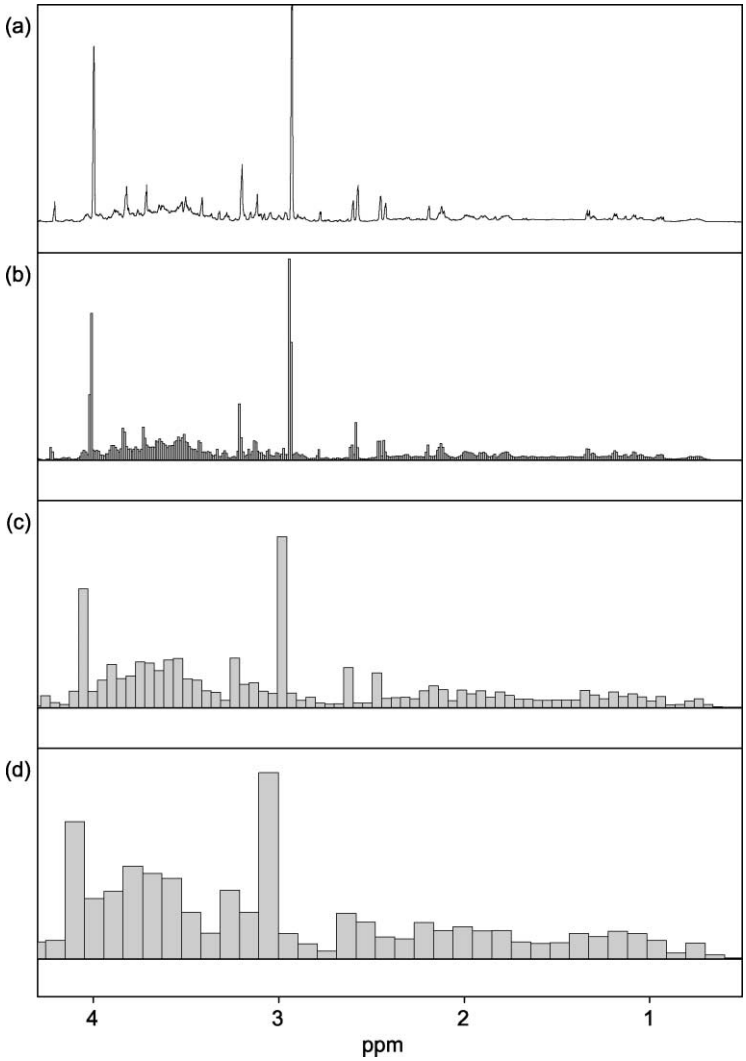

Fig. 4. The influence of binning and the resulting spectral descriptor as demonstrated on a portion of the ^{1}H NMR (600 MHz) spectra of human urine. The (a) original, un-binned NMR spectrum, digital resolution ~0.0002 ppm per point, 25,500 points, (b) 0.01 ppm bin interval, 432 resulting points (or bins), (c) 0.05 ppm bin interval, 86 resulting points, and (d) 0.10 ppm bin interval, 43 resulting points.

example of the preprocessing binning on a ^{1}H NMR spectrum. With increasing bin width, there is a corresponding reduction in the number of points or variables in the resulting 'spectrum', plus a reduction in the spectral resolution. While binned NMR data can greatly improve the efficiency of spectral classification schemes and allow general identification of spectral regions responsible for this discrimination, the loss of the fine structure in the NMR spectra removes spin-coupling information and exact

chemical shift information that might be useful for final identification of important molecular species.

2.4. Instrumental transfer

The influence of NMR spectrometer performance and the efficiency of different pulse sequences should also be evaluated when producing and analyzing NMR data sets. Recently, Potts and coworkers[52] did a detailed analysis of the impact of NMR parameters on the PCA classification of biofluid NMR. They studied the variance in high resolution ^{1}H NMR spectra of urine samples due to implementation of different solvent suppression techniques: (1) Presaturation, (2) NOESY (Nuclear Overhauser Effect Spectroscopy)-presaturation, (3) WET (water suppression through T_1 effects), and (4) WATERGATE (water suppression by gradient tailored excitation). In many biofluid investigations the spectral region containing water and urea ($\delta = +6.3-4.5$ ppm) are often excluded to reduce variance that result from differential solvent saturation and selective attenuation due to exchangeable protons. Potts and coworkers[52] demonstrated that other spectral regions show variation depending on the solvent suppression technique. For example, the $\delta = +4.3$ to $+3.3$ ppm spectral region revealed additional attenuation when spectra were collected utilizing the Watergate water-suppression pulse sequence, due to differences in the baseline response and differential attenuation of other spectral regions near water. It was also shown that these variations between the different NMR spectra were produced by changes in the bionomial 90° pulse length. These results show that pulse sequences involving significant parameter optimization resulted in increased spectral variations. Keun and co-workers[53] analyzed the PCA results for two ^{1}H NMR data sets on urine taken on different instruments in different laboratories, and demonstrated that the PCA results were very similar. They also demonstrated that the efficiency of the water suppression method produced the largest spectral variations between the two NMR data sets. Beckwith-Hall and co-workers[49] have also shown that for ^{1}H NMR studies of biofluids, intra- and inter-instrumental variations will often obscure the separation of groups during classification. These researchers utilized the OSC method (Section 2.3) to eliminate or greatly reduce the impact of these types of NMR instrumental variations.

These studies also revealed the difficulty in transfer of training sets between different NMR instruments without some type of standardization to minimize spectral variation. In many instances large data sets may be compiled from individual NMR experiments run over several months (if not years), as well as data collected on different instruments and from different groups. There is no guarantee that the performance of an NMR instrument over time, or different NMR instruments, are equivalent. Gislason and co-workers have recently reported a study on the protocol for transferring PLS methods between low field process NMR spectrometers in which they found that a piece-wise direct standardization methods for accurate model transfer. This study appears to be one of the few concerning instrumental transfer of chemometric models in NMR.[54] The development of efficient methods that allow for accurate transfer and combination of NMR spectral data from a variety of sources is an important area for future research.

3. UNSUPERVISED METHODS

Due to the increasing complexity of NMR data sets, it has become important to utilize data reduction and chemometric techniques to accurately access the latent chemical information within the data. In the next two sections, a mathematical overview of the different chemometric methods commonly employed for NMR analysis will be presented. In many NMR studies the initial goal during analysis may be the classification of the data into different classes (origin of the material, response to a toxin, etc.). To accomplish this goal, pattern recognition (PR) methods can be employed to reduce the complexity and size of NMR data (typically to 2D and 3D representations) so that classification can be visually pursued. The simplest of these techniques are referred to as 'unsupervised methods', since there is no operator input (attempts to force samples into predefined classes or define the number of classes *a priori*). These methods are often used as exploratory techniques during the initial stages of data analysis. Examples of chemometric analysis of NMR data using these unsupervised methods are discussed in Section 5.

3.1. Principle component analysis

Principle components analysis (PCA), a form of factor analysis (FA), is one of the most common unsupervised methods used in the analysis of NMR data.[8,55] Also known as Eigenanalysis or principal factor analysis (PFA), this method involves the transformation of data matrix **D** into an orthogonal basis set which describes the variance within the data set. The data matrix **D** can be described as the product of a scores matrix **T**, and a loading matrix **P**,

$$\mathbf{D} = \mathbf{T}\mathbf{P}^{\mathrm{T}} \tag{15}$$

where **T** is proportional to the eigenvectors of the transposed covariance matrix $\mathbf{Z} = (\mathbf{D}^{\mathrm{T}}\mathbf{D})^{\mathrm{T}}$, and **P** is equal to eigenvectors of $(\mathbf{D}^{\mathrm{T}}\mathbf{D})$. Since $(\mathbf{D}^{\mathrm{T}}\mathbf{D})$ is symmetric, the eigenvalues are real and non-negative. The influence of a given principal component is given by the corresponding eigenvalues.[55]

When examining spectroscopic data, the loading vectors **P** can be viewed as the spectral, or frequency variations, while the scores **T** represent the amount, or importance, of the loading vector in the sample under consideration. The first loading, P_1, describes the maximum variance in the data. The subsequent loadings or principal components explain decreasing amounts of the data variance, while accurately reproducing the original data. At some point these later principal components will contain only noise (if data set has random noise structure). For a data set **D** where $n_{\mathrm{samp}} < n_{\mathrm{freq}}$ there will be a maximum n_{samp} of principal components. However, the NMR data set is often a linear combination of a limited number of components n_{comp} [see Eq. (2)], such that **D** is now described by n_{comp} principal components, where $n_{\mathrm{comp}} < n_{\mathrm{samp}}$. These loadings and scores in Eq. (15) are linear combinations of the product between the concentration and pure component spectra described in Eq. (4). Determining the number of components to

retain in PCA as well as other FA methods (detailed in Section 4) can be somewhat arbitrary. Malinowski presents a number of methods that have been used to estimate the number of factors to keep.[6] For PCA, a common method used to determine the number of factors is to monitor the cumulative percent variance, whereby the percentage of the original data explained is calculated using an increasing number of factors. The cut-off point is arbitrary, often set at 90–99% of the original data. For spectroscopic data, later loading vectors can often appear as noise, further aiding in selecting the cut-off point. For supervised FA methods, the selection process becomes slightly less arbitrary, and is often based on the resulting model's prediction performance.[56]

It is important to know how many principal components (factors) should be retained to accurately describe the data matrix **D** in Eq. (15), and still reduce the amount of noise. A common method used is the cross validation technique, which provides a pseudo-predictive method to estimate the number of factors to retain. The cross validation technique leaves a percentage of the data ($\gamma\%$) out at a time.[12,56] Using this reduced data set, PCA is again carried out to provide new loading and scores. These are then used to predict the deleted data ($D_{i,j}(p)$) and then used to calculate the ensuing error defined by

$$E_{i,j} = D_{i,j} - \hat{D}_{i,j}(p) \tag{16}$$

This procedure is then calculated [100/($\gamma\%$)] times, ensuring that a given data grouping is only deleted once. The predicted residual error sum of squares (PRESS) is then calculated[12]

$$\mathrm{PRESS}(n_{\mathrm{comp}}) = \sum_i \sum_j E_{i,j}^2 \tag{17}$$

As the number of important components or factors is included in the analysis, PRESS will decrease. When noise begins to be included in the analysis PRESS will begin to increase or slow its rate of decline. An initial estimate of the number of factors to use can be made using the minimum in PRESS, but this can lead to overfitting. Criteria for the selection of the optimal number of factors using methods involving PRESS and F statistics have been described.[56]

Plotting the first few scores (e.g., T_1 versus T_2 or T_2 versus T_3) provides a 2D representation of the data set and is called a scores plot. An example of a scores plot is shown in Fig. 5, where the clustering of the data can be readily visualized. Plotting the first three scores (T_1, T_2, and T_3) results in a stereo plot, and is used for classification of more difficult data sets. An example of this can be seen in Fig. 6b in Section 5. If the noise within the data matrix is randomly varying, it will be contained in later factors of the PCA decomposition. Thus, estimating the NMR data set by using only the significant PCA loadings effectively filters random noise. The major benefit of PCA is that it provides a simple representation of the data matrix **D**, and describes the data with fewer variables than in the original description, allowing the design of a classifier method. The use of PCA for quantification of NMR spectral data has also been discussed.[40,55]

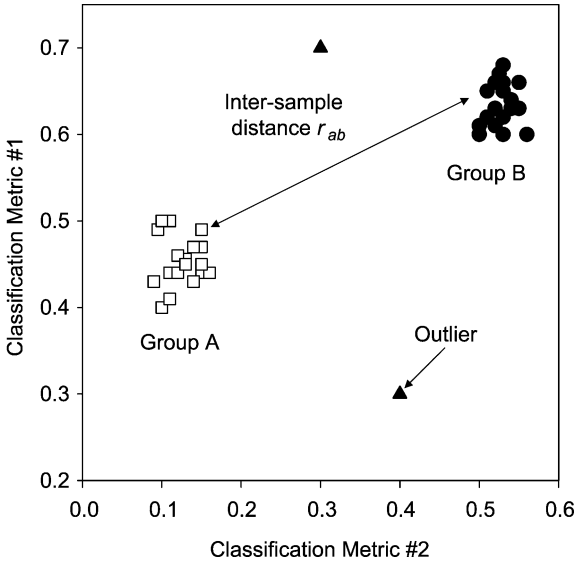

Fig. 5. An example of a scores plot as one might obtain in a principal components analysis. Distinct clustering or grouping of NMR spectra is observed in this type of plot, where the discrimination results from the analyzed metric used (e.g., principal components). The distance between samples (r_{ab}) within groups is used by many supervised methods to further describe and improve class or group separation. There are different chemometric techniques that can be used to identify outliers, or to provide a group assignment.

There are a variety of methods used to obtain the loading and scores matrix in Eq. (15). Perhaps, the most common methods employed are non-linear iterative partial least squares (NIPALS), and the singular value decomposition (SVD). Being an iterative method, NIPALS allows the user to calculate a minimum number of factors, whereas the SVD is more accurate and robust, but in most implementations provides all the factors, thus can be slow with large data sets. During SVD the data matrix can be expressed as

$$\mathbf{D} = \mathbf{U}\boldsymbol{\Sigma}\mathbf{V}^{\mathrm{T}} \tag{18}$$

Because $\mathbf{U}$ and $\mathbf{V}$ are orthonormal, working with the SVD decomposition is relatively simple, as the inverses of $\mathbf{U}$ and $\mathbf{V}$ are defined by their transposes. The diagonal matrix $\boldsymbol{\Sigma}$ contains the singular values of $\mathbf{D}$ along its diagonal. The singular values are equal to the square root of the eigenvalues, $\boldsymbol{\Sigma} = \mathbf{L}^{1/2}$ of $\mathbf{D}^{\mathrm{T}}\mathbf{D}$. By comparing Eqs. (18) and (15) it can be seen that $\mathbf{U} = \mathbf{T}$, and $\boldsymbol{\Sigma}\mathbf{V}^{\mathrm{T}} = \mathbf{P}^{\mathrm{T}}$ (or $\mathbf{U}\boldsymbol{\Sigma} = \mathrm{T}$ and $\mathbf{V}^{\mathrm{T}} = \mathbf{P}^{\mathrm{T}}$). SVD is easily implemented in MATLAB.

The NIPALS method is also a relatively straightforward method to understand. To start, an arbitrary vector is selected to be used as a starting point for the first loading vector P_1^{T}. It is also possible to start with an arbitrary scores vector T_1 and estimate P_1^{T}. The starting point can be from the data set, or it can be created from random numbers.

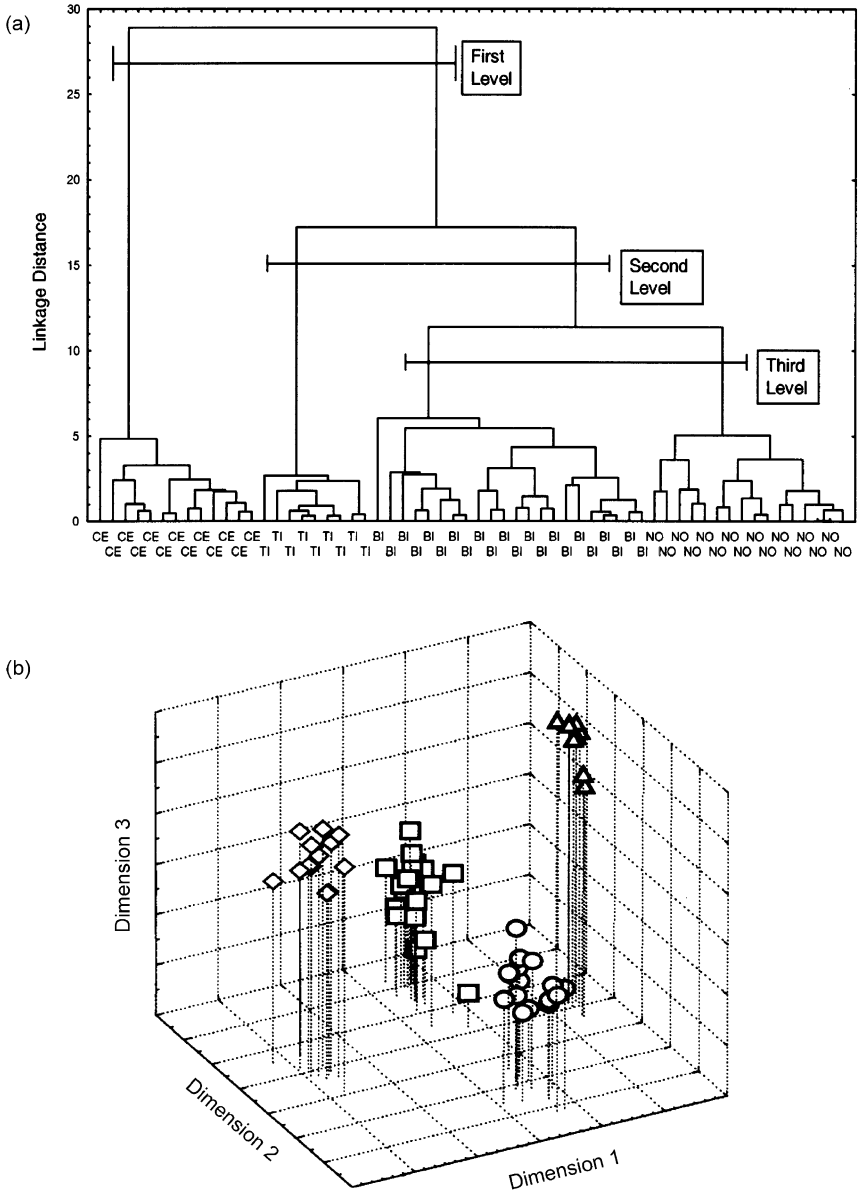

Fig. 6. An example of (a) TCA and (b) LDA analysis for the discrimination of 60 monovarietal Sicilian extra virgin olive oils from different cultivars. The TCA results were based on 46 selected ^{13}C NMR peaks. Samples with the same letters belong to the same cultivar. In the TCA dendrogram all samples start as individual clusters. Three levels of discrimination in the TCA analysis are marked. The 3D scores plot (dimensions 1, 2, and 3) obtained from LDA reveals good separation of the different cultivars, with the different symbols denoting oil samples from the same cultivar: ○, NO, Nocellara; □, BI, Biancolilla; ◇, CE, Cerasuola; △, TI, Tonda Iblea. Adapted figure reprinted with permission from Hanneguelle *et al*.[77] Copyright 2003 American Chemical Society.

Here, we will start with an arbitrary loading vector selected from the spectral data matrix:

$$P_{\text{start}} = D_{\text{arbitrary}} \tag{19}$$

The loading vector P is then used to solve for scores vector T, according to

$$T_{\text{start}} = \frac{\mathbf{D}P_{\text{start}}}{P_{\text{start}}^{\text{T}}P_{\text{start}}} \tag{20}$$

The starting scores vector T is normalized to unit length.

$$T_{\text{new}} = \frac{T_{\text{start}}}{\|T_{\text{start}}\|} \tag{21}$$

A new loading vector can now be calculated using this normalized scores vector via

$$P_{\text{new}} = \frac{\mathbf{D}^{\text{T}}T_{\text{new}}}{T_{\text{new}}T_{\text{new}}^{\text{T}}} \tag{22}$$

This now becomes an iterative process. If $P_{\text{new}} = P_{\text{start}}$, continue; if not, replace P_{start} in Eq. (20) with P_{new} and continue with Eqs. (21) and (22) again. Then, repeat Eqs. (20)–(22) until $P_{\text{new}} = P_{\text{start}}$. Once the convergence level is fulfilled the first factor is complete. This factor is stripped from the data matrix to produce the first residual matrix $\mathbf{E}_1$, where the residuals are obtained via

$$\mathbf{E}_k = \mathbf{D} - \sum_{i=1}^{k} \mathbf{D}_i \tag{23}$$

where $\mathbf{D}_i = T_{\text{new}}P_{\text{new}}$ for each subsequent factor. The second, third, fourth, etc. factors are calculated by replacing $\mathbf{D}$ with the residual matrix, $\mathbf{E}_j$, and repeating the steps described in Eqs. (20)–(23). The procedure is continued until all the desired factors are calculated. The resulting matrix $\mathbf{T}$ is orthonormal, while the matrix $\mathbf{P}$ is orthogonal. If one starts the procedure with an arbitrary T and normalizes P, these properties are reversed.

3.2. Hierarchical cluster analysis

Hierarchical cluster analysis (HCA) and the closely related tree cluster analysis (TCA) provide a simple view of distances between samples, often viewed in a tree-like structure called a dendrogram (see Fig. 6a as an example). These types of analyses methods allow for the development of quick and simple classification schemes. Distances are calculated between all samples within the data set where the data parameters are the coordinates in a multidimensional variable parameter space (of dimension n_{var}). The general distance

r_{ab} between two points a and b is given by

$$r_{ab} = \left[\sum_{i=1}^{n_{\text{var}}} (x_a(i) - x_b(i))^p \right]^{1/p} \tag{24}$$

where p is the order of the distance, $x_a(i)$ and $x_b(i)$ are the ith coordinate of samples a and b, respectively, and the summation over all the variables used to describe the system. For $p = 2$ the distance is the conventional Euclidian distance, but for certain cases the $p = 1$ ('city block' distance) has also been used. These calculated distance between samples can be compared directly or can be normalized to create a similarity matrix, $\mathbf{S}_{ab}$, between pairs of points a and b using

$$\mathbf{S}_{ab} = 1 - \frac{r_{ab}}{r_{\max}} \tag{25}$$

where r_{ab} is the distance between a selected pair of samples, and $r_{\max}$ the maximum distance found between points in the data set. The two most distant data points in the data set (most dissimilar) have $S = 0.0$, while identical data points would have $S = 1.0$.

During HCA, each sample point is originally assumed to be a lone cluster. The similarity matrix $\mathbf{S}_{ab}$ is evaluated to find the largest value (largest similarity, smallest distance). The corresponding points are linked into a new cluster. The similarity matrix is now recalculated, and the process repeated until only one cluster remains. As the number of samples within the cluster increases, there are different ways to determine the distance between a sample and a cluster, which is composed of many different samples. These include single link method (nearest neighbor method), the complete link (farthest neighbor technique), and the centroid method. Details of these different linking methods can be found elsewhere.[8,12] The resulting dendrogram (Fig. 6a) allows the different links to be visualized, with the branch lengths being proportional to the distances between the linked clusters. There are other methods that allow for the display or mapping of the distances. One example is non-linear mapping (NLM) which creates the best 2D representation of the data while attempting to preserve the n-dimensional parameter space distances.[12,14]

4. SUPERVISED METHODS

In complex systems where the number of groups to be separated during classification becomes larger, the performance of simple unsupervised methods (Section 3) degrades, requiring the use of more sophisticated supervised chemometric techniques. Additionally, in fields such a process NMR where there is a need for quantifying a component, the use of supervised methods becomes necessary. The different supervised methods described in the sections below have all been utilized in the chemometric analysis of NMR data for classification and/or quantitation. Examples utilizing these different techniques are discussed in Section 5.

4.1. Principle components regression

Principle components regression (PCR) is one of the supervised methods commonly employed to analyze NMR data. This method is typically used for developing a quantitative model. In simple terms, PCR can be thought of as PCA followed by a regression step. In PCR, the scores matrix ($\mathbf{T}$) obtained in PCA (Section 3.1) is related to an external variable in a least squares sense. Recall that the data matrix can be reconstructed or estimated using a limited number of factors (n_{fact}), such that only the $k = n_{\text{fact}}$ PCA loadings (1:k) are required to describe the data matrix. Eq. (15) can be reconstructed as

$$\hat{\mathbf{D}} = \mathbf{T}_{1:k}\mathbf{P}_{1:k}^{\mathrm{T}} \tag{26}$$

In PCR a least squares solution can be found to relate the vector containing the state of an external variable (C) with dimensions $n_{\text{samp}} \times 1$ to the scores matrix, $\mathbf{T}$

$$C \propto \mathbf{T} \tag{27}$$

The vector C can be any parameter that is appropriate to model through $\mathbf{D}$. Examples of C include species concentration, time of data collection, length of hydrocarbon chain or other performance parameters. The estimated relation between C and $\mathbf{T}$ is called the regression vector, B. Using a calibration set of data where, for each NMR spectrum, the concentration is known, B is estimated using the $\mathbf{T}$ matrix estimated from the PCA step.

$$C = \mathbf{T}B + E_C \tag{28}$$

where E_C is the error vector associated with C. Solving for B gives

$$\hat{B} = [\mathbf{T}^{\mathrm{T}}\mathbf{T}]^{-1}\mathbf{T}^{\mathrm{T}}C \tag{29}$$

Once B is estimated using calibration data, the C_{unknown} value of an unknown data vector (spectrum) can be estimated from the unknown scores $\mathbf{T}_{\text{unknown}}$. $\mathbf{T}_{\text{unknown}}$ is estimated from an unknown sample using $\mathbf{P}$ from the calibration ($\mathbf{T}_{\text{unknown}} = \mathbf{D}\mathbf{P}_{\text{cal}}^{+}$). Once the scores have been estimated, the concentration associated with the spectrum can be estimated using the regression vector

$$C_{\text{unknown}} = \mathbf{T}_{\text{unknown}}\hat{B} + E_C \tag{30}$$

More details on the least squares procedure, orthonormal matrices, and the SVD can be found in Strang.[57]

4.2. Partial least squares

PLS method is also a regression algorithm, relating concentration information, in this case, to spectral information. In PCR scores and loading are calculated strictly using spectral information. However, in PLS, concentration information is included during the calculation of the loadings and scores. By incorporating concentration information in the calculation of the loading and score vectors, more predictive ability is included into earlier loading vectors than is the case for PCR. If C is a matrix, the technique is referred to as PLS-2. In most applications C is a vector. The standard method for calculating PLS loading and scores uses the NIPALS algorithm introduced in Section 3.1 in the discussion of PCA. To begin, the first PLS spectral space weight vector, $W_k(k = 1)$ is calculated as the least squares solution of the relationship between the external variable (concentration) vector (C) and the data matrix (**D**):

$$\mathbf{D} = CW_k^{\mathrm{T}} + E_{\mathrm{D}}$$

$$\hat{W}_k = \frac{\mathbf{D}^{\mathrm{T}}C}{C^{\mathrm{T}}C} \tag{31}$$

$$\hat{W}_k = \frac{\hat{W}_k}{\|\hat{W}_k\|}$$

where E_D is the error associated with the data matrix **D**. The PLS weight vector is then used to calculate the PLS scores vector T_k:

$$\mathbf{D} = T_k\hat{W}_k^{\mathrm{T}} + E_{\mathrm{D}} \tag{32}$$

$$\hat{T}_k = \frac{\mathbf{D}\hat{W}_k}{\hat{W}_k^{\mathrm{T}}\hat{W}_k} = \mathbf{D}\hat{W}$$

Next, the least squares relationship is found between the scores vector $T_{k,}$ and concentration vector C, defining the concentration space weight vector V_k

$$C = V_k\hat{T}_k + E_C \qquad \hat{V}_k = \frac{C\hat{T}_k^{\mathrm{T}}}{\hat{T}_k^{\mathrm{T}}\hat{T}_k} \tag{33}$$

where E_C is the error associated with the concentration. Similarly, we find the least squares relationship between the scores vector, $\hat{T}_k$ and the spectral data matrix, resulting in the PLS loading vector, P_k

$$\mathbf{D} = \hat{T}_kP_k^{\mathrm{T}} + E_{\mathrm{D}}, \qquad \hat{P}_k = \frac{\hat{T}_k\mathbf{D}^{\mathrm{T}}}{\hat{T}_k^{\mathrm{T}}\hat{T}_k} \tag{34}$$

with the loading and score calculated for step k, the residuals are calculated for both the concentration and the spectral space using

$$E_{\mathrm{D}} = \mathbf{D} - \hat{T}_k \hat{P}_k^{\mathrm{T}}, \qquad E_C = C - \hat{V}_k \hat{T}_k \tag{35}$$

To calculate the subsequent T_{k+1} and P_{k+1} scores and loadings, the residuals E_{D} and E_C are substituted for $\mathbf{D}$ and C in Eqs. (31)–(35). This procedure continues until all n_{fact} PLS factors have been calculated. To predict C_{unknown} from $\mathbf{D}_{\mathrm{unknown}}$ using the PLS model, the $\mathbf{D}_{\mathrm{unknown}}$ matrix is decomposed, building up the C_{unknown} values, factor by factor. Using the estimated weight vectors of step k from the calibration, the scores for the unknown are estimated using

$$T_k = \hat{W}_k^{\mathrm{T}} \mathbf{D}_{\mathrm{unknown}} \tag{36}$$

The concentration at step k is then estimated using the score from Eq. (36) and the $\hat{V}_k$ calculated during calibration and summed with the previously $k - 1$ concentration values.

$$C_k = C_{k-1} + \hat{V}_k T_k \tag{37}$$

The spectral residuals, E_D, is calculated and replaces $\mathbf{D}_{\mathrm{unknown}}$ in Eq. (36). Calculation continues until all n_{fact} factors have been included in the calculation of C. Alternatively, PLS prediction can be done using a calculated regression vector. A detailed discussion on the PLS method has been previously presented in the literature.[56,58]

4.3. Soft independent modeling of class analogies

Soft independent modeling of class analogies (SIMCA), is a supervised classification method based on PCA. For each known class of samples, a PCA model is created. Unknown samples are compared to each PCA model and the degree of fit determined. The goodness of fit for an unknown sample to a particular class can be estimated through standard metrics such as lack of fit to a particular model as well as Student T tests.[59,60] These metrics allow SIMCA to determine an incoming sample to be an outlier (i.e., does not belong, see Fig. 5) to any of the known classes, an advantage where incoming samples may not belong to a finite set (e.g., polymer classification).

4.4. Linear discriminant analysis

Linear discriminant analysis (LDA) is a classification method that uses the distance between the incoming sample and the class centroid to classify the sample. For LDA using Mahalanobis distances, the classification metric uses the pooled variance–covariance matrix to weight the Mahalanobis distance $r^2_{(D_i,\bar{D}_g)}$ between the incoming

sample spectrum (D_i) and the mean of the samples in class g

$$r^2_{(D_i,\bar{D}_g)} = [(D_i - \bar{D}_g)\mathrm{Cov}^{-1}_{\mathrm{pooled}}(D_i - \bar{D}_g)^{\mathrm{T}}] \tag{38}$$

The pooled covariance matrix is calculated as the weighted average of the covariance matrices of the individual classes

$$\mathrm{Cov}_{\mathrm{pooled}} = 1/(n_{\mathrm{samp}} - 1)\sum_{g=1}^{G} n_g \mathrm{Cov}_g \tag{39}$$

where $\mathrm{Cov}_{\mathrm{pooled}}$ is the resulting pooled covariance matrix, n_{samp} is the total number of samples in the set, G is the total number of classes, n_g is the number of samples in class g, and Cov_g is the covariance matrix for class g. LDA will classify all incoming samples, a disadvantage if an incoming sample may not belong to any of the g groups within the classification scheme created. It does a good job at binary classification and it may, however, tolerate small interferences slightly better than SIMCA. Because it will classify every sample, it will tolerate gradations in sample class, such as classification of biological samples (e.g., grades of cancer).

4.5. K nearest neighbors

K nearest neighbors (KNN) is simple, non-parametric method of classification that determines the class of an incoming sample based on the distance between the incoming sample and its nearest neighbors, whose classes are known. Examination of the distances between the incoming sample and K neighbors can be used to classify the sample. For a two-class system the number of neighbors, K is typically set to three, and the incoming sample is classified according to the majority class of the nearest three neighbors. Traditionally, the distance metric used for KNN has been the Euclidean distance in n-space[61]

$$r_{i,g} = [(D_i - D_g)(D_i - D_g)^{\mathrm{T}}]^{1/2} \tag{40}$$

where $r_{i,g}$ is the resulting distance between incoming sample i and a sample within class g, D_i is the vector of points representing the incoming sample i, and D_g is the vector of points representing a sample from class g. However, the use of the Euclidean distance can lead to poor conclusions when the variables are correlated.[62] Alternatively, the Mahalanobis distance between samples can be used

$$r^2_{(D_i,D_g)} = [(D_i - D_g)\mathrm{Cov}^{-1}_{g}(D_i - D_g)^{\mathrm{T}}] \tag{41}$$

where Cov_g is the estimated variance–covariance matrix from class g, and D_i and D_g are the vectors described above. Wu *et al.*[62] describe an alternative form of KNN used with the Mahalanobis distance, termed linear nearest neighbor (LNN) to identify its similarity to LDA, in which the class covariance matrix in Eq. (41) is replaced by the pooled

covariance matrix, described by Eq. (39). The pooled covariance matrix is to be used where the covariance matrices of each class are similar, or the number of samples is small with respect to the number of variables.[63] Being a non-parametric method, KNN analysis can work well when there may be a limited number of calibration samples or in situations where there may be gradations in sample type.

4.6. Other methods

As to be expected there are a number of other methods and variants in addition to those described above. Recent examples include the utilization of Bayesian methods for class recognition,[64] wavelet transforms, artificial neural networks (ANN) in biomedical NMR (see Table 1 of Ref. 20) and PR,[65,66] plus genetic and evolutionary computing.[20]

5. EXAMPLES OF SUPERVISED AND UNSUPERVISED INVESTIGATIONS

5.1. Food science

In food chemistry high resolution NMR has proven to be a valuable tool for the assessment of quality, degree of adulteration along with identification of region or cultivar of origin. The application of NMR spectroscopy to detect adulterations in wines, fruit juices, and olive oils has been reported. Chemometric analysis of NMR spectral data is widely used in the analysis of olive oils.[67–74] These studies include cluster analysis of olive oil ^{1}H NMR spectra (intensity of 11 selected resonances) to demonstrate that cultivar identity governs the chemical composition of the resulting olive oil.[67] Cluster analysis on the minor components in the ^{1}H NMR spectra of virgin olive oils has also been reported for classification of olive oils.[70] Discriminant analysis (DA) allowed mixtures of pure olive oil and olive oils adulterated with oil from hazelnut and sunflowers to be identified based on ^{1}H NMR spectra.[69] LDA analysis of the ^{13}C NMR spectra have also been used to identify the cultivar of origin for 60 Sicilian extra virgin olive oils,[71] while LDA analysis of the ^{1}H NMR of olive oils from five different geographical districts in Italy was able to distinguish the different origins even for oils from different cultivars and grown in different years.[68,71] Similarly, cluster analysis and LDA was used to characterize the geographic origin of 42 extra virgin olive oils based on 11 selected resonances as independent variables.[75] The TCA and LDA analysis of the ^{1}H NMR for 216 extra virgin olive oils from different geographical areas in Italy, different cultivars and different production years, showed that discrimination based on the geographical origin could be realized.[72] PCA and TCA methods have been used to analyze ^{1}H and ^{13}C NMR data of olive oils obtained from matched Mediterranean cultivars grown in experimental fields in Argentina and in Italy.[68,71] Most of the olives grown in the mild conditions of Italy could be distinguished from the corresponding cultivar grown in Argentina. The TCA analysis did reveal some of the Argentine-produced olive oils were grouped together with the Italian oils, suggesting that these cultivars were less affected by the climatic conditions in Argentina, and might be the best candidates for transfer

to the extreme climatic conditions of Argentina. Eleven NMR resonances that were sensitive to the different cultivars were selected using multivariate analysis of variance (MANOVA) prior to the PCA, TCA, and LDA analysis.[68,71] PCA, PCR, and PLS methods have been used to identify variety and origin of extra virgin olive oils based on the ^{13}C NMR spectra. In this study 41 variables (^{13}C NMR chemical shifts) were used for the discrimination. Different methods of variable selection including the Fisher Ratio and the ratio of inner variance within classes to outer class-to-class variance were explored to improve separation during the PCA analysis and improve PCR and PLS predictive results.[73]

Figure 6 shows an example of the impact of chemometrics on the analysis of olive oils. The cultivar–composition relationship in Sicilian olive oils was recently explored through the use of high-resolution ^{13}C NMR spectra.[76] For 60 monovarietal extra virgin olive oils, MANOVA selected 46 variables (^{13}C resonances) as input for the PCA, TCA, MDS, (multidimensional scaling) and LDA analysis. Figure 6a shows the dendrogram resulting from the TCA analysis. Several distinct clusters based on the cultivar were identified, with three levels of discrimination observed. The LDA results are shown in Fig. 6b where the first scores for the first three principal components are displayed. The four different olive oil cultivars are clearly separated. These ^{13}C NMR results were also able to show that the cultivar separation is dominated by the identity of the fatty acids in the *sn*-1,3 position of the glycerol triesters.[76]

Site-specific natural isotope fractionation (SNIF) NMR, which determines different $(D/H)_i$ isotope ratios from the ^{2}H NMR spectra, has been used to characterize essential oils derived from a variety of botanicals (lavender, spike lavender, bose de rose oil, bergamont, germanium, clary sage, petit grain, coriander, Formosan, and camphor oil) and geographical regions versus synthetically produced oils. These SNIF–NMR results combined with DA allowed the natural and synthetic oils to be unambiguously indentified.[77]

The ability to detect adulteration of orange juices using PCA and KNN chemometric methods on the high-resolution ^{1}H spectra of juices has also been reported.[78] NMR proved to be an excellent general screening tool for the detection of pulp wash, beet sugars, preservatives or other adulterants in authentic orange juice samples. In this study, the PLF method of Vogels *et al.*[41] (see Section 2.2) was used to correct for shifts in peak resonances due to variation in the relative concentrations of sample components (in particular a series of organic acids). PCA and LDA methods applied to the ^{1}H NMR spectra of >300 orange and pulp wash juices has also been reported, and identified dimethylproline as a possible marker of orange juice adulteration. The chemometric results revealed an additional 21 NMR resonances that might be used as markers in the future.[79] Analysis of the ^{1}H NMR spectra for apple juices from three different varieties (Bramley, Russett and Sparten) were studied using PCA and LDA methods, and were able to obtain 100% success rate in the classification.[80] From the PCA analysis it was revealed that malic acid and sucrose were the two most important chemical species involved in the discrimination of the different apple classes.

Chemometrics has been used to classify Apulian and Slovenian wines from ^{1}H NMR.[81,82] PCA, FA, LDA, and KNN analysis of ^{2}H nuclear magnetic resonance SNIF-NMR coupled with isotope ratio mass spectrometry (IRMS) has also been reported

for the identification of geographical origin and adulteration of wines.[83–85] In these studies the NMR spectra were not used directly to create the data matrix **D**, but instead utilized the deuterium/hydrogen (D/H) ratios of the methyl and methylene groups in ethanol, the ratio (R) of the methyl and methylene intensity in a ^{2}H NMR spectra, along with the $^{13}C/^{12}C$ ($\delta^{13}C$) and the $^{18}O/^{16}O$ ($\delta^{18}O$) ratios obtained from IRMS. A PCA–DA analysis of ^{1}H and ^{13}C NMR spectra of German white wines has also been reported, and has allowed for the identification and classification of geographical origin in these wines.[86]

Chemometric techniques have also been used to identify grapevine cultivars and clones based on the ^{1}H and ^{13}C NMR of polyphenols observed in extracts.[73,87] Extractions from crushed grape seeds and vines obtained in France were analyzed using HMBC and HMQC (heteronuclear multiple quantum correlation) 2D $^{1}H-^{13}C$ NMR experiments. From these 2D spectra between 48 and 120 correlation peaks were integrated, and these integrals were used as input variables in the data matrix **D**. The analysis of variance (ANOVA) routines were used to select the variables (typically between 6 and 13) used by the subsequent PCA and HCA methods. These studies demonstrated that it was possible to differentiate between grape vine cultivars and clones. SNIF–NMR was used to provide D/H ratios in concentrated rectified grape musts (grape sugar solutions) along with finite mixture distribution analysis rules based on Mahalanobis distance measurements to identify adulterations by addition of sugars from sources other than grape (beet and cane).[88]

Chemometrics and NMR have also been extended to other food science areas beyond the oil, wine, and juice sector. For example, chemometrics has been used to develop correlations between parameters of meat and sausage quality, and the ^{1}H Carr-Purcell-Meiboom-Gill (CPMG) transverse T_2 relaxation and spin-lattice T_1 relaxation.[30,31,36] Closely related experiments have been reported for ^{1}H NMR studies of fish flesh.[32] The ^{1}H CPMG T_2 and T_1 relaxation time domain signal have been analyzed in a series of butters and margarines to correlate these parameters with water content and type of fat within the spread.[34] ^{1}H CPMG T_2 and spin-lattice T_1 relaxation time domain signals in gelatins have been studied using ANOVA and PLS.[89,90] Process ^{1}H NMR on bread used PCA and PLS methods to correlate the CPMG T_2 relaxation to characterize the role of water during the bread baking and staling process.[33] Finally, solid state ^{1}H MAS NMR spectra of durum wheat flours have been analyzed using PCA methods allowing for the identification of flour origin.[91]

5.2. Materials chemistry

Some of the earliest chemometric NMR analysis of materials involved the PCA of organic peat using ^{13}C CPMAS NMR spectra,[92] and the analysis of ^{1}H and ^{13}C NMR relaxation parameters in coal.[93] Chemometrics and ^{13}C CPMAS has also been applied to classify soil organic matter.[94] Clayden and co-workers have used FA of the time domain ^{19}F NMR signal in poly(tetrafluoroethane), PTFE polymers as a method to measure crystallinity. It was demonstrated that the dominant principal component did not correlate well, but that the scores of second and third principal component show an excellent correlation with the PTFE crystallinity. PLS methods have also been used to determine

the total styrene content in styrene/butadiene copolymers from the solid state ^{1}H NMR time domain signal from a process NMR.[27]

Multivariate techniques have also proven important in the analysis of cellulose-based material and wood pulps. PLS analysis of the solid state ^{13}C CPMAS NMR spectra of softwood kraft pulp allowed models for the variation of the kappa number to be developed[26] while PLS methods on the ^{1}H NMR free induction decay allowed for the calibration of both water content and wood density.[35] Additional ^{13}C CPMAS NMR studies of pulp composition and kinetics have been reported.[95,96] By combining the result of both ^{13}C, ^{31}P NMR and size exclusion chromatography (SEC), multivariate techniques were used to establish relationships between the chemical structure of the hardwood and softwood lignins within the kraft black liquors and the combustion properties of these woods such as burning times and swelling values.[97] In these combustion and swelling studies the input variables included defined spectral regions from both the ^{31}P and the ^{13}C NMR spectra, such that inspection of the loadings of the significant principal components from the ^{31}P NMR spectra revealed the existence of different lignin–carbohydrate complexes within the woods. PLS methods have also allowed for the correlation between wood pulp processing variables such as filter clogging and alkali resistance and combined spectral results from both solid state ^{13}C CPMAS NMR spectra and NIR spectroscopy.[98] A combination of PCA and PLS methods have been reported in the analysis of ^{13}C CPMAS NMR spectra of lignocellulosic materials to identify and quantify the two crystalline forms of cellulose (I_α and I_β) along with the amorphous fraction,[99] the transformation of cellulose due to alkali treatment,[100] along with the characterization of the non-crystalline form of cellulose in birch pulp and cotton linters.[101] PCA analysis of ^{13}C CPMAS NMR spectra allowed for the identification of pulp fibers from different wood species.[102]

5.3. Chemistry

The early investigations of multivariate and chemometric analysis as applied to NMR spectra was directed towards complex mixtures, including analysis of substituent and solvent shifts, and isolation of ^{13}C NMR spectra for individual components.[103] In a very interesting application of PCA, KNN, and SIMCA methods Goux and coworkers[104–106] were able to classify unknown peracetylated oligosaccharide residues. Using a series of homonuclear and heteronuclear 2D NMR experiments they assigned specific ^{13}C and ^{1}H resonances, along with a set of $^{1}H-^{1}H$ J couplings. Instead of using the actual NMR spectra to form the input data matrix [**D** in Eq. (4)] these researchers used select chemical shifts and J couplings (up to 15 variables) to form **D**. This is an excellent example of using mixed NMR variables for the chemometric analysis. PR methods using LDA were also used in the analysis of 2D $^{1}H-^{13}C$ HMBC NMR experiments on the urine of steers and cows undergoing hormonal treatment.[107] This study utilized a two-step algorithm for filtering of input variables, combining an ANOVA and a step-wise introduction of informative variables, to select the most important variables while eliminating those variables that are correlated to those already in the candidate variable set.[107]

The combination of NMR and near-infrared (NIR) spectral data prior to chemometric analysis has also been reported. Rutledge and co-workers[29] used the time-domain

NMR signal along with the NIR spectra to investigate sugar solutions. By using outer product analysis (OPA), correlations between the NMR and NIR signals could be discerned, and provided insight into the hydration phenomena. This unique combination of spectral data should prove to be another fruitful area of future research.

The ^{1}H NMR spectra of Australian gasoline was analyzed using HCA and FA methods, allowing the influence of different chemical species on the octane number to be evaluated.[108] Correlations between the biological demand (BOD) in industrial waste water and the ^{1}H NMR spectra were developed using a PLS model.[109]

Chemometric analysis of the ^{17}O NMR in primary alcohol mixtures has also been described.[110] Figure 7a shows the solution ^{17}O NMR spectra for 26 mixtures of five different primary alcohols (3-methyl-1-butanol, butanol, propanol, pentanol, and ethanol). The rapid quadrupolar relaxation produces significant spectral broadening, such that the individual species are not visually discernable. Initial PLS models revealed poor precision due to spectral overlap between the different alcohols. Through the use of net analyte signal (NAS) analyses these overlapping resonances were identified, allowing grouping of similar alcohol species and the development of more robust calibration methods. Significant improvement in the prediction for the concentration of the different alcohol species was achieved. The resulting predictions using these modified PLS models are shown in Fig. 7b where propanol and butanol species were combined.

5.4. Hyphenated NMR

In the future multivariate or chemometric analysis will see significant utilization in hyphenated NMR analysis. Hyphenated NMR techniques, including LC–NMR, HPLC–NMR, and LC–MS–NMR, can produce large amounts of NMR data in a short period of time requiring automated data analysis methods. In LC–NMR and HPLC–NMR there have been several demonstrations of the power of chemometrics. In these hyphenated NMR studies, chemometrics can be used to resolve components in the chromatographic profile, as well as extract the NMR spectra for individual components in the spectra dimension. PCA analysis of the LC–NMR separation of three region-isomers of dihydroxynapthalene has been reported.[111] In this study, the researchers explored the impact of including the full dataset versus selected components containing the most important PC, as well as different methods to present the PCA analysis. The impact of different scaling techniques prior to PCA analysis on the results was also evaluated. These authors further extended the procedure for the chemometric analysis of LC–NMR with the case study analysis involving the separation of three polyaromatic hydrocarbons.[112] In that study the authors used a combination of evolving principal component analysis (EPCA), canonical correlation analysis (CCA) and constrained non-negative least squares to determine the number and relationship of analytes between spectroscopic peak clusters. Additional work comparing the different chemometric methods to determine the number and elution position of components in HPLC–NMR studies of dihydroxynapthalene mixtures has also been reported.[51] This work showed that the performance of various chemometric techniques were different for

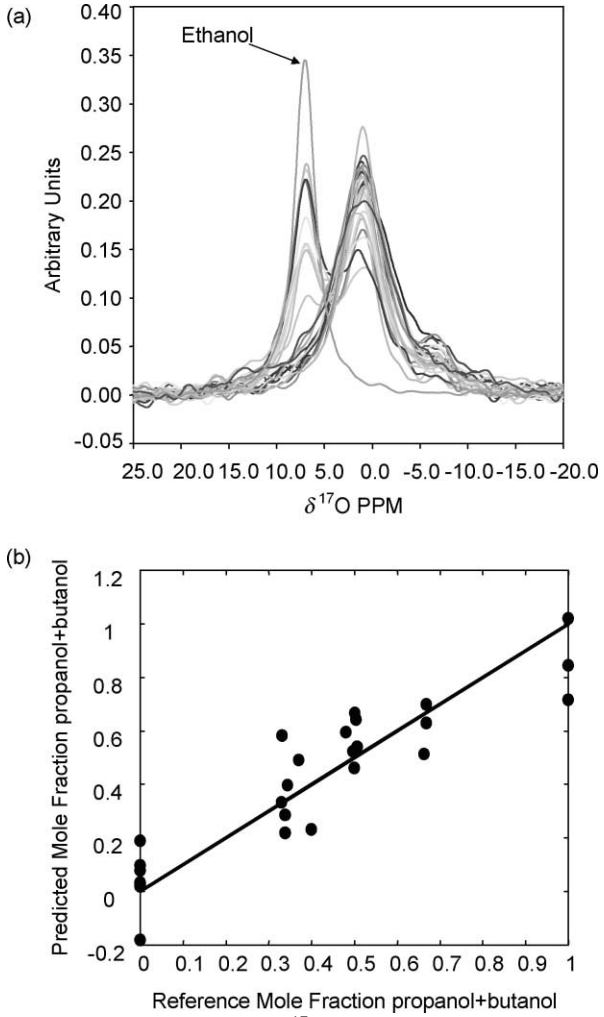

Fig. 7. A data set containing (a) the solution ^{17}O NMR spectra for 26 mixtures of five primary alcohols. Broad line shapes are observed in the ^{17}O NMR due to rapid quadrupolar relaxation, making the discrimination of the individual resonance difficult. Original PLS predictions for the primary alcohols in these complex mixtures were very poor. Through the utilization of net analyte signal (NAS) methods, the combination of propanol and butanol alcohols into a single analysis group (based on carbon chain length) greatly improved the resulting (b) PLS predictions. Figure adapted from the work of Alam and Alam.[110]

the HPLC–NMR versus diode array detector (DAD)–HPLC data, demonstrating the need to optimize the analysis methods to a particular detection scheme. It is expected that chemometrics will play an increasing role in the analysis of hyphenated NMR data in the future.

6. SPECTRAL RESOLUTION METHODS

In some investigations it may be important to extract the pure component spectra (**S**) and the associated concentration (**C**) for the different species present within a mixture. A generalized solution to Eq. (4) has an infinite number of solutions available, while analysis methods such as PCA produce abstract factors that are linear combinations of the pure component spectra and concentrations [Eq. (15)]. An additional transformation step is required to rotate these abstract factors into the pure component spectra and pure concentration profiles. Two specific examples that allow this transformation step are presented below.

6.1. Multivariate curve resolution

The objective of multivariate curve resolution (MCR) methods is to obtain the pure component spectra and concentrations described by Eq. (4). The concentration information obtained is relative percent. By imposing constraints on the possible solutions, through either chemical or physical bounds, the resulting concentrations and spectra will hopefully reflect the true result. A common way to implement MCR is using constrained alternating least-squares (ALS) optimization.[113] Constraints that can be applied include:[114,115] non-negativity, unimodality, common concentration profiles in chromatography runs, and equality. In NMR both the concentration and spectra are assumed to be non-negative, while unimodality and common concentration profile constraints can be imposed during hyphenated NMR analysis. Equality constraints can be applied if there are spectra or concentrations that are known and are not to change during the optimization. Under ALS, initial input guesses to either the concentration ($\mathbf{C}_{\text{init}}$) or pure component spectra matrix ($\mathbf{S}_{\text{init}}$) are made. Recall that the data matrix is described by the product of a concentration and pure component spectra matrix.

$$\mathbf{D} = \mathbf{CS} \tag{42}$$

The alternative matrix (**C** or **S**) is then estimated ($\hat{\mathbf{C}}$ or $\hat{\mathbf{S}}$), followed by applying the constraints to that specific matrix ($\tilde{\mathbf{C}}$ or $\tilde{\mathbf{S}}$)

$$\hat{\mathbf{S}} = \mathbf{C}_{\text{init}}^{\text{T}}\mathbf{D}, \qquad \tilde{\mathbf{S}} \Leftarrow \hat{\mathbf{S}} \qquad \text{(constraints)} \tag{43}$$

$$\hat{\mathbf{C}} = \mathbf{D}\tilde{\mathbf{S}}^{\text{T}}, \qquad \tilde{\mathbf{C}} \Leftarrow \hat{\mathbf{C}} \qquad \text{(constraints)} \tag{44}$$

The estimated and constrained concentration and pure component spectra matrices are then used to estimate the data matrix, allowing the error to be evaluated and checked for convergence. If convergence is not reached the process is repeated using $\tilde{\mathbf{C}}$ as the initial input into Eq. (43).

$$\mathbf{D} = \tilde{\mathbf{C}}\tilde{\mathbf{S}}, \qquad E_{\text{D}} = \hat{\mathbf{D}} - \mathbf{D} \tag{45}$$

Additional details are described in the literature.[114–117]

6.2. Direct exponential curve resolution algorithm

Chemometrics has seen an increased presence in the analysis of NMR spectral data,[9] especially the analysis of multidimensional data. One of the more important advances in spectral resolution methods or three-way data analysis techniques has been the implementation of the direct exponential curve resolution algorithm (DECRA)[118] to a wide range of different NMR experiments. In NMR, spin-lattice relaxation, spin–spin relaxation or diffusion can be used to produce NMR data sets where the variation of signal intensities can be described by a simple exponential. It is these decay or relaxation data matrices for which DECRA was developed. The underlying basis of the DECRA method involves the creation of two proportional data sets from a single data matrix. When utilizing DECRA the decay in the original data matrix must be described by single-exponential behavior, and the individual spectra within the data matrix must be obtained at equally spaced intervals along the decay profile. Analysis of data sets containing several overlapped spectral components is one situation where DECRA has proven superior in its ability to resolve complex mixtures.[119]

Recall that the data matrix can be described as the product of the concentration and the pure component spectra [Eq. (42)], but that the solution to this relationship is not trivial or unique. It was demonstrated by Kubista[120] that if two proportional data sets can be obtained for a sample, then an unambiguous unique solution (i.e., the single correct solution) is obtained through a self-modeling analysis of the spectral data sets. These two proportional data sets **A** and **B** can be formulated as

$$\mathbf{A} = \mathbf{CS}, \qquad \mathbf{B} = \mathbf{C}\alpha\mathbf{S} \tag{46}$$

where α is the diagonal proportionality matrix. Booksh and Kowalski[121] reformulated the Kubista method in terms of the generalized rank annihilation method (GRAM).[122,123] Note that we have elected to use the nomenclature **A** and **B** instead of the previously used **D** [Eq. (4)] to denote the different data matrices, and to clearly distinguish these matrices as proportional data sets. In addition, many of the previous DECRA derivations decompose the data matrices as $\mathbf{A} = \mathbf{CS}^{\mathrm{T}}$ where the transpose is utilized because in those descriptions the pure component spectral matrix is in a column representation $(n_{\mathrm{freq}} \times n_{\mathrm{comp}})$, and is the transpose of the definitions we presented in Section 2.1. Rearrangement of Eq. (46) leads to the generalized eigenvalue problem

$$\mathbf{AS}^{+}\alpha = \mathbf{BS}^{+}, \qquad \mathbf{AZ}\alpha = \mathbf{BZ} \tag{47}$$

where $\mathbf{Z} = \mathbf{S}^{+}$, and $+$ designates the pseudoinverse of the matrix. The matrix **Z** can be calculated using standard numerical routines if the **A** and **B** matrices are square. If they are not square they can be projected into a common space in order to obtain an equation with square matrices. As discussed in detail by Windig and Antalek[118] there are several common spaces that can be utilized. For example the latent variables of **A** can be chosen

for the projection. The matrix **A** is now estimated using the significant factors of the SVD

$$\mathbf{A} = \overline{\mathbf{U}\mathbf{\Sigma}\mathbf{V}}^{\mathrm{T}} \tag{48}$$

where the bar refers to truncation of the matrices to significant factors within the experimental noise range. Combining Eqs. (47) and (48) leads to a standard eigenvalue problem.

$$\mathbf{Z}^{*}\alpha = (\overline{\mathbf{U}}^{\mathrm{T}}\mathbf{B}\overline{\mathbf{V}\mathbf{\Sigma}}^{-1})\mathbf{Z}^{*} \tag{49}$$

where $\mathbf{Z}^{*} = \overline{\mathbf{\Sigma}\mathbf{V}}^{\mathrm{T}}\mathbf{Z}$. Since $(\mathbf{U}^{\mathrm{T}}\mathbf{B}\overline{\mathbf{V}\mathbf{S}}^{-1})$ is square, $\mathbf{Z}^{*}$ will contain the eigenvectors and α will contain the eigenvalues. The pure component spectra, pure component concentrations and the reconstructed spectral data set are then derived from the eigenvectors $\mathbf{Z}^{*}$ as follows:

$$\hat{\mathbf{S}} = (\overline{\mathbf{V}\mathbf{\Sigma}}^{-1}\mathbf{Z}^{*})^{+} \tag{50}$$

$$\hat{\mathbf{C}} = \bar{\mathbf{U}}\mathbf{Z}^{*} \tag{51}$$

$$\hat{\mathbf{D}} = \hat{\mathbf{C}}\hat{\mathbf{S}} \tag{52}$$

where $\hat{\mathbf{S}}, \hat{\mathbf{C}}$ and $\hat{\mathbf{D}}$ designate the predicted pure component spectra, concentrations and reconstructed data set, respectively.

Schulze and Stilbs reported an example for PGSE NMR experiments in which two individual proportional data sets were collected by using different gradient ratios.[124] Antalek and Windig[118,125] later demonstrated that for data matrices, where each spectral component decays exponentially, a single data set could be split into the two proportional data sets required in Eq. (47). For equally spaced intervals along the exponential relaxation function this proportionality constant is easily recognized if one determines the ratio of the signal intensity of the ith component, $I_i(\omega)$, for any two adjacent time points (τ_n and τ_{n+1}) with an exponential decay of rate R_i. This ratio of signal intensities for two adjacent time points is given by

$$\frac{I_i(t = \tau_n)}{I_i(t = \tau_{n+1})} \approx \exp[-R_i(\tau_n - \tau_{n+1})] = \exp[-R_i(\Delta\tau)] = \alpha \tag{53}$$

To obtain the two proportional data sets, one data set (**A**) can be built from the 1 to $n_{\mathrm{samp}} - 1$ spectra (along the exponential decay), while the second data set (**B**) can be constructed using the 2 to n_{samp} spectra in the decay profile. Figure 8 shows a graphical representation detailing the creation of these two proportional data sets from a single decay or relaxation NMR data set. This splitting of spectral data sets is rather unique to the DECRA algorithm. The use of two proportional data sets can reduce many difficulties with instrumental stability, spectral distortions, non-linear behavior of gradients or differences in the rank of the data matrices.

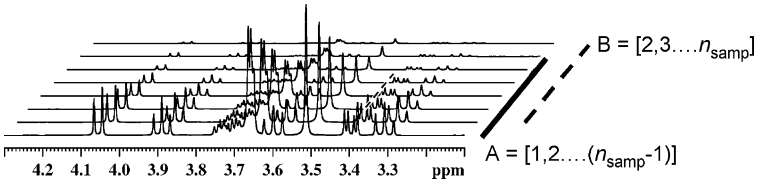

Fig. 8. A representation of how two proportional data sets are extracted from a single NMR data set during the direct exponential curve resolution algorithm (DECRA). Data set **A** uses spectra 1 through $(n_{samp} - 1)$, while data set **B** used spectra 2 through n_{samp}.

6.3. Examples of MCR and DECRA

MCR has been used to analyze the kinetic ^{1}H NMR data for studies involving the interaction of *cis*-platinum (cisplatin) and polynucleotides.[126] By imposing non-negativity constraints on both the concentrations and NMR spectra of the pure components, the constraint of unimodal concentration profiles and a fixed total polynucleotide concentration during the experiment, pure component spectra of the different polynucleotide interaction species formed were quickly identified through alternating least squares (ALS) methods. The use of MCR–ALS has also been used for the resolution of overlapping spectral features in the ^{1}H NMR investigation of hydrolysis kinetics for a sulfonylurea herbicide.[127] In this MCR example, a kinetic constraint was employed during the analysis.

Eads and co-workers described a method called molecular factor analysis (MFA) that utilizes self-modeling curve resolution in conjunction with ALS.[128] By applying non-negativity to the NMR spectra and to the concentration matrix, along with a minimal complexity constraint, MFA was able to provide a realistic solution to Eq. (42). The authors demonstrated that MFA can extract the pure component spectra from data sets of complex mixtures. They also demonstrated that the principal components obtained using PCA for the same NMR data have very little resemblance to the pure component spectra obtained using MFA. The ability to determine the NMR spectra of the pure components, along with the corresponding concentrations, allows researchers to follow changes in the relative concentration of the different species in complex mixtures. A study utilizing the interactive self-modeling mixture analysis (SIMPLISMA) approach to analyze NMR of surfactants has also been recently reported.[129] This curve resolution method utilizes the combination of both conventional and second-derivative spectra to help resolve overlap in NMR spectra containing both narrow and broad components.

Implementations of the DECRA method include analysis of pulsed gradient spin echo (PGSE) NMR studies of mixtures,[130] PGSE NMR studies of surfactants,[118,125,131] PGSE NMR studies of polymers,[119,132] and magnetic resonance imaging (MRI).[131,132] In an interesting study, the solid state ^{13}C CPMAS NMR data sets for a pharmaceutical compound were analyzed using DECRA. In these experiments the exponential decay of the signal intensity in the data matrix **D** decayed as a result of ^{1}H spin lattice T_1 relaxation. The DECRA results allowed the resolution of two distinct crystalline polymorphs within the compound.[133,134] DECRA has also used to analyze the ^{13}C MAS NMR spectra of irradiated cross-linked polyolefin cable insulation. In this study, the two proportional data

sets were created from a data set based on differences in the ^{13}C T_1 relaxation times.[135] Using DECRA the line shapes for the intermediate and amorphous polymer components were directly obtained, which allowed the changes in morphology during irradiation to be determined. DECRA has also been used to analyze both the ^{1}H and ^{19}F time domain signals in low-field NMR applications.[136]

As an example of the pure component spectral resolution power of DECRA, Fig. 9 shows the results obtained from the ^{1}H PGSE NMR investigation of a mixture of glucose and sucrose. DECRA nicely resolved the individual spectra for these two molecular species, even though there was a high degree of spectral overlap. The resulting extracted glucose and sucrose spectra are almost identical to pure solutions of the individual components. Spectral 'mixing' within the extracted pure component spectra was noted in some instances, but was the result of experimental artifacts that produced non-exponential relation behavior during the diffusion experiment. Antalek was able to devise an elegant series of modified pulse sequences to eliminate these effects.[130]

There has also been a recent assessment of different methods for the processing of diffusion ordered spectroscopy (DOSY) NMR experiments.[137] This included the evaluation of iterative single channel methods including single channel methods such as

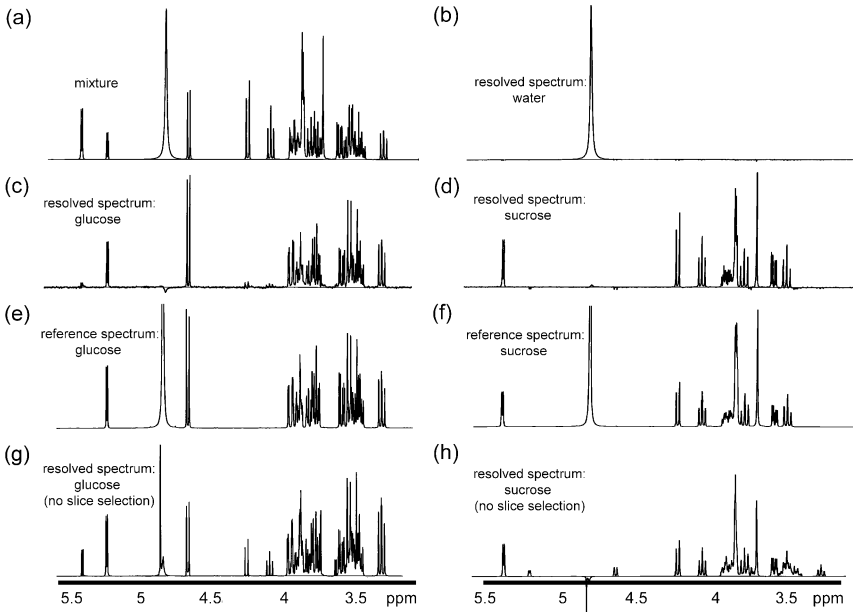

Fig. 9. DECRA results for a PGSE NMR study of a complex mixture, allowing the resolution of individual pure component spectra. The (a) original ^{1}H NMR (first spectra in the PGSE data matrix) for a solution of glucose and sucrose, the DECRA-resolved (b) H_2O spectrum, (c) glucose spectrum, and (d) sucrose spectrum, along with the reference spectra for (e) glucose, and (f) sucrose. In addition, the DECRA-resolved NMR spectra from a data set acquired without the use of slice selection for (g) glucose and (h) sucrose. Note the large residual signals (mixing) of other components in each of the resolved spectra in (g) and (h) due to the non-exponential decay. This spectral mixing is dramatically reduced with the use of slice selection during the PGSE experiment as seen in (c) and (d). Figure obtained from Antalek [130] and reprinted by permission of Wiley.

the routine SPLMOD and continuous diffusion coefficient (CONTIN) method versus multivariate DECRA and MCR methods. On a limited experimental example, the separation of true pure components and related diffusion decay profiles using the PCA–VARIMAX–MCR and iterative principal component analysis (IPCA)–MCR methods were cleaner than those obtained using the DECRA methods. It was shown that for the example studied that the IPCA–MCR overall gave the superior results. Part of this difference in methods was attributed to the dependence of DECRA on a single-exponential relaxation, which Hou and co-workers attributed to non-linearity in the gradient strengths (g) and subsequent spacing of g^2. The MCR analysis does not depend on the nature of the signal decay (i.e., not required to be exponential). Other experimental causes of non-exponential decay in DOSY experiments have been previously discussed, and demonstrated to be significant in producing mixed pure component spectra (see Fig. 9).[130] A more thorough investigation into the impact of non-exponential relaxation and decay behavior on the DECRA experiment has also been recently reported, in which it was demonstrated that the existence of components with non-exponential relaxation behavior can impact the quantification and extraction of the NMR spectra of other components (with pure exponential decay) within the mixture.[138]

7. CONCLUSIONS AND FUTURE DIRECTIONS

The impact of chemometrics on the analysis of NMR spectral data from a wide range of disciplines is becoming significant. The increased complexity and dimensionality of NMR data produced in a wide range of disciplines has made visual interpretation of spectra challenging. The coupling of NMR with other spectroscopies, and the increased utilization of hyphenated NMR techniques, requires automated analysis for the rapid and accurate interpretation of the resulting data. Outside of the metabonomic field, the use of chemometrics will most significantly benefit the analysis of hyphenated NMR data. Chemometrics provides a set of promising methods for the analysis of NMR data, and with further development will become an important tool within the NMR community.

ACKNOWLEDGEMENTS

Sandia is a multiprogram laboratory operated by Sandia Corporation, a Lockheed Martin Company, for the United States Department of Energy's National Nuclear Security Administration under contract DE-AC04-94AL85000. The authors are indebted to the numerous researchers who supplied copies of their figures, and preprints of ongoing research.

REFERENCES

1. P. A. Keifer, *Magn. Reson. Chem.*, 2003, **41**, 509.
2. H. Pham-Tuan, L. Kaskavelis, C. A. Daykin and H.-G. Janssen, *J. Chromatogr. B*, 2003, **789**, 283.
3. G. C. Leo, A. Krikava and G. W. Caldwell, *Anal. Chem.*, 2003, **75**, 1954.
4. W. Maas, Monitoring Metabolism. *Today's Chemist at Work*, 2004, 21.
5. K. Albert, ed., *On-Line LC-NMR and Related Techniques*, Wiley, Chichester, 2002.
6. E. Malinowski, *Factor Analysis in Chemistry*, Wiley, New York, 1991.
7. E. Holmes and H. Antti, *Analyst*, 2002, **127**, 1549.
8. J. C. Lindon, E. Holmes and J. K. Nicholson, *Prog. NMR Spectrosc.*, 2001, **39**, 1.
9. T. M. Alam and M. K. Alam, *Spectroscopy*, 2001, **16**, 18.
10. U. Edlund and H. Grahn, *J. Pharm. Biomed. Anal.*, 1991, **9**, 655.
11. H. Grahn, F. Delaglio, M. A. Delsuc and G. C. Levy, *J. Magn. Reson.*, 1988, **77**, 294.
12. M. A. Sharaf, D. L. Illman and B. R. Kowalski, *Chemometrics*, Wiley, New York, 1986.
13. H. Martens and T. Næs, *Multivariate Calibration*, Wiley, New York, 1989.
14. R. A. Johnson and D. W. Wichern, *Applied Multivariate Statistical Analysis*, Prentice-Hall, Upper Saddle River, 2002.
15. J. K. Nicholson, J. C. Lindon and E. Holmes, *Xenobiotica*, 1999, **29**, 1181.
16. J. K. Nicholson, J. C. Connelly, J. C. Lindon and E. Holmes, *Nature Reviews Drug Discovery*, 2002, **1**, 153.
17. J. C. Lindon, J. K. Nicholson and J. R. Everett, *Ann. Rep. NMR Spectrosc.*, 1999, **38**, 1.
18. J. C. Lindon, J. K. Nicholson, E. Holmes and J. R. Everett, *Concepts Magn. Reson.*, 2000, **12**, 289.
19. H. Grahn and P. Geladi, *Signal Treatment and Signal Analysis in NMR*, D. N. Rutledge, ed., Elsevier, Amsterdam, 1996.
20. W. El-Deredy, *NMR Biomed.*, 1997, **10**, 99.
21. G. E. P. Box, W. G. Hunter and J. S. Hunter, *Statistics for Experimenters: An Introduction to Design, Data Analysis, and Model Building*, Wiley, New York, 1978.
22. Cornell, *Experiments with Mixtures*, Wiley, New York, 1990.
23. R. R. Ernst, G. Bodenhausen and A. Wokaun, *Principles of Nuclear Magnetic Resonance in One and Two Dimensions*, Oxford University Press, New York, 1987.
24. X. Lai, M. Sardashti, B. J. Lane, J. J. Gislason and D. J. O'Donnell, *Appl. Spectrosc.*, 2000, **54**, 54.
25. N. J. Clayden, R. J. Lehnert and S. Turnock, *Anal. Chim. Acta*, 1997, **344**, 261.
26. J. B. Hauksson, U. Edlund and J. Trygg, *Magn. Reson. Chem.*, 2001, **39**, 267.
27. M. Sardashti, J. J. Gislason, X. Lai, C. A. Stewart and D. J. O'Donnell, *Appl. Spectrosc.*, 2001, **55**, 467.
28. D. N. Rutledge, A. S. Barros and F. Gaudard, *Magn. Reson. Chem.*, 1997, **35**, S13.
29. D. N. Rutledge, A. S. Barros and R. Giangiacomo, *R. Soc. Chem. Spec. Publ.*, 2001, **262**, 179.
30. R. J. S. Brown, F. Capozzi, C. Cavani, M. A. Cremonini, M. Petracci and G. Placucci, *J. Magn. Reson.*, 2000, **147**, 89.
31. J. Brødum, D. V. Byrne, L. S. Bak, G. Bertelsen and S. B. Engelsen, *Meat Sci.*, 2000, **54**, 83.
32. S. M. Jepsen, H. T. Pedersen and S. B. Engelsen, *J. Sci. Food Agric.*, 1999, **79**, 1793.
33. S. B. Engelsen, M. K. Jensen, H. T. Pedersen, L. Nørgaard and L. Munck, *J. Cereal Sci.*, 2001, **33**, 59.
34. D. N. Rutledge and A. S. Barros, *Analyst*, 1998, **123**, 551.
35. L. G. Thygesen, *Holzforschung*, 1996, **50**, 434.
36. A. Gerbanowski, D. N. Rutledge, M. H. Feinberg and C. J. Ducauze, *Sci. Aliments*, 1997, **17**, 309.
37. M. Spraul, P. Neidig, U. Klauck, P. Kesseler, E. Holmes, J. K. Nicholson, B. C. Sweatman, S. R. Salman, R. D. Farrant, E. Rahr, C. R. Beddell and J. C. Lindon, *J. Pharm. Biomed. Anal.*, 1994, **12**, 1215.
38. T. R. Brown and R. Stoyanova, *J. Magn. Reson. Ser. B*, 1996, **112**, 32.
39. H. Witjes, W. J. Melssen, H. J. A. in 't Zandt, M. van der Graff, A. Heerschap and L. M. C. Buydens, *J. Magn. Reson.*, 2000, **144**, 35.
40. R. Stoyanova and T. R. Brown, *J. Magn. Reson.*, 2002, **154**, 163.
41. J. T. W. E. Vogels, A. C. Tas, J. Venekamp and J. van der Greef, *J. Chemom.*, 1996, **10**, 425.
42. R. J. O. Torgrip, M. Åberg, B. Karlberg and S. P. Jacobsson, *J. Chemom.*, 2003, **17**, 573.

43. H. C. Keun, T. M. D. Ebbels, H. Antti, M. E. Bollard, O. Beckonert, E. Holmes, J. C. Lindon and J. K. Nicholson, *Anal. Chim. Acta*, 2003, **490**, 265.
44. S. Wold, H. Antti, F. Lindgren and J. Öhman, *Chemom. Intell. Lab. Syst.*, 1998, **44**, 175.
45. J. Sjöblom, O. Svensson, M. Josefson, H. Kullberg and S. Wold, *Chemom. Intell. Lab. Syst.*, 1998, **44**, 229.
46. J. A. Westerhuis, S. de Jong and A. K. Smilde, *Chemom. Intell. Lab. Syst.*, 2001, **56**, 13.
47. O. Svensson, T. Kourti and J. F. MacGregor, *J. Chemom.*, 2002, **16**, 176.
48. J. Trygg and S. Wold, *J. Chemom.*, 2002, **16**, 119.
49. B. M. Beckwith-Hall, J. T. Brindle, R. H. Barton, M. Coen, E. Holmes, J. K. Nicholson and H. Antti, *Analyst*, 2002, **127**, 1283.
50. C. L. Gavaghan, I. D. Wilson and J. K. Nicholson, *FEBS Lett.*, 2002, **530**, 191.
51. M. Wasim, M. S. Hassan and R. G. Brereton, *Analyst*, 2003, **128**, 1082.
52. B. C. M. Potts, A. J. Deese, G. J. Stevens, M. D. Reily, D. G. Robertson and J. Theiss, *J. Pharm. Biomed. Anal.*, 2001, **26**, 463.
53. H. C. Keun, T. M. D. Ebbels, H. Antti, M. E. Bollard, O. Beckonert, G. Schlotterbeck, H. Senn, U. Niederhauser, E. Holmes, J. C. Lindon and J. K. Nicholson, *Chem. Res. Toxicol.*, 2002, **15**, 1380.
54. J. Gislason, H. Chan and M. Sardashti, *Appl. Spectrosc.*, 2001, **55**, 1553.
55. R. Stoyanova, A. C. Kuesel and T. R. Brown, *J. Magn. Reson., Ser. A*, 1995, **115**, 265.
56. D. M. Haaland and E. V. Thomas, *Anal. Chem.*, 1988, **60**, 1193.
57. G. Strang, *Linear Algebra and its Applications*, Harcourt, Brace and Jovanovich, New York, 1988.
58. P. Geladi and B. R. Kowalski, *Anal. Chim. Acta*, 1986, **185**, 1.
59. M. A. Dempster, B. F. MacDonald, P. J. Gemperline and N. R. Boyer, *Anal. Chim. Acta*, 1995, **310**, 43.
60. M. Sjostrom and B. R. Kowalski, *Anal. Chim. Acta, Comput. Tech. Optimization*, 1979, **112**, 11.
61. B. R. Kowalski and C. F. Bender, *Anal. Chem.*, 1972, **44**, 1405.
62. W. Wu and D. L. Massart, *Anal. Chim. Acta*, 1997, **349**, 253.
63. I. E. Frank and J. H. Friedman, *J. Chemom.*, 1989, **3**, 463.
64. C. Antz, K.-P. Neidig and H. R. Kalbitzer, *J. Biomol. NMR*, 1995, **5**, 287.
65. B. J. Hare and J. H. Prestegard, *J. Biomol. NMR*, 1994, **4**, 35.
66. S. A. Corne, *Signal Treatment and Signal Analysis in NMR*, Vol. 18, D. N. Rutledge, ed., Elsevier, Amsterdam, 1996.
67. L. Mannina, P. Barone, M. Patumi, P. Fiordiponti, M. C. Emanuele and A. Serge, *Recent Res. Devel. Oil Chem.*, 1999, **3**, 85.
68. L. Mannina, C. Calcagni, E. Rossi and A. Serge, *Annali di Chim.*, 2003, **93**, 97.
69. C. Fauhl, F. Reniero and C. Guillou, *Magn. Reson. Chem.*, 2000, **38**, 436.
70. S. Sacchi, M. Patumi, G. Fontanazza, P. Barone, P. Fiordiponti, L. Mannina, E. Rossi and A. L. Serge, *J. Am. Oil Chem. Soc.*, 1996, **73**, 747.
71. L. Mannina, A. P. Sobolev and A. Serge, *Spectrosc. Europe*, 2003, **15**, 6.
72. L. Mannina, M. Patumi, N. Proietti, D. Bassi and A. L. Serge, *J. Agric. Food Chem.*, 2001, **49**, 2687.
73. A. D. Shaw, A. di Camillo, G. Vlahov, A. Jones, G. Bianchi, J. Rowland and D. B. Kell, *Anal. Chim. Acta*, 1997, **348**, 357.
74. G. Vlahov, A. D. Shaw and D. B. Kell, *J. Am. Oil Chem. Soc.*, 1999, **76**, 1223.
75. L. Mannina, M. Patumi, N. Proietti and A. L. Serge, *Ital. J. Food Sci.*, 2001, **1**, 53.
76. L. Mannina, G. Dugo, F. Salvo, L. Cicero, G. Ansanelli, C. Calcagni and A. Serge, *J. Agric. Food Chem.*, 2003, **51**, 120.
77. S. Hanneguelle, J.-N. Thibault, N. Naulet and G. J. Martin, *J. Agric. Food Chem.*, 1992, **40**, 81.
78. J. T. W. E. Vogels, L. Terwel, A. C. Tas, F. van den Berg, F. Dukel and J. van der Greef, *J. Agric. Food Chem.*, 1996, **44**, 175.
79. G. Le Gall, M. Puaud and I. J. Colquhoun, *J. Agric. Food Chem.*, 2001, **49**, 580.
80. P. S. Belton, I. J. Colquhoum, E. K. Kemsley, I. Delgadillo, P. Roma, M. J. Dennis, M. Sharman, E. Holmes, J. K. Nicholson and M. Spraul, *Food Chem.*, 1998, **61**, 207.
81. I. J. Kosir and J. Kidric, *Anal. Chim. Acta*, 2002, **458**, 77.
82. M. A. Brescia, I. J. Kosir, V. Caldarola, J. Kidric and A. Sacco, *J. Agric. Food Chem.*, 2003, **51**, 21.
83. G. J. Martin, C. Guillou, M. L. Martin, M.-T. Cabanis, Y. Tep and J. Aerny, *J. Agric. Food Chem.*, 1988, **36**, 316.

84. N. Ogrinc, I. J. Kosir, M. Kocjancic and J. Kidric, *J. Agric. Food Chem.*, 2001, **49**, 1432.
85. I. J. Kosir, M. Kocjancic, N. Ogrinc and J. Kidric, *Anal. Chim. Acta*, 2001, **429**, 195.
86. J. T. W. E. Vogels, A. C. Tas, F. van den Berg and J. van der Greef, *Chemom. Intell. Lab. Syst.*, 1993, **21**, 249.
87. L. Forveille, J. Vercauteren and D. N. Rutledge, *Food Chem.*, 1996, **57**, 441.
88. A. Monetti, G. Versini, G. Dalpiaz and F. Reniero, *J. Agric. Food Chem.*, 1996, **44**, 2194.
89. M. C. Vackier, A. S. Barros and D. N. Rutledge, *J. Magn. Reson. Anal.*, 1996, **2**, 321.
90. M. C. Vackier and D. N. Rutledge, *J. Magn. Reson. Anal.*, 1996, **2**, 311.
91. A. Sacco, I. N. Bolsi, R. Massini, S. Manfred, E. Humpfer and S. Ghelli, *J. Agric. Food Chem.*, 1998, **46**, 4242.
92. B. Nordén and C. Albano, *Fuel*, 1989, **68**, 771.
93. D. E. Axelson, *Magnetic Resonance of Carbonaceous Solids*, Vol. 229, R. E. Botto and Y. Sanada, eds., American Chemical Society, Washington, DC, 1993.
94. H. Wilcken, C. Sorge and H.-R. Schulten, *Geoderma*, 1997, **76**, 193.
95. L. Wallbäcks, U. Edlund, B. Nordèn and I. Berglund, *Tappi J.*, 1991, 201.
96. L. Wallbäcks, U. Edlund, B. Nordèn and J. Wood, *Chem. Tech.*, 1989, **9**, 235.
97. P. Malkavaara, R. Alèn and E. Kolehmainen, *Magn. Reson. Chem.*, 1999, **37**, 407.
98. K. Elg-Christofferson, J. Hauksson, U. Edlund, M. Sjöström and M. Dolk, *Cellulose*, 1999, **6**, 233.
99. H. Lennholm, T. Larsson and T. Iversen, *Carbohydr. Res.*, 1994, **261**, 119.
100. T. Lindgren, U. Edlund and T. Iversen, *Cellulose*, 1995, **2**, 273.
101. K. Wickholm, P. T. Larsson and T. Iverson, *Carbohydr. Res.*, 1998, **312**, 123.
102. H. Lennholm and T. Iversen, *Holzforschung*, 1995, **49**, 462.
103. R. A. Hearmon, J. H. Scrivens, K. R. Jennings and M. J. Farncombe, *Chemom. Intell. Lab. Syst.*, 1987, **1**, 167.
104. W. J. Goux, *J. Magn. Reson.*, 1989, **85**, 457.
105. D. S. Weber and W. J. Goux, *Carbohydr. Res.*, 1992, **233**, 65.
106. G. Okide, D. S. Weber and W. J. Goux, *J. Magn. Reson.*, 1992, **96**, 526.
107. M.-E. Dumas, C. Canlet, F. André, J. Vercauteren and A. Paris, *Anal. Chem.*, 2002, **74**, 2261.
108. R. Meusinger, *Fuel*, 1996, **75**, 1235.
109. M. B. Seasholtz, *Chemom. Intell. Lab. Syst.*, 1999, **45**, 55.
110. M. K. Alam and T. M. Alam, *Spectrochem. Acta A*, 2000, **56**, 729.
111. C. Y. Airiau, H. Shen and R. G. Brereton, *Anal. Chim. Acta*, 2001, **447**, 199.
112. H. Shen, C. Y. Airiau and R. G. Brereton, *J. Chemom.*, 2002, **16**, 165.
113. R. Tauler and D. Barceló, *Trends Anal. Chem.*, 1993, **12**, 319.
114. R. Tauler, *J. Chemom.*, 2001, **15**, 627.
115. M. H. Van Benthem, M. R. Keenan and D. M. Haaland, *J. Chemom.*, 2002, **16**, 613.
116. A. K. Smilde, R. Tauler, J. Saurina and R. Bro, *Anal. Chim. Acta*, 1999, **398**, 237.
117. A. de Jaun, S. Rutan, R. Tauler and D. L. Massart, *Chemom. Intell. Lab. Syst.*, 1998, **40**, 19.
118. W. Windig and B. Antalek, *Chemom. Intell. Lab. Syst.*, 1997, **37**, 241.
119. B. Antalek, J. M. Hewitt, W. Windig, P. D. Yacobucci, T. Mourey and K. Le, *Magn. Reson. Chem.*, 2002, **40**, S60.
120. M. Kubitsa, *Chemom. Intell. Lab. Syst.*, 1990, **7**, 273.
121. K. S. Booksh and B. R. Kowalski, *J. Chemom.*, 1994, **8**, 287.
122. E. Sanchez and B. R. Kowalski, *Anal. Chem.*, 1986, **58**, 496.
123. B. E. Wilson, E. Sanchez and B. R. Kowalski, *J. Chemom.*, 1989, **3**, 493.
124. D. Schulze and P. Stilbs, *J. Magn. Reson. Ser. A*, 1993, **105**, 54.
125. B. Antalek and W. Windig, *J. Am. Chem. Soc.*, 1996, **118**, 10331.
126. M. Vives, R. Tauler, V. Moreno and R. Gargallo, *Anal. Chim. Acta*, 2001, **446**, 439.
127. E. Bezemer and S. Rutan, *Anal. Chim. Acta*, 2002, **459**, 277.
128. C. D. Eads, C. M. Furnish, I. Noda, K. Juhlin, D. A. Cooper and S. W. Morrall, *Anal. Chem.*, 2004, **76**, 1982.
129. W. Windig, B. Antalek, J. L. Lippert, Y. Batonneau and C. Brémard, *Anal. Chem.*, 2002, **74**, 1371.
130. B. Antalek, *Concepts Magn. Reson.*, 2002, **14**, 225.

131. W. Windig and B. Antalek, *Chemom. Intell. Lab. Syst.*, 1999, **46**, 207.
132. W. Windig, B. Antalek, L. J. Sorrierro, S. Bijlsma, D. J. Louwerse and A. K. Smilde, *J. Chemom.*, 1999, **13**, 95.
133. N. Zumbulyadis, B. Antalek, W. Windig, R. P. Scaringe, A. M. Lanzafame, T. Blanton and M. Helber, *J. Am. Chem. Soc.*, 1999, **121**, 11554.
134. W. Windig, B. Antalek, M. J. Robbins, N. Zumbulyadis and C. E. Heckler, *J. Chemom.*, 2000, **14**, 213.
135. D. J. Harris and M. K. Alam, *Polymer*, 2002, **43**, 5147.
136. A. Nordon, P. J. Gemperline, C. A. McGill and D. Littlejohn, *Anal. Chem.*, 2001, **73**, 4286.
137. R. Huo, R. Wehrens, J. van Duynhoven and L. M. C. Buydens, *Anal. Chim. Acta*, 2003, **490**, 231.
138. T. M. Alam and M. K. Alam, *J. Chemom.*, 2003, **17**, 583.

Multiple-Quantum Magic-Angle Spinning: High-Resolution Solid-State NMR of Half-Integer Spin Quadrupolar Nuclei

AMIR GOLDBOURT[1] AND P.K. MADHU[2]

[1]*Department of Chemical Physics, Weizmann Institute of Science, Rehovot 76100, Israel*
[2]*Department of Chemical Sciences, Tata Institute of Fundamental Research, Homi Bhabha Road, Colaba, Mumbai 400 005, India*

ANNUAL REPORTS ON NMR SPECTROSCOPY
VOLUME 54 ISSN 0066 4103
DOI 10.1016/S0066-4103(04)54003-6

Of the several techniques introduced to obtain high-resolution solid-state NMR spectra of nuclei with half-integer spins larger than one-half, the multiple-quantum magic-angle-spinning (MQMAS) method remains the most popular. This technique is easy to implement and spectral analysis is straightforward. MQMAS has now become the method of choice for the characterization of materials containing half-integer spin quadrupolar nuclei such as ^{11}B, ^{17}O, ^{23}Na, and ^{27}Al. The combination of MQMAS with other solid-state NMR techniques has resulted in hetero- and homo-correlation experiments. They have helped in obtaining connectivity information and are expected to yield a wealth of geometry constraints in systems of quadrupolar nuclei. In this chapter, we review the technique of MQMAS in detail covering the basic theory, experimental implementation, signal optimization, data analysis and interpretation, signal enhancement schemes, applications, and give an overview of the hetero- and homo-correlation experiments involving MQMAS.

1. INTRODUCTION

Quadrupolar nuclei with integer and half-integer spins make up the majority of the elements in the periodic table. Prominent nuclei among them are ^{2}H and ^{14}N (spin-1), ^{11}B, ^{23}Na, ^{65}Cu, and ^{87}Rb (*spin-*$\frac{3}{2}$), ^{17}O, ^{25}Mg, ^{27}Al, ^{47}Ti, and ^{67}Zn (spin-$\frac{5}{2}$), ^{45}Sc, ^{49}Ti, ^{59}Co, and ^{139}La (spin-$\frac{7}{2}$), and ^{93}Nb and ^{209}Bi (spin-$\frac{9}{2}$). Most of these nuclei have proven industrial applications, such as in catalysis, zeolites, polymers, glasses, and superconductors.[1] NMR characterization of these elements is often rendered difficult due to quadrupolar interaction strengths which range from zero to several MHz. Hence, obtaining a high-resolution spectrum of quadrupolar nuclei in these systems is a challenging task.[1,2]

For all nuclei with spin quantum number $I \geq 1$ an electric quadrupole moment exists that couples with the gradient of the inhomogeneous internal electric fields that are created by other charges in the system.[3,4] The quadrupole moment and the magnitude of the electric field gradient (EFG) are given by eQ and eq, respectively. The strength of the quadrupolar interaction is, therefore, dictated by the molecular or crystalline environment, and is denoted by $\chi = e^2qQ/\hbar$, the nuclear quadrupolar coupling constant (NQCC). When the molecular environment is perfectly symmetric, the quadrupolar interaction vanishes. In the case of spins-$\frac{1}{2}$, this happens due to the symmetry of the nucleus itself.

Generally, among the anisotropic interactions present in solid state it is observed that $\mathcal{H}_Z \gg \mathcal{H}_Q > \mathcal{H}_{RF} > \mathcal{H}_{DD} > \mathcal{H}_{CSA} > \mathcal{H}_J$ where the Hamiltonian terms $\mathcal{H}_\lambda$ correspond to the Zeeman (Z), quadrupolar (Q), radio frequency (RF), dipole–dipole (DD), chemical-shift anisotropy (CSA), and scalar (J) interactions, respectively. Normally, in NMR, the Zeeman interaction is much larger than the rest, which are hence treated as perturbations to the main Hamiltonian, $\mathcal{H}_Z$. For the majority of cases, a first-order perturbation approach suffices to describe the experimental results. However, due to the relatively large size of $\mathcal{H}_Q$, one has to consider both the first- and second-order terms in the perturbation expansion, namely, $\mathcal{H}_Q^{(1)}$ and $\mathcal{H}_Q^{(2)}$.[2]

Magic-angle spinning (MAS) has proved to be extremely useful to obtain high-resolution spectra of spin-$\frac{1}{2}$ nuclei.[5] Spinning the sample at the magic angle

of $\theta_M = 54.7^\circ$ with respect to the static external magnetic field B_0 averages to zero the second-rank Legendre polynomial, $P_2(\cos\theta) = \frac{1}{2}(3\cos^2\theta - 1)$. Since the time-independent part of the first-order perturbation terms is proportional to $P_2(\cos\theta)$, as long as $\mathcal{H}_\lambda$ commutes with $\mathcal{H}_Z$, high-resolution spectra can be obtained with MAS devoid of interactions such as CSA. However, this is not enough to completely average out the second-order quadrupolar Hamiltonian $\mathcal{H}_Q^{(2)}$, which is governed by both $P_2(\cos\theta)$ and $P_4(\cos\theta)$ terms, as will be shown in detail in Section 2. The second- and fourth-rank Legendre polynomials do not have a common root, and hence, MAS alone cannot provide a high-resolution quadrupolar spectrum.[2]

Variable-angle sample spinning (VASS),[6] nutation spectroscopy,[7,8] double rotation (DOR),[9] dynamic-angle spinning (DAS),[10,11] and satellite-transition spectroscopy (SATRAS)[12] are some of the methods that were introduced to improve the resolution of the spectra of quadrupolar nuclei. While the extraction of information content from a nutation spectrum is numerically challenging, both DAS and DOR, though yielding 'real' high-resolution spectrum, are technically challenging.

The subject of this review is the elegant two-dimensional (2D) method that was introduced by Frydman and Harwood[13,14] to obtain high-resolution spectra of half-integer spin quadrupolar nuclear systems. This method, called multiple-quantum magic-angle spinning (MQMAS), uses manipulation of spin coherences rather than sophisticated mechanical manipulations of the sample like its predecessors. Due to its methodological simplicity, it may not be a gross overstatement to say that with the introduction of MQMAS, NMR spectroscopy of half-integer spin quadrupolar nuclei got a tremendous boost resulting in the characterization of several classes of industrially useful materials (see Section 7). Further theoretical and experimental advancements have led to correlation experiments and investigation of higher-order terms in and cross terms among various interactions.[15–18] Promising areas of research include recoupling of heteronuclear dipolar interactions between half-integer spin quadrupolar nuclei and spins-$\frac{1}{2}$.[19]

A related high-resolution technique that was introduced by Gan in 2001 is the satellite-transition MAS (STMAS).[20,21] Routine use of STMAS is still in an infancy stage as various groups are exploring several features of this scheme and improving it further.[22–24]

This review will concentrate on MQMAS with the following outline: Section 2 presents the basic theory of quadrupolar spins with emphasis on the averaging of the second-order quadrupolar interaction in terms of MQMAS and other line narrowing techniques. For an extensive discussion of the theory of quadrupolar nuclei the reader is referred to other reviews.[2,25–27] Section 3 presents the basic MQMAS pulse scheme and discusses the acquisition of pure absorption 2D lineshapes in MQMAS. The processing, labelling, and analysis of MQMAS spectra are discussed in Section 4. In Section 5, strategies for improving the MQMAS signal sensitivity are discussed with an emphasis on the gain that can be obtained by the use of fast amplitude-modulated (FAM) pulses.[28,29] Section 6 discusses combination of MQMAS with other experimental schemes to obtain additional structural information in the form of hetero- and homo-correlation experiments. Representative lists of applications using MQMAS

are presented in Section 7 and finally Section 8 is dedicated to recent developments in STMAS.

2. THEORY OF QUADRUPOLAR SPINS: LINE NARROWING TECHNIQUES

The MQMAS experiment in its simplest form is a 2D NMR experiment consisting of two RF pulses.[13] The first pulse excites symmetric multiple-quantum coherences (MQCs) of order $p = 2m$, or equivalently, creates non-zero $|m\rangle\langle -m|$ elements in the density matrix. Here, m values represent the magnetic quantum numbers which identify the energy levels in Fig. 1. After an evolution time t_1, during which the density matrix elements accumulate a certain phase, a conversion pulse transfers the MQCs to observable $p = -1$ single-quantum coherences (SQCs) $|-1/2\rangle\langle 1/2|$. The MQMAS experiment thus correlates a p-quantum coherence to a SQC, $p\text{QC} \leftrightarrow \text{SQC}$. An echo forms at time $t_2 = k(I, m, -1/2)t_1$ provided that the total phase accumulated by the density matrix elements becomes a constant, and independent of the crystallite orientation. The coefficient k depends on the spin quantum number I and on the order of coherence $p = 2m$, and is a constant for all the crystallites. The 2D experiment provides an isotropic spectrum along the F_1 dimension (after proper shearing of the data when necessary[13]) depending only on the isotropic chemical shift and the isotropic component of the second-order quadrupolar interaction, $\mathcal{H}_Q^{(2)}$.

A typical MQMAS spectrum is shown in Fig. 2. The 2D spectrum is a MQMAS ^{87}Rb spectrum of a sample of rubidium nitrate clearly showing the three well-resolved Rb sites. The F_1 projection shows the isotropic spectrum and the F_2 projection shows the MAS anisotropic spectrum. The slices across the 2D contours give the anisotropic lineshape of each of the sites. An analysis of both these projections (and the anisotropic lineshapes) aided by numerical methods yields the isotropic chemical shift and the quadrupolar interaction parameters of ^{87}Rb in this sample.

In the following, we show how an MQMAS echo is formed. The quadrupolar Hamiltonian under MAS will be derived as a perturbation to the strong static magnetic field B_0. The evolution of the density matrix under this Hamiltonian will be then shown to form an echo under a suitable selection of symmetric coherences. The manipulation of spin coherences by RF pulses will be assumed to be ideal here. The effects of non-idealities were discussed by the group of Vega.[29,31] From the expression for the elements of the quadrupolar Hamiltonian, line narrowing by DOR experiment and echo formation by two alternative experiments, DAS and STMAS, will also be demonstrated and briefly discussed. Finally, some additional line narrowing schemes will be mentioned.

Since we will be discussing only the echo formation, for details regarding the MAS spectra and expressions of the NMR lineshapes of quadrupolar nuclei, the reader is directed to some excellent reviews concerning quadrupolar nuclei by Freude,[25] Smith and VanEck,[26] Man,[27] Frydman,[32–34] and Kentgens.[35] Additional reviews of interest on MQMAS include those of Amoureux and Pruski,[19] and Goldbourt and Madhu.[36]

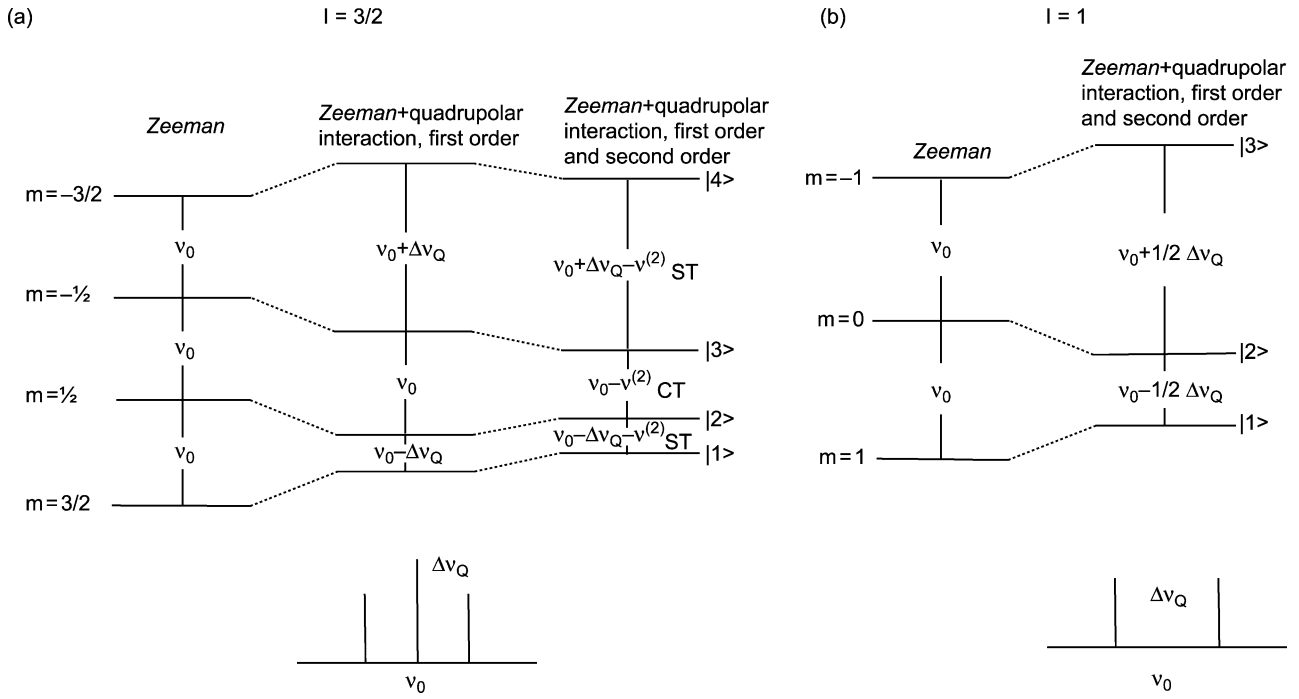

Fig. 1. Energy level diagram of a -spin-$\frac{3}{2}$ and spin-1 quadrupolar nuclei. In the bottom are shown the stick spectrum of a single crystal of each nuclear spin. ν_0 is the Larmor frequency, $\Delta\nu_Q\left(=\frac{\Delta\omega_Q}{2\pi}\right)$ is the orientation dependent quadrupolar splitting [Eq. (18) for the static case and Eq. (34c) for MAS], and $\nu_{CT}^{(2)}$ and $\nu_{ST}^{(2)}$ are the second-order quadrupolar contribution to the central and satellite transition frequencies, respectively [Eqs. (30) and (31) for the static case and Eqs. (35) and (36) for MAS].

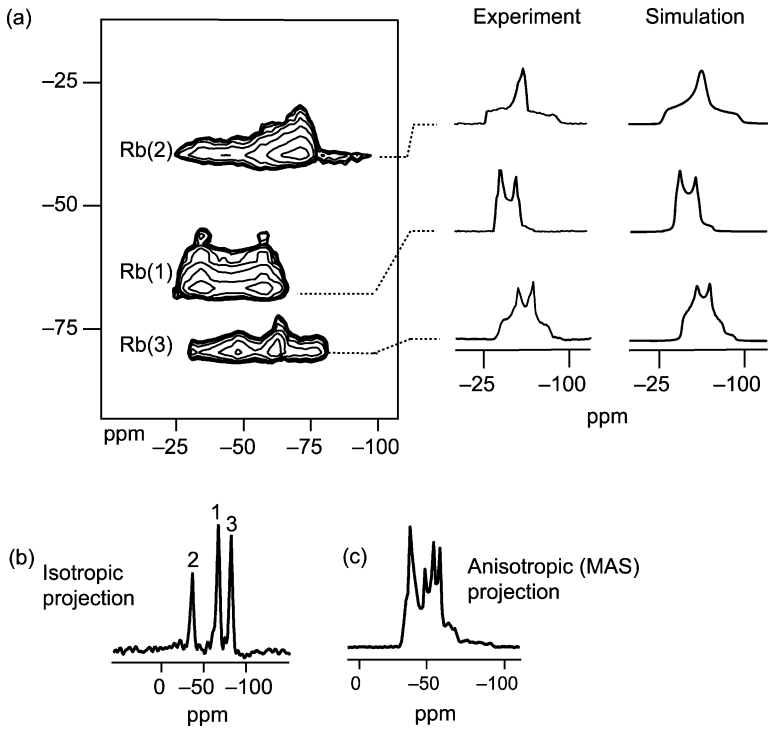

Fig. 2. (a) 2D ^{87}Rb MQMAS spectrum of a sample of $RbNO_3$ at a magnetic field of 4.7 T with a MAS rate of 10 kHz. The anisotropic slices corresponding to the three sites in the sample are indicated along with simulations assuming the known η and χ values for each site. (b) The high-resolution isotropic projection, and (c) the MAS anisotropic projection from (a). (Reprinted with permission from Madhu and Levitt[30] Copyright (2002) Elsevier.)

2.1. Spherical tensor representation in NMR

Local interactions in NMR can be conveniently described as scalar products of spatial and spin irreducible spherical tensors[5,37]

$$\mathcal{H}_\lambda = C_\lambda \sum_{l=0}^{2} \sum_{m=-l}^{l} (-1)^m V_{l,-m} T_{l,m} \tag{1}$$

Here C_λ represents the strength of a specific interaction λ and $V_{l,-m}$ and $T_{l,m}$ are the spatial and spin spherical tensor components of the interaction λ, respectively. Their explicit form depends on the interaction λ and can be found in many text books.[5,37] l is the principal quantum number and m is the azimuthal quantum number.[38]

With $K_{l,m}$ a spherical tensor of arbitrary rank, either spatial or spin, irreducible spherical tensors are defined by their commutation relations with linear Cartesian operators in the following manner

$$[I_z, K_{l,m}] = mK_{l,m} \tag{2}$$

$$[I_\pm, K_{l,m}] = \sqrt{\frac{1}{2}(l \mp m)(l \pm m + 1)}K_{l,m\pm 1} \tag{3}$$

with $I_\pm = (I_x \pm iI_y)$.[38] The rotation properties of spherical tensors are well defined and thoroughly described by Rose[39] and Edmonds.[40] A spherical tensor $K^{\mathcal{A}}_{l,m}$ of rank l (of an interaction λ) in an arbitrary axis system $\mathcal{A}$ may be represented as a linear combination of irreducible tensors of the same rank in a different axis system, for example, its principal axis system (PAS) $\mathcal{P}$, as

$$K^{\mathcal{A}}_{l,m} = \sum_{m'=-l}^{l} K^{\mathcal{P}}_{l,m'}\mathcal{D}^{(l)}_{m'm}(\Omega_{\mathcal{PA}}) \tag{4}$$

where $\mathcal{D}^{(l)}_{m'm}(\Omega_{\mathcal{PA}})$ are the Wigner rotation matrix elements and $\Omega_{\mathcal{PA}} = \{\alpha_{\mathcal{PA}}, \beta_{\mathcal{PA}}, \gamma_{\mathcal{PA}}\}$ are the Euler angles describing the transformation from $\mathcal{P}$ to $\mathcal{A}$. The Wigner rotation matrix elements can be explicitly expressed as

$$\mathcal{D}^{(l)}_{m'm}(\Omega_{\mathcal{PA}}) = \mathrm{e}^{-\mathrm{i}m'\alpha_{\mathcal{PA}}}d^{(l)}_{m'm}(\beta_{\mathcal{PA}})\mathrm{e}^{\mathrm{i}m\gamma_{\mathcal{PA}}} \tag{5}$$

where $d^{(l)}_{m'm}(\beta_{\mathcal{PA}})$ are called the reduced Wigner matrix elements. For $l = 2, 4$ they are given in Table 1.

With these simple rules, the quadrupolar Hamiltonian of a powder sample can be presented.

2.2. The quadrupolar Hamiltonian

The quadrupolar interaction arises from the coupling of the EFG surrounding the nucleus with that of its nuclear quadrupole moment, as described by Cohen and Reif.[4] The EFG tensor (or the quadrupolar tensor) is defined in its PAS by three Cartesian elements, $Q'_{zz} \geq Q'_{yy} \geq Q'_{xx}$, with the quadrupolar tensor in the PAS notated as Q'_{PAS}. Like any other tensor, the anisotropic contribution can be defined by a magnitude $(Q'_{zz} - \frac{1}{3}\sum_{\alpha\alpha} Q'_{\alpha\alpha})$ and an asymmetry parameter η. For the EFG tensor, the isotropic part (the trace) vanishes as the diagonal elements satisfy the Laplace equation[4] and therefore its magnitude eq and asymmetry η are given by

$$eq = Q'_{zz}; \eta = \frac{Q'_{xx} - Q'_{yy}}{Q'_{zz}} \tag{6}$$

Table 1. The values of the reduced Wigner matrix elements $d^{(l)}_{mn}(\beta)$

Definition	$D^{(l)}_{mn}(\alpha,\beta,\gamma) = \mathrm{e}^{-ima} d^{(l)}_{mn}(\beta) \mathrm{e}^{-in\gamma}$
Reduced elements	$d^{(l)}_{mn}(\beta) = \sum_k (-1)^{k-m+n} \frac{\sqrt{(l+m)!(l-m)!(l+n)!(l-n)!}}{(l+m-k)!(l-k-n)!(k-m+n)!}$
	$\left(\cos\frac{\beta}{2}\right)^{2l-2k+m-n} \left(\sin\frac{\beta}{2}\right)^{2k-m+n}$
Symmetry relations	$d^{(l)}_{mn}(\beta) = (-1)^{m-n} d^{(l)}_{nm}(\beta)$
	$d^{(l)}_{mn}(\beta) = (-1)^{m-n} d^{(l)}_{-m-n}(\beta)$
	$d^{(l)}_{mn}(\beta) = (-1)^{l-n} d^{(l)}_{m-n}(\beta+\pi)$

$d^{(2)}_{mn}(\beta)$	$n=2$	1	0	-1	-2
$m=2$	$\cos^4(\beta/2)$	$-\frac{1}{2}(1+\cos\beta)\sin\beta$	$\sqrt{\frac{3}{8}}\sin^2\beta$	$\frac{1}{2}(\cos\beta-1)\sin\beta$	$\sin^4(\beta/2)$
1	$-d^{(2)}_{21}(\beta)$	$\left(\cos\beta-\frac{1}{2}\right)(\cos\beta+1)$	$-\sqrt{\frac{3}{8}}\sin 2\beta$	$\left(\cos\beta+\frac{1}{2}\right)(1-\cos\beta)$	$d^{(2)}_{2-1}(\beta)$
0	$d^{(2)}_{20}(\beta)$	$-d^{(2)}_{10}(\beta)$	$\frac{1}{2}(3\cos^2\beta-1)$	$d^{(2)}_{10}(\beta)$	$d^{(2)}_{20}(\beta)$
-1	$-d^{(2)}_{2-1}(\beta)$	$d^{(2)}_{1-1}(\beta)$	$-d^{(2)}_{10}(\beta)$	$d^{(2)}_{11}(\beta)$	$d^{(2)}_{21}(\beta)$
-2	$d^{(2)}_{2-2}(\beta)$	$-d^{(2)}_{2-1}(\beta)$	$d^{(2)}_{20}(\beta)$	$-d^{(2)}_{21}(\beta)$	$d^{(2)}_{22}(\beta)$

$d^{(4)}_{mn}(\beta)$ (only minimal set)			
$d^{(4)}_{00}(\beta)$	$\frac{1}{8}(35\cos^4\beta-30\cos^2\beta+3)$	$d^{(4)}_{24}(\beta)$	$\frac{\sqrt{7}}{8}(\cos\beta+1)^2\sin^2\beta$
$d^{(4)}_{10}(\beta)$	$\frac{\sqrt{5}}{4}(7\cos^3\beta-3\cos\beta)\sin\beta$	$d^{(4)}_{30}(\beta)$	$-\frac{\sqrt{35}}{4}\cos\beta\sin^3\beta$
$d^{(4)}_{20}(\beta)$	$\frac{\sqrt{10}}{8}(7\cos^2\beta-1)\sin^2\beta$	$d^{(4)}_{40}(\beta)$	$\frac{\sqrt{70}}{16}\sin^4\beta$
$d^{(4)}_{21}(\beta)$	$\frac{\sqrt{2}}{8}(16\cos^3\beta+10\cos^2\beta$ $-10\cos\beta-3)\sin\beta$	$d^{(4)}_{41}(\beta)$	$-\frac{\sqrt{14}}{8}(\cos\beta+1)\sin^3\beta$
$d^{(4)}_{22}(\beta)$	$\frac{1}{4}(\cos\beta+1)(7\cos^3\beta-6\cos\beta+1)$	$d^{(4)}_{43}(\beta)$	$-\frac{\sqrt{2}}{8}(\cos\beta+1)^3\sin\beta$
$d^{(4)}_{23}(\beta)$	$\frac{\sqrt{14}}{8}(\cos\beta+1)^2(2\cos\beta-1)\sin\beta$	$d^{(4)}_{44}(\beta)$	$\frac{1}{16}(\cos\beta+1)^4$

The spherical tensor representation of the non-zero elements of the EFG tensor in its PAS is given by *

$$Q'_{2,0} = \sqrt{\frac{3}{2}}Q'_{zz} = \sqrt{\frac{3}{2}}eq \quad Q'_{2,\pm 2} = \frac{1}{2}(Q'_{xx} - Q'_{yy}) \pm \mathrm{i}Q'_{xy} = \frac{1}{2}\eta eq \tag{7}$$

In angular units of frequency, the NQCC is given by $\chi = eqe\mathrm{Q}/\hbar$.[4] The quadrupolar frequency is defined in angular units as (see Ref. 2)

$$\omega_{\mathrm{Q}} = \frac{3e^2\mathrm{Q}q}{2I(2I-1)\hbar} \tag{8}$$

and depends on the spin quantum number I.

The quadrupolar splitting $\omega_{\mathrm{Q}}(\Omega_{\mathcal{PL}})$ defines the separation between the NMR spectral lines of a single crystal. Here, $\Omega_{\mathcal{PL}}$ describes a transformation from the PAS of the EFG $\mathcal{P}$ to the laboratory frame (the magnetic field) $\mathcal{L}$ ($\Omega_{\mathcal{PL}}$ defines the orientation of $\mathcal{L}$ in $\mathcal{P}$). When the principal axis system of the EFG tensor is aligned parallel to the magnetic field B_0, this value equals the quadrupolar frequency and is, therefore, a better measure of the quadrupolar interaction than χ.

Therefore, we choose to define the quadrupolar Hamiltonian in terms of the quadrupolar frequency as

$$\mathcal{H}_{\mathrm{Q}} = \frac{\omega_{\mathrm{Q}}}{3}\sum_{m=-2}^{2}(-1)^m V_{2,-m}T_{2,m} \tag{9}$$

In this definition, the magnitude eq of the EFG tensor is eliminated from the spatial tensor ($Q_{zz} = Q'_{zz}/eq$) and absorbed into ω_{Q}. Equation (7) now becomes

$$Q_{2,0} = \sqrt{\frac{3}{2}}, \quad Q_{2,\pm 2} = \frac{1}{2}\eta \tag{10}$$

The elements $V_{2,-m}$ describe the spatial interaction in a reference axis system of choice and are connected to $Q_{2,m}$ by a rotation as shown in Eq. (4). The spin tensor elements $T_{2,m}$ are given in terms of the Cartesian angular momentum operators by †

$$T_{2,0} = \frac{1}{\sqrt{6}}(3I_z^2 - I(I+1)) \quad T_{2,\pm 1} = \mp\frac{1}{\sqrt{2}}(I_zI_+ + I_-I_z) \quad T_{2,\pm 2} = \frac{1}{2}(I_\pm)^2 \tag{11}$$

* An alternative convention uses the principal components $Q'_{zz} \geq Q'_{xx} \geq Q'_{yy}$ and $\eta = (Q'_{yy} - Q'_{xx})/Q'_{zz}$. In this case, $Q'_{2,\pm 2} = -\frac{1}{2}\eta eq$.

† Some authors express the elements $T_{2,m}$ in terms of the spherical angular momentum operators $I_{\pm 1} = \frac{1}{\sqrt{2}}(I_{1x} \pm iI_{1y})$ and then accordingly, $T_{2,\pm 1} = \mp(I_zI_{+1} + I_{-1}I_z)$, $T_{2,\pm 2} = (I_{\pm 1})^2$.

In the presence of a strong static magnetic field, all interactions are described as perturbations to the dominant Zeeman interaction, given by

$$\mathcal{H}_0 = -\gamma B_0 I_z = \omega_0 I_z \tag{12}$$

Here, γ is the gyromagnetic ratio of the nucleus of interest, B_0 the strength of the z-component of the static magnetic field, and I_z is the angular momentum projection operator along the magnetic field. The Larmor frequency is given by $\omega_0 = -\gamma B_0$ (corresponding to clockwise precession of the spin angular momenta for nuclei with positive γ[41]).

We now calculate the perturbation to the Zeeman field due to the quadrupolar interaction by means of average Hamiltonian theory.[37] This is accomplished by transforming $\mathcal{H}_Q$ to the Zeeman interaction frame and then applying the spherical tensor rotation properties to the spin elements $T_{2,k}$. The resulting quadrupolar Hamiltonian $\tilde{\mathcal{H}}_Q$ in the rotating frame is given by:

$$\begin{aligned}\tilde{\mathcal{H}}_Q &= e^{i\mathcal{H}_0 t}\mathcal{H}_Q e^{-i\mathcal{H}_0 t} = \frac{\omega_Q}{3}\sum_m V_{2,-m}\sum_k T_{2,k}\mathcal{D}^{(2)}_{km}(-\omega_0 t, 0, 0) \\ &= \frac{\omega_Q}{3}\sum_m V_{2,-m}\sum_k T_{2,k}e^{ik\omega_0 t}\delta_{km} \quad = \frac{\omega_Q}{3}\sum_m V_{2,-m}T_{2,m}e^{im\omega_0 t}\end{aligned} \tag{13}$$

Averaging over the Larmor period $\omega_0/2\pi$ is performed by taking the zero- and first-order terms in the Magnus expansion.[37] They are notated here as $\tilde{\mathcal{H}}^{(1)}_Q$ and $\tilde{\mathcal{H}}^{(2)}_Q$ in order to stress their equivalence to the first- and second-order terms of standard perturbation theory:[2]

$$\tilde{\mathcal{H}}^{(1)}_Q = \frac{\omega_0}{2\pi}\int_0^{2\pi/\omega_0}\tilde{\mathcal{H}}_Q(t)dt = \frac{\omega_Q}{3}V_{2,0}T_{2,0} \tag{14}$$

$$\begin{aligned}\tilde{\mathcal{H}}^{(2)}_Q &= -\tfrac{i\omega_0}{4\pi}\int_0^{2\pi/\omega_0}dt\int_0^t dt'[\tilde{\mathcal{H}}_Q(t), \tilde{\mathcal{H}}_Q(t')] \\ &= \tfrac{\omega_Q^2}{4\pi}\int_0^{2\pi/\omega_0}dt\left[\sum_m V_{2,-m}T_{2,m,}\frac{1}{n}\sum_n V_{2,-n}T_{2,n}\right]e^{-i(m+n)\omega_0 t} \\ &= \frac{\omega_Q^2}{18\omega_0}\left\{V_{2,1}V_{2,-1}[T_{2,-1},T_{2,1}] + \tfrac{1}{2}V_{2,2}V_{2,-2}[T_{2,-2},T_{2,2}]\right\}\end{aligned} \tag{15}$$

In the derivation of Eq. (15) terms with $m \neq n$ have been dropped, as they do not commute with I_z, and equivalence to perturbation theory is achieved.[5]

The rotating frame quadrupolar Hamiltonian is, therefore, given by the sum of Eqs. (14) and (15):

$$\tilde{\mathcal{H}}_Q = \tilde{\mathcal{H}}^{(1)}_Q + \tilde{\mathcal{H}}^{(2)}_Q \tag{16}$$

2.3. Spectra of quadrupolar spins

In order to calculate the evolution of the density matrix and consequently the positions of the spectral lines, the transition frequencies have to be calculated. The first-order transition frequencies are given by [following Eq. (14)]

$$\omega^{(1)}_{m-1,m} = \langle m-1|\tilde{\mathcal{H}}^{(1)}_{\mathrm{Q}}|m-1\rangle - \langle m|\tilde{\mathcal{H}}^{(1)}_{\mathrm{Q}}|m\rangle = \frac{\omega_{\mathrm{Q}}}{\sqrt{6}}(1-2m)V_{2,0} \tag{17}$$

The central transition (CT) $\omega^{(1)}_{-1/2,1/2}$ is clearly independent of the quadrupolar interaction to first order, as shown in Fig. 1. On the other hand, the frequency of the satellite transitions depends on ω_{Q}. For a single crystal all frequencies can be calculated by expressing $V_{2,0}$ in the LAB frame as a function of the elements of the quadrupolar tensor in its PAS using the Euler angles $\alpha = \alpha_{\mathcal{PL}}$ and $\beta = \beta_{\mathcal{PL}}$. The third Euler angle γ vanishes since the magnetic field has only a z-component, B_0. The first-order transition frequencies are then given by

$$\begin{aligned}
\omega^{(1)}_{m-1,m} &= \frac{\omega_{\mathrm{Q}}}{\sqrt{6}}(1-2m)\sum_{n=-2}^{2} Q_{2,n}\mathcal{D}^{(2)}_{n0}(\Omega_{\mathcal{PL}}) \\
&= \frac{\omega_{\mathrm{Q}}}{\sqrt{6}}(1-2m)\{Q_{2,2}d^{(2)}_{20}(\beta)(\mathrm{e}^{-2\mathrm{i}\alpha}+\mathrm{e}^{2\mathrm{i}\alpha}) + Q_{2,0}d^{(2)}_{00}(\beta)\} \\
&= \omega_{\mathrm{Q}}(1/2-m)\left\{\frac{3\cos^2\beta - 1}{2} + \eta\frac{\sin^2\beta\cos 2\alpha}{2}\right\}
\end{aligned} \tag{18}$$

For a single crystal having the z-axis of its PAS parallel to B_0, Eq. (18) gives for the *nth* satellite transition $|n-1/2\rangle \rightarrow |n+1/2\rangle$ (ST_n), a frequency $\omega^{(1)}_{n-1/2,n+1/2} = n\omega_{\mathrm{Q}}$ (Fig. 1, $n = \pm 1$) and the spectrum has lines at $\omega_0 \pm n\omega_Q$.

In order to calculate the second-order transition frequencies according to Eq. (15), we first express the spin terms in terms of the linear Cartesian operators. The commutators $[T_{2,-m},T_{2,m}]$ are calculated by expanding the products according to

$$T_{2,m}T_{2,-m} = \sum_{k=0}^{4}\langle 22; m-m|k0\rangle T_{k,0} \tag{19}$$

where the relevant Clebsch–Gordon coefficients $\langle j_1 j_2; m_1 m_2|jm\rangle$ are given in Table 2. (For simplicity, we notate the Clebsch–Gordon coefficients as $\langle j_1 j_2; m_1 m_2|jm\rangle$ instead of $\langle j_1 j_2; m_1 m_2|j_1 j_2; jm\rangle$.) The Clebsch–Gordon coefficients obey the following properties:

(i) j spans the range $|j_1 - j_2| < j < |j_1 + j_2|$.
(ii) $\langle j_1 j_2; m_1 m_2|jm\rangle = (-1)^{m_1+m_2+1}\langle j_1 j_2; m_2 m_1|jm\rangle$.
(iii) $m = m_1 + m_2$.

Table 2. The Clebsh–Gordon coefficients $\langle 22; m_1 m_2 | jm \rangle = \langle 22; -m_2 - m_1 | j - m \rangle$

$\langle 22; m_1 m_2 \vert j4 \rangle$	m_1,m_2\j	4				
	2,2	1				
$\langle 22; m_1 m_2 \vert j3 \rangle$	m_1,m_2\j	4	3			
	2,1	$1/\sqrt{2}$	$1/\sqrt{2}$			
	1,2	$1/\sqrt{2}$	$-1/\sqrt{2}$			
$\langle 22; m_1 m_2 \vert j2 \rangle$	m_1,m_2\j	4	3	2		
	2,0	$\sqrt{3/14}$	$1/\sqrt{2}$	$\sqrt{2/7}$		
	1,1	$2/\sqrt{7}$	0	$-\sqrt{3/7}$		
	0,2	$\sqrt{3/14}$	$-1/\sqrt{2}$	$\sqrt{2/7}$		
$\langle 22; m_1 m_2 \vert j1 \rangle$	m_1,m_2\j	4	3	2	1	
	2, −1	$1/\sqrt{14}$	$\sqrt{3/10}$	$\sqrt{3/7}$	$1/\sqrt{5}$	
	1,0	$\sqrt{3/7}$	$1/\sqrt{5}$	$-\sqrt{1/14}$	$-\sqrt{3/10}$	
	0,1	$\sqrt{3/7}$	$-1/\sqrt{5}$	$-\sqrt{1/14}$	$\sqrt{3/10}$	
	−1,2	$1/\sqrt{14}$	$-\sqrt{3/10}$	$\sqrt{3/7}$	$-1/\sqrt{5}$	
$\langle 22; m_1 m_2 \vert j0 \rangle$	m_1,m_2\j	4	3	2	1	0
	2, −2	$\sqrt{1/70}$	$\sqrt{1/10}$	$\sqrt{2/7}$	$\sqrt{2/5}$	$\sqrt{1/5}$
	1, −1	$\sqrt{8/35}$	$\sqrt{2/5}$	$\sqrt{1/14}$	$-\sqrt{1/10}$	$-\sqrt{1/5}$
	0,0	$\sqrt{18/35}$	0	$-\sqrt{2/7}$	0	$\sqrt{1/5}$
	−1,1	$\sqrt{8/35}$	$-\sqrt{2/5}$	$\sqrt{1/14}$	$\sqrt{1/10}$	$-\sqrt{1/5}$
	−2,2	$\sqrt{1/70}$	$-\sqrt{1/10}$	$\sqrt{2/7}$	$-\sqrt{2/5}$	$\sqrt{1/5}$

Since $m_1 = -m_2$ in Eq. (19) only terms with odd k remain and using the definitions of $T_{k,0}$ in terms of the Cartesian operators[42]

$$T_{1,0} = \sqrt{\frac{2}{5}} I_z \left(I(I+1) - \frac{3}{4} \right) \tag{20a}$$

$$T_{3,0} = \sqrt{\frac{2}{5}} I_z (3I(I+1) - 5I_z^2 - 1) \tag{20b}$$

the commutators in Eq. (15) can be easily calculated and give

$$[T_{2,-1}, T_{2,1}] = \frac{1}{2} I_z (8I_z^2 - 4I(I+1) + 1) \tag{21a}$$

$$[T_{2,-2}, T_{2,2}] = I_z(2I_z^2 - 2I(I+1) + 1) \tag{21b}$$

The spatial part is calculated by first transforming the products $V_{2,m}V_{2,-m}$ to the LAB frame using Eq. (4), giving

$$V_{2,m}V_{2,-m} = \sum_{j=-2}^{2} Q_{2,j}\mathcal{D}^{(2)}_{jm}(\Omega_{\mathcal{PL}}) \sum_{k=-2}^{2} Q_{2,k}\mathcal{D}^{(2)}_{k-m}(\Omega_{\mathcal{PL}}) \tag{22}$$

and collecting products of Wigner matrices according to[39,40]

$$\mathcal{D}^{(2)}_{jm}(\Omega_{\mathcal{PL}})\mathcal{D}^{(2)}_{k-m}(\Omega_{\mathcal{PL}}) = \sum_{l=0}^{4} \langle 22; m-m|l0\rangle\langle 22; jk|l\, j+k\rangle \mathcal{D}^{(l)}_{j+k0}(\Omega_{\mathcal{PL}}) \tag{23}$$

The symmetry of the Clebsch–Gordon coefficients is again used in conjunction with Eq. (10) ($Q_{2,m} = Q_{2,-m}$) resulting in the elimination of terms with $l = 1, 3$. For example, the terms with $l = 1$ have (where only $(k,j) = (\pm 2, \mp 2)$ are shown explicitly)

$$\begin{aligned}
&\langle 22; m-m|10\rangle\{Q_{2,2}Q_{2,-2}\langle 22; 2-2|10\rangle + Q_{2,2}Q_{2,-2}\langle 22; -22|10\rangle + \cdots\} \\
&\quad = \langle 22; m-m|10\rangle\{(Q_{2,2})^2(\langle 22; 2-2|10\rangle + \langle 22; -22|10\rangle) + \cdots\} \\
&\quad = \langle 22; m-m|10\rangle\{(\eta^2/4)^2 \cdot 0 + \cdots\}
\end{aligned} \tag{24}$$

Accordingly, only terms with even l are retained.

Finally, collecting the spin and spatial elements, the second-order quadrupolar Hamiltonian can be expressed as

$$\begin{aligned}
\mathcal{H}^{(2)}_{\mathrm{Q}} &= \frac{\omega_{\mathrm{Q}}^2}{36\omega_0} \sum_{l=0}^{2} A^{(2l)}(I, I_z) \sum_{j,k=-2}^{2} Q_{2j}Q_{2k}\langle 22; jk|2l\, j+k\rangle \mathcal{D}^{(l)}_{j+k0}(\Omega_{\mathcal{PL}}) \\
&= \frac{\omega_{\mathrm{Q}}^2}{36\omega_0} \sum_{l=0}^{2} A^{(2l)}(I, I_z) \sum_{n=-l}^{l} B^{(2l)}_{2n}(\eta)\mathcal{D}^{(2l)}_{2n0}(\Omega_{\mathcal{PL}})
\end{aligned} \tag{25}$$

where the coefficients $\langle 22; m-m|2l0\rangle$ were absorbed into the operator $A^{(2l)}(I, I_z)$:

$$A^{(2l)}(I, I_z) = 4\langle 22; 1-1|2l\ 0\rangle[T_{2,-1}, T_{2,1}] + 2\langle 22; 2-2|2l\ 0\rangle[T_{2,-2}, T_{2,2}] \tag{26}$$

and explicitly given by

$$A^{(0)}(I,I_z) = -\frac{2}{\sqrt{5}}[2I_z(3I_z^2 - I(I+1))] \tag{27a}$$

$$A^{(2)}(I,I_z) = \frac{1}{\sqrt{14}}[2I_z(12I_z^2 - 8I(I+1)+3)] \tag{27b}$$

$$A^{(4)}(I,I_z) = \frac{1}{\sqrt{70}}[2I_z(34I_z^2 - 18I(I+1)+5)] \tag{27c}$$

The $B_{2n}^{(2l)}(\eta)$ functions are defined as

$$B_{2n}^{(2l)} = \sum_{j+k=2n} Q_{2j}Q_{2k}\langle 22;jk|2l\,j+k\rangle \tag{28}$$

or explicitly

$$\begin{aligned} B_0^{(0)} &= \frac{3+\eta^2}{2\sqrt{5}} \\ B_0^{(2)} &= \frac{\eta^2-3}{2\sqrt{7}} \quad B_{\pm 2}^{(2)} = \eta^2\sqrt{\frac{3}{7}} \\ B_0^{(4)} &= \frac{\eta^2+18}{2\sqrt{70}} \quad B_{\pm 2}^{(4)} = \frac{3\eta}{\sqrt{28}} \quad B_{\pm 4}^{(4)} = \frac{\eta^2}{4} \end{aligned} \tag{29}$$

The central-transition (CT) frequencies are obtained by substituting for the $A(I,I_z)$ operators their eigenvalues $A(I,m)$ in the basis set of the quadrupolar Hamiltonian, with $A(I,I_z)|m>=A(I,m)|m>$, and by substituting $m=-1/2$ in the following general expression for the symmetric transitions (for the static case)

$$\omega_{m,-m}^{2,\text{static}} = \frac{\omega_Q^2}{18\omega_0}\sum_{l=0}^{2} A^{(2l)}(I,m)\sum_{n=-l}^{l} B_{2n}^{(2l)}(\eta)\mathcal{D}_{2n0}^{(2l)}(\Omega_{\mathcal{PL}}) \tag{30}$$

The satellite-transition frequencies are given by

$$\omega_{m-1,m}^{2,\text{static}} = \frac{\omega_Q^2}{18\omega_0}\sum_{l=0}^{2} \mathcal{A}^{(2l)}(I,m)\sum_{n=-l}^{l} B_{2n}^{(2l)}(\eta)\mathcal{D}_{2n0}^{(2l)}(\Omega_{\mathcal{PL}}) \tag{31}$$

with

$$\mathcal{A}^{(0)}(I,m) = \frac{-2}{\sqrt{5}}[-9m^2+9m-3+I(I+1)] \tag{32a}$$

Table 3. The values of $A^{(l)}(I,m)$ (for MQMAS)

l	$A^{(l)}$(3/2,1/2)	$A^{(l)}$(3/2,3/2)			
0	−3	9			
2	−24	0			
4	−54	42			
l	$A^{(l)}$(5/2,1/2)	$A^{(l)}$(5/2,3/2)	$A^{(l)}$(5/2,5/2)		
0	−8	−6	50		
2	−64	−120	40		
4	−144	−228	300		
l	$A^{(l)}$(7/2,1/2)	$A^{(l)}$(7/2,3/2)	$A^{(l)}$(7/2,5/2)	$A^{(l)}$(7/2,7/2)	
0	−15	−27	15	147	
2	−120	−288	−240	168	
4	−270	−606	−330	966	
l	$A^{(l)}$(9/2,1/2)	$A^{(l)}$(9/2,3/2)	$A^{(l)}$(9/2,5/2)	$A^{(l)}$(9/2,7/2)	$A^{(l)}$(9/2,9/2)
0	−24	−54	−30	84	324
2	−192	−504	−600	−336	432
4	−432	−1092	−11440	−168	2232

$$\mathcal{A}^{(2)}(I,m) = \frac{2}{\sqrt{14}}[-36m^2 + 36m - 15 + 8I(I+1)] \tag{32b}$$

$$\mathcal{A}^{(4)}(I,m) = \frac{1}{\sqrt{70}}[-102m^2 + 102m - 39 + 18I(I+1)] \tag{32c}$$

where $\mathcal{A}^{(l)}(I,m)$ is obtained from $A(I,m)$ by $\mathcal{A}^{(l)}(I,m) = \frac{1}{2}[A^{(l)}(I,m-1) - A^{(l)}(I,m)]$. The values of $A^{(2l)}(I,m)$ and $\mathcal{A}^{(2l)}(I,m)$ are summarized in Tables 3 and 4, respectively,

Table 4. The values of $\mathcal{A}^{(l)}(I,m)$ (for STMAS)

l	$\mathcal{A}^{(l)}$(3/2,3/2)			
0	−6			
2	−12			
4	−48			
l	$\mathcal{A}^{(l)}$(5/2,3/2)	$\mathcal{A}^{(l)}$(5/2,5/2)		
0	−1	−28		
2	28	−80		
4	42	−264		
l	$\mathcal{A}^{(l)}$(7/2,3/2)	$\mathcal{A}^{(l)}$(7/2,5/2)	$\mathcal{A}^{(l)}$(7/2,7/2)	
0	6	−21	−66	
2	84	−24	−204	
4	168	−138	−648	
l	$\mathcal{A}^{(l)}$(9/2,3/2)	$\mathcal{A}^{(l)}$(9/2,5/2)	$\mathcal{A}^{(l)}$(9/2,7/2)	$\mathcal{A}^{(l)}$(9/2,9/2)
0	15	−12	−57	−120
2	156	48	−132	−384
4	330	24	−486	−1200

and will be used in the Section 2.4 where manipulation of selected transitions will be shown to yield high-resolution spectra of quadrupolar spins. *

2.3.1. *Magic-angle spinning*

For a powder sample all orientations exist in equal probabilities. This results in broad lines centred around $\omega_Q(m-1/2)$ for a transition $m-1 \rightarrow m$. MAS is designed to narrow these lines and is introduced into the first- and second-order quadrupolar transition frequencies by applying a proper transformation $\Omega_{\mathcal{PL}} = \Omega_{\mathcal{PR}}\Omega_{\mathcal{RL}}$, where $\mathcal{R}$ represents the rotor frame. The Euler angles corresponding to rotation from $\mathcal{P}$ (quadrupolar PAS) to $\mathcal{R}$ are $\alpha_{\mathcal{PR}}, \beta_{\mathcal{PR}}, \gamma_{\mathcal{PR}}$ and depend on the orientation of the atoms in the molecule. Rotation of $\mathcal{R}$ to the LAB frame $\mathcal{L}$ depends on the rotor tilt-angle θ ($\theta = \theta_M = \arctan\sqrt{2}$ for MAS) and $\omega_{\mathcal{R}}t$, the phase obtained by the rotor for an angular spinning frequency $\omega_{\mathcal{R}}$. In order to redefine the transformation $\Omega_{\mathcal{PL}}$ the corresponding Wigner matrix $\mathcal{D}^{(l)}_{mn}(\Omega_{\mathcal{PL}})$ is decomposed according to

$$\mathcal{D}^{(l)}_{mn}(\Omega_{\mathcal{PL}}) = \sum_{m'=-l}^{l} \mathcal{D}^{(l)}_{mm'}(\Omega_{\mathcal{PR}})\mathcal{D}^{(l)}_{m'n}(\Omega_{\mathcal{RL}}) \tag{33}$$

The first-order quadrupolar transition frequency under MAS is then given by

$$\omega^{(1)}_{m-1,m} = \frac{\omega_Q}{\sqrt{6}}(1-2m)\sum_{k,j=-2}^{2} Q_{2,k}\mathcal{D}^{(2)}_{kj}(\Omega_{\mathcal{PR}})\mathcal{D}^{(2)}_{j0}(\Omega_{\mathcal{RL}}) \tag{34a}$$

$$= \frac{\omega_Q}{\sqrt{6}}(1-2m)\sum_{k,j=-2}^{2} Q_{2,k}e^{-ik\alpha_{\mathcal{PR}}}d^{(2)}_{kj}(\beta_{\mathcal{PR}})d^{(2)}_{j0}(\theta)e^{-ij(\gamma_{\mathcal{PR}}+\omega_{\mathcal{R}}t)} \tag{34b}$$

$$= \omega_Q(1/2-m)\sum_{k=-2}^{2} g_k(\alpha,\beta,\theta,\eta)e^{ik(\gamma+\omega_{\mathcal{R}}t)} \tag{34c}$$

with Eq. (34c) being the well known MAS frequencies, expressed as a Fourier series. Setting $\theta = \theta_M$ nullifies g_0

$$\left(g_0 \propto \frac{3\cos^2\beta - 1}{2}\,\frac{3\cos^2\theta - 1}{2}\right)$$

and produces a first-order quadrupolar spectrum with a CT $-1/2 \rightarrow 1/2$ line at the Larmor frequency, not broadened to first order, and a manifold of sidebands for the satellites centred at $\omega_Q(1/2-m)$ and separated by $\omega_{\mathcal{R}}$. This is illustrated in Fig. 3.

* Normally, one eliminates the coefficients in front of the square brackets of Eqs. (27a–c) and (32a–c) absorbing them into $B^{(2l)}_{2n}$ (e.g., Ref. 43). However, this complicates the definition of the A terms considerably. In Tables 3 and 4 the values of $A^{(2l)}(I,m)$ and $\mathcal{A}^{(l)}(I,m)$ are given without these coefficients, since, for the purpose of echo position calculation, only their ratios are required.

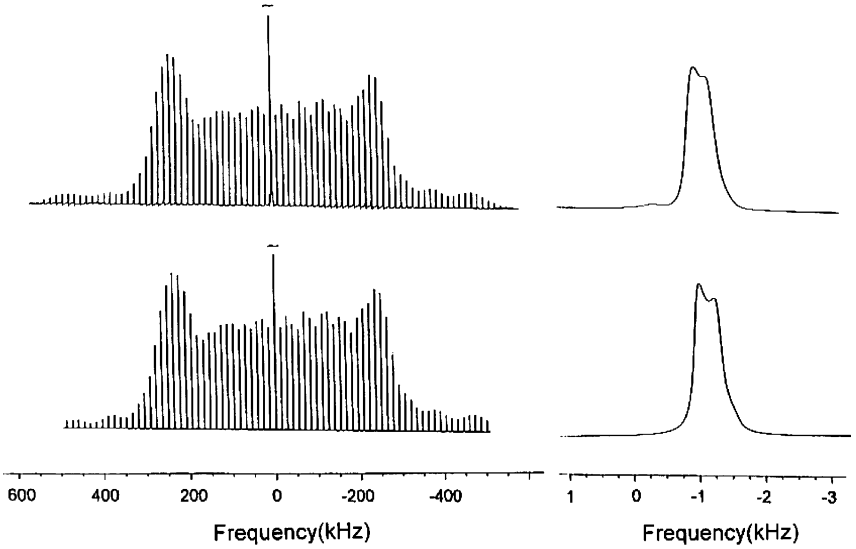

Fig. 3. ^{23}Na spectrum of a sample of $NaNO_2$ showing the satellite-transition sidebands (left column) and the CT peak (right column). The top trace is experimental and the bottom trace is a result of numerical simulation. From both the experimental and simulated spectra the quadrupolar parameters were estimated as $\chi = 1.1 \pm 0.03$ MHz and $\eta = 0.10 \pm 0.03$. In the left column the CT line has been chopped off for a better view of the satellite-transition sidebands. (Reprinted with permission from Jung *et al.*[44] Copyright (1999) Elsevier.)

The contribution of the second-order quadrupolar Hamiltonian to the frequencies of the symmetric transitions is given by *

$$\omega^{(2)}_{m,-m} = \frac{\omega_Q^2}{18\omega_0} \sum_{l=0}^{2} A^{(2l)}(I,m) \sum_{j,k=-l}^{l} B^{(2l)}_{2j}(\eta) \mathrm{e}^{-2j\mathrm{i}\alpha} d^{(2l)}_{2j\ 2k}(\beta) d^{(2l)}_{2k0}(\theta) \mathrm{e}^{-2k\mathrm{i}(\gamma+\omega_R t)} \quad (35)$$

The lineshape of the CT is obtained by setting $m = -1/2$ in Eq. (35). The second-order contribution to the satellite transitions $\omega^{(2)}_{m-1,m}$ is given by:

$$\omega^{(2)}_{m-1,m} = \frac{\omega_Q^2}{18\omega_0} \sum_{l=0}^{2} \mathcal{A}^{(2l)}(I,m) \sum_{j,k=-l}^{l} B^{(2l)}_{2j}(\eta) \mathrm{e}^{-2j\mathrm{i}\alpha} d^{(2l)}_{2j\ 2k}(\beta) d^{(2l)}_{2k\ 0}(\theta) \mathrm{e}^{-2k\mathrm{i}(\gamma+\omega_R t)} \quad (36)$$

2.4. High-resolution spectra of half-integer quadrupolar spins

High-resolution spectra of half-integer quadrupolar spins can be obtained if the observable elements of the density matrix $|-1/2\rangle\langle 1/2|$ have accumulated the same

* with $\alpha = \alpha_{\mathcal{PR}}, \beta = \beta_{\mathcal{PR}}, \gamma = \gamma_{\mathcal{PR}}$.

phase for all crystallites simultaneously. In such cases, an echo is formed, the modulation of which is affected only by isotropic terms. In the following, the formation of this echo is explained by a simple manipulation of Eqs. (35) and (36) and accordingly, the basics of the DAS, MQMAS and STMAS experiments are derived. Finally, high resolution by DOR, VASS, nutation spectroscopy and SATRAS will be briefly outlined.

In the evaluation of the echo positions we retain only those terms in Eqs. (35) and (36), which contribute to the inhomogeneous broadening of the spectrum and the isotropic part $(l = 0)$ is neglected. It has no net contribution to the inhomogeneous phase dispersion that results from the distribution of crystallite orientations in the powder, and will be reentered in the calculation in Section 4. In the limit of fast MAS, time-dependent terms $(k \neq 0)$ may also be dropped, as they contribute only to the sideband formation. After elimination of $l = 0$ and $k \neq 0$ terms, Eqs. (35) and (36) reduce to

$$\omega^{(2)}_{m,-m} = \omega^{(2)}_{\mathrm{Q}} A^{(2)}(I,m) d^{(2)}_{00}(\theta) + \omega^{(4)}_{\mathrm{Q}} A^{(4)}(I,m) d^{(4)}_{00}(\theta) \tag{37}$$

$$\omega^{(2)}_{m-1,m} = \omega^{(2)}_{\mathrm{Q}} \mathcal{A}^{(2)}(I,m) d^{(2)}_{00}(\theta) + \omega^{(4)}_{\mathrm{Q}} \mathcal{A}^{(4)}(I,m) d^{(4)}_{00}(\theta) \tag{38}$$

where $\omega^{(2l)}_{\mathrm{Q}} = \omega^{(2l)}_{\mathrm{Q}}(\alpha,\beta,\eta) = \frac{\omega^2_{\mathrm{Q}}}{18\omega_0}\left(\sum_{j=-l}^{l} B^{(2l)}_{2j}(\eta) d^{(2l)}_{2j0}(\beta) \mathrm{e}^{-2\mathrm{i}j\alpha}\right)$ are the spatial terms of the quadrupolar tensor that do not depend on either m or θ. Manipulation of these two free experimental parameters induces echo formation in DAS, MQMAS, and STMAS experiments. In Eqs. (37) and (38) the $d^{(2)}_{00}$ and $d^{(4)}_{00}$ terms are equivalent to the Legendre polynomials of the second- and fourth-rank, respectively.

2.4.1. *Dynamic-angle spinning*

In the DAS experiment three pulses are applied.[10,11] The first creates SQCs, evolving under $\tilde{\mathcal{H}}_{\mathrm{Q}}$ with the rotor spinning at an angle of θ_1 with respect to the magnetic field. A second pulse stores the magnetization along z, allowing time for an angle hop ($\approx$30 ms), which is achieved by specialized hardware. Finally, another pulse creates SQCs, which are detected with the sample spinning at an angle θ_2. Since the value of m remains either 1/2 or $-1/2$ and since during t_1 $\theta = \theta_1$ and during t_2 $\theta = \theta_2$, the overall phase accumulated by the $|-1/2\rangle\langle 1/2|$ term of the density matrix will be

$$\begin{aligned}\phi(\{\theta_1,t_1\},\{\theta_2,t_2\}) = &\left\{A^{(2)}\left(I,-\frac{1}{2}\right)\omega^{(2)}_{\mathrm{Q}} d^{(2)}_{00}(\theta_1) + A^{(4)}\left(I,-\frac{1}{2}\right)\omega^{(4)}_{\mathrm{Q}} d^{(4)}_{00}(\theta_1)\right\} t_1 \\ &+ \left\{A^{(2)}\left(I,-\frac{1}{2}\right)\omega^{(2)}_{\mathrm{Q}} d^{(2)}_{00}(\theta_2) + A^{(4)}\left(I,-\frac{1}{2}\right)\omega^{(4)}_{\mathrm{Q}} d^{(4)}_{00}(\theta_2)\right\} t_2 \end{aligned} \tag{39}$$

An echo will form at a time $t_2 = kt_1$ if simultaneously the two following equations hold

$$d^{(2)}_{00}(\theta_1) = -k d^{(2)}_{00}(\theta_2) \tag{40a}$$

$$d_{00}^{(4)}(\theta_1) = -k d_{00}^{(4)}(\theta_2) \tag{40b}$$

If a value of $k = 1$ is chosen so that the CSA is refocused, then for the pair of angles $\theta_1 = 37.38°$ and $\theta_2 = 79.19°$, Eqs. (40a) and (40b) are satisfied.

2.4.2. *Multiple-quantum magic-angle spinning*

As was mentioned in the beginning of this section, MQMAS was the first experiment that utilized RF and spin manipulation, retaining the normal MAS spatial averaging and avoiding angle hopping.[13,14] Spin coherences are manipulated by first exciting higher-order symmetric coherences (± 3, ± 5, ± 7, or ± 9), which are free of first-order quadrupolar broadening, and then transferring them to CT coherences. An echo is formed when the MQC frequencies and the symmetric SQC frequencies have opposite signs, since their ratio is independent of the crystallite orientation. With a constant spinning angle $\theta = \theta_M(d_{00}^{(2)}(\theta_M) = 0)$ the total phase accumulated by the detectable elements of the density matrix becomes

$$\phi(\{m_1, t_1\}, \{m_2, t_2\}) = \omega_Q^{(4)} d_{00}^{(4)}(\theta_M)\{A^{(4)}(I, m_1)t_1 + A^{(4)}(I, m_2)t_2\} \tag{41}$$

and an echo forms at a time $t_2 = kt_1$ with

$$k(I, m_1, m_2) = -\frac{A^{(4)}(I, m_1)}{A^{(4)}(I, m_2)} \tag{42}$$

also known as the MQMAS ratio. In the simplest case $m_2 = -1/2$ (The CT with coherence order -1 used for echo and detection) leading to the creation of both echo ($k > 0$) and antiecho ($k < 0$), as long as a suitable phase cycling is applied (see Section 3). Using the values $A^{(4)}(I, m)$ appearing in Table 3 and the relation $A^{(4)}(I, m) = -A^{(4)}(I, -m)$, the values of $k(I, m_1, -1/2)$ for the echo pathway can be calculated and for spins-$\frac{3}{2}$ to $\frac{7}{2}$ they are given by:

$$\begin{aligned} k(3/2, -3/2, -1/2) &= 7/9 \quad & k(7/2, +3/2, -1/2) &= 101/45 \\ k(5/2, +3/2, -1/2) &= 19/12 \quad & k(7/2, +5/2, -1/2) &= 11/9 \\ k(5/2, -5/2, -1/2) &= 25/12 \quad & k(7/2, -7/2, -1/2) &= 45/166 \end{aligned} \tag{43}$$

Thus, an echo will be obtained if a correlation $m_1 \leftrightarrow -1/2$ for a spin I is chosen with negative m_1 for $|m_1| = I$ and positive m_1 if $|m_1| < I$. MQMAS can be performed using values of m_2 that are different from $-1/2$. For example, it was shown that correlation of five-quantum and triple-quantum coherences in spins-$\frac{5}{2}$ ($k(5/2, \pm 5/2, \pm 3/2) = 25/19$) can be exploited and in fact results in a better resolution than $5Q \rightarrow 1Q$ or $3Q \rightarrow 1Q$ MQMAS[45] (see also Section 3.3).

2.4.3. *Pictorial representation of the MQMAS echo*

Equation (41) is modelled qualitatively in Fig. 4 for the simplest MQMAS experiment involving two pulses (which can be easily adapted to STMAS experiment also). Four subspaces of the density matrix describe the phase accumulated by two arbitrary crystallites. From left to right, the first subspace, Fig. 4a, corresponds to the MQC $|m\rangle\langle -m|$ at time $t_1 = 0$ (or $|-m><m|$, depending on $|m|$ and I). When perfect excitation is assumed the coherence of all crystallites will have the same phase and amplitude. In Fig. 4b the same subspace is shown for time $t_1 = \tau$, with a coherence phase accumulated according to Eq. (41). The two crystallites accumulate a different phase depending on their $\Omega_{\mathcal{PL}}$ values. In Fig. 4c1 the projection of the density matrix on to the CT subspace is shown following a conversion pulse. Ideally, this is similar in phase and amplitude to its predecessor and corresponds to time $t_2 = 0$. Finally, in Fig. 4d1 the phase accumulation at $t_2 = k(I, m_1, -1/2)t_1$ is shown. All crystallites refocus at the same k value and therefore no phase dispersion is observed. Normal evolution following $t_2 > k(I, m_1, -1/2)t_1$ (not shown) yields the MAS dimension in the 2D experiment.

Figure 4c2 describes a case in which the conversion pulse is non-ideal. Therefore, the coherence in the second subspace is not mapped directly on to its analogue in the third subspace, leading to phase dispersion and amplitude attenuation. (The dashed arrows

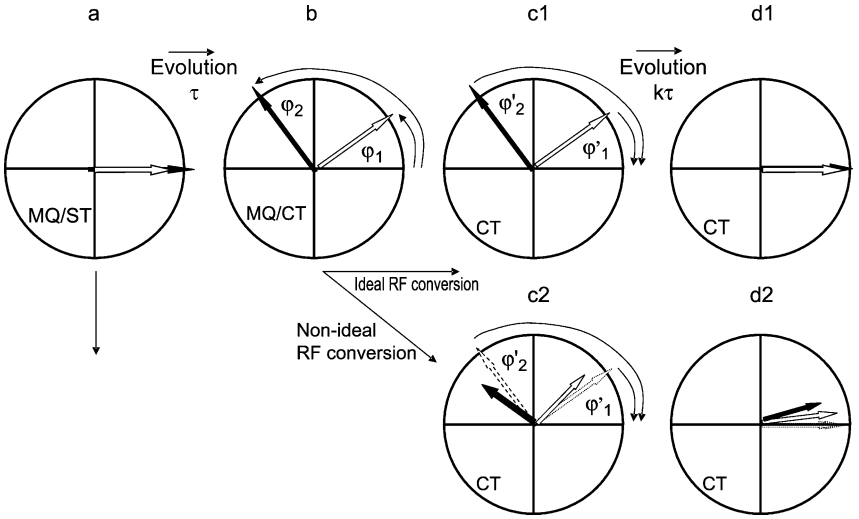

Fig. 4. The formation of the MQMAS echo following the trajectory of two crystallites. The circles from left to right denote (a) initial ideal triple- (or multiple-) quantum coherence ($|m\rangle\langle -m|(\Omega_{\mathcal{PL}})$ or $|-m\rangle\langle m|(\Omega_{\mathcal{PL}})$, see text) of two arbitrary crystallites. (b) The multiple-quantum density matrix element after some time τ, where each crystallite had evolved with a different frequency according to Eq. (41). (c1) An ideal conversion to observable SQC ($|1/2\rangle\langle -1/2|(\Omega_{\mathcal{PL}})$) following an ideal RF pulse. (d1) An echo is formed after an additional evolution time, $k\tau$. (c2) and (d2) show the MQMAS echo formation after an inefficient conversion pulse. The conversion from multiple- to singe-quantum subspace results in signal reduction and phase dispersion of the final echo. The broken arrows represent the ideal case.

represent the ideal case, as in Fig. 4c1 and d1.) This results in a reduced echo as shown in the fourth subspace picture (Fig. 4d2). Another consequence will be the deformation of the lineshapes along the MAS dimension as a result of the non-uniform initial conditions at time $t_2 = kt_1$. Several pulse sequences have been designed to overcome this problem using amplitude and frequency modulation, rotary resonance phenomena or simple adiabatic transfer properties of quadrupolar nuclei. These issues will be discussed at length in Section 5. In real experiments, non-ideality is generated both in the excitation and conversion RF pulses. Such non-ideality can be quantified with a single parameter which can be used to compare the efficiency of modifications to the basic MQMAS scheme.[31]

2.4.4. *Satellite-transition magic-angle spinning*

In the STMAS experiment,[20,21] like in MQMAS, spin coherences are manipulated rather than the spinning angle. However, instead of creating symmetric MQCs, the single-quantum satellite transition coherences, $|n - 1/2 >< n + 1/2|$, are now excited. After an evolution period t_1, these are then refocused with the symmetric CT SQCs evolving during t_2. The relevant accumulated phase thus becomes

$$\phi(\{m_1, t_1\}, \{m_2, t_2\}) = \omega_{\mathrm{Q}}^{(4)} d_{00}^{(4)}(\theta_{\mathrm{M}})\{\mathcal{A}^{(4)}(I, m_1)t_1 + A^{(4)}(I, -1/2)t_2\} \tag{44}$$

and an echo is formed at a time $t_2 = kt_1$ where

$$k(I, m_1, -1/2) = -\frac{\mathcal{A}^{(4)}(I, m_1)}{A^{(4)}(I, -1/2)} \tag{45}$$

The relevant satellite transition coherences $\mathrm{ST_n}$ correspond to the $|n - 1/2\rangle\langle n + 1/2|$ elements of the density matrix, where $n = m_1 - 1/2$. The STMAS ratios can be again calculated from Table 4 in a similar fashion to the MQMAS ratios and for an $m_1 \leftrightarrow -1/2$ STMAS experiment one obtains explicitly the following values for spins-$\frac{3}{2}$ to $\frac{7}{2}$:

$$\begin{aligned}
&\mathrm{ST}_{-1} : k(3/2, +3/2, -1/2) = 8/9 \quad \mathrm{ST}_{+1} : k(7/2, -3/2, -1/2) = 28/45 \\
&\mathrm{ST}_{+1} : k(5/2, -3/2, -1/2) = 7/24 \quad \mathrm{ST}_{-2} : k(7/2, +5/2, -1/2) = 23/45 \\
&\mathrm{ST}_{-2} : k(5/2, +5/2, -1/2) = 11/6 \quad \mathrm{ST}_{-3} : k(7/2, +7/2, -1/2) = 12/5
\end{aligned} \tag{46}$$

Like MQMAS the basic STMAS scheme is a two-pulse experiment, with satellite transition coherences evolving during t_1 and refocused by SQC evolution during t_2. Some requirements of the experiment are stroboscopic sampling during t_1 and very accurate setting of the magic angle (no more than 0.004° variation[21]) in order to average out the first-order quadrupolar interaction of the satellite transitions.

In Section 8 we will highlight some of the features of STMAS as well as the recent developments of this technique, which allow for some level of compromise in the setting of the magic angle.

We now briefly outline some additional high-resolution techniques for half-integer spin quadrupolar nuclei.

2.4.5. *Double rotation*

The double-rotation technique was introduced by Samoson *et al*. in 1988.[9] This was the first real high-resolution method for half-integer spin quadrupolar nuclei. DOR is performed as a 1D experiment in which the sample is spun simultaneously by an inner rotor that is inclined along an axis making an angle of 30.56° with respect to an outer rotor axis, and an outer rotor at an angle of 54.7° with respect to B_0. Unlike Eq. (35), here, the Hamiltonian contains instead of $d_{00}^{(2l)}(\theta_1)$, a product term of the form $d_{00}^{(2l)}(\theta_1)d_{00}^{(2l)}(\theta_2)$ $(l = 0 - 2)$ due to an additional transformation from one rotor PAS $\mathcal{R}_1$ to the second rotor PAS $\mathcal{R}_2$. The angles $\theta_1 = 30.56°$ and $\theta_2 = 54.7°$ are a pair of possible solutions chosen to nullify this term. The achievable spinning rates of DOR rotors are of the order of 5–7 kHz for the inner rotor and 2–3 kHz for the outer rotor. The resultant spectrum has a central peak that is often flanked by a large number of spinning sidebands, unless a spinning sideband suppression technique is used.[46] The limitation of this technique is the requirement of dedicated and mechanically complex probes, limiting the application of DOR to a few laboratories.

2.4.6. *VASS, SATRAS and nutation spectroscopy*

In the VASS technique,[6] the sample is spun at angles other than the magic angle of 54.7°. It was shown that the linewidth depends greatly on the asymmetry parameter η and that the narrowest lines are achieved for samples spinning at the angles 36° and 75°, corresponding approximately to the roots of the fourth-order Legendre polynomials, which appear in Eq. (35). Since this technique gives only a partial narrowing of the CT lineshapes and in parallel reintroduces parts of the dipolar and CSA interactions, it is limited to compounds having well isolated half-integer quadrupolar spins of low CSA values.

SATRAS is a regular single-pulse MAS experiment where the satellite transitions of a half-integer quadrupolar spin nucleus are probed rather than the CT. An accurate setting of the magic-angle along with stable spinning speeds are needed in order to obtain decent spectra, since the strength of the quadrupolar interaction is normally much higher than that of the spinning frequency. The individual satellite spectra can be analysed separately for information regarding the quadrupolar and chemical shifts.[47] SATRAS spectra can be simulated and fitted to experimental results providing the NMR parameters[12] (see Fig. 3). Spectral resolution that is better than that of the CT lineshape can be detected by observing the sideband manifold of the individual satellite spectra. Since the second-order broadening of the central and satellite transitions both obey the same orientation dependence [Eqs. (35) and (36)], it is the ratio $A(I, -1/2)/\mathcal{A}(I, m)$ that determines the line narrowing of a single sideband in the $|m - 1\rangle \leftrightarrow |m\rangle$ satellite transition manifold.

In fact, the $|3/2\rangle \rightarrow |5/2\rangle$ ST_2 satellite (or its equivalent ST_{-2}) transition of a spin-9/2 yields sidebands that are narrower with respect to the CT by about a factor of 18,[21] and provides almost complete high-resolution chemical shift spectra.

Nutation spectroscopy is a 2D scheme in which the signal intensity is monitored during the t_2 interval following a single pulse of increasing length t_1. A 2D Fourier transform (FT) and a projection on to the indirect dimension give a nutation spectrum that reflects the distribution of nutation frequencies of the spins during the pulse.[7,8] Three regimes of RF frequencies, ν_1 (where ν_1 is the strength of the RF field), can be identified with respect to $\nu_Q(\Omega_{\mathcal{PL}})(=\omega_Q(\Omega_{\mathcal{PL}})/2\pi)$. (i) When $\nu_1 > \nu_Q(\Omega_{\mathcal{PL}})$, a non-selective excitation of the first-order quadrupolar spectrum results in a nutation frequency $\nu_{nut} \cong \nu_1$ and a spectral line at that frequency. (ii) When $\nu_1 < \nu_Q(\Omega_{\mathcal{PL}})$, the RF field excites the CT selectively and a spectrum with a line at $\nu_{nut} = (I + \frac{1}{2})\nu_1$ results. (iii) In the most complex case, when $\nu_1 \sim \nu_Q(\Omega_{\mathcal{PL}})$, a nutation spectrum is observed with a characteristic second-order powder lineshape from which ν_Q/ν_1 and η may be deduced. However, ideal lineshapes are difficult to get in this case and numerical fitting procedures are hard to perform. Off-resonance nutation spectroscopy[48] was shown to have several advantages over regular nutation spectroscopy. Here, a wider range of quadrupolar interactions can be probed and the off-resonance variable can be used as an additional parameter that facilitates the separation of sites with similar ν_Q values. Finally, the reduction in signal-to-noise due to the off-resonance excitation and the existence of intense $F_2 = 0$ lines can be almost completely eliminated by using frequency stepped adiabatic half-passage pulses.[49,50] In conclusion, nutation spectroscopy results in complex lineshapes containing all the necessary information to deduce quadrupolar parameters. However, this deduction involves extensive numerical fitting that is error-prone and needs to be applied with extreme caution.

3. BASIC MQMAS PULSE SCHEMES

The essential requirements of a 2D MQMAS pulse scheme are a pulse or a set of pulses that excite MQCs, followed by an evolution under $\mathcal{H}_Q^{(2)}$ during t_1, another set of pulses to convert the MQC into SQCs, and an acquisition period t_2, during which an echo is formed.

3.1. The two-pulse sequence

A single RF pulse is sufficient to create MQC in half-integer quadrupolar spin systems, as long as the strength of the RF pulse $\nu_1 < \nu_Q$, which is often the case.[79] Similarly, a single RF pulse can also convert the MQC to observable SQC. We denote such a basic sequence as P_H–P_H, which is sketched in Fig. 5a, where P_H denotes a hard unmodulated rectangular pulse often called CW pulse. The first pulse is optimized to excite MQC and has a phase ϕ_1. The second pulse with a phase ϕ_2 converts MQC to SQC which is detected by the receiver. The receiver phase ϕ_{rec} is cycled to select the required coherence pathways and to eliminate the undesired ones. The value of the receiver phase equals $-[\sum_i \Delta p_i \phi_i]$ where Δp_i is the difference between the coherence order after and

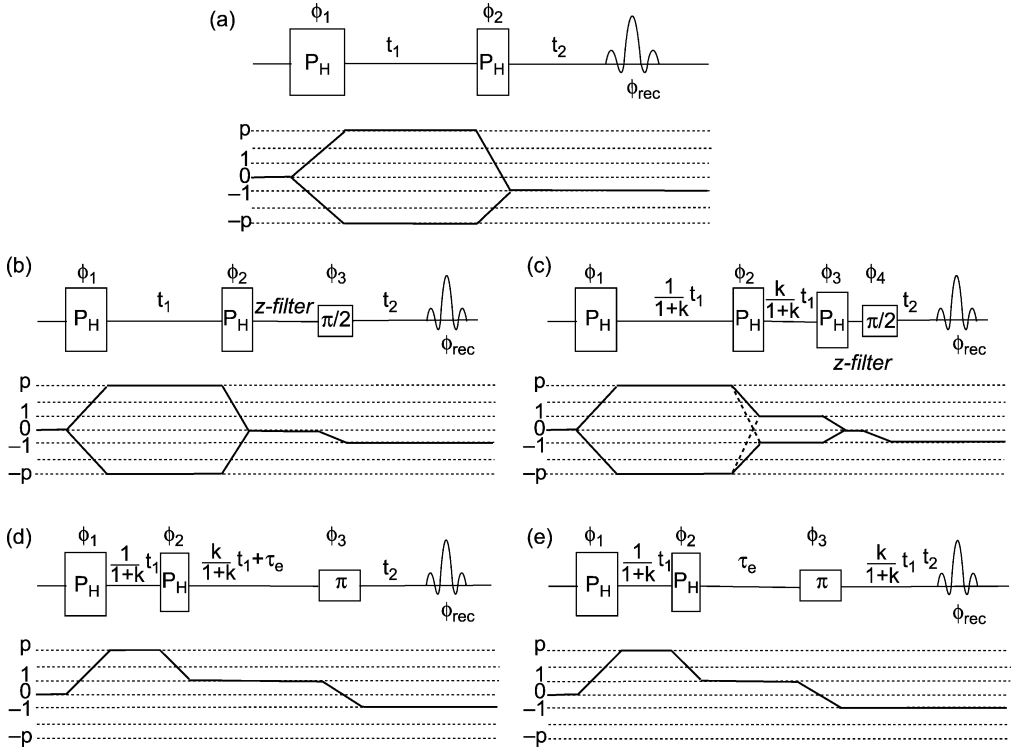

Fig. 5. Schematic of the various MQMAS pulse schemes along with their coherence transfer pathways. (a) The basic two-pulse MQMAS scheme (denoted as $P_H - P_H$), (b) z-filter, (c) z-filter with split-t_1 where the dotted pathway indicates the required coherence transfer for experiments on a spin I correlating pQC with SQC with $|p| < 2I$ and the solid pathway corresponds to the case $|p| = 2I$, (d) shifted-echo split-t_1 pulse sequence for the case $|p| = 2I$, and (e) shifted-echo split-t_1 pulse sequence for the case $|p| < 2I$. The value of k is positive here.

Table 5a. The phase table for 3Q-, 5Q-, 7Q, and 9QMAS P_H–P_H two-pulse experiments

Experiment	Number of phase-cycle steps, N	ϕ_1	ϕ_2	ϕ_{rec}
3QMAS	6	$\frac{2\pi}{6}\mathcal{M}$	0	$-\frac{2\pi}{2}\mathcal{M}$
5QMAS	10	$\frac{2\pi}{10}\mathcal{M}$	0	$-\frac{2\pi}{2}\mathcal{M}$
7QMAS	14	$\frac{2\pi}{14}\mathcal{M}$	0	$-\frac{2\pi}{2}\mathcal{M}$
9QMAS	18	$\frac{2\pi}{18}\mathcal{M}$	0	$-\frac{2\pi}{2}\mathcal{M}$

prior to the application of a pulse with a phase ϕ_i, the summation done for all the pulses in a given sequence.[51] In the simple case of the two-pulse MQMAS experiment, correlating 3QC $\leftrightarrow$ SQC called 3QMAS experiment (called 3QMAS experiment) the receiver phase is designed to select a coherence pathway that follows $\Delta p = \pm 3$ during the first pulse and $\Delta p = -4$, and $+2$ simultaneously during the second pulse. Table 5a shows the values of ϕ_1, ϕ_2, and ϕ_{rec} for the selection of various MQC orders in various half-integer spin systems following the nested phase cycle procedure.[51,52] In the Table, $\mathcal{M}$ is the transient counter that takes values from 0 to $N-1$ where N is the number of phase-cycle steps.

The two-pulse scheme results in an MQ echo at $t_2 = kt_1$ which leads to a 2D time domain data set with echoes forming along a line with a slope k, as shown in Fig. 6a. Fourier transform of such a time-domain data set leads to an 'unsheared spectrum', a typical example of which is shown in Fig. 6b where FT was done only along the t_2 dimension. In order to get a pure isotropic F_1 projection, the MQMAS data set needs to be sheared as shown in Fig. 6c with the sheared 2D ^{23}Na 3QMAS spectrum of a sample of $Na_2\ C_2O_4$ shown in Fig. 6d.

When the receiver phase selects both the $+p$ and $-p$ coherences following the excitation pulse, as shown in Fig. 5a, positive and negative values of k together contribute to the signal. A positive k value corresponds to an echo signal having its maximum at a time $t_2 = kt_1$ and a negative k corresponds to an antiecho signal having a virtual maximum at a time $t_2 = -kt_1$ (before the conversion pulse). If $|p| = 2I$ is selected (3Q in spins-$\frac{3}{2}$, 5Q in spins-$\frac{5}{2}$, etc.), the echo signal corresponds to the pathway with a $p < 0$ evolution, and when $|p| < 2I$ is selected (3Q in spins-$\frac{5}{2}$, 3Q and 5Q in spins-$\frac{7}{2}$, etc.) the echo pathway emerges from $p > 0$. This implies that whilst the echo propagates forward in time, the antiecho pathway generates signals propagating backward in time as t_1 is increased.

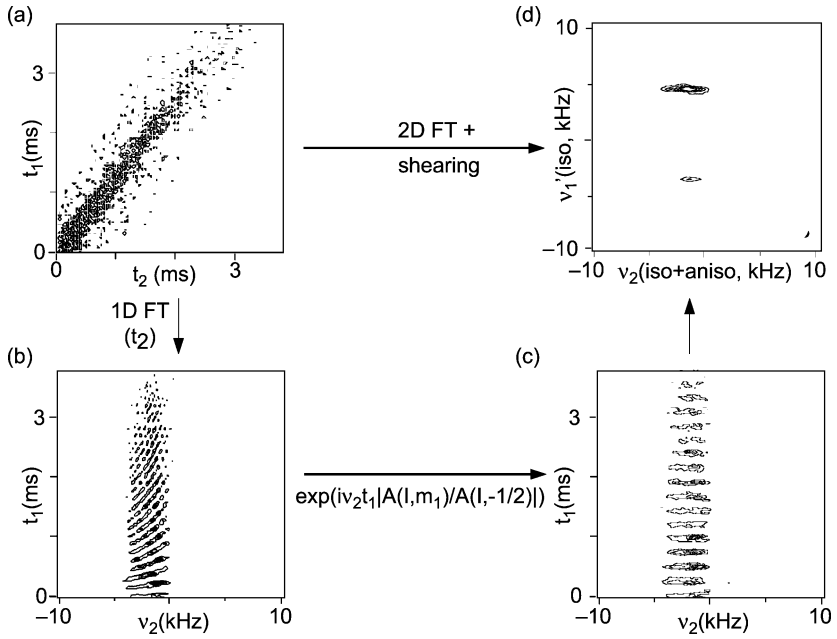

Fig. 6. Schematic of the 2D time domain data set, shearing, and frequency representation of a ^{23}Na MQMAS experiment on a sample of $Na_2C_2O_4$. (a) 3QMAS time domain data set obtained with the pulse sequence shown in Fig. 5a. (b) Unsheared spectrum following a Fourier transformation along t_2 of the data in (a). (c) Sheared spectrum (FT along only t_2) after applying a first-order t_1 dependent phase correction along the F_2 axis (ν_2). (d) ^{23}Na 2D 3QMAS spectrum of $Na_2C_2O_4$ obtained from either (a) with both 2D FT and shearing transformation or from (a), (b), and (c), with FT along the t_2 dimension followed by a shearing transformation. (Reprinted with permission from Frydman and Harwood[13] Copyright (1995) American Chemical Society.)

Fourier transform of the data from the basic MQMAS scheme has the following properties: (i) When the antiecho contribution is long lived, a linear combination of the echo and antiecho signals may be accomplished leading to a time domain data set that is amplitude modulated (AM). This leads to a pure phase absorptive spectrum with ambiguity in the sign of the frequencies. It was shown that if the $+3 \rightarrow -1$ transfer ($\Delta p = -4$) and $-3 \rightarrow -1$ transfer ($\Delta p = +2$) (for 3QMAS in spins-$\frac{3}{2}$) have the same efficiency sine amplitude-modulated data set results by acquiring both echo and antiecho pathways.[53] TPPI or STATES method[54] may be then used for frequency sign discrimination. In the above, if both $\Delta p = -4$ and $\Delta p = +2$ transfers are not of the same efficiency, contributions of mixed absorptive and dispersive lineshapes appear in the spectrum. Hence, a careful optimization of the conversion pulse is required.[53] (ii) When the antiecho signal is short lived, proper combination of echo and antiecho signals is not possible leading to phase modulation (PM) of at least part of the acquired data resulting in the formation of twisted 2D lineshapes. (iii) As indicated before, the position

of the echo is shifted as t_1 is propagated resulting in a sheared spectrum, i.e., the isotropic axis appears along a ridge with a slope k. Therefore, a shearing transformation needs to be applied that aligns the ridges along the isotropic dimension, F_1.

In the following, we outline strategies for achieving pure absorption lineshapes in 2D NMR experiments in general, with specific emphasis on the MQMAS experiment.

3.2. Pure absorption 2D NMR lineshapes

A 2D NMR experiment can lead to a data set that is either phase modulated or amplitude modulated as a function of t_1, depending on the particular experiment and coherence pathways selected. A regular 1D spectrum consists of absorption $\mathcal{A}(\nu)$ and dispersion $\mathcal{D}(\nu)$ peaks corresponding to the real and imaginary parts of the spectral lines, respectively. In 2D experiments, phase modulation in t_1 results in twisted 2D real lineshapes as a result of the Fourier transformation of bi-exponential time domain signals:

$$\mathrm{Re}(\mathrm{FT}[\mathrm{e}^{-2\pi i\nu_1 t_1}\mathrm{e}^{-2\pi i\nu_2 t_2}]) = \mathcal{A}(\nu_1)\mathcal{A}(\nu_2) - \mathcal{D}(\nu_1)\mathcal{D}(\nu_2) \tag{47}$$

When the data is amplitude modulated in t_1, sign discrimination in the F_1 frequency dimension cannot be obtained since the real part of the Fourier transform becomes:

$$\mathrm{Re}(\mathrm{FT}[(\mathrm{e}^{-2\pi i\nu_1 t_1} + \mathrm{e}^{2\pi i\nu_1 t_1})\mathrm{e}^{-2\pi i\nu_2 t_2}] = \{\mathcal{A}(\nu_1) + \mathcal{A}(-\nu_1)\}\mathcal{A}(\nu_2) \tag{48}$$

The result of Eq. (48) is obtained by applying a complex Fourier transform in t_2 followed by real Fourier transform in t_1. For either phase or amplitude modulation, 2D NMR signals have to be acquired in such a manner that both pure absorption spectra and sign discrimination will be obtained.

Several schemes have been suggested in the literature to overcome the twisted lineshapes in phase modulated experiments and the sign ambiguity in amplitude modulated 2D experiments. Provided an echo can be detected, phase modulated experiments can yield pure absorption lineshapes by acquiring the whole echo.[55] A schematic of the underlying process shown in Fig. 7 depicts symmetric FID time domain signals from an experiment with negligible relaxation effects. For an echo appearing at time $t_2 = \tau_e$ (Fig. 7a) the FID can be rearranged so that the acquisition points from τ_e onwards appear at $t_2 = 0$ and all points originating from $t_2 = 0$ to τ_e are shifted to the end of the FID (Fig. 7c). The Fourier transform of such a signal has a zero imaginary part ($\mathcal{D}(\nu_2) = 0$) contribution (dotted line in Fig. 7d) and thus provides pure absorption 2D lineshapes according to Eq. (47). An alternative is to first Fourier transform the echo signal in Fig. 7a to get a spectrum in Fig. 7b and then perform a first-order phase correction amounting to $360\tau_e/\Delta t_2$, where Δt_2 is the dwell time during the t_2 period, or the time difference between adjacent points in the acquisition time domain. In both the cases, the real part of the resulting 2D spectrum will be devoid of the $\mathcal{D}(\nu_1)\mathcal{D}(\nu_2)$ term appearing in Eq. (47). For antisymmetric signals, $\mathcal{D}(\nu_2)$ is small but non-zero

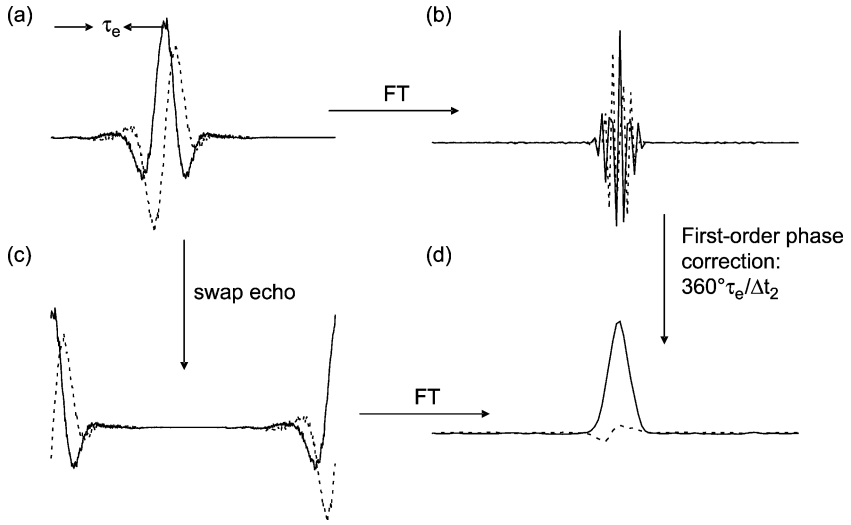

Fig. 7. (a) Schematic profile of the whole echo. There are two ways of getting a pure absorption lineshape from the whole echo. The echo maximum is shifted to $t_2 = 0$ and all points from 0 to τ_e are shifted to the end of the FID as in (c), Fourier transform of which gives the spectrum shown in (d). Alternatively, the spectrum in (b) obtained after a Fourier transform of (a) may be corrected to first-order in phase by $360°\tau_e/\Delta t_2$ to obtain the spectrum in (d). Here, τ_e is the echo delay and Δt_2 is the t_2 dwell time. The solid lines are the real component of the time and frequency domain signal and the dotted lines indicate the contribution of the imaginary component.

(proportional to the amount of asymmetry), and the dispersive parts result in some twisting of the 2D lineshapes.

The major schemes for obtaining pure absorption 2D lineshapes in MQMAS are phase modulated whole-echo acquisition, amplitude modulated hypercomplex acquisition, and shifted echo hypercomplex acquisition suggested by Massiot and coworkers,[56] *z*-filtering[57] introduced into MQMAS by Brown *et al.*[58] and by Amoureux *et al.*[59] and the shifted-echo split-t_1 method introduced by Brown and Wimperis.[60] The split-t_1 technique does away with the shearing transformation. It provides shearing in the time domain by splitting the t_1 evolution between MQC and SQC and not whilst processing the data.

In the following, we discuss the *z*-filter experiment[59] and the shifted-echo split-t_1 MQMAS schemes.[60] Although the latter scheme of whole-echo acquisition has been shown to be the most efficient in terms of signal-to-noise and is especially suited for sensitivity enhancement schemes, which are discussed extensively in Section 5, for samples with short T_2 the *z*-filter scheme may prove to be more beneficial.

3.2.1. *z-Filtered amplitude-modulated MQMAS scheme*

The pulse sequences for the amplitude-modulated *z*-filter MQMAS experiment are shown in Fig. 5, with Fig. 5b showing the regular three pulse sequence and Fig. 5c

the split-t_1 scheme. The z-filter sequence was described in detail by Amoureux.[19] This sequence provides pure absorption lineshapes since the $\pm p \rightarrow 0 \rightarrow -1$ pathway has an intermediate stage where the magnetization is stored along z, thus eliminating any phase memory from all crystallites. The first two pulses are non-selective hard pulses, whilst the third pulse is a selective $\pi/2$ pulse, with a power level of 10–20 kHz. The zero-quantum (ZQ) storage time can be very short, if a full phase cycling is applied filtering only this coherence during that period. For ZQ storage duration of a few rotor periods, the z-filter should eliminate all residual transverse coherences. In general, the ZQ storage duration is short enough to prevent any possible spin diffusion. The pulses can be optimized with a short fixed t_1 delay of 5 μs.

The three-pulse sequence and the split-t_1 version of the z-filter scheme yield pure absorptive lineshapes, and may be combined with either TPPI or STATES for frequency sign discrimination. For the split-t_1 version no shearing is required, however, its coherence pathway, and thus the phase cycling depends on the values of I and desired p after the excitation pulse. For a pQMAS experiment, if $|p| < 2I$, the second pulse transfer has a value of $\Delta p = \pm(p+1)$ (for 3QMAS in spins-$\frac{5}{2}$, $\frac{7}{2}$, $\frac{9}{2}$, 5QMAS in spins-$\frac{7}{2}$, $\frac{9}{2}$, and 7QMAS in spins-$\frac{9}{2}$), indicated by the dotted line in Fig. 5c, and for $|p| = 2I, \Delta p = \pm(p-1)$, indicated by the solid line in Fig. 5c.

For the schemes in Fig. 5b and c a 3QMAS experiment requires 24- and 96-step nested phase cycles, respectively. Table 5b gives the phase cycle for all possible MQMAS experiments employing the scheme in Fig. 5b, where floor(x) corresponds to the largest integer which is not greater than x.

3.2.2. *Phase-modulated shifted-echo split-t_1 MQMAS scheme*

Figure 5d depicts the phase-modulated shifted-echo split-t_1 experiment for $|p| = 2I$ and Fig. 5e the scheme for $|p| < 2I$, p being the desired coherence level after the excitation pulse. Their corresponding coherence pathways are also shown. The first pulse excites MQC and the second pulse converts them into SQC. The third pulse is a selective π pulse, i.e., ideally it operates on the CT only and converts $+1Q \rightarrow -1Q$ coherences, and is normally applied at a RF power level of 10–20 kHz. The experiment relies on the fact that with a soft 180° pulse after the conversion pulse an additional echo can be generated after the MQ echo without any substantial signal loss. As discussed above, this minimizes the imaginary components produced by the whole-echo FT, as shown by the dotted lines in Fig. 7d. This scheme, introduced by Brown and Wimperis,[60] was derived from the shifted-echo experiments, proposed by Massiot *et al.*[56] by changing the definitions of the t_1 and t_2 evolution periods. This leads to shearing in the time domain during the experiment rather than applying the shearing transformation to the data set after the completion of the acquisition.

Since the experiment relies on a second echo formation, either the echo or the antiecho pathway can be chosen. However, choosing the antiecho pathway requires a much longer echo delay, which can lead to unwanted relaxation or exchange effects generating antisymmetric echoes. It is, therefore, preferable to choose the echo pathway, which is also the choice depicted in Fig. 5d and 5e.

Table 5b. The phase table for 3Q-, 5Q-, 7Q, and 9QMAS z-filtered amplitude-modulated experiments

Experiment	Number of phase-cycle steps, N	ϕ_1	ϕ_2	ϕ_3	ϕ_{rec}
3QMAS	24	$\frac{2\pi}{6}\mathcal{M}$	0	$\frac{2\pi}{4}\ \text{floor}\left(\frac{\mathcal{M}}{6}\right)$	$\mp 3\frac{2\pi}{6}\mathcal{M} + \frac{2\pi}{4}\ \text{floor}\left(\frac{\mathcal{M}}{6}\right)$
5QMAS	40	$\frac{2\pi}{10}\mathcal{M}$	0	$\frac{2\pi}{4}\ \text{floor}\left(\frac{\mathcal{M}}{10}\right)$	$\mp 5\frac{2\pi}{10}\mathcal{M} + \frac{2\pi}{4}\ \text{floor}\left(\frac{\mathcal{M}}{10}\right)$
7QMAS	56	$\frac{2\pi}{14}M$	0	$\frac{2\pi}{4}\ \text{floor}\left(\frac{\mathcal{M}}{14}\right)$	$\mp 7\frac{2\pi}{14}\mathcal{M} + \frac{2\pi}{4}\ \text{floor}\left(\frac{\mathcal{M}}{14}\right)$
9QMAS	72	$\frac{2\pi}{18}\mathcal{M}$	0	$\frac{2\pi}{4}\ \text{floor}\left(\frac{\mathcal{M}}{18}\right)$	$\mp 9\frac{2\pi}{18}\mathcal{M} + \frac{2\pi}{4}\ \text{floor}\left(\frac{M}{18}\right)$

Depending on the sign of k, different experimental approaches are required in order to select the echo pathway. The first delay after the excitation pulse always amounts to $t_1/(1 + |k|)$. For the pulse scheme in Fig. 5d, applied when $|p| = 2I$ pathway is desired, the evolution of $+p$ coherences is refocused by $+1Q$ coherences (Table 3) and therefore, the delay between the conversion pulse and the echo (π) pulse is $|k|t_1/(1 + |k|) + \tau_e$, where τ_e is the echo delay time. For the pulse sequence shown in Fig. 5e, applied when $|p| < 2I$ pathway is desired, the refocusing must be performed during $p = -1$. Therefore, the second delay only shifts the echo and equals τ_e, and the refocusing of MQ coherences by SQ coherences is done after the π pulse during the delay $|k|t_1/(1 + |k|)$ prior to acquisition.

The nested phase cycle schemes that are employed for the shifted-echo split-t_1 scheme are listed in Table 5c for a variety of MQMAS experiments. Table 5d gives the phase cycle values following the recently suggested cogwheel phase cycle procedure[61] for shifted-echo split-t_1 MQMAS experiments. This phase cycling scheme may prove convenient especially for higher-spin systems. Optimization can be accomplished with a fewer scans using cogwheel phase cycle method on model compounds. The notation used for the cogwheel phase cycle is (assuming three pulses with phases ϕ_1, ϕ_2, and ϕ_3) $COGN(\nu_1, \nu_2, \nu_3; \nu_{\text{rec}})$ where N is the number of phase cycle steps and ν_1, ν_2, ν_3, and ν_{rec} are the winding numbers of each of the pulses and the receiver, respectively. The pulses and the receiver are phase cycled simultaneously with phase increments of $2\pi/\nu_1, 2\pi/\nu_2, 2\pi/\nu_3$, and $2\pi/\nu_{\text{rec}}$, respectively. The phase cycle repeats itself after N phase increments. Additionally, it may be noted that the nested phase cycle list given here is not the optimum ones for 3QMAS of spins-$\frac{7}{2}$ and $\frac{9}{2}$, for instance. Nevertheless, the amplitude of the undesired pathways is negligibly small. On the other hand, the cogwheel phase list ensures the selection of only the desired pathways and is the optimal one.

3.3. Mixed MQMAS experiments

For a given half-integer spin quadrupolar nucleus, there is a distinct advantage of obtaining higher resolution by following the time evolution of the highest MQC possible, such as 5QC in a spin-$\frac{5}{2}$ system as compared with 3QC in the same spin system.[62] The impediment is of course the severe sensitivity problem associated with the excitation of such higher-order MQ coherences.

In general, the best MQMAS sequence for the highest resolution in any quadrupolar spin system is obtained with the use of an MQNQ experiment.[45] Here, for instance, in a spin-$\frac{5}{2}$ system, instead of correlating either the 5Q or 3Q with SQC, the second-order quadrupolar frequencies resulting from a 5QC evolution period are refocused with 3QC evolution and only then transferred and detected via SQC. The pulse sequence for this is shown in Fig. 8a where both 5QC and 3QC are subjected to a t_1 evolution (split-t_1) to refocus second-order quadrupolar broadening. This, though yielding a better resolution, is prone to sensitivity problems more than other MQMAS schemes.

Table 5c. The phase table for 3Q-, 5Q-, 7Q, and 9QMAS phase-modulated shifted-echo split-t_1 experiments

Experiment	Number of phase-cycle steps, N	ϕ_1	ϕ_2	ϕ_3	ϕ_{rec}
3QMAS	96	$\frac{2\pi}{12}\mathcal{M}$	0	$\frac{2\pi}{8}\ \mathrm{floor}\left(\frac{\mathcal{M}}{12}\right)$	$-3\frac{2\pi}{12}\mathcal{M}+2\frac{2\pi}{8}\ \mathrm{floor}\left(\frac{\mathcal{M}}{12}\right)$
5QMAS	160	$\frac{2\pi}{20}\mathcal{M}$	0	$\frac{2\pi}{8}\ \mathrm{floor}\left(\frac{\mathcal{M}}{20}\right)$	$-5\frac{2\pi}{20}\mathcal{M}+2\frac{2\pi}{8}\ \mathrm{floor}\left(\frac{\mathcal{M}}{20}\right)$
7QMAS	224	$\frac{2\pi}{28}\mathcal{M}$	0	$\frac{2\pi}{8}\ \mathrm{floor}\left(\frac{\mathcal{M}}{20}\right)$	$-7\frac{2\pi}{28}M+2\frac{2\pi}{8}\ \mathrm{floor}\left(\frac{\mathcal{M}}{28}\right)$
9QMAS	288	$\frac{2\pi}{36}\mathcal{M}$	0	$\frac{2\pi}{8}\ \mathrm{floor}\left(\frac{\mathcal{M}}{36}\right)$	$-9\frac{2\pi}{36}\mathcal{M}+2\frac{2\pi}{8}\mathrm{floor}\left(\frac{\mathcal{M}}{36}\right)$

Table 5d. The cogwheel phase table for phase-modulated shifted-echo split-t_1 MQMAS experiments

Spin	Experiment	Cogwheel solution, COG$N(\nu_1, \nu_2, \nu_3; \nu_{rec})$
$\frac{3}{2}$	3QMAS	COG23(−3,0,1;11)
$\frac{5}{2}$	3QMAS	COG51(−5,0,3;21)
	5QMAS	COG57(−5,0,1;27)
$\frac{7}{2}$	3QMAS	COG87(−7,0,5;31)
	5QMAS	COG97(−7,0,3:41)
	7QMAS	COG107(−7,0,1:51)
$\frac{9}{2}$	3QMAS	COG131(−9,0,7:41)
	5QMAS	COG145(−9,0,5:55)
	5QMAS	COG159(−9,0,3:69)
	9QMAS	COG173(−9,0,1:83)

The mixed MQNQ scheme was first demonstrated on a spin-$\frac{5}{2}$ system acquiring a ^{27}Al spectrum of AlPO-41. Both the 5Q1Q (conventional 5QMAS) and 5Q3Q (mixed 5Q3QMAS) spectra are shown in Fig. 8b and c, demonstrating the resolution enhancement offered by the MQNQ approach. The phase list used for this experiment, based on the nested phase cycle scheme, may be denoted as: $\phi_1 = \frac{2\pi}{20}\mathcal{M}$, $\phi_2 = \frac{2\pi}{4}$ floor $(\frac{\mathcal{M}}{20})$, $\phi_3 = \frac{2\pi}{8}$ floor $(\frac{\mathcal{M}}{80})$, $\phi_4 = 0$, $\phi_{rec} = -5\frac{2\pi}{20}\mathcal{M} + 2\frac{2\pi}{4}$ floor $(\frac{\mathcal{M}}{20}) + 2\frac{2\pi}{8}$ floor $(\frac{\mathcal{M}}{80})$. The first, second, and third pulse are phase cycled in 20, 4, and 8 steps, respectively, leading to a total phase cycle of 640 steps. It may be noted that this is a compromise with respect to the minimum required number of phases of 693 where the first, second, and third pulses are phase cycled in steps of

Table 5e. The phase table for STMAS and SCAM–STMAS experiments

Experiment	Number of phase-cycle steps, N	ϕ_1	ϕ_2	ϕ_3	ϕ_4	ϕ_{rec}
STMAS, Fig. 24a	32	0	$\frac{2\pi}{8}\mathcal{M}$	$\frac{2\pi}{4}\,\text{floor}\left(\frac{\mathcal{M}}{8}\right)$		$\frac{2\pi}{2}\,\text{floor}\left(\frac{\mathcal{M}}{8}\right)$
SCAM –STMAS, Fig. 24b	100	0	$\frac{2\pi}{5}\mathcal{M}$	$\frac{2\pi}{5}\,\text{floor}\left(\frac{\mathcal{M}}{5}\right)$	$\frac{2\pi}{4}\,\text{floor}\left(\frac{\mathcal{M}}{25}\right)$	$\frac{2\pi}{2}\,\text{floor}\left(\frac{\mathcal{M}}{25}\right)$

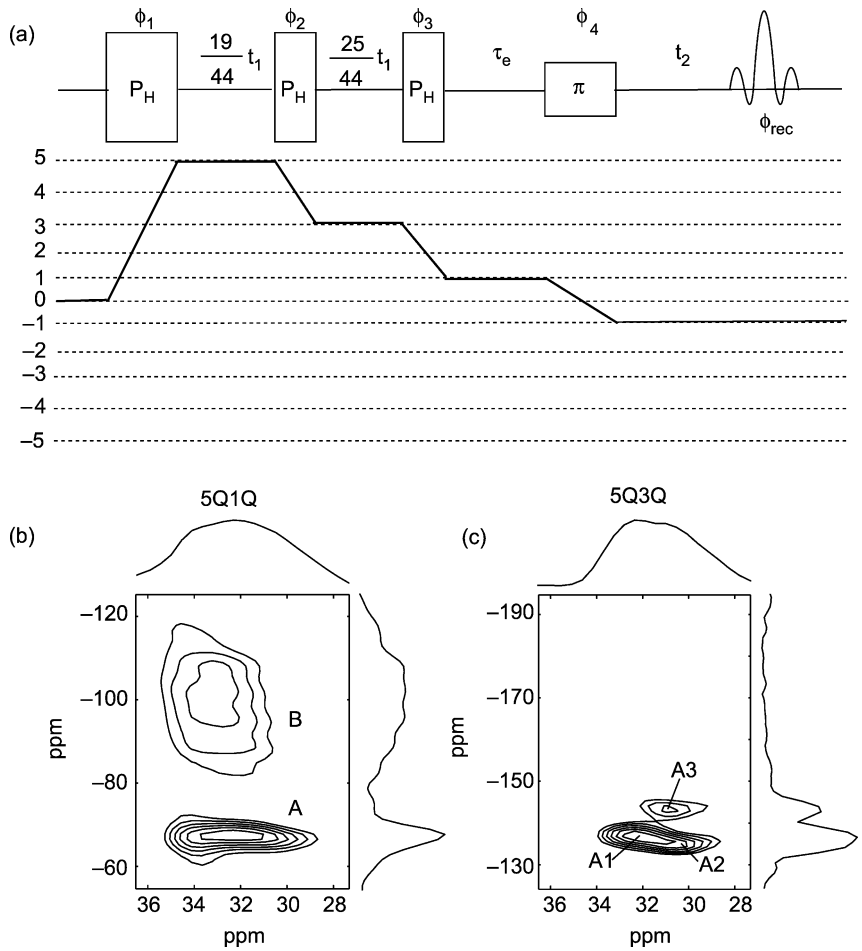

Fig. 8. (a) Pulse sequence for the shifted-echo split-t_1 5Q3QMAS experiment. ^{27}Al spectra of $AlPO_4$-41 shown in (b) was acquired with a 5Q1QMAS scheme and that in (c) with the 5Q3QMAS scheme shown in (a). The 5Q1QMAS experiment resolved two sites, *A* and *B*, while the 5Q3QMAS experiment provided higher resolution, showing the three Al sites for *A*, indicated as A_1, A_2, and A_3. Site *B* is not shown in this case. The hard pulses in (a) and (b) may be replaced with amplitude-modulated RF pulses (Section 5) for signal sensitivity enhancement. (Reprinted with permission from Jerschow *et al.*[45] Copyright (2001) Elsevier.)

11, 9, and 7, respectively. The cogwheel phase table for this experiment can be denoted as COG201(−15,0,5,8;101), reducing the minimal number of phases by a factor of 3.

4. MQMAS DATA INTERPRETATION

This section describes the presentation of MQMAS data by exploring various ways to label the F_1 frequency axis and accordingly, deriving the isotropic chemical shifts

and quadrupolar parameters from the spectral data. From the centres of gravity of the 2D spectral peaks along F_1 and F_2, the product $\chi\sqrt{1+\eta^2/3}$ can be derived. Summation of slices parallel to F_2 of individual 2D peaks (primarily in crystalline materials) provides the complete assignment of χ and η by either simulating the extracted lineshapes[63] or by other means such as moment analysis[64] and direct observation.[65] Data from amorphous materials are harder to interpret since the projection of their 2D peaks on to the F_2 dimension exhibits distributions rather than well-defined second-order quadrupolar MAS lineshapes. Yet, they can be analysed by spectral inversion, full 2D simulations or direct observation, as will be shown at the end of this section.

4.1. Isotropic shifts in MQMAS

The isotropic shifts in MQMAS are governed by both the chemical shift and the second-order quadrupolar shift. The isotropic chemical shift is given in angular frequency units by

$$\omega_{\mathrm{iso},m}^{\mathrm{CS}} = -2m\omega^{\mathrm{c}}\,\delta_{\mathrm{iso}}^{\mathrm{CS}} \tag{49}$$

where ω^{c} is the carrier frequency of the RF pulses, $2m$ is the MQC order ($p = 2m$) and $\delta_{iso}^{\mathrm{CS}}$ is the normal CT chemical shift in ppm units. The induced quadrupolar second-order shift of a symmetric transition, which is derived from Eq. (35) by taking only the isotropic terms ($l = 0$), is

$$\omega_{\mathrm{iso},m}^{\mathrm{Q}} = \frac{\omega_{\mathrm{Q}}^2}{18\omega_0}A^{(0)}(I,m)B_0^{(0)}(\eta) = -2m\frac{3\left(\chi\sqrt{1+\eta^2/3}\right)^2}{10[2I(2I-1)]^2\omega_0}(3m^2 - I(I+1)) \tag{50}$$

with the second-order quadrupole effect $\mathrm{SOQE} = \chi\sqrt{1+\eta^2/3}$ (sometimes also called the quadrupolar product, Pq). The centre of gravity of the spectral lines in a regular MAS experiment of a quadrupolar spin-I is then (in ppm units, setting $m = -1/2$)

$$\delta_{\mathrm{iso}}^{\mathrm{MAS}} = \delta_{\mathrm{iso}}^{\mathrm{CS}} + \frac{3[\mathrm{SOQE}]^2(\frac{3}{4} - I(I+1))}{[2I(2I-1)]^2 10\omega^{\mathrm{c}}\omega_0} \tag{51}$$

Table 6a. The contribution to the isotropic shift by the second-order quadrupole interaction of different spin quantum numbers

Spin (I)	Shift ($\times[\mathrm{SOQE}]^2/\omega^c\omega_0$)
3/2	1/40
5/2	3/500
7/2	1/392
9/2	1/720

Table 6b. The values λ and k for spins-$\frac{3}{2}$ and $\frac{5}{2}$ with the top sign corresponding to echo signals and bottom sign corresponding to antiecho signals

Experiment: I	m	λ	k
3QMAS: 3/2	$\mp 3/2$	∓ 3	$\mp 7/9$
3QMAS: 5/2	$\mp 3/2$	$\mp 3/4$	$\mp 19/12$
5QMAS: 5/2	$\mp 5/2$	$\mp 25/4$	$\mp 25/12$

The shifts induced by the quadrupolar interactions are inversely proportional to the field strength.* The shifts for different spin quantum numbers are summarized in Table 6a.

In MQMAS the isotropic component of the phase accumulated by the detectable elements of the density matrix at the echo (or antiecho) position is governed by both MQ and SQ evolution periods. The angular frequency of the spectral line in F_1 of each quadrupolar site $\omega_{F_1,\mathrm{iso}}$ may be conveniently expressed as

$$\omega_{F_1,\mathrm{iso}} = (k(I,m) - 2m)\omega^{\mathrm{CS}}_{\mathrm{iso},-1/2} + (\lambda(I,m) + k(I,m))\omega^{\mathrm{Q}}_{\mathrm{iso},-1/2} \tag{52}$$

Here, $k(I,m) = A^{(4)}(I,m)/A^{(4)}(I,-1/2)$ is the MQMAS ratio and $\lambda(I,m) = A^{(0)}(I,m)/A^{(0)}(I,-1/2)$ is the ratio of the isotropic contribution of $(2m)$Q and (-1)Q coherences. The values of λ and k can be easily calculated from Table 3 and are given for spins-$\frac{3}{2}$ and spins-$\frac{5}{2}$ in Table 6b.

4.2. Axis labelling

The convention for labelling the F_2 axis in ppm units is similar in all the MAS experiments and is obtained by dividing the angular frequency ω_{F_2} by ω^{c}. The frequency offset is given by Ω_{F_2} and corresponds to the chemical-shift value of the centre of the spectrum relative to some reference. The off-resonance $\Delta\omega_{F_2}$ denotes the frequency of a given spectral line with respect to Ω_{F_2}. However, labelling of the F_1 axis has been performed in several ways by different authors. Mostly, the carrier frequency was replaced with a scaled apparent carrier frequency using different scaling factors. These conventions were nicely described by Millot and Man[66] and we follow their description. Four different apparent carrier frequencies were used, resulting in the following δ_{F_1} values in ppm units:

(i) $\omega_{F_1,\mathrm{iso}}/\omega^{\mathrm{c}}$, similar to F_2, which has been used in Refs. 13,67.
(ii) $\omega_{F_1,\mathrm{iso}}/2m\omega^{\mathrm{c}}$, which scales the axis with an apparent multiple-quantum carrier frequency (used in Ref. 68).
(iii) $\omega_{F_1,\mathrm{iso}}/(k-2m)\omega^{\mathrm{c}}$, the coefficient of $\omega^{\mathrm{CS}}_{\mathrm{iso},-1/2}$ in Eq. (52) (used in Refs. 69,70).
(iv) $\omega_{F_1,\mathrm{iso}}/(k+\lambda)\omega^{\mathrm{c}}$, the coefficient of $\omega^{\mathrm{Q}}_{\mathrm{iso},-1/2}$ in Eq. (52) (used in Ref. 66).

*This is exactly opposite to the chemical shift, a phenomena that can lead to loss of resolution when increasing the magnetic field!

An additional set of conventions scales the evolution period by $(1 + k)$ so that $\Delta t_1 \rightarrow \Delta t_1(1 + k)$, or alternatively, scales the spectral width by $(1 + k)$. The two options are similar in terms of the axis labelling in ppm and the following results a–d are merely the ratio of results i–iv with $(1 + k)$:

(a) $\omega_{F_1,\mathrm{iso}}/[(1 + k)\omega^{\mathrm{c}}]$.[56]
(b) $\omega_{F_1,\mathrm{iso}}/[2m(1 + k)\omega^{\mathrm{c}}]$.[68]
(c) $\omega_{F_1,\mathrm{iso}}/[(1 + k)(k - 2m)\omega^{\mathrm{c}}]$.[69,70]
(d) $\omega_{F_1,\mathrm{iso}}/[(1 + k)(k + \lambda)\omega^{\mathrm{c}}]$.[66]

It is noted here that Δt_1 is defined as the increment of the time during which MQCs evolve. Another important property which should be taken into account is the apparent carrier frequency positions with respect to the reference frequency (Ω_{F_1}) and the line position with respect to the apparent carrier frequency $(\Delta\omega_{F_1})$. Since the evolution in t_1 is governed by both MQCs and SQCs, these values scale with Ω_{F_2} and $\Delta\omega_{F_2}$, and depend on the definition of the dwell time, on the MQMAS ratio k and on the MQC value, $2m$.

$$\left.\begin{aligned} \Omega_{F_1} &= (k - 2m)\Omega_{F_2} \\ \Delta\omega_{F_1} &= (k - 2m)\Delta\omega_{F_2} \end{aligned}\right\} \quad \text{dwell time : } \Delta t_1 \tag{53}$$

$$\left.\begin{aligned} \Omega_{F_1} &= \frac{k - 2m}{1 + k}\Omega_{F_2} \\ \Delta\omega_{F_1} &= \frac{k - 2m}{1 + k}\Delta\omega_{F_2} \end{aligned}\right\} \quad \text{dwell time : } (1 + k)\Delta t_1 \tag{54}$$

4.3. Derivation of the chemical shift and quadrupolar parameters

If we define the apparent carrier frequency as $\omega^{\mathrm{ac}} = \kappa\omega^{\mathrm{c}}$, κ denoting the scaling factor, the derivation of the chemical shift and quadrupolar parameters is merely by an inversion of the two following equations to obtain $\delta_{\mathrm{iso}}^{\mathrm{CS}}$ and $\delta_{\mathrm{iso}}^{\mathrm{Q}} = \omega_{\mathrm{iso},-1/2}^{\mathrm{Q}}/\omega^{\mathrm{c}}$:

$$\delta_{F_1} = \frac{k(I,m) - 2m}{\kappa}\delta_{\mathrm{iso}}^{\mathrm{CS}} + \frac{\lambda(I,m) + k(I,m)}{\kappa}\delta_{\mathrm{iso}}^{\mathrm{Q}} \tag{55}$$

$$\delta_{F_2} = \delta_{\mathrm{iso}}^{\mathrm{CS}} + \delta_{\mathrm{iso}}^{\mathrm{Q}} \tag{56}$$

and $\delta_{\mathrm{iso}}^{\mathrm{CS}}$ and $\delta_{\mathrm{iso}}^{\mathrm{Q}}$ are obtained as

$$\delta_{\mathrm{iso}}^{\mathrm{CS}} = -\frac{\kappa}{\lambda + 2m}\delta_{F_1} + \frac{10}{27}\delta_{F_2} \tag{57}$$

$$\delta_{\mathrm{iso}}^{\mathrm{Q}} = \frac{\kappa}{\lambda + 2m}\delta_{F_1} + \frac{17}{27}\delta_{F_2} \tag{58}$$

where the numerical factors 10/27 and 17/27 correspond to the ratios $(\lambda + k)/(2m + \lambda)$ and $(k - 2m)/(\lambda + 2m)$, respectively. The value $\mathrm{SOQE} = \chi\sqrt{1 + \eta^2/3}$ can be derived directly from Eq. (50).

Millot and Man[66] have provided detailed tables of solutions of Eqs. (57) and (58) for all cases (i–iv) and (a–d), with respect to dwell times Δt_1 and Δt_1 $(1 + k)$. Here, we describe two solutions, the first giving intuitive results in which axes correspond directly to the (split-t_1) experimental parameters and the second resulting in a unified representation of all the MQMAS experiments. The first choice corresponds to option (a) and takes $\kappa = (1 + k)$. In addition, $\Delta t_1(1 + k)$ is the increment time since it corresponds to both single- and multiple-quantum evolution and Eq. (54) is used for the offset values. This results in the following relations for spins 3/2 and 5/2:

spin $3/2$, 3QMAS	spin $5/2$, 3QMAS	spin $5/2$, 5QMAS
$\delta_{\mathrm{iso}}^{\mathrm{CS}} = \frac{8}{27}\delta_{F_1} + \frac{10}{27}\delta_{F_2}$	$\delta_{\mathrm{iso}}^{\mathrm{CS}} = -\frac{31}{27}\delta_{F_1} + \frac{10}{27}\delta_{F_2}$	$\delta_{\mathrm{iso}}^{\mathrm{CS}} = \frac{37}{135}\delta_{F_1} + \frac{10}{27}\delta_{F_2}$
$\delta_{\mathrm{iso}}^{\mathrm{Q}} = -\frac{8}{27}\delta_{F_1} + \frac{17}{27}\delta_{F_2}$	$\delta_{\mathrm{iso}}^{\mathrm{Q}} = \frac{31}{27}\delta_{F_1} + \frac{17}{27}\delta_{F_2}$	$\delta_{\mathrm{iso}}^{\mathrm{Q}} = \frac{37}{135}\delta_{F_1} + \frac{17}{27}\delta_{F_2}$

(59)

The second option includes in κ all terms depending on I and m so that the resulting axis is uniform for all MQMAS experiments. In options (iii) and (iv) $\kappa = (k - 2m)$ and $\kappa = (k + \lambda)$, respectively, and the dwell time is defined to be Δt_1. This results in

$\kappa = (k - 2m)$ (option iii)	$\kappa = (k + \lambda)$ (option iv)
$\delta_{iso}^{\mathrm{CS}} = \frac{17}{27}\delta_{F_1} + \frac{10}{27}\delta_{F_2}$	$\delta_{\mathrm{iso}}^{CS} = -\frac{10}{27}(\delta_{F_1} - \delta_{F_2})$
$\delta_{\mathrm{iso}}^{\mathrm{Q}} = -\frac{17}{27}(\delta_{F_1} - \delta_{F_2})$	$\delta_{\mathrm{iso}}^{\mathrm{Q}} = \frac{10}{27}\delta_{F_1} + \frac{17}{27}\delta_{F_2}$

(60)

with the following shifts, $(k - 2m)\Omega_{F1}$ and $(k - 2m)\Delta\omega_{F1}$ [Eq. (53)].

4.4. Interpretation of spectra

After the 2D spectra have been obtained and the axes labelled by a method of choice, the centre of gravity along F_1 and F_2 can be used to derive the chemical shift and second-order quadrupolar effect, according to Eqs. (57) and (58) or specifically by Eqs. (59) or (60). However, more information can be obtained by summing slices parallel to F_2 of specific 2D peaks. These result in quadrupolar MAS lineshapes for each site separately. From the second-order quadrupolar MAS lineshapes, χ and η can be unambiguously determined. Lineshape simulations can be performed, for example,

by using the program DMFIT written by Massiot and coworkers.[63] Alternatively, the lineshapes can be analysed using moment analysis[64] or in the case of a good signal-to-noise ratio directly from the discontinuities in the spectrum.[65] An example of a MQMAS spectrum is shown in Fig. 2 of a sample of $RbNO_3$, with lineshape simulation of the three Rb sites. In this case, simulations were done using the package SIMPSON[71] by varying the χ and η values for each site and searching for the best fit.

The case of amorphous materials is somewhat more complex. No distinct lineshapes are normally visible due to the distribution in chemical shift and quadrupolar parameters. Iuga *et al.*[72] have used full 2D simulations incorporating distributions in both quadrupolar and chemical-shift parameters. Another elegant method was initially proposed by Zwanziger for the case of DAS[73] and further developed for MQMAS.[74,75] This method uses a transformation from the F_1/F_2 axis system to a χ/δ_{iso}^{CS} axis system, providing visual knowledge of chemically meaningful parameters, separating the quadrupolar, chemical-shift and broadening contributions in a clear manner. Yet, the method requires high-quality data and further constraints to discard mathematically allowed, but physically irrelevant, solutions.[76] Figure 9 gives an example of MQMAS, model simulation and inversion spectra of an organically modified aluminosilicate xerogel.[76]

Another method which can be used is the extraction of the parameters by direct observation of the spectra. Drawing the distribution directions of the chemical shift and quadrupolar coupling on the F_1/F_2 2D spectra was already demonstrated by Fernandez and Amoureux[77] in their first demonstration of 5QMAS experiment. Goldbourt *et al.*[78] have shown that by drawing the full $SOQE/\delta_{iso}^{CS}$ grid it is possible to estimate immediately the distribution of the NMR parameters. An example for the case of a 5QMAS experiment on γ-Al_2O_3 is shown in Fig. 10.

5. SENSITIVITY ENHANCEMENT SCHEMES IN MQMAS EXPERIMENTS

MQMAS involves the excitation of MQCs, 3Q, 5Q, 7Q, and 9Q, and their conversion into observable SQC. Both these processes are intrinsically inefficient. The distribution of crystallites spanning a wide range of quadrupolar splittings (on the order of ν_Q) and the low values of the available RF power are some of the reasons for this inefficiency (for 3Q excitation in the case of a single crystal see Ref. 79). Hence, the basic MQMAS pulse schemes suffer from low sensitivity. Whilst increasing the RF power and the spinning frequency can provide some improvement, for spins with large ν_Q, this solution is limited for current instruments, which normally provide RF intensities of 50–200 kHz. Signal sensitivity enhancement may be achieved via two routes. One is the improvement of the detection schemes by using t_1 increments synchronous with the rotor period[80] or by adding echoes generated by CPMG pulse trains[81] during detection. The other more important route for signal enhancement is by improving the RF performance. In the following, we will treat in detail one of the most practical schemes for sensitivity enhancement in MQMAS experiments entitled FAM (fast amplitude modulation),[28,82] and sketch additional methods such as DFS (double-frequency sweeps),[83] RIACT

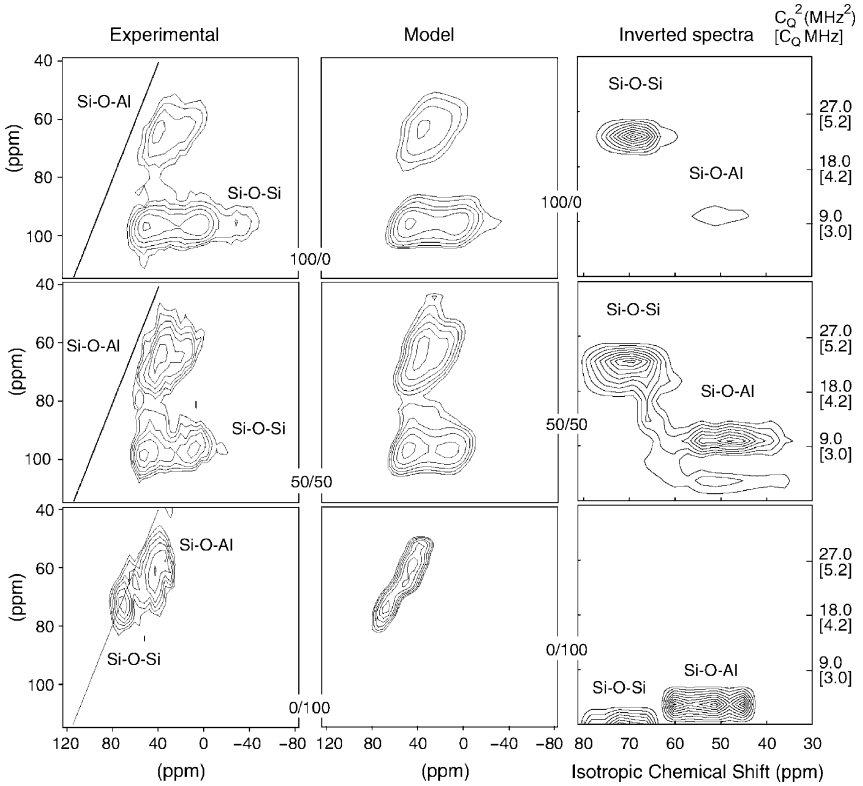

Fig. 9. Experimental ^{17}O 3QMAS NMR spectra of TDA 100/0 (top), TDA 50/50 (middle) and TDA 0/100 (bottom) glass samples, with their respective computer model spectra and inversion figures. The line drawn on the experimental spectra represents the isotropic chemical-shift direction corresponding to a virtual site with negligible quadrupolar coupling. Experimental and modelled MQMAS spectra are reported using bottom (F_2) and left (F_1) ppm scales, whilst inversion figures are given as correlation between isotropic chemical shift ($\delta_{\mathrm{iso}}^{\mathrm{CS}}$) and squared quadrupolar coupling constant (χ^2) assuming $\eta = 0$. Distributions of chemical shift and quadrupolar parameters can be directly obtained from the inversion figures whereas they give rise to spreading over the diagonal or away from the diagonal in the standard MQMAS experiments. (Reprinted with permission from Lafuma *et al.*[76] Copyright (2003) Wiley.)

(rotation induced adiabatic coherence transfer)[84] and FASTER-MQMAS, which exploits rotary resonance conditions.[85]

5.1. Amplitude- and frequency-modulated pulse schemes

Interconversion of single- and triple-quantum coherences was first suggested by Vega and Naor,[79] who demonstrated how application of amplitude-modulated pulses, having a modulation frequency ν_m equal to the $|3/2\rangle \leftrightarrow |1/2\rangle$ satellite transition frequency $\nu_{1/2,3/2}$, results in perfect inversion of the populations of the $|3/2\rangle$ and $|1/2\rangle$ levels, leading to

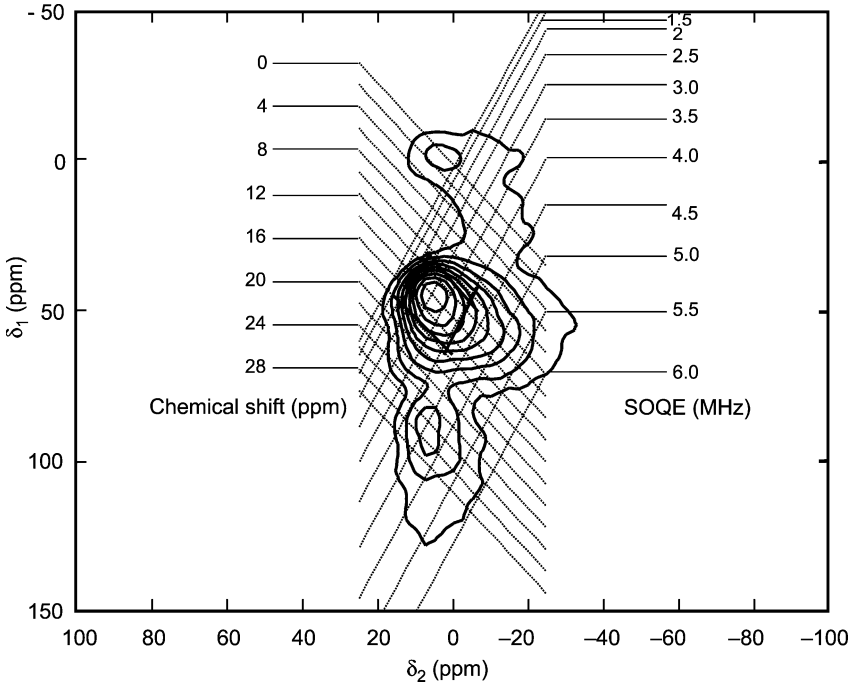

Fig. 10. Data extraction strategy: An example of the octahedral region in the 5QMAS spectra of γ-A_2O_3 overlaid with a grid of constant SOQE and δ_{iso}^{CS} lines. The SOQE spacing is 0.5 MHz and the chemical shift spacing is 2 ppm. Contours are drawn between 10 and 90% of the maximum spectral intensity. The box around the contour lines indicates 70% of the peak maximum. Values of 11–18 ppm and 2.2–4.1 MHz for δ_{iso}^{CS} and SOQE were determined, respectively. (Reprinted with permission from Goldbourt *et al.*[78] Copyright (2003) American Chemical Society.)

an increase in the CT signal intensity.[79,86] Whilst the effect of these pulses on the satellite transitions of a single crystal were calculated already in the 1970s,[86] it was not until 1991 that Haase, Conradi, and Kentgens used frequency-stepped adiabatic half-passage (FSAHP) pulses in order to enhance the powder MAS spectra of half-integer spin quadrupolar nuclei.[49,87] The FSAHP pulses achieved an almost complete inversion of the populations across the satellite transitions by virtue of an adiabatic transfer of populations.

It is not surprising, therefore, that upon the introduction of the MQMAS experiment, frequency and amplitude modulations were suggested to replace the hard pulses applied for the transfer of MQ ↔ SQ coherences. DFS[83,88,89] and FAM[28,29,82] methods have been shown to yield approximately a three- to four-fold enhancement of MQMAS signal intensities. FAM pulses were also utilized to enhance 1D central-transition MAS spectra resulting in enhancement factors of around 2 in spin-$\frac{3}{2}$ systems[90] 2.5–3 in spin-$\frac{5}{2}$ systems,[91] and 3–3.5 in spin-$\frac{7}{2}$ systems.[92]

Both FAM and DFS methods yield relatively undistorted lineshapes.[31] Prior to the introduction of FAM and DFS, Wu *et al.*[84] suggested to replace both excitation and conversion pulses by long RF irradiation pulses lasting for quarter of the rotor period, a scheme that was entitled RIACT. Such pulses have been shown to induce adiabatic transitions between different orders of transitions in an efficient way.[93] RIACT results in enhancements similar to those of FAM and DFS and, whilst it provides uniform excitations for a large range of ν_Q values, it results in ill-defined lineshapes.[31,94]

In the following, we will primarily deal with FAM pulses. The hard pulses are denoted as P_H and soft RF pulses as P_S which act selectively on the central-transition SQC. In all the figures and discussions below we denote groups of pulses with an overall 180° phase shift by an over-bar.

5.2. Fast amplitude-modulation pulses

Figure 11a shows how an ideal cosine amplitude modulation of the RF carrier wave could be approximated by a rectangular RF pulse scheme, which is much easier to implement. Such a scheme comprises of pulses with alternating phases of 0° and 180° and is referred to as FAM. As was already mentioned, the modulation frequency should be tuned such that ν_m matches ν_Q, at least during part of the excitation. Due to the sample spinning, the quadrupolar splitting of many crystallites will pass through the ν_m value. It was shown that mismatches between ν_m and the powder ν_Qs do not create large phase distortions[29] and simultaneous adiabatic and direct coherence transfer processes result in relatively pure MQ ↔ SQ transfers. By pure we mean that no significant phase dispersions are observed when looking at the transfer of each crystallite separately.

Two cases need attention: Improving the excitation and conversion efficiency of MQC in 2D MQMAS experiments and implementing appropriate modulation techniques to

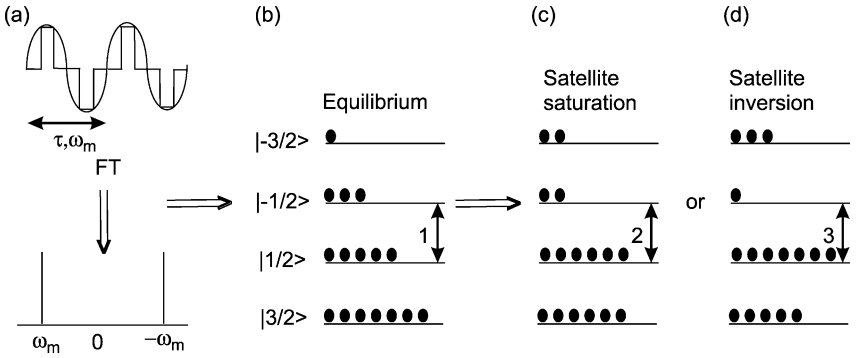

Fig. 11. (a) Cosine modulation and amplitude-modulated rectangular pulses approximating the cosine modulation, along with their schematic Fourier transform (additional bands at $2\omega_m$ and $3\omega_m$ are not shown). τ and ω_m correspond to the period and the frequency of the modulation. The FT of the wave form generates peaks at the frequency of modulation, ω_m. Also shown are the population distribution across the central and satellite transition of a spin-spin-$\frac{3}{2}$ nucleus: (b) Boltzmann distribution, (c) upon saturation of populations across the satellite transitions, and (d) upon inversion of populations across the satellite transitions.

manipulate populations to enhance the central-transition signal intensity in 1D MAS experiments. Two types of RF modulations, involving rectangular pulses that are experimentally easy to implement, were suggested toward this goal. In general, they are called FAM pulses of type I and II, FAM-I and FAM-II, and are generated by amplitude modulation of a single carrier frequency.

Whilst FAM-I is mainly used in the excitation or conversion processes involving SQC and the highest order of coherences (3QC $\leftrightarrow$ SQC in spin-$\frac{3}{2}$, 5QC $\leftrightarrow$ SQC in spins-$\frac{5}{2}$, etc.), FAM-II is used in pQC $\leftrightarrow$ SQC conversion processes with $|p| < 2I$ (e.g., 3QC $\leftrightarrow$ SQC in spins $> \frac{3}{2}$). We now deal with the classification and notation of FAM pulses for an easier description. The notations are built upon previous works.[92,96]

5.3. FAM-I sequence

FAM-I pulses were suggested first in Ref. 28 (initially referred to as AM pulses) and analysed thoroughly in Ref. 29. A schematic of FAM-I is shown in Fig. 12a. This consists of a train of rectangular pulses of equal duration that are equally spaced with alternating phases of 0° and 180°. Such a scheme is denoted as $F_n^I(\tau)$. Here, n is the number of pulses (always an even number) and τ is the repetition period. $\tau = 2\tau_p + 2\tau_w$ where τ_p and τ_w are the duration of the pulse and the interpulse delay, respectively. The scheme $F_n^I(\tau)$ may be treated as an approximation to a smoothly modulated cosine wave with a modulation frequency of τ^{-1}. A FAM sequence of the type $F_n^I(\tau)$ may be used in 3QMAS experiments of spins-$\frac{3}{2}$ systems.

In the case of spins-$\frac{5}{2}$ to $\frac{9}{2}$ the number of pairs of satellite transitions increases and is given by $I - \frac{1}{2}$. Adiabaticity arguments show that interconversion, during sample spinning, of higher-order coherences with SQC may be achieved with a single FAM pulse

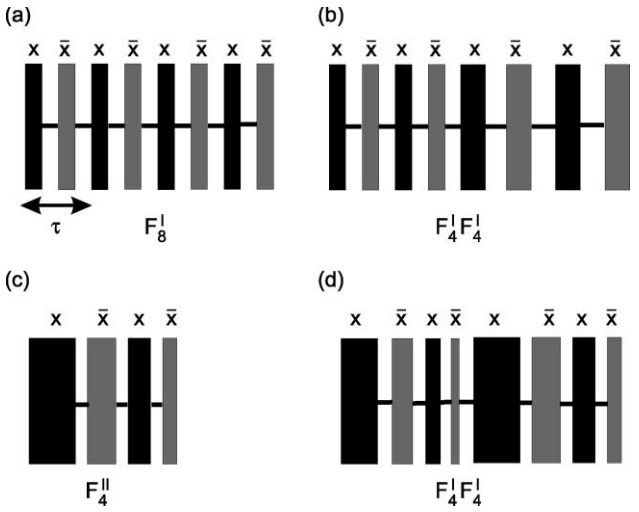

Fig. 12. Schematic of (a,b) FAM-I sequences and (c,d) FAM-II sequences. The modulation frequency is given as $1/\tau$ for FAM-I sequence.

of modulation frequency τ^{-1}. However, sequential transfer from the outer satellite transitions to the inner satellite transitions may prove beneficial due to the existence of direct non-adiabatic excitation processes. The additional sequential modulation of the frequency has also been shown to be beneficial for obtaining more quantitative results, even for a spins-$\frac{3}{2}$ system.[31] Such a scheme may be realized by a series of $F_n^I(\tau)$ pulse trains with different τ values where the number of modulation trains is given by $I - \frac{1}{2}$. For example, two sets of modulation trains for spins-$\frac{5}{2}$ with $\tau < \tau'$ need to be applied to obtain a transfer from 5QC to SQC.[95,96] These pulses are denoted as $F_n^I(\tau)\ F_{n'}^I(\tau')$ and are sketched in Fig. 12b.

5.4. FAM-II sequence

FAM-II pulses were initially shown to enhance the 3QC $\leftrightarrow$ SQC conversion process in a spin-5/2 system.[82] Later they were also used for excitation purposes by transferring 3QC $\leftrightarrow$ 5QC coherences in 5QMAS experiments.[97] Figure 12c shows a schematic of a FAM-II sequence, which consists of a train of pulses of progressively decreasing duration with alternating phases of 0° and 180° separated by an interpulse delay. The interpulse delay is normally kept to the minimum value required for stabilization of the phase jumps between the pulses, say 0.2–0.4 μs. Such a FAM-II sequence is denoted as $F_n^{II}(\Gamma)$, where n again corresponds to the number of pulses (it can be odd or even in contrast to the $F_n^I(\tau)$ case) and Γ is a vector containing the durations of the pulses and interpulse delays, $\Gamma = \{\tau_p^{(1)}, \tau_w, \tau_p^{(2)}, \ldots, \tau_p^{(n)}\}$. In general, $\tau_p^{(1)} > \tau_p^{(2)} >, \ldots, \tau_p^{(n)}$, and all the interpulse delays are equal to τ_w. All the odd-numbered pulses are applied with phase 0° and even-numbered pulses are applied with phase 180°. The FAM-II scheme shown in Fig. 12c may be notated as $F_4^{II}(\Gamma)$. Such a scheme may be used in the conversion of 3QC $\leftrightarrow$ SQC in any spin system with $I > \frac{3}{2}$ and can also provide 3Q signal enhancement in spins-$\frac{3}{2}$.

As mentioned before, in the case of spins-$\frac{5}{2}$ to $\frac{9}{2}$, for an optimum signal sensitivity enhancement the satellite transitions need to be sequentially perturbed. In the conversion of MQC $\leftrightarrow$ SQC, where MQC may represent any order of coherence larger than 3, the perturbation should proceed from the outer satellite transitions to the inner satellite transitions. Such a transfer may be envisioned by an application of a series of $F_n^{II}(\Gamma)$ pulses with multiple modulation frequencies as in the case of 5QC $\leftrightarrow$ SQC for $I > \frac{5}{2}$. Such a FAM-II pulse sequence may be denoted as $F_n^{II}(\Gamma)F_{n'}^{II}(\Gamma')$ with $\Gamma < \Gamma'$. A schematic of such a FAM-II sequence is shown in Fig. 12d which was used to interconvert 5QC $\leftrightarrow$ SQC in a spin-$\frac{5}{2}$ system.[78,97]

5.5. FAM sequences for excitation of MQC

$F_n^I(\tau)$ sequences when applied after an unmodulated RF pulse P_{H}, can enhance the MQC excitation efficiency. A $P_H F_n^I(\tau)F_{n'}^I(\tau')$ sequence can be applied for the excitation of 7QC of spin-$\frac{7}{2}$, with $\tau > \tau'$. Here, the FAM trains are such that they first perturb the inner transitions and then the outer ones sequentially. Such FAM excitation blocks have been implemented for 5QMAS in spin-$\frac{5}{2}$ systems[78,96,97] and 5QMAS and 7QMAS in spin-$\frac{7}{2}$ systems.[92]

5.6. Optimization of FAM sequences

Optimum values for both the excitation pulse and the conversion pulse are found for a $P_H - P_H$ two pulse scheme by monitoring the echo intensity in a 1D MQMAS experiment.

In experiments involving the FAM-I scheme, first the conversion pulse is replaced with a $F_n^I(\tau)$ pulse block with $n = 4$ and $\tau_p = \tau_w = 1$ μs. The duration of the pulses, delays, and the number of blocks are then optimized in a 1D experiment. Subsequent FAM-I blocks, such as $F_{n'}^I(\tau')$, are added if necessary and optimized for the best conversion of MQC to SQC. The FAM blocks should be in decreasing order of modulation frequency.

When excitation of higher-order coherences are sought, $F_n^I(\tau)$ blocks may be added right after a 3Q excitation P_H pulse and optimized in the same manner as above with the sole difference that blocks are inserted in increasing order of their modulation frequencies. Here, we should point out the it may be beneficial to insert FAM-II blocks rather than FAM-I blocks to provide better transfer of $3Q \leftrightarrow MQ$. Sometimes, the composite pulse applied cannot be really classified as FAM-I or FAM-II and a good example is the single $\bar{x} - x$ scheme used in Refs. 78 and 97.

FAM-II optimization was initially performed in a similar manner. The duration of the first pulse with phase 0° is optimized for the maximum echo intensity followed by

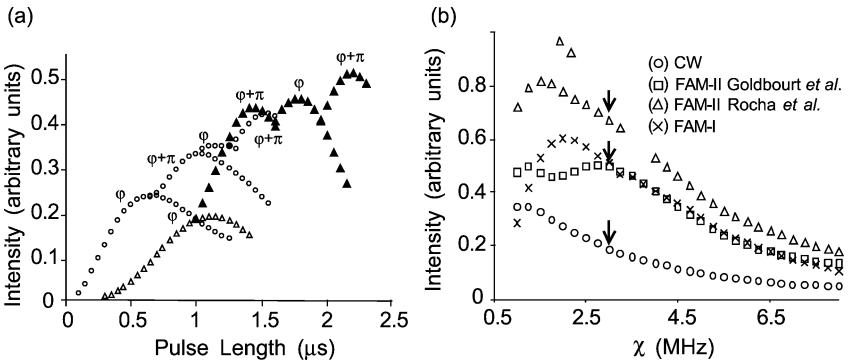

Fig. 13. (a) Optimization of FAM-II pulses for triple-quantum to SQC transfer using two different approaches of Goldbourt *et al.*[82] and Rocha *et al.*[99] where the echo intensity is plotted as a function of the conversion pulse duration. In the Goldbourt *et al.* method (denoted by ○) FAM-II segment durations are optimized by sequential maximization of the echo signal. The phase of each of the segment is altered from 0 to π when an echo maximum is encountered. In the Rocha *et al.* method the length of the first segment of the FAM-II pulse was determined by the intersection point of the echo (denoted by ○) and antiecho (denoted by △) curves. The lengths of the other segments (denoted by filled ▲) do not correspond to the maximum intensity point of the $-3QC \leftrightarrow SQC$ coherence transfer curve, but rather to a point after the maximum. These numerical simulations were performed with $\chi = 3.8$ MHz, $\nu_{nut} = 250$ kHz, and MAS rate of 30 kHz. It is evident from the plot that the Rocha *et al.* optimization method is superior to Goldbourt *et al.* method. (b) Intensity of the MQC to SQC conversion as a function of χ for different conversion methods, using the pulse values corresponding to the maximum intensity transfer obtained for $\chi = 3.8$ MHz, value to which the arrows point to. Again Rocha *et al.* method gives a superior performance than the other methods. (Reprinted with permission from Morais *et al.*[99] Copyright (2003) Wiley.)

insertion of additional pulses with alternating phases till no more enhancement in the echo intensity can be obtained. Although, in principle, the FAM-II scheme is not the ideal choice for 3QMAS in spin-$\frac{3}{2}$ systems, it has proved to be of immense practical interest in the observation of NMR resonances in distorted local environments, which normally have large quadrupolar coupling constants in the range of 10–24 MHz.[98,99]

Recently, Morais *et al.*[99] introduced an alternative and very efficient strategy for the optimization of FAM-II pulse segment durations. After optimizing the duration of the excitation pulse, the intensity of both the echo- and antiecho-signals is plotted as a function of the conversion pulse length (the first segment of FAM-II at a phase of 0°). The optimum duration of the first pulse in a FAM-II block is taken as the point of intersection of these curves and not the point of maximum echo intensity (Fig. 13). A second segment is then added to the FAM-II block which is phase altered by 180°. The duration of this segment does not correspond to the subsequent maximum in the echo intensity, but to a point after this, which is normally 0.1–0.2 μs after the maximum. The subsequent segments in the FAM-II block are optimized in a similar manner. Practically, the length of each pair of FAM-II pulses is optimized by setting the second pulse constant and modifying the preceding pulse until maximum intensity is achieved.

Figure 14 shows representative 3QMAS spectra obtained with the application of FAM-II schemes on a variety of samples having half-integer quadrupolar spins-$\frac{3}{2}$, $\frac{5}{2}$, $\frac{7}{2}$, and $\frac{9}{2}$.

5.7. Alternative sensitivity enhancement schemes for MQMAS

Before we deal with the experimental examples of FAM we outline some of the other signal sensitivity enhancement schemes.

5.7.1. *Rotation induced adiabatic coherence transfer*

One of the first MQMAS signal sensitivity enhancement schemes was the RIACT method which achieves signal sensitivity enhancement by applying the conversion pulse for quarter of a rotor period $(\tau_r/4)$, called RIACT-I[100] scheme or by employing both an excitation and a conversion pulse of duration $\tau_r/4$, called RIACT-II scheme,[84] where the excitation pulse is preceded by a selective 90° pulse. The sensitivity enhancement by RIACT is often accompanied by a severe distortion in the line shapes.[31,94] The applicability of this approach was never shown beyond spins-$\frac{3}{2}$ except in a couple of instances in spins-$\frac{5}{2}$.[101,102]

5.7.2. *Double-frequency sweep*

A very effective signal sensitivity enhancement scheme for MQMAS as well as for MAS is the DFS introduced by the group of Kentgens.[83] The underlying principles of DFS and FAM are similar and they have been explicitly dealt with already.[29,88,89] In a nutshell, a cosine amplitude modulated RF carrier wave irradiates the sample at two frequencies, namely, $\omega_0 + \omega_m$ and $\omega_0 - \omega_m$, where ω_0 is the on-resonant Larmor frequency of the spins and ω_m is the frequency of modulation. This means that if $\omega_m = \omega_Q$ for a crystallite the two SQ satellite transitions of a static spins-$\frac{3}{2}$ system will be simultaneously

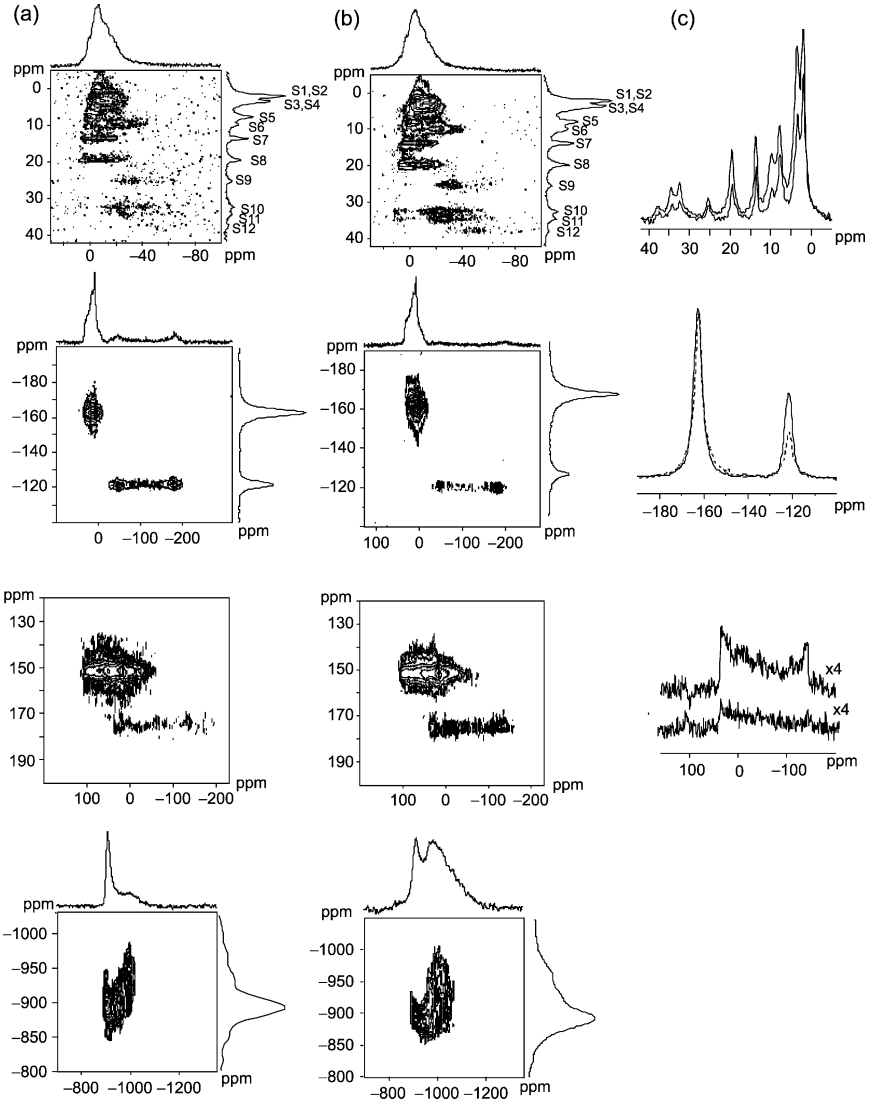

Fig. 14. 3QMAS spectra acquired with FAM-II as conversion block in a split-t_1 scheme of various samples. Column (a) corresponds to the spectra acquired with the two-pulse $P_H - P_H$ scheme, column (b) corresponds to the spectra acquired with FAM-II conversion block, and column (c) shows either the isotropic slices or the anisotropic slices obtained from both the experiments. The first row depicts ^{23}Na spectrum of $Na_3YSi_3O_9$ acquired with a MAS rate of 30 kHz and a comparison of the isotropic slices. The excitation pulse was 2.5 μs long, and the FAM-II block consisted of pulses of duration 1.1, 0.8, 0.45, 0.4, 0.3, and 0.2 μs. The second row depicts the ^{27}Al spectrum of andalusite acquired with a MAS rate of 31 kHz and a comparison of the isotropic slices. The excitation pulse was 1.4 μs long, and the FAM-II block consisted of pulses of duration 0.7, 0.45, 0.3, 0.25, 0.2, and 0.15 μs. The third row depicts the ^{45}Sc spectrum of Sc_2O_3 acquired with a MAS rate of 28 kHz and a comparison of the anisotropic slices. The excitation pulse was 1.4 μs

irradiated on-resonance. However, due to sample spinning, the on-resonant irradiation time is very short and the individual resonance frequency of the crystallites can cross adiabatically through ν_m. In DFS, both the sample spinning (ν_R) and the frequency sweep $(\nu_m(t))$ control this mechanism. Such a crossing results in a very efficient, coherent and relatively broadband coherence transfer for a large number of crystallites. In DFS, both converging and diverging sweeps may be implemented to effect the best MQC $\leftrightarrow$ SQC transfer. For instance, diverging sweeps are the most effective in the conversion of 3QC $\leftrightarrow$ SQC in spin-$\frac{5}{2}$ systems by preventing the unwanted 3QC $\leftrightarrow$ 5QC transfer process. For a successful implementation of DFS, extra hardware is required which can provide sweeps over broad frequency ranges with fast switching of frequency and this is not routinely available.

5.7.3. *Faster-MQMAS*

FASTER-MQMAS is an approach suggested by Vosegaard *et al.*[85] for MQ signal enhancements where two long pulses with a duration of 2–3 rotor periods are applied for both the excitation and conversion of MQC. The experiment uses low RF fields and high spinning rates. It was found that an excitation minimum occurs when $2\omega_1 = n\omega_R$ $(n = 0, 1, \ldots)$ ascribed to rotary resonance conditions. In between these conditions, enhanced signals were obtained. For the conversion pulse a maximum was found at $\omega_1 = n\omega_R$. Although this scheme reportedly achieved a three-fold enhancement of 3Q signal on a sample of $RbClO_4$,[84] it provided distorted line shapes, and has not found much application till this date. FASTER-MQMAS approach was successfully employed to enhance the signal sensitivity of mixed MQMAS experiment (5Q3QMAS on a spin-$\frac{5}{2}$ system) by a factor of two on a sample of aluminium acetyl acetonate using very low RF fields with a concomitant deterioration of the anisotropic line shapes.[103]

5.8. Optimum MQMAS sequences with FAM

We now outline pulse sequences that have been found to be the optimal ones for MQMAS spectra of spins-$\frac{3}{2}$, $\frac{5}{2}$, and $\frac{7}{2}$ using FAM for signal sensitivity enhancement. Here, we discuss some specific cases, showing in addition the experimental results. All the pulse sequences are based on the shifted-echo split-t_1 scheme.

5.8.1. *3QMAS in* spins-$\frac{3}{2}$

The best performance for 3QMAS in spins-$\frac{3}{2}$ is obtained by combining FAM with RIACT, the pulse sequence for which is shown in Fig. 15.[30,31] The excitation part

---

long, and the FAM-II block consisted of pulses of duration 0.6, 0.4, 0.2, and 0.15 μs. The fourth row depicts the ^{93}Nb spectrum of PMN [$Pb(Mg_{1/3}Nb_{2/3})O_3$] acquired with a MAS rate of 15 kHz. The excitation pulse was 1.7 μs long, and the FAM-II block consisted of pulses of duration 0.55 and 0.3 μs. In all the spectra the signal enhancement provided by the FAM-II conversion block over the two-pulse scheme is evident. (Reprinted with permission from Morais *et al.*[99] Copyright (2003) Wiley.)

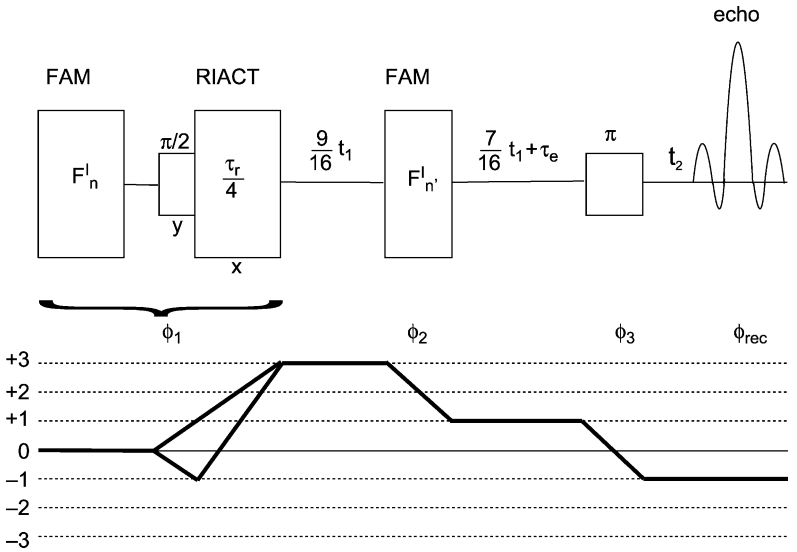

Fig. 15. The FAM–RIACT–FAM split-t_1 shifted-echo pulse sequence for sensitivity enhancement in the 3QMAS experiments of spin-$\frac{3}{2}$ systems. Also shown are the coherence transfer pathways.

consists of a $F^I_n(\tau)$ block lasting nearly a rotor period which enhances the population difference across the CT. The selective 90° pulse acts on this and converts the enhanced population difference to an enhanced central-transition SQC. The RIACT pulse, lasting for quarter of a rotor period, converts the enhanced SQC to 3QC. This is then converted to observable SQC by a $F^I_{n'}(\tau')$ block where n is generally 2–12. This sequence is called FAM–RIACT–FAM or $F^I_n(\tau)$–RIACT–$F^I_{n'}(\tau')$. A typical 2D 3QMAS spectrum acquired with this sequence is shown in Fig. 2.

The performance efficiency of FAM–RIACT–FAM may be seen from Fig. 16. Isotropic projection from a 2D 3QMAS spectrum, anisotropic projection, and an anisotropic slice across one of the Rb sites are shown of a sample of $^{87}RbNO_3$ with the application of several 3QMAS schemes, *namely*, $P_H - P_H$, RIACT–II, P_H–$F^I_n(\tau)$, RIACT–$F^I_n(\tau)$, and $F^I_n(\tau)$–RIACT–$F^I_{n'}(\tau')$. The superior performance of the $F^I_n(\tau)$–RIACT–$F^I_{n'}(\tau')$ sequence is very evident from this figure.

5.8.2. *3Q and 5QMAS in* spins-$\frac{5}{2}$

Figure 17a and b respectively show the pulse sequences for the 3Q- and 5QMAS experiments in a spin-$\frac{5}{2}$ system. Figure 17a is a P_H–$F^{II}_n(\Gamma)$ scheme, the result of which is shown in Fig. 18a (top trace) which is compared with the result from a P_H–P_H scheme shown in Fig. 18a (bottom trace). Figure 17b is a $P_H\overline{F^I_n}(\tau)$–$F^I_{n'}(\tau')F^I_{n''}(\tau'')$ scheme where two FAM-I blocks are used for the conversion of 5QC ↔ SQC and one FAM-I block is used for the excitation of 5QC from 3QC. The result of this is shown

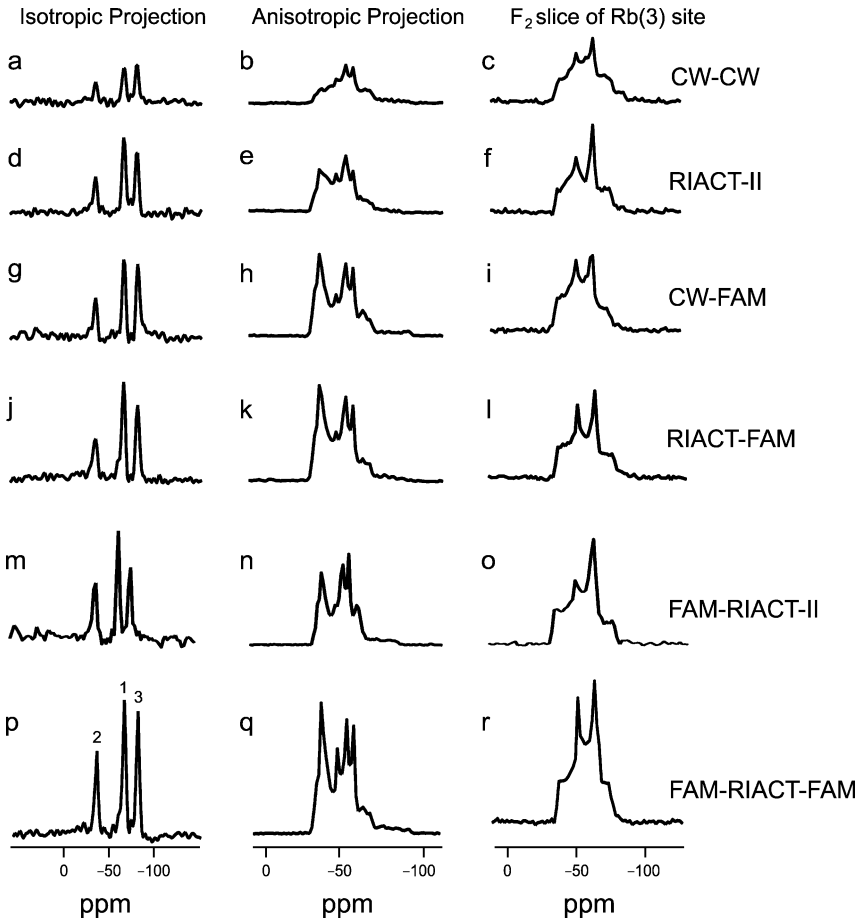

Fig. 16. The isotropic projection from a 2D 3QMAS spectrum, the anisotropic projection, and an anisotropic slice across one of the Rb sites of a sample of $^{87}RbNO_3$ with the pulse sequences indicated across each trace. All the spectra were acquired under identical conditions at an external field of 4.7 T and a MAS frequency of 10 kHz. Split-t_1 acquisition was employed for all the spectra. (Reprinted with permission from Madhu and Levitt[30] Copyright (2002) Elsevier.)

in Fig. 18c (for this spectrum only one FAM-I block was used for the conversion of 5QC to SQC) which is compared with the result from the $P_H - P_H$ scheme shown in Fig. 18b. A similar sequence was also implemented by Goldbourt *et al.*[78]

5.8.3. *3Q, 5Q, and 7QMAS in* spins-$\frac{7}{2}$

Figure 19a shows the pulse sequence for 3QMAS in a spin-$\frac{7}{2}$ system. A hard pulse P_H is used for the excitation of the 3Q coherences which are converted back to SQC following

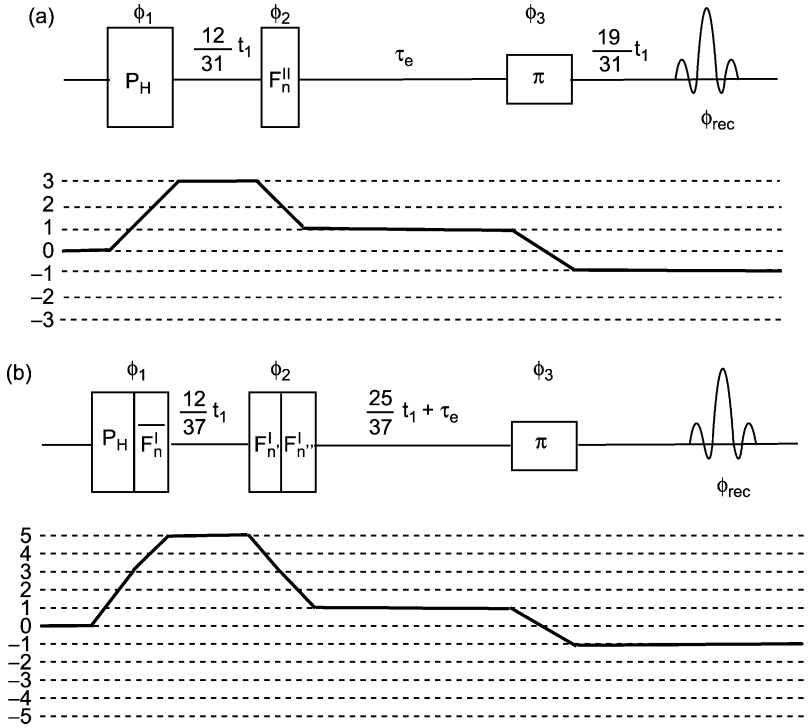

Fig. 17. Pulse sequences with FAM for (a) 3QMAS experiments and (b) 5QMAS experiments of spin-$\frac{5}{2}$ systems. In the P_{H}–$F_n^{II}(\Gamma)$ scheme depicted in (a), the P_{H} pulse excites 3QC which is then converted to SQC by a FAM-II block. In the $P_{\mathrm{H}}F_n^I(\tau) - F_{n'}^I(\tau')F_{n''}^I(\tau'')$ scheme depicted in (b), the $P_{\mathrm{H}}F_n^I(\tau)$ block creates 5QC which is then converted into SQC by two FAM-I blocks, $F_{n'}^I(\tau')F_{n''}^I(\tau'')$, such that $\tau' < \tau''$.

a FAM-II sequence of the type $F_n^{II}(\Gamma)$. The second column of Fig. 20 shows a comparison of the results of this sequence with those from a regular two-pulse P_{H}–P_{H} sequence, the results of which are shown in the first column of Fig. 20.

Figure 19b shows the pulse sequence for 5QMAS in a spin-$\frac{7}{2}$ system. A hard pulse P_{H} followed by $\overline{F_n^I(\tau)}$ excites the 5Q coherence which gets converted into SQC by a FAM sequence of the type $F_n^{II}(\Gamma)F_{n'}^{II}(\Gamma')(\Gamma < \Gamma')$. The second column of Fig. 21 shows a comparison of the results of this sequence with those from a regular two-pulse P_{H}–P_{H}sequence, the results of which are shown in the first column of Fig. 21.

Figure 19c shows the pulse sequence for 7QMAS in a spin-$\frac{7}{2}$ system. A hard pulse P_{H} followed by $\overline{F_n^I(\tau)F_{n'}^I(\tau')}(\tau > \tau')$ excites the 7Q coherence which gets converted into SQC by a FAM sequence of the type $F_{n''}^I(\tau'')F_{n'''}^I(\tau''')(\tau'' < \tau''')$. The second column of Fig. 22 shows a comparison of the results of this sequence with those from a regular two-pulse P_{H}–P_{H} sequence, the results of which are shown in the first column of Fig. 22. It may be mentioned here that ideally one should make use of a sequence like $F_n^I(\tau)F_{n'}^I(\tau')F_{n''}^I(\tau'')(\tau < \tau' < \tau'')$ for the conversion of 7QC to SQC.

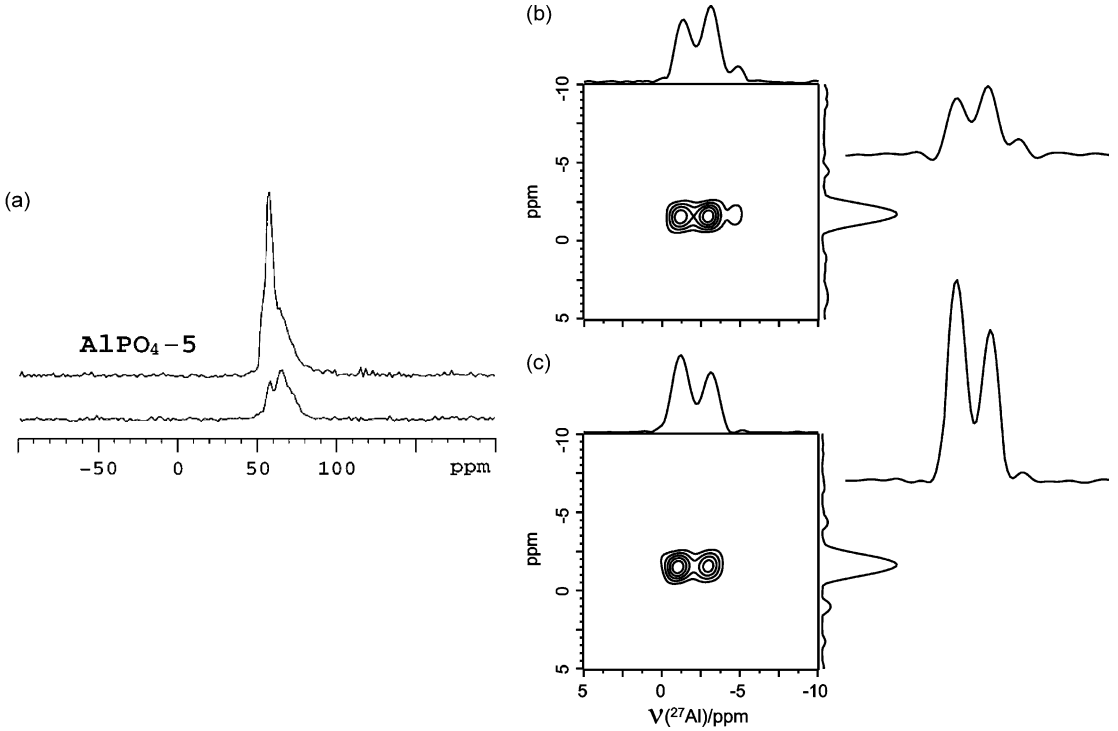

Fig. 18. (a) Comparison of the isotropic projection from a 3QMAS spectrum of a sample of $AlPO_4$ obtained with both a $P_H - P_H$ (bottom trace) and $P_{H^-}F_n^{II}(\Gamma)$ (top trace) schemes showing the superior performance of the latter. The experiment was performed at an external magnetic field of 7.1 T. The central-transition RF nutation frequency was 80 kHz and the MAS frequency was 10 kHz. The FAM-II pulses were of duration 0.9 and 0.7 μs. (b&c) Comparison of the 2D 5QMAS spectrum of a sample of aluminium acetyl acetonate obtained with a $P_H - P_H$ (b) and $P_H F_n^I(\tau) - F_{n'}^I(\tau')$ (c) schemes showing the superior performance of the latter. The experiment was performed at an external magnetic field of 14.1 T. The central-transition RF nutation frequency was 80 kHz and the MAS frequency was 10 kHz. Also shown along side the 2D spectra are the anisotropic slices. (Reprinted with permission from Bräuniger[96] and Goldbourt and Vega.[97] Copyright (2003, 2002) Elsevier.)

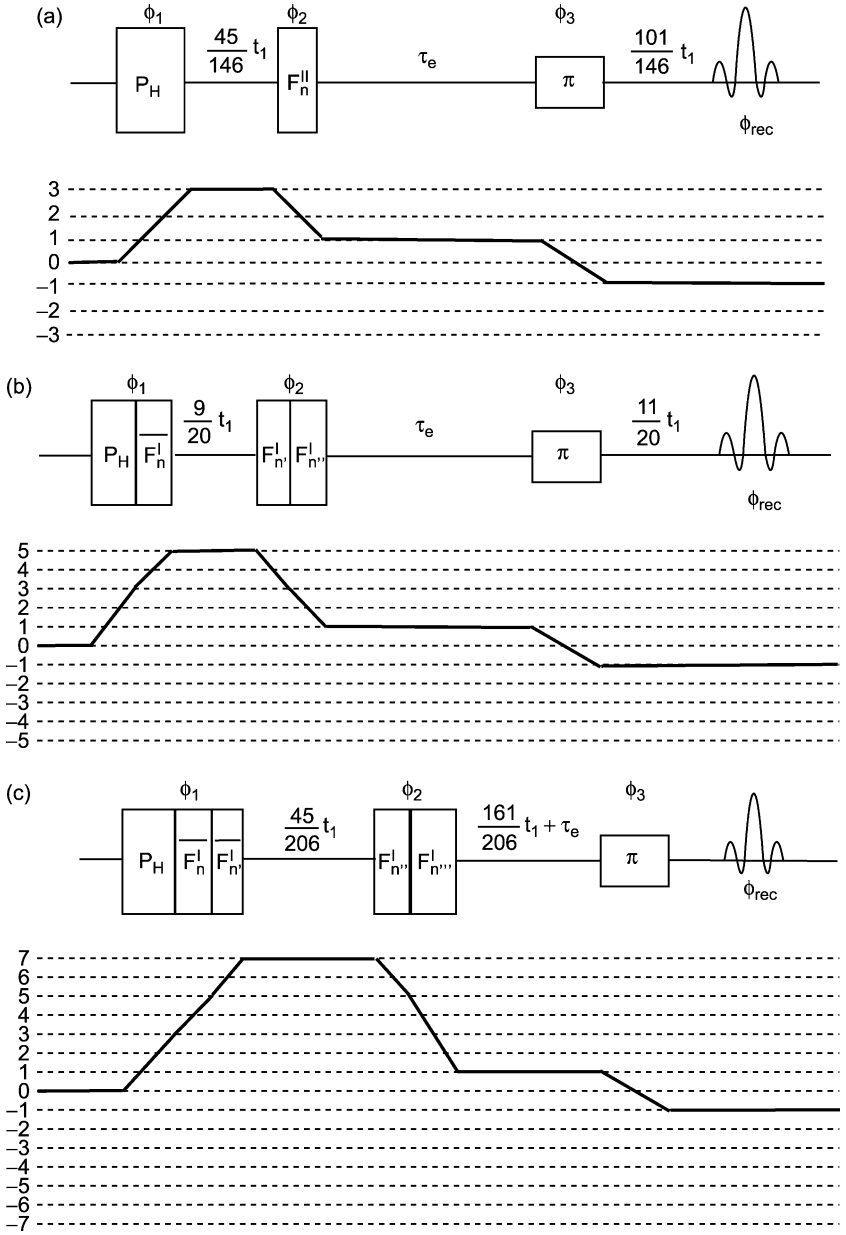

Fig. 19. Pulse sequences with FAM for (a) 3QMAS (b) 5QMAS, and (c) 7QMAS experiments of spin-$\frac{7}{2}$ systems.

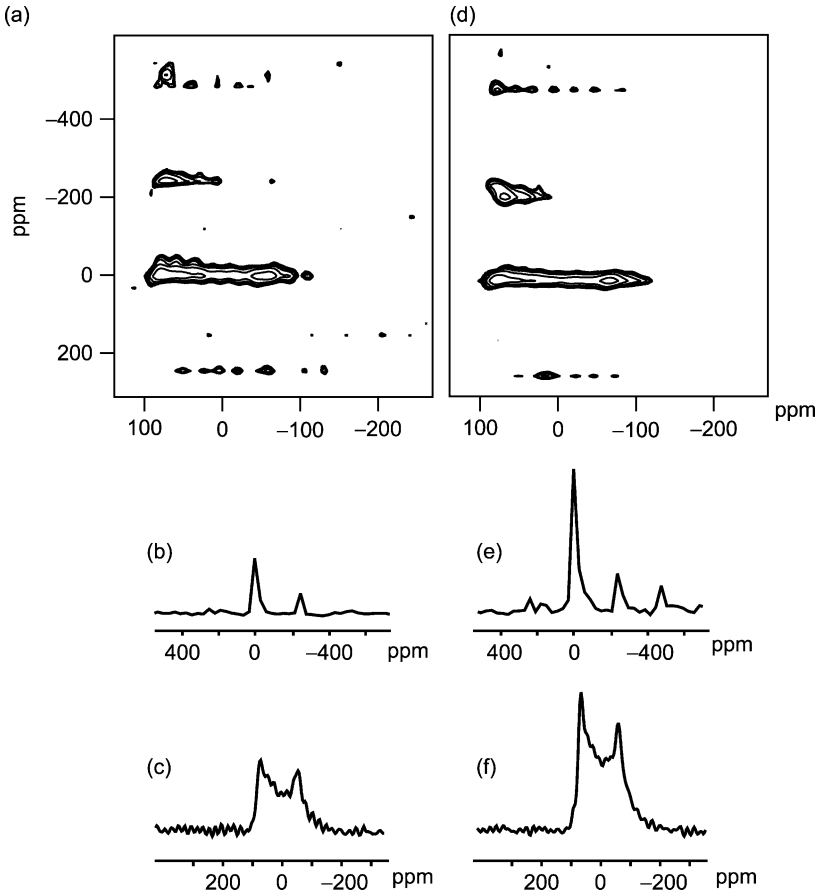

Fig. 20. Comparison of the ^{139}La 3QMAS spectrum of a sample of $LaAlO_3$ recorded with both (a–c) $P_H - P_H$ scheme and (d–f) $P_H - F_n^{II}(\Gamma)$ scheme. (a) and (d) correspond to the 2D spectra, (b) and (e) correspond to the isotropic projection, and (c) and (f) correspond to the anisotropic projection. A sensitivity enhancement by a factor of 2.0 is obtained with the application of FAM. The experiments were performed at an external magnetic field of 7.1 T. The central-transition RF nutation frequency was 80 kHz and the MAS frequency was 10 kHz. The optimum conversion block was $F_2^{II}(\Gamma)$, with $\Gamma = \{1.8, 0.2, 1.4\}$ μs. (Reprinted with permission from Madhu *et al.*[92] Copyright (2003) Elsevier.)

In Figs. 20, 21, 22 the experimental results are from ^{139}La spectrum of a sample of $LaAlO_3$.

5.9. FAM for 1D MAS signal enhancement

In this section, we will digress to show how FAM schemes lead to sensitivity enhancement in the 1D MAS spectra of half-integer quadrupolar spin systems.

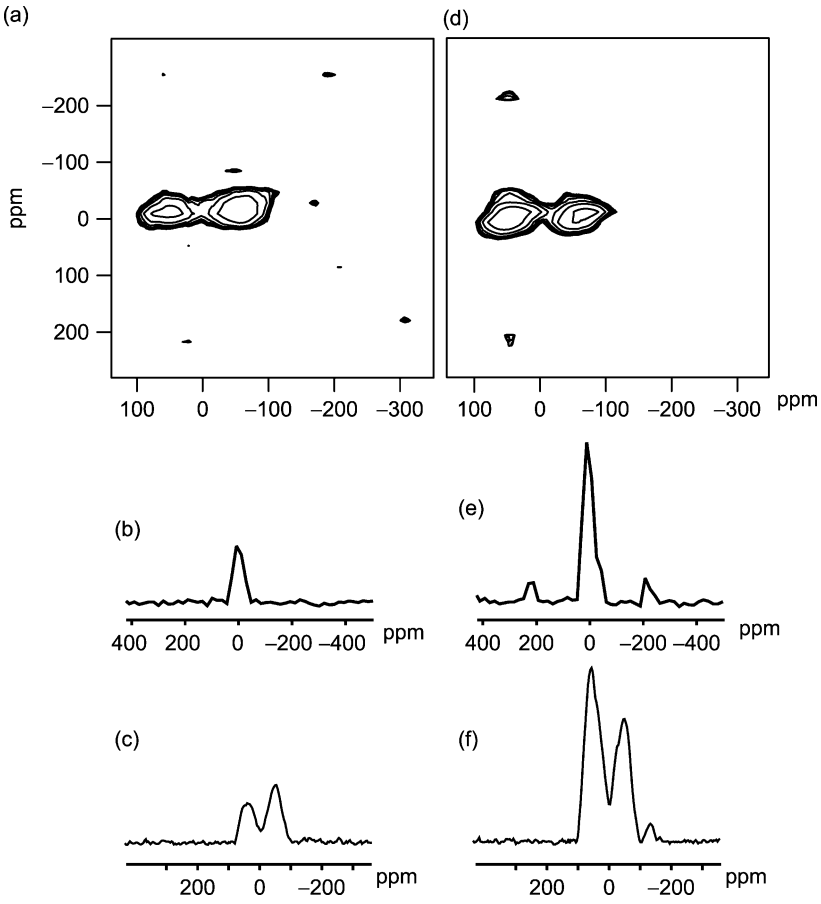

Fig. 21. Comparison of the ^{139}La 5QMAS spectrum of a sample of $LaAlO_3$ recorded with both (a–c) $P_{\mathrm{H}} - P_H$ scheme and (d–f) $P_H F_n^I(\tau) - F_n^{II}(\Gamma)\, F_{n'}^{II}(\Gamma')$ scheme. (a) and (d) correspond to the 2D spectra, (b) and (e) correspond to the isotropic projection, and (c) and (f) correspond to the anisotropic projection. A sensitivity enhancement by a factor of 3.0 is obtained with the application of FAM. The experiments were performed at an external magnetic field of 7 T. The central-transition RF nutation frequency was 80 kHz and the MAS frequency was 10 kHz. The parameters for the optimal pulse sequence for the spectrum in (d) were $P_H F_2^I(2.4\ \mu\mathrm{s}) - F_2^{II}(\Gamma) F_2^{II}(\Gamma')$ with $\Gamma = \{1.8, 0.2, 1.0\}$ μs and $\Gamma' = \{2.2, 0.2, 1.4\}$ μs. (Note that there is an error in the above in Ref. 92) (Reprinted with permission from Madhu *et al.*[92] Copyright (2003) Elsevier.)

The population distribution across the energy levels of a spin-$\frac{3}{2}$ is shown in Fig. 11b. A saturation of the populations across the satellite transitions leads to a scenario as shown in Fig. 11c where an enhancement of the population difference across the CT is equal to $I + 1/2$. An inversion of the populations across the satellite transitions leads to a scenario as shown in Fig. 11d where an enhancement of the population difference across the CT is $2I$.

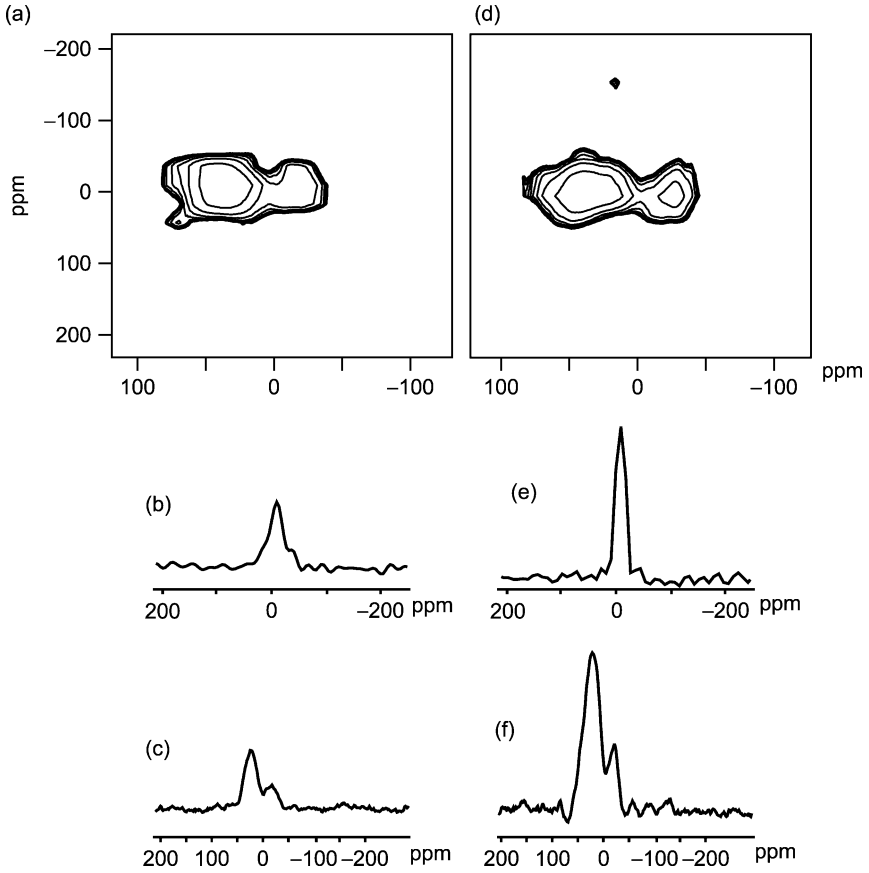

Fig. 22. Comparison of the ^{139}La 7QMAS spectrum of a sample of $LaAlO_3$ recorded with both (a–c) $P_H - P_H$ scheme and (d–f) $P_H F_n^I(\tau)\, F_{n'}^I(\tau') - F_{n''}(\tau'')F_{n'''}^I(\tau''')(\tau > \tau'$ and $\tau'' < \tau''')$ scheme. (a) and (d) correspond to the 2D spectra, (b) and (e) correspond to the isotropic projection, and (c) and (f) correspond to the anisotropic projection. A sensitivity enhancement by a factor of 3.0 is obtained with the application of FAM. The experiments were performed at an external magnetic field of 11.7 T. The central-transition RF nutation frequency was 80 kHz and the MAS frequency was 10 kHz. The optimized pulse sequence for the spectrum in (d) was $P_H\overline{F_4^I}(6\ \mu s)\overline{F_4^I}(4.0\ \mu s) - F_8^I(2.4\ \mu s)F_8^I(4.8\ \mu s)$. (Note that there is an error in the above in Ref. 92) (Reprinted with permission from Madhu *et al.*[92] Copyright (2003) Elsevier.)

The enhancement of the population difference across the CT leads to an enhancement of the spectral intensity of a static or MAS experiment of half-integer quadrupolar spins with either a single 90° pulse experiment or a Hahn-echo experiment preceded by a FAM block.[90–92,104] The schematic of the former is shown in Fig. 23b.

The maximum signal enhancement of $2I$ may be possible to achieve in the case of single-crystals, but in a spinning powder, especially with a large distribution of ν_Q, amplitude-modulated pulses result in a mixture of inversion, saturation and partial

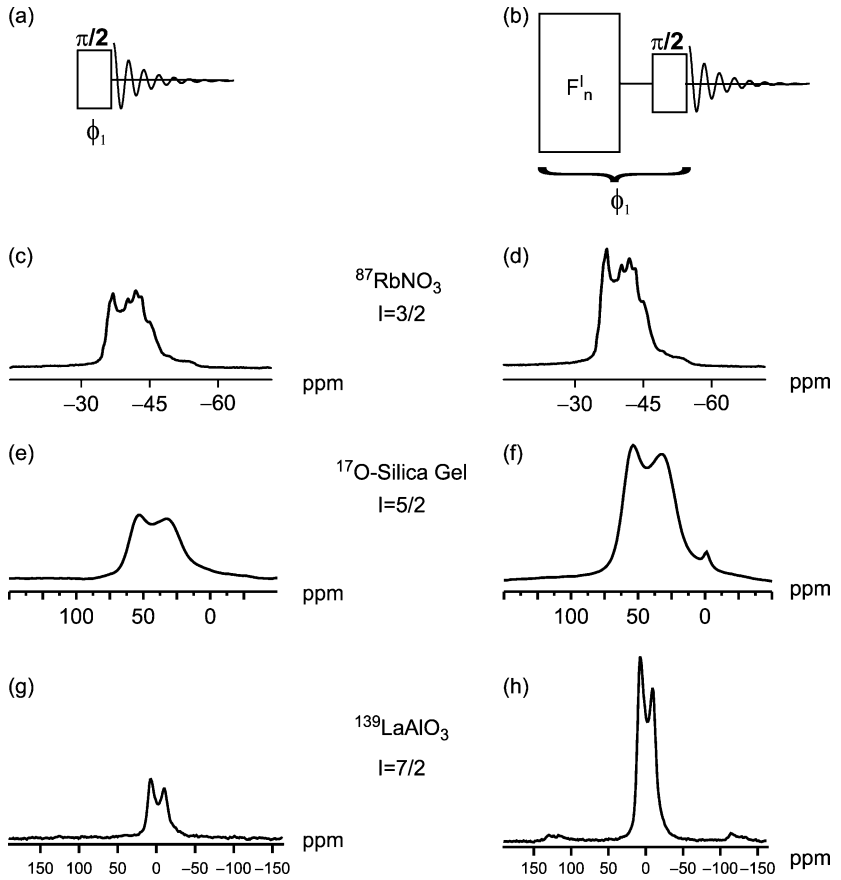

Fig. 23. (a) and (b) MAS pulse sequences with (a) the conventional experiment employing only a 90° pulse and (b) employing FAM pulses for enhancing the central-transition signal intensity of a spin-$\frac{3}{2}$ where FAM pulses precede a 90° pulse. Whilst for spins-$\frac{3}{2}$ FAM block with only one modulation frequency is required, for spins-$\frac{5}{2}$ and spins-$\frac{7}{2}$ additional blocks may have to be added in the form of $F_n^I(\tau)\, F_{n'}^I(\tau')$ and $F_n^I(\tau)\, F_{n'}^I(\tau')\, F_{n''}^I(\tau'')$, respectively, where $\tau < \tau' < \tau''$. FAM enhanced ^{87}Rb, ^{17}O, and ^{139}La spectra of $RbNO_3$, silica gel, and $LaAlO_3$ samples. (c), (e), and (g) correspond to the spectra acquired with the pulse sequence in (a) and (d), (f), and (h) correspond to the spectra acquired with the pulse sequence in (b). The signal enhancement factors vary from 1.8, 2.5, and 3.1 for ^{87}Rb, ^{17}O, and ^{139}La nuclei, respectively. (Reprinted with permission Madhu *et al.*[91, 92] Copyright (2003) Elsevier.)

population exchange, leading to enhancements different from the ideal values. Nevertheless, substantial signal increase is observed for any quadrupolar site. Figure 23c, e, and g shows the MAS spectra acquired with the pulse sequence shown in Fig. 23a. Figure 23d, f, and h shows the FAM enhanced MAS spectra acquired with the pulse sequence shown in Fig. 23b. The enhancements with FAM are on the order of 1.7–1.8 for spin-$\frac{3}{2}$, Fig. 23d, 2.0–2.5 for spin-$\frac{5}{2}$, Fig. 23f, and 3.2–3.5 for spin-$\frac{7}{2}$, Fig. 23h.

6. HETERO- AND HOMONUCLEAR CORRELATION EXPERIMENTS INVOLVING MQMAS

MQMAS has further opened up vistas by making it possible to design high-resolution hetero- and homonuclear correlation experiments. These lead to connectivity information, distance measurements, and spectral editing.

Connectivity information and spectral editing may be performed by combining cross-polarization (CP) and MQMAS. These include direct CP from a spin-$\frac{1}{2}$ to the quadrupolar spin and subsequently its detection with MQMAS scheme.[105,106] CP can be performed by polarizing either the CT of the quadrupolar nucleus followed by an inverse split-t_1 MQMAS scheme, allowing the incorporation of FAM pulses,[107] or by directly polarizing the multiple-quantum transitions during the CP contact time.[108–110]

Another very important experiment for spectral editing is a heterocorrelation experiment combining MQMAS (in the indirect dimension) with CP. Introducing CP at the MQMAS echo position following a split-t_1 MQMAS scheme creates a spin-$\frac{1}{2}$ detected spectra (in the F_2 dimension), which is modulated by the isotropic frequency of the quadrupolar nucleus in F_1. HETCOR has been demonstrated on ^{23}Na–^{31}P pairs,[111] on ^{27}Al–^{31}P pairs[112] and lately on ^{23}Na–^{1}H pairs,[113] where proton resolution during F_2 was obtained with the wPMLG5 multiple pulse decoupling technique.[114]

Distance information could be obtained between a spin-$\frac{1}{2}$ and a quadrupolar spin by combining REDOR[115] with MQMAS. Two distinct experiments have been suggested. In MQ-t_2-REDOR,[116] the dephasing π pulses of REDOR were applied during the SQ evolution period of the MQMAS scheme. In MQ-t_1-REDOR,[117] the dephasing pulses were applied during the MQ evolution period, resulting in enhanced dipolar dephasing, however, at the cost of requiring a triple-quantum inversion pulse ($+3 \rightarrow -3$ inversion), which is normally inefficient.

MQMAS is being developed to obtain further structural information in terms of residual dipolar coupling between quadrupolar nuclei,[18] by investigating the cross-terms between quadrupolar and homonuclear dipole–dipole interactions that induce field-dependent broadening in the isotropic dimension,[16] and by determining relative orientations among quadrupolar nuclei by incorporating into the z-filter period of MQMAS pulse sequence a proton driven spin diffusion scheme resulting in orientation-dependent lineshapes.[118]

7. APPLICATIONS OF MQMAS

Applications of MQMAS have been enormous since its inception in 1995. MQMAS has been implemented in numerous different types of materials such as glasses, clays, ceramics, zeolites, organic, and biological substances. Whilst the most commonly observed nuclei are ^{11}B, ^{17}O, ^{23}Na, and ^{27}Al, other examples also exist for nuclei such as ^{25}Mg, ^{45}Sc, ^{51}V, ^{87}Rb, and ^{93}Nb.

In this section we have tried to compile most of the applications that use partially or fully MQMAS results in order to assign, characterize and study the systems of interest. Among the large number of applications, the most popular are the study of aluminium

Table 7. Representative ^{11}B applications of MQMAS

Nucleus	Material class	Substances	Year	Reference
^{11}B,^{23}Na	Glass	$(Na_2S)_x(B_2S_3)_{1-x}$	1998	124
^{11}B,^{27}Al	Glass	Na-borate,Na-borosilicate, Li-boroaluminate	1998	125
^{11}B	Gels	$SiO_2-B_2O_3$	1999	126
^{11}B	Ceramics	Polyborazilene (precursor of h-BN)	2001	127
^{11}B	Glass	SiC_xO_{4-x},BC_yO_{3-y}	2001	128
^{11}B	Glass	$xB_2O_3(1-x)SiO_2$	2002	129
^{11}B	Ceramics	h−BN and precursors: polyborazilene, polyaminoborane	2002	130
^{11}B	Boron content materials	B_4C, SiB_4, h−BN	2002	131
^{11}B,^{17}O	Glass	Na Borosilicate glass	2003	132
^{11}B,^{17}O	Glass	Alkali-borosilicate glass	2003	133
^{11}B,^{17}O	Glass	Li-, Na-, K-borosilicates	2003	134
^{11}B	Polymer	Silyl-carborane (1,7-$C_2B_{10}H_{10}$) hybrid diethynylbenzene-silylene	2003	135

sites in zeolites, where aluminium coordination is probed as a function of chemical modifications such as heating, drying, dealumination, and cation insertion. Another example is the evolution of glass, in which detection of ^{11}B, ^{17}O, and ^{27}Al gives information regarding coordination, bond length and bond angle distributions. The vast majority of applications has been in inorganic systems, and the existence of only a very few examples in biological systems is somewhat surprising. There is no doubt that a development in this direction is overdue in the near future.

Several reviews have already described the potential uses of MQMAS in the systems mentioned above. Examples are reviews on glasses,[119] clay,[120] zeolites,[121] aluminophosphate molecular sieves,[122] and possible biological applications.[123] Tables 7–11 summarize studies done solely with MQMAS or using it as complementary source of information, starting immediately after the introduction of the experiment in 1995. They are organized according to the observed nuclei and contain information regarding the class of materials, the type of materials and the year of study.

8. SATELLITE-TRANSITION MAGIC-ANGLE SPINNING

This section gives an overview of the recent developments in STMAS spectroscopy. This method is expected to be complimentary to MQMAS in the study of materials containing quadrupolar nuclei.

STMAS, as indicated in Section 3, correlates the single-quantum satellite transitions to single-quantum CT leading to an echo of the Fourier transformation which gives rise to high-resolution spectra of half-integer quadrupole spins. A possible correlation is between the $|\pm\frac{3}{2}><\pm\frac{1}{2}|$ satellite transitions ($ST^{\pm}$) in the t_1 period of a 2D experiment and the CT in the t_2 period. Such a correlation leads to an echo free of the second-order

Table 8. Representative ^{17}O applications of MQMAS

Nucleus	Material class	Substances	Year	Reference
^{17}O	Zeolite	ZSM-5	1998	136
^{17}O	Glass	Boro-silicate	1998	137
^{17}O	Glass	$Na_2Si_4O_9$ (sodium tetrasilicate, NTS), $NaAlSi_3O_8$ (albite) $NaAlSi_2O_6{\cdot}H_2O$ (crystalline analcime)	1998	138
^{17}O,^{27}Al	Glass	Y^{3+} and La^{3+} aluminosilicates	1998	139
^{17}O	Glass	$NaAlO_2$, $CaAl_2O_4$ (model compounds for Al-O-Al sites in glasses)	1999	140
^{17}O	Glass	Boron-oxide glasses	1999	141
^{17}O	Zeolite(natural)	Stilbite	1999	142
^{17}O	Nano-objects	Ti-oxo clusters, nanoparticles of titanium anatase	1999	143
^{17}O	Mineral	Forsterite (Mg_2SiO_4)	1999	144
^{17}O	Glass	Nepheline ($NaAlSiO_4$), β-eucryptite ($LiAlSiO_4$)	2000	145
^{17}O	Glass	Barium borosilicate	2000	146
^{17}O	Glass	Sodium aluminoborosilicate	2001	147
^{17}O	Mineral	Hydroxyl-chondrodite ($2Mg_2SiO_4{\cdot}Mg(OH)_2$), hydroxyl-clinohumite ($4Mg_2SiO_4{\cdot}Mg(OH)_2$)	2001	148
^{17}O	Zeolites	A, LSX zeolites with Si:Al = 1:1	2001	149
^{17}O	Glass	$CaAl_4O_7$(crystalline calcium dialuminate, grossite) $CaAl_2O_4$ (crystalline calcium monoaluminate)	2001	150
^{17}O	Organic	D-alanine, potassium hydrogen dibenzoate, glutamic-acid·HCl, uracil	2001	151
^{17}O	Gels	V_2O_5, $V_2O_5{\cdot}nH_2O$ gels	2002	152
^{17}O	Zeolite	Na–A, Ca–A	2002	153
^{17}O	Mineral	Pyroxenes: $CaMgSi_2O_6$: diopside, $MgSiO_3$ polymorphs: *ortho*-, clino- and proto-enstatite	2002	154
^{17}O	Glass	$xNa_2O{\cdot}(1-x)P_2O_5$	2002	155
^{17}O	Glass	Alkali aluminosilicate glasses	2002	156
^{17}O	Zeolite	$AlPO_4$	2002	157
^{17}O	Silicate	Wadsleyite (β-Mg_2SiO_4)	2003	158
^{17}O	Glass	Ca–Na soda-lime silicate glass	2003	159
^{17}O	Mineral	Kaolinite, musovite	2003	160
^{17}O	Composite	Aluminosilicate xerogels	2003	76

quadrupole broadening with the first-order broadening averaged to zero by MAS.[20,21] The pulse sequence for STMAS using split-t_1 method is shown in Fig. 24a.

STMAS has higher sensitivity in comparison with MQMAS since the correlation is between two single-quantum transitions, the excitation and conversion of which are more efficient than those of MQ transitions. However, an accurate setting of the magic angle (to about 0.004°) is necessary for averaging out the first-order effects. Any minor deviation in the setting of the magic angle reintroduces the first-order effects and broadening of the spectral lines.[21]

Table 9. Representative ^{23}Na applications of MQMAS

Nucleus	Material class	Substances	Year	Reference
^{23}Na	Microporous	ETS-10	1998	161
^{23}Na,^{27}Al	Zeolite	NH4-ferrierites (ZSM-35)	1998	162
^{23}Na	Microporous	AV-3 (Na-Zr-silicate)	1998	163
^{23}Na	Microporous	AV-1 (Y-silicate), AV-2 (Ca-silicate)	1998	164
^{23}Na	Mineral	Makatite, kanemite, octosilicate, magadiite, kenyaite	1998	165
^{23}Na		$(Na_2SO_4)_x$-$(Na_3PO_4)_{1-x}$	1999	166
^{23}Na	Microporous	ETS10	1999	167
^{23}Na		$Na_5P_3O_{10}$	1999	168
^{23}Na	Mineral	Zr silicate (analogue of AV-3)	1999	169
^{23}Na	Biological	Hydrated disodium ATP	2000	170
^{23}Na	Phosphate	$NaMg(PO_3)_3$, $NaZn(PO_3)_3$	2000	171
^{23}Na		$Na_6[P_2MO_5O_{23}]7H_2O$	2000	172
^{23}Na	Zeolite	NaX, NaY	2000	173
^{23}Na	Glass	$(Na_2O)_x$:B_2O_3:SiO_2:$(Al_2O_3)_{25}$	2000	174
^{23}Na	Glass	$Na_2O - M - 3SiO_2$, $M = 2SiO_2$, 2CaO, Al_2O_3 B_2O_3	2000	175
^{23}Na	Biological	Na^+ in DNA quadruplex	2000	176
^{23}Na		$Na_2Ga_6Te_{10}$, $Li_2Ga_6Te_{10}$	2000	177
^{23}Na	Zeolite	Li,Na-Chabazite	2000	178
^{23}Na	Catalysts	Na-doped V_2O_5–TiO_2	2000	179
^{23}Na	Zeolite	Sodium cerium silicate AV-5	2000	180
^{23}Na	Salts	Na_2–EDTA $2H_2O$ and Na_4–EDTA $5H_2O$	2001	181
^{23}Na	Zeolite	LSX, X, Y dehydrated	2001	182
^{23}Na	Zeolite	LiNaX	2001	183
^{23}Na	Zeolite	K^+ effect on Li,Na-Chabazite	2001	184
^{23}Na	Silicate	Amorphous Na–Ga silicate	2002	185
^{23}Na	Glass	$Na_2O{\cdot}3SiO_2$	2002	186
^{23}Na		Na-disilicate SKS-5	2002	187
^{23}Na	Biological	Na + in lipophilic G-quadruplex channel	2002	188
^{23}Na,^{27} Al	Clay	Laponite,synthetic saponites	2003	189
^{23}Na	Biological	dCMP, dGMP, dUMP, ATP	2003	190
^{23}Na, ^{27}Al	Mineral	Sodalite	2003	191
^{23}Na	Biological	Guanosine 5′-monophosphate	2003	192
^{23}Na	Glass	Na^+/silicate glasses	2003	193
^{23}Na	Silicate	Na-disilicates SKS-5, SKS-6	2003	194

Several modifications have been proposed for STMAS. Some were aimed at achieving pure absorption lineshapes such as z-filter[20] and phase-modulated shifted-echo schemes.[279] Another modification proposed was to create CT coherences first and detecting the satellite transitions (iSTMAS).[280] Perhaps, the most interesting modification involves pure absorption lineshapes with a compensation to the magic-angle misset, the SCAM–STMAS experiment.[22,23]

The SCAN–STMAS pulse sequence is shown in Fig. 24b. The extra pulse in the middle of the t_1 period transfers the coherence between the two satellite transitions. The two satellite transitions, ST^+ and ST^-, have first-order quadrupole frequencies that

Table 10. Representative ^{27}Al applications of MQMAS

Nucleus	Material class	Substances	Year	Reference
^{27}Al	Zeolite	$AlPO_4$-34	1998	195
^{27}Al	Ceramic	Mullite (+andalusite)	1998	68
^{27}Al	Cement	Calcium aluminate hydrates	1998	196
^{27}Al	Mineral	Andalusite	1998	197
^{27}Al		$SrAl_{12}O_{19}$	1998	198
^{27}Al	Glass	Na_2O-B_2O_3-Al_2O_3	1998	199
^{27}Al	Zeolite	$AlPO_4$-H3, $CoAPO_4$-H3	1998	200
^{27}Al	Cement	Ca-silicate-hydrate	1998	201
^{27}Al	Micorporous	AlMePO-β/AlMePO-a	1999	202
^{27}Al	Zeolite	Levyne	1999	203
^{27}Al	Glass	$(R_2O_3)_x$ $(P_2O_5)_{1-x}$ R ≡ Ce,Nd,Tb	1999	204
^{27}Al		$(La_2O_3)_x$ $(Al_2O_3)_{1-x}$	1999	72
^{27}Al		$MgAl_2O_4$ precursor	1999	205
^{27}Al	Zeolite	Offretite	1999	206
^{27}Al	Sodalite	$Ag_6[AlSiO_4]_6$, $Tl_6[AlSiO_4]_6$	1999	207
^{27}Al	Zeolite	AlPO4-CJ2	1999	208
^{27}Al	Mesoporous	MCM-22	1999	209
^{27}Al		Ca-silicate-hydrate	1999	210
^{27}Al	Clay mineral	Kaolinite	1999	211
^{27}Al		Phosphorus modified alumina	1999	212
^{27}Al	Zeolite	$AlPO_4$-41	1999	213
^{27}Al,^{11}B	Glass	Na-borate,Na-borosilicate, Li-boroaluminate	1999	214
^{27}Al	Mineral	Kyanite, andalusite	1999	215
^{27}Al	Zeolite	Mordenite	2000	216
^{27}Al	Zeolite	H-USY, La_x NaY	2000	217
^{27}Al		Pigments of TiO_2 coated with $SiO_2-Al_2O_3$	2000	218
^{27}Al	Zeolite	USY	2000	219
^{27}Al	Zeolite	Y	2000	220
^{27}Al	Glass	$MgO-Al_2O_3-SiO_2$	2000	221
^{27}Al	Glass	Ca^+ in sodium aluminosilicate	2000	222
^{27}Al	Mineral	Kaolinite, gibbsite	2000	223
^{27}Al	Zeolite	$ALPO_4$ − 34	2000	224
^{27}Al	Mesoporous	Mesostructured aluminophosphates	2000	225
^{27}Al	Blue luminis-cent compound	Al_2 $(CH_3)_2$ (7-azain)$_4$, $Al_3(\mu 3-O)(CH_3)$ (7-azain)$_4$$(OCH(CF_3)_2)_2$	2000	226
^{27}Al	Catalyst	Mo-alumina, Mo-P−alumina	2000	227
^{27}Al	Zeolite	$Al_{100}P_xV_y$	2000	228
^{27}Al	Zeolite	H-Beta	2000	229
^{27}Al,^{17}O	Glass	Aluminosilicate	2000	230
^{27}Al	Silicates	Amorphous types of $3Al_2O_32SiO_2$ (mullite)	2001	231
^{27}Al	Ceramic	Mixtures of bayerite and silicic acid/silica-gel	2001	232
^{27}Al	Garnets	$Y_{3-x}Lu_xAl_5O_{12}(0 \leq \times \geq 3)$	2001	233
^{27}Al	Mineral/zeolite	Natural barrerite (Alaska)	2001	234

(*continued*)

Table 10. Continued

Nucleus	Material class	Substances	Year	Reference
^{27}Al	Polycations	Al13 ε-Keggin Johansson-type, Al13Mogel-type and Al30 δ-Taulelle-type	2001	235
^{27}Al	Zeolite	Ultrastable Y	2001	236
^{27}Al		$Al_{22}Cl_{20}$·12THF, $Al_{22}Cl_{20}$·12THP	2001	237
^{27}Al	Zeolite	H-ZSM acid site	2001	238
^{27}Al	Glass	AlF_3-BaF_2-CaF_2	2001	239
^{27}Al	Zeolite	Aluminophosphates	2001	240
^{27}Al		$CaAl_4O_7$, $CaAl_{12}O_{19}$	2001	241
^{27}Al	Composite	Aluminosilicate-PEO	2001	242
^{27}Al	Zeolite	USY	2001	243
^{27}Al	Zeolite	$AlPO_4$-5/TPAF	2001	244
^{27}Al	Ceramic	Lithium-α-sianols (Li_mSi_{12}-$(_{m+n)}$-$_{m+n)}Al_{m+n}O_nN_{16-n}$)	2001	245
^{27}Al		Alumina-pillared γ-zirconium phosphate	2001	246
^{27}Al		2D layered aluminophosphate: $(C_8N_2H_{22})_8[Al_{13}P_{18}O_{72}]\cdot 6H_2O$	2001	247
^{27}Al	Clay	Al13(heidi)63 + polycation	2002	248
^{27}Al	Zeolite	High silica USY	2002	249
^{27}Al		Drying process of precasting materials in a steel-making converter	2002	250
^{27}Al	Mesoporous	Alumina formation	2002	251
^{27}Al	Zeolite	ZSM-5	2002	252
^{27}Al		$Sr_3Al_{10}SiO_{20}$	2002	253
^{27}Al		2D layered aluminophosphate	2002	254
^{27}Al	Zeolite	HZSM-5	2002	255
^{27}Al,^{23}Na	Sodalite	Na_8 $[Al_6Si_6O_{24}]$ $Br_x\cdot(H_3O_2)_{2-x}$	2002	256
^{27}Al	Zeolite	MCM-22, Mo/MCM-22	2002	257
^{27}Al		Aluminium hydroxides	2002	258
^{27}Al	Zeolites	$AlPO_4$ -11	2003	259
^{27}Al	Zeolites	SAPO-34	2003	260
^{27}Al	Zeolites	H-USY, amorphous silica	2003	261
^{27}Al	Mineral	Phlogopite	2003	262
^{27}Al	Zeolite	$AlPO_4$ -18	2003	263
^{27}Al	Zeolite	Yi-USY	2003	264
^{27}Al	Mineral	Zunyite	2003	265
^{27}Al	Mineral	Montmorillonite	2003	266
^{27}Al	Zeolite	USY	2003	267
^{27}Al	Zeolite	BETA	2003	268
^{27}Al	Super-sodalite	Zn–Al phosphate	2003	269
^{27}Al	Composite	Aluminophosphate-oxalate	2003	270
^{27}Al	Mesoporous	γ-Al_2O_3,Alumina grafted MCM-41	2003	78
^{27}Al		$Sr_4Al_{14}O_{25}$	2003	272

Table 11. Representative ^{25}Mg, ^{45}Sc, ^{51}V, ^{87}Rb, and ^{93}Nb applications of MQMAS

Nucleus	Material class	Substances	Year	Reference
^{25}Mg	Biological	Mg^{2+} ATP	2000	273
^{25}Mg	Biological, Mg complex as models for inner-sphere Mg^{2+} coordination	$Mg(H_2O)_4L_2$, L = methylmalonte, formate, acetate, orotate	2000	271
^{87}Rb	Polycrystalline	$LiRbSO_4$ – phase transitions	2001	274
^{93}Nb	Inorganic niobates	$LiNbO_3$, $NaNbO_3$, $PbNb_2O_6$, $Pb_2Nb_2O_7$, $Pb_3Nb_2O_8$, $Pb_5Nb_4O_{15}$, $Pb_3Nb_4O_{13}$, $Pb_{1.83}Nb_{1.71}Mg_{0.29}O_{6.39}$	2001	275
^{93}Nb	Ferroelectric pyrochlore(mineral)	$Pb(Mg_{1/3}Nb_{2/3})O_3$ (PMN)	1999	276
^{45}Sc	Phosphate	$Sc(HPO_4)_2{\cdot}0.5(N_2C_2H_{10})$	2002	277
^{51}V		$LaVO_4$	2003	278

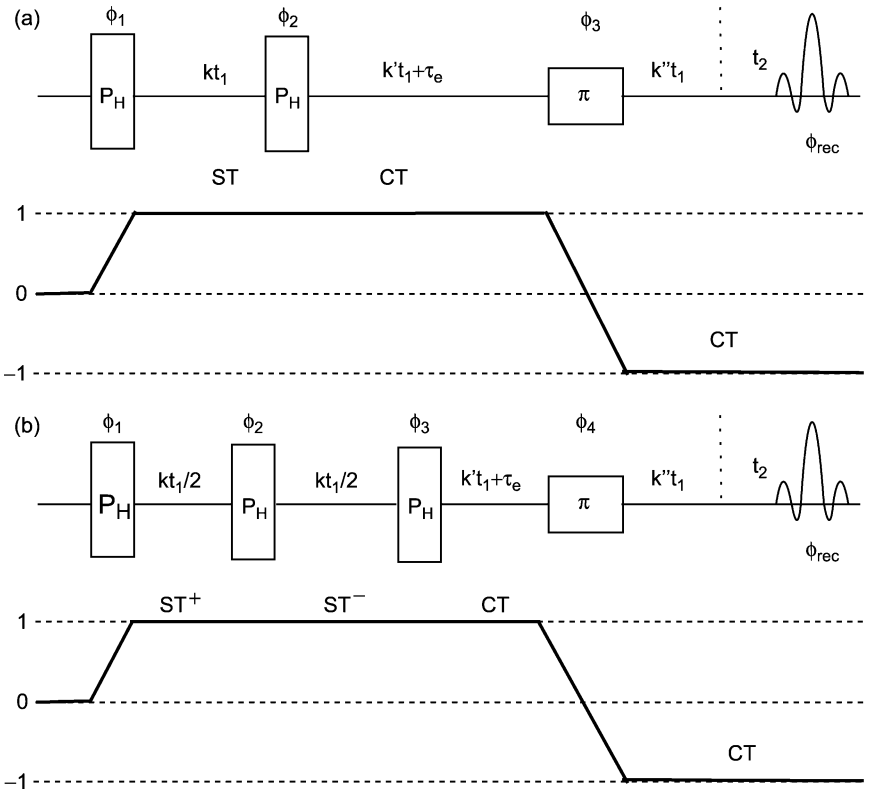

Fig. 24. Shifted-echo split-t_1 pulse sequences for (a) STMAS and for (b) SCAM–STMAS which compensates for a mis-set in the magic angle. Also shown are the coherence level diagrams along with an indication of which transition, satellite transition (ST) or central transition (CT), is being tracked by the pulses. The phase-cycle list, $\phi_1,\phi_2,\phi_3,\phi_4$, and ϕ_{rec} is given in Table 5e.

are equal in magnitude and opposite in sign. Compensation is obtained by correlating ST_n^+ with ST_n^- thus retaining the sign of the second-order quadrupolar frequency of the satellite coherences while inverting that of the first-order quadrupolar frequency. For example, the t_1 period of an STMAS experiment is split into two halves to allow evolution of ST^+ coherences ($|+1/2><+3/2|$ coherences) for a period of τ followed by evolution of ST^- coherences ($|-3/2><-1/2|$ coherences) for another period of τ. The STMAS echo will be observed at time $t_2 = 2k\tau t_1$, with $k = 8/9$ as given in Eq. (46). FAM pulses may be used in place of the extra pulse in SCAM–STMAS scheme to boost the signal sensitivity such that the overall intensity is higher than that obtained with MQMAS scheme.[23]

A high-resolution ^{87}Rb STMAS spectrum of a sample of $RbNO_3$ is shown in Fig. 25a with very accurate magic-angle setting. The diagonal peaks, resulting from CT–CT echo formation, may be removed by employing a soft presaturation pulse before the STMAS pulses at the cost of spectral sensitivity.[21] Figure 25b shows the STMAS spectrum of the same sample with the magic-angle mis-set by 0.07° which greatly affects the resolution and sensitivity. Figure 25c shows the SCAM–STMAS spectrum of the same sample with

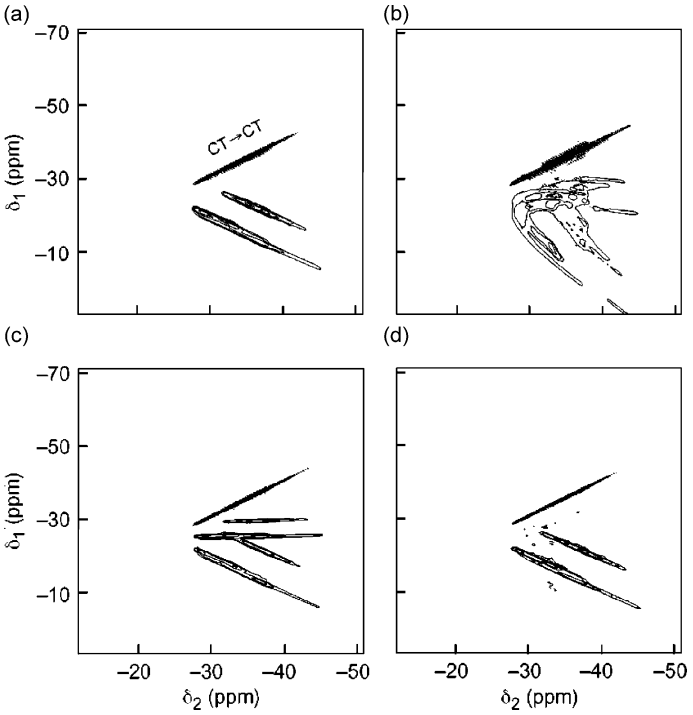

Fig. 25. ^{87}Rb spectra of $RbNO_3$ acquired with (a) regular STMAS scheme with very accurate magic-angle setting, (b) regular STMAS scheme with a magic-angle mis-set of 0.07°, (c) SCAM–STMAS scheme with very accurate magic-angle setting, and (d) SCAM–STMAS scheme with a magic-angle mis-set of 0.07°. (Reprinted with permission from Ashbrook and Wimperis[22] Copyright (2002) American Chemical Society.)

accurate magic-angle setting, which also suffers from low resolution due to certain unwanted coherence transfers.[22] Figure 25d shows the SCAM–STMAS spectrum of the same sample with the magic-angle mis-set by 0.07° showing good resolution, although now the sensitivity is equivalent to that obtained with a FAM-assisted MQMAS experiment.[22]

As the field stands now, STMAS is a difficult experiment to perform, confining its implementation to a handful of groups. Attempts are in progress to make the experiment less demanding on hardware requirements. Pulse schemes are being introduced to remove several artefacts, for instance, the strong diagonal peaks by performing double-quantum filtered STMAS.[24] Despite all these, both MQMAS and STMAS are expected to supplement each other for better characterization of materials containing quadrupolar nuclei. We can probably expect in the future to see correlation of single-quantum satellite transitions with MQCs, heteronuclear experiments involving STMAS and more.

9. CONCLUSIONS

We have attempted to give a broad overview of the field of MQMAS, the technique and its different facets. It is expected that more and more applications with MQMAS will result in material science and in biological fields. Development of MQMAS signal enhancement schemes is an on-going process. Although we have emphasized the role of FAM pulses in signal enhancement, a variety of other approaches are being introduced which may have an impact in the field of MQMAS in the near future.[281,282] We expect, in the future, a routine implementation of both MQMAS and STMAS for a speedy and high-resolution characterization of half-integer spin quadrupolar nuclear systems along with various homo- and hetero-correlation experiments.

ACKNOWLEDGEMENTS

The authors acknowledge fruitful discussions with Shimon Vega on various aspects of the theory of quadrupolar spins and MQMAS. We also acknowledge Shimon Vega and Thomas Bräuniger for a very careful reading of the manuscript and their critical comments.

REFERENCES

1. K. J. D. MacKenzie and M. E. Smith, *Multinuclear Solid-State NMR of Inorganic Materials*, Pergamon Press, Oxford, 2002.
2. A. Vega, *Quadrupolar Nuclei in Solids*, Encyclopedia of NMR, Vol. 6, D. M. Grant and R. K. Harris eds., Wiley, Chichester, 2002, 3869.
3. A. Abragam, *The Principles of Nuclear Magnetism*, Clarendon Press, Oxford, 1961.
4. M. H. Cohen, F. Reif, *Solid State Physics*, Vol. 5. Academic Press, 1957.
5. M. Mehring, *Principles of High Resolution NMR in Solids*, Springer, Berlin, 1983.
6. S. Ganapathy, S. Schramm and E. Oldfield, *J. Chem. Phys.*, 1982, **77**, 4360.
7. A. Samoson and E. Lippmaa, *Phys. Rev.*, 1983, **B28**, 6567.
8. A. Samoson and E. Lippmaa, *Chem. Phys. Lett.*, 1983, **100**, 205.

9. A. Samoson, E. Lippmaa and A. Pines, *Mol. Phys.*, 1988, **65**, 1013.
10. A. Llor and J. Virlet, *Chem. Phys. Lett.*, 1988, **152**, 248.
11. B. F. Chmelka, K. T. Müller, A. Pines, J. F. Stebbins, Y. Wu and J. W. Zwanziger, *Nature*, 1989, **339**, 42.
12. H. J. Jakobsen, J. Skibsted, H. Bildsøe and N. C. Nielsen, *J. Magn. Reson.*, 1989, **85**, 173.
13. L. Frydman and J. S. Harwood, *J. Am. Chem. Soc.*, 1995, **117**, 5367.
14. A. Medek, J. S. Harwood and L. Frydman, *J. Am. Chem. Soc.*, 1995, **117**, 12779.
15. G. Wu and K. Yamada, *Chem. Phys. Lett.*, 1999, **313**, 519.
16. J. McManus, R. Kemp-Harper and S. Wimperis, *Chem. Phys. Lett.*, 1999, **311**, 292.
17. S. Wi and L. Frydman, *J. Chem. Phys.*, 2000, **112**, 3248.
18. S. Wi, V. Frydman and L. Frydman, *J. Chem. Phys.*, 2001, **114**, 8511.
19. J. P. Amoureux and M. Pruski, *Advances in MQMAS NMR* Encyclopedia of NMR, Vol. 9, D. M. Grant and R. K. Harris, eds., Wiley, Chichester, 2002.
20. Z. Gan, *J. Am. Chem. Soc.*, 2000, **122**, 3242.
21. Z. Gan, *J. Chem. Phys.*, 2001, **114**, 10845.
22. S. E. Ashbrook and S. Wimperis, *J. Am. Chem. Soc.*, 2002, **124**, 11603.
23. S. E. Ashbrook and S. Wimperis, *J. Magn. Reson.*, 2003, **162**, 402.
24. H-T. Kwak and Z. Gan, *J. Magn. Reson.*, 2003, **164**, 369.
25. D. Freude, Quadrupolar nuclei in solid-state nuclear magnetic resonance. *Encyclopedia of Analytical Chemistry*, R. A. Meyers, ed., Wiley, Chichester, 2000, 12188.
26. M. E. Smith and E. R. H. van Eck, *Prog. Nucl. Magn. Reson. Spectrosc.*, 1999, **34**, 159.
27. P. P. Man, Quadrupole couplings in nuclear magnetic resonance, general. *Encyclopedia of Analytical Chemistry*, R. A. Meyers, ed., Wiley, Chichester, 2000, 12224.
28. P. K. Madhu, A. Goldbourt, L. Frydman and S. Vega, *Chem. Phys. Lett.*, 1999, **307**, 41.
29. P. K. Madhu, A. Goldbourt, L. Frydman and S. Vega, *J. Chem. Phys.*, 2000, **112**, 2377.
30. P. K. Madhu and M. H. Levitt, *J. Magn. Reson.*, 2002, **155**, 150.
31. A. Goldbourt, P. K. Madhu, S. Kababya and S. Vega, *Solid State Nucl. Magn. Reson.*, 2000, **18**, 1.
32. A. Medek and L. Frydman, *J. Braz. Chem. Soc.*, 1999, **10**, 263.
33. L. Frydman, *Annu. Rev. Phys. Chem.*, 2001, **52**, 463.
34. L. Frydman, *Fundamentals of Multiple-quantum Magic-angle Spinning NMR on Half-integer Quadrupolar Nuclei*, Encyclopedia of NMR, Vol. 9, D. M. Grant and R. K. Harris, eds., Wiley, Chichester, 2002.
35. A. P. M. Kentgens, *Geoderma*, 1997, **80**, 271.
36. (a) A. Goldbourt and P. K. Madhu, *Monatsh. Chem.*, 2002, **133**, 1497. (b) A. Goldbourt and P. K. Madhu, *Current Developments in Solid State NMR Spectroscopy* Vol. 133 N. Müller, and P. K. Madhu, SpringerWien 2002.
37. U. Haeberlen, *High resolution NMR of solids*, Adv. Magn. Reson., Suppl. 1. Academic Press, San Diego, 1976.
38. J. J. Sakuari, *Modern Quantum Mechanics*, Addison-Wesley, Reading, MA, 1994.
39. M. E. Rose, *Elementary Theory of Angular Momentum*, Wiley, New York, 1957.
40. A. R. Edmonds, *Angular Momentum in Quantum Mechanics*, Princeton University Press, Princeton, NJ, 1957.
41. M. H. Levitt, *Spin Dynamics*, Wiley, Chichester, 2001.
42. A. Samoson and E. Lippmaa, *J. Magn. Reson.*, 1989, **84**, 410.
43. J.-P. Amoureux, *Solid State Nucl. Magn. Reson.*, 1993, **2**, 83.
44. J. K. Jung, O. H. Han and S. K. Choh, *Solid State Nucl. Magn. Reson.*, 1999, **13**, 255.
45. A. Jerschow, J. W. Logan and A. Pines, *J. Magn. Reson.*, 2001, **149**, 268.
46. D. Kuwahara and T. Nakai, *Chem. Phys. Lett.*, 1996, **260**, 249.
47. A. Samoson, *Chem. Phys. Lett.*, 1985, **119**, 29.
48. A. P. M. Kentgens, *J. Magn. Reson.*, 1993, **A104**, 302.
49. A. P. M. Kentgens, *J. Magn. Reson.*, 1991, **95**, 619.
50. A. P. M. Kentgens, *Prog. Nucl. Magn. Reson. Spectrosc.*, 1998, **32**, 141.
51. G. Bodenhausen, H. Kogler and R. R. Ernst, *J. Magn. Reson.*, 1984, **58**, 370.
52. A. D. Bain, *J. Magn. Reson.*, 1984, **56**, 418.
53. J.-P. Amoureux, C. Fernandez and L. Frydman, *Chem. Phys. Lett.*, 1996, **259**, 347.

54. R. R. Ernst, G. Bodenhausen and A. Wokaun, *Principles of NMR in One and Two Dimensions*, Clarendon Press, Oxford, 1987.
55. A. Bax, A. F. Mehlkopf and J. Smidt, *J. Magn. Reson.*, 1979, **35**, 373.
56. D. Massiot, B. Touzo, D. Trumeau, J. P. Coutures, J. Virlet, P. Florian and P. J. Grandinetti, *Solid State Nucl. Magn. Reson.*, 1996, **6**, 73.
57. O. W. Sørensen, M. Rance and R. R. Ernst, *J. Magn. Reson.*, 1984, **56**, 527.
58. S. P. Brown, S. J. Heyes and S. Wimperis, *J. Magn. Reson.*, 1996, **A119**, 280.
59. J. P. Amoureux, C. Fernandez and S. Steuernagel, *J. Magn. Reson.*, 1996, **A123**, 116.
60. S. P. Brown and S. Wimperis, *J. Magn. Reson.*, 1997, **124**, 279.
61. M. H. Levitt, P. K. Madhu and C. H. Hughes, *J. Magn. Reson.*, 2002, **155**, 300.
62. K. J. Pike, R. P. Malde, S. E. Ashbrook, J. McManus and S. Wimperis, *Solid State Nucl. Magn. Reson.*, 2000, **16**, 203.
63. D. Massiot, F. Fayon, M. Capron, I. King, S. L. Calvè, B. Alonso, J.-O. Durand, B. Bujoli, Z. Gan and G. Hoatson, *Magn. Reson. Chem.*, 2002, **40**, 70.
64. B. Herreros, A. W. Metz and G. S. Harbison, *Solid State Nucl. Magn. Reson.*, 2000, **16**, 141.
65. G. Engelhardt, A. P. M. Kentgens, H. Koller and A. Samoson, *Solid State Nucl. Magn. Reson.*, 1999, **15**, 171.
66. Y. Millot and P. P. Man, *Solid State Nucl. Magn. Reson.*, 2002, **21**, 21.
67. M. Hanaya and R. K. Harris, *J. Phys. Chem.*, 1997, **A101**, 6903.
68. P. R. Bodart, J. Parmentier, R. K. Harris and D. P. Thompson, *J. Phys. Chem. Sol.*, 1998, **60**, 223.
69. J.-P. Amoureux and C. Fernandez, *Solid State Nucl. Magn. Reson.*, 1998, **10**, 211.
70. J.-P. Amoureux and C. Fernandez, *Solid State Nucl. Magn. Reson.*, 2000, **16**, 339.
71. M. Bak, J. T. Rasmussen and N. C. Nielsen, *J. Magn. Reson.*, 2000, **147**, 296.
72. D. Iuga, S. Simon, E. De Boer and A. P. M. Kentgens, *J. Phys. Chem.*, 1999, **B103**, 7591.
73. J. W. Zwanziger, *Solid State Nucl. Magn. Reson.*, 1994, **3**, 219.
74. F. Angeli, T. Charpentier, P. Faucon and J.-C. Petit, *J. Phys. Chem.*, 1996, **B103**, 10356.
75. C. Fernandez, *Stud. Surf. Sci. Catal.*, A. Galarneau, F. Di Renzo, F. Fajula and J. Vedrine, eds., Proceedings of the 13th International Zeolite Conference, Montpellier, France, Vol. 135. 2002, 183.
76. A. Lafuma, F. Fayon, D. Massiot, S. Chodorowski-Kimmes and C. Sanchez, *Magn. Reson. Chem.*, 2003, **41**, 944.
77. C. Fernandez and J.-P. Amoureux, *Chem. Phys. Lett.*, 1995, **242**, 4951.
78. A. Goldbourt, M. V. Landau and S. Vega, *J. Phys. Chem.*, 2003, **B107**, 724.
79. S. Vega and Y. Naor, *J. Chem. Phys.*, 1981, **75**, 75.
80. D. Massiot, *J. Magn. Reson.*, 1996, **A122**, 240.
81. T. Vosegaard, F. H. Larsen, H. J. Jakobsen, P. D. Ellis and N. C. Nielsen, *J. Am. Chem. Soc.*, 1997, **119**, 9055.
82. A. Goldbourt, P. K. Madhu and S. Vega, *Chem. Phys. Lett.*, 2000, **320**, 448.
83. A. P. M. Kentgens and R. Verhagen, *Chem. Phys. Lett.*, 1999, **300**, 435.
84. G. Wu, D. Rovnyak and R. G. Griffin, *J. Am. Chem. Soc.*, 1996, **118**, 9326.
85. T. Vosegaard, P. Florian, D. Massiot and P. J. Grandinetti, *J. Chem. Phys.*, 2001, **114**, 4618.
86. S. Vega, *J. Chem. Phys.*, 1978, **68**, 5518.
87. J. Haase and M. S. Conradi, *Chem. Phys. Lett.*, 1993, **209**, 287.
88. H. Schäfer, D. Iuga, R. Verhagen and A. P. M. Kentgens, *J. Chem. Phys.*, 2001, **114**, 3073.
89. D. Iuga and A. P. M. Kentgens, *J. Magn. Reson.*, 2002, **158**, 65.
90. Z. Yao, H.-T. Kwak, D. Sakellariou, L. Emsley and P. J. Grandinetti, *Chem. Phys. Lett.*, 2000, **327**, 85.
91. P. K. Madhu, K. J. Pike, R. Dupree, M. H. Levitt and M. E. Smith, *Chem. Phys. Lett.*, 2003, **367**, 150.
92. P. K. Madhu, O. G. Johannessen, K. J. Pike, R. Dupree, M. E. Smith and M. H. Levitt, *J. Magn. Reson.*, 2003, **163**, 310.
93. A. J. Vega, *J. Magn. Reson.*, 1992, **96**, 50.
94. H. K. Lim and C. P. Grey, *Solid State Nucl. Magn. Reson.*, 1998, **13**, 101.
95. T. Vosegaard, D. Massiot and P. J. Grandinetti, *Chem. Phys. Lett.*, 2000, **326**, 454.
96. T. Bräuniger, K. J. Pike, R. K. Harris and P. K. Madhu, *J. Magn. Reson.*, 2003, **163**, 64.
97. A. Goldbourt and S. Vega, *J. Magn. Reson.*, 2002, **154**, 280.

98. J. P. R. Ananias, A. Ferreira, C. M. Morais, M. Lopes, J. Rocha and L. D. Carlos, *Chem. Mater.*, 2002, **24**, 1767.
99. C. M. Morais, M. Lopes, C. Fernandez and J. Rocha, *Magn. Reson. Chem.*, 2003, **41**, 679.
100. G. Wu, D. Rovnyak, B. Q. Sun and R. G. Griffin, *Chem. Phys. Lett.*, 1996, **249**, 210.
101. T. Mildner, M. E. Smith and R. Dupree, *Chem. Phys. Lett.*, 1999, **306**, 297.
102. S. Caldarelli and F. Ziarelli, *J. Am. Chem. Soc.*, 2000, **122**, 12015.
103. J. Logan, J. T. Urban, J. D. Walls, K. H. Lim, A. Jerschow and A. Pines, *Solid State Nucl. Magn. Reson.*, 2002, **22**, 97.
104. T. Bräuniger, K. Ramaswamy and P. K. Madhu, *Chem. Phys. Lett.*, 2004, **383**, 403.
105. M. Pruski, D. P. Lang, C. Fernandez and J.-P. Amoureux, *Solid State Nucl. Magn. Reson.*, 1997, **7**, 327.
106. C. Fernandez, L. Develoye, J.-P. Amoureux, D. P. Lang and M. Pruski, *J. Am. Chem. Soc.*, 1997, **119**, 6858.
107. S. E. Ashbrook and S. Wimperis, *Chem. Phys. Lett.*, 2001, **340**, 500.
108. S. E. Ashbrook, S. P. Brown and S. Wimperis, *Chem. Phys. Lett.*, 1998, **288**, 509.
109. S. E. Ashbrook and S. Wimperis, *J. Magn. Reson.*, 2000, **147**, 238.
110. D. Rovnyak, M. Baldus and R. G. Griffin, *J. Magn. Reson.*, 2000, **142**, 145.
111. S. H. Wang, S. M. De Paul and L. M. Bull, *J. Magn. Reson.*, 1997, **125**, 364.
112. C. Fernandez, L. Delevoye, J.-P. Amoureux, D. P. Lang and M. Pruski, *Solid State Nucl. Magn. Reson.*, 2002, **21**, 61.
113. A. Goldbourt, E. Vinogradov, G. Goobes and S. Vega, *J. Magn. Reson.*, 2004, **169**, 342.
114. E. Vinogradov, P. K. Madhu and S. Vega, *Chem. Phys. Lett.*, 2002, **354**, 193.
115. T. Gullion and J. Schaefer, *J. Magn. Reson.*, 1989, **81**, 196.
116. C. Fernandez, D. P. Lang, J.-P. Amoureux and M. Pruski, *J. Am. Chem. Soc.*, 1998, **120**, 2672.
117. M. Pruski, A. Baily, D. P. Lang, J.-P. Amoureux and C. Fernandez, *Chem. Phys. Lett.*, 1999, **307**, 35.
118. N. G. Dowell, S. E. Ashbrook, J. McManus and S. Wimperis, *J. Am. Chem. Soc.*, 2001, **123**, 8135.
119. J. F. Stebbins, J. V. Oglesby and S. K. Lee, *Chem. Geol.*, 2001, **174**, 63.
120. J. Rocha, C. M. Morais and C. Fernandez, *Clays Clay Miner.*, 2003, **38**, 259.
121. G. Engelhardt, *Introduction to Zeolite Science and Practice*, Stud. Surf. Sci. Catal., 2nd edition Vol. 137. 2001pp. 387.
122. P. R. Bodart, J.-P. Amoureux, M. Pruski, A. Bailly and C. Fernandez, *Magn. Reson. Chem.*, 1999, **37**, S69.
123. G. Wu, *Biochem. Cell Biol.*, 1998, **76**, 429.
124. S.-J. Hwang, C. Fernandez, J.-P. Amoureux, J.-W. Han, J. Cho, S. W. Martin and M. Pruski, *J. Am. Chem. Soc.*, 1998, **120**, 7337.
125. S. Sen, Z. Xu and J. F. Stebbins, *J. Non-Cryst. Solids*, 1998, **226**, 29.
126. G. D. Soraru, N. Dallabonna, C. Gervais and F. Babonneau, *Chem. Mater.*, 1999, **11**, 910.
127. C. Gervais, J. Maquet, F. Babonneau, C. Duriez, E. Framery, M. Vaultier, P. Florian and D. Massiot, *Chem. Mater.*, 2001, **13**, 1700.
128. C. Gervais, F. Babonneau, N. Dallabonna and G. D. Soraru, *J. Am. Cer. Soc.*, 2001, **84**, 2160.
129. L. van Wuellen and G. Schwering, *Solid State Nucl. Magn. Reson.*, 2002, **21**, 134.
130. C. Gervais and F. Babonneau, *J. Organomet. Chem.*, 2002, **657**, 75.
131. K. Kanehashi and K. Saito, *J. Mol. Struct.*, 2002, **602/603**, 105–113.
132. L.-S. Du and J. F. Stebbins, *J. Phys. Chem.*, 2003, **B107**, 10063.
133. L.-S. Du and J. F. Stebbins, *Chem. Mater.*, 2003, **15**, 3913.
134. L.-S. Du and J. F. Stebbins, *J. Non-Cryst. Solids*, 2003, **315**, 239.
135. H. Kimura, K. Okita, M. Ichitani, T. Sugimoto, S. Kuroki and I. Ando, *Chem. Mater.*, 2003, **15**, 355.
136. J.-P. Amoureux, F. Bauer, H. Ernst, C. Fernandez, D. Freude, D. Michel and U.-T. Pingel, *Chem. Phys. Lett.*, 1998, **285**, 10.
137. S. Wang and J. F. Stebbins, *J. Non-Cryst. Solids*, 1998, **231**, 286.
138. Z. Xu, H. Maekawa, J. V. Oglesby and J. F. Stebbins, *J. Am. Chem. Soc.*, 1998, **120**, 9894.
139. T. Schaller and J. F. Stebbins, *J. Phys. Chem.*, 1998, **B102**, 10690.
140. J. F. Stebbins, S. K. Lee and J. V. Oglesby, *Am. Mineral.*, 1999, **84**, 983.
141. S. Wang and J. F. Stebbins, *J. Am. Ceram. Soc.*, 1999, **82**, 1519.
142. J. F. Stebbins, P. Zhao, S. K. Lee and X. Cheng, *Am. Mineral.*, 1999, **84**, 1680.

143. E. Scolan, C. Magnenet, D. Massiot and C. Sanchez, *J. Mater. Chem.*, 1999, **9**, 2467.
144. S. E. Ashbrook, A. J. Berry and S. Wimperis, *Am. Mineral.*, 1999, **84**, 1191.
145. S. K. Lee and J. F. Stebbins, *J. Non-Cryst. Solids*, 2000, **270**, 260.
146. P. Zhao, S. Kroeker and J. F. Stebbins, *J. Non-Cryst. Solids*, 2000, **276**, 122.
147. F. Angeli, T. Charpentier, S. Gin and J. C. Petit, *Chem. Phys. Lett.*, 2001, **341**, 23.
148. S. E. Ashbrook, A. J. Berry and S. Wimperis, *J. Am. Chem. Soc.*, 2001, **123**, 6360.
149. D. Freude, T. Loeser, D. Michel, U.-T. Pingel and D. Prochnow, *Solid State Nucl. Magn. Reson.*, 2001, **20**, 46.
150. J. F. Stebbins, J. V. Oglesby and S. Kroeker, *Am. Mineral.*, 2001, **86**, 1307.
151. G. Wu and S. Dong, *J. Am. Chem. Soc.*, 2001, **123**, 9119.
152. C. J. Fontenot, J. W. Wiench, G. L. Schrader and M. Pruski, *J. Am. Chem. Soc.*, 2002, **124**, 8435.
153. J. E. Readman, N. Kim, Z. Namjun, G. Martine and C. P. Grey, *Chem. Commun.*, 2002, **23**, 2808.
154. S. E. Ashbrook, A. J. Berry and S. Wimperis, *J. Phys. Chem.*, 2002, **B106**, 773.
155. M. Zeyer, L. Montagne, V. Kostoj, G. Palavit, D. Prochnow and C. Jäger, *J. Non-Cryst. Solids*, 2002, **311**, 223.
156. J. V. Oglesby, P. Zhao and J. F. Stebbins, *Geochim. Cosmochim. Acta*, 2002, **66**, 291.
157. K. Kanehashi and K. Saito, *Chem. Lett.*, 2002, **7**, 668.
158. S. E. Ashbrook, A. J. Berry, W. O. Hibberson, S. Steuernagel and S. Wimperis, *J. Am. Chem. Soc.*, 2003, **125**, 11824.
159. S. K. Lee and J. F. Stebbins, *J. Phys. Chem.*, 2003, **B107**, 3141.
160. S. K. Lee and J. F. Stebbins, *Am. Mineral.*, 2003, **88**, 493.
161. S. Ganapathy, T. K. Das, R. Vetrivel, S. Ray, T. Sen, S. Sivasanker, L. Delevoye, C. Fernandez and J.-P. Amoureux, *J. Am. Chem. Soc.*, 1998, **120**, 4752.
162. P. Sarv, B. Wichterlová and J. Čejka, *J. Phys. Chem.*, 1998, **B102**, 1372.
163. J. Rocha, P. Ferreira, Z. Lin, J. R. Agger and M. W. Anderson, *Chem. Commun.*, 1998, **12**, 1269.
164. J. Rocha, P. Ferreira, Z. Lin, P. Brandão, A. Ferreira, J. D. Pedrosa and de Jesus, *J. Phys. Chem.*, 1998, **B102**, 4739.
165. M. Hanaya and R. K. Harris, *J. Mater. Chem.*, 1998, **8**, 1073.
166. M. Witschas and H. Eckert, *J. Phys. Chem.*, 1999, **A103**, 10764.
167. M. W. Anderson, J. R. Agger, D.-P. Luigi, A. K. Baggaley and J. Rocha, *Phys. Chem. Chem. Phys.*, 1999, **1**, 2287.
168. C. Fyfe, H. M. Z. Altenschildesche and S. Jorgen, *Inorg. Chem.*, 1999, **38**, 84.
169. Z. Lin, J. Rocha, P. Ferreira, A. Thursfield, J. R. Agger and M. W. Anderson, *J. Phys. Chem.*, 1999, **B103**, 957.
170. S. Ding and C. A. McDowell, *Chem. Phys. Lett.*, 2000, **320**, 316.
171. I. Abrahams, A. Ahmed, C. J. Groombridge, G. E. Hawkes and T. G. Nunes, *J. Chem. Soc. Dalton Trans.*, 2000, **2**, 155.
172. J. Skibsted, M. Brorson, J. Villadsen and H. J. Jakobsen, *Inorg. Chem.*, 2000, **39**, 4130.
173. K. H. Lim and C. P. Grey, *J. Am. Chem. Soc.*, 2000, **122**, 9768.
174. J. M. Egan and K. T. Müller, *J. Phys. Chem.*, 2000, **B104**, 9580.
175. F. Angeli, J.-M. Delaye, T. Charpentier, J.-C. Petit, D. Ghaleb and P. Faucon, *J. Non-Cryst. Solids*, 2000, **276**, 132.
176. D. Rovnyak, M. Baldus, G. Wu, N. V. Hud, J. Feigon and R. G. Griffin, *J. Am. Chem. Soc.*, 2000, **122**, 11423.
177. H. J. Deiseroth, L. Kienle, H. Günther and M. Hartung, *Z. Anorg. Allg. Chem.*, 2000, **626**, 302.
178. L. J. Smith, H. Eckert and A. K. Cheetham, *J. Am. Chem. Soc.*, 2000, **122**, 1700.
179. V. V. Terskikh, O. B. Lapina and V. M. Bondareva, *Phys. Chem. Chem. Phys.*, 2000, **2**, 2441.
180. J. Rocha, P. Ferreira, L. D. Carlos and A. Ferreira, *Angew. Chem. Int. Ed.*, 2000, **39**, 3276.
181. A. Wong and G. Wu, *Can. J. Anal. Sci. Spectrosc.*, 2001, **46**, 188.
182. S. Caldarelli, A. Buchholz and M. Hunger, *J. Am. Chem. Soc.*, 2001, **123**, 7118.
183. R. J. Accardi, R. F. Lobo and M. Kalwei, *J. Phys. Chem.*, 2001, **B105**, 5883.
184. L. J. Smith, H. Eckert and A. K. Cheetham, *Chem. Mater.*, 2001, **13**, 385.
185. S. Antonijevic, S. E. Ashbrook, R. I. Walton and S. Wimperis, *J. Mater. Chem.*, 2002, **12**, 1469.

186. H. Masui, D. P. Chen, T. Akai and T. Yazawa, *Z. Naturforsch A*, 2002, **57**, 473.
187. X. Ai, F. Deng, J. Dong, L. Chen and C. Ye, *J. Phys. Chem.*, 2002, **B106**, 9237.
188. A. Wong, J. C. Fettinger, S. L. Forman, J. T. Davis and G. Wu, *J. Am. Chem. Soc.*, 2002, **124**, 742.
189. L. Delevoye, J.-L. Robert and J. Grandjean, *Clays Clay Miner.*, 2003, **38**, 63.
190. A. Wong and G. Wu, *J. Phys. Chem.*, 2003, **A107**, 579.
191. H. Trill, H. Eckert and V. I. Srdanov, *J. Phys. Chem.*, 2003, **B107**, 8779.
192. A. Wong and G. Wu, *J. Am. Chem. Soc.*, 2003, **125**, 13895.
193. S. K. Lee and J. F. Stebbins, *Geochim. Cosmochim. Acta*, 2003, **67**, 1699.
194. C. Xuanjun, D. Lei, Y. Jinxiang, D. Chaohui and J. Feng, *Chem. Mater.*, 2003, **13**, 614.
195. N. Rajic, A. Meden, P. Sarv and V. Kaucic, *Micropor. Mesopor. Mater.*, 1998, **24**, 83.
196. P. Faucon, T. Charpentier, D. Bertrandie, A. Nonat, J. Virlet and J. C. Petit, *Inorg. Chem.*, 1998, **37**, 3726.
197. J. Rocha, *Chem. Commun.*, 1998, **22**, 2489.
198. S. R. Jansen, T. H. Hintzen, R. Metselaar, J. W. de Haan, L. J. M. van de Ven, A. P. M. Kentgens and G. H. Nachtegaal, *J. Phys. Chem.*, 1998, **102**, 5969.
199. L. Zuechner and J. C. C. Chan, *J. Phys. Chem.*, 1998, **B102**, 4495.
200. L. Canesson, I. Arcon, S. Caldarelli and A. Tuel, *Micropor. Mesopor. Mater.*, 1998, **36**, 117.
201. P. Faucon, T. Charpentier, A. Nonat and J. C. Petit, *J. Am. Chem. Soc.*, 1998, **120**, 12075.
202. S. P. Brown, S. E. Ashbrook and S. Wimperis, *J. Phys. Chem.*, 1999, **B103**, 812.
203. P. Lentz, J. B. Nagy, L. Delevoye, C. Fernandez, J.-P. Amoureux, C. V. Tuoto and A. Nastro, *Stud. Surf. Sci. Catal.*, 1999, **125**, 205.
204. J. M. Cole, E. R. H. van Eck, G. Mountjoy, R. J. Newport, T. Brennan and G. A. Saunders, *J. Phys.: Condens. Mater.*, 1999, **11**, 9165.
205. V. Montouillout, D. Massiot, A. Douy and J. P. Coutures, *J. Am. Ceram. Soc.*, 1999, **82**, 3299.
206. P. Lentz, A. Carvalho, L. Delevoye, C. Fernandez, J.-P. Amoureux and J. B. Nagy, *Magn. Reson. Chem.*, 1999, **37**, S55.
207. S. E. Latturner, J. Sachleben, B. B. Iversen, J. Hanson and G. D. Stucky, *J. Org. Chem.*, 1999, **B103**, 7135.
208. F. Taulelle, M. Pruski, J.-P. Amoureux, D. Lang, A. Bailly, C. Huguenard, M. Haouas, C. Gerardin, T. Loiseau and G. Ferey, *J. Am. Chem. Soc.*, 1999, **121**, 12148.
209. P. Mèriaudeau, A. Tuel and T. T. H. Vu, *Catal. Lett.*, 1999, **61**, 89.
210. P. Faucon, J.-C. Petit, T. Charpentier, J. F. Jacquinot and F. Adenot, *J. Am. Ceram. Soc.*, 1999, **82**, 1307.
211. J. Rocha, *J. Phys. Chem.*, 1999, **B103**, 9801.
212. J. Quartararo, M. Guelton, M. Rigole, J.-P. Amoureux, C. Fernandez and J. Grimblot, *J. Mater. Chem.*, 1999, **10**, 2637.
213. S. Caldarelli, A. Meden and A. Tuel, *J. Phys. Chem.*, 1999, **B103**, 5477.
214. S. Sen, *J. Non-Cryst. Solids*, 1999, **253**, 84.
215. L. B. Alemany, S. Steuernagel, J.-P. Amoureux, R. L. Callender and A. R. Barron, *Solid State Nucl. Magn. Reson.*, 1999, **14**, 1.
216. T.-H. Chen, B. H. Wouters and P. J. Grobert, *Eur. J. Inorg. Chem.*, 2000, **2000**, 281.
217. J. A. van Bokhoven, A. L. Roest, D. C. Koningsberger, J. T. Miller, G. H. Nachtegaal and A. P. M. Kentgens, *J. Phys. Chem.*, 2000, **B104**, 6743.
218. C. Magnenet, D. Massiot, I. Klur and J. P. Coutures, *J. Mater. Sci.*, 2000, **35**, 115.
219. C. A. Fyfe, J. L. Bretherton and L. Y. Lam, *Chem. Commun.*, 2000, **17**, 1575.
220. A. Gola, B. Rebours, E. Milazzo, J. Lynch, E. Benazzi, S. Lacombe, L. Delevoye and C. Fernandez, *Micropor. Mesopor. Mater.*, 2000, **40**, 73.
221. M. J. Toplis, S. C. Kohn, M. E. Smith and I. J. F. Poplett, *Am. Mineral.*, 2000, **85**, 1556.
222. F. Angeli, J.-M. Delaye, T. Charpentier, J.-C. Petit, D. Ghaleb and P. Faucon, *Chem. Phys. Lett.*, 2000, **320**, 681.
223. S. E. Ashbrook, J. McManus, K. J. D. MacKenzie and S. Wimperis, *J. Phys. Chem.*, 2000, **B104**, 6408.
224. A. Tuel, S. Caldarelli, A. Meden, L. B. McCusker, C. Baerlocher, A. Ristic, N. Rajic, G. Mali and V. Kaucic, *J. Phys. Chem.*, 2000, **B104**, 5697.
225. M. Schulz, M. Tiemann, M. Fröba and C. Jäger, *J. Phys. Chem.*, 2000, **B104**, 10473.
226. J. Ashenhurst, S. Wang and G. Wu, *J. Am. Chem. Soc.*, 2000, **122**, 3528.
227. J. Quartararo, J.-P. Amoureux and J. Grimblot, *J. Mol. Catal.*, 2000, **A162**, 345.

228. R. D. Gougeon, P. R. Bodart, R. K. Harris, D. M. Kolonia, D. E. Petrakis and P. J. Pomonis, *Phys. Chem. Chem. Phys.*, 2000, **2**, 5286.
229. J. A. van Bokhoven, D. C. Koningsberger, P. Kunkeler, H. van Bekkum and A. P. M. Kentgens, *J. Am. Chem. Soc.*, 2000, **122**, 12842.
230. S. K. Lee and J. F. Stebbins, *J. Phys. Chem.*, 2000, **B104**, 4091.
231. J. McManus, S. E. Ashbrook, K. J. D. MacKenzie and S. Wimperis, *J. Non-Cryst. Solids*, 2001, **282**, 278.
232. S. E. Ashbrook, K. J. D. MacKenzie and S. Wimperis, *Solid State Nucl. Magn. Reson.*, 2001, **20**, 87.
233. E. V. Charnaya, C. Tien, J. Lu, R. R. Wu, S. N. Ivanov and E. N. Khazanov, *J. Phys.: Condens. Mater.*, 2001, **13**, 8775.
234. A. Sani, L. Delmotte, C. Marichal, Z. Gabelica and C. Forte, *Eur. J. Mineral.*, 2001, **13**, 101.
235. L. Allouche, C. Huguenard and F. Taulelle, *J. Phys. Chem. Solids*, 2001, **62**, 1525.
236. S. M. C. Menezes, V. L. Camorim, Y. L. Lam, R. A. S. San Gil, A. Bailly and J.-P. Amoureux, *Appl. Catal. A: Gen.*, 2001, **207**, 367.
237. C. Klemp, M. Bruns, J. Gauss, U. Haeussermann, G. Stoesser, L. van Wuellen and M. Jansen, *J. Am. Chem. Soc.*, 2001, **123**, 9099.
238. A. P. M. Kentgens, D. Iuga, M. Kalwei and H. Koller, *J. Am. Chem. Soc.*, 2001, **123**, 2925.
239. J. C. C. Chan and H. Eckert, *J. Non-Cryst. Solids*, 2001, **284**, 16.
240. M. Tiemann, M. Schulz, C. Jäger and M. Fröba, *Chem. Mater.*, 2001, **13**, 2885.
241. C. Gervais, K. J. D. MacKenzie and M. E. Smith, *Magn. Reson. Chem.*, 2001, **39**, 23.
242. L. M. Bronstein, C. Joo, R. Karlinsey, A. Ryder and J. W. Zwanziger, *Chem. Mater.*, 2001, **13**, 3678.
243. C. A. Fyfe, J. L. Bretherton and L. Y. Lam, *J. Am. Chem. Soc.*, 2001, **123**, 5285.
244. R. D. Gougeon, E. B. Brouwer, P. R. Bodart, L. Delmotte, C. Marichal, J.-M. Chezeau and R. K. Harris, *J. Phys. Chem.*, 2001, **B105**, 12249.
245. P. Kempgens, R. K. Harris, Z. B. Yu and D. P. Thompson, *J. Mater. Chem.*, 2001, **11**, 2507.
246. E. Rodriguez-Castellon, A. Jimenez-Lopez, P. Maireles-Torres, J. Merida-Robles, P. Braos-Garcia, G. Aguilar-Armenta, E. Flores-Loyola, F. Marmottini and E. Felici, *Langmuir*, 2001, **17**, 3769.
247. A. Tuel, V. Gramlich and C. Baerlocher, *Micropor. Mesopor. Mater.*, 2001, **47**, 217.
248. J.-B. d'Espinose de la Caillerie, P. P. Man, M. A. Vicente and J.-F. Lambert, *J. Phys. Chem.*, 2002, **B106**, 4133.
249. K. U. Gore, A. Abraham, S. G. Hegde, R. Kumar, J.-P. Amoureux and S. Ganapathy, *J. Phys. Chem.*, 2002, **B106**, 6115.
250. K. Saito, K. Kanehashi, Y. Saito and J. Godward, *Appl. Magn. Reson.*, 2002, **22**, 257.
251. W. Deng, P. Bodart, M. Pruski and B. H. Shanks, *Micropor. Mesopor. Mater.*, 2002, **52**, 169.
252. O. H. Han, C.-S. Kim and S. B. Hong, *Angew. Chem. Int. Ed.*, 2002, **41**, 469.
253. M. Capron, F. Fayon, J. Coutures, D. Massiot and A. Douy, *J. Solid State Chem.*, 2002, **169**, 53.
254. A. Tuel, V. Gramlich and Ch. Baerlocher, *Micropor. Mesopor. Mater.*, 2002, **56**, 119.
255. J. O. Ehresmann, W. Wang, B. Herreros, D.-P. Luigi, T. N. Venkatraman, W. Song, J. B. Nicholas and J. F. Haw, *J. Am. Chem. Soc.*, 2002, **124**, 10868.
256. H. Trill, H. Eckert and V. I. Srdanov, *J. Am. Chem. Soc.*, 2002, **124**, 8361.
257. D. Ma, X. Han, D. Zhou, Z. M. Yan, R. Fu, Y. Xu, X. Bao, H. Hu and S. C. F. Au-Yeung, *Chem. Eur. J.*, 2002.
258. K. Damodaran, P. R. Rajamohanan, D. Chakrabarty, U. S. Racherla, V. Manohar, C. Fernandez, J.-P. Amoureux and S. Ganapathy, *J. Am. Chem. Soc.*, 2002, **124**, 3200.
259. Y. Huang, R. Richer and C. W. Kirby, *J. Phys. Chem.*, 2003, **B106**, 1327.
260. Z. M. Yan, J. Q. Zhuang, L. Xu, X. W. Han, Z. M. Liu and X. H. Bao, *Chin. Chem. Lett.*, 2003, **14**, 87.
261. A. Omegna, J. A. van Bokhoven and R. Prins, *J. Phys. Chem.*, 2003, **B107**, 8854.
262. M. Fechtelkord, H. Behrens, F. Holtz, J. L. Bretherton, C. A. Fyfe, L. A. Groat and M. Raudsepp, *Am. Mineral.*, 2003, **88**, 1046.
263. Y. Huang, A. B. Demko and C. W. Kirby, *Chem. Mater.*, 2003, **15**, 2437.
264. S. Ganapathy, K. U. Gore, R. Kumar and J.-P. Amoureux, *Chem. Phys. Lett.*, 2003, **367**, 150.
265. B. Zhou, B. L. Sherriff, F. Taulelle and G. Wu, *Can. Mineral.*, 2003, **41**, 891.
266. T. Ohkubo, K. Kanehashi, K. Saito and Y. Ikeda, *Clays Clay Miner.*, 2003, **51**, 513.

267. Z. Yan, D. Ma, J. Zhuang, X. Liu, X. Han, X. Bao, F. Chang, L. Xu and Z. Liu, *J. Mol. Catal. A: Chem.*, 2003, **194**, 153.
268. A. E. W. Beers, J. A. van Bokhoven, K. M. de Lathouder, F. Kapteijn and J. A. Moulijn, *J. Catal.*, 2003, **218**, 239.
269. L. Beitone, C. Huguenard, A. Gansmueller, M. Henry, F. Taulelle, T. Loiseau and G. Ferey, *J. Am. Chem. Soc.*, 2003, **125**, 9102.
270. G. Mali, N. Rajic, N. Z. Logar and V. Kaucic, *J. Phys. Chem.*, 2003, **B107**, 1286.
271. S. Sham and G. Wu, *Inorg. Chem.*, 2000, **39**, 4.
272. M. Capron, F. Fayon, D. Massiot and A. Douy, *Chem. Mater.*, 2003, **15**, 575.
273. C. V. Grant, V. Frydman and L. Frydman, *J. Am. Chem. Soc.*, 2000, **122**, 11743.
274. H. J. Kim, M. Pruski, J. W. Wiench, D. Y. Jeong and S. H. Choh, *Phys. Rev.*, 2001, **B63**, 064107/1-6.
275. S. Prasad, P. Zhao, J. Huang, J. J. Fitzgerald and J. S. Shore, *Solid State Nucl. Magn. Reson.*, 2001, **19**, 45.
276. L. P. Cruz, J. Rocha, J. D. Pedrosa, de Jesus, J. M. Savariault and J. Galy, *Solid State Nucl. Magn. Reson.*, 1999, **23**, 213.
277. D. Riou, F. Fayon and D. Massiot, *Chem. Mater.*, 2002, **14**, 2416.
278. U. G. Nielsen, H. J. Jakobsen and J. Skibsted, *Solid State Nucl. Magn. Reson.*, 2003, **23**, 107.
279. K. J. Pike, S. E. Ashbrook and S. Wimperis, *Chem. Phys. Lett.*, 2001, **345**, 400.
280. J.-P. Amoureux, C. Morais, J. Trebosc, J. Rocha and C. Fernandez, *Solid State Nucl. Magn. Reson.*, 2003, **23**, 213.
281. R. Siegel, T. Nakashima and R. Wasylishen, *Chem. Phys. Lett.*, 2004, **388**, 441.
282. Z. Gan and H.-T. Kwak, *J. Magn. Reson.*, 2004, **168**, 346.

^{73}Ge NMR Spectroscopy of Organogermanium Compounds

YOSHITO TAKEUCHI[1] AND TOSHIO TAKAYAMA[2]

[1]*Department of Chemistry, Faculty of Science, Kanagawa University, 2946 Tsuchiya, Hiratuka 259-1293, Japan*
[2]*Department of Applied Chemistry, Faculty of Engineering, Kanagawa University, 3-27-1 Rokkakubashi, Yokohama 221-8686, Japan*

Recent advances in ^{73}Ge NMR spectroscopy are reviewed. Following the introduction (Section 1), Section 2 describes recently determined chemical shifts and linewidths for a variety of organogermanium compounds which range from normal (tetravalent) to hypercoordinated (up to heptavalent) species. The role of linewidth as evidence for hypercoordination is discussed. In Section 3, coupling constants, relaxation times and relaxation mechanisms are discussed in detail, showing that in some cases a mechanism other than quadrupolar is involved. In the last section, high-resolution solid-state ^{73}Ge NMR spectroscopy is covered which has not been treated in previous reviews.

1. INTRODUCTION

In the beginning of his recent review on the NMR spectroscopy of germanium, tin and lead, Marsmann[1] quoted very interesting figures: "…in the period 1995–2000, *Chemical Abstracts* lists more than 500 entries for ^{119}Sn NMR results and nearly 50 entries for

ANNUAL REPORTS ON NMR SPECTROSCOPY
VOLUME 54 ISSN 0066 4103
DOI 10.1016/S0066-4103(04)54004-8

^{207}Pb NMR. In contrast, only a limited number of germanium resonances is found in the literature."

Although the statement itself may be justified, there have also been advances in this field in recent years. The present authors believe these examples of progress are worthwhile to be evaluated and reviewed.

There are two reasons why ^{73}Ge NMR spectroscopy has been rather leisurely studied. One is the difficulty of its measurement due to its quadrupolar nature, and the other is the limited popularity of organogermanium compounds to the chemical industry. It must be pointed out, however, that germanium is by no means a rare element at least in the earth's core. The abundance, 1.5 ppm for Ge, is comparable to that for Si (2 ppm), while for Pb it is 12.5 ppm.

The first reason may be summarized as follows. The measurement of ^{73}Ge (a quadrupolar nucleus; quadrupolar moment $q = -0.2$) NMR spectra is generally difficult because of excessive line broadening unless the germanium atom is symmetrically substituted. This broadening occurs through the interaction of the electric field gradient at the nucleus with the quadrupole moment of germanium. Thus, in the absence of chemical exchange processes, the extent of line broadening may be related to the local symmetry at the germanium centre.

The nuclear properties of group 14 elements are summarized in Table 1.

Table 1. Properties of isotopes of group 14 elements[a,b]

Nucleus	Natural abundance (%)	Nuclear spin I	Magnetic moment μ[a]	Frequency Ratio Ξ/%[b]
^{13}C	1.108	1/2	0.7022	25.145020
^{29}Si	4.7	1/2	-0.5548	19.867
^{73}Ge	7.76	-9/2	-0.8768	3.488
^{115}Sn	0.35	1/2	-0.9132	32.718
^{117}Sn	7.61	1/2	-0.9949	35.632
^{119}Sn	8.58	1/2	-1.0409	37.290
^{207}Pb	22.6	1/2	0.5843	20.920
	Sensitivity rel.[c]	Receptivity abs.[d]	Receptivity relative to ^{13}C	Reference compound
^{13}C	1.59×10^{-2}	1.76×10^{-4}	1	Me_4Si
^{29}Si	7.84×10^{-3}	3.69×10^{-4}	2.1	Me_4Si
^{73}Ge	1.4×10^{-3}	1.08×10^{-4}	0.61	Me_4Ge
^{115}Sn	3.5×10^{-2}	1.22×10^{-4}	0.69	Me_4Sn
^{117}Sn	4.52×10^{-2}	3.44×10^{-3}	19.5	Me_4Sn
^{119}Sn	5.18×10^{-3}	4.44×10^{-3}	25.2	Me_4Sn
^{207}Pb	9.16×10^{-3}	2.07×10^{-3}	11.8	Me_4Pb

[a] In multiples of the nuclear magneton.

[b] Ratios of resonance frequency of the reference to that of the protons of tetramethylsilane (TMS) at infinite dilution in $CDCl_3$.

[c] At constant field or for equal number of nuclei.

[d] Product of the relative sensitivity and the natural abundance.

Notwithstanding this difficulty, ^{73}Ge NMR spectroscopy has occasionally been reviewed. In the first important review on ^{73}Ge NMR in 1978, Harris *et al.*[2] could compile chemical shift values for only 20 compounds. The introduction of the FT technique in the early 1970s improved the situation to a considerable extent, and ^{73}Ge NMR spectra of a large number of relatively simple (but not completely symmetrical) organogermanium compounds were examined. As a result, a few reviews were published in the 1980s by several authors.[3–5]

Another milestone in ^{73}Ge NMR was made by the introduction of high field instruments coupled with the advancement of software technology. Use of high field instruments is particularly advantageous for low frequency nuclei such as ^{73}Ge. Observation of the ^{73}Ge resonance of larger and less symmetric compounds became possible in certain cases. Use of advanced software has also widened the scope of ^{73}Ge NMR spectroscopy. Thus, INEPT and DEPT pulse sequences achieved several fold signal enhancement (and hence corresponding reduction in machine time). Application of 2D techniques to ^{73}Ge NMR spectroscopy has also been reported.

Such advances have been rather briefly described in a recent review,[6] which highlighted the problems of measuring NMR spectra of nuclei with high spin and low frequency. The baseline roll resulting from 'acoustic ringing' creates difficulties in observing the expected broader line signals from non-symmetric species within wide spectral windows. To observe broad line resonance, several pulse sequences have been used, including RIDE (RIng down DElay),[7] ACOUSTIC (Alternate Compound One-eighties Used to Suppress Transients In the Coil),[8] and EXSPEC (EXtended SPin ECho sequence).[9]

The authors pointed out that use of a higher field (300 MHz or higher) magnet, and a dedicated germanium probe will make the observation of this low resonance frequency more accessible (Table 2). They added, however, that more powerful pulses are needed to maintain reasonable observation windows, and that this aggravates the 'acoustic ring'.

It is expected that the current generation of spectrometers will allow for a greater use of composite pulses, and greater phase cycling. This assists in providing better suppression of rolling baselines using the various pulse sequences available. In Fig. 1, the spectra of ethyltriphenylgermane (**1**) show what can be achieved using the more detailed pulse sequences, and Table 2 features some recent results that were first obtained with advanced techniques.

The upper trace is a standard one pulse experiment and shows no obvious signal. The middle trace was obtained using the RIDE sequence and, while showing a signal from the sample, it still contains considerable baseline roll. The lower trace was obtained using the EXSPEC sequence and shows very good removal of the rolling baseline. Each spectrum was acquired over 8 h.

Thus, there are several advances, e.g., solid state high resolution ^{73}Ge NMR spectroscopy, ^{73}Ge spectra of hypercoordinated organogermanium species, and relaxation phenomena, which have not been fully covered in previously published reviews. This review will cover these topics in addition to the general one of recent topics in ^{73}Ge NMR spectroscopy.

Table 2. Recently observed ^{73}Ge chemical shifts

Compound	δ_{Ge} [a,b]	$\Delta\nu_{1/2}$ [c]
Observations made at 3.1 MHz		
GeH_3GeMe_2Cl (**2**)	−280.5	39
$GeH_3GeH_2Mn(CO)_5$ (**3**)	−291.8	68
$GeH_3GeH(Me)Mn(CO)_5$ (**4**)	−277.9	17
GeH_4 (**5**)	−283.7	1.1
GeH_3D (**6**)	−293.3	1.95
GeD_4 (**7**)	−299.1	3.1
D_3GeGeD_3 (**8**)	−318.0	63
Observations made at 10.5 MHz		
$Ph_3GeGePh_3$ (**9**)	−67	90
$Me_3GeGeMe_3$ (**10**)	−59	–
$MeGePh_3$ (**11**)	−22.9	43
$EtGePh_3$ (**1**)	−19.7	–
$(Ph_3Ge)_3$*Ge*H (**12**)	−314	200
$(Ph_3Ge)_3SiH$ (**13**)	−53.2	40
$(Ph_3Sn)_4Ge$ (**14**)	−480.4	24

Reproduced, with permission, from Thomson *et al.*,[6] Copyright 1999, Overseas Publishers Association.

[a] In ppm relative to external Me_4Ge. This notation is used throughout this review.

[b] Only the Ge nuclei in italics were observed.

[c] Half-height linewidth in Hz. This notation is used throughout this review.

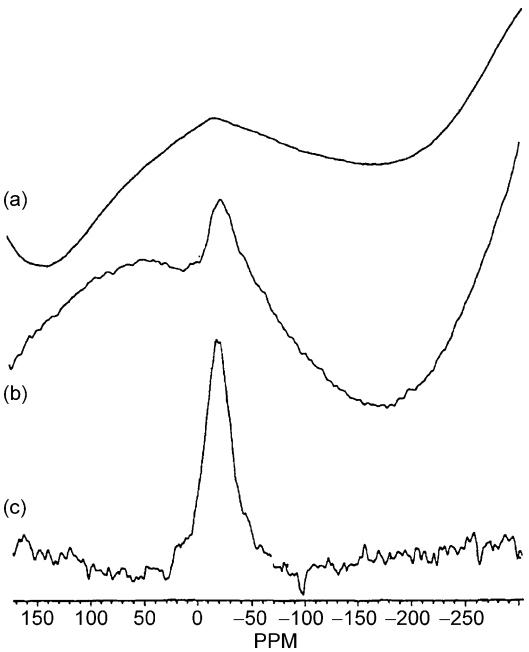

Fig. 1. ^{73}Ge NMR spectra of Ph_3GeEt (1). (a) The standard trace of one pulse experiment. (b) The trace obtained using the RIDE sequence. (c) The trace obtained using the EXSPEC sequence. Reproduced, with permission, from Thomson *et al.*,[6] Copyright 1999, Overseas Publishers Association.

2. RECENT TOPICS IN ^{73}Ge NMR

2.1. Some interesting compounds

In the 1980s and early 1990s, ^{73}Ge NMR spectra of a large number of relatively simple organogermanium compounds were determined using FT NMR instruments (in most cases 90–100 MHz instruments) with low frequency probes. One such example is the conformational analysis of a series of germacyclohexanes based on ^{73}Ge resonances.[10–12]

Less symmetric species, e.g., germanium compounds substituted with a combination of saturated and unsaturated hydrocarbon moieties, were also investigated. For instance, a series of methylvinylgermanes $Me_{4-n}Ge(CH{=}CH_2)_n$ ($n = 0, 1, 2, 3, 4$) **15–19**, respectively) were prepared and their ^{73}Ge NMR spectra were determined (Table 3).[13]

The chemical shifts were compared with those of the corresponding methylvinylsilanes ($Me_{4-n}Si(CH{=}CH_2)_n$, **20–24** and a very good correlation was found. The correlation between the ^{29}Si chemical shifts of **20–24** and the ^{73}Ge chemical shifts of **15–19** is given by Eq. (1), where R is the correlation coefficient.

$$\delta_{Ge} = 1.96\delta_{Si} + 2.37; \qquad R = 0.999 \tag{1}$$

The chemical shift data for these germanes and silanes are summarized in Table 3.

In a similar manner, the ^{73}Ge chemical shifts of alkyl-, alkenyl- and aryl-germanes can be correlated with the corresponding organosilicon compounds in one plot. Thus, Lukevics *et al.*[14] reported the ^{73}Ge NMR spectra of 2-furyl-, 2-thienyl and 2-(4,5-dihydrofuryl)germanes. Though the range of ^{73}Ge chemical shifts studied is large (ca. 100 ppm), the observed correlation is reasonable, indicating the factors determining the chemical shifts of ^{29}Si and ^{73}Ge are similar so far as these compounds have the same structural features (Table 4).

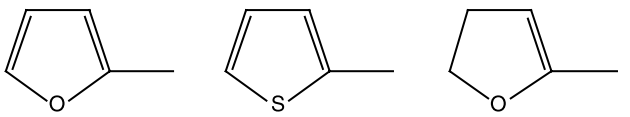

Table 3. ^{73}Ge and ^{29}Si chemical shifts[a] of $Me_{4-n}Ge(CH{=}CH_2)_n$ **15–19** and $Me_{4-n}Si(CH{=}CH_2)_n$ **20–24**

Compound	δ_{Ge}	Compound	δ_{Si}
Me_4Ge (**15**)	0.00	Me_4Si (**20**)	0.00
$Me_3Ge(CH{=}CH_2)$ (**16**)	−15.62	$Me_3Si(CH{=}CH_2)$ (**21**)	−10.68
$Me_2Ge(CH{=}CH_2)_2$ (**17**)	−30.61	$Me_2Si(CH{=}CH_2)_2$ (**22**)	−17.35
$MeGe(CH{=}CH_2)_3$ (**18**)	−44.98	$MeSi(CH{=}CH_2)_3$ (**23**)	−24.06
$Ge(CH{=}CH_2)_4$ (**19**)	−58.73	$Si(CH = CH_2)_4$ (**24**)	−30.31

Reproduced, with permission, from Takeuchi et al.,[13] Copyright 1989, Wiley.

[a] Reference standards; internal TMS for ^{29}Si.

Table 4. ^{73}Ge NMR data for isostructural heteroaromatic compounds

	δ_{Ge}	$\Delta\nu_{1/2}$
(2-furyl)$GeMe_3$ (**25**)	−22.1	140
(2-furyl)$_2GeMe_2$ (**26**)	−56.1	340
(2-furyl)$_3$GeMe (**27**)	−79.5	390
(2-furyl)$_4$Ge (**28**)	−115.0	30
(2-thienyl)$GeMe_3$ (**29**)	−10.1	200
(2-thienyl)$_2GeMe_2$ (**30**)	−23.5	450
(2-thienyl)$_3$GeMe (**31**)	−39.4	600
(2-thienyl)$_4$Ge (**32**)	−56.5	18
(4,5-dihydro-2-furyl)$GeMe_3$ (**33**)	−25.5	180
(4,5-dihydro-2-furyl)$_2GeMe_2$ (**34**)	−59.5	250
(4,5-dihydro-2-furyl)$_3$GeMe (**35**)	−89.7	440
(4,5-dihydro-2-furyl)$_4$Ge (**36**)	−119.1	65
Me_2Ph_2Ge (**37**)	18.5	120
Ph_4Ge (**38**)	−32.9	15
(2-furyl)$_2GePh_2$ (**39**)	−73.0	400
(2-furyl)$_3$GePh (**40**)	−93.9	320

Reproduced, with permission, from Liepins *et al.*,[14] Copyright 1990, Elsevier.

They concluded that an increase in the number of heteroaromatic substituents cause almost additive low frequency shifts of the resonance signals (Fig. 2). High frequency shifts with an increase in the number of electronegative substituents at the germanium atom should be expected.

Linear relationships of the type δ_{Ge}/σ^* (inductive constants) are observed for the series R_nGeMe_{4-n} in which the substituent R is fixed, but n varies, i.e., analogous with the relation δ_{Ge}/n. Two different correlations are evident (Fig. 3).

The authors suggest that the inductive constants for the heteroaromatic substituents, previously determined for carbon compounds, might not adequately reflect the electronic effects of these groups in the germanium compounds.

The ^{73}Ge NMR spectra of methylethynylgermanes (Table 5) have been studied by Liepins *et al.*[15]

The chemical shifts were compared with those of the corresponding isostructural tin compounds and a good correlation was found (Table 5).

Takeuchi *et al.* reported the ^{13}C and ^{73}Ge NMR spectra of germamacrocycles, ranging from 10- to 22-membered rings (**45–49**) and tetragermamacrocycles ranging from 20- to 44-membered rings (**50–54**) in which germanium atoms are symmetrically positioned. (Table 6).[16]

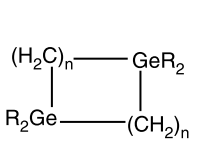

digermacycloalkane(**45-49**)

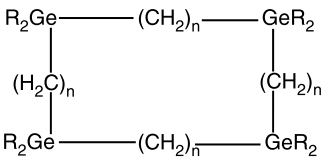

tetragermacycloalkane(**50-54**)

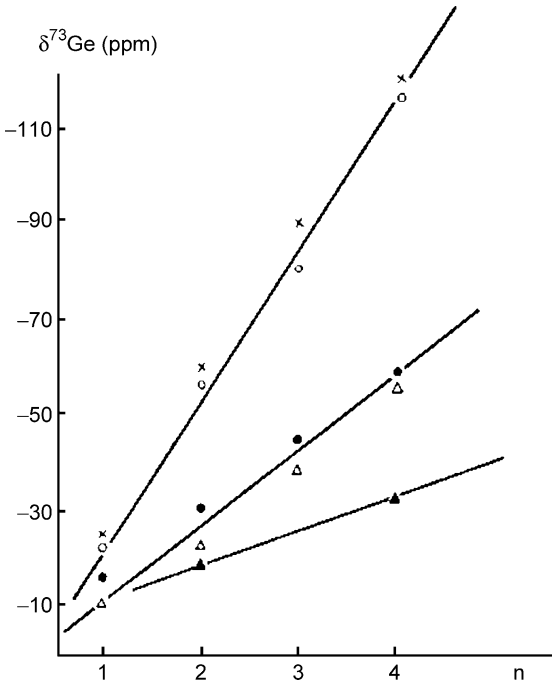

Fig. 2. The dependence of ^{73}Ge chemical shifts in hetaryl- and vinylgermanes R_nGeMe_{4-n} on the number of unsaturated substituents: $R = C_4H_3O$(○) (**25–28**); C_4H_5O(x) (**33–36**); $H_2C{=}CH$(●) (**21–24**); C_4H_3S(△) (**29-32**); C_6H_5(▲) (**37–38**). Reproduced, with permission, from Liepins *et al.*,[14] Copyright 1990, Elsevier.

Since broadening of the ^{73}Ge resonance is usually enhanced as the molecular weight of the sample is increased, it is rather surprising that all of the germamacrocycles gave ^{73}Ge signals. The width at half height is in the range of 35–130 Hz, which is reasonable in view of the other examples of unequally substituted tetraalkylgermanes. The chemical shifts are uniform, and there is a very small effect due to the difference in the ring size. The shifts are in the range 1.2–6.2 ppm and there is no direct correlation with ring size since the shift of **55** is $\delta = -13.7$.[17] and that of 1,1-dimethyl-1-germacyclopentan-3-ene (**63**) is $\delta = 37$.[18]

In the case of germamacrocycles, digermacycloalkanes and tetragermacycloalkanes, the bond angles associated with germanium are essentially similar to those for **15** ($\delta = 0$). This is in a good agreement with the structure determined by the X-ray analysis.[19]

The effect of ring size upon chemical shift is large when the ring is small. The ^{73}Ge chemical shifts of the *gem*-dimethylgermyl moiety are sensitive to ring size. Thus, those of **55** ($\delta = -13.7$)[17] and 1,1-dimethyl-1-germacyclopentane (**62**) ($\delta = 40.0$) differ by 53.7 ppm.[18]

The ^{73}Ge chemical shifts of germamacrocycles, digermacycloalkanes and of some reference compounds (germacyclohexanes) together with the linewidths of the ^{73}Ge signals are summarized in Table 6.

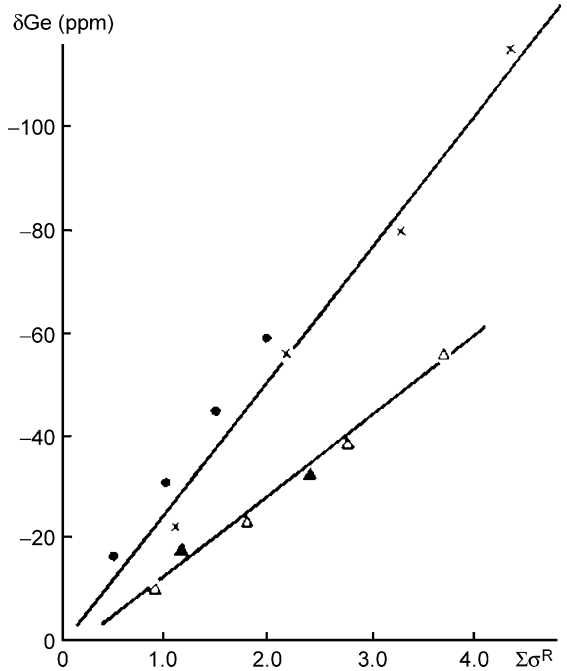

Fig. 3. The dependence of ^{73}Ge chemical shifts in hetaryl- and vinylgermanes R_nGeMe_{4-n} on the sum of substituent inductive constants: R = C_4H_5O(×) **(33–36)**; $H_2C=CH$(●) **(21–24)**; C_4H_3S(△) **(29–32)**; C_6H_5(▲) **(37–38)**. Reproduced, with permission, from Liepins *et al.*,[14] Copyright 1990, Elsevier.

The linewidths of the ^{73}Ge resonances also provide information on the molecular structure. The values for **47** ($\delta = -9; \Delta\nu_{1/2} = 470$Hz) which contrast with the values for **56** ($\delta = -33; \Delta\nu_{1/2} = 370$Hz) are in line with the corresponding pair, **46** ($\delta = +5; \Delta\nu_{1/2} = 35$Hz)[16] and **55** ($\delta = -13.7; \Delta\nu_{1/2} = 22$Hz).[17] The shifts for **47** and **46** reflect the C–Ge–C angles, which are close to the tetrahedral value. The linewidths of **47** and **46** are also very informative. It was established that the linewidth is a good

Table 5. NMR spectral parameters of methylethynylgermanes $(CH_3)_{4-n}Ge(C{\equiv}CH)_n$

Compounds	δ_{Ge}	$\Delta\nu_{1/2}$
Me_4Ge (**15**)	0	1.4
$Me_3Ge(C{\equiv}CH)$ (**41**)	−34	300
$Me_2Ge(C{\equiv}CH)_2$ (**42**)	−77	750
$MeGe(C{\equiv}CH)_3$ (**43**)	−118	800
$Ge(C{\equiv}CH)_4$ (**44**)	−173	14

Reproduced, with permission, from Liepins *et al.*,[15] Copyright 1991, Elsevier.

Table 6. ^{73}Ge chemical shifts of digermacycloalkanes and tetragermacycloalkanes

Compound	Ring size	δ_{Ge}	$\Delta\nu_{1/2}$
Digermacycloalkanes			
1,1,6,6-Tetramethyl-1,6-digermacyclodecane (**45**)	10	6.2	67
1,1,8,8-Tetramethyl-1,8-digermacyclotetradecane (**46**)	14	5.0	35
1,1,8,8-Tetraphenyl-1,8-digermacyclotetradecane (**47**)	14	−9	470
1,1,10,10-Tetramethyl-1,10-digermacyclooctadecane (**48**)	18	3.7	45
1,1,12,12-Tetramethyl-1,12-digermacyclodocosane (**49**)	22	1.9	100
Tetragermacycloalkanes			
1,1,6,6,11,11,16,16-Tetramethyl-1,6,11, 16-tetragermacycloeicosane (**50**)	20	5.0	60
1,1,7,7,13,13,20,20-Tetramethyl-1,7,13, 10-tetragermacyclotetraeicosane (**51**)	24	6.2	100
1,1,8,8,15,15,22,22-Tetramethyl-1,8,15, 22-tetragermacyclooctaeicosane (**52**)	28	1.9	70
1,1,10,10,19,19,28,28-Tetramethyl-1,9,17, 25-tetragermacyclohexatriacontane (**53**)	34	1.2	130
1,1,12,12,23,23,34,34-Tetramethyl-1,12,23, 34-tetragermacyclotetratetracontane (**54**)	44	5.0	120
Germacyclohexanes			
1,1-Dimethyl-1-germacyclohexane (**55**)	6	−13.7	22
1,1-Diphenyl-1-germacyclohexane (**56**)	6	−33	370

Reproduced, with permission, from Aoyagi *et al*.,[16] Copyright 1992, Royal Society of Chemistry.

indication of relaxation times for alkylgermanes, and that the correlation times (hence the relaxation times) are related to molecular radius.[20]

The relaxation times of **47** and **46** are expected to be much shorter (hence the linewidths are much larger) than those of corresponding germacyclohexane derivatives unless the extent of asymmetry of the electric field gradient around germanium is essentially identical for germamacrocycles and germacyclohexanes. Thus, the observed linewidths of **47** and **46** are a very good indication of higher symmetry around germanium.

Takeuchi *et al*. also synthesized germamacrocycles with halogen or phenyl groups on germanium.[21] These compounds failed to give ^{73}Ge resonances. This is not unexpected since it is well known that only highly symmetrical tetrahalogermanes and tetraarylgermanes show narrow ^{73}Ge signals.[5]

Takeuchi *et al*.[22] studied a congested system, i.e., a germanium analogue of the bicyclo[3.1.0]hexane system. The molecular structure predicted for the 3-germabicyclo [3.1.0]hexanes(GBCH) by means of molecular mechanics (MM) calculations is in a good agreement with the observation from ^{73}Ge NMR spectra.

The structure was confirmed by means of X-ray crystallographic analysis of a solid derivative of GBCH, spiro[3-germabicyclo[3.1.0]hexane-3,9′-[9]germafluorene] **57**.[23] Thus, GBCH prefers the boat form, even if highly substituted at Ge3. The ^{73}Ge NMR chemical shifts for selective GBCH are given below.

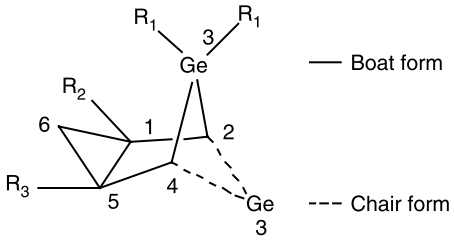

3-germabicyclo[3.1.0] hexanes(**58-61**)

For accessing the effect of the adjoining cyclopropane ring, and its relative orientation to the germacyclopentane moiety (i.e., boat or chair) upon ^{73}Ge chemical shifts of GBCH, the shift for 1,1-dimethyl-1-germacyclopentane (**62**) ($\delta = 40$) and that for 1,1-dimethyl-1-germacyclopent-3-ene (**63**) ($\delta = 37$) will be the reference values. From the chemical shift for 3.3-dimethyl-3-germabicyclo[3.1.0]hexane (**58**) ($\delta = 57$), it is assumed that the effect of fused (possibly *cis*-fused) cyclopropane is ca. 17 ppm. The effect of 3-ethyl groups causes an additional high frequency shift of 19 ppm for 3,3-diethyl-3-germabicyclo[3.1.0]hexane (**59**) ($\delta = 76$). This is a reasonable value in view of the shifts for 1,1,3-trimethyl-1-germacyclopent-3-ene (**64**) ($\delta = 44.6$) and 1,1-diethyl-3-methyl-1-germacyclopent-3-ene (**65**) ($\delta = 70.9$).[17]

The shift observed for 3,3-diethyl-1-methyl-3-germabicyclo[3.1.0]hexane (**60**) ($\delta = 82$) is along this line, and compounds **58–60** seem to have the same (i.e., boat) structure. The shift ($\delta = 46$) observed for 3,3-diethyl-1,5-dimethyl-3-germabicyclo [3.1.0]hexane (**61**) ($\delta = 46$) is anomalous since a similar shift to that of **60** is expected. The most possible explanation is that the compound has a chair structure where the γ-effect is expected because of the interaction between the germanium moiety and the two methyl groups at C1,5.

Schmidbaur *et al.*[24] reported an interesting series of ^1J(Ge–H) couplings. So far, ^1J(Ge–H) has been determined only for molecules with high symmetry. Thus, solutions of GeH_4 (**5**) in solvents of low polarity show the famous 10-line ^{1}H NMR signal from which the coupling ^1J(Ge–H) = 97.6 Hz can be extracted.[25]

Mackay *et al*. reported the *J* values of Et_3GeH,[26] and Schmidbaur also reported a series of simple germa/silaalkanes for which ^{73}Ge NMR spectra of surprisingly good resolution have been obtained.[27] The observed ^1J(Ge–H) couplings range from 88 to 99 Hz. Owing to their low molecular symmetry (point groups C_s, C_2, or C_3), arylgermanes are not expected to give high quality ^{73}Ge NMR spectra, and in fact, for several series of aryl- and heteroarylgermanes only broad resonances ($\Delta\nu_{1/2} = 15–600$ Hz) have been reported.[14]

With this background, it was surprising that ^{73}Ge NMR spectra of excellent quality (Fig. 4) were obtained for all arylgermanes reported in that work.

As a representative example, phenylgermane (**66**) shows a well-resolved 1:3:3:1 quartet at $\delta = -190$ ppm (^1J(Ge–H) = 98 Hz). The same pattern is found for *p*-tolyl, mesityl, and even *p*-anisylgermane as summarized in Table 7. Accordingly, diphenylgermane (**67**) and triphenylgermane (**68**) show triplet and doublet signals, respectively, at -108.8 ppm (^1J(Ge–H) = 94 Hz) and -55.4 ppm (^1J(Ge–H) = 98 Hz). Conversely, none of these

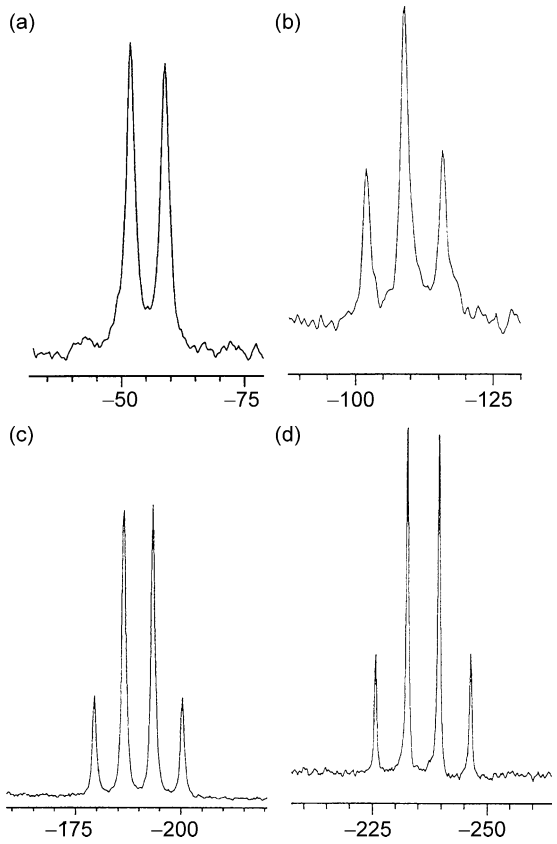

Fig. 4. ^{73}Ge NMR spectra of (a) Ph_3GeH **68**; (b) Ph_2GeH_2 **67**; (c) $PhGeH_3$ **66**; (d) $MesGeH_3$ **69** (in C_6D_6 at 20°C). Reproduced, with permission, from Schmidbaur *et al.*,[24] Copyright 1999, American Chemical Society.

Table 7. ^{73}Ge NMR parameters of arylgermanes Ar_nGeH_{4-n} $(n = 1, 2, 3)$

Compound	Multiplicity	δ_{Ge}	^1J(Ge−H) (Hz)
p-Anisylgermane (**71**)	Quartet	−189.9	97
Bis (*p*-anisyl)germane (**72**)	Broad singlet	−112.0	–
p-Tolylgermane (**69**)	Quartet	−190.6	96
Mesitylgermane (**70**)	Quartet	−234.3	95
Phenylgermane (**66**)	Quartet	−190.0	98
Diphenylgermane (**67**)	Triplet	−108.8	94
Triphenylgermane (**68**)	Doublet	−55.4	98

Reproduced, with permission, from Reidmiller *et al.*,[24] Copyright 1999, American Chemical Society.

^1J(Ge–H) couplings are observed in the ^{1}H NMR spectra of the compounds. It thus appears that ^{73}Ge NMR spectroscopy is in fact a very helpful tool for the identification and for a more detailed study of alkyl- and arylgermanes. The authors offer several suggestions which help to explain this phenomenon:

(1) Because of the discontinuities in the electronegativity sequence of group 14 elements, the Ge–C bond has an inherently low polarity.
(2) It is known from microwave and vibrational spectroscopy that H_3Ge–R bonds have very low barriers of rotation, and this is, of course, particularly true for bonds to sp^2 and sp carbon atoms where virtually free rotation can be assumed.
(3) The linewidth factor ι is a function of both the quadrupole moment Q and the nuclear spin I of the isotope under observation. Apparently, an internal compensation of the two contributions according to $\iota = (2I+3)Q_2/[I^2(2I-1)] = 2.4 \times 10^{-59}\mathrm{m}^4$ leads to an appreciable sharpness of the lines generated in the spin–spin coupling.[28] The data are summarized in Table 7.

Note that the sensitivity of the ^{73}Ge nucleus is close to that of frequently observed nuclei such as ^{29}Si (3.7×10^{-4}), but the frequency range is one of the lowest of all nuclei.

2.2. Compounds with hypercoordinated Ge nuclei

Hypercoordination (or hypervalency) of main group elements has attracted considerable attention since the end of the last century.[29] In this regard, hypercoordination of the germanium atom should be discussed in connection with ^{73}Ge NMR spectroscopy. As early as 1989, Lukevics *et al*. explained that ^{73}Ge chemical shifts can be a very good indicator of hypercoordination.[30] They claimed that the formation of hexacoordinated Ge species in solution and its associated decrease in the rate of intermolecular exchange were accompanied by the dramatic low frequency shift of $\Delta\delta - 350$ ppm for ethoxygermatrane (**73**), relative to the tetracoordinate parent compound, tetraethoxygermane (**74**), in ^{73}Ge NMR spectra.

Table 8. ^{73}Ge NMR data for 1,3-dioxa-6-aza-2-germacyclooctanes in CD_3CN at 343 K and for model compounds[a]

Compounds	R	X	δ_{Ge}	$\Delta\nu_{1/2}$
75	H	$(CH_2)_2$	−57	280
76	Me	$(CH_2)_2$	−55	320
77	*i*-Pr	$(CH_2)_2$	−56	500
78	Me	$(CMe_2)_2$	−57	170
79	Me	*o*-C_6H_4	−82	150
80[a]	H	$(CH_2CH_2O)_2$	−94	240
Tetraethoxygermane (**74**)			−44	30
Ethoxygermatrane (**73**)[b]			−68	165

Reproduced, with permission, from Kupce *et al*.,[30] Copyright 1989, Elsevier.
[a]In DMSO-d_6.
[b]In $CDCl_3$.

An increase in ^{73}Ge shielding in derivatives of **73** (see Table 8)[31] as compared to that observed for the model compound **74**, provides evidence for the existence of a transannular donor–acceptor (DA) N–Ge bond in **73** in solution.

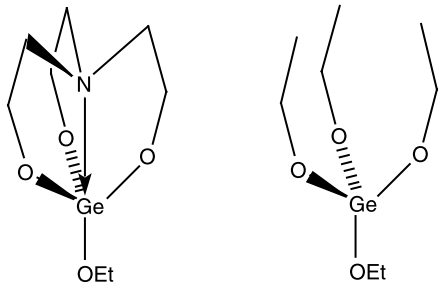

ethoxygermatran (**73**) tetraethoxygermane (**74**)

The 1,3-dioxa-6-aza-2-germacyclooctanes, which are the analogues of germatrane, are another interesting series of compounds. Judging from the linewidth, it is certain that there is a coordination between germanium and nitrogen, making the former pentacoordinate. This agrees well with the results of an X-ray diffraction study of crystalline **76** in which the distance between the N and Ge atoms is decreased to 2.159 Å.[32]

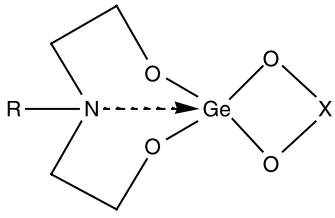

1,3-dioxa-6-aza-2-germacyclooctane (**75-80**)

Substitution of the H atom at N by a Me or *i*–Pr group does not appreciably affect the ^{73}Ge shielding and, consequently the DA N–Ge bond strength.

The insignificant low frequency shift of the ^{73}Ge resonance in **78** compared with that of **76** is attributable to the inductive effect of the Me groups in the β-position which is consistent with the effects observed in tetraalkoxygermanes. A similar effect is observed for compound **79**, but the lack of ^{73}Ge data for the appropriate model compounds prevents any definite conclusion to be drawn. Decreased ^{73}Ge shielding in the series **75–80**, as compared to **73**, alkoxy derivatives of $ROGe(OCH_2CH_2)_3N$ ($\delta_{Ge} = -60$ to -68),[33,34] suggests a stronger DA N–Ge bond in germatrane. However, the differences in the conditions under which ^{73}Ge spectra were recorded must be taken into account.

A substantial increase in ^{73}Ge shielding in compound **80** is indicative of a pseudohexacoordinate Ge atom resulting from additional 1,5-transannular O–Ge bonding. At present, unambiguous interpretation of the results obtained is not possible because of insufficient information regarding the influence of ring size on the ^{73}Ge chemical shifts.

The spectra depicted in Fig. 5 and summarized in Table 9 reflect the possible applications of ^{73}Ge NMR to the study of chemical reactions involving hexacoordinated Ge derivatives. The key compound is the hexacoordinated 2.2′-bipyridyl–$GeCl_4$ complex **81**, the hypercoordinated nature of this compound is depicted by both the ^{73}Ge chemical shift and the linewidth when compared with those of tetracoordinated $GeCl_4$ **88**.

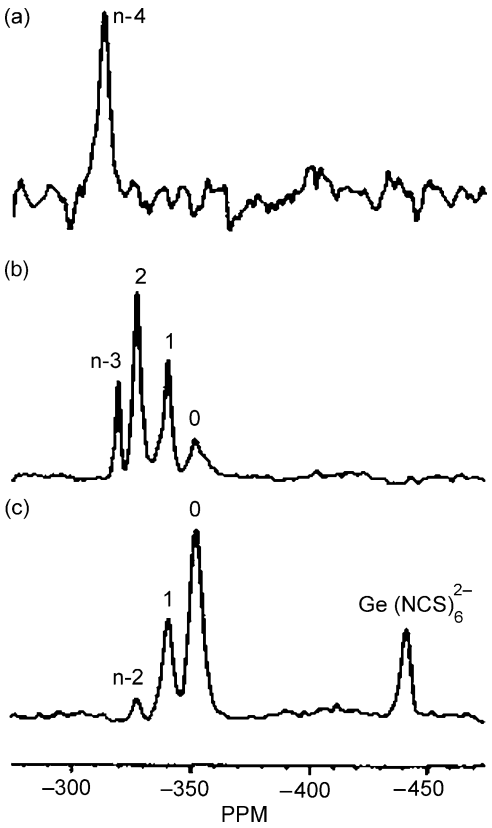

Fig. 5. 12.56 MHz ^{73}GeNMR spectra of hexacoordinate Ge complexes. (a) $GeCl_4$·Bpy in DMDO-d_6; (b) $GeCl_4$·Bpy + KSCN(1:1) in acetone-d_6 (the ^{73}Ge signal of $GeCl_4$·$GeCl_4$ Bpy does not appear because of the low solubility of the compound in acetone); (c) the same starting compounds in the ratio 1:4. Reproduced, with permission, from Kupce *et al.*,[31] Copyright 1989, Elsevier.

Table 9. ^{73}Ge NMR parameters of hexacoordinated organogermanium derivatives in acetone-d_6

Compound	δ_{Ge}	$\Delta\nu_{1/2}$
$GeCl_4Bpy^a$ (**81**)	−313.7	35
$GeCl_3(NCS)Bpy$ (**82**)	−319.5	22
$GeCl_2(NCS)_2Bpy$ (**83**)	−327.1	35
$GeCl(NCS)_3Bpy$ (**84**)	−340.2	32
$Ge(NCS)_4Bpy$ (**85**)	−351.8	48
$GeCl_4Phen$ (**86**)	−319.4	150
$[Ge(NCS)_6]^{2-}$ (**87**)	−442.5	50
$GeCl_4$ (**88**)	+30.9	2

Reproduced, with permission, from Kupce *et al.*,[30] Copyright 1989, Elsevier.
[a]In dimethylsulphoxide-d_6.

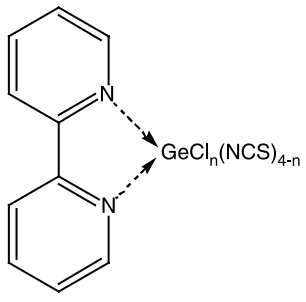

81-85

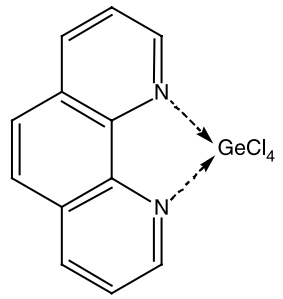

86

Thus, it is possible to estimate from ^{73}Ge NMR the degree of substitution of the Cl atoms by NCS groups when KSCN is added to a suspension of compound **81** in acetone-d_6 and to observe the formation of the anion **87** in an excess of KSCN. These spectra also indicate that intermolecular exchange between Ge substituents in hexacoordinated derivatives **81–85** proceeds slowly (on the NMR time scale), in contrast to their tetracoordinated derivatives $GeCl_n(NCS)_{4-n}$, i.e., complex formation stabilizes the $GeCl_4(NCS)_{4-n}$ molecules.

The shifts ($\Delta\delta$) of −313.7 ppm for **81** and −319.4 ppm for **86** suggest the formation of a stronger complex in **86**. The transition from the neutral complex **85** to anion **87** is accompanied by an additional low frequency shift of the ^{73}Ge resonance. This agrees well with the results of CNDO/2 calculations which indicate an increase in ^{73}Ge shielding with increasing negative charge on the germanium atom in tetracoordinated derivatives.[35]

In connection with hypercoordination in molecules that are not as congested, triarylsilanes and -germanes are particularly interesting. Corriu *et al.*[36,37] found by X-ray crystallographic analysis that tris(2-dimethylaminomethylphenyl)germane (**93**) is heptacoordinated, and is a tricapped tetrahedron in which the three carbon atoms bonded to germanium and the hydrogen atom form a tetrahedron with the germanium atom at the core, and three nitrogen atoms coordinate with germanium from outside of the tetrahedron.

Takeuchi *et al.*[38] synthesized and determined X-ray crystallographic analysis and ^{73}Ge NMR spectra of tris[2-(*t*-butoxymethyl)phenyl]germane (**91**) and tris[(2-methylthiomethyl)phenyl]germane (**92**) which were proved to have the incipient dative bonding between germanium and oxygen or sulphur atoms to make the germanium hyperconjugated.

It is generally accepted that multinuclear NMR spectroscopy is a very useful means to prove whether a hypercoordinated state is involved or not. Thus, hypercoordination is often associated with a low frequency shift of the ^{29}Si signal in the case of silicon compounds. A large line broadening was also reported for germanium hypercoordination. Takeuchi *et al.* determined the ^{73}Ge chemical shifts and linewidths for all of the compounds they prepared.[38] In addition, they prepared and determined the ^{73}Ge NMR spectra of **66**, **93**, **96** and other compounds for reference. The results are summarized in Table 10.

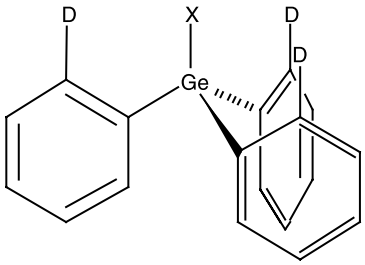

triarylgermanes (**89-93**)

Although compounds **89–93** exhibit a substantial low frequency shift as compared with **66**, compound **95** shows much the same low frequency shift. Hence, this shift should be due to a γ-effect[10] rather than to hypercoordination. It is interesting to note, however, that there is a rough linear relation ($\delta_{Ge} = 0.025\ \delta_{Si} - 0.049\ (R = 0.972)$) between the ^{73}Ge chemical shifts of **89, 92, 93, 66** and ^{29}Si chemical shifts of related silanes. Such linear relations have long been known to exist between related organogermanium and organosilicon compounds.[5]

Table 10. ^{73}Ge NMR parameters of triarylgermanes

Compounds	δ_{Ge}	$\Delta\nu_{1/2}$
Tris(2-methoxymethylphenyl)germane (**89**)	− 85	350
Tris(2-ethoxymethylphenyl)germane (**90**)	− 85.4	350
Tris(2-*t*-butoxymethylphenyl)germane (**91**)	− 84	350
Tris(2-methylthiomethylphenyl)germane (**92**)	− 93	270
Tris(2-dimethylaminomethylphenyl)germane (**93**)	− 89	900
Bis(2-methoxymethylphenyl)(2-hydroxyphenyl) germane (**94**)	− 85	250
Tris(2-tolyl)germane (**95**)	− 84	70
Tetraphenylgermane (**38**)	− 32.6	6
Triphenylgermane (**66**)	− 57.0	20
Tris(2-methoxymethylphenyl)phenylgermane (**96**)	− 27.8	75

As previously described, the broadening of the signal seems to be always accompanied by hypercoordination. A typical example is the linewidth of **73** (165 Hz) vs. that of **74** (30 Hz).[31] The lines of **38**, **68** and **95** are narrow, corresponding to the absence of coordination. In the case of **89–93** the broadening is large, and this is particularly so for **93**, where, as indicated by the interatomic distance, coordination seems stronger.

Thus, both X-ray crystallographic analysis and NMR linewidth study support the interpretation that in compounds **89–92** incipient dative bonding between oxygen (or sulphur) and germanium takes place though it may be weaker than that between nitrogen and germanium in the similar structure **93**.

Takeuchi *et al.*[39] also determined ^{73}Ge NMR spectra of some phenylgermanes. The chemical shifts and linewidths are discussed in terms of structure and in relation to hypercoordination of germanium atoms. It appears that the linewidth can be a measure of hypercoordination.

In the course of their investigations on organogermanium compounds with anion transport capability, these authors noticed that aryl substituent(s) on germanium are effective in enhancing its Lewis acidity. Since the observed anion transport capability is most likely due to the hypercoordination in which the germanium atom can be involved with anions, chloride ion in particular, a suitable method of evaluation of germanium hypercoordination is needed.

Hypercoordination of silicon in organosilicon compounds has often been associated with a considerable low frequency shift of ^{29}Si signals.[40] It is expected that the same effect will be observed for the ^{73}Ge NMR spectra of hypercoordinated organogermanium compounds. The ^{73}Ge NMR spectra of tris(*o*-substituted phenyl)germanes were examined and it was found that the ^{73}Ge chemical shifts (summarized in Table 11) are not necessarily correlated with hypercoordination.

On the other hand, it was noticed that the linewidths of the ^{73}Ge signals are a good indication of the hypercoordination of germanium atoms.[38] The linewidths of **73** (165 Hz) and **74** (30 Hz) are good examples of this phenomenon.[31] Thus, the linewidth of

Table 11. ^{73}Ge chemical shifts and linewidths of some phenylgermanes[a]

Compounds	δ_{Ge}	$\Delta\nu_{1/2}$	^1J (Ge–H) (Hz)
Phenylgermane (**68**)	−187.5 (−190.0)	25	96.9 (98)
Diphenylgermane (**67**)	−108.5 (−108.8)	28	96.9 (94)
Triphenylgermane (**66**)	−56.0 (−55.4)	87	98.6 (98)
Tetraphenylgermane (**38**)	−31.6	5.9	
Dimethyldiphenylgermane (**37**)	−19.5	92	
Bis(2-hydroxyethyl)diphenylgermane (**97**)	−25	370	
Bis(2-acetoxyethyl)diphenylgermane (**98**)	−25	58	
Bis(2-methoxycarbonyl)diphenylgermane (**99**)	−14.0	33	
Bis(3-hydroxypropyl)diphenylgermane (**100**)	−14	580	
2-Hydroxyethyltriphenylgermane (**101**)	−30	117	
2-Cyanoethyltriphenylgermane (**102**)	−26	95	
2-Acetoxyethyltriphenylgermane (**103**)	−30	35	

Reproduced, with permission, from Takeuchi *et al.*,[39] Copyright 2002, Wiley.

[a]Values in parentheses are taken from Ref. 24.

tris(*o*-tolyl)germane is 70 Hz, whereas that of **89** is 350 Hz. The linewidth of **93**, which has a stronger donor, nitrogen, is even as large as 900 Hz. By contrast, the chemical shift values of these three compounds lie in a narrow range of −84 to −89 ppm. The linewidths of these and related compounds are summarized in Table 11. The authors extended their study to some diphenylgermanes and triphenylgermanes with a variety of substituents on the germanium atom to observe the relation between the hypercoordinate state of germanium and the ^{73}Ge resonance linewidth.

The ^{73}Ge chemical shifts and linewidths of compounds **97–103** together with those of **66–68, 38, 37** and the ^{1}J(Ge–H) values, are summarized in Table 12. The ^{1}J(Ge–H) values obtained are in good agreements with those reported previously.[24]

Since the solution concentrations were similar throughout the study, so that the viscosities of the solutions were nearly the same, the linewidth may be determined by any of four factors: the coalescence phenomenon, extent of asymmetry of the electric field gradient around the germanium nucleus, the molecular weight and any hydrogen bonding. The first possibility can be discounted since the exchange process involved in this kind of hypervalence should be very rapid on the NMR time scale.[41]

The ^{73}Ge resonance linewidths of **66–68, 38 and 37**, measured as the reference, clearly reflect the effects of two factors mentioned. Thus, the narrowest signal for **38** is due to its high symmetry. The difference between the linewidths of **66** and **68** largely reflects the difference in molecular weights. Much the same is true for **67** and **37**. The fact that the value for **67** is close to that of **68** rather than **66** seems to be due to the greater symmetry. These results clearly indicate that a comparison of linewidths should be made among compounds with similar molecular weights and similar symmetry.

Among the linewidths of **97–103,** it is noticeable that those with a terminal hydroxy group uniformly have a large linewidth. The very large value for **100**, for instance, is explained by favourable hypercoordination as shown below, although the possible role of hydrogen bonding cannot be excluded. An analogue of **100** with a shorter side-chain, **97**, also exhibits a large linewidth which seems to indicate that hypercoordination is also involved to some extent in this compound. The smaller linewidths for **98** and **99** suggest the role of hypercoordination in relation to the linewidth. The same is true for **102** and **103**.

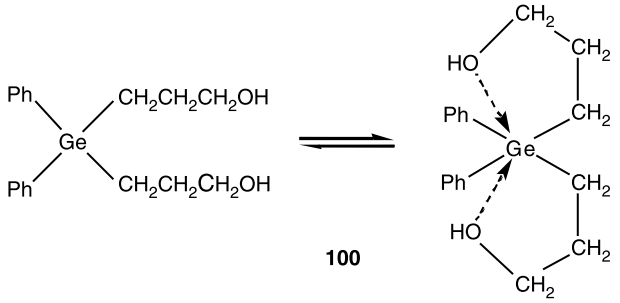

100

In most cases, a large linewidth for the ^{73}Ge signal can be associated with hypercoordination between the germanium atom and, in their case, the oxygen donor. A contribution from hydrogen bonding is likely, but this cannot be the sole reason for

line broadening since compounds without any hydroxy group often have a large linewidth.

2.3. Miscellaneous compounds

There are a few reports in which dynamic processes are traced by ^{73}Ge NMR spectroscopy. ^{73}Ge and ^{14}N NMR spectra were used to study reaction products and chemical exchange processes in the system $GeCl_4$ **88** + KSCN in acetone-d_6.[42] At the $GeCl_4$ to KSCN ratios from 2:1 to 1:4, germanium (IV) derivatives of the type $Ge(NCS)_nCl_{4-n}$ were formed. Rapid intermolecular exchange with Cl and NCS groups was observed between the $Ge(NCS)_nCl_{4-n}(n = 0–4)$ molecules with varying n. The formation of dimeric and/or larger intermediate complexes was suggested. This is accompanied by simultaneous formation of $[Ge(NCS)_nCl_{6-n}]^{2-}$ anions $(n = 4–6)$. Addition of a KSCN solution in acetone-d_6 to $GeCl_4$ results in considerable broadening of the ^{73}Ge signal and its displacement to lower frequency. This is accompanied by the occurrence of a ^{73}Ge signal at -443 ppm corresponding to the $[Ge(NCS)_6]^{2-}$ ion (see Fig. 6).

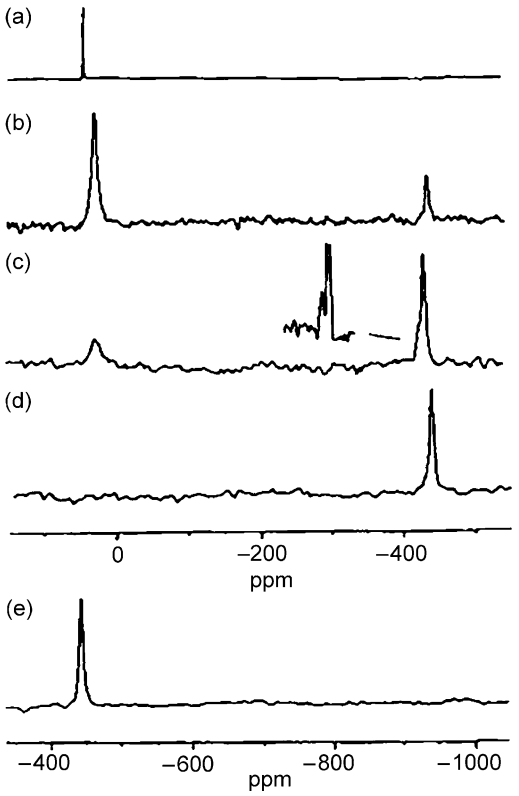

Fig. 6. ^{73}Ge NMR spectra of $GeCl_4$ + KSCN in acetone-d_6 at (a) 1:0, (b) 1:1, (c) 1:2, (d) 1:6 and (e) 1:20 ratios. Reproduced, with permission, from Kupce *et al.*,[42] Copyright 1989, Pergamon Press.

The most plausible mechanism for the observed exchange is the formation of dimeric and/or larger intermediate structures. The involvement of the $[Ge(NCS)_6]^{2-}$ anion in this exchange is insignificant, as the chemical shift was not subject to appreciable variation. The low intensity signals also detected in the ^{73}Ge spectra (see Fig. 6) indicate the formation of small amounts of $[Ge(NCS)_nCl_{6-n}]^{2-}$ $(n = 5–6)$ type derivatives.

Germanium dioxide (**104**) occurs as a component of natural minerals and meteorites. It has been widely used as a starting material in inorganic synthesis and recently in the synthesis of organogermanium compounds. For these reasons the possibility of detecting **104** by means of NMR spectroscopy is intriguing not only from a theoretical but also from a purely practical point of view. Lukevics *et al.*[43] were able to detect a relatively narrow ^{73}Ge resonance at -16.7 ppm ($\Delta\nu_{1/2} = 22$ Hz) for a neutral solution of **104** in $2H_2O$ (see Fig. 7(a)) despite the considerably lower solubility of **104** under these conditions.

The small linewidth (implying high symmetry of the charge distribution around Ge) and substantial high frequency shift for the observed signal as compared with the resonances of tetramethoxygermane (**105**) $(\delta = -37.8)$ or tetraisopropyloxygermane (**106**) $(\delta = -49.7)$[22] allow one to assign it to $Ge(OH)_4$.

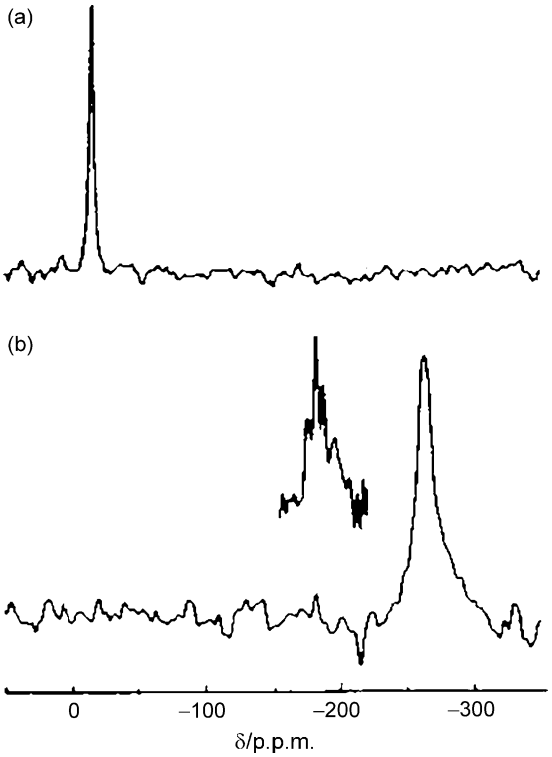

Fig. 7. 12.56 MHz ^{73}Ge NMR spectra of **104** dissolved (a) in ^2H_2O and (b) in a 3:1 mixture of ^2H_2O and NEt_3 at 303 K. Reproduced, with permission, from Kupce and Lukevics,[43] Copyright 1990, Royal Society of Chemistry.

The solubility of **104** in water increases substantially in the presence of triethylamine, indicating some kind of complex formation. Indeed, a ^{73}Ge NMR signal was observed at -269.1 ppm, replacing that at -16.7 ppm (Fig. 7(b)). The large shift ($\Delta\delta = -252.4$) suggests the formation of a hexacoordinate germanium complex.[30,44] Because an interaction between **74** and 2,2′-pyridine was not observed (by means of ^{1}H,^{14}N and ^{73}Ge NMR spectroscopy), the authors prefer to assign this signal to the $[Ge(OH)_6]^{2-}$ (**107**) type anion rather than to a $Ge(OH)_4(NEt_3)_2$ complex. The former can arise as a result of the increased pH of the solution ($pK_a = 11.0$ for NEt_3). It is noteworthy that a very weak signal was detected despite the high content of **104** in the solution. A resolution-enhanced spectrum indicates that the observed resonance consists of at least of four ($\delta = -262.5$, -269.3, -274.5 and -282.2) closely spaced signals. It is reasonable to assign these to six-coordinate–O–$Ge(OH)_5^{2-}$ end-groups oligomeric germoxanes of different length and structure.

3. RECENT DEVELOPMENTS IN THE STUDY OF NMR PARAMETERS

3.1. Prediction of ^{73}Ge chemical shifts

In certain cases, MM or semiempirical molecular orbital (e.g., MNDO) calculations are useful in predicting ^{73}Ge chemical shifts. For instance, a variety of *t*-butylgermacyclohexanes was prepared and their ^{73}Ge (when possible) NMR spectra were determined.[45]

It was estimated that the conformational energy of a *t*-butyl group bonded to germanium is about 5.4 kJ (1.3 kcal) mol^{-1} by NMR data though the MM calculations gave variable results depending on the parameters used for germanium; Thus, 1.38 kJ (0.33 kcal) mol^{-1} by Allinger's parameter, but 5.15 kJ (1.23 kcal) mol^{-1} by Ouellette's parameter. The origin of this discrepancy was discussed. The molecular orbital calculations (MNDO) gave an intermediate value (2.51 kJ (0.60 kcal) mol^{-1}).

In the case of 1-methyl-1-germacyclohexane derivatives,[10,17] the ^{73}Ge chemical shifts are very sensitive to the stereochemistry of a methyl group bonded to germanium.

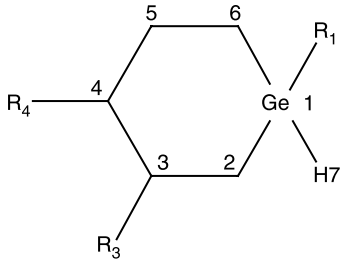

germacyclohexanes (**108 - 117**)

Thus, that of *cis*-**112** (**112ae**) is ca. 12 ppm upfield when compared with that of *trans*-**112** (**112ee**). Hence, it is possible to estimate the ratio of *e*quatorial and *a*xial isomers of **109** based on its ^{73}Ge chemical shifts (see Table 12).

It will be interesting to see if 1-*t*-butylgermacyclohexanes are also sensitive to the stereochemistry of the *t*-butyl group and can be a means to distinguish whether

Table 12. ^{73}Ge NMR parameters of germacyclohexanes

Compounds	δ_{Ge}	$\Delta\nu_{1/2}$
Germacyclohexane (**108**)	−131.2	
1-Methylgermacyclohexane (**109**)	−65.3	
3-Methylgermacyclohexane (**110**)	−131.2	
4-Methylgermacyclohexane (**111**)	−134.3	
trans-1,4-dimethylgermacyclohexane (*trans*-**112**)	−61.5	
cis-1,4-dimethylgermacyclohexane (*cis*-**112**)	−73.4	
1-*t*-Butylgermacyclohexane (**113**)	−27.8	
4-*t*-Butylgermacyclohexane (**114**)	−131.6	
trans-1-*t*-Butyl-3-methylgermacyclohexane (*trans*-**115**)	−37.5[a]	ca. 150
cis-1-*t*-Butyl-3-methylgermacyclohexane (*cis*-**115**)	−37.5[a]	
trans-1-*t*-Butyl-4-methylgermacyclohexane (*trans*-**116**)	−41.2[a]	ca. 150
cis-1-*t*-Butyl-4-methylgermacyclohexane (*cis*-**116**)	−41.2[a]	
trans-1,4-di-*t*-Butylgermacyclohexane (*trans*-**117**)	[b]	
cis-1,4-di-*t*-Butylgermacyclohexane (*cis*-**117**)	[b]	

Reproduced, with permission, from Takeuchi et al.,[45] Copyright 1990, Chemical Society of Japan.
[a]Unresolved.
[b]Inseparable broad peak.

the molecule has an axial *t*-butyl group, or a twist form. Unfortunately, however, due to the enhanced asymmetry of the electric field gradient around the germanium nuclei together with the increased molecular weights, the linewidths of the ^{73}Ge resonances of **115** and **116** are large (ca. 150 Hz or 30 ppm) and cannot be resolved. Furthermore, no separable signal was recorded for **117** although a reasonable concentration was employed. Nevertheless, the chemical shift values are very revealing. For **115** and **116**, the centres of the signals are at ca. −38 and −41 ppm, respectively, both are to low frequency that of **113** ($\delta = -27.8$ ppm). Since the substituent effect of Me-3 or Me-4 on ^{73}Ge shifts is small if any, this shift is accounted for by a contribution from an axial *t*-butyl group.

Germacyclopentane **118**, its 1-methyl and 1,1-dimethyl derivatives together with some germacyclopentenes were prepared and their ^{73}Ge NMR spectra were determined by the same author[46]

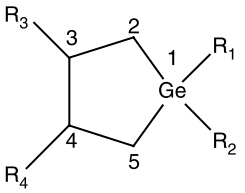

germacyclopentanes

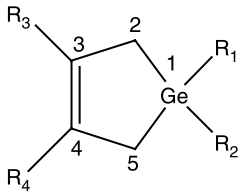

germacyclopentenes

MM calculations of germacyclopentanes indicate that the symmetric twist form is the most stable in contrast to cyclopentane where the envelope and twist forms have much

the same energy. Though ^{73}Ge chemical shifts are less sensitive to the stereochemistry of the methyl group when compared with the corresponding germacyclohexanes, the spectroscopic results can be explained in terms of the structures as depicted by the MM calculations.

For the input structures for MM2 calculations, the germacyclopentane ring can either be an envelope or a twist and in each structure the germanium atom can have three different positions(a, b, and c for an envelope and d, e, and f for a twist). In other words, there are six possible input structures for **118** (Fig. 8). A similar situation should be involved in the case of **62**. In the case of 1-methyl-1-germacyclopentane (**119**) the situation is more complicated since for each of the input structures a–f, there are two orientations, equatorial (abbreviated as eq-**119**) and axial (ax-**119**), of the methyl group. For the input structure f, the equatorial and axial structures are degenerate, and hence for **119** altogether 11 input structures were considered. In Table 13, ^{73}Ge chemical shifts of germacyclopentanes and germacyclopentenes are listed.

The values in parentheses are those of the corresponding germacyclohexanes. The chemical shifts of three compounds **118**, **119** and **62** indicate that the effect of a methyl group is similar in magnitude to that in **108**. Thus the span is ca. 140 ppm for germacyclopentanes and ca. 120 ppm for germacyclohexanes. In germacyclopentanes, however, the resonances are considerably to higher frequency. This shift is most likely due to the reduced bond angle. ^{73}Ge chemical shifts for **63–65** and **120** are, however, puzzling. In view of a very small chemical shift difference between **55** ($\delta = -13.7$) and 1,1,3-trimethylgermacyclohexane (**132**) ($\delta = -12.2$), similarly small differences are expected for the chemical shifts of the compounds, **63**, **64** and **120** since the effect of a pseudo-equatorial methyl group at C3 should not be large. In fact, the difference

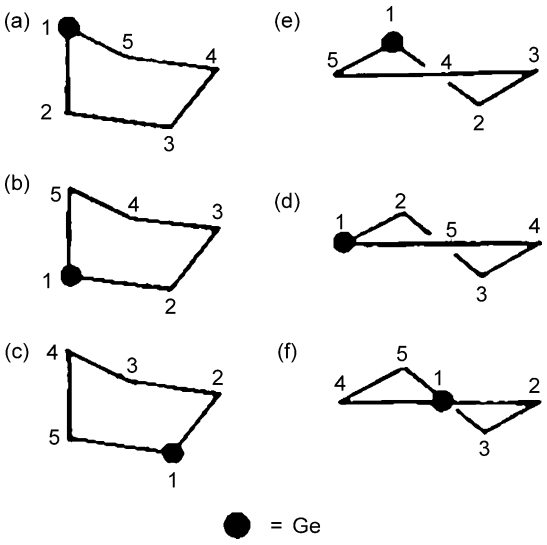

Fig. 8. Input structures for MM2 calculation of germacyclopentane. Reproduced, with permission, from Takeuchi *et al.*,[46] Copyright 1991, Chemical Society of Japan.

Table 13. ^{73}Ge chemical shifts of germacyclopentanes and germacyclopentenes[a]

Compounds GBCH	δ_{Ge}
Germacyclopentane (**118**)	−101.1 (−130.3)
1-Methylgermacyclopentane (**119**)	−27.4 (−65.6)
1,1-Dimethylgermacyclopentane (**62**)	40.0 (−11.3)
1,1-Dimethyl-1-germacyclopent-3-ene (**63**)	37.0
1,1,3-Trimethyl-1-germacyclopent-3-ene (**64**)	44.6
1,1-Diethyl-3-methyl-1-germacyclopent-3-ene (**65**)	70.9
1,1,3,4-Tetramethylgermacyclopent-3-ene (**120**)	9.7

[a] Values in parentheses are corresponding germacyclohexanes.

between **63** and **64** is 7.6 ppm, a rather unexpectedly large value. Furthermore, the shift for **120** is considerably to low frequency. The most possible explanation is the change in the most stable structure in **120**. According to MM calculations, the most stable conformation of cyclopentene is an envelope with a nearly planar double bond moiety.[47] The *cis*-dimethyl substituents will suffer from a strong repulsion, and the deviation from the planarity will be increased. One of the methyl group will be bent to the direction opposite to the flap, while the other is to the direction of the flap. The latter methyl is expected to induce a substantial high field shift induced by the steric interaction with the 1,1-dimethyl moiety. A lack of the relevant parameters inhibited the authors from carrying out MM calculations to prove this explanation. The ^{73}Ge chemical shift of **65** is also puzzling. Since the shift for tetraethylgermane (**121**) is δ17.8, a large difference of $\Delta\delta$ 26.3 between **64** and **65** is unexpected. Here, the deviation of germanium from a tetrahedral structure seems to be involved, although more extensive data should be accumulated before a concrete conclusion can be drawn.

Nakatsuji and Nakao[48] studied theoretically germanium chemical shifts by the *ab initio* molecular orbital method. The compounds studied were $GeMe_{4-x}Cl_x$ and $GeMe_{4-x}H_x$ $(x = 0–4)$. The calculated values of the germanium chemical shifts agreed well with the available experimental values. The germanium chemical shift is due to the p-electron mechanism that reflects the ligand electronic effect on the pp^* excitation in the second order paramagnetic term. For $GeMe_{4-x}H_x$, the chemical shift is almost linear to the number of the ligands, x. On the other hand, a U-shaped dependence is predicted for the chemical shifts of the $GeMe_{4-x}Cl_x$ series and is shown to be caused by the strong and non-additive electron-withdrawing ability of the Cl ligand. The diamagnetic contribution is relatively small for the chemical shift and is determined solely by a structural factor.

The germanium chemical shifts are calculated by the *ab initio* finite perturbation method.[49] The details of the method have been described in a previous paper.[50] For the SCF calculations, a modified version of the HONDOG program is used.[51] The gauge origin is taken at the position of the germanium nucleus. The geometries of the germanium compounds are summarized in Table 14.[52]

Table 14. Geometries of the germanium compounds used in the calculations[a]

Compounds	Ge–C	Ge–Cl	Ge–H	C–H	⟨CGeC	⟨GeCH	⟨HGeC	⟨ClGeC	⟨HGeH	⟨ClGeCl
GeH_4 (**5**)	–	–	1.5251	–	–	–	–	–	109.47	–
$GeMeH_3$ (**122**)	1.9453	–	1.5290	1.083	–	110.52	109.64	–	109.30	–
$GeMe_2H_2$(**123**)	1.9500	–	1.5320	1.083	110.00	110.43	109.47	–	109.47	–
$GeMe_3H$(**124**)	1.9470	–	1.5320	1.095	109.60	110.97	109.34	–	–	–
$GeMe_4$(**15**)	1.9450	–	–	1.120	109.47	108.20	–	–	–	–
$GeMe_3Cl$ (**125**)	1.9400	2.170	–	1.105	112.62	109.47	–	106.1	–	–
$GeMe_2Cl_2$ (**126**)	1.9260	2.155	–	1.105	121.70	107.79	–	107.0	–	106.10
$GeMeCl_3$ (**127**)	1.9450	2.135	–	1.103	–	110.50	–	112.3		106.40
$GeCl_4$(**88**)	–	2.113	–	–	–	–	–	–	–	109.47

Reproduced, with permission, from Nakatsuji and Nakao,[48] Copyright 1994, Wiley.
[a]In angstrom for length and in degree for angle.

The basis sets are taken from the book by Huzinaga *et al.*[53] For Ge, the basis set (13s10p4d)/[5s4p1d] plus d-functions with the exponent of 0.246 are used. For the atoms directly connected to Ge, the basis set is as follows: (9s6p)/[4s3p] plus polarization d-functions ($\zeta = 1.0$) for Cl,(6s3p)/[3s2p] for C, and (3 s)/[2s] plus polarization p-functions ($\zeta = 1.0$) for H.21. For the other atoms, the minimal basis sets with the same exponents are used.

The germanium chemical shift of the compound M is defined relative to the reference compound, $GeMe_4$, as

$$\Delta\delta_M = \sigma(GeMe_4) - \sigma(M) \tag{2}$$

The nuclear magnetic shielding constant σ is the sum of the diamagnetic term, σ^{dia}, and the paramagnetic term, σ^{para},

$$\sigma = \sigma^{dia} + \sigma^{para} \tag{3}$$

where σ^{dia} and σ^{para} are the first- and second-order terms, respectively, in the perturbation theory view. In Table 15 are summarized the germanium nuclear magnetic shielding constants and the chemical shifts for all of the compounds studied in the work.

The calculated values are broken down into σ^{dia} and σ^{para} and further into valence and core MO contributions. The experimental values are shown in the last column of the Table 16. For $GeMe_{4-x}Cl_x$ $(x = 1-3)$, the experimental values are not available, so that the values are estimated from the Ge/Si correlations which are shown in parentheses in the last column of Table 16. The correlation between the theoretical and experimental values of the chemical shift is shown in Fig. 9.

The U-shaped dependence of the metal chemical shifts on the number x of electronegative ligands is well known for Si and Sn chemical shifts in series like $SiMe_{4-x}Cl_x$ and $SnMe_{4-x}Cl_x$. Therefore, a similar U-shaped relationship for the $GeMe_{4-x}Cl_x$ series is expected. In Fig. 10, the theoretical results for the $GeMe_{4-x}Cl_x$ and $GeMe_{4-x}H_x$ $(x = 0-4)$ series are plotted against x.

The authors predicted that the $GeMe_{4-x}Cl_x$ series certainly shows the U-shaped relationship, but the $GeMe_{4-x}H_x$ series does not behave as expected. The origin of the U-shaped dependence lies in the non-additivity of the electronic effect of Cl on the 4p orbital of Ge as the number x in the complexes, $GeMe_{4-x}Cl_x$ $(x = 0-4)$, increases.

3.2. Coupling constants

For nuclei with $I > 1$, the quadrupole coupling constant is defined as the product of the nuclear quadruple moment eQ and the maximum principle value of electric field gradient tensor q.

The quadrupole coupling constants in the symmetric tetrasubstituted germanes(GeR_4), $GeMe_4$(**15**), tetraethylgermane (**121**), tetrapropylgermane (**128**), tetrabutylgermane (**129**), tetrachlorogermane (**88**) and tetrabromogermane (**130**) were obtained by

Table 15. Diamagnetic and paramagnetic contributions, σ^{dia} and σ^{para}, to the germanium nuclear magnetic shielding constants σ and their analyses into core and valence MO contributions (in ppm)

Compound	σ^{dia}				σ^{para}				σ^{total}		
	Core	Valence	Total	Shift	Core	Valence	Total	Shift	Total	Shift	Expt.
GeH_4 (**5**)	2716	62	2777	136	−16	−991	−1007	−403	1771	−267	−283.7
$GeMeH_3$ (**122**)	2725	86	2811	102	−24	−1107	−1131	−279	1680	−177	−209.2
$GeMe_2H_2$(**123**)	2734	111	2845	68	−32	−1209	−1241	−168	1604	−100	−127.6
$GeMe_3H$(**124**)	2744	135	2879	34	−41	−1286	−1327	−83	1552	−48	−57.2
$GeMe_4$(**15**)	2753	160	2914	0	−49	−1361	−1410	0	1504	0	0.0
$GeMe_3Cl$ (**125**)	2787	159	2946	−33	−51	−1469	−1520	110	1426	78	(56.8–147.8)[a]
$GeMe_2Cl_2$ (**126**)	2882	159	2981	−67	−54	−1537	−1592	182	1389	115	(60.4–146.7)[a]
$GeMeCl_3$ (**127**)	2857	158	3015	−101	−58	−1539	−1597	187	1418	86	(24.1–81.3)[a]
$GeCl_4$ (**88**)	2893	159	3052	−139	−63	−1544	−1607	197	1446	58	30.9

Reproduced, with permission, from Nakatsuji and Nakao,[48] Copyright 1994, Wiley.

[a]Estimated value.

Table 16. The physico-chemical values necessary to determine quadrupolar coupling constants of germanium in tetrasubstituted germanes

Compounds	Concn. mol dm^{-3}	ρ (30°C)	η (30°C) cP^a	r Å	T_1 (IR)^b ms	τ_c(30°C) 10^{-11} s	e^2Qq/h MHz
$GeMe_4$(**15**)	3.67	1.26	0.537	3.75	290	0.69	1.51
$GeEt_4$(**121**)	2.63	1.21	0.573	5.11	220	2.2	0.97
$GePr_4$(**128**)	1.95	1.20	0.720	5.83	100	4.5	1.00
$GeBu_4$(**129**)	1.55	1.19	0.910	6.90	80	10.9	0.72
$GeCl_4$(**88**)	4.37	1.67	0.586	3.89	280	0.78	1.45
$GeBr_4$(**130**)	4.02	2.29	0.986	4.24	160	1.8	1.25

[a] 1 $P = 0.1$ Pa.

[b] T_1 (IR); T_1 determined by inversion-recovery method.

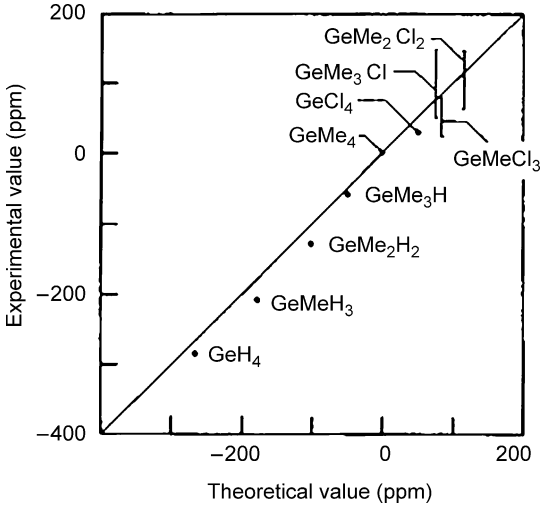

Fig. 9. Correlation between the experimental and theoretical values of the ^{73}Ge chemical shifts of the germanium compounds. Reproduced, with permission, from Nakatsuji and Nakao,[48] Copyright 1994, Wiley.

measuring the ^{73}Ge spin-lattice relaxation times (T_1) and the reorientational correlation times (τ_c) in the chloroform solutions. Quadrupole coupling constants of GeR_4 are in the range of 0.72 MHz (**129**) to 1.51 MHz (**15**), and these decrease slightly as the molecular radius increases.[54]

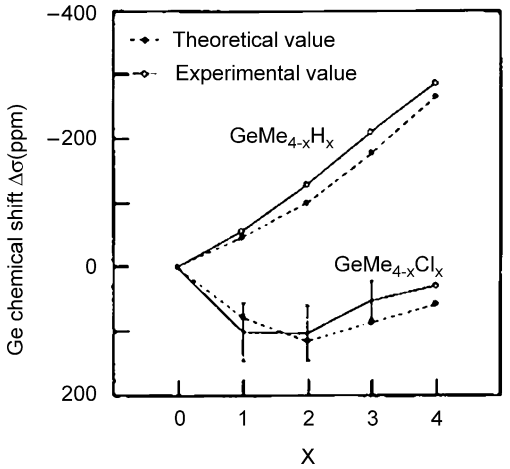

Fig. 10. The dependence of the ^{73}Ge chemical shift on the number of ligands x in the $GeMe_{4-x}H_x$ and $GeMe_{4-x}Cl_x$ series. The values estimated in the text are used for the experimental values of the $GeMe_{4-x}Cl_x$ ($x = 1 - 3$) compounds. Reproduced, with permission, from Nakatsuji and Nakao,[48] Copyright 1994, Wiley.

It is generally accepted that if electric field gradients occur at the nucleus site, the quadrupole relaxation times, T_1^q and T_2^q, of nuclei with nuclear spin $I > 1/2$ are related to the reorientational correlation time τ_c at the extreme-narrowing limit as given below.[55]

$$\pi\Delta\nu_{1/2} = 1/T_1 = 1/T_2 = 3\pi^2/10 \times (2I+3)/I^2(2I-1) \times (e^2Qq/h)^2(1+\zeta^2/3)\tau_c \quad (4)$$

where e^2Qq/h is quadrupole coupling constant and ζ is the asymmetry parameter. Takeuchi *et al*. estimated the quadrupole coupling constants of GeR_4 with the aid of Eq. (4). The values of the concentration, density (ρ), viscosity (η), and radius (r) of tetrasubstituted germanes are shown in Table 16.[56]

The correlation times, τ_c, are given by Eq. (5)

$$\tau_c = 4\pi r^3 \eta f/3kT \quad (5)$$

where r is the molecular radius, η solution viscosity, f microviscosity, k the Boltzmann constant and T the absolute temperature. Gierer and Wirtz have introduced the idea of a microviscosity, which is defined by Eq. (6).[57]

$$f = [6a_s/a + (1 + a_s/a)^{-3}]^{-1} \quad (6)$$

The mean radius of solvent molecule $CHCl_3$ a_s was estimated as 3.13 Å. The quadrupole coupling constants for GeR_4 were found to be in the range 0.72–1.7 MHz, as shown in Table 16.

For **15** and **129** in $CDCl_3$, the values of quadrupole coupling constants have been reported as 1.7 and 1.1 MHz, respectively,[58] in which τ_c was calculated from dipole–dipole interaction of the CH_3 group. This discrepancy of the quadrupole coupling constants may be due to the different methods of determining τ_c values.

Since the relaxation rate is proportional to the correlation time and to the square of the quadrupole coupling constant, it is interesting to determine which of the two mainly determines the relaxation rate. They found that the difference of relaxation rate is mainly governed by the correlation time rather than by the quadrupole coupling constant from the data for GeR_4 shown in Table 16. A linear relationship exists between $\ln\tau_c$ and the molecular radius as shown in a previous paper.[56]

On the other hand, the value of the quadrupole coupling constant slightly decreases as the molecular radius increases. A plot of the quadrupole coupling constants vs. molecular radius, r, is given in Fig. 11. The larger the radius, the smaller is the quadrupole coupling constant. It seems that in the symmetrical germanium compounds investigated the smaller complex molecules will be instantaneously distorted by the molecular vibration and rotation, or by collision.

Wrackmeyer *et al*.[59] prepared tetrakis(trimethylstannyl)germanium (**131**) and studied this compound by ^{73}Ge and ^{119}Sn NMR spectroscopy. Quadrupolar relaxation of the ^{73}Ge nucleus is slow, which allows one to measure $^1J(^{117/119}Sn-^{73}Ge) = 37$ Hz and to determine its positive sign by a 2D heteronuclear $^{73}Ge-^1H$ shift correlation. The absolute

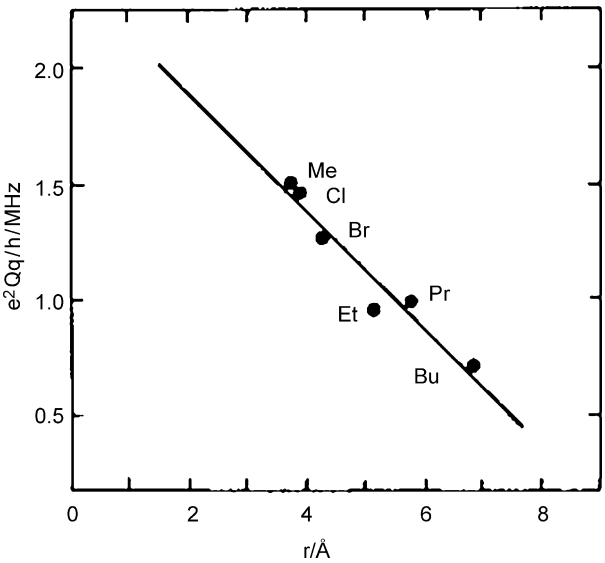

Fig. 11. Plot of e^2Qq/h vs. radius r of GeR_4. Reproduced, with permission, from Harazono *et al.*,[54] Copyright 1989, Chemical Society of Japan.

signs of other couplings involving the nuclei ^{1}H, ^{13}C and $^{117/119}$Sn were also determined by appropriate 2D shift correlation. The ^{73}Ge chemical shift for **131** in C_6D_6 is $\delta - 515.2$.

The ^{73}Ge signal of **131** is a fairly sharp singlet ($\Delta\nu_{1/2} = 2.5$ Hz), accompanied by $^{117/119}$Sn satellites with correct intensity for four equivalent tin atoms in the molecule, and corresponding to $^1J(^{117/119}\text{Sn}-^{73}\text{Ge}) = 37$ Hz. This indicates that all inter- and intramolecular dynamic processes are fast and that quadrupolar effects are almost completely averaged. In fact, it proved possible to detect the ^{73}Ge NMR signal of **131** by polarization transfer from the 36 equivalent ^{1}H nuclei, assuming a coupling constant $^3J(^{73}\text{Ge}-^1\text{H}) = 1.5$ Hz (unresolved). Therefore, 2D heteronuclear ^{73}Ge–^{1}H shift correlation (HETCOR) was carried out in order to determine the sign (positive) of $^1J(^{117/119}\text{Sn}-^{73}\text{Ge})$ (Fig. 12).

The presence of magnetically active ^{1}H, ^{13}C, ^{117}Sn and ^{119}Sn nuclei is attractive for the determination of all absolute coupling signs in **131**. It turned out that the determination of the sign of ^2J(Sn–Sn) is not straightforward, since the HETCOR experiment based on the long-range coupling constant $^4J(^{119}\text{Sn}-\text{Ge}-\text{Sn}-\text{C}-\text{H})$ failed to produce the desired result.

In the present case, it might be that the magnitude of $^4J(^{119}\text{Sn}-\text{Ge}-\text{Sn}-^{13}\text{C}-^1\text{H})$ is too small ($\ll 1$ Hz), leading to insufficient polarization transfer.

3.3. Relaxation times and exchange phenomena

The ^{73}Ge spin-lattice relaxation time (T_1) and spin–spin relaxation time (T_2) in such alkylgermanes as symmetrical GeR_4, **15, 121, 128, 129** and the unsymmetrical

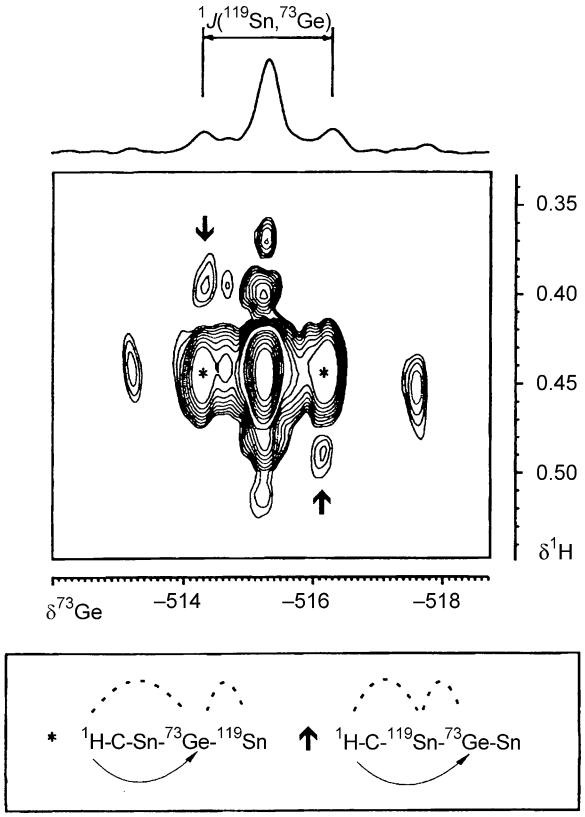

Fig. 12. Contour plot of the $^{73}Ge/^{1}H$ HETCOR experiment. Note the negative tilt of the cross peaks for the $^{117/119}Sn$ satellites marked by arrows. The pathway of polarization transfer (drawn line) and the coupling constants for comparison of signs (dashed lines) are shown. Reproduced, with permission, from Wrackmeyer *et al.*,[59] Copyright 1999, Wiley.

germacyclohexane derivatives, 1,1,3-trimethyl-1-germacyclohexane (**132**), 1,1,4-trimethyl-1-germacyclohexane (**133**), and 1,1,3,5-tetramethyl-1-germacyclohexane (**134**) have been measured at several temperatures in order to elucidate the relaxation mechanism of germanium nuclei in organogermanium compounds.

Furthermore, the viscosities of the solutions of symmetrical alkylgermanes were measured to obtain the reorientational correlation times. T_1 and T_2 are the same for all compounds investigated at room temperature, and these become shorter as the molecular radii become larger. The relaxation times of unsymmetrical germacyclohexane derivatives are even shorter than those of symmetrical GeR_4. T_1 and T_2 of germanium nuclei in alkylgermanes are found to be dominated by the quadrupole relaxation. The reorientational correlation times ($(0.69 - 10.9) \times 10^{-11}$ s) and the activation energies (9.6–13.2 kJ mol^{-1}) for GeR_4 were also discussed.[20]

In Fig. 13 plots of $\ln(1/T_1)$ and $\ln(1/T_2)$ for **15** and **121** against $1/T$ are given.

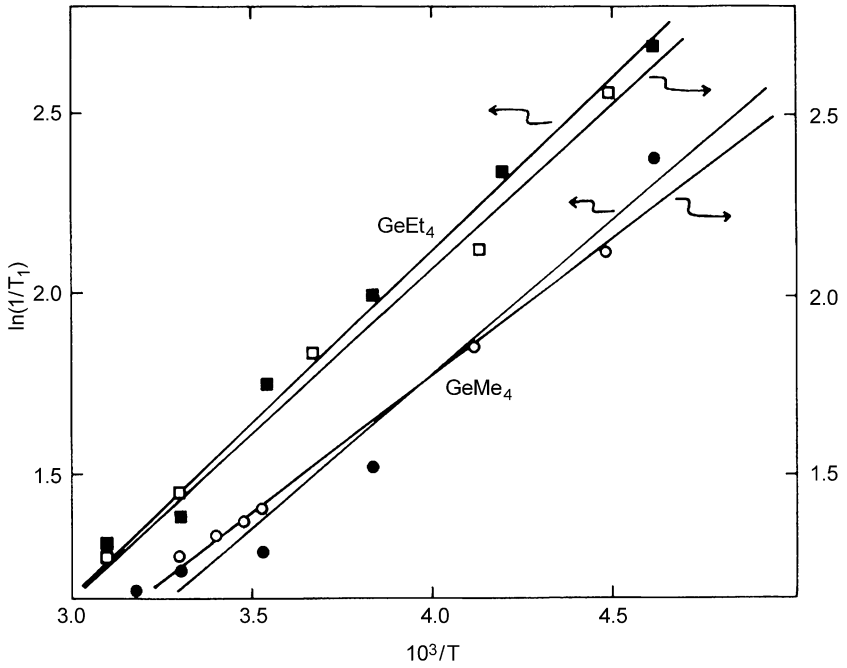

Fig. 13. Plots of $\ln(1/T_1)$ and $\ln(1/T_2)$ vs. $1/T$ in tetraalkylgermanes:(■) $\ln(1/T_1)$ of $Ge(C_2H_5)_4$ **121** ($R = 0.997$); (□) $\ln(1/T_2)$ of $Ge(C_2H_5)_4$ **121** ($R = 0.914$); (●) $\ln(1/T_1)$ of $Ge(CH_3)_4$ **15** ($R = 0.873$); (○) $\ln(1/T_2)$ of $Ge(CH_3)_4$ **15** ($R = 0.921$). R is the correlation coefficient. Reproduced, with permission, from Harazono *et al.*,[56] Copyright 1987, American Chemical Society.

Both of the two plots give straight lines with positive slopes which are nearly equal for each compound in the temperature range of +50 to −50°C. These results indicate that the spin–spin relaxation of ^{73}Ge nuclei in **15** and **121** occurs also solely via the quadrupole mechanism. The relaxation mechanism of ^{73}Ge nuclei in other compounds listed in Table 17 proved similar to that for the two compounds above.

Table 17. Values of T_1(IR), T_2(CPMG) and T_2 ($\Delta\nu_{1/2}$) of tetraalkylgermanes at 303 K

Compounds	T_1(IR), ms	T_2(CPMG)[a], ms	$T_2(\Delta\nu_{1/2})$[b], ms
$GeMe_4$ (**15**)	290	270	280
$GeEt_4$ (**121**)	220	200	240
$GePr_4$ (**128**)	100	100	90
$GeBu_4$ (**129**)	80	80	80
1,1,3-Trimethyl-1-germacyclohexane (**132**)	16	14	14
1,1,4-Trimethyl-1-germacyclohexane (**133**)	16	15	15
1,1,3,5-Tetramethyl-1-germacyclohexane (**134**)	24	24	24

[a] T_2 (CPMG); T_2 determined by CPMG method.
[b] $T_2(\Delta\nu_{1/2})$; T_2 determined from linewidth.

The possibility of a contribution of relaxation other than quadrupole is excluded as discussed below. The ^{73}Ge signal strength was not changed by the Overhauser effect within experimental error in the ^{73}Ge{^{1}H} experiment, which excludes the dipole–dipole mechanism. The shielding anisotropy mechanism is also excluded because the germanium atom has a tetrahedral environment in the symmetrical GeR_4. The spin-rotation mechanism shows a reverse temperature dependency to that of the quadrupole relaxation. Fig. 14 suggests the absence of the spin-rotation mechanism in the temperature range studied.

The scalar-coupling mechanism contributes to the spin–spin relaxation mechanism as the temperature is increased; on the other hand, it contributes to the spin-lattice relaxation mechanism in the lower temperature region. The scalar-coupling mechanism is also absent.

To elucidate the relationships between the molecular motion and the molecular structure or the molecular motion and the relaxation time, the reorientational correlation times were obtained from the viscosity measurements of solutions.

The correlation time, τ_c, in Eq. (4) is generally used in the rotational diffusion model of a liquid, which is concerned with the reorientational motion of a molecule as being impelled by a viscosity-related frictional force (Stokes-Einstein-Debye model). Gierer and Wirtz have introduced the idea of a microviscosity, f.[57] The reorientational

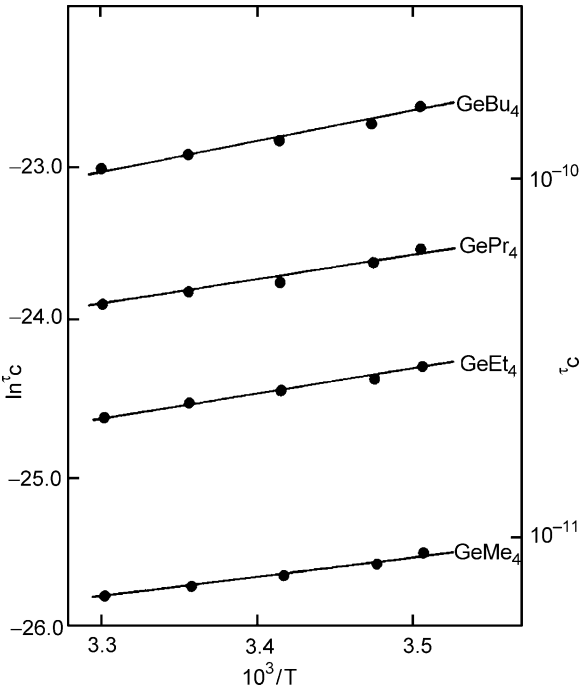

Fig. 14. Relationship between the correlation times of alkylgermanes and the reciprocal of the temperatures: **15** ($R = 0.996$); **121** ($R = 0.999$); **128** ($R = 1.000$); **129** ($R = 1.000$). Reproduced, with permission, from Harazono *et al.*,[56] Copyright 1987, American Chemical Society.

correlation time τ_c is given by Eq. (5). They determined τ_c at various temperatures from viscosity measurement. In Table 18, τ_c values at 30°C and the activation energies are listed.

In Fig. 14, plots of $\ln\tau_c$ of symmetrical tetraalkylgermanes against $1/T$ are given.

The plots gave straight lines. τ_c is usually well represented by an Arrhenius-type equation (Eq. (7)), where τ_c^0 is a constant and ΔE an activation energy for the reorientation. R is the gas constant.

$$\tau_c = \tau_c^0 \exp(\Delta E/RT) \tag{7}$$

with τ_c thus obtained, ΔE was estimated on the basis of Eq. (7). The correlation times become longer and the activation energies increase as the molecular radius increases in accordance with Eqs. (5) and (7). In Fig. 15, a plot of $\ln\tau_c$ vs. the molecular radius r is given. The correlation coefficient R is unity. In Fig. 16 a plot of the activation energy of reorientation ΔE vs. r is given. The linearity is also excellent.

The spin-lattice relaxation time (T_1) and spin–spin relaxation time (T_2) of ^{73}Ge nuclei in $GeBr_4$ and GeI_4 have been measured at various temperatures. It has been shown that T_1 is almost exclusively dominated by the quadrupole relaxation mechanism, while T_2 is dominated by the combination of the scalar coupling and the quadrupole relaxation mechanisms in the high-temperature region.[60]

As described elsewhere,[56] ^{73}Ge relaxes mostly via the quadrupole mechanism. Indeed, in the tetraalkylgermanes, T_1 is equal to T_2 within experimental error.[20] On the other hand, it was shown that T_1 is longer than T_2 for tetrahalogermanes. This is most remarkable for **88** in $CDCl_3$ at low temperature.[56] The T_1 (IR) and T_2 ($\Delta\nu_{1/2}$) values for **130** and **135** were also determined in toluene-d_8 at higher temperatures. Results for **130** at 25°C and **135** at 45°C in toluene-d_8 together with results for **130** in chloroform and **135** in a CS_2/benzene mixture are presented in Table 19.

T_1 is slightly longer than T_2 for **130**. On the other hand, for **135**, T_1 is identical with T_2 at 45°C. The relaxation times of compounds in toluene-d_8 were shown to be shorter than those in $CDCl_3$ or a CS_2/benzene mixture.[56] This is likely to be due to the higher viscosity of toluene-d_8 than that of chloroform-d_1 or a CS_2/benzene mixture. The authors further investigated the temperature dependency on T_1 and T_2 for ^{73}Ge in **130** and **135** in order to elucidate the relaxation mechanism.

Table 18. Values of τ_c and ΔE for tetraalkylgermanes

Compounds	$10^{11}\tau_c$(30°C), s	ΔE, kJ mol^{-1}
$GeMe_4$ (**15**)	0.69	9.6
$GeEt_4$ (**121**)	2.2	11.4
$GePr_4$ (**128**)	4.5	11.9
$GeBu_4$ (**129**)	10.9	13.2

Reproduced, with permission, from Harazono *et al.*,[20] Copyright 1987, American Chemical Society.

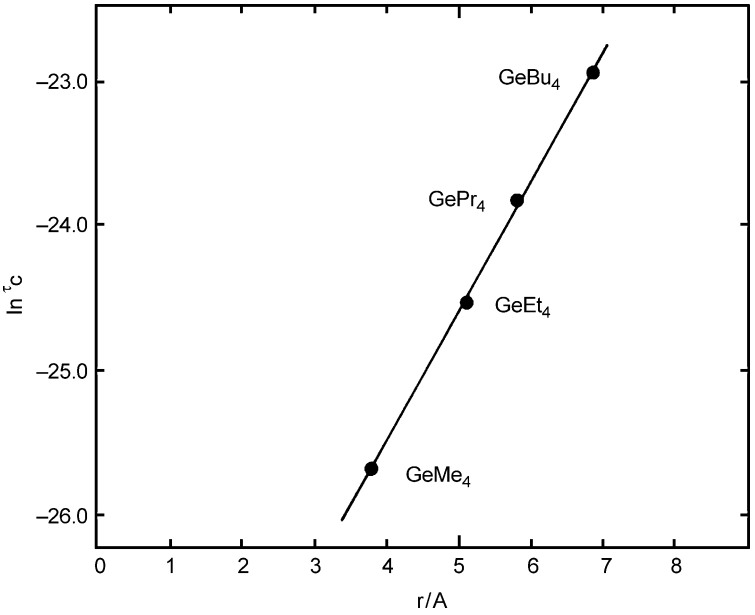

Fig. 15. Relationship between the correlation times and the molecular radii of alkylgermanes ($R = 1.000$). Reproduced, with permission, from Harazono *et al.*,[56] Copyright 1987, American Chemical Society.

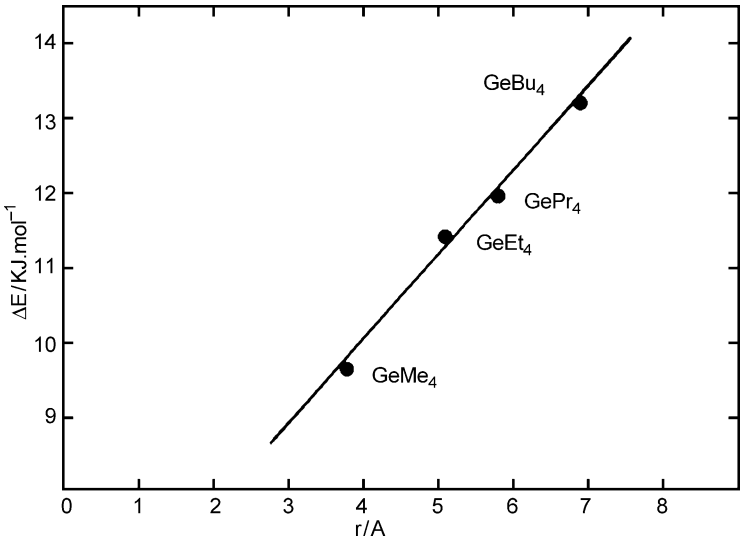

Fig. 16. Relationship between the activation energies and the molecular radii of alkylgermanes ($R = 0.996$). Reproduced, with permission, from Harazono *et al.*,[56] Copyright 1987, American Chemical Society.

Table 19. Values of T_1(IR) and $T_2(\Delta\nu_{1/2})$ for ^{73}Ge in tetrahalogermanes

Compound	Solvent	T_1(IR)/ms	$T_2(\Delta\nu_{1/2})$/ms	Temp/°C
Tetrabromogermane (**130**)	CDCl3	160	130	30
	toluene-d_8	88	81	25
Tetraiodogermane (**135**)	CS_2–C_6D_6 (1:1)	80	80	30
	toluene-d_8	51	50	45

Reproduced, with permission, from Harazono *et al.*,[20] Copyright 1987, American Chemical Society.

The reciprocals of the quadrupole relaxation time, $1/T_1^q$ and $1/T_2^q$, are reasonably represented by an Arrhenius-type equation as given in Eq. (8),

$$1/T_1^q = 1/T_2^q = A\exp(\Delta E/RT) \tag{8}$$

where A is a constant, ΔE is the activation energy, and R is the gas constant. The superscript 'q' indicates the quadrupole relaxation. If the relaxation occurs solely via the quadrupole relaxation mechanism, ln $(1/T_1^q)$ and $\ln(1/T_2^q)$ are proportional to the reciprocal of the absolute temperature, $1/T$(K). The plots of $\ln(1/T_1^q)$ or $\ln(1/T_2^q)$ against

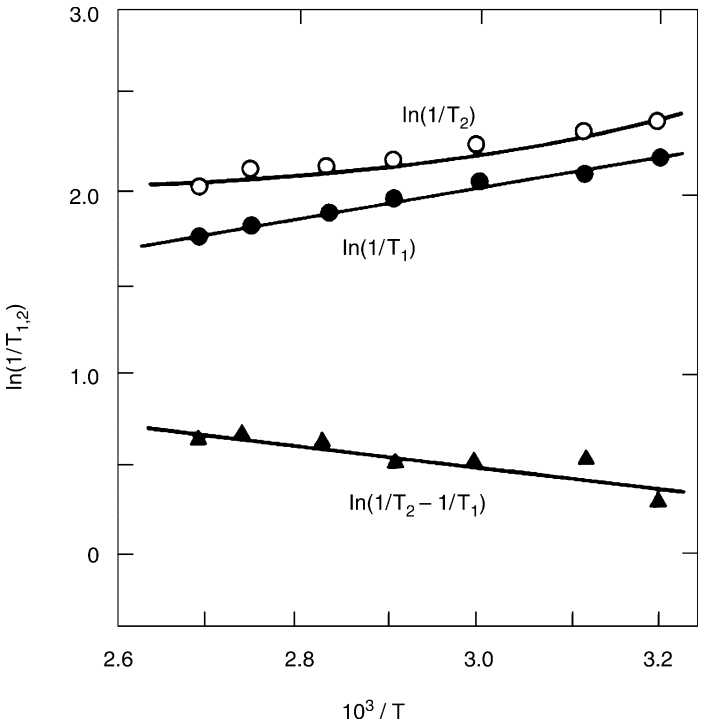

Fig. 17. Plot of $\ln(1/T_1)$, $\ln(1/T_2)$ and $\ln(1/T_2 - 1/T_1)$ vs. $1/T$ for ^{73}Ge in $GeBr_4$ **130**. Reproduced, with permission, from Harazono *et al.*,[60] Copyright 1989, American Chemical Society.

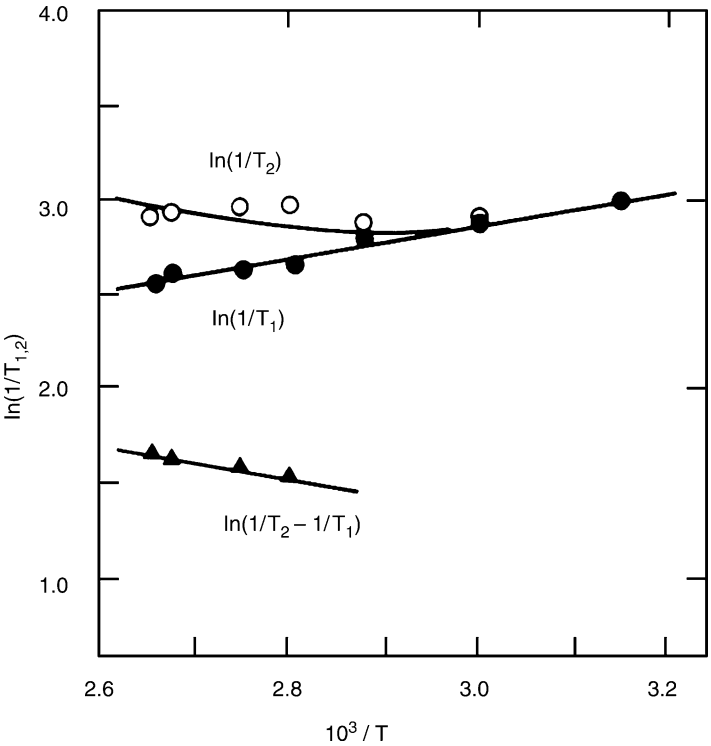

Fig. 18. Plot of $\ln(1/T_1)$, $\ln(1/T_2)$ and $\ln(1/T_2 - 1/T_1)$ vs. $1/T$ for ^{73}Ge in GeI_4 **135**. Reproduced, with permission, from Harazono *et al*.,[60] Copyright 1989, American Chemical Society.

$1/T$(K) should give straight lines with positive slopes. Plots of ln $(1/T_1)$ vs. $1/T$ and ln $(1/T_2)$ vs. $1/T$ for **130** and **135** are given in Figs. 17 and 18, respectively.

The plots of $\ln(1/T_1)$ vs. $1/T$ for both compounds give straight lines with positive slopes, which indicate that the spin-lattice relaxation of ^{73}Ge in both **130** and **135** is dominated by the quadrupole relaxation mechanism.

4. RECENT DEVELOPMENTS IN SOLID-STATE ^{73}Ge NMR

4.1. Introduction

In solution ^{73}Ge NMR spectroscopy, it is observed that when the symmetry of the structure around the germanium atom was high, a sharp signal could be observed (as found for ^{14}N NMR) while the signal tended to broaden as the symmetry was lost. For instance, the linewidth of tetramethylgermane **15**, a compound with the highest symmetry, is only 1.4 Hz.[61] while the corresponding values for germacyclohexane **108**,

1-methylgermacyclohexane **109** and 1,1-dimethylgermacyclohexane **55** are 15.4, 22.3 and 15.6 Hz, respectively.[17]

It is also observed that when either halogen or oxygen atoms are unsymmetrically substituted, as found in 1-bromo-1-methyl-1-germacyclohexane (**136**), an excessive broadening takes place to such an extent that observation of the signals is impossible. Given these factors, it has generally been accepted that observation of ^{73}Ge signals in the solid state would be even more difficult, and there had been no reports on ^{73}Ge signals of organogermanium compounds in the solid state.

The rapid development of NMR hard- and soft-ware has, however, made observation of ^{73}Ge signals more feasible. An appropriate modification of hardware might make it possible to observe solid-state high-resolution ^{73}Ge NMR spectra of organogermanium compounds with the aid of high field instruments. This was realized a few years ago.

4.2. Chemical shifts

Verkhovskii *et al.*[62] studied the influence of isotopic disorder on the local deformations in Ge single crystals from both experimental and calculation points of view. The NMR spectra of ^{73}Ge nuclei in perfect single crystals of germanium with different isotopic content were measured at temperatures 80, 300 and 450 K. Abnormal broadening of the spectrum was found to occur when the magnetic field was aligned along the [111] axis of a crystal. The observed specific angular dependence of the quadrupole broadening was attributed to isotopic disorder among atoms of germanium sited around the ^{73}Ge NMR probe. Local lattice deformations in the germanium crystal lattice due to isotopic impurity atoms were calculated in the framework of the adiabatic bond charge model. The results obtained were applied to study random non-cubic crystal field interactions with the nuclear quadrupole moments and corresponding effects in NMR spectra.

High resolution solid-state MAS ^{73}Ge NMR spectra of organogermanium compounds have been observed for the first time; the chemical shifts and linewidths of tetraphenylgermane (**38**) and tetrabenzylgermane (**137**) were recorded with and without high-power decoupling.[63]

The authors chose these two compounds for the first attempt because of their high symmetry. **38** gave an unexpectedly sharp signal, even without high-power proton decoupling, after an accumulation of a few hundred FIDs. Under similar measurement conditions, the linewidth of the signal of **137** is much broader, and required much more accumulation for signal recording. ^{73}Ge chemical shifts and the linewidth of the signals for **38** and **137** are given in Table 20. There is a small shift, in comparison to values to values in solution, arising from a solid-state effect. When high-power proton decoupling was applied to **38**, the linewidth became slightly smaller. Fig. 19 shows the ^{73}Ge NMR spectra of **38** and **137**.

The ^{73}Ge NMR spectrum for tetraethylgermane **121** (liquid) filled in a cell was measured without rotation and it was assumed that the chemical shift under this measurement condition was δ17.3 (the same value as in solution). The chemical shifts of **38** and **137** in the solid state are reference values.

Table 20. ^{73}Ge NMR parameters for **38** and **137** in the solid state[a]

Compound	δ_{Ge}	$\Delta\nu_{1/2}$ (Hz)
Tetraphenylgermane (**38**) (proton decoupled)	−31.0 (−3.6)	40 (6)
Tetraphenylgermane (**38**) (proton coupled)	−31.0	49
Tetrabenzylgermane (**137**) (proton decoupled)	0.14 (0.04)	ca. 350 (24)

Reproduced, with permission, from Takeuchi *et al.*,[63] Copyright 2000, Royal Society of Chemistry.
[a]Values in parentheses are solution data for the same compounds.

4.3. Relaxation times

The temperature dependence of the spin-lattice relaxation time corresponding to the inelastic scattering of phonons by the ^{73}Ge quadrupole moment in Ge single crystals is calculated in the framework of the adiabatic bond charge model. The results obtained agree with the experimental data.[64]

From the comparison of the measured and calculated temperature dependences of the relaxation time (see Fig. 20), it follows that the inelastic phonon scattering is the most essential mechanism of the spin-lattice relaxation for Ge. It is evident that only at low temperatures ($T < 30$K) some other mechanisms (the most probable one is the relaxation due to a small amount of paramagnetic impurities) become dominant. At $T > 300K$ some additional mechanism of relaxation may also exist. The interaction of the nuclear quadrupole moment with vibrations of the nearest four Ge atoms brings about the main contribution to the spin-lattice relaxation rate. The effective modulation of the EFG by the nearest bond charges is greatly reduced because of strong correlations between their displacements. As the main result of the present investigation of spin-lattice relaxation,

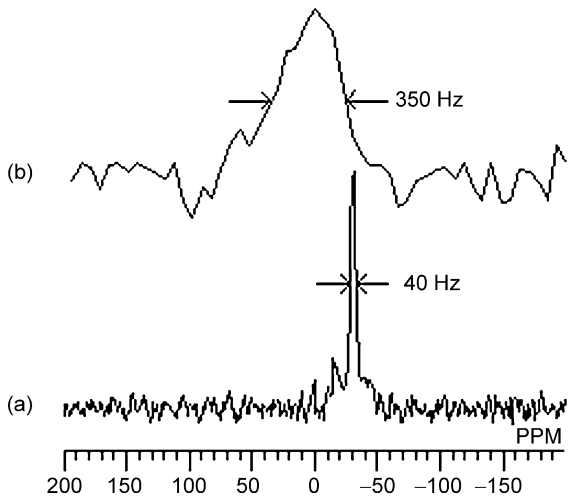

Fig. 19. Solid-state high-resolution ^{73}Ge NMR spectra of **38** (lower) and **137** (upper). Reproduced, with permission, from Takeuchi *et al.*,[63] Copyright 2000, Royal Society of Chemistry.

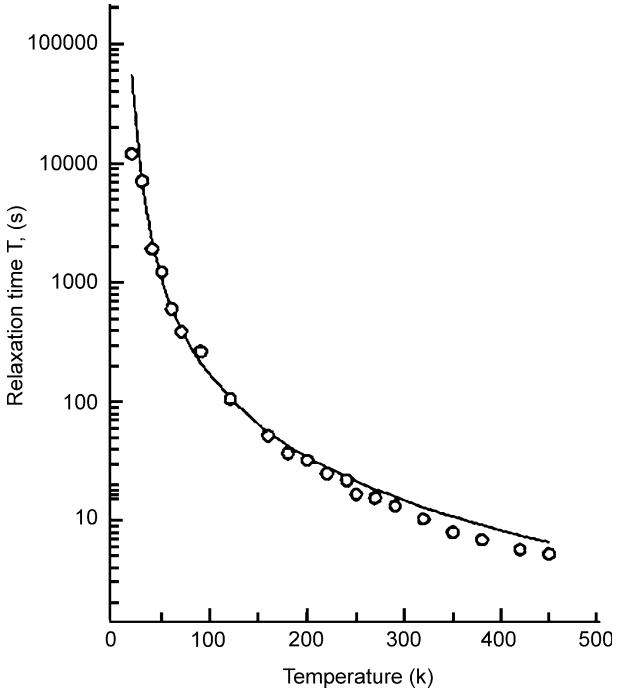

Fig. 20. The spin-lattice relaxation time for $^{73}Ge^{74}_{0.022}Ge_{0.97}$ sample. Results of calculations are presented by a solid line, open circles correspond to the measured data. Reproduced, with permission, from Malkin *et al.*,[64] Copyright 1998, Springer Verlag.

a simple model has been derived which can be used to estimate the quadrupole splittings for the ^{73}Ge nuclei induced by local deformations of the crystal lattice. This fact makes it possible to develop investigations of the NMR spectra as a method for the isotopic composition control in Ge crystals.

T_1 of ^{73}Ge nuclei of **38** and some other organogermanes in solid state and metallic germanium were determined under the high-resolution conditions.[65,66] The authors could determine T_1 of **38** with the inversion-recovery method. The measured T_1 of **38** with 2.6 s makes a sharp contrast with T_1 of the same compound in solution (0.42 s). Since it was rather hopeless to determine T_1 of **137** which has a large linewidth (350 Hz), the authors prepared some other symmetrically substituted tetraarylgermanes, $(p\text{-}C_6H_5C_6H_4)_4Ge$ (**138**) and $(p\text{-}MeC_6H_4)_4Ge$ (**139**). The linewidth of **138** is 78 Hz while that of **139** is as large as 390 Hz. It was possible to determine T_1 of **138** (ca. 1.2 s) although the error might be proportionally large. T_1 values for **137** and **139** could not be obtained accurately, but it was possible to estimate safely, from the null-points of inversion-recovery stack plots, these are of the order of 0.1 s (e.g., ca. 0.6 s for **139**). Now it may be concluded that T_1 values of symmetrically substituted germanes are of the order of seconds, and that the value decreases to the order of 0.1 s as the linewidths of the signals increase.

T_1 values are found to be of the order of seconds in agreement with the reported value for metallic germanium determined in the static condition. Since the measurement of T_1

for germanium single crystals (**140**) by Russian investigators[62] was carried out without MAS, the measurement of powdered germanium (**141**) (natural isotopic abundance sample) was repeated with and without MAS by the inversion-recovery method. A typical stacked plot is given in Fig. 21.

The T_1 value obtained is 10.6 s, which is essentially identical with the reported value. At the natural abundance level, the linewidth of germanium is ca. 40–80 Hz.[67]

The measurement without MAS also gives the value of 60 Hz, but with MAS the signal is substantially sharpened, and the linewidth is 18 Hz, which indicates that the MAS does affect on the linewidth to a considerable extent. Since there is little, if any, dipolar interaction among germanium nuclei in the solid state, MAS seems to reduce the broadening due to the quadrupolar interaction to some extent.

One interesting aspect as for the linewidth is the value for the isotopically enriched germanium compound. The linewidth and T_1 value of the isotopically enriched germanium compound ($>$98 at. wt%) were determined. Although there is no change in T_1, the linewidth is increased to 230 Hz (Fig. 22). This can be explained in terms of the homonuclear dipole interaction[68,69] among the same isotopes which makes difficult the measurement of solid state NMR for some abundant nuclei. Since ^{73}Ge is a quadrupolar nucleus, the spin-lattice relaxation would most likely proceed via a quadrupolar mechanism. The authors determined T_1 of **141** at temperatures ranging from 290 to 370 K. Although the range is narrow, the temperature dependence of T_1 is clear; there is a negative dependence, i.e., as the temperature increases, T_1 linearly decreases (Fig. 23). The investigators also determined the temperature dependence of T_1 of **140** at lower temperatures; at 300 K, T_1 is ca. 12 s while at 50 K it is as long as 1300 s, and based on this, they concluded that the relaxation proceeds via a quadrupolar mechanism.

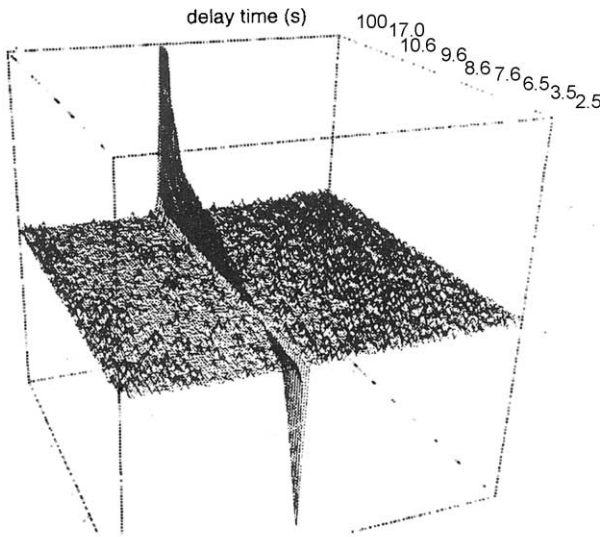

Fig. 21. ^{73}Ge inversion-recovery spectra of germanium. Reproduced, with permission, from Takeuchi *et al.*,[65] Copyright 2001, Chemical Society of Japan.

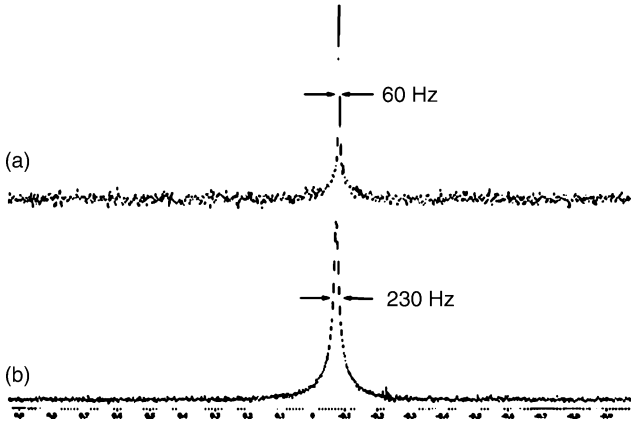

Fig. 22. ^{73}Ge linewidth of natural abundance and enriched germanium metal. (a) Natural abundance sample. (b) ^{73}Ge enriched sample. Reproduced, with permission, from Takeuchi *et al*.,[65] Copyright 2001, Chemical Society of Japan.

The authors believe that in the case of organogermanium compounds, the relaxation mechanism in the solid state is the same as that in solution where the quadrupolar mechanism was proved predominant.[61] They could confirm the absence of a dipolar mechanism by determining that the NOE enhancement factor is zero for **38**.

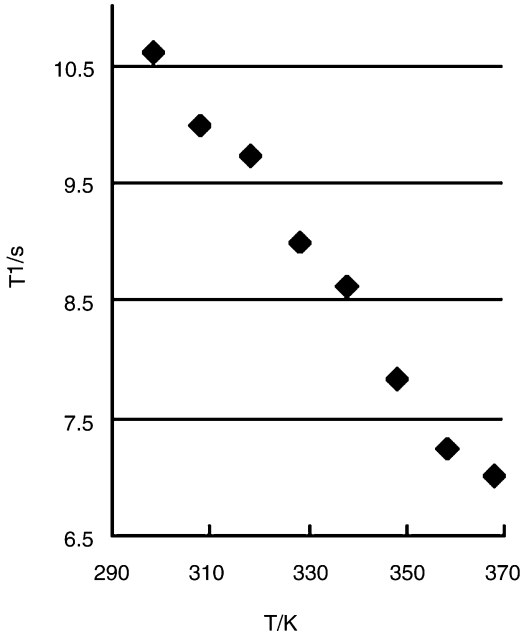

Fig. 23. Temperature dependence of T_1 of **141**. Reproduced, with permission, from Takeuchi *et al*.,[65] Copyright 2001, Chemical Society of Japan.

5. CONCLUSIONS

Recent progress in ^{73}Ge NMR spectroscopy has been briefly reviewed. The crucial point of heteronuclear NMR spectroscopy is the extent to which it can achieve that which may be carried out by ^{1}H and ^{13}C NMR spectroscopy. As described in this review, ^{73}Ge NMR spectroscopy can employ almost all techniques used in ^{1}H and ^{13}C NMR spectroscopy. There exists, however, a severe limitation in ^{73}Ge NMR spectroscopy. ^{73}Ge is a quadrupolar nucleus and a high symmetry of electric field gradient around germanium is required for proper observation of signals. Acoustic ringing is another problem associated with ^{73}Ge NMR spectroscopy.

Although the latter can now be substantially reduced with the aid of modern pulse techniques, at the moment there is no complete remedy for the broadening inherent to quadrupolar nuclei. A breakthrough which will make ^{73}Ge NMR spectroscopy a more feasible technique is highly desired.

Recently high resolution solid state ^{73}Ge NMR spectra of hexacoordinated germanium species, i.e., diiodogermylene and bis(1-pyrrolyl)(*meso*-tetraphenylporphyrinato)germanium were determined.[70]

ACKNOWLEDGEMENTS

Y. T. thanks The Ministry of Education, Culture, Sports, Science and Technology for the grant to the High-Tech Research Center Project, with the aid of which this review was prepared.

REFERENCES

1. H. C. Marsmann, *The Chemistry of Organic Germanium, Tin and Lead Compounds*, Vol. 2, Z. Rappoport and Y. Apeloig, eds., Wiley, New York, 2002.
2. R. K. Harris, J. D. Kennedy and W. McFalane, *NMR and the Periodic Table*, R. K. Harris and B. E. Mann, eds., Academic Press, London, 1978, p. 309.
3. J. D. Kennedy and W. McFalane, *Multinuclear NMR*, J. Mason, ed., Plenum Press, New York, 1987, p. 305.
4. K. M. Mackay and R. A. Thomson, *Main Group Metal Chem.*, 1987, **10**, 83.
5. E. Liepins, I. Zicmane and E. Lukevics, *J. Organomet. Chem.*, 1988, **341**, 315.
6. R. A. Thomson, A. L. Wilkins and K. M. Mackay, *Phosphorus, Sulfur and Silicon*, 1999, **150–151**, 319.
7. P. S. Belton, I. J. Cox and R. K. Harris, *J. Chem. Soc. Faraday Trans.*, 1985, **81**, 63.
8. S. L. Patt, *J. Magn. Reson.*, 1982, **49**, 161.
9. A. L. Wilkins, R. A. Thomson and K. M. Mackay, *Main Group Metal Chem.*, 1990, **13**, 219.
10. Y. Takeuchi, M. Shimoda, K. Tanaka, S. Tomoda, K. Ogawa and H. Suzuki, *J. Chem. Soc. Perkin Trans.*, 1988, **2**, 7.
11. Y. Takeuchi, *Frontiers of Organogermanium, -Tin and -Lead Chemistry*, E. Lukevics and L. Ignatovich, eds., Latvian Institute of Organic Synthesis, Riga, 1993, p. 121.
12. Y. Takeuchi, *Nippon Kagaku Kaishi*, 1994, 185.
13. Y. Takeuchi, H. Inagaki, K. Tanaka and S. Yoshimura, *Magn. Reson. Chem.*, 1989, **27**, 72.
14. E. Liepins, I. Zicmane, L. M. Ignatovich and E. Lukevics, *J. Organomet. Chem.*, 1990, **389**, 23.
15. E. Liepins, M. V. Petrova, E. T. Bogoradovsky and V. S. Zavgorodny, *J. Organomet. Chem.*, 1991, **410**, 287.
16. S. Aoyagi, K. Tanaka, L. Zicmane and Y. Takeuchi, *J. Chem. Soc. Perkin Trans.*, 1992, **2**, 2217.

17. Y. Takeuchi, M. Shimoda and S. Tomada, *Magn. Reson. Chem.*, 1985, **23**, 580.
18. I. Zicmane, E. Liepins, E. Lukevics and T. K. Gar, *Zh. Obshch. Khim.*, 1982, **52**, 896.
19. K. Ogawa, K. Tanaka, S. Yoshimura and Y. Takeuchi, *Acta Crystallogr.*, 1991, **C47**, 2558.
20. T. Harazono, K. Tanaka and Y. Takeuchi, *Inorg.Chem.*, 1987, **26**, 1894.
21. S. Aoyagi, K. Tanaka and Y. Takeuchi, *J. Chem. Soc. Perkin Trans.*, 1994, **2**, 1549.
22. Y. Takeuchi, K. Ogawa, G. Manuel, R. Boukherroub and I. Zicmane, *Main Group Metal Chem.*, 1994, **17**, 121.
23. K. Ogawa, Y. Takeuchi, G. Manuel and R. Boukherroub, *Acta Cryst.*, 1994, **C50**, 1337.
24. F. Reidmiller, G. L. Wegner, A. Jockish and H. Schmidbaur, *Organometallics*, 1999, **18**, 4317.
25. E. A. V. Ebsworth, D. W. H. Rankin and S. Cradock, *Structural Methods in Inorganic Chemistry*, 2nd edition, Blackwell, Oxford, 1987.
26. (a) K. M. Mackay, P. J. Watkinson and A. L. Wilkins, *J. Chem. Soc. Dalton Trans.*, 1984, **2**, 133; (b) A. L. Wilkins, P. J. Watkinson and K. M. Mackay, *J. Chem. Soc. Dalton Trans.*, 1987, **10**, 2365.
27. (a) H. Schmidbaur and J. Rott, *Z. Naturforsch*, 1990, **45b**, 961; (b) H. Schmidbaur and J. Rott, *Z. Naturforsch*, 1989, **44b**, 285; (c) H. Schmidbaur, J. Rott, G. Reber and G. Z. Muller, *Z. Naturforsch*, 1988, **43b**, 727.
28. R. K. Harris, *Proceedings of the NATO Advanced Study on the Multinuclear Approach to NMR-Spectroscopy*, J. P. Lambert, F. G. Reidel and D. Reidel, eds., Kluwer, Dordrecht, 1987.
29. K.-Y. Akiba, ed., *Chemistry of Hypervalent Compounds*, Wiley-VCH, 1998.
30. E. Kupce, L. M. Ignatovitch and E. Lukevics, *J. Organomet. Chem.*, 1989, **372**, 189.
31. E. Kupce, E. Lukevics, O. D. Flid, N. A. Viktorov and T. K. Gar, *J. Organomet. Chem.*, 1989, **372**, 187.
32. A. Viktorov, S. N. Gurkova, A. I. Gusev, T. K. Gar and V. F. Mironov, *Metalloorg. Khim.*, 1988, **1**, 715.
33. G. I. Zelcans, A. F. Lapsina, I. I. Solomennikova, E. Lukevics, E. E. Liepins and E. L. Kupce, *Zh. Obshch. Khim.*, 1983, **53**, 1069.
34. V. A. Pestunovich, S. N. Tandura, B. Z. Shterenberg, N. Yu. Khromova, T. K. Gar, V. F. Mironov and M. G. Voronkov, *Izv. Akad. Nauk SSSR, Ser. Khim.*, 1980, 959.
35. P. Geerlings and C. Van Alsenoy, *J. Organometal. Chem.*, 1976, **117**, 13.
36. C. Brelière, F. Carré, R. J. P. Corriu and G. Royo, *Organometallics*, 1988, **7**, 1006.
37. C. Brelière, F. Carré, R. J. P. Corriu, G. Royo and M. W. C. Man, *Organometallics*, 1994, **13**, 307.
38. Y. Takeuchi, H. Yamamoto, K. Tanaka, K. Ogawa, J. Harada, T. Iwamoto and H. Yuge, *Tetrahedron*, 1998, **54**, 9811.
39. Y. Takeuchi, K. Tanaka, S. Aoyagi and H. Yamamoto, *Magn. Reson. Chem.*, 2002, **40**, 241.
40. C. Chuit, R. J. P. Corriu, C. Reye and J. C. Young, *Chem. Rev.*, 1993, **93**, 1371.
41. Y. Takeuchi, M. Nishikawa, K. Tanaka and G. Yamamoto, *Heteroatom Chem.*, 2001, **12**, 451.
42. E. Kupce, E. Upena, M. Trusule and E. Lukevics, *Polyhedron*, 1989, **8**, 2641.
43. E. Kupce and E. Lukevics, *J. Chem. Soc. Dalton Trans.*, 1990, 2319.
44. E. Kupce and E. Lukevics, *J. Magn. Reson.*, 1988, **79**, 325.
45. Y. Takeuchi, K. Tanaka, T. Harazono and S. Yoshimura, *Bull. Chem. Soc. Jpn*, 1990, **63**, 708.
46. Y. Takeuchi, K. Tanaka and T. Harazono, *Bull. Chem. Soc. Jpn*, 1991, **64**, 91.
47. U. Burkert, *Angew. Chem. Int. Ed. Engl.*, 1981, **20**, 572.
48. H. Nakatsuji and T. Nakao, *Int. J. Quantum Chem.*, 1994, **49**, 279.
49. H. Nakatsuji, *J. Chem. Phys.*, 1974, **61**, 3728.
50. H. Nakatsuji, K. Kanda, K. Endo and T. Yonezawa, *J. Am. Chem. Soc.*, 1984, **106**, 4653.
51. H. F. King, M. Dupuis and J. Rys, *Program Library HONDOG (No. 343)*, The Computer Center of the Institute for Molecular Science, Okazaki, 1979.
52. J. H. Callomon, E. Hirota, K. Kuchitsu, W. J. Lafferty, A. G. Maki and C. S. Pote, *Landolt-Bornstein New Series Supplement II/7*, K. H. Hellwege and A. M. Hellwege, eds., Springer, Berlin, 1987.
53. S. Huzinaga, J. Andzelm, M. Klobukowski, E. Radzio-Andzelm, Y. Sakai and H. Tatewaki, *Gaussian Basis Sets for Moleculations*, Elsevier, New York, 1984.
54. T. Harazono, K. Tanaka and Y. Takeuchi, *Bull. Chem. Soc. Jpn*, 1989, **62**, 919.
55. A. Abragam, *The Principles of Nuclear Magnetism*, Oxford University Press, London, 1961, Chapter 8.
56. T. Harazono, K. Tanaka, Y. Takeuchi and H. Fukutomi, *Inorg.Chem.*, 1987, **26**, 3851.
57. A. Gierer and K. Wirtz, *Z. Naturforsch*, 1953, **A8**, 532.

58. I. P. Sekatsis, E. E. Liepin'sh, I. A. Zitmane and E. Lukevits, *Zh. Obshch.*, 1983, **53**, 2064.
59. B. Wrackmeyer and P. Bernatowicz, *Magn. Reson. Chem.*, 1999, **37**, 418.
60. T. Harazono, K. Tanaka and Y. Takeuchi, *Inorg. Chem.*, 1989, **28**, 1813.
61. Y. Takeuchi, T. Harazono and N. Kakimoto, *Inorg. Chem.*, 1984, **23**, 3835.
62. S. V. Verkhovskii, A. Y. Yakubovskii, A. Trokiner, B. Z. Malkin, S. K. Saikin, V. I. Ozhogin, A. V. Tikhomirov, A. V. Ananyev, A. P. Gerashenko and Y. V. Piskunov, *Appl. Magn. Reson.*, 1999, **17**, 557.
63. Y. Takeuchi, M. Nishikawa, K. Tanaka, T. Takayama, M. Imanari, K. Deguchi, T. Fujito and Y. Sugisawa, *Chem. Commun.*, 2000, 687.
64. B. Z. Malkin, S. K. Saikin and V. I. Ozhogin, *Appl. Magn. Reson.*, 1998, **14**, 513.
65. Y. Takeuchi, M. Nishikawa, K. Tanaka and T. Takayama, *Chem. Lett.*, 2001, 572.
66. Y. Takeuchi and M. Nishikawa, Unpublished results.
67. S. V. Verkhovskii, B. Z. Malkin, A. Trokiner, A. Yakubovskii, E. Haller, A. Ananyev, A. Gerashenko, Yu. Piskunov, S. Saikin, A. Tikhomirov and V. Ozhogin, *Z. Naturforch.*, 2000, **55**, 105, and references therein.
68. I. J. Lowe, *Phys. Rev. Lett.*, 1959, **2**, 285.
69. E. R. Andrew, A. Bradbury and R. G. Eades, *Nature*, 1959, **183**, 1802.
70. Y. Takeuchi, M. Nishikawa and H. Yamamoto, *Magn. Reso. Chem.*, in press.

NMR Studies of Purines

RADEK MAREK AND VLADIMÍR SKLENÁŘ

National Center for Biomolecular Research, Faculty of Science, Masaryk University, Kotlářská 2, CZ-61137 Brno, Czech Republic

This contribution reviews applications of NMR spectroscopy in the investigation of the structure and the intra- and intermolecular interactions of purine derivatives. Purines represent a highly important class of heterocyclic compounds that are widely distributed in all living organisms, not only as constituents of nucleic acids, but also as signal molecules. Their structure, electron distribution, and proton-transfer processes determine their chemical reactivity, interactions with solvents, and, subsequently, also

ANNUAL REPORTS ON NMR SPECTROSCOPY
VOLUME 54 ISSN 0066 4103
DOI 10.1016/S0066-4103(04)54005-X

their biological activity and function. Along with X-ray diffraction, NMR spectroscopy represents one of the most important experimental tools for investigating molecular topology at the atomic level. In the following text, NMR methods suitable for studying the purine structure and their application to exploring samples at natural levels of the ^{13}C and ^{15}N isotopes are briefly reviewed. As will be shown, isotropic ^{13}C and ^{15}N chemical shifts, $^{1}H-^{13}C$ one- and three-bond J-coupling constants and $^{1}H-^{15}N$ one- and two-bond couplings are the commonly used characteristic parameters for NMR in the solution state. In the solid state, CP MAS spectra of powder samples provide the principal values of the chemical-shift tensors. Quantum-chemical calculations on the DFT level support and explain the experimental data. Due to the extremely wide scope of the topic, no attempt is made to cover the area completely. Rather, typical examples of applications and recently published contributions in all of the areas identified above are included to provide the reader with a summary of the current efforts to increase our knowledge and understanding of the interactions at the atomic, molecular and intermolecular levels in purine and its derivatives.

1. INTRODUCTION

1.1. Purine skeleton

Purine (**1**), systematic name 9H-imidazo[4,5-*d*]pyrimidine, consists of two fused, nitrogen-containing aromatic rings. Purine derivatives represent an integral part of all living organisms,[1] not only as basic constituents of nucleic acids, but also as ligands interacting with enzymes and proteins, and as a part of the cofactors and signal molecules involved in recognition processes. Adenine (**2**) and guanine (**3**), the two most important and widely distributed derivatives of the purine base, are the essential building elements of nucleic acids. Intracellular ATP plays a fundamental role in energy metabolism, nucleic acid synthesis, pump activities, and enzyme regulation. Additionally, extensive evidence indicates that extracellular adenine nucleos(t)ides mediate signals via membrane-associated adenosine and ATP receptors.[2]

Other key derivatives, xanthine (2,6-dihydroxypurine, **4**) and hypoxanthine (6-hydroxypurine, **5**), are formed by the hydrolytic decomposition of nucleic acids. As their systematic names indicate, the well-known CNS stimulants caffeine (1,3,7-trimethylxanthine, **6**), theophylline (1,3-dimethylxanthine), and theobromine (3,7-dimethylxanthine), found in coffee, tea, and cocoa beans, respectively, are all derived from xanthine.

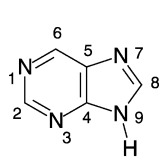

1

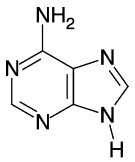

2

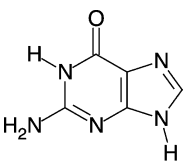

3

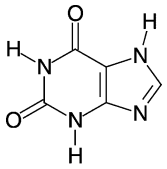

4

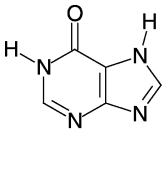

5

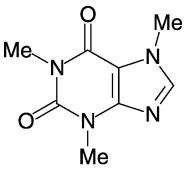

6

The acid–base character of the purines affects a number of phenomena such as self-association, interaction with metal ions, molecular recognition by proteins, and the base-pairing of nucleic acids.[3–5] For many years, the interest of numerous laboratories has been focused mainly on the natural purine bases adenine and guanine. However, chemical investigations in the second half of the 20th century and the resulting substitutions and modifications of the purine skeleton, have opened new horizons in purine chemistry. Myriad purine derivatives have now been synthesized. Many of them exhibit significant and attractive pharmacological properties. Purine analogs have been used to develop highly successful drugs to treat AIDS and associated disorders because of their antiviral[6] and antitumor activity.[7] Various purine derivatives interact with proteins as biological targets, e.g., as inhibitors of the reverse transcriptase or the cyclin-dependent kinase.

A purine base contains one pyrimidine and one imidazole ring connected via a shared (C4–C5) aromatic bond. One nitrogen atom in the purine base is generally protonated. Due to the presence of several nitrogen sites, several tautomers usually co-exist both in solution and in the solid state. The populations of individual tautomers are strongly influenced by the substitution of the purine base, the temperature, the pH, the solvent, and the salt concentration.

As with other aromatic compounds, the distribution of electrons plays a crucial role in the intermolecular interactions and controls the reactivity of the purine base. The electron densities differ substantially in five- and six-membered rings of heterocycles. The electron density in a five-membered ring is usually larger and is responsible for the predominant populations of the N^7-H and N^9-H tautomers. The number of tautomers increases when the purine moiety carries substituents such as amino, oxo, or thioxo groups. Amino tautomers and oxo- or thioxo-tautomers are the main species formed in solution. However, minor tautomers are of considerable importance. They can form odd base pairs within nucleic acids, thereby causing mutagenic events.

In general, the N-7 and N-9 nitrogens are also the centers of the N-alkylation processes.[8] But not exclusively; some N^3-alkylated adenine derivatives (discadenine), possessing cytokinine activity, have also been isolated from natural sources.

As will be discussed in the following sections, the NMR chemical shifts and coupling constants reflect the electron distribution very sensitively and can be used to investigate the structure and electron distribution in great detail.

1.2. Detection of NMR parameters and referencing of chemical shifts

The NMR parameters of purines can be obtained by directly measuring the nucleus of interest or by using a wide variety of inverse-detected experiments. Experiments based on proton detection are significantly more sensitive than techniques that directly observe the nucleus in question. Although, enhancements in signal-to-noise ratio of 31.96 (^{13}C) and 305.92 (^{15}N) represent only the theoretical, practically unachievable limits, inverse experiments are preferred in most cases, especially for investigating ^{15}N nuclei.

One-bond ^{1}H–^{13}C chemical-shift correlation experiments facilitate the assignment of protonated carbons (C-2 or C-8 or both). Both multiple-quantum-HMQC[9] and single-quantum-HSQC[10] versions, optimized for $^{1}J_{H,C} \sim 200$ Hz can be applied. The quaternary carbons C-4, C-5, and C-6 are identified using long-range ^{1}H–^{13}C correlation techniques (gradient-selected heteronuclear multiple bond correlation (g-HMBC);[11,12] gradient-selected single-quantum multiple bond correlation (GSQMBC)[13,14]), based on the spin–spin scalar interactions of H-2 with C-4 and C-6 and of H-8 with C-4 and C-5. These experiments are typically adjusted for the coupling constant $^{3}J_{H,C} \sim 7.5$ Hz. The actual values of the three-bond ^{1}H–^{13}C coupling constants can be extracted from the INEPT, HMBC, or GSQMBC spectra.[15,16] For derivatives substituted at both positions 2 and 6 (or 6 and 8), four-bond interactions H8–C6 (or H2–C5) can be detected using experiments with an evolution delay $\tau \sim 120$–200 ms ($^{4}J \sim 2.5$–4.2 Hz). The presence of chemical exchange processes necessitates a compromise between relaxation and quantitative *J*-coupling evolution and substantially shorter evolution periods (16–20 ms) are used.

Similarly, the measurements of ^{15}N chemical shifts and two-bond ^{1}H–^{15}N coupling constants at natural abundance is usually based on INEPT and variants of multiple-quantum and single-quantum multiple-bond correlation experiments.[17]

The ^{1}H and ^{13}C chemical shifts reported in this review are referenced to tetramethylsilane (TMS) as the internal standard on the δ scale (ppm). Liquid NH_3 has been used as the external standard for the ^{15}N chemical shifts, with the following values employed to correct the chemical shifts originally reported relative to other commonly used standards: liquid NH_3 (0.0 ppm), 1 M urea in DMSO (77.0 ppm), 1 M HNO_3 in H_2O (377.3), liquid $MeNO_2$ (381.7 ppm).[18] Liquid nitromethane and 1 M urea in DMSO-d_6 are frequently used as secondary external standards for measurements in coaxial systems or in separate experiments. A more detailed discussion can be found in recently published review articles on nitrogen NMR spectroscopy.[17,19–21]

The use of Ξ ratios allows the indirect referencing of ^{13}C and ^{15}N chemical shifts through direct referencing to a single, well-determined ^{1}H standard.[18] The Ξ ratio is independent of both the spectrometer design and the sample geometry and therefore provides an accurate and consistent way to reference ^{13}C and ^{15}N chemical shifts.

All spin–spin scalar coupling constants are reported in Hertz.

2. NMR METHODOLOGY

The distribution of electrons around the purine skeleton affects not only its chemical properties and reactivity but also the basic parameters of its NMR spectra – chemical

shielding and spin–spin scalar interactions. The ^{13}C and ^{15}N NMR chemical shifts and the $^{1}H-^{13}C$ and $^{1}H-^{15}N$ coupling constants are characteristic indicators of the substitution patterns, proton exchange, and electron-mediated interactions associated with the purine skeleton. Since our review is focused mainly on samples with a natural abundance of ^{13}C and ^{15}N isotopes, we do not discuss the $^{13}C-^{13}C$, $^{13}C-^{15}N$, and $^{15}N-^{15}N$ coupling constants. However, these couplings were determined experimentally for a limited number of compounds.[22,23] Theoretical values obtained by DFT calculations for the free bases and the AU and GC base-pairs have also been published recently.[24] The chemical synthesis of C-13 and N-15 labeled nucleosides for site-specific incorporation into the RNA and DNA oligonucleotides used in numerous biochemical studies has recently been reviewed.[25]

2.1. ^{1}H chemical shifts

The ^{1}H NMR chemical shifts of the H-2 and H-8 atoms in purine derivatives are significantly deshielded due to the aromatic nature of the purine ring. Their NMR signals are located in the relatively narrow region ($\sim$7.5–9.5 ppm). The resonance frequencies, however, are characteristically influenced by substitution, protonation, alkylation, complexation, and intermolecular interactions. For example, when a hydrogen atom at position C-2 is replaced by an NH_2 group, the H-8 resonance becomes more shielded (by $\sim$0.3–0.6 ppm) because of the conjugation of the NH_2 group with the aromatic purine system. Because they are the most NMR sensitive, proton resonances are currently the most commonly used for monitoring the protonation and weak coordination processes of biological samples. ^{1}H chemical shifts are highly sensitive to solvent effects, which makes it more complicated to use them to elucidate structure. This is of no surprise, considering the fact that both hydrogen atoms H-2 and H-8 are located in the outer sphere of the molecule.

The measurement of various NMR parameters is demonstrated for 6-methoxy-N^7-benzylpurine in DMSO-d_6 solution. Its ^{1}H NMR spectrum is shown in Fig. 1. The ^{1}H-NMR chemical shifts[26–34] of selected purine derivatives **7** are summarized in Tables 1–3.

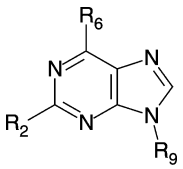

7

2.2. ^{13}C chemical shifts

The ^{13}C chemical shifts of the purine carbon atoms are found in the range typical for heteroaromatic compounds.[35] For purine and adenine derivatives without heavy-atom substitution, the resonances of the C-2 and C-8 atoms are located between 135 and 155 ppm. Their chemical shifts are significantly influenced by the presence of the lone

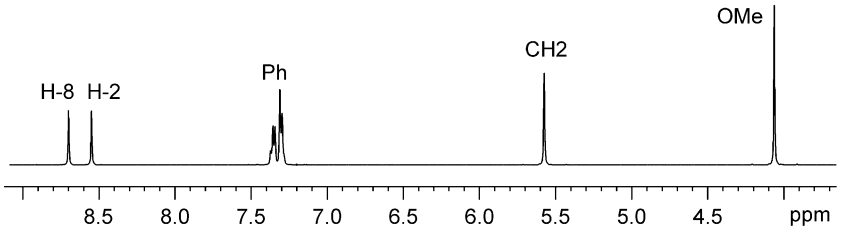

Fig. 1. ^{1}H NMR spectrum of 6-methoxy-N^{7}-benzylpurine.

pair of electrons on the neighboring nitrogen atoms. For example, the chemical shift of C-8 is ~6–18 ppm larger for N^{1}- and N^{3}- than for N^{7}- and N^{9}- isomers.[36] Further, the C-8 atom is always 2–6 ppm more shielded in the N^{9}-isomer than in the corresponding N^{7}-substituted compound due to the different electron distribution in the aromatic skeleton, and the C-8 atom is slightly more shielded in the N^{3}-isomer than in the corresponding N^{1}-analog.

The effect of a neighboring nitrogen atom is also observed for the C-2 resonance. While the C-2 atom in N^{1}-methylpurine and N^{3}-methylpurine resonates at ~144 ppm, the chemical shift of the same carbon atom in N^{7}-methylpurine and N^{9}-methylpurine is ~152 ppm.

C-5 is typically the most shielded quaternary carbon atom due to the presence of only one neighboring electron-accepting nitrogen atom. Depending on the substitution of the purine ring, this atom resonates in the range of approximately 110–140 ppm. The second bridgehead carbon atom C-4 is usually more deshielded due to the electronic effects of the two neighboring nitrogens N-3 and N-9. The resonance of C-4 is typically located in the range 145–165 ppm. The C-6 resonance is always more shielded (~4–12 ppm) in N^{7}-substituted compounds than in N^{9}-derivatives. For C^{6}-substituted derivatives, the chemical shift of the C-6 atom increases in the order of substituents I < Cl < NH_2 < MeO. Replacement of the 6-Cl by 6-I thus increases the shielding of the C-6 atom by ~12–25 ppm. A similar effect is observed if the 6-Cl

Table 1. ^{1}H NMR chemical shifts (ppm)[26] of selected 6-substituted purines in DMSO-d_6

6-Substituent	H-2	H-8
$-N(CH_3)_2$	8.19	8.07
$-NH_2$	8.20	8.17
$-OCH_3$	8.57	8.40
–I	8.63	8.60
$-SCH_3$	8.75	8.47
$-CH_3$	8.80	8.55
–Cl	8.80	8.73
–H	9.00	8.67
–CN	9.12	8.93

Table 2. ^{1}H NMR chemical shifts (ppm)[27] of selected 2,6-disubstituted purines in DMSO-d_6

2-Substituent	6-Substituent	H-8
$-N(CH_3)_2$	$-NH_2$	7.72
$-NH_2$	$-NH_2$	7.76
$-NH_2$	$-SCH_3$	7.93
$-NH_2$	$-CH_3$	7.98
$-SCH_3$	$-NH_2$	8.02
$-Cl$	$-NH_2$	8.13
$-F$	$-NH_2$	8.16
$-SCH_3$	$-SCH_3$	8.32
$-Cl$	$-OCH_3$	8.45
$-Cl$	$-CH_3$	8.64
$-H$	$-H$	8.68
$-Br$	$-Br$	8.70
$-Cl$	$-Cl$	8.77
$-CF_3$	$-Cl$	8.97

atom is displaced by 6-C≡CH group. ^{13}C NMR chemical shifts of selected purine derivatives are summarized in Table 4. The ^{13}C NMR spectrum of 6-methoxy-N^7-benzylpurine is shown in Fig. 2A along with partial spectra with (Fig. 2B) and without (Fig. 2C) ^{1}H-decoupling.

Table 3. ^{1}H NMR chemical shifts (ppm) of selected purine derivatives **7** in DMSO-d_6 (D) and $CDCl_3$ (C)[28–34]

Compound			H-2	H-8	Solvent
2-Substituent	6-Substituent	N9-Substituent			
$-H$	$-CN$	$-H$	9.04	8.65	D[28]
$-NH_2$	$-CN$	$-H$	–	8.32	D[28]
$-H$	$-CF_3$	$-H$	9.09	8.84	C[29]
$-H$	$-CF_3$	$-R$	9.19	9.14	D[30]
$-NH_2$	$-CF_3$	$-H$	–	8.27	D[29]
$-NH_2$	$-CF_3$	$-R$	–	8.53	D[30]
$-H$	$-Ph$	$-H$	8.96	8.64	D[31]
$-NH_2$	$-Ph$	$-H$	–	8.14	D[31]
$-I$	$-Cl$	$-H$	–	8.68	D[32]
$-Cl$	$-Me$	$-H$	–	8.59	D[33]
$-Cl$	$-Me$	$-Bz$	–	7.96	D[33]
$-Cl$	$-Me$	$-R$	–	8.80	D[33]
$-Me$	$-Me$	$-H$	–	8.44	D[33]
$-Me$	$-Me$	$-Bz$	–	7.86	C[33]
$-Me$	$-Me$	$-R$	–	8.63	D[33]
$-H$	$-Cl$	$-P$	8.75	8.11	C[34]
$-H$	$-I$	$-P$	8.63	8.13	C[34]
$-H$	$-CCH$	$-P$	8.95	8.14	C[34]

Bz is benzyl; R is (β-D-ribofuranosyl); P is pentyl.

Table 4. ^{13}C NMR chemical shifts (ppm)[28–34] of *N*-methyl purines, adenines, and selected purine derivatives **7**

Compound	Solv.	C-2	C-4	C-5	C-6	C-8
1-Me-purine	DMS	144.71	142.37	134.95	136.47	166.28
3-Me-purine	DMS	143.78	155.93	140.89	145.72	162.31
7-Me-purine	DMS	152.04	159.88	125.79	140.72	149.78
9-Me-purine	DMS	151.86	151.38	133.46	147.44	147.44
7-Me-adenine	DMS	152.31	159.82	111.77	151.91	145.94
9-Me-adenine	DMS	152.50	149.94	118.72	155.98	141.47
R_7=P, R_2=H, R_6=Cl	$CDCl_3$	152.35	162.05	122.34	142.96	148.87
R_9=P, R_2=H, R_6=Cl	$CDCl_3$	151.86	151.02	131.62	151.02	145.03
R_9=P, R_2=H, R_6=I	$CDCl_3$	151.85	148.06	122.08	138.58	144.36
R_9=P, R_2=H, R_6=CCH	$CDCl_3$	152.39	151.72	134.91	140.49	145.59
R_9=Bz, R_2=Cl, R_6=Me	$CDCl_3$	154.1	152.3	132.0	161.8	144.1
R_9=Bz, R_2=Me, R_6=Me	$CDCl_3$	162.1[a]	151.2	130.6	158.8[a]	142.8
R_9=Bz, R_2=Ph, R_6=Me	$CDCl_3$	159.0[a]	151.4	131.4	158.9[a]	143.3
R_9=RF, R_2=Me, R_6=Me	DMS	160.6[a]	150.6	130.9	158.0[a]	143.3
R_9=RF, R_2=Ph, R_6=Me	DMS	157.3[a]	151.1	131.7	158.2[a]	144.4
R_9=RF, R_2=H, R_6=CF_3	DMS	151.58	153.60	130.09	142.53	147.90
R_9=RF, R_2=H, R_6=4-MeOPh	DMS	151.98	152.07	130.36	152.96	144.51

DMS is DMSO-d_6; P is pentyl; Bz is benzyl; RF is β-D-ribofuranosyl.
[a]May be interchanged.

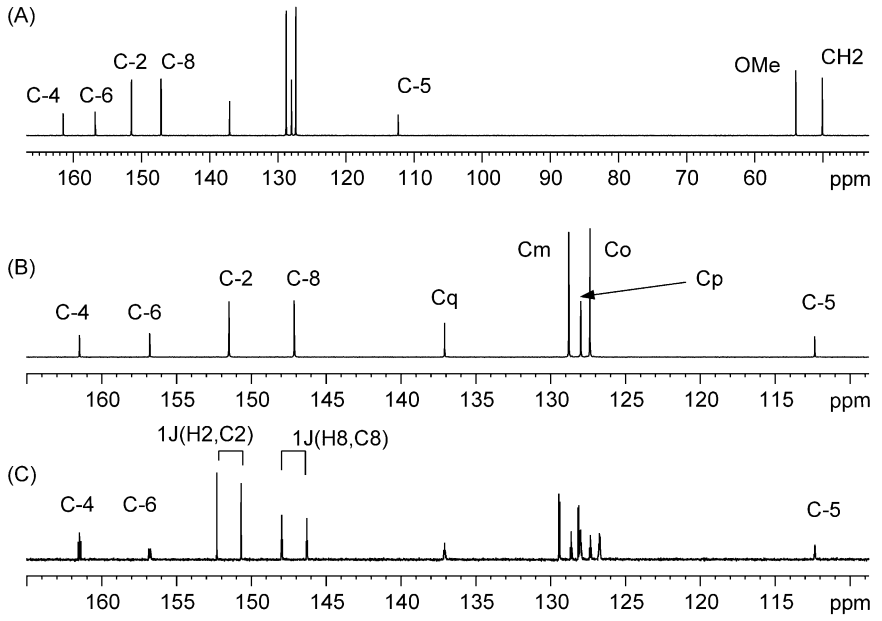

Fig. 2. ^{13}C NMR spectrum of 6-methoxy-N^7-benzylpurine (Panel A). Portions of ^{13}C NMR spectra with (Panel B) and without (Panel C) ^1H-decoupling.

2.2.1. *Carbon chemical-shift tensors*

Atoms in molecules rarely possess spherically symmetric electron distributions due to the presence of chemical bonds or nonbonding π-orbitals. The chemical shielding, therefore, depends on the orientation of the molecule with respect to the static magnetic field and the chemical shift is described by a second-rank tensor. The chemical-shift tensor is fully described by three principal values and three Euler angles that orient the principal axis system of the diagonalized chemical-shift tensor with respect to the molecular frame. δ_{11}, δ_{22}, and δ_{33} (ppm) represent the three principal components of the shift tensor with the following rule: $\delta_{11} \geq \delta_{22} \geq \delta_{33}$. In order to describe the approximate orientation of the principal shielding axis in the molecular frame and to establish some simple rules, the principal components are denoted as $\delta_{\perp}$ (perpendicular to the aromatic ring), δ_t (approximately tangential to the purine ring), and δ_r (radial with the chemical bond or lone pair of electrons). The most shielded components (δ_{33}) of the carbon and nitrogen atoms in the aromatic rings are always oriented perpendicular to the purine skeleton ($\delta_{33} = \delta_{\perp}$).

The highly asymmetric molecular skeleton of the aromatic purine system results in relatively large asymmetries of the ^{13}C chemical-shift tensors. The orientations of the components of the ^{13}C tensor of the carbon atoms in the purine ring follow the simple rules found for the trigonal sp^2 carbon atoms in polycyclic aromatic hydrocarbons.[37] As already mentioned, the most shielded components (δ_{33}) are always oriented perpendicular to the purine ring. These perpendicular components of the ^{13}C shift tensor ($\delta_{\perp}$) of the protonated and alkyl-substituted aromatic carbons are larger than those of aromatic bridgehead carbons. The components δ_{11} and δ_{22} lie within the plane of the purine skeleton. If two adjacent, more or less equal bonds have less π-character than the third adjacent bond, then δ_{11} tends to be oriented approximately perpendicular to the adjacent bond with the most π-character. This situation applies to the carbonyl carbon atom C-6 in guanine.[38] When the bond orders of two adjacent π-bonds are similar and larger than that of the third adjacent bond, δ_{11} lies approximately along the bond with the lowest bond order. This has been observed for the C-2 and C-8 carbon atoms in A and G, and also for the C-5 atom in A. The ^{13}C shift-tensor orientations and the principal values for the bridgehead carbons, C-4 in A and G and C-5 in G, deviate from the established rules. These deviations can likely be attributed to the different character of C–N bonds as compared to C–C bonds.[38]

2.3. ^{15}N chemical shifts

Several excellent reviews and chapters in books that are specifically devoted to the general applications of ^{15}N NMR spectroscopy to structural studies are currently available.[17,19–21] The interested reader is referred to these reviews for more detailed treatment. Most attention has been focused on isotropic chemical shifts and their relationship to the elucidation of structure, the importance of solvent effects, and tautomeric equilibria. The combination of a large range of chemical shifts – approximately 600 ppm for organic molecules ($\sim$1200 ppm for –NO

compounds) – and sensitivity to the electronic interactions involving the lone pair has made the ^{15}N chemical shift a very sensitive probe for both structural changes and intermolecular interactions. The NMR chemical shift of the nitrogen nucleus is the parameter most sensitive to N-alkylation, protonation, complexation, and hydrogen-bond formation. In fact, nitrogen atoms are at the center of each of these interactions. In all the above-mentioned cases, the electron lone pair is directly affected.

It has been know for a long time that the involvement of the nitrogen electron lone pair in a chemical reaction or intermolecular interaction is reflected mainly in the $n-\pi^*$ transition, causing remarkable changes in the chemical shielding of the ^{15}N nucleus. The protonation (or N-alkylation) of a pyridine-type nitrogen leads to a significant increase in its magnetic shielding, often 50 ppm or more, and makes nitrogen NMR an important tool in studies of protonation–deprotonation sites and equilibria. The resonances of the nitrogen atoms of the pyridine type of 6-substituted purines bearing an electron lone pair are found in the range of $\sim 225-300$ ppm.

The effect of NH_2 substitution at the C-2 position on the chemical shifts of the N-1 and N-3 atoms has been investigated for various purine derivatives. The data have shown that the N-1 and N-3 resonances are always shielded by 40 ppm more than the C-2 unsubstituted analogs. The substitution at the N-7 and N-9 positions also has a significant long-range effect on the chemical shielding of the N-3 nitrogen. As documented, this chemical shift is always 20–30 ppm greater for the N^7-alkylated compound than for the related N^9-regioisomers, indicating substantial deshielding of the N-3 atom. This effect was first systematically investigated for a series of halogenated derivatives and amino derivatives.[39] Similar effects were also observed for N^7- and N^9-substituted adenine and protected adenine derivatives.[40] A more comprehensive study, including quantum chemical calculations of the ^{15}N chemical shifts and the CP/MAS measurements for powdered samples of adenine and guanine derivatives has recently been published.[41] To conclude this short summary, the resonances of nitrogen atoms of the pyrrole type are usually located between 140 and 170 ppm. The ^{15}N NMR chemical shifts of selected purine derivatives,[39–45] together with the relevant references are summarized in Table 5. The $^1H-^{15}N$ g-HMBC spectrum of 6-methoxy-N^7-benzylpurine is shown in Fig. 3.

2.3.1. *Nitrogen chemical-shift tensors*

The contributions of the principal components of the chemical-shift tensors to the isotropic shielding and the orientation of individual components in the molecular coordinate system are discussed in the following paragraphs. This is believed to be important for understanding the problem and for further discussion.

A paper describing the experimental values of the principal components of the shielding tensors of the nitrogen atoms in various nitrogen heterocycles was published in 1997.[46] Based on quantum chemical calculations, this chapter reported the orientations of the individual components of the shielding tensors. The dramatic differences in the nitrogen tensors resulting from changes in the nitrogen hybridization may be rationalized as follows. The largest shift component, δ_{11}, generally orients

Table 5. Experimental ^{15}N chemical shifts of various purine derivatives[39–45] in DMSO-d_6 (unless otherwise indicated)

Compound	N-1	N-3	N-7	N-9	N-6	N-X	CN
Purine[a]	267.6	252.5	195.7	191.6	–	–	–
Purine	278.9	261.3	210.5	190.0	–	–	–
7-Me-purine[a]	267.0	258.8	146.1	232.5	–	–	–
9-Me-purine[a]	266.2	242.8	230.5	131.4	–	–	–
7-Me-purine	279.4	272.3	144.1	244.7	–	–	–
9-Me-purine	278.3	251.7	240.9	150.9	–	–	–
6-Cl-7R-purine	276.0	269.5	164.3	247.5	–	–	–
6-Cl-9R-purine	274.4	248.9	241.6	171.7	–	–	–
2-NH_2-6-Cl-7R-purine	237.9	217.4	152.7	240.2	80.3	–	–
2-NH_2-6-Cl-9R-purine	234.8	198.8	240.1	159.4	83.3	–	–
2-NH_2-7R-purine	240.6	221.1	151.7	243.3	78.3	–	–
2-NH_2-9R-purine	241.9	201.9	241.5	156.7	81.1	–	–
Adenine	236.0	230.2	241.4	159.1	80.5	–	–
2-hexylS-adenine	227.2	218.3	241.4	156.7	81.4	–	–
8-Br-adenine	236.9	230.2	242.3	157.5	76.9	–	–
2-Bu-adenine	233.8	227.5	228.5	169.1	79.5	–	–
8-Bu-adenine	234.7	230.4	224.6	170.0	81.2	–	–
7-Et-adenine	236.9	243.2	158.9	244.1	78.5	–	–
9-Et-adenine	234.7	224.9	239.5	165.5	80.6	–	–
8	236.7	224.8	240.9	152.7	81.9	–	–
N^6,N^6-diMe-adenine	235.8	227.2	244.9	160.0	77.0	–	–
N^6,N^6-diEt-adenine	234.7	226.7	247.0	158.5	105.8	–	–
Adenosine	238.7	225.5	243.5	172.3	84.8	–	–
N^6-Bz-adenosine	232.7	224.1	241.4	171.7	91.0	–	–
Guanosine	149.3	167.8	248.7	172.0	75.3	–	–
Inosine	176.6	216.1	250.6	176.6	–	–	–
ATP	217.2	217.5	232.8	170.7	79.0	–	–
2-MeS-ATP	217.0	212.1	230.5	168.7	77.7	–	–
2-Cl-ATP	223.7	214.8	232.7	170.7	84.0	–	–
8-Br-ATP	220.0	221.1	240.4	167.3	80.4	–	–
9	152.4	201.1	165.6	250.5	137.1	–	–
10	153.5	182.8	249.2	156.6	137.4	–	–
11	238.8	242.4	144.2	246.2	141.6	121.3	–
12	235.6	221.8	239.4	153.6	142.1	120.9	–
13	248.3	256.4	141.1	248.7	202.1	107.2	253.1
14	252.2	234.3	246.6	146.2	211.2	105.2	253.2
15	249.1	256.5	138.9	249.8	202.1	106.6	–
16	252.8	234.6	247.4	145.2	211.4	105.0	–
17	267.3	242.9	238.7	172.7	–	–	–
18	277.4	245.6	237.7	174.6	–	–	–

R is β-D-ribofuranosyl.
[a] Measured in water.

perpendicular to the plane defined by the bonding–antibonding or HOMO–LUMO pair of orbitals with the smallest energy gap.[47,48] This orientation is a result of the mixing in the occupied and vacant molecular orbitals described by the angular momentum operator specified in the Ramsey expression of the chemical shifts.[49,50] Since

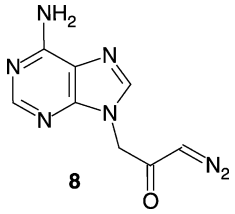

8

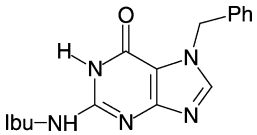

9

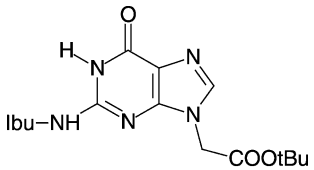

10

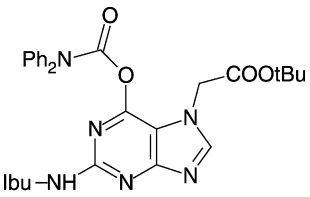

11

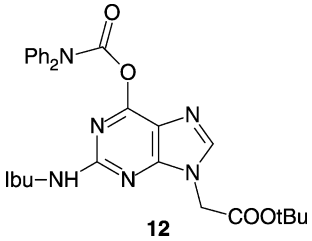

12

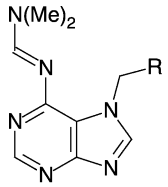

13: R = CN
15: R = CF_3

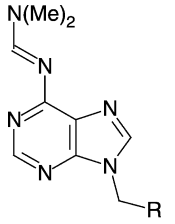

14: R = CN
16: R = CF_3

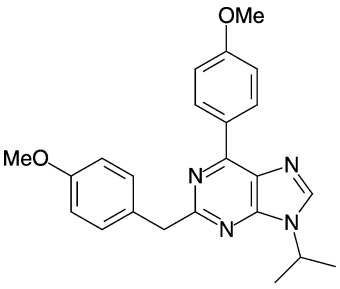

17

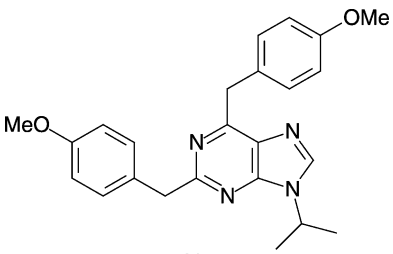

18

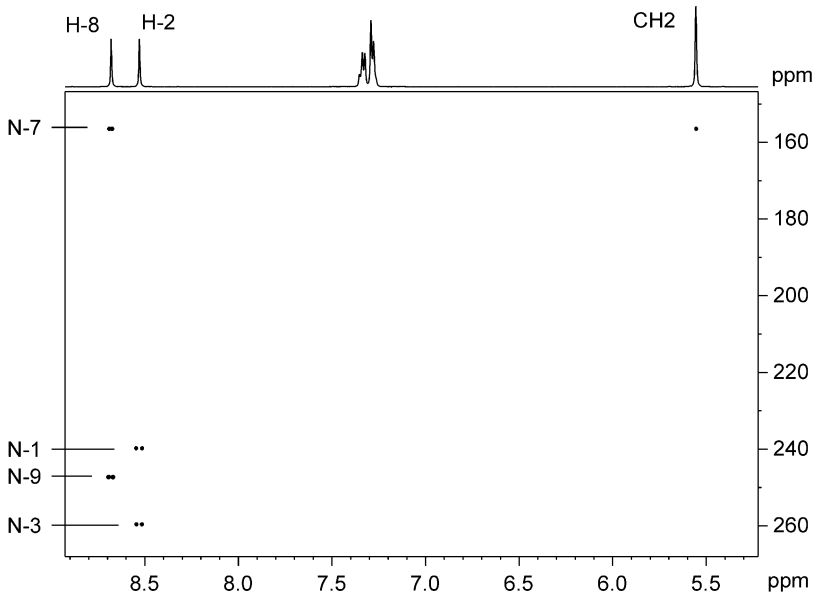

Fig. 3. $^{1}H-^{15}N$ g-HMBC spectrum of 6-methoxy-N^{7}-benzylpurine with assignment of nitrogen resonances.

the paramagnetic term in the Ramsey expression is inversely proportional to the energy gap between the pair of orbitals, the term with the smallest energy gap makes the largest paramagnetic contribution, and the largest chemical-shift component is oriented perpendicular to these two orbitals (Fig. 4).

As mentioned previously, two different types of nitrogen atoms are generally found in the purine skeleton. Pyridine-type nitrogen bears an electron lone pair which may be considered a part of the relevant σ-bond system and which supplies one π-electron to the delocalized aromatic π-bonds. Its chemical shielding is dominated by an $n-\pi^{*}$ transition with a relatively small energy gap. Consequently, this transition dominates the δ_{11} component of the shift tensor, which is approximately tangential to the purine ring (δ_{t}). The orientations of the δ_{11}, δ_{22}, and δ_{33} components of the two different types of nitrogen are depicted in Fig. 5.

The δ_{22} component is oriented radially with the electron lone pair. This component is dominated by a $\sigma_{N-C}-\pi^{*}$ transition. The δ_{33} component is always perpendicular to the plane of the aromatic ring ($\delta_{\perp}$) and is dominated by the σ-electronic structure.

In N-substituted derivatives, the nature of the electronic environment of the pyrrole-type nitrogen is different from that of its pyridine-type counterpart. Each of these pyrrole-type nitrogens is bound covalently to three neighboring atoms, and supplies two electrons to the delocalized π-bond system. In this case, the δ_{11} component, which is oriented radially with the bond N–R (R = H, alkyl, metal), is dominated by a $\sigma_{N-C}-\pi^{*}$ transition. The δ_{22} component, which is dominated by a $\sigma_{N-R}-\pi^{*}$ transition, is approximately tangential to the aromatic ring. In other words, the tangential component (δ_{t}) is dominated by an $n-\pi^{*}$ (lone-pair) transition for a pyridine-type nitrogen,

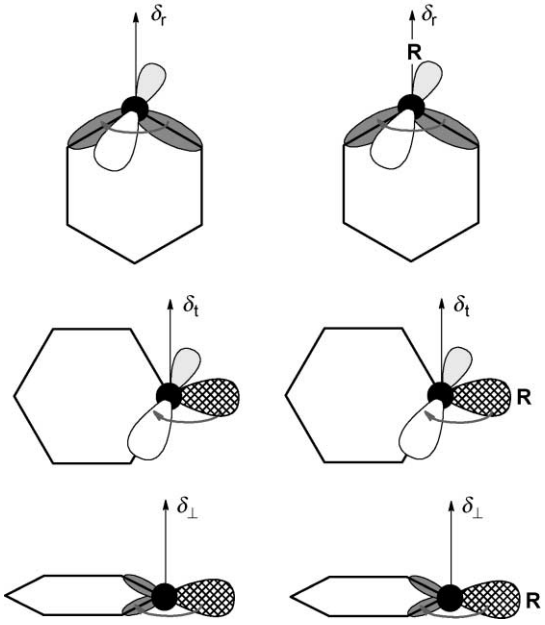

Fig. 4. Schematic drawings of the electron orbitals[46] making the largest contributions to the principal components of the chemical shifts in pyridine and N-substituted (R = H, alkyl) pyridine.

whereas a $\sigma_{N-R}-\pi^*$ transition dominates this shielding direction for a pyrrole-type nitrogen. Because the energy gap corresponding to an $n-\pi^*$ transition is quite small, the tangential component becomes the largest component of the chemical shift (δ_{11}) for pyridine-type nitrogens. In N-substituted compounds the tangential component, δ_t, is dominated by a $\sigma_{N-R}-\pi^*$ transition which has a much larger energy gap, resulting in its decrease by $\sim$300 ppm. Consequently, the δ_{11} becomes δ_r and δ_{22} is now δ_t. Note that δ_r is dominated by $\sigma_{N-C}-\pi^*$ transitions for both types of nitrogen because these

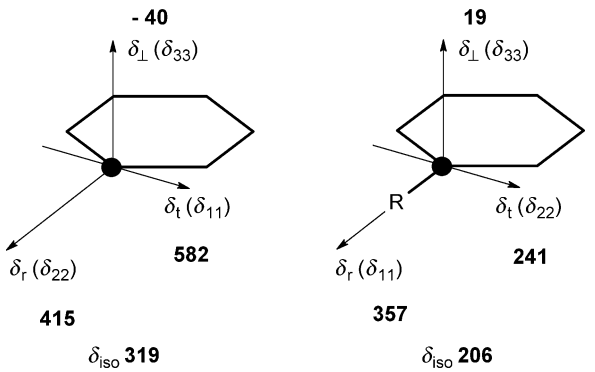

Fig. 5. Principal components of the nitrogen chemical-shift tensors (ppm) and their orientations in the molecular frame in pyridine and *N*-methylpyridinium.[46]

transitions are not generally affected by protonation, N-alkylation, or complexation phenomena. The values of δ_r are quite similar for both pyridine-type and pyrrole-type nitrogens. The smallest $\delta_\perp$ component, perpendicular to the ring and dominated by the σ-electronic structure, is not substantially affected by structural changes and remains relatively invariant.

The principal components of the chemical-shift tensor are strongly affected by intermolecular contacts and hydrogen bonding (HB) and can be used as a highly sensitive probe to investigate weak interactions.[51] For protonated (N–H) nitrogens that behave as proton donors, the δ_{22} principal shift component shows the largest HB effects. This component lies approximately perpendicular to the N–H direction (δ_t, tangential to the purine ring), which is always along the direction of the HB forces. HB produces deshielding in this δ_t direction. For the non-protonated nitrogens that serve as proton acceptors, the largest effects are also observed along the direction perpendicular to the HB in the plane of the molecule (δ_{11}). In summary, the largest HB effects are observed in the chemical-shift components that are in the plane of the molecule and perpendicular to the direction of the HB ($\sim \delta_t$).

2.4. One-bond ^{1}H–^{13}C coupling constants

Like the carbon chemical shift, the magnitude of the one-bond coupling constant is significantly influenced by the electron lone pair present on each of the neighboring nitrogen atoms. For example, in N^7- and N^9-substituted purine or adenine derivatives the one-bond H2–C2 coupling constant is always smaller than the H8–C8 coupling constant. Analogously, the value of the one-bond ^{1}H–^{13}C coupling constant is also strongly affected by protonation of the neighboring nitrogen atom. In purine itself, a significant increase (+14.8 Hz) was found for ^1J(H8,C8) upon transition from the purine anion **19** to the neutral purine **1**. The fact that ^1J(H2,C2) and ^1J(H6,C6) are also affected, although less strongly, is due to conjugation between the pyrimidine and imidazole partial structures in purine, as already explained by Pugmire and Grant[52] to rationalize the changes in the ^{13}C chemical shifts observed for the pair **19/1**. The ^{1}H–^{13}C g-HMQC spectrum of 6-methoxy-*N*^{7}-benzylpurine is shown in Fig. 6.

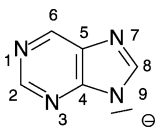

19

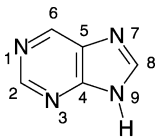

1

2.5. Three-bond ^{1}H–^{13}C coupling constants

Long-range ^{1}H–^{13}C spin–spin coupling constants have long been known to be useful parameters for determining protonation sites[53] and studying tautomeric equilibria.[54] In 1982, Schumacher and Günther published the first report describing the advantages of

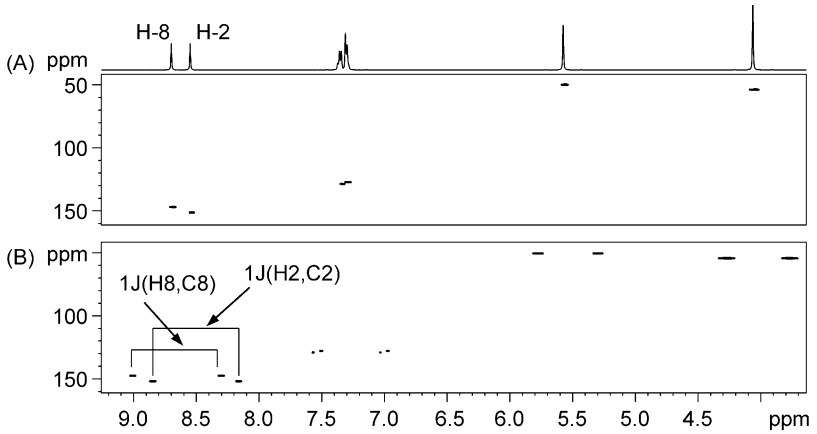

Fig. 6. $^{1}H-^{13}C$ g-HMQC spectra of 6-methoxy-N^{7}-benzylpurine with (Panel A) and without (Panel B) heteronuclear ^{13}C-decoupling during acquisition.

using coupling constants to determine the protonation sites and tautomeric equilibria in purine.[55] It has been recognized, that the three-bond coupling constant in the **H**C**N**C fragment is greatly reduced by changing the =N– type of nitrogen to –NH–. This approach seemed of interest since coupling parameters are normally far less sensitive to the effects of medium and concentration than chemical shifts and, therefore, might yield more reliable estimates of tautomer equilibria than measurements of the chemical shifts. The $^{1}H-^{13}C$ spin–spin coupling constants for purine and the *N*-methyl purines are summarized in Table 6. A portion of the $^{1}H-^{13}C$ GSQMBC spectrum of 6-methoxy-N^{7}-benzylpurine with a depiction of the three-bond coupling constants is shown in Fig. 7.

2.6. One-bond $^{1}H-^{15}N$ coupling constants

The value of the $^{1}J(^{1}H,^{15}N)$ coupling is greatly influenced by the s character of the electron lone pair of N, which in turn depends on the pyramidality at the N atom.

Table 6. Experimental $^{1}H-^{13}C$ *J*-coupling constants of purine, its N–Me derivatives, and the protonated and deprotonated forms[55]

Compound	Solvent	$^{1}J_{H2,C2}$	$^{1}J_{H8,C8}$	$^{3}J_{H2,C6}$	$^{3}J_{H2,C4}$	$^{3}J_{H8,C4}$	$^{3}J_{H8,C5}$
7-Me-purine	D_2O	205.9	211.6	10.6	10.8	12.5	4.9
	DMSO-d_6	202.9	210.9	10.8	10.9	13.0	4.3
9-Me-purine	D_2O	207.0	213.5	10.0	11.0	5.5	11.0
	DMSO-d_6	204.3	212.4	10.4	11.0	5.5	11.5
Purine	D_2O	206.6	213.0	10.3	10.9	9.2	8.1
	DMSO-d_6	203.3	210.8	10.5	11.2	8.2	9.3
Purine^{-}	NaOD	201.5	198.2	10.2	10.2	10.2	9.3
Purine^{+}	TFA	221.5	221.1	6.9	11.5	7.8	9.8

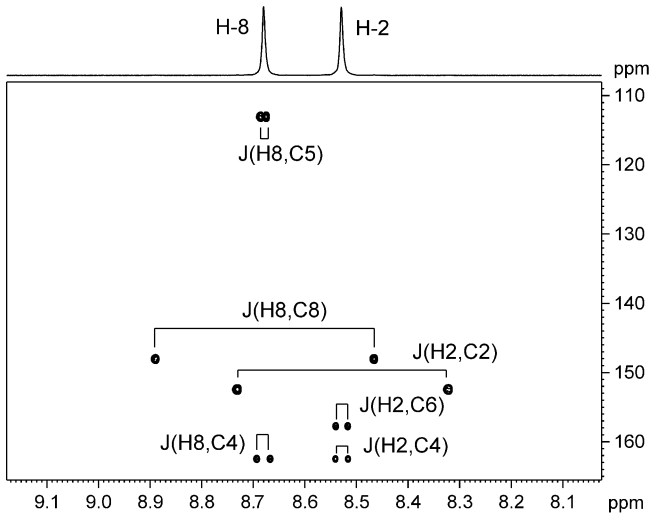

Fig. 7. Portion of the $^{1}H-^{13}C$ GSQMBC spectrum of 6-methoxy-N^{7}-benzylpurine with assigned *J*-couplings.

In pyrrol, where the N lone pair is of purely p character, $^{1}J_{H,N} \sim 96$ Hz, which is quite close to the $^{1}J_{H,N}$ coupling in ammonia for a planar configuration.[56]

Similar values ranging between 89 and 96 Hz can be detected for the imidazole portion of the purine system.[57] Unfortunately, due to the fast chemical exchange of these labile N–H protons, the ^{1}H NMR signals are very broad (hundreds of Hz), precluding observation of the corresponding coupling constant. Similar values and behavior are also detected for the exocyclic NH_2 groups. However, the corresponding proton signals are generally sharper and the determination of NMR parameters is easier.

The chemical exchange processes can be slowed down by HB the N–H groups of the purines to other molecules or by decreasing the temperature of the system. Under these special conditions, the values of the coupling constants can be determined and the scalar interactions used for polarization transfer in chemical-shift correlation experiments (e.g., nucleic acids).

2.7. Two-bond $^{1}H-^{15}N$ coupling constants

Like three-bond $^{1}H-^{13}C$ coupling constants, two-bond $^{1}H-^{15}N$ coupling constants can be employed to identify the positions of protons or alkyl groups on the purine skeleton. It has been demonstrated that the scalar coupling of a proton to a pyrrole-type nitrogen atom is somewhat smaller than to a pyrimidine-type nitrogen. The $^{1}H-^{15}N$ coupling constants determined for purine, N^{7}-methylpurine, and N^{9}-methylpurine[58] in various solvents are summarized in Table 7. A portion of $^{1}H-^{15}N$ GSQMBC spectrum of 6-methoxy-N^{7}-benzylpurine with a depiction of the two-bond coupling constants is shown in Fig. 8.

A complementary study to determine the sites of protonation, alkylation, or complexation by using ^{13}C and ^{15}N chemical shifts and $^{1}H-^{13}C$ and $^{1}H-^{15}N$ coupling

Table 7. Experimental $^{1}H-^{15}N$ *J*-coupling constants of purine, its N–Me derivatives, and the protonated and deprotonated forms[58]

Compound	Solvent	$^{2}J_{H2,N1}$	$^{2}J_{H2,N3}$	$^{2}J_{H8,N7}$	$^{2}J_{H8,N9}$	$^{2}J_{H6,N1}$
Purine	5% NaOH	13.9	13.4	12.6	12.6	9.7
	H_2O	14.1	14.1	–	–	9.6
	20% D_2SO_4	8.3	12.7	8.4	9.2	2.6
	90% D_2SO_4	8.8	13.3	6.3	6.3	–
	DMSO-d_6	14.9	15.1	11.9	9.7	10.9
	TFA	8.9	13.0	10.2	8.3	–
	HSO_3F	7.3	12.8	–	3.7	–
7Me-purine	D_2O	11.9	14.0	9.6	13.5	11.9
	20% D_2SO_4	11.8	12.3	9.3	10.9	–
	90% D_2SO_4	8.7	13.3	7.8	5.7	–
	DMSO-d_6	12.9	14.9	9.6	12.4	12.9
	TFA	10.9	12.9	8.9	11.4	–
9Me-purine	D_2O	13.8	14.6	11.4	9.9	9.7
	20% D_2SO_4	7.9	12.9	11.1	11.1	2.6
	90% D_2SO_4	9.3	13.5	5.8	7.7	–
	DMSO-d_6	13.1	15.6	12.4	10.4	13.1
	TFA	9.5	13.4	9.7	9.0	–

constants is generally recommended. A schematic graphical representation of the characteristic values of the ^{13}C and ^{15}N chemical shifts and the $^{1}H-^{13}C$ and $^{1}H-^{15}N$ coupling constants for N^7-methylpurine and N^9-methylpurine pair is shown in Figs. 9 and 10.

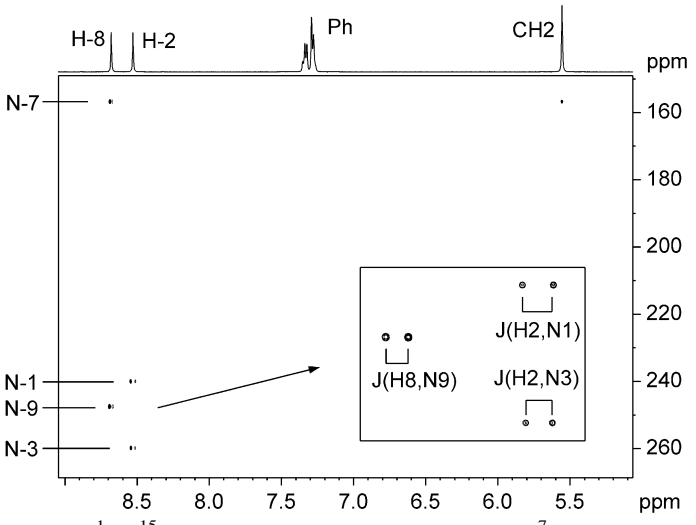

Fig. 8. Portion of the $^{1}H-^{15}N$ GSQMBC spectrum of 6-methoxy-N^7-benzylpurine with assigned *J*-couplings.

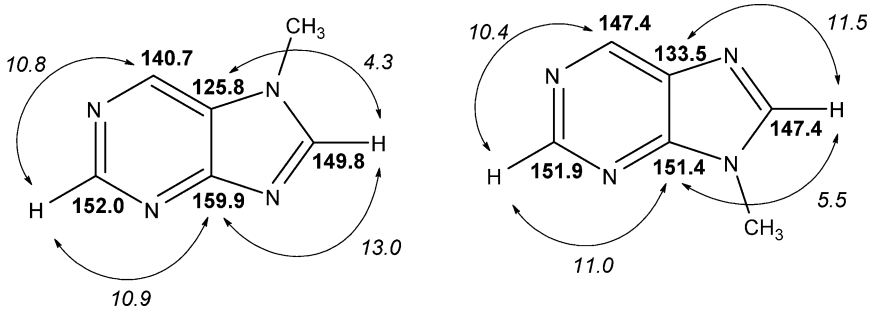

Fig. 9. ^{13}C-NMR chemical shifts (ppm) and three-bond ^{1}H–^{13}C coupling constants (Hz) for N^7-methyl and N^9-methyl purine in DMSO-d_6.

2.8. ^{19}F chemical shifts and ^{19}F–^{13}C coupling constants

Fluorinated purines have been increasingly investigated during the past few years due to their significant biological activities. In the original literature, $CFCl_3$ was used as an internal standard to reference the ^{19}F signal. Generally, fluorine atoms can be substituted for H-2 or H-8 hydrogen atoms, a trifluoromethyl group can be connected to the C-2, C-6, or C-8 position or a fluorine atom can be connected to various carbon substituents at these positions.

The one-bond ^{19}F–^{13}C coupling constant of C-2 fluorinated compounds[59] ranges between 212 and 222 Hz. For the three-bond coupling constant with carbons C-4 and C-6, $^{3}J_{F,C} \sim 15–17$ Hz. The ^{19}F resonance of a trifluoromethyl group connected to the purine aromatic skeleton[29] is usually located at around -65 ppm. The one-bond ^{19}F–^{13}C coupling constant is $\sim$275 Hz. For 6-trifluoromethylpurine and its derivatives, a two-bond ^{19}F–^{13}C-6 coupling constant of $\sim$36 Hz is detected. For the 6-(4-fluorophenyl)-purine derivatives[31] the fluorine chemical shift is -110 ppm and the corresponding $^{1}J_{F,C} \sim 247$ Hz.

2.9. Dynamic NMR and chemical exchange processes

As will be discussed in detail later, chemical exchange processes are frequently observed in solutions of purine bases (tautomerism, HB), salts (protonation sites), and complexes

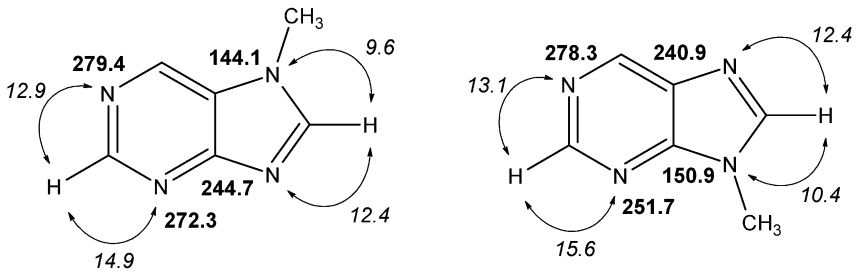

Fig. 10. ^{15}N-NMR chemical shifts (ppm) and two-bond ^{1}H–^{15}N coupling constants (Hz) for N^7-methyl and N^9-methyl purine in DMSO-d_6.

(complexation sites). These phenomena are characterized by the energy of the individual components and by the magnitude of the interconversion barrier. They determine the appearance of the resulting NMR spectrum and the values of the individual NMR parameters. In a fast NMR regime, only those signals reflecting the time-averaged contributions of the individual components are observed.

Very recently, novel applications of dynamic NMR in organic chemistry have been reviewed.[60] A similar report on recent advances in the study of tautomerism in solution and in the solid state has been published by Kleinpeter.[61]

Analysis of the NMR parameters and the dynamic processes depends on the exchange rates. The basic one-dimensional band-shape analysis is best suited to intermediate rates ($10-10^3$ per s). Slow exchange rates ($\sim 0.1-10$ per s) are most accurately measured by using magnetization transfer experiments and T_1-relaxation times. Fast dynamic processes ($> 10^3$ per s) can be elucidated by investigating the spin–spin relaxation times.

Traditionally, dynamic NMR studies have been time consuming, requiring extensive measurements under varied conditions (solvent, temperature, etc.). Despite this drawback, NMR has been essential in providing unique insights into equilibrium phenomena. However, novel theoretical methods, such as DFT calculations (vide infra), are changing the role of NMR remarkably. Using currently available computational resources, it is possible to estimate the NMR parameters of the major contributors involved in dynamic processes within a reasonable time. Contemporary trends in computational approaches are discussed in Section 5. When the NMR parameters of the individual components are known, calculating the statistical average of all the signals, which one can observe in a fast-exchange regime is often straightforward. More sophisticated calculation procedures for multi-spin systems have also become available, as reviewed by Orrell.[62]

Slowing down the chemical exchange by decreasing the temperature of the system is a historically well-established experimental approach in NMR spectroscopy. However, this

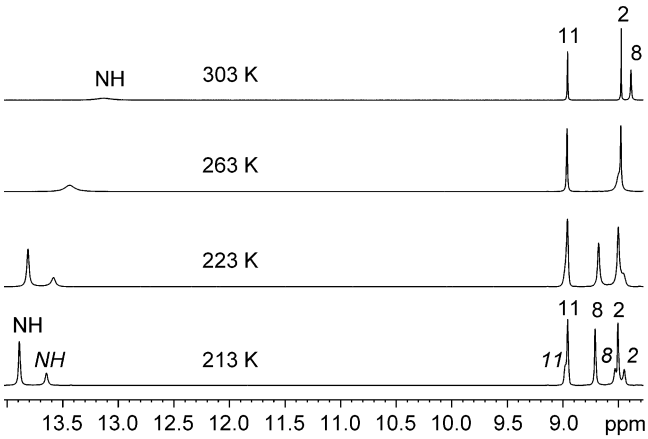

Fig. 11. Temperature dependence of the ^{1}H-NMR spectrum[63] of *N*,*N*-dimethyl-*N*′-(7(9)-*H*-purin-6-yl)-formamidine in DMSO-d_6.

methodology has rarely been used to study purines since exchange studies of purine derivatives have been performed primarily in water. Very recently, temperature-dependence and low-temperature studies (213 K) in DMF-d_7 solutions have been reported (see Section 3.2).[63] The temperature dependence of the ^{1}H NMR spectrum of *N*,*N*-dimethyl-*N*′-(7(9)-*H*-purin-6-yl)-formamidine is shown in Fig. 11.

Recently, a study of HB between adenosine and acetic acid at very low temperature has been published. The system was investigated using a deuterated freon mixture as the solvent (128 K).[64] This experimental set-up made it possible to investigate the system in a slow-exchange regime using ^{1}H NMR and 2D NOE experiments.

3. APPLICATIONS

3.1. Regioisomerism

^{13}C and ^{15}N NMR chemical shifts and ^{1}H–X coupling constants can be used as significant markers of the purine structure attained through alkylation processes. As described in the previous chapters, the alkylation of nitrogen atom N-7 or N-9 produces a 5–10 ppm shielding of the neighboring quaternary carbon atom C-5 or C-4, respectively.

The N-3 resonance is always 20–30 ppm more shielded in N^9-substituted compounds than in the comparable N^7-isomers. This feature has been used together with the characteristic three-bond ^{1}H–^{13}C coupling pathways to study the structures of various N-substituted purine derivatives.[39–41] Very recently, an identical approach has been used to determine the position of alkylation for several purine derivatives reacted with 4-vinylbenzyl chloride.[65]

The characteristic coupling pathways obtained in ^{1}H–^{13}C g-HMBC experiments have been used to determine the constitution of guanosine- and adenosine-derived N-alkylated regioisomers.[66,67] The three-bond couplings of the protons of the N^1-bonded CH_2 groups with carbon atoms C-2 and C-6 have been obtained for the N^1-alkylated isomers. ^{1}H–^{13}C HMBC experiments have also made possible the complete regiochemical assignment of the coupling product of 6-chloropurine and tetrahydropyran-2-yl.[32] The three-bond coupling constants for H-8 with C-4, C-5, and C-1′, and of H-1′ with C-4 and C-8, unequivocally confirm the formation of the N^9-isomer. An identical three-bond ^{1}H–^{13}C coupling pattern for the subsequent reaction step verified the C^2-stannylation and excluded the formation of the C^8-isomer.

3.2. Tautomerism

Proton-transfer processes in solution are generally characterized by a low inter-conversion barrier. Measurements at laboratory temperature typically fall into a fast-exchange regime. Under these conditions, the experimentally observed NMR parameters represent the time-averaged contributions of the individual forms. Exact knowledge of the NMR parameters of the individual components is essential for determining

the tautomeric ratio. These parameters can be obtained either theoretically, using quantum chemical calculations, or experimentally, from model compounds.

Analogously to the studies of N-alkylation processes, the characteristic values of ^{13}C NMR chemical shifts can be used to determine the tautomeric equilibria existing at the purine skeleton.[68] In the original work, the ^{13}C chemical-shift data were obtained for a series of pyrrolo[2,3-*d*]pyrimidines and purines.[69] These data were used to determine sets of substituent parameters, which in turn could be used to correct the chemical shifts of the bridgehead carbons for the effect of substitution on a purine when a proton at either the N^7- or N^9-position is replaced with either a methyl group or a β-D-ribofuranosyl moiety. Other substituent effects on the chemical shifts of the aromatic carbons caused by replacing the hydrogen atom at the C^6-position of purine with an amino, oxo, or thieno function have been discussed. The differences in the chemical shifts of the carbon atoms between the purines and their corresponding pyrrolo[2,3-*d*]pyrimidines were observed to be highly reproducible.[69] Sets of α- and β-substituent parameters relative to the bridgehead carbons (C-4 and C-5) have been determined and are summarized in Table 8.

It has been demonstrated that the α- and β-substituent parameters for the C^4- and C^5-positions can be used in a reverse process, i.e., to determine whether the substituent resides in the N^7- or the N^9-position of the purine ring. Thus, the prototropic tautomerism that occurs in the imidazole portion of the purine ring was investigated by using the chemical shifts of the C-4 and C-5 carbons. Using the chemical shift for either the C-4 or the C-5 atom allowed the percentage of the N^7–H tautomer to be calculated using Eqs. (1) and (2).

$$\%(N^7\text{–H})_{C4} = 100\{\delta(\text{Pu})_{C4} - [\delta(N^9\text{–R})_{C4} - \alpha]\}/\{[\delta(N^7\text{–R})_{C4} - \beta] - [\delta(N^9\text{–R})_{C4} - \alpha]\} \quad (1)$$

$$\%(N^7\text{–H})_{C5} = 100\{\delta(\text{Pu})_{C5} - [\delta(N^9\text{–R})_{C5} - \beta]\}/\{[\delta(N^7\text{–R})_{C5} - \alpha] - [\delta(N^9\text{–R})_{C5} - \beta]\} \quad (2)$$

where $\delta(\text{Pu})_i$ is the average chemical shift of either C-4 or C-5 in the unsubstituted purine; $\delta(N^9\text{–R})_i$ and $\delta(N^7\text{–R})_i$ are the chemical-shift values for C-4 or C-5 of

Table 8. Sets of α- and β-substituent parameters relative to the bridgehead carbons (C-4 and C-5) in purine derivatives (in ppm)[69]

Nature of the substituent at N-7 or N-9	Substituent at C6							
	α-parameter				β-parameter			
	H	NH_2	=O	=S	H	NH_2	=O	=S
ribosyl-H	−0.5	−0.5	−0.3	−0.2	1.1	1.0	0.8	0.8
ribosyl-CH_3	−0.3	−0.9	−0.7	−0.6	0.8	0.9	0.7	0.7
CH_3-H	−0.2	0.4	0.4	0.4	0.3	0.1	0.1	0.1

the N^9- or N^7-substituted purine, respectively, and α and β are the substituent parameters that must be used to correct the chemical shifts of the model compounds for the effect of the substituent. Naturally, these parameters depend on the properties of the substituent R.

Lactam–lactim interconversion and the tautomerism between the thione and thiol forms, which could occur in the pyrimidine portion of hypoxanthine and 6-mercaptopurine, respectively, have been investigated by using the chemical shift of the C-6 carbon. The relative position of the C-6 resonance made it possible to calculate the amount of N^1–H tautomer by using Eq. (3)

$$\%(N^1\text{–H})_{C6} = 100\{\delta(\text{Pu})_{C6} - [\delta(C^6\text{–R})_{C6} - y]\}/\{[\delta(N^1\text{–R})_{C6} - z] - [\delta(C^6\text{–R})_{C6} - y]\} \quad (3)$$

where $\delta(\text{Pu})_{C6}$ is the C-6 chemical shift of the purine possessing lactam–lactim or thione–thiol tautomerism, i.e., C6═X ↔ C6–XH, and $\delta(C^6\text{–R})_{C6}$ is the C-6 chemical shift for a purine with an XCH_3 group at position 6, $\delta(N^1\text{–R})_{C6}$ is the C-6 chemical shift when a methyl group is attached to the N^1-position of the purine, and y and z are correction factors used for the XCH_3 and N^1–CH_3 substituents, respectively. The C-13 NMR chemical shifts of variously substituted purine bases are summarized in Table 9.

Table 9. Experimental ^{13}C chemical shifts of various purine derivatives[32,36,52,69]

Compound	Solvent	C-2	C-4	C-5	C-6	C-8
7-Me-purine	Water	152.11	159.27	126.14	140.91	150.65
9-Me-purine	Water	151.89	150.93	132.89	147.42	148.77
Purine −	Water	149.52	160.70	134.47	143.67	156.91
Purine	Water	152.00	154.86	128.40	144.84	147.87
Purine +	Water	148.33	158.10	128.42	139.86	125.99
9R-purine	DMS	152.22	151.09	134.28	148.32	145.53
7R-adenine	DMS	152.85	160.74	110.27	151.73	144.64
9R-adenine (adenosine)	DMS	152.60	149.27	119.57	156.30	140.20
7-Me-hypoxanthine	DMS	144.37	157.02	115.48	154.63	144.37
7R-hypoxanthine	DMS	144.80	157.72	114.79	154.14	142.49
9R-hypoxanthine (inosine)	DMS	146.19	148.46	124.63	156.88	139.11
1-Me-9R-hypoxanthine	DMS	148.77	147.63	123.68	156.42	139.22
6-MeO-9R-purine	DMS	151.67	151.83	121.24	160.46	142.33
7-Me-purine-6-thione	DMS	144.74	152.68	125.87	170.40	148.33
7R-purine-6-thione	DMS	144.99	153.34	125.32	169.83	144.99
9R-purine-6-thione	DMS	145.49	144.12	135.61	176.19	141.45
1-Me-9R-purine-6-thione	DMS	148.49	142.01	135.78	177.43	141.60
6-MeS-9R-purine	DMS	151.53	148.01	131.34	160.46	143.06
R_9═H, R_2═H, R_6═Cl	DMS	151.4	154.2	129.4	147.7	146.1
R_9═H, R_2═I, R_6═Cl	DMS	129.3	155.9	117.1	147.1	146.8

DMS is DMSO-d_6; R is β-D-ribofuranosyl; Me is methyl.

Table 10. Investigation of lactam–lactim and thione–thiole tautomerism in the pyrimidine rings of inosine and 9-(β-D-ribofuranosyl)purine-6-thione from C-6 chemical-shift data[69]

Compound	C-6
Inosine	156.9
1-Me-9R-hypoxanthine	156.4
NMe-H correction	−0.5 (*z*)
6-OMe-9R-purine	160.5
%N1–H	100
9R-purine-6-thione	176.2
1-Me-9R-purine-6-thione	177.4
6-SMe-9R-purine	160.5
%N1–H	93

As already discussed, purine exists in water and DMSO solutions as a mixture of N^7- and N^9-tautomers.[52] The N^7/N^9 tautomeric ratios for several purine derivatives were determined from the ^{13}C chemical shifts of C-4, C-5, or C-6 by using the α, β, and z parameters. The results obtained for selected derivatives are summarized in Tables 10–13.

The characteristic ^{13}C chemical shift of the C-6 atom was used as a significant qualitative marker for the thione–thiol tautomerism in C^2-substituted adenine derivatives.[59] Introducing a fluorine atom at the C^2-position of **21** instead of an NH_2 group in **20** causes a change in the shielding of the C-6 atom (~17 ppm) which is considered to be induced by the conversion to the thiol form. The effect on the C-2 atom is very weak (~3 ppm). The magnitude of the one-bond C–F coupling constant at C-2 (212–221 Hz) is in agreement with those of related fluorinated compounds. However, a significant C^2-substituent effect (~43 ppm as compared with the NH_2 derivative) was found in the purine ring for 2-iodo derivatives. This shielding is a typical heavy-element effect.

Table 11. Calculation of the percentages of the N7–H tautomeric forms of purine and adenine from C-4 and C-5 chemical shifts[69]

Compound	C-4	C-5
Purine	154.8	130.4
7Me-purine	159.9	125.8
Me–H parameters	0.3 (α)	−0.2 (β)
9Me-purine	151.4	133.5
Me–H parameters	−0.2 (β)	0.3 (α)
% N7–H	40	39
Adenine	151.3	117.5
7R-adenine	160.7	110.3
R–H parameters	1.0 (β)	−0.5 (α)
Adenosine	149.3	119.6
R–H parameters	−0.5 (α)	1.0 (β)
% N7–H	15	14

Table 12. Calculation of the percentages of the N7–H tautomeric forms of 1-methylhypoxanthine and 6-methoxypurine from C-4 and C-5 chemical shifts[69]

	C-4	C-5
1-Methylhypoxanthine		
1-Methylhypoxanthine	153.0	118.3
1Me-9R-hypoxanthine	147.6	123.7
R–H parameters	−0.3 (α)	0.8 (β)
% N7–H	63	53
Average %		58
6-Methoxypurine		
6-Methoxypurine	155.2	118.1
6-OMe-9R-purine	151.8	121.2
R–H parameters	−0.3 (α)	0.8 (β)
% N7–H	38	26
Average %		32

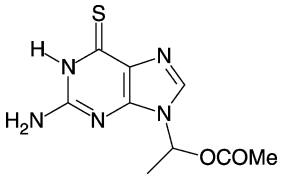

20

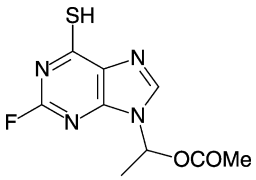

21

Table 13. Calculation of the percentages of the N7–H tautomeric forms of 1-methyl-6-mercaptopurine and 6-methylthiopurine from C-4 and C-5 chemical shifts[69]

	C-4	C-5
1-Methyl-6-mercaptopurine		
1Me-6-mercaptopurine	149.2	128.3
1Me-9R-purine-6-thione	142.0	135.8
R–H parameters	−0.2 (α)	0.8 (β)
% N7–H	85	72
Average %		79
6-Methylthiopurine		
6-Methylthiopurine	150.1	129.4
6-SMe-9R-purine	148.0	131.3
R–H parameters	−0.2 (α)	0.8 (β)
% N7–H	23	12
Average %		18

Similarly to the chemical shifts of carbon, the chemical shifts of nitrogen atoms N-7 and N-9 were used with Eqs. (4) and (5) to quantify the populations of individual tautomers:[70]

$$\%(\mathrm{N^7{-}H}) = 100\{\delta(\mathrm{N7})_{\mathrm{exp}} - \delta(\mathrm{N7})_{\mathrm{N9-R}}\}/\{[\delta(\mathrm{N7})_{\mathrm{N7-R}} + x] - \delta(\mathrm{N7})_{\mathrm{N9-R}}\} \quad (4)$$

$$\%(\mathrm{N^7{-}H}) = 100\{[\delta(\mathrm{N9})_{\mathrm{N9-R}} + x] - \delta(\mathrm{N9})_{\mathrm{exp}}\}/\{[\delta(\mathrm{N9})_{\mathrm{N9-R}} + x] - \delta(\mathrm{N9})_{\mathrm{N7-R}}\} \quad (5)$$

where x is the substituent parameter that must be used to correct the chemical shift of the model compound for the effect of the substituent.

Using the ^{15}N NMR chemical shifts approach, the population of the N^7–H tautomer of adenine in DMSO was determined to be 13.5% at 323 K.

^{15}N NMR spectroscopy was used to study the tautomerism of adenine derivatives enriched by the N-15 isotope.[43] These enriched samples were prepared as probes for further biochemical studies. While tautomeric mixtures of N^7–H and N^9–H were reported for adenine and 2-MeS-adenine based on the ^{15}N NMR spectra, an N^3–H species was suggested for the solution of 8-Br-adenine. These observations were supported by quantum chemical calculation of the individual tautomeric forms for isolated molecules and for the inclusion of solvent effects (both continuum and discrete models).

8-Hydroxyadenosine is a naturally occurring oxidized nucleic acid adduct. ^{15}N NMR chemical shifts and coupling constants indicate that the modified base exists in the 8-keto form.[71] The pH dependence of the ^{15}N NMR spectra showed the presence of two pK_a values, 2.9 and 8.7, corresponding to protonation at N-1 and ionization at N-7, respectively. The N-7 ionization results in the formation of an 8-enolate structure. Unusual values of the ^{1}H and ^{15}N resonances of the NH_2 group indicate an unfavorable steric or electronic interaction between the NH_2 group and the adjacent N^7–H proton.

Owing to the characteristic dependence of the ^{1}H–^{13}C coupling constants on the substitution, experimental values can be used for determining not only the N-alkyl position but also the position of any labile proton and hence of any tautomeric form of the compound being studied. In a fast NMR regime, the individual tautomers are rapidly interconverting, resulting in the observation of scalar coupling constants corresponding to the time-averaged contributions of the individual forms (see Section 2.9). The ratio of the components in equilibrium can be determined if the spin–spin couplings of the individual tautomers are known. Since these parameters are often experimentally unavailable, the coupling constants for appropriate model compounds must be applied. As for the methodology based on the chemical shifts, N^7- and N^9-alkylated derivatives usually serve as suitable models. The population of the N^7–H tautomer can be calculated based on the $^3J(^1\mathrm{H},^{13}\mathrm{C})$ values that have been measured for the **H8**C8N9**C4** and **H8**C8N7**C5** interactions in purine derivatives and evaluated using a correction[55] for the substituent effect of the N-alkyl group in N^7- and N^9-isomers.

For the model compounds, *N*-methylimidazole and protonated imidazole, the effects of a methyl group on the value of the corresponding three-bond coupling constant were

determined to be 0.6 and 0.8 Hz, respectively. The following equations were used to calculate the tautomeric ratio:

$$\%(\mathrm{N^7{-}H}) = 100\{[{}^3J(\mathrm{H8,C4})_{\mathrm{N9-R}} + \alpha] - {}^3J(\mathrm{H8,C4})_{\mathrm{Pu}}\}/\{[{}^3J(\mathrm{H8,C4})_{\mathrm{N9-R}} + \alpha] - [{}^3J(\mathrm{H8,C4})_{\mathrm{N7-R}}]\} \quad (6)$$

$$\%(\mathrm{N^7{-}H}) = 100\{[{}^3J(\mathrm{H8,C5})_{\mathrm{N9-R}}] - {}^3J(\mathrm{H8,C5})_{\mathrm{Pu}}\}/\{[{}^3J(\mathrm{H8,C5})_{\mathrm{N9-R}}] - [{}^3J(\mathrm{H8,C5})_{\mathrm{N7-R}} + \alpha]\} \quad (7)$$

Protonation of the purine anion significantly decreases ^3J(H8,C4) and ^3J(H8,C5). This observation points to the tautomeric equilibrium N^7–H, N^9–H, present in purine.[55] Based on the values of the three-bond coupling constants and taking the correction factor for a methyl group (0.6 Hz) into account a ratio of ~1:1 is obtained for N^7/N^9 tautomers in D_2O solution at laboratory temperature. This indicates that the energy of the two tautomers in water solution is nearly equal. In contrast, the content of the N^7–H form in DMSO solution has been determined to be 30 and 33% using the values of the $^3J_{\mathrm{H8,C4}}$ and $^3J_{\mathrm{H8,C5}}$ coupling constants, respectively.

Very recently, a low-temperature NMR study of tautomerism in purine derivatives has been conducted.[63] The temperature dependences of the ^{1}H NMR spectra were studied in DMF-d_7 solution. Two sets of signals were observed in the NMR spectra of the two purine derivatives at 213 K, whereas at laboratory temperature, there was only a single set of signals, reflecting the time-averaged contribution of the two components. Based on the characteristic values of the ^{13}C and ^{15}N chemical shifts and the three-bond ^{1}H–^{13}C scalar coupling constants, the two components were determined to be the N^7–H and N^9–H tautomers. The NMR parameters obtained for the two tautomers of 6-methoxypurine are shown in Fig. 12.

3.3. Protonation

The protonation equilibria of various derivatives have long been extensively explored. These studies led to an understanding of the principal chemical and biological

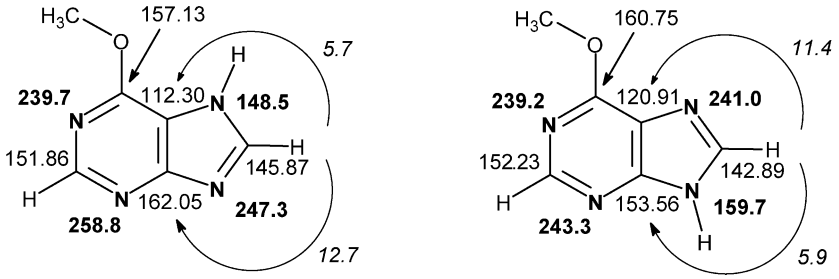

Fig. 12. ^{13}C- and ^{15}N-NMR chemical shifts (ppm) and three-bond ^{1}H–^{13}C scalar coupling constants (Hz) for the N^7–H and N^9–H tautomers of 6-methoxypurine in DMF-d_7 at 213 K.[63]

interactions that determine the biological activity of purine heterocycles. As indicated in previous sections, ^{15}N NMR spectroscopy has proven to be particularly useful for investigating proton-transfer processes in great detail.

A protonation study of purine and its N^7-methyl and N^9-methyl derivatives revealed that purine itself is protonated exclusively at position N-1, whereas N^1-H, N^9-H and N^1-H, N^7-H tautomers coexist in solution.[52,72] The dependence of the ^{13}C chemical shifts of purine, adenine, and adenosine on pH showed that protonation in an $HClO_4$-containing solution leads to the singly protonated species BH^+ClO4^-, whereas solutions containing HCl, TFA, and HSO_3F gave mixtures of singly, doubly, and triply protonated species, respectively.[73]

In the case of guanosine, the N-7 resonance shifts upfield by *ca* 40 ppm upon the addition of 1 molar equivalent of TFA, indicating that this is the preferred site of protonation. In contrast, the N-3 resonance shows only a minor upfield shift (*ca* 1 ppm), whereas N-9 and the NH_2 groups shift downfield by *ca* 3 ppm. N-1 is essentially unaffected. Similar work done on the structurally related inosine molecule also led to the conclusion that N-7 is the preferred site for protonation.

Upon the addition of 1 molar equivalent of TFA, adenosine protonates predominantly at the N-1 site, accompanied by a shielding of *ca* 70 ppm of the N-1 resonance. Like adenosine, N^9-ethyladenine is protonated predominantly at N-1, with a resonance shift of 77.2 ppm. With N^7-ethyladenine, there is compelling evidence of more than one protonation site. When 1.5 M equivalent of TFA was added, the nitrogen resonances of N-1, N-3, and N-9 all were shielded by 53.8, 29.9, and 9.9 ppm, respectively. These results are quite decisive in showing that the N^7-R forms have a rather more basic N-3 nitrogen than the N^9-R forms.

The protonation of compounds **22** and **23** using a DMSO solution and TFA has been similarly investigated.[39] The N^7-isomer is protonated at nitrogen atom N-9 whereas the N^9-isomer is protonated at N-7. Protonation at atom N-3 was, however, observed only for the N^7-derivative. The enhanced basicity of the N-3 and N-9 atoms in the N^7-isomers compared with those in the N^9-isomers can be explained by the absence of extensive delocalization of the electron lone pair on the corresponding atom of the N^7-isomer.

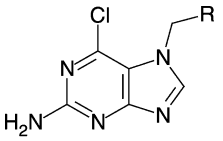

22

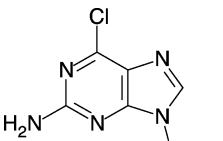

23

The nucleophilicity of the N-7 atom of guanosine, and some of its O^6- and N^1-substituted derivatives, has been studied by following the ^{15}N chemical shifts of the protonated species.[74] The effect of protecting groups of the nucleobases during

the acidic hydrolysis of the glycosidic bond of 2′-deoxyadenosine was investigated by ^{15}N NMR spectroscopy.[75] In a nonpolar environment, the N^1-alkyladenine derivatives were shown to exist predominantly in their imino forms. The content of the amino form increases with the dielectric constant of the medium.[76] In aqueous solution, the amino form predominates, and ^{13}C NMR spectroscopy indicates that mainly the N^9-position is protonated. In contrast, theoretical calculations and experimental measurements of the acidity confirm that N^3-methyladenine adopts predominantly the amino form.[77]

A protonation study of several ATP analogs has recently been reported.[44] The derivatives studied included C-2, C-8, and N-6 modified adenine and ATP compounds. Substituents of different nature and in various positions on the adenine ring do not change the preferred protonation site, which remains N-1. However, for 2-thioether-ATP derivatives, differences in the ^{15}N NMR chemical shifts have indicated a mixed population of N-1 and N-7 singly protonated species. All the ATP derivatives evaluated have shown basicity 0.4–1 pK_a units lower than ATP, except for 2-Cl-ATP, for which K_a was *ca* 10,000-fold lower. The ^{15}N NMR chemical shifts of the ATP analogs measured at pH 5.1–5.4 are summarized in Table 3.

A recent protonation study has investigated the behavior of N^6-benzoyl-3′,5′-diamino-2′,3′,5′-trideoxyadenosine.[78] Protonation constants of log K 9.21 and 6.57 were determined based on pH measurements and NMR spectroscopy.

8-Amino, 8-methylamino, and 8-dimethylamino-adenosines have been studied by ^{1}H and ^{15}N NMR in order to delineate the influences on the relative rate of cleavage of the glycosyl bond.[79] Analysis of the ^{15}N data showed that the relative amounts of protonation at N-1 in 8-aminoadenosine and 8-methylaminoadenosine are 66% (34% N^7H^+) and 85% (15% N^7H^+), respectively, while 96% (4% N^7H^+) has been found for 8-dimethylanimoadenosine.

3.4. Hydrogen bonding

HB belongs to the fundamental intermolecular interactions that determine the formation of supramolecular complexes and the interactions of small ligands with biological targets. The lone electron pairs of the nitrogen atoms and the hydrogen atoms bonded to nitrogens along with other heteroatoms, play crucial roles in primary molecular recognition. ^{15}N NMR spectroscopy is the method of choice for probing HB, since the nitrogen atoms are directly involved in this process.[80,81]

The stability of solute–solvent complexes is governed by the capacity of the solvent to form the specific hydrogen bonds. A comparative study of the chemical shifts of ^{15}N in adenosine and ATP in dimethylsulfoxide-d_6 and water was performed to gain insight into the HB effects. The N-1 resonance of ATP in water is *ca* 12 ppm more shielded than the N-1 of adenosine in dimethylsulfoxide-d_6. This clearly indicates significant interaction between the N-1 atom and the water molecule. For the protonated molecules, the chemical shift of N-1 for ATP in water is almost equivalent to that for adenosine in DMSO-d_6.

The self-association of guanosine (G), cytidine (C), and adenosine (A) and the base pairing between guanosine, cytidine, adenosine, and uridine in dimethylsulfoxide have

been investigated by following the changes in the ^{15}N NMR chemical shifts as the concentration and temperature were changed.[82] G, C, and A all showed evidence of self association by means of HB. In G–C mixtures, a hydrogen-bonded dimer formed; however, no base pairing could be detected in the A–C or A–U mixtures.

The loss of Hoogsteen pairing ability brought about by N^1-binding adenine to platinum has recently been studied using low-temperature NMR spectroscopy[83] in D_2O, DMF-d_7, and $CDClF_2/CDF_3$ mixtures. Comparison of the association of uridine with free and N^1-platinated adenine derivatives suggests that the interaction is inherently weaker in the case of the platinated compound. Complementary *ab initio* studies indicate that counter ions reduce the effective positive charge of the heavy metal ion Pt^{2+}, and thus diminish the interaction energies.

The binding of an acetic acid ligand to adenosine has been studied by ^1H spectroscopic techniques.[64] Using a low-melting deuterated Freon mixture as the solvent, liquid-state measurements could be performed in a slow-exchange regime and allowed the detailed characterization of the associates formed. It was found that at 128 K, trimolecular complexes with both the Watson–Crick and the Hoogsteen sites of the central adenine base occupied, coexist in various amounts, depending on the adenosine:acetic acid molar ratio. For acetic acid bound to an adenosine–thymidine base pair in either a Watson–Crick or a Hoogsteen configuration, the hydrogen bonds to the available adenine binding site are stronger than in the A-HAc_2 complex.

3.5. Metal complexation

A large number of NMR applications have focused on investigating purine complexes with metal ions or salts of transition metals.[84] These systematic studies of the interactions between metal ions and nucleobases started around 1950 and have many roots. The fact that nucleic acids are strong acids, present mostly as the salts of metal ions or protonated amines, was among the first discoveries. The discovery that cisplatin (*cis*-$[Pt(NH_3)_2Cl_2]$) is a potent antitumor agent, and the subsequent work that determined that the binding of Pt-complexes to DNA was responsible for triggering the killing of tumor cells, significantly stimulated the field. Metal-nucleobase studies have burgeoned ever since. The interested reader is referred to the review by Lippert[84] to learn the details of the binding patterns of metal ions to nucleobases.

A recent contribution[85] described the use of NMR spectroscopy for studying the solution and solid-state structures of Zn(II) chloride complexes with purine and methylpurine ligands. The formation of Zn(II)–N coordination bonds resulted in 3–15 ppm low-frequency shifts for the respective ^{15}N NMR signals. The nitrogen atoms coordinated were N-7 for purine, N-1 and N-9 for N^7-methylpurine, and N-1 and N-7 for N^9-methylpurine.

A series of Zn(II) and Cd(II) complexes of adenine and guanine derivatives has been characterized by single-crystal X-ray analysis and NMR spectroscopy (^1H, ROESY, and ^{113}Cd).[86] A wide range of structural types, including monomeric, dimeric, tetrameric, and polymeric architectures incorporating the N-7 atoms of the nucleobases, has been obtained. Additional metal–nucleobase coordination has generally been observed at the N^3-site of the adenine derivatives.

The effect of Pt^{2+} coordination on the acid–base properties of the purine ligands N^9-ethylguanine, N^9-methylhypoxanthine, inosine, N^9-methyladenine, and N^6,N^6,N^9-trimethyladenine has been quantitatively evaluated.[87] The acidity constants of the complexes were calculated by curve-fitting procedures, using the pH (pD) dependence of the ^{1}H NMR shift data. It was found that Pt^{2+} coordinated to the N^1-site acidifies the N-7 unit to the same extent as N^7-coordinated Pt^{2+} acidifies the N-1 site.

The value of ^{15}N relaxation rates (T_1) for examining the association of platinum-tetraamine cations with the mononucleotide 5′-GMP (guanosine-5′-monophosphate) has been demonstrated by incorporating labeled $^{15}NH_3$ into the Pt complex.[88] No major differences between the mononuclear and dinuclear complexes were detected. Recently, the time-dependence of the reaction of several new platinum complexes with 5′-GMP was followed by using ^{1}H-NMR analysis of the chemical shifts of the H-8 of GMP.[89] All these complexes interact with the mononucleotide at the N^7-position to form *bis*-GMP adducts. A small quantity of mono-GMP adduct is formed and subsequently diminishes within the first 10 h.

The migration of coordinated Pt(II) about the adenine ring has been studied using Pt(II) complexes of N^9-methyladenine in basic aqueous solution.[90] Upon displacement of an NH_2 proton the coordinated Pt(II) migrates from the endocyclic nitrogen N-7 or N-1 to the exocyclic amino group. Prolonged treatment of the N^6,N^7-bound complex in strongly basic solution resulted in the deamination of the N^7-bound 9-methyladenine, yielding a mixed-ligand complex consisting of N^6-bound 9-methyladenine and N^7-bound 9-methylhypoxanthine. Products of this unusual deamination reaction were characterized by ^{1}H and ^{195}Pt NMR spectroscopy and by X-ray crystallography.

A detailed ^{15}N NMR study of variously coordinated Pt(II)-9-methyladenine complexes has recently been published.[91] The compounds investigated represent various binding modes: $N^1 + N^6$; $N^6–N^7$; $N^1 + N^7$; N^1; $N^1 + N^6–N^7$. In Fig. 13, selected compounds are depicted with the corresponding ^{15}N and ^{13}C NMR chemical shifts.

The interactions of guanine, guanosine, and 5′-GMP with Pd(II) complexes have been studied by pH measurements and ^{1}H NMR.[92] In strongly acidic solution, where $N^1–H$ is still protonated, only N-7 is coordinated to the metal ion, but as the pH increases to ~3, ^{1}H NMR shows that both N^7-only and N^1-only coordinated species come into existence. At pH 4–5, both N^1-only and N^1,N^7-bridged coordination to Pd(II) complexes are found.

Organometallic ruthenium(II)-arene anticancer complexes specifically target the guanine bases of DNA oligomers and form monofunctional adducts. The structures of several monofunctional adducts with guanine derivatives have been investigated in solution by using 2D NOESY and $^1H–^{15}N$ HSQC.[93] NOE studies have revealed that a syn orientation predominates for all the biphenyl-G adducts. This predominance can be attributed to hydrophobic interactions between the arene and purine rings. The NH protons of the donor complex are involved in strong H-bonding with the 5′-phosphate and O-6 of 5′-GMP. The strong H-bonding from the G O-6 to the NH protons partly accounts for the strong preference of the Ru(II) complex for binding to G rather than A.

^{1}H NMR studies of AMP, ADP, and ATP in the presence of Mg^{2+} give no indication of the existence of an interaction between Mg^{2+} and the adenine ring in the Mg^{2+}–nucleotide complexes under the experimental conditions used.[94] However, a conformational study of 2′-deoxyguanosine 5′-methylmonophosphate and 2′-deoxyguanosine

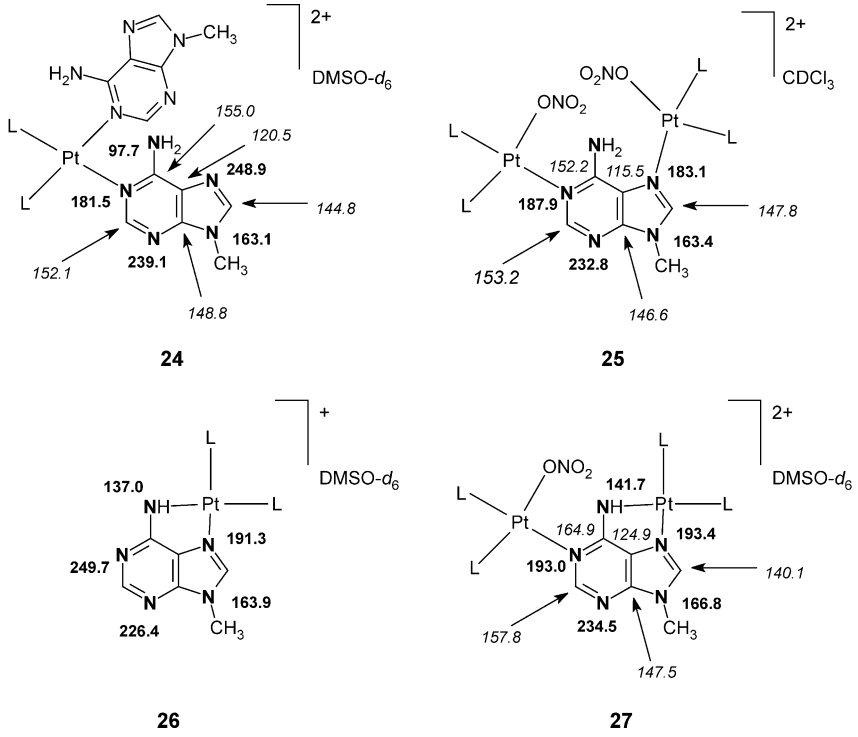

Fig. 13. ^{13}C- and ^{15}N-NMR chemical shifts (ppm) for various Pt(II)-9-methyladenine complexes in DMSO-d_6 or $CDCl_3$.

3′-methylmonophosphate and their interactions with Mg^{2+}, Zn^{2+}, and Hg^{2+} ions has been reported more recently.[95] The conformation of these compounds in D_2O solution was inferred from vicinal proton–proton, proton–phosphorus, and carbon–phosphorus NMR coupling constants and nuclear Overhauser effects. The chemical changes showed that hard Mg^{2+} ions interact preferentially with the phosphate oxygen atoms and the C^6═O carbonyl group. Softer Zn^{2+} and Hg^{2+} ions were found to show a strong binding affinity towards N-7. This study also revealed the strengthening of the anomeric effect by soft M^{2+} ions.

4. SOLID-STATE NMR

Currently, solid-state NMR spectroscopy is a rapidly developing technique in all branches of chemistry.[96] Solid-state NMR spectra are capable of providing information that is difficult or impossible to obtain from measurements in solution. In isotropic solutions, or in the fast Magic Angle Spinning (MAS) spectra of solids, the observed isotropic chemical shift represents the result of motional averaging of the principal components (δ_{11}, δ_{22}, and δ_{33}) of the chemical-shift tensors. The spinning rate decreases,

an increasing number of spinning sidebands appears in the spectrum because the chemical-shift anisotropy (CSA) is no longer completely averaged out by rotation. The intensities of the spinning sidebands contain information about the shift tensor, and through an appropriate analysis,[97] one can determine the principal components of the shift tensor, δ_{11}, δ_{22}, and δ_{33}. This method is conceptually straightforward, requiring only the acquisition of a slow-spinning 1D MAS spectrum.

If the spectra are too crowded with sidebands, 2D NMR spectroscopy can advantageously spread the overlapping CSA patterns across a second dimension. An array of these techniques is currently available (PASS, MAT, VACSY, FIREMAT, etc.), and they are described in excellent review articles.[96,98,99] However, the analysis of powdered samples with the natural abundance of ^{13}C and ^{15}N is not capable of providing information about the orientation of individual shielding-tensor components in the molecular frame. At present, the orientation of the principal components in the molecular frame is available from quantum chemical calculations. This topic will be discussed briefly in Section 5.

The principal components of the chemical-shift tensor are usually determined by fitting the theoretically predicted data to the experimentally obtained values. A number of simulation and fitting programs are currently available, e.g., SIMPSON,[100] DMFIT,[101] etc. Due to the strong and complicated dipole–dipole interactions of ^{1}H nuclei, only the ^{13}C and ^{15}N spectra are discussed briefly in the following paragraphs.

4.1. ^{13}C NMR

The carbon atoms of the purine skeleton form part of an aromatic system. Their electronic environment is reflected in relatively large CSA values. The most-shielded components of the ^{13}C shift tensors, δ_{33}, are always oriented perpendicular to the purine ring. Generally, the perpendicular ^{13}C shift-tensor components ($\delta_{\perp}$) of protonated and alkyl-substituted aromatic carbons are larger than those of aromatic bridgehead carbons.[102] The orientations of the in-plane δ_{11} and δ_{22} components are strongly dependent on the atomic environment (the presence of electron lone pairs on neighboring nitrogen atoms, the p-character of the chemical bonds). Some general trends have been discussed in Section 2.2.

The chemical shifts and principal values of the shift tensors determined for adenosine and guanosine in the solid state by using the FIREMAT experiment[38] are summarized in Table 14.

4.2. ^{15}N NMR

As already mentioned, a paper comprehensively describing the experimental values of the principal components of the shielding tensors of the nitrogen atoms in various nitrogen heterocycles was published[46] by Grant and co-workers in 1997. Based on quantum chemical calculations, the same paper reports the orientations of the individual components of the shielding tensors. The findings and generalizations are described in Section 2.3. This study was later extended by investigating nucleic acid bases, including adenine and guanine.[51] Recently, the same group has also published the values of

Table 14. Experimental principal values of the ^{13}C chemical-shift tensor and the isotropic MAS (ppm) for adenosine and guanosine dihydrate[38]

Compound	Atom	MAS	δ_{11}	δ_{22}	δ_{33}
Adenosine	C-2	154.8	239	158	66
	C-4	148.5	221	166	58
	C-5	119.7	167	145	47
	C-6	155.2	222	191	52
	C-8	137.8	216	136	61
Guanosine dihydrate	C-2	152.2	223	165	66
	C-2		223	165	66
	C-4	151.4	223	165	66
	C-4	150.0	223	165	66
	C-5	115.2	159	138	49
	C-5	115.9	160	140	49
	C-6	157.7	237	154	82
	C-6	157.7	237	154	82
	C-8	138.2	214	141	59
	C-8	136.9	214	134	66

the ^{13}C and ^{15}N chemical-shifts tensors for adenosine and guanosine dehydrate among others.[38] The experimental and theoretical values of the ^{15}N chemical-shift tensors of some purine derivatives have been reported recently.[41] The values for several adenine and guanine derivatives are summarized in Table 15.

5. QUANTUM-CHEMICAL CALCULATIONS OF NMR PARAMETERS

5.1. Geometry

Many approaches ranging from molecular mechanics to electron-correlation second-order Møller-Plesset (MP2) methods have been used for optimizing the geometry of molecular systems. Here, no attempt is made to cover the technical details of various methods, and the reader is referred to the original literature for a comprehensive treatment.

Ab initio quantum-chemical calculations including electron correlation have significantly contributed to understanding the molecular interactions of DNA and RNA bases. High-level approaches have been extremely useful in addressing the planarity and flexibility of the amino groups in DNA bases.[103] *Ab initio* calculations unambiguously predicted that the amino groups of bases are intrinsically non-planar, with partial sp^3 hybridization of the nitrogen atoms of the amino groups. Very recently, this theoretically predicted non-planarity has been confirmed experimentally.[104] The non-planarity of guanine is larger than that of adenine and the amino group is also substantially rotated due to repulsion between the N^1–hydrogen and the amino hydrogen. The amino group hydrogen atoms are very flexible and can form efficient out-of-plane hydrogen bonds. Further, the nitrogen atom of the amino group can serve as a weak H-bond acceptor.

Table 15. Experimental principal values of the ^{15}N chemical-shift tensor and the isotropic MAS (ppm) for various purine derivatives[38,41,51]

Compound	Atom	MAS	δ_{11}[a]	δ_{22}[a]	δ_{33}[a]
Adenine	N-1	226.7	364	306	9
	N-3	216.7	356	303	−9
	N-7	234.7	413	284	9
	N-9	162.7	240	182	65
	NH_2	92.7	161	58	58
Guanine	N-1	150.7	223	150	80
	N-3	175.7	296	222	10
	N-7	234.7	388	280	39
	N-9	153.7	247	155	58
	NH_2	79.7	132	62	44
Adenosine	N-1	224.3	353	298	22
	N-3	217.2	355	300	−4
	N-7	237.6	422	288	3
	N-9	172.8	234	184	101
	NH_2	85.2	153	57	48
Guanosine dihydrate	N-1	154.2	239	147	75
		151.5	233	151	74
	N-3	163.5	273	218	1
			282	223	−2
	N-7	232.7	406	278	14
		234.0	420	283	0
	N-9	168.3	232	183	91
		170.5	230	193	90
	NH_2	78.4	133	54	48
		82.3	141	72	34
12	N-1	229.0	421.4	190.5	75.1
	N-3	220.8	428.0	215.7	18.8
	N-7	236.4	487.4	211.3	10.5
	N-9	153.1	242.1	146.4	70.8
	NH−C2	144.9	214.1	132.6	87.8
	N−X	119.8	–[b]	–[b]	–[b]
15	N-1	248.5	448.0	317.6	−19.9
	N-3	255.5	462.5	321.7	−16.0
	N-7	141.4	238.0	104.1	83.9
	N-9	251.1	425.6	308.0	26.7
	N-6	204.5	369.2	234.4	3.6
	N−X	107.2	204.1	63.1	55.8
14	N-1	261.0	457.4	347.5	−13.1
	N-3	233.0	449.0	273.0	−20.1
	N-7	244.3	450.3	273.7	12.2
	N-9	147.1	–[b]	–[b]	–[b]
	N-6	216.3	401.4	215.4	36.4
	N−X	112.0	–[b]	–[b]	–[b]
	CN	257.1	398.8	398.8	−23.6

[a] δ_{11}, δ_{22}, and δ_{33} (ppm) represent the three components of the shift tensor expressed in its principal axis system with the following rule: $\delta_{11} \geq \delta_{22} \geq \delta_{33}$.

[b] Not obtained.

Studies based on *ab initio* optimized geometries (B3LYP/6-311 + G** and MP2/6-311 + G** levels) and on experimental structures retrieved from the Cambridge Structural Database (CSD) reveal that the nucleobases constituting DNA and RNA differ significantly in their aromatic character, as shown by the geometry-based index of aromaticity HOMA.[105] The aromaticity of the bases decreases markedly with an increase in the number of double-bond C═X substituents at the rings. H-bonds involving C═O groups in Watson–Crick pairs cause an increase in the aromatic character of the rings. The alternative approach for determining the index of aromaticity is based on the nucleus-independent chemical shifts (NICS).[106]

DNA bases can undergo proton shifts while forming various tautomers. Studies of tautomerism in the gas phase can show the relative stabilities of the individual tautomers. However, a bulk solvent and also a microhydrated environment can change the relative stabilities substantially.[107,108]

Studying the complexes of purines with the transition metals or the interactions of purines with metal ions requires relativistic effective core potentials (RECP), as implemented, e.g., in the Gaussian program package (gaussian basis functions), or the relativistic correction terms included in the Hamiltonian, as implemented, e.g., in the ADF software (STO orbitals). Heavy-metal electron shells, which contain significant contributions from diffuse outer orbitals, are less suitable for representation by means of gaussian orbitals (which drop off too rapidly in the outer region) than the shells of lighter atoms.[109]

The inclusion of intermolecular interactions is important, especially when calculating the chemical shielding of a nitrogen nucleus. Whereas the experimental chemical shielding of the carbon atom is relatively well reproduced by using the isolated-molecule approach, inclusion of the molecular environment is essential for ^{15}N calculations. Two principally different approaches are currently used for these calculations. The first is represented by a continuum model that usually incorporates the dielectric constant of the environment. The supramolecular approach is based on simulating the environment by including a few solvent molecules explicitly at the same computational level. This approach, however, gives the local minimum and one has to look for the different conformations. For simple molecules this can be done by using a systematic conformational search. However, molecular dynamics is frequently used to explore the potential hyperface for large and complicated molecules. Unfortunately, because of its dependence on experimental parameterization, this approach is not generally applicable. Quantum dynamics may become the method of choice for such studies in the near future.

The molecular geometry obtained by experimental methods can be used to calculate the NMR parameters (especially for solid-state studies). These experimental techniques include diffraction methods (especially X-ray, electron, and neutron). However, specifically in the case of the widely used X-ray diffraction technique, the position of the hydrogen atoms is poorly described and must be corrected or re-optimized before the topology is used to calculate the NMR parameters. The application of the embedded ion method (EIM) as a general approach to efficiently include intermolecular interactions and to optimize the positions of protons has recently been described.[110]

For optimized or experimentally determined molecular topology, NMR parameters can be calculated at various levels of theory. The tremendous progress in

the quantum-chemical calculation of NMR parameters allows one to obtain reliable results, even for systems of considerable size, using density-functional theory (DFT), to take into account the relativistic effect in compounds containing heavier elements, and to get highly accurate data for difficult cases employing the post-Hartree–Fock (HF) approaches.

5.2. Chemical shifts

Currently, several methods are available for calculating the chemical shifts.[111] The gauge including atomic orbital (GIAO) method uses basis functions with explicit field dependence and was first adopted for quantum-chemical calculations of the NMR parameters by Ditchfield.[112] The individual gauge for localized orbitals (IGLO) alternative method, which uses molecular orbitals with explicit field dependence, was developed by Kutzelnigg.[113] These methods supply the NMR shielding tensors (values of σ_{11}, σ_{22}, and σ_{33} and their orientations in the molecular reference frame). From these values, the isotropic shieldings can be calculated as $\sigma_{iso} = 1/3(\sigma_{11} + \sigma_{22} + \sigma_{33})$, where $\sigma_{33} > \sigma_{22} > \sigma_{11}$. These values are related to the chemical shifts by adding or subtracting the shielding constant of the reference compound. The calculations thus not only allow extracting the values of the principal components but also provide the orientations of the individual components in the molecular system. This information is frequently used in solid-state studies to orient the experimentally determined principal values δ_{11}, δ_{22}, and δ_{33} into the axis system of the molecule.

The earliest calculations of the chemical-shift tensors for some purine bases employed an IGLO method of the HF type.[114] The general findings agree well with the results obtained recently by a combination of experimental solid-state measurements and GIAO calculations.[38]

Nowadays, NMR parameters are frequently calculated at the DFT level.[115] This approach produces better results than the HF method with comparable computational requirements. A review article describing the calculation of chemical shifts in heterocyclic compounds has recently been published.[116]

As already discussed in previous sections, the ^{15}N chemical shielding is very sensitive to the formation of hydrogen bonds. This phenomenon has also been explored by using theoretical calculations. The principal values of the shielding tensors of nitrogen atoms and their orientations in the molecular frame system, as a function of the hydrogen-bond length, have been systematically investigated for nucleic acid base pairs. Both the magnitudes and the orientations of the principal components strongly depend on the distance between the bases.[117]

A study investigating the influence of the stacking $\sigma-\pi$ and $\pi-\pi$ interactions on the shielding tensors has also been discussed recently. However, only the model systems of benzene and formamidine dimers were investigated.[118]

Calculated NMR shifts can be used to explore the composition of a fast-exchange system (tautomerism, protonation). The theoretically calculated NMR chemical shifts of the N^7–H and N^9–H purine tautomers have been used to analyze the experimentally observed chemical shifts and to calculate the tautomeric ratio.[119]

5.3. Coupling constants

As described previously, the coupling constants also represent valuable parameters for studying the structure of purine derivatives. Unfortunately, the extraction of relevant chemical information (geometry and electronic structure) is not always straightforward, and couplings often require careful analysis and interpretation.[56,120]

In the non-relativistic treatment, there are four contributions to the indirect nuclear spin–spin coupling constant: the Fermi-contact (FC), paramagnetic spin-orbit (PSO), spin-dipolar (SD), and diamagnetic spin-orbit (DSO) terms. Splitting the total coupling constant into these four contributions may be considered the first level of interpretation.[121]

Several approaches relying on the decomposition of couplings into contributions from different sorts of orbitals are currently available (sum-over-states – SOS, finite perturbation theory – FPT). However, the decomposition of the couplings into separate contributions is by no means unique. An alternative way is to look at the distribution of some functions, closely related to the coupling, in 3-D space, without further separation.[121]

A paper describing the DFT calculations of spin–spin scalar coupling constants in N^9-methyladenine and N^9-methylguanine has recently appeared. The calculated values of various coupling constants agree remarkably well with those previously reported.[24]

A comprehensive monograph covering the state-of-the-art theoretical tools for calculating NMR parameters has recently been published, and the interested reader is referred to this book for a more detailed treatment of the subject.[122]

6. MISCELLANEOUS

During the last decade many novel purine derivatives have been isolated from natural sources.

The structure of mucronatine, a new *N*-methyl purine obtained from *Stryphnus mucronatus*, was investigated by using an $^1H-^{15}N$ GHMBC experiment.[123] Three new purine derivatives have recently been isolated from New Zealand ascidians. N^2,N^2,N^7-trimethylguanine[124] has been isolated from *Lissoclinum notti*, and N^1,N^3,N^7-trimethylisoguanine[125] and N^1,N^3-dimethyl-8-oxoisoquanine[126] have been isolated from *Pseudodistoma cereum*. The structures of these compounds were elucidated by the use of standard spectroscopic techniques, including $^1H-^{15}N$ 2D NMR at natural abundance. A new purine, N^3,N^7-dimethylguanine, has been isolated from the marine sponge *Zyzzya fuliginosa* and analyzed by 1D and 2D NMR, including $^1H-^{15}N$ g-HMBC.[127]

Several condensation products with an additional ring formed by bridging the N-1 or N-3 with the NH_2 nitrogen of a guanine analog[128] and the N-1 and NH_2 nitrogen atoms of 2-aminopurine with several aldehydes, have been described very recently.[129] $^1H-^{13}C$ long-range correlations have been used to determine the mode of cyclization during the chemical preparation of asmarine alkaloids from substituted purines.[130]

7. CONCLUSIONS

To conclude this review, several important aspects should be highlighted. The nitrogen atoms of the purine skeleton are the centers for the intermolecular interactions between the purine molecule and its environment. The changes in the electron distribution induced by these interactions are reflected in changes of several NMR parameters which can be obtained from the samples at natural ^{13}C and ^{15}N abundance, namely the ^{13}C and ^{15}N NMR chemical shifts and the $^{1}H-^{13}C$ and $^{1}H-^{15}N$ scalar coupling constants. All these parameters can be used to study the purine structure in detail.

Solid-state NMR spectroscopy is capable of providing NMR parameters that are unobtainable by solution-state NMR. Probably the most important parameters for investigating small molecules are the magnitudes and orientations of the principal components of the shielding tensors.

At present, theoretical calculations are capable of reproducing and predicting NMR parameters with high accuracy. This is especially important in solution-state NMR for predicting the parameters of the individual components involved in dynamic processes. A theoretical approach is also used to calculate the solid-state parameters (e.g., the orientations of the principal components of the chemical shift), which are unavailable from measurements on powdered samples.

The combination of NMR spectroscopy in solution and in the solid state, X-ray analysis, and theoretical calculations, thus represents a powerful tool for investigating the electronic structure of purines in great detail.

ACKNOWLEDGEMENTS

The financial support of the Ministry of Education of the Czech Republic (LN00A016) is gratefully acknowledged. We would like to thank Dr. Michal Hocek (Institute of Organic Chemistry and Biochemistry, AS CR, Prague) for the sample of 6-methoxy-N^7-benzylpurine.

REFERENCES

1. J. H. Lister, *The Purines*, Wiley, New York, 1996.
2. S. S. Bhagwat and M. Williams, *Eur. J. Med. Chem.*, 1997, **32**, 183.
3. P. Legault and A. Pardi, *J. Am. Chem. Soc.*, 1997, **119**, 6621.
4. A. Gforer, M. Schnetter, J. Wolfrum and K. D. Greulich, *Ber. Bunsen-Ges. Phys. Chem.*, 1989, **93**, 300.
5. R. Cali, S. Musumeci, C. Rigano and S. Sammartano, *Inorg. Chim. Acta*, 1981, **56**, L11.
6. E. De Clercq, *Nat. Rev. Drug Discov.*, 2002, **1**, 13.
7. M. Kidwai, R. Venkataramanan, R. Mohan and P. Sapra, *Curr. Med. Chem.*, 2002, **9**, 1209.
8. B. Pullman and A. Pullman, *Adv. Heterocycl. Chem.*, 1971, **13**, 77.
9. L. Müller, *J. Am. Chem. Soc.*, 1979, **101**, 4481.
10. G. Bodenhausen and D. J. Ruben, *Chem. Phys. Lett.*, 1980, **69**, 185.
11. A. Bax and M. F. Summers, *J. Am. Chem. Soc.*, 1986, **108**, 2093.
12. W. Willker, D. Leibfritz, R. Kerssebaum and W. Bermel, *Magn. Reson. Chem.*, 1993, **31**, 287.
13. R. Marek, L. Králík and V. Sklenář, *Tetrahedron Lett.*, 1997, **38**, 665.

14. H. Koskela, I. Kilpeläinen and S. Heikkinen, *J. Magn. Reson.*, 2003, **164**, 228.
15. M. Eberstadt, G. Gemmecker, D. F. Mierke and H. Kessler, *Angew. Chem., Int. Ed. Engl.*, 1995, **34**, 1671.
16. B. L. Marquez, W. H. Gerwick and R. T. Williamson, *Magn. Reson. Chem.*, 2001, **39**, 499.
17. R. Marek and A. Lyčka, *Curr. Org. Chem.*, 2002, **6**, 35.
18. D. S. Wishart, C. G. Bigam, J. Yao, F. Abildgaard, H. J. Dyson, E. Oldfield, J. L. Markley and B. D. Sykes, *J. Biomol. NMR*, 1995, **6**, 135.
19. M. Witanowski, L. Stefaniak and G. A. Webb, *Annu. Rep. NMR Spectrosc.*, 1993, **25**, 1.
20. G. W. Buchanan, *Tetrahedron*, 1989, **45**, 581.
21. G. E. Martin and C. E. Hadden, *J. Nat. Prod.*, 2000, **63**, 543.
22. P. Büchner, W. Maurer and H. Rüterjans, *J. Magn. Reson.*, 1978, **29**, 45.
23. S. S. Wijmenga and B. N. M. van Buuren, *Prog. NMR Spectrosc.*, 1998, **32**, 287.
24. R. Fiala, M. L. Munzarová and V. Sklenář, *J. Biomol. NMR*, 2004, **29**, 477.
25. I. M. Lagoja and P. Herdewijn, *Synthesis*, 2002, 301.
26. J. H. Keck, Jr., R. A. Simpson and J. L. Wong, *J. Org. Chem.*, 1978, **43**, 2587.
27. W. C. Coburn, Jr., M. C. Thorpe, J. A. Montgomery and K. Hewson, *J. Org. Chem.*, 1965, **30**, 1110.
28. M. Hocek and A. Holý, *Collect. Czech. Chem. Commun.*, 1995, **60**, 1386.
29. M. Hocek and A. Holý, *Collect. Czech. Chem. Commun.*, 1999, **64**, 229.
30. D. Hocková, M. Hocek, H. Dvořáková and I. Votruba, *Tetrahedron*, 1999, **55**, 11109.
31. M. Hocek, A. Holý, I. Votruba and H. Dvořáková, *J. Med. Chem.*, 2000, **43**, 1817.
32. D. Taddei, P. Kilian, A. M. Z. Slawin and J. Derek Woollins, *Org. Biomol. Chem.*, 2004, **2**, 665.
33. M. Hocek and H. Dvořáková, *J. Org. Chem.*, 2003, **68**, 5773.
34. M. Hocek, H. Dvořáková and I. Císařová, *Collect. Czech. Chem. Commun.*, 2002, **67**, 1560.
35. M. C. Thorpe, W. C. Coburn and J. A. Montgomery, *J. Magn. Reson.*, 1974, **15**, 98.
36. R. J. Pugmire, D. M. Grant, L. B. Townsend and R. K. Robins, *J. Am. Chem. Soc.*, 1973, **95**, 2791.
37. J. C. Facelli and D. M. Grant, *Top. Stereochem.*, 1989, **19**, 1.
38. D. Stueber and D. M. Grant, *J. Am. Chem. Soc.*, 2002, **124**, 10539.
39. G. Remaud, J. Kjellberg, H. Bazin, N. G. Johansson and J. Chattopadhyaya, *Tetrahedron*, 1986, **42**, 5073.
40. D. Hocková, M. Buděšínský, R. Marek, J. Marek and A. Holý, *Eur. J. Org. Chem.*, 1999, 2675.
41. R. Marek, J. Brus, J. Toušek, L. Kovács and D. Hocková, *Magn. Reson. Chem.*, 2002, **40**, 353.
42. V. Markowski, G. R. Sullivan and J. D. Roberts, *J. Am. Chem. Soc.*, 1977, **99**, 714.
43. A. Laxer, D. T. Major, H. E. Gottlieb and B. Fischer, *J. Org. Chem.*, 2001, **66**, 5463.
44. D. T. Major, A. Laxer and B. Fischer, *J. Org. Chem.*, 2002, **67**, 790.
45. M. Hocek, I. Votruba and H. Dvořáková, *Tetrahedron*, 2003, **59**, 607.
46. M. S. Solum, K. L. Altmann, M. Strohmeier, D. A. Berges, Y. Zhang, J. C. Facelli, R. J. Pugmire and D. M. Grant, *J. Am. Chem. Soc.*, 1997, **119**, 9804.
47. J. C. Facelli, D. M. Grant and J. Michl, *Int. J. Quant. Chem.*, 1987, **31**, 45.
48. M. S. Solum, J. C. Facelli, J. Michl and D. M. Grant, *J. Am. Chem. Soc.*, 1986, **108**, 6464.
49. J. C. Facelli, *Encyclopedia of Nuclear Magnetic Resonance*, D. M. Grant and R. K. Harris, eds., Wiley, London, 1996, 4299.
50. N. F. Ramsey, *Phys. Rev.*, 1950, **77**, 567.
51. J. Z. Hu, J. C. Facelli, D. W. Alderman, R. J. Pugmire and D. M. Grant, *J. Am. Chem. Soc.*, 1998, **120**, 9863.
52. R. J. Pugmire and D. M. Grant, *J. Am. Chem. Soc.*, 1971, **93**, 1880.
53. U. Ewers, A. Gronenborn and H. Günther, *Chemistry and Biology of Pteridines*, W. Pfleiderer, ed., W. De Gruyter, Berlin, 1976.
54. R. E. Wasylishen and G. Tomlinson, *Can. J. Biochem.*, 1977, **55**, 579.
55. M. Schumacher and H. Günther, *J. Am. Chem. Soc.*, 1982, **104**, 4167.
56. R. H. Contreras and J. E. Peralta, *Prog. NMR Spectrosc.*, 2000, **37**, 321.
57. R. M. Claramunt, D. Sanz, C. López, J. A. Jiménez, M. L. Jimeno, J. Elguero and A. Fruchier, *Magn. Reson. Chem.*, 1997, **35**, 35.
58. M. Schumacher and H. Günther, *Chem. Ber.*, 1983, **116**, 2001.
59. S. Prekupec, D. Svedružić, T. Gazivoda, D. Mrvoš-Sermek, A. Nagl, M. Grdiša, K. Pavelić, J. Balzarini, E. De Clercq, G. Folkers, L. Scapozza, M. Mintas and S. Rais-Malić, *J. Med. Chem.*, 2003, **46**, 5763.

60. E. Kolehmainen, *Annu. Rep. NMR Spectrosc.*, 2003, **49**, 1.
61. E. Kleinpeter, *Adv. Mol. Struct. Res.*, 2000, **6**, 97.
62. K. Orrell, *Annu. Rep. NMR Spectrosc.*, 1999, **37**, 2.
63. P. Sečkářová, R. Marek, K. Maliňáková, E. Kolehmainen, D. Hocková, M. Hocek and V. Sklenář, *Tetrahedron Lett.*, 2004, **45**, 6259.
64. E. M. B. Janke, H.-H. Limbach and K. Weisz, *J. Am. Chem. Soc.*, 2004, **126**, 2135.
65. M. Sedlák, P. Šimůnek and M. Antonietti, *J. Heterocycl. Chem.*, 2003, **40**, 671.
66. F. Lemière, K. VanHoutte, T. Jonckers, R. Marek, E. L. Esmans, M. Claeys, E. Van den Eeckhout and H. Van Onckelen, *J. Mass Spectrom.*, 1999, **34**, 820.
67. W. F. Veldhuyzen, A. J. Shallop, R. A. Jones and S. E. Rokita, *J. Am. Chem. Soc.*, 2001, **123**, 11126.
68. M.-T. Chenon, R. J. Pugmire, D. M. Grant, R. P. Panzica and L. B. Townsend, *J. Am. Chem. Soc.*, 1975, **97**, 4636.
69. M.-T. Chenon, R. J. Pugmire, D. M. Grant, R. P. Panzica and L. B. Townsend, *J. Am. Chem. Soc.*, 1975, **97**, 4627.
70. N. C. Gonnella, H. Nakanishi, J. B. Holtwick, D. S. Horowitz, K. Kanamori, N. J. Leonard and J. D. Roberts, *J. Am. Chem. Soc.*, 1983, **105**, 2050.
71. B. P. Cho and F. Evans, *Nucleic Acid Res.*, 1991, **19**, 1041.
72. N. C. Gonnella and J. D. Roberts, *J. Am. Chem. Soc.*, 1982, **104**, 3162.
73. R. L. Benoit and M. Fréchette, *Can. J. Chem.*, 1984, **62**, 995.
74. G. Remaud, X.-X. Zhou, C. J. Welch and J. Chattopadhyaya, *Tetrahedron*, 1986, **42**, 4057.
75. G. Remaud, X.-X. Zhou, J. Chattopadhyaya, M. Oivanen and H. Lŏnnberg, *Tetrahedron*, 1987, **43**, 4453.
76. M. Dreyfus, G. Dodin, O. Bensaude and J. E. Dubois, *J. Am. Chem. Soc.*, 1977, **99**, 7027.
77. S. Sharma and J. K. Lee, *J. Org. Chem.*, 2002, **67**, 8360.
78. I. Lavandera, S. Fernández, M. Ferrero and V. Gotor, *Tetrahedron*, 2003, **59**, 5449.
79. J. Hovinen, C. Glemarec, A. Sandstom, C. Sund and J. Chattopadhyaya, *Tetrahedron*, 1991, **47**, 4693.
80. L. Stefaniak, *Polish J. Chem.*, 1999, **73**, 173.
81. W. Schilf and L. Stefaniak, *Bull. Pol. Acad. Sci., Chem.*, 1998, **46**, 15.
82. C. Dyllick-Brenzinger, G. R. Sullivan, P. P. Pang and J. D. Roberts, *Proc. Natl Acad. Sci USA*, 1980, **77**, 5580.
83. K. S. Schmidt, J. Reedijk, K. Weisz, E. M. B. Janke, J. E. Sponer, J. Sponer and B. Lippert, *Inorg. Chem.*, 2002, **41**, 2855.
84. B. Lippert, *Coord. Chem. Rev.*, 2000, **200**, 487.
85. E. Szłyk, L. Pazderski, I. Łakomska, A. Wojtczak, L. Kozerski, J. Sitkowski, B. Kamieński and H. Günther, *Polyhedron*, 2003, **22**, 391.
86. M. A. Shipman, C. Price, A. E. Gibson, M. R. J. Elsegood, W. Clegg and A. Houlton, *Chem. Eur. J.*, 2000, **6**, 4371.
87. R. Griesser, G. Kampf, L. E. Kapinos, S. Komeda, B. Lippert, J. Reedijk and H. Sigel, *Inorg. Chem.*, 2003, **42**, 32.
88. Y. Qu and N. Farrell, *Inorg. Chim. Acta*, 1996, **245**, 265.
89. S. Moradell, J. Lorenzo, A. Rovira, M. S. Robillard, F. X. Avilés, V. Moreno, R. de Llorens, M. A. Martinez, J. Reedijk and A. Llobet, *J. Inorg. Biochem.*, 2003, **96**, 493.
90. J. Arpalahti and K. D. Klika, *Eur. J. Inorg. Chem.*, 2003, 4195.
91. B. Longato, L. Pasquato, A. Mucci, L. Schenetti and E. Zangrando, *Inorg. Chem.*, 2003, **42**, 7861.
92. S. Zhu, A. Matilla, J. M. Tercero, V. Vijayaragavan and J. A. Walmsley, *Inorg. Chim. Acta*, 2004, **357**, 411.
93. H. Chen, J. A. Parkinson, S. Parsons, R. A. Coxall, R. O. Gould and P. J. Sadler, *J. Am. Chem. Soc.*, 2002, **124**, 3064.
94. P. Wang, R. M. Izatt, J. L. Oscarson and S. E. Gillespie, *J. Phys. Chem.*, 1996, **100**, 9556.
95. M. Polak and J. Plavec, *Eur. J. Inorg. Chem.*, 1999, 547.
96. D. D. Laws, H.-M. L. Bitter and A. Jerschow, *Angew. Chem. Int. Ed.*, 2002, **41**, 3096.
97. J. Herzfeld and A. E. Berger, *J. Chem. Phys.*, 1980, **73**, 6021.
98. M. J. Potrzebowski, *Eur. J. Org. Chem.*, 2003, 1367.
99. O. N. Antzutkin, *Prog. NMR Spectrosc.*, 1999, **35**, 203.

100. M. Bak, J. T. Rasmussen and N. C. Nielsen, *J. Magn. Reson.*, 2000, **147**, 296.
101. D. Massiot, F. Fayon, M. Capron, I. King, S. Le Calve, B. Alonso, J. O. Durand, B. Bujoli, Z. H. Gan and G. Hoatson, *Magn. Reson. Chem.*, 2002, **40**, 70.
102. R. J. Iuliucci, C. G. Phung, J. C. Facelli and D. M. Grant, *J. Am. Chem. Soc.*, 1996, **118**, 4880.
103. J. Šponer and P. Hobza, *Collect. Czech. Chem. Commun.*, 2003, **68**, 2231.
104. F. Dong and R. E. Miller, *Science*, 2002, **298**, 1227.
105. M. K. Cyrański, M. Gilski, M. Jaskólski and T. M. Krygowski, *J. Org. Chem.*, 2003, **68**, 8607.
106. P. V. Schleyer, C. Maerker, A. Dransfeld, H. Jiao and N. J. R. V. Hommes, *J. Am. Chem. Soc.*, 1996, **118**, 6317.
107. M. Hanus, F. Ryjáček, M. Kabeláč, T. Kubař, T. V. Bogdan, S. A. Trygubenko and P. Hobza, *J. Am. Chem. Soc.*, 2003, **125**, 7678.
108. M. Hanus, M. Kabeláč, J. Rejnek, F. Ryjáček and P. Hobza, *J. Phys. Chem. B*, 2004, **108**, 2087.
109. J. Kozelka and J. Bergès, *J. Chim. Phys.*, 1998, **95**, 2226.
110. D. Stueber, F. N. Guenneau and D. M. Grant, *J. Chem. Phys.*, 2001, **114**, 9236.
111. T. Helgaker, M. Jaszuński and K. Ruud, *Chem. Rev.*, 1999, **99**, 293.
112. R. Ditchfield, *Mol. Phys.*, 1974, **27**, 789.
113. W. Kutzelnigg, *Isr. J. Chem.*, 1980, **19**, 193.
114. M. Schindler, *J. Am. Chem. Soc.*, 1988, **110**, 6623.
115. P. Geerlings, F. De Proft and W. Langenaeker, *Chem. Rew.*, 2003, **103**, 1793.
116. I. Alkorta and J. Elguero, *Struct. Chem.*, 2003, **14**, 377.
117. J. Czernek, R. Fiala and V. Sklenář, *J. Magn. Reson.*, 2000, **145**, 142.
118. J. Czernek, *J. Phys. Chem. A*, 2003, **107**, 3952.
119. A. Dokalik, H. Kalchhauser, W. Mikenda and G. Schweng, *Magn. Reson. Chem.*, 1999, **37**, 895.
120. J. Vaara, J. Jokisaari, R. E. Wasylishen and D. L. Bryce, *Prog. NMR Spectrosc.*, 2002, **41**, 233.
121. O. L. Malkina, *in: Calculation of NMR and EPR Parameters: Theory and Applications*, M. Kaupp, M. Bühl and V. Malkin, eds., Wiley-VCH Verlag, Weinheim, 2004, 307.
122. M. Kaupp, M. Bühl and V. Malkin, *Calculation of NMR and EPR Parameters: Theory and Applications*, Wiley-VCH Verlag, Weinheim, 2004.
123. M. L. Bourguet-Kondracki, M. T. Martin, J. Vacelet and M. Guyot, *Tetrahedron Lett.*, 2001, **42**, 7257.
124. A. N. Pearce, R. C. Babcock, G. Lambert and B. R. Copp, *Nat. Prod. Lett.*, 2001, **15**, 237.
125. B. R. Copp, C. M. Wassvik, G. Lambert and M. J. Page, *J. Nat. Prod.*, 2000, **63**, 1168.
126. D. R. Appleton, M. J. Page, G. Lambert and B. R. Copp, *Nat. Prod. Res.*, 2004, **18**, 39.
127. D. Tasdemir, G. C. Mangalindan, G. P. Concepcion, M. K. Harper and C. M. Irelanda, *Chem. Pharm. Bull.*, 2001, **49**, 1628.
128. G. Remaud, J. Kjellberg, N. G. Johansson and J. Chattopadhyaya, *Tetrahedron*, 1987, **43**, 365.
129. P. Virta, T. Holmström, M. U. Roslund, P. Mattjus, L. Kronberg and R. Sjöholm, *Org. Biomol. Chem.*, 2004, **2**, 821.
130. D. Pappo, A. Rudi and Y. Kashman, *Tetrahedron Lett.*, 2001, **42**, 5941.

Numerical Simulations in Biological Solid-State NMR Spectroscopy

ASTRID C. SIVERTSEN[1], MORTEN BJERRING[1], CINDIE T. KEHLET[1,2], THOMAS VOSEGAARD[1] AND NIELS CHR. NIELSEN[1]

[1]*Interdisciplinary Nanoscience Center (iNANO) and Laboratory for Biomolecular NMR Spectroscopy, Department of Chemistry, University of Aarhus, DK-8000 Aarhus C, Denmark; E-mail: ncn@chem.au.dk (N.C. Nielsen)*

[2]*Institut für Organische Chemie und Biochemie, Technische Universität München, D-85747 Garching, Germany*

Numerical simulations play an increasingly important role in biological solid-state NMR spectroscopy. In this chapter, we describe some of the most important tools currently used for numerical simulations in solid-state NMR, including a brief theoretical section to provide the basic definitions. The most powerful tools involve general computer software packages, enabling simulations of essentially all types of experiments with flexibility similar to that of a modern NMR spectrometer. Supplementary software includes programs that allow easy establishment of typical

ANNUAL REPORTS ON NMR SPECTROSCOPY
VOLUME 54 ISSN 0066 4103
DOI 10.1016/S0066-4103(04)54006-1

anisotropic tensor information for the numerical simulations as well as visualization of molecular structures with attached graphics of NMR-relevant information such as peptide planes, chemical shielding tensors, etc. Based on these tools, we describe the use of numerical simulations for experiment evaluation, with examples from rotating as well as uniaxially oriented samples. The subsequent part describes the use of computer software for design of solid-state NMR experiments, based on standard non-linear optimization methods as well as optimal control theory. The final section demonstrates the use of numerical simulations for extraction of information about structure and dynamics from experimental spectra based on various widely different applications.

1. INTRODUCTION

Since its discovery in 1946, nuclear magnetic resonance (NMR) has with an increasing pace found use in more and more diverse fields stretching from biological structure elucidation to materials science, nanotechnology, whole body imaging, and quantum computing. This evolution – constantly motivated by perspectives to expand the field of applications into increasingly challenging studies and new disciplines – has been supported by the development of advanced NMR instrumentation, analytical and numerical tools, and of increasingly advanced NMR experiments.[1–5] The fundamental NMR pulse sequences have to a large extent been developed using intuition and analytical tools such as the product operator formalism,[6] effective Hamiltonian theory,[7–10] Floquet theory,[11,12] and similar tools, where the primary limitation is the ingenuity of the 'spin engineer' and our ability to handle complex mathematical expressions. With the increasing capability of the experimental methods – and the following increasing complexity of the NMR data – the data analysis has undergone a similar evolution, however, gradually being more extensively computerized although a lot of manual work is still involved in the vast majority of the studies today.

Looking at the state of NMR today and the ever increasing perspectives of the method for analyzing increasingly complex molecular spin systems to unravel structure and dynamics for small and large molecules in liquid and solid phases, it is evident that there will be an accelerating need for automation and many-variable analysis using advanced computer programs to handle all elements from experiment design, through experiment evaluation to data interpretation. This applies to liquid-state NMR spectroscopy – which already has 'matured' to be one of the prime methods for atomic-resolution structural analysis of biological macromolecules – to take an example close to the topic of this chapter.[1,5] The need for numerical procedures, maybe even to a larger extent, applies to solid-state NMR spectroscopy which is a much 'younger' method evolving extremely fast to take up similar use for immobilized biological macromolecules, such as membrane proteins, fibrils/amyloids, and protein aggregates/assemblies.[13–31]

The demand for efficient numerical methods in biological solid-state NMR may be explained not only by the interest in studying larger and more complex molecular systems, but also by the fact that most of the nuclear spin interactions are anisotropic (i.e., dependent on the orientation of the molecule relative to the external magnetic field) which complicates the NMR spectra as well as the transfers of polarization and coherence

between spins. The chemical shielding interactions as well as dipole–dipole, J, and quadrupolar couplings are examples of anisotropic spin interactions that may affect the nuclear spin evolution and therefore the spectra in solid-state NMR directly, whereas in liquid-state NMR, these interactions can only be probed indirectly in relaxation studies. The fact that dipole–dipole couplings influence solid-state NMR experiments through an $1/r^3$ (where r is the internuclear distance) rather than the indirect $1/r^6$ dependency render them effective over longer distances (up to tens of Å) with the consequence of considerably larger spin systems to consider – thereby further increasing the need for numerical simulations. But the very same interactions that complicate matters are also the ones that bring us exciting perspectives for detailed structural analysis – provided we manipulate the interactions such that the information can be extracted from the NMR spectra. To overcome the substantial resolution and sensitivity problems caused by the anisotropic interactions in solid-state NMR spectroscopy, the molecular systems need to be subjected to fast spinning around an axis inclined by the magic angle (54.74°) relative to the external magnetic field or need to be oriented in crystals or uniaxially oriented membrane samples. These conditions have an adverse effect on the pulse techniques to be applied in order to manipulate the nuclear spin interactions, i.e., the Hamiltonian, in the best way to achieve high spectral resolution while restoring the information from specific interactions to establish structure and dynamics information. Often, the desired shaping of the Hamiltonian is obtained by combining advanced rf pulse sequences in synchrony with the potential sample spinning – the effect of which is easily understood under ideal conditions, but is more difficult to appreciate straightforwardly under less ideal (albeit more typical) experimental conditions.

Numerical methods in biological solid-state NMR spectroscopy will face many challenges in the coming years. Among the important questions to be addressed are: (i) How can we efficiently evaluate the many pulse sequences and pulse sequence building blocks presently available to ensure that we are working with the best experiments available for the given purpose? (ii) How do we predict and interpret the outcome of advanced experiments on large molecular systems without preparing many expensive samples with different isotope labeling patterns? (iii) How do we design the best pulse sequences – can this be done by numerical means? (iv) How can we extract structural information from complex solid-state NMR spectra recorded using ‘non-ideal’ pulse sequences and experimental conditions? These questions provide us with good arguments for developing efficient numerical simulation procedures for biological solid-state NMR with the aim of evaluating, designing, and interpreting advanced experimental methods.

2. THEORETICAL BACKGROUND

It is necessary to establish an appropriate analytical framework for the calculations, and through this a clear definition of the variables mapping all information about molecular structure and dynamics. Over the past decades, there has been many excellent texts on the statistical (i.e., density matrix) quantum theory providing the basis for analytical and numerical evaluations of solid-state NMR experiments.[3,4,32–38] Unfortunately,

however, many of these texts use different notations, definitions, and conventions, e.g., with regard to signs of interactions, definition of rotation angles, and definition of the parameters used to describe the anisotropic interactions. From an isolated perspective this may not be a problem, but for use in public numerical simulation software it is crucial that all parameters influencing the spin evolution to be simulated and potentially extracted from the experimental spectra are clearly and unambiguously defined. With reference to more thorough descriptions,[36,38] we will briefly review the mathematical model forming the basis for simulations of NMR experiments.

The state of an NMR-relevant physical system changes over time as described by the Schrödinger equation which within a statistical density operator formalism may be recast in form of the so-called Liouville-von Neuman equation

$$\frac{\mathrm{d}}{\mathrm{d}t}\rho(t) = -i[H(t), \rho(t)], \tag{1}$$

where $\rho(t) = \overline{|\Psi(t) >< \Psi(t)|}$ is the density operator representing an ensemble average over a large number of identical spin systems each of which are described fully by a wave function $\Psi(t)$.

The dynamics of the spin system is governed by the Hamiltonian $H(t)$, which in addition to a term reflecting external radio-frequency (rf) manipulations displays dependencies on chemical shifts, scalar (electron-mediated) J coupling, dipole–dipole coupling, and quadrupolar coupling, i.e.,

$$H = H_{\mathrm{rf}} + H_{\mathrm{CS}} + H_J + H_{\mathrm{D}} + H_{\mathrm{Q}}. \tag{2}$$

For simplicity, the direct Zeeman interaction with the external magnetic field is parametrized out by representing the system in the standard rotating frame. Within the high-field approximation, the Hamiltonian for the *external* rf irradiation may be expressed as

$$H_{\mathrm{rf}} = \sum_j |\omega_{\mathrm{rf}}^j(t)|(I_{jx}\cos\,\phi_i + I_{jy}\sin\,\phi_i), \tag{3}$$

where I_x and I_y are standard Cartesian spin operators, while ω_{rf} and ϕ represent the amplitude (angular units) and phase of the rf irradiation, respectively. The summation reflects contributions to all spins j. To take the most general approach of rotating samples (of which static samples may be considered a special case), the high-field truncated first-order Hamiltonians for the *internal* chemical shift, J coupling, dipole–dipole coupling, and quadrupolar coupling interactions may be written as

$$H_\lambda^{(1)} = \sum_j \omega_{\lambda,0}^j(t)O^\lambda, \tag{4}$$

with $\lambda = CS$, J, D, or Q and where O^{λ} is the associated spin operator. For rotating samples, the angular frequency of the Hamiltonian may conveniently be described in terms of a Fourier series

$$\omega^{j}_{\lambda,m'}(t) = \sum_{m=-2}^{2} \omega^{(m)}_{\lambda,m'} e^{im\omega_r t}, \tag{5}$$

where ω_r denotes the angular sample spinning frequency, while $\omega^{(m)}_{\lambda,m'}$ represents the frequency Fourier coefficients. The latter may be expressed as

$$\omega^{(m)}_{\lambda,m'} = \omega^{\lambda}_{iso}\delta_{m,0} + \omega^{\lambda}_{aniso}\left\{D^{(2)}_{0,-m}(\Omega^{\lambda}_{PR}) - \frac{\eta^{\lambda}}{\sqrt{6}}[D^{(2)}_{-2,-m}(\Omega^{\lambda}_{PR}) + D^{(2)}_{2,-m}(\Omega^{\lambda}_{PR})]\right\} \times d^{(2)}_{-m,m'}(\beta_{RL}), \tag{6}$$

where $D^{(2)}$ and $d^{(2)}$ are second-rank Wigner and reduced Wigner rotation matrices[3,33] depending on the Euler angles $\Omega = \{\alpha, \beta, \gamma\}$ and mutually related by

$$D^{(2)}_{m',m}(\Omega) = e^{-im'\alpha} d^{(2)}_{m',m}(\beta) e^{-im\gamma}, \tag{7}$$

with direct parameterization of the α and γ Euler angles while dependencies on β appear through the reduced Wigner elements in Table 1.

The Wigner rotations describe the coordinate transformations from the principal axis frame (P^{λ}) in which the tensor describing the interaction λ is diagonal, via a molecule-fixed frame (C) and the rotor-fixed frame (R) to the laboratory frame (L) as illustrated in an ORTEP representation[39] in Fig. 1.

Table 1. Second-rank reduced Wigner matrix elements $d^{(2)}_{m',m}(\beta)$[a]

m'	m				
	-2	-1	0	1	2
-2	$\frac{1}{4}(1+c_\beta)^2$	$\frac{1}{2}(1+c_\beta)s_\beta$	$\sqrt{\frac{3}{8}}s^2_\beta$	$\frac{1}{2}(1-c_\beta)s_\beta$	$\frac{1}{4}(1-c_\beta)^2$
-1	$-\frac{1}{2}(1+c_\beta)s_\beta$	$c^2_\beta - \frac{1}{2}(1-c_\beta)$	$\sqrt{\frac{3}{8}}s_{2\beta}$	$\frac{1}{2}(1+c_\beta) - c^2_\beta$	$\frac{1}{2}(1-c_\beta)s_\beta$
0	$\sqrt{\frac{3}{8}}s^2_\beta$	$-\sqrt{\frac{3}{8}}s_{2\beta}$	$\frac{1}{2}(3c^2_\beta - 1)$	$\sqrt{\frac{3}{8}}s_{2\beta}$	$\sqrt{\frac{3}{8}}s^2_\beta$
1	$-\frac{1}{2}(1-c_\beta)s_\beta$	$\frac{1}{2}(1+c_\beta) - c^2_\beta$	$-\sqrt{\frac{3}{8}}s_{2\beta}$	$c^2_\beta - \frac{1}{2}(1-c_\beta)$	$\frac{1}{2}(1+c_\beta)s_\beta$
2	$\frac{1}{4}(1-c_\beta)^2$	$-\frac{1}{2}(1-c_\beta)s_\beta$	$\sqrt{\frac{3}{8}}s^2_\beta$	$-\frac{1}{2}(1+c_\beta)s_\beta$	$\frac{1}{4}(1+c_\beta)^2$

[a] c_β is cos β, s_β is sin β.

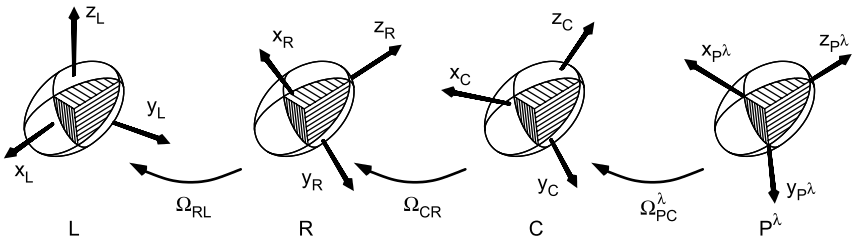

Fig. 1. ORTEP-type representation of a spatial second-rank anisotropic interaction tensor in its principal-axis system (P^λ), a molecule (or crystallite) fixed coordinate system (C), the rotor-fixed coordinate system (R), and the laboratory-fixed coordinate system (L) along with the Euler angles $\Omega_{XY} = \{\alpha_{XY}, \beta_{XY}, \gamma_{XY}\}$ describing transformation between the various frames X and Y. Reproduced from Ref. 36 with permission.

Based on the formulae in Eqs. (4) and (6) along with the relevant constants and operators in Table 2, it is a straightforward matter to set up all internal Hamiltonians to the first order. For the quadrupolar coupling interaction, it is often necessary to include second-order terms, as expressed by the Hamiltonian

$$H_{\mathrm{Q}}^{(2)} = \sum_i \frac{1}{2\omega_0^i}\left\{\omega_{\mathrm{Q},-2}^i(t)\omega_{\mathrm{Q},2}^i(t)(2\mathbf{I}_i^2 - 2I_{iz}^2 - 1)I_{iz} + \omega_{\mathrm{Q},-1}^i(t)\omega_{\mathrm{Q},1}^i(t)(4\mathbf{I}_i^2 - 8I_{iz}^2 - 1)I_{iz}\right\}, \tag{8}$$

where ω_0^i denotes the Larmor frequency of spin i and the relevant angular frequency components can be found using Eqs. (5) and (6) along with Tables 1 and 2.

Table 2. Operators and constants used for computation of the first-order internal Hamiltonians $H_\lambda^{(1)a}$

λ	Spins	O^λ	$\omega_{\mathrm{iso}}^\lambda$	$\omega_{\mathrm{aniso}}^\lambda$	η^λ
CS	i	I_{iz}	$\omega_0^i\delta_{\mathrm{iso}}^i - \omega_{\mathrm{ref}}$	$\omega_0^i\delta_{\mathrm{aniso}}^i$	η_{CS}^i
D	i,j	$3I_{iz}Ijz - \mathbf{I}_i{\cdot}\mathbf{I}_j$	0	$\sqrt{6}b_{ij}$	0
J_{iso}	i,j	$\mathbf{I}_i{\cdot}\mathbf{I}_j$	$-2\pi\sqrt{3}J_{\mathrm{iso}}^{ij}$	0	0
J_{aniso}	i,j	$3I_{iz}I_{jz} - \mathbf{I}_i{\cdot}\mathbf{I}_j$	0	$2\pi\sqrt{6}J_{\mathrm{aniso}}^{ij}$	η_J^{ij}
Q	i	$3I_{iz}^2 - \mathbf{I}_i^2$	0	$2\pi\sqrt{6}C_{\mathrm{Q}}^i/(4I_i(2I_i - 1))$	η_{Q}^i

[a]All frequencies are given in angular units. For the chemical shift interaction, the following applies: $\omega_{\mathrm{iso}}^{\mathrm{CS}} = \omega_0^i\delta_{\mathrm{iso}}^i$ and $\omega_{\mathrm{aniso}}^{\mathrm{CS}} = \omega_0^i\delta_{\mathrm{aniso}}^i$, and i is the spin, $\delta_{\mathrm{iso}}^i = \frac{1}{3}(\delta_{xx}^i + \delta_{yy}^i + \delta_{zz}^i)$, $\delta_{\mathrm{aniso}}^i = \delta_{zz}^i - \delta_{\mathrm{iso}}^i$, $\eta_{\mathrm{CS}}^i = (\delta_{yy}^i - \delta_{xx}^i)/\delta_{\mathrm{aniso}}^i$. The dipolar coupling constant is defined as $b_{ij} = -\gamma_i\gamma_j\mu_0\hbar/(r_{ij}^3 4\pi)$, r_{ij} is the internuclear distance (SI units). The quadrupolar coupling constant is defined as $C_{\mathrm{Q}}^i = (e^2Qq)/h$. I_i denotes the spin-quantum number for spin i.

Equipped with the Hamiltonian at any time of the experiment, the next step in a numerical evaluation is to solve the Liouville-von Neuman equation in Eq. (1). The formal solution is given by

$$\rho(t) = U(t,0)\rho(0)U^{\dagger}(t,0) \tag{9}$$

where $\rho(0)$ is the density operator at thermal equilibrium and $U(t'',t')$ is the unitary propagator (i.e., exponential operator) defined by

$$U(t'',t') = \hat{T}\exp\left\{-i\int_{t'}^{t''} H(t)\mathrm{d}t\right\}, \tag{10}$$

where $\hat{T}$ is the so-called Dyson time-ordering operator. For time-independent Hamiltonians (e.g., free precession for static samples), Eq. (10) is simply evaluated as a single matrix exponential. In the general (typical) time-dependent case, Eq. (10) may be evaluated as a product of propagators taken over n time intervals sufficiently small that to a good approximation, the Hamiltonian may be considered time independent in each interval, i.e.,

$$\rho(t) = U_n \ldots U_2 U_1 \rho(0) U_1^{\dagger} U_2^{\dagger} \ldots U_n^{\dagger}. \tag{11}$$

where $U_i = \exp\{-iH_i\Delta t_i\}$ and H_i is the average Hamiltonian in the time interval from t_{i-1} to t_i and $\Delta t_i = t_i - t_{i-1}$.

With $I^{+} = I_x + {}^{i}I_y$ denoting the detection operator, the time-domain signal (i.e., the free-induction decay (FID)) may be evaluated as

$$s(t) = \sum_{\Omega_{\mathrm{PR}}} \mathrm{Tr}\{\rho(t)I^{+}\}w_{\Omega_{\mathrm{PR}}} \tag{12}$$

where the contribution from every crystallite to $\rho(t)$ in Eq. (11) is determined by the principal-axis to rotor frame Euler angles $\Omega_{\mathrm{PR}} = \{\alpha_{\mathrm{PR}}, \beta_{\mathrm{PR}}, \gamma_{\mathrm{PR}}\}$ according to Eq. (6). The crystallite angles α_{PR} and β_{PR} and their associated weight factors $w_{\Omega_{\mathrm{PR}}}$ may be derived using the methods of Zaremba, Conroy, and Wolfsberg,[40–42] REPULSION,[43] or Lebedev.[44] For static samples, the γ_{PR} crystallite angle is redundant, while for rotating samples, this angle is typically treated separately in conjunction with the sample rotation angle $\omega_{\mathrm{r}}t$, for example using the COMPUTE,[45] γ-COMPUTE,[46] or related methods.[47–49]

3. NUMERICAL TOOLS

Simulations of solid-state NMR experiments can provide the user with information about the spin system or the pulse sequence. The programs take a given pulse sequence and parameters for a nuclear spin system as input, and their output allow extraction of information about structure and dynamics for the molecular system or evaluation

of the performance of the pulse sequence. The latter may be either as a support in the design of the sequence or as a means of comparing the performances of different pulse sequences for a given purpose. Software for these applications will be addressed in the first part of this section. Another important concern in numerical simulations is the establishment of reliable nuclear spin interaction parameters for structurally relevant molecular systems. Also, it is important to visualize and demonstrate graphically the relation between anisotropic nuclear spin interaction tensors (magnitude, orientation) and molecular structures. Tools facilitating translation of structures into typical nuclear spin parameters (and in the long term, vice versa) will be the subject of the second part of this section.

Before entering a description of the tools, we should note that there has been an increasing interest in numerical simulations with more general relevance for solid-state NMR spectroscopy in the past 10–15 years. This has led to the development of several general-purpose programming platforms,[36,50–53] some new analytical[43–49] and molecular tools,[38,54] and recently to a couple of reviews discussing various aspects of solid-state NMR numerical simulations.[55,56] To a large extent, these reviews focus on theoretical and technical aspects of numerical simulations, and thereby the basis for establishment of efficient tools for simulations in solid-state NMR spectroscopy. In the following, we will describe some of the most important and widespread tools – but we will not go into too much detail on programming issues, our approach will rather be to illustrate the prospects of numerical simulations and establish the link between the computer simulations and practical experiments – which in the following sections will be exemplified by typical numerical simulations.

3.1. Software for simulation of solid-state NMR experiments

Numerical simulations in solid-state NMR spectroscopy is by no means a new idea. Over the years, a large number of programs have been written for simulation of the outcome of solid-state NMR experiments. In fact, numerical simulations have typically been regarded as an intrinsic part of the presentation of new techniques – to demonstrate new features as well as provide an objective basis for comparison with previous methods. Also, numerical simulations have been used extensively to extract structurally relevant nuclear spin interaction parameters from experimental spectra. However, until quite recently the vast majority of these simulations have been performed in the developer's laboratory only, using home-made programs designed for specific purposes rather than providing a more general platform for numerical simulations. Accordingly, most programs were made on an ad-hoc basis, typically not very user-friendly, and they were, of course, based on the prevailing choice of notation in the developer's lab – and as so not suited for nor distributed for public use. A few exceptions exist, in particular in the area of quadrupolar nuclei, where software such as STARS[57,58] and QUASAR[59] have been distributed via NMR instrument manufacturers for fast simulation and iterative fitting of spectra resulting from single-pulse (or other simple) experiments. Highly specialized programs of this sort are useful for popular NMR experiments, since the programs can be highly optimized and often provide fast results even when combined with time-consuming iterative fitting procedures.

To the best of our knowledge, the first general purpose program for simulation of solid-state NMR experiments was the program ANTIOPE[52] developed by de Bouregas and Waugh in 1992. This program allowed the user to implement pulse sequences in the form of a table and define sample acquisition/spinning conditions for anisotropy influenced spin systems of up to five spins, on basis of which the calculations were conducted. ANTIOPE did not attract much attention, and was (in 1994) followed by the more general GAMMA (General Approach to Magnetic resonance Mathematical Analysis) platform presented by Smith and co-workers for numerical simulations of virtually all kinds of NMR experiments.[53] GAMMA was developed as an extension of the object-oriented computer language C++,[60] adding data types needed for the simulation of NMR experiments, such as operators, matrices, and tensors. It contains a set of definitions of simple Hamiltonians, and functions for applying pulses and acquiring FIDs and thereby serves as an excellent platform for numerical simulations in NMR spectroscopy. In order to simulate an NMR experiment, the user writes a C++ program that makes use of the data types and functions in GAMMA. The first versions of the program were primarily developed under consideration of the needs of a liquid-state NMR spectroscopist, although elements facilitating the use in solid-state NMR were incorporated. For solid-state NMR, the user has to write code that (i) calculates the components of the Hamiltonian which depend on the tensor orientation for each crystallite orientation by performing Wigner rotations, (ii) calculates the Hamiltonian for one crystallite, (iii) acquires an FID, and finally (iv) sums the FIDs for all crystallites. This gives a tremendous degree of freedom to calculate essentially all kinds of experiments, but unfortunately leaves the user with quite some work on setting up the program. In many respects, this programming effort may be similar to that of establishing an independent program in, e.g., Fortran or C – much work has to be devoted to efficient incorporation of, e.g., the loops controlling the orientation dependency of the Hamiltonians for powder samples. In all respects, this requires a decent knowledge on the theory underlying NMR spectroscopy and good programming skills. For those with these skills, however, GAMMA is a very powerful program which has been used extensively for numerical simulations in broad areas of NMR spectroscopy, and many of its tools have also found applications as a fundament for other simulation software[55,56] written in C++ or in the framework of MATLAB.[61]

To alleviate some of the spin-engineering and programming qualification demands to the users of GAMMA, SIMPSON (SIMulation Program for SOlid-state NMR)[36] was introduced in 2000. This program is designed to operate essentially like a spectrometer, i.e., a computer spectrometer, in the sense that the programming load and the required expertise of the programmer would be similar to the demands required for implementing new experiments on a state-of-the-art NMR spectrometer. The hope was to (i) expand the group of users of numerical simulation software to include the people actually using solid-state NMR for structural analysis, (ii) provide researchers with software where they can demonstrate the applicability of a method on a typical molecular system, and (iii) shift some of the 'explorations' of new NMR technology to the computer rather than doing tests on the spectrometer with request for expensive labeled samples and the use of spectrometer time for testing purposes. In SIMPSON, most of the theoretical details are hidden below the surface of the program with the arguments that most of the theory

(see previous section) and the most common procedures (such as powder averaging, transformations between different coordinate systems, sample spinning, execution of rf pulses, etc.) are sufficiently simple and reasonably structured that there is no need for the user to bother with these issues on a practical level. SIMPSON is released as open source software under the GNU conditions,[62] implying that the specialist in 'spin engineering' with standard programming skills quite easily can modify or incorporate new C-code elements into SIMPSON. This is the typical way to include new features and elements which will operate too slowly when incorporated on the scripting level.

In SIMPSON, the user writes an input file in the scripting language Tcl,[63,64] organized as follows: a 'spinsys' part defining the spin system (types of nuclei, specific spins, etc.) and the nuclear spin interactions to automatically generate the internal part of the Hamiltonian. Experimental conditions, such as external field, powder averaging methods, initial and target spin operators, sample spinning, etc. are defined in the 'par' section, while the rf irradiation and timing of the pulse sequence are specified in the 'pulseq' part of the program using mnemonic simple commands to define pulses, delays, etc. Finally, the flow of the program and data handling/processing are controlled in the 'main' section of the program. All programming in these elements makes extensive use of a large number of specific SIMPSON commands as well as the general features of the Tcl scripting language to allow for calculations, instructions to input/output, and operation in combination with other software if needed. The latter could be specific programs for visualization of spectra, numerical optimization, or even the NMR spectrometer software for optimization purposes. The SIMPSON software makes extensive use of state-of-the-art mathematical procedures for data manipulation, matrix algebra, Fourier transformation, etc. – but also incorporates, e.g., commands[65] to control software such as MINUIT for non-linear optimization[66] and features for performing parallel calculations in clusters of CPUs, as also discussed in by Kristensen and Farnan in another context.[67] Parallelization may allow the response from different crystallites, rf isochromats, etc. to be distributed on different computers to speed up the calculations. Many of the specific features of SIMPSON and the associated SIMPLOT plotting program, as well as a large number of practically relevant examples can be found in the SIMPSON paper[36] and various later papers illustrating new features and examples of SIMPSON calculations.[65,68–70]

Recently, two programs based on similar principles have been introduced: BlochLib[50] and SPINEVOLUTION.[51] These programs should offer the same sort of flexibility as SIMPSON with similar or different procedures for fast execution of numerical simulations. Examples of the use of these programs can be found in the respective publications. In the following, we will show typical examples of numerical simulations primarily based on SIMPSON calculations, as it is our impression that SIMPSON is currently the most widely distributed and used program for calculation of solid-state NMR spectra.

3.2. Auxiliary programs

One of the main features of numerical simulations in biological solid-state NMR spectroscopy is the ability to investigate the impact of advanced pulse sequences on

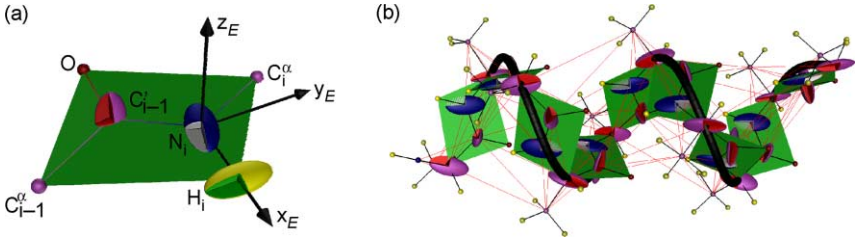

Fig. 2. (a) Peptide plane showing the amide ^{15}N, amide ^{1}H, and carbonyl ^{13}C chemical shielding tensors with typical orientations relative to the peptide plane. (b) An α-helical fragment illustrated with peptide planes and typical chemical shielding tensors. The thin lines indicate $^{13}C-^{13}C$ and $^{13}C-^{15}N$ dipolar couplings larger than 75 Hz. The graphics and calculations were generated using SIMMOL[38] and reproduced from Ref. 38 (a) and Ref. 69 (b) with permission.

complicated spin systems influenced by anisotropic nuclear spin interactions. With the increasing use of uniformly ^{15}N and ^{13}C labeled proteins, the number of spins that participate in the spin evolution of a given NMR experiment may be quite high, as illustrated in Fig. 2 showing chemical shift tensors as ellipsoids, peptide planes, and lines indicating through-space $^{13}C-^{13}C$ and $^{13}C-^{15}N$ dipole–dipole couplings exceeding 75 Hz. The presence of many spins with differently oriented anisotropic shielding tensors may render the establishment of the 'spinsys' part of the SIMPSON input file (this part describes the magnitude and orientation of the tensorial interactions) quite cumbersome. One can easily envisage situations where establishment of the orientation of even three tensors may be difficult, even more so for 5–6 tensors – and the eagerness to test pulse sequences numerically for several typical spin systems of this size may be reduced significantly unless numerical procedures for this work can be established.

It is a well-known fact that the magnitudes of the peptide backbone ^{13}C, ^{15}N, and amide ^{1}H chemical shielding tensors and their orientations relative to the peptide planes are quite similar for all amino acids. Although the details of the tensor parameters may vary, this feature is fundamental for powerful new techniques exploiting residual anisotropies in liquid-state NMR of partially aligned samples, and for the general utility of PISEMA type solid-state NMR experiments.[68,71,72] Exactly the same feature is very useful for our aim: Fast and reliable establishment of typical anisotropic interaction tensors (magnitude and orientation) for solid-state NMR simulations. This may be accomplished using the recently introduced SIMMOL program.[38] SIMMOL takes atomic coordinates in the form of a PDB (Protein Data Bank)[73] file containing a structure established by NMR, X-ray crystallography, electron microscopy, or molecular dynamics modeling, as input. According to the specifications of the user, SIMMOL takes the full structure, parts of the structure, or specified atoms, and generates typical parameters for relevant dipole–dipole couplings and chemical shielding tensors.

The dipole–dipole coupling parameters are generated straightforwardly from the atomic coordinates based on the internuclear distances and the orientations of the internuclear vectors. The peptide plane chemical shielding tensors are established according to the type of atom and its typical orientation relative to the peptide plane (Fig. 2). If amide protons and H^{α} are not present (as would be the case with X-ray

structures), these may be attached to the structure. SIMMOL contains tools for establishment of local coordinate systems and specific tensor orientations for side-chain atoms using empirical relations between these tensors and the closely attached atoms. Typical parameters for chemical shielding tensors, dipole–dipole couplings, and *J* couplings are given in Table 3 and visualized in Fig. 2. We note that SIMMOL automatically assigns typical parameters to the selected atoms but if more detailed information is available for specific residues or atoms, this may be entered straightforwardly. The most important issue is that numerical simulations on peptide/protein structures use the most realistic parameters possible - to improve the quality and reliability of the calculations. The flexible operation of SIMMOL, through a Tcl scripting interface, ensures that it is relatively easy to generate useful 'spinsys' parameters for SIMPSON - or for that matter any other software – based on a representative structure for which a given experiment is intended.

In addition to the spin system parameters, SIMMOL may also provide an OOGL (Object Oriented Graphics Language) formatted graphical file which allows interactive 3D visualization of the molecular structure with indication of the selected peptide planes, shielding tensors, and dipole–dipole couplings. The OOGL file may be visualized by the open source software Geomview.[74] This visualization feature proves extremely useful for tests of the selection of the correct spin system and of the orientation of the shielding tensors relative to the molecular frame. Another important issue is that SIMMOL allows visualization of the tensorial interactions related to – or determined by – a given NMR experiment for the purpose of teaching or publication. We note that similar software such as Moleculix and the later version Gullringen, as preliminarily described in Ref. 54, has recently been developed.

Table 3. Typical magnitudes and orientations of anisotropic interaction tensors[a]

Chemical shift	Spin	δ_{iso}^{CS}	δ_{aniso}^{CS}	η^{CS}	α_{PE}^{CS}	β_{PE}^{CS}	γ_{PE}^{CS}
	$^{1}H^{N}$	9.3	7.7	0.65	90	−90	90
	$^{13}C^{\alpha}$	50	−20	0.43	90	90	0
	$^{13}C'$	170	−76	0.90	0	0	94
	^{15}N	119	99	0.19	−90	−90	−17
J and dip. couplings	Spins	J_{iso}^{IS}	$b_{IS}/2\pi$	r_{IS}	β_{PE}^{D}	γ_{IS}^{D}	
	$^{1}H^{\alpha}$–$^{13}C^{\alpha}$	140	−23,328	1.090	[b]	[b]	
	$^{1}H^{N}$–^{15}N	−92	11,341	1.024	90	0	
	$^{13}C^{\alpha}$–$^{13}C'$	55	−2142	1.525	90	120.8	
	$^{13}C^{\alpha}$–$^{13}C^{\beta}$	35	−2159	1.521	[b]	[b]	
	$^{13}C^{\alpha}$–^{15}N	−11	988	1.458	90	115.3	
	$^{13}C'$–^{15}N	−15	1305	1.329	90	57	

[a] The Euler angles represent transformations between the principal axis frame (P) and the peptide plane (E) coordinate system, see Figure 2a.

[b] The parameter is dependent on the secondary structure.

4. PULSE SEQUENCE EVALUATION

The development of biological solid-state NMR spectroscopy has largely followed two tracks, where one is focused on rotating samples[14] and the other on macroscopically oriented samples.[13] The former approach takes advantage of magic-angle spinning (MAS) to eliminate line broadening, which for powder samples (i.e., samples with a uniform distribution of all molecular orientations relative to the external magnetic field) originate from anisotropic nuclear spin interactions. This elimination is followed by selective recoupling (i.e., reintroduction) of the effects from specific interactions of interest to drive certain coherence/polarization transfers or probe specific effects to extract structural information. Using intricate combinations of sample spinning and advanced rf irradiation schemes to de- or recouple specific interactions, it has proven possible to 'tailor' the Hamiltonian largely to any desired form. This provides a large degree of freedom to create advanced multiple-dimensional solid-state NMR experiments, which provide high spectral resolution and detailed structural information from the anisotropic interactions at the same time. The other approach – which is specifically developed for the study of proteins embedded in planar native membranes or phospholipid bilayers – exploits macroscopic alignment of the bilayers, and thereby the embedded proteins, relative to the external magnetic field (the bilayer normal is along B_0) to obtain high-resolution solid-state NMR spectra with the resonance position depending on isotropic as well as anisotropic nuclear spin interactions from which it is possible to extract detailed structural information. For both approaches – and more recent combinations[75] between the two – it applies that a large number of pulse sequences have been developed to mediate the necessary coherence/polarization transfers and interaction probing in multiple-dimensional experiments which in many respects resemble the methods which two to three decades ago introduced liquid-state NMR as a prime method in structural biology.[1,5]

With hundreds of pulse sequence elements being proposed for different purposes, often developed by different research groups using different tools and with different quality criteria, it is crucial to be able to compare these elements on similar grounds to choose the best possible element for a given purpose. Considering, in addition, the complexity of multiple-dimensional solid-state NMR experiments where leakage from one element may be transferred to another element and considering potential non-idealities or limitations in the performance of the NMR instrumentation, it is clear that numerical simulations have an important mission in pulse sequence evaluation. In the following subsections we will exemplify these aspects for rotating samples as well as static, macroscopically oriented samples by simulating and numerically comparing various popular solid-state NMR experiments. We should note that other, complementary, examples may be found in previous broadly oriented accounts on numerical simulations[31,36,38,54,65,69,76,77] as well as in more specialized papers to be discussed below.

4.1. Coherence transfers in rotating samples

Based on a substantial improvement of the NMR hardware in terms of higher fields, better probes, etc. and a parallel improvement of solid-state NMR pulse sequence

elements for re- and decoupling of specific anisotropic nuclear spin interactions in the past couple of decades,[69,78,79] solid-state NMR has now reached a level where many of these pulse sequence building blocks may be assembled into advanced multiple-dimensional solid-state NMR experiments for structural analysis of uniformly labeled peptides/proteins. These potentials have recently been demonstrated by partial/full assignments and structure determination of polypeptides ranging from a few up to about 100 residues.[16–30]

Addressing solid-state NMR experiments on proteins, a typical spin system is given in Fig. 3a, where three peptide planes with typical chemical shift tensor orientations are shown. The arrows indicate typical coherence transfer pathways for HNCACB and HNCOCA type of experiments being instrumental in the establishment of resonance assignments and correlations between spins in uniformly ^{15}N, ^{13}C- labeled proteins. A schematic of a pulse sequence for such purposes is given in Fig. 3b. The $^{1}H \rightarrow {}^{15}N$ transfer is normally conducted by Hartmann–Hahn cross-polarization (CP),[80] or ramped variants of this experiment.[81] The other building blocks typically consist of special re- and decoupling pulse schemes with varying complexity depending on their specific role. When dealing with large uniformly labeled proteins, it is relevant to establish powerful methods for assignment as well as methods for extraction of precise structural constraints in terms of internuclear distances and torsion angles. Typically these methods are developed under careful attention to the distinct chemical shift and dipolar coupling parameters for the various nuclei in the peptide backbone and side chains. Figure 3c,d show the frequency areas relevant for coherence transfers in multiple-dimensional triple-resonance experiments. Taking, as an example, the NCA building block carrying out magnetization transfer from amide ^{15}N (chemical shift range 110–130 ppm) to the C^{α} (chemical shift range approximately 45–65 ppm) the dipolar recoupling should be sufficiently broadbanded that all $^{15}N,^{13}C^{\alpha}$ pairs in a given molecule are covered, but simultaneously sufficiently narrowbanded that magnetization does not leak to the directly attached carbonyl $^{13}C'$ (chemical shift range 170–185 ppm) nor the more distant aliphatic ^{13}C in the side chains (chemical shift range approximately 20–43 ppm). Leakage of magnetization will cause loss of sensitivity and/or increase the risk of ambiguous assignments.

The optimal building blocks and their combinations in multi-dimensional pulse sequences are not always easily predicted and often depend highly on the experimental conditions (spinning speed, rf inhomogeneity, the external field, etc.) as well as on the spin system. Several aspects should be observed in the selection of the best building blocks. (i) Typically it is preferable to use elements with a large scaling on the dipolar couplings to ensure fast magnetization build-up and prevent loss of signal due to relaxation. (ii) The method should give as modest dependency on crystallite orientations as possible. (iii) The experiments should use the weakest possible rf fields to avoid excessive sample heating. (iv) The experiment should be band-selective to ensure the desired coherence transfers without leakage to undesired spins. Careful analysis taking all these aspects into account should be carried out before setting up multi-dimensional experiments – an analysis in which numerical simulations may prove indispensable.

As an example illustrating the use of numerical evaluation for selection of a specific pulse sequence element, we consider pulse sequences conducting coherence transfer

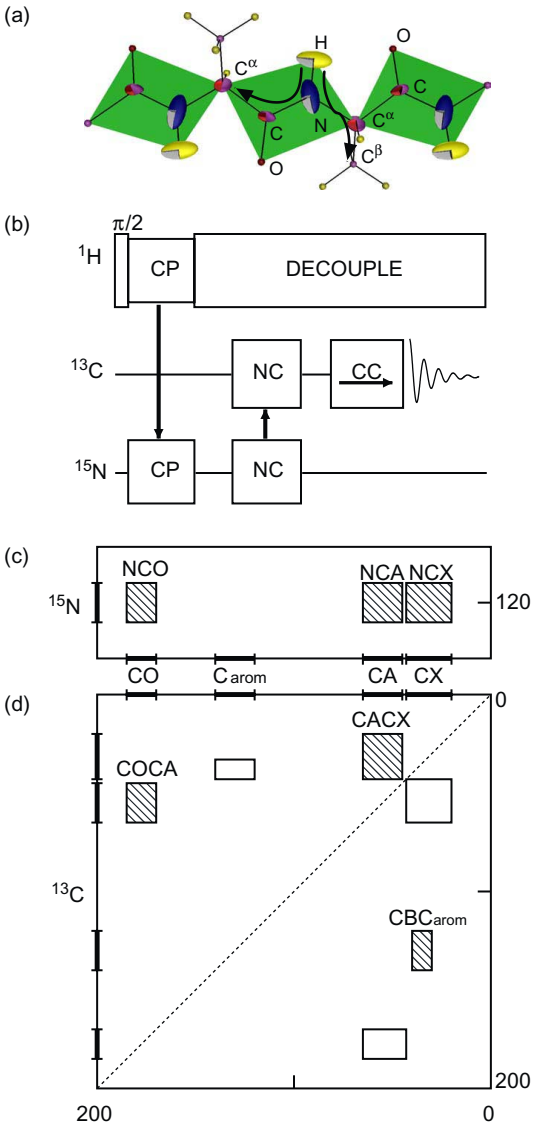

Fig. 3. (a) A typical spin system of three peptide planes with chemical shielding tensors and typical coherence transfer pathways shown. Reproduced from Ref. 69 with permission. (b) A schematic representation of a pulse sequence for HNC triple-resonance experiments. (c,d) Typical chemical shift ranges for ^{13}C and ^{15}N in peptides/proteins. The boxes indicate the 'frequency areas' to be covered by the different types of recoupling building blocks.

from ^{15}N to $^{13}C^{\alpha}$ or $^{13}C'$ under MAS conditions. This transfer – which is intrinsic to all NCOCA, NCACB, NCACX type experiments – is most efficiently conducted via the dipolar couplings, although through-bond experiments exploiting J couplings have also been proposed.[82] During fast MAS, all anisotropic interactions, including the dipolar

couplings, are eliminated to first order, and the purpose of the block is to recouple the $^{15}N-^{13}C$ dipolar coupling by quenching of the spatial averaging by rf pulses imposing similar time dependence on the spin operators. There exist a large number of different pulse sequences for heteronuclear dipolar recoupling, of which the γ-encoded[83] experiments are known to be more efficient (max. transfer efficiency of 73%) than non-γ-encoded ones (max. transfer efficiency of approx. 50%), due to refocusing of the influence from the γ_{CR} Euler angle. An alternative could be adiabatic pulses sequences[84] which in principle may provide 100% transfer for powder samples, however, using much longer mixing times than those typical for the γ-encoded experiments. Therefore, we will leave the adiabatic pulse sequences out of the present discussion and return with an evaluation of such experiments in the following section.

Through SIMPSON numerical simulations, Fig. 4 compares the coherence transfer curves for a variety of the most popular and efficient heteronuclear dipolar recoupling schemes. Specifically, we evaluate the C7,[85] POST-C7,[86] off-resonance C7,[87] $R14^1_2$,[88] DCP,[89] SPICP,[90] SPECIFIC,[91] and *i*DCP[92] pulse sequences, realizing that many new powerful schemes enter the scene every year. For the present purpose, we address a three-spin $^{13}C'-^{15}N-^{13}C^{\alpha}$ system in a peptide backbone using parameters established for a typical fragment of ubiquitin using SIMMOL, a spinning speed of 7 kHz, and a magnetic field of 14.1 T (^{1}H Larmor frequency of 600 MHz). The curves in Fig. 4a,c and b,d show the efficiency of transfer from the amide ^{15}N to $^{13}C^{\alpha}$ and $^{13}C'$, respectively, as a function of the excitation time τ_{exc}. For DCP, SPICP, *i*DCP, and SPECIFIC, effective rf fields of

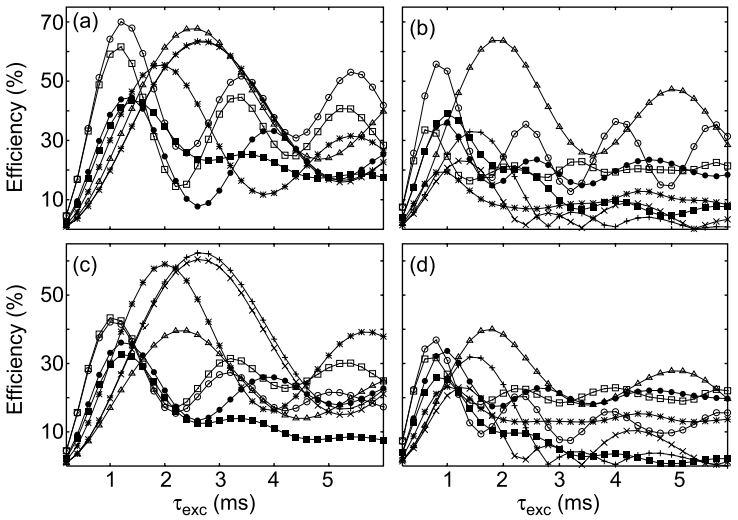

Fig. 4. Magnetization transfer build-up curves for (a,c) a $^{15}N \rightarrow {}^{13}C^{\alpha}$ transfer and (b,d) a $^{15}N \rightarrow {}^{13}C'$ transfer in a three-spin system with (N = ^{15}N, CA = $^{13}C^{\alpha}$, CO = $^{13}C'$) $b_{NCA}/2\pi =$ 947.6 Hz, $b_{NCO}/2\pi = 1281.8$ Hz, $b_{CACO}/2\pi = -514.9$ Hz, $\delta_N^{aniso} = 99$ ppm, $\delta_{CA}^{aniso} = -20$ ppm, $\delta_{CO}^{aniso} = -76$ ppm, $\eta_N = 0.19$, $\eta_{CA} = 0.43$, $\eta_{CO} = 0.90$ subjected to a static magnetic field of 14.1 T and $\omega_r/2\pi = 7$ kHz, and (a,b) neglecting rf inhomogeneity, (c,d) assuming a 5% Lorentzian rf inhomogeneity profile. The pulse schemes used are (+) C7, (×) POST-C7, (∗) off-resonance C7, (□) DCP, (■) SPICP, (○) *i*DCP, (•) SPECIFIC, (△) $R14^1_2$.

$\omega_{\mathrm{rf}}^{\mathrm{C}}/2\pi = 35$ kHz and $\omega_{\mathrm{rf}}^{\mathrm{N}}/2\pi = 28$ kHz are used, whereas for the symmetry-based schemes, the rf field strengths are related to the spinning speed, i.e., for the C7 sequences the effective fields on the two channels are matched to seven times the spinning frequency (i.e., 49 kHz) as is the case for $R14_2^1$ using the 90_0270_{180} R element.[88] We assume on-resonance rf irradiation for all experiments, except for SPECIFIC where $\Omega_{\mathrm{C}}/2\pi =$ 20232 Hz, and for off-resonance C7, where $\Omega_{\mathrm{C}}/2\pi = -\Omega_{\mathrm{N}}/2\pi = 28325$ Hz. Based on this setup, Fig. 4a,b show transfer curves for the various recoupling experiments calculated under the assumption of homogeneous rf fields. In practical applications, however, the experiments are always influenced by rf inhomogeneity to a certain degree, depending on the specific NMR probe. To explore the effects of typical rf inhomogeneities, we have determined an rf inhomogeneity of 5% Lorentzian shape or a simulation-wise very similar 9.2% Gaussian distribution for a typical 4 mm triple-resonance probe by numerical fitting of nutation spectra (not shown). The former rf profile has been included in the simulations shown in Fig. 4c,d.

Neglecting rf inhomogeneity, Fig. 4a reveals that *i*DCP (an improved DCP experiment)[92] offers the best compromise between fast (ca. 1.2 ms) and efficient (70%) $^{15}\mathrm{N} \rightarrow {}^{13}\mathrm{C}^{\alpha}$ coherence transfer. Also, DCP and the symmetry-based schemes C7, POST-C7, off-resonance C7, and $R14_2^1$ operate reasonably well at these conditions, although they are slightly less efficient and display substantially slower excitation (except DCP). These findings match very well with the known dipolar scaling factors for the various recoupling experiments. The symmetry-based sequences generally suffer from lower scaling factors than DCP-type experiments, as discussed in Ref. 87, where we introduced off-resonance C7 as a means for maximizing the scaling factor for heteronuclear symmetry-based experiments. Consequently, the symmetry-based sequences are slower than DCP-types, and this can be considered as 'the price to pay' for larger robustness of the recoupling block. Depending on the particular application, the larger robustness may or may not be needed. The $^{15}\mathrm{N} \rightarrow {}^{13}\mathrm{C}'$ transfer is influenced by the large chemical shift anisotropy (CSA) on the carbonyl generally leading to lower magnetization transfer efficiency as illustrated in Fig. 4b. Again, a good choice seems to be the *i*DCP scheme which, with 57% magnetization transfer, is more compensated against large CSAs than DCP, as discussed in Ref. 92, or possibly $R14_2^1$ which is slightly more efficient but has a twice as long build-up.

Figure 4c,d demonstrates that the 'self-compensating' C7, POST-C7, and off-resonance C7 recoupling experiments are relatively insensitive to a moderate rf inhomogeneity, whereas the other experiments examined are substantially influenced by such effects. Under inhomogeneous conditions, it would be recommendable to use C7, POST-C7, or off-resonance C7 for the $^{15}\mathrm{N} \rightarrow {}^{13}\mathrm{C}^{\alpha}$ transfer since they have efficiencies around 60%, with off-resonance C7 showing the fastest transfer in approx. 2 ms. As shown in Fig. 4d, the maximum efficiency for the $^{15}\mathrm{N} \rightarrow {}^{13}\mathrm{C}'$ transfer is less than 40% when rf inhomogeneity is taken into account. However, it is seen that *i*DCP or $R14_2^1$ should still be good choices for this type of coherence transfer.

In conclusion, the calculations in Fig. 4 demonstrate, for one particular type of coherence transfer, that careful analysis prior to experiment setup can provide important information on the performance of different pulse sequence elements. It should be realized that one element that is optimal for one application, may not be the best for

others. Simple changes in the spinning speed, the external magnetic field, the shielding effects (isotropic as well as anisotropic), and potential limitations on the maximum available rf field strenghts (e.g., for simultaneous ^{1}H decoupling) or the wish to reduce effects from rf-induced sample heating, may completely change the picture. Thus, the curves and the accompanying recommendations are by no means universal – our recommendation is to perform a numerical comparison of relevant experiments using the intended experimental conditions. This is quite simple to establish using available software such as SIMPSON and SIMMOL. We note that similar comparison of experiments for, e.g., ^{13}C to ^{13}C coherence transfer, double-quantum filtration, or longitudinal spin-order recoupling may be found elsewhere.[38,54,69,76,93]

4.2. Correlation experiments for uniaxially oriented samples

As an alternative approach to MAS experiments on immobilized proteins, membrane proteins may be incorporated into planar lipid bilayers, which may be uniaxially oriented with the bilayer normal parallel to the external magnetic field. This implies that the sample will display single-crystal like spectra and hence sample spinning is not needed to provide high resolution. In this section, we will numerically investigate some of the fundamental aspects one needs to consider when performing experiments on uniaxially oriented membrane proteins.

In the solid state, the most efficient transfer of coherences between nuclei is mediated by through-space dipolar couplings. In static, uniaxially oriented samples, it will be the *effective* dipolar coupling, proportional to $b_{IS}(3\cos^2\beta_{IS}^{PL} - 1)$, that comes into play.[68] In this expression β_{IS}^{PL} represents the angle between the internuclear vector and the external magnetic field. It is obvious that protein fragments with different conformation and thereby different molecular orientation relative to the bilayer normal will have different effective dipolar couplings. Figure 5 quantifies this statement by calculating the effective dipolar couplings between amide nitrogen and the directly bonded amide proton (Fig. 5a), amide nitrogen and carbonyl carbon of the preceding residue (Fig. 5b), amide nitrogen and C^{α} in the same residue (Fig. 5c), and intra-residue C^{α} and carbonyl (Fig. 5d) for an ideal α-helix with the tilt angles shown on the right. From this figure, it is evident that even small tilts of the helix relative to the bilayer normal will cause a broad distribution of the effective dipolar couplings. One of the most severe examples is the ^{1}H–^{15}N dipolar couplings for a helix tilted by $\sim 30°$. In this case, the effective dipolar couplings will range from 1 to 9 kHz for the individual residues. Considering real samples, this effect is also illustrated by Fig. 5e–h displaying the number of residues having a certain effective dipolar coupling in the G-protein coupled receptor rhodopsin.[68] These numbers are obtained from SIMMOL[38] simulations using the atomic coordinates for rhodopsin from Palczewski's X-ray structure (PDB-ID: 1F88)[94] oriented with the average helical axis oriented parallel to the magnetic field (i.e., in normal transmembrane fashion). Here, it turns out that the distribution of effective ^{1}H–^{15}N dipolar couplings is almost uniform in the entire range from 0 to 10 kHz.

Clearly, the variations in the dipolar couplings need to be considered in the design of experiments for uniaxially oriented samples, and they need to be taken into account in the subsequent interpretation of the data. The reason is that it is very challenging to achieve

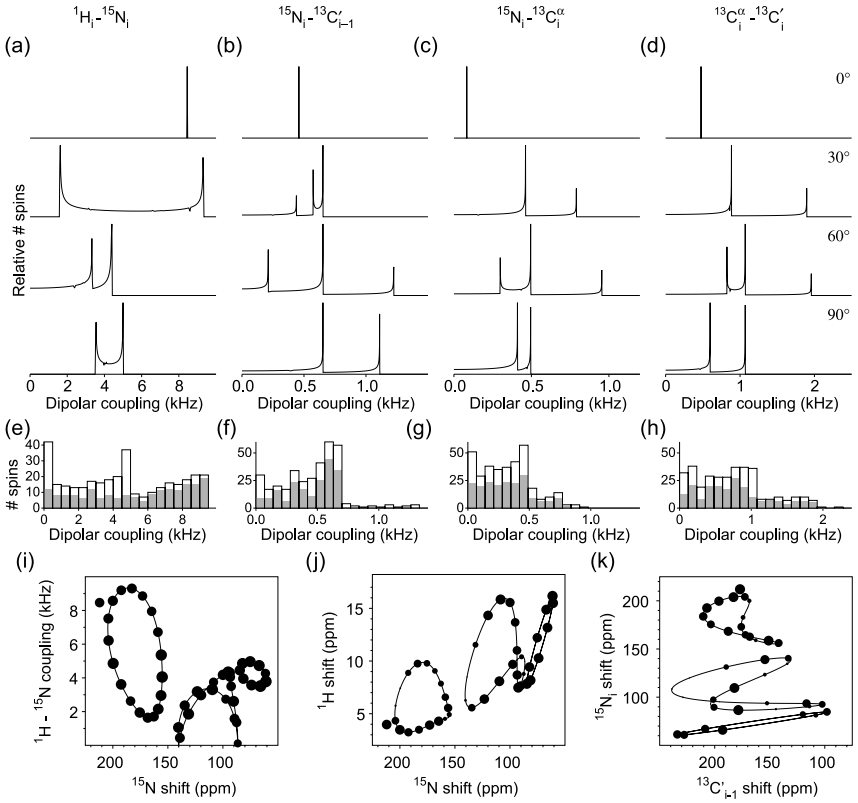

Fig. 5. (a–h). Distributions of the (a,e) $^{1}H_i-^{15}N_i$, (b, f) $^{15}N_i-^{13}C'_{i-1}$, (c, g) $^{15}N_i-^{13}C_i^{\alpha}$, and (d,h) $^{13}C_i^{\alpha}-^{13}C_i'$ effective dipolar couplings determined using SIMMOL. The simulations correspond to (a–d) an ideal α-helix tilted by (from top to bottom) 0°, 30°, 60°, and 90° relative to the bilayer normal and (e–h) rhodopsin with the average helix axis oriented parallel to the external magnetic field. (i–k) SIMPSON/SIMMOL simulated PISA wheels illustrating the orientational dependence on the transfer efficiencies for different one-bond coherence transfers for an ideal 18-residue α-helix. The solid lines represent the PISA wheels and the filled circles represent the resonance position for the 18 residues. The diameters of the circles are proportional to the signal intensities. The three spectra are (i) PISEMA using an 1 ms contact time, (j) $^{1}H-^{15}N$ HETCOR using a short mixing time to achieve completely selective transfer, and (k) $^{15}N_i-^{13}C'_{i-1}$ transfer. Reproduced from Ref. 68 with permission.

a uniform coherence transfer when the effective dipolar couplings vary significantly. To substantiate this postulate, we performed a series of simulations of the signal intensity for the individual residues in an ideal α-helix tilted by 0°, 30°, 60°, and 90° relative to the bilayer normal.[68] Selective simulations are shown in Fig. 5i–k, where the solid lines represent the ideal PISA wheels[68,71,72,95] and the filled circles represent the resonance positions for the individual residues. In these plots, the diameters of the filled circles are proportional to the signal intensity achieved by optimizing the CP coherence transfer to maximize the sum intensity for the entire helix.[68] Specifically, the three figures represent normal $^{1}H\rightarrow{}^{15}N$ CP with a contact time of 1 ms as typically used in PISEMA

experiments[96] (Fig. 5i), selective $^{1}H_i \rightarrow ^{15}N_i$ transfer as used in $^{1}H-^{15}N$ HETCOR experiments (Fig. 5j), and selective $^{15}N_i \rightarrow ^{13}C'_{i-1}$ (Fig. 5k) typically used in ^{1}H, ^{15}N, ^{13}C triple-resonance experiments.[97]

These simulations stress the point that when using CP for the coherence transfer, the variation in effective dipolar couplings will also greatly influence the signal intensity for experiments where the transfer is conducted through specific one-bond dipolar couplings. One notable exception is the PISEMA experiment, which does not rely on selective one-bond coherence transfer but typically relies on CP with relatively long mixing time. Therefore, the effective dipolar coupling to the directly bonded proton becomes less important since the mixing time is sufficiently long to bring other neighboring protons into play. Hence, the PISEMA experiment displays virtually uniform signal intensity independently on the orientation of the protein. Because of this attractive feature, along with its ability to provide high resolution in crowded spectra,[68] this experiment is the most widely used experiment for selectively and uniformly ^{15}N labeled peptides and proteins in uniaxially oriented lipid bilayers. We also note that most of the membrane protein structures solved by solid-state NMR and reported to the protein data bank have been determined from PISEMA spectra. For the other experiments, which have very important potentials for improving the resolution of crowded spectra, we note that some of the resonances have close to zero intensity because the effective dipolar coupling vanishes, i.e., the internuclear axis approaches the magic angle relative to the external field.

A very important aspect of solid-state NMR studies of uniaxially oriented peptides is the possibility to directly determine the conformation of the protein in the bilayer. The PISA wheels[71,72] for regular secondary structures, which may be considered a direct NMR mapping of the so-called helical wheels, help interpreting the experimental spectra. More recently, Opella and co-workers have suggested to exclusively use the effective dipolar couplings in the analysis of such spectra[98–100] to alleviate uncertainties from small residue/structure-specific variations in the chemical shifts.

To illustrate the power of PISA wheels and dipolar waves to determine the structure of helical peptides and proteins in uniaxially oriented lipid bilayers, Fig. 6a–c show SIMPSON/SIMMOL-simulated PISEMA spectra of an ideal 18-residue α-helix with a tilt angle of 10°–30° relative to B_0. In these simulations, we have tried to mimic experimental conditions by including a random distribution of the principal components of the chemical shift tensor and the dipolar coupling. The chemical shift distribution is ±6 ppm for each principal element and has been established as follows: we obtained ~85000 ^{15}N isotropic chemical shifts reported to the BioMagResBank[101] and selected only the ~31000 located in helical secondary structures to have a data set independent on secondary chemical shifts. The standard deviation on the ^{15}N chemical shifts for these resonances was ~6 ppm. With the lack of other statistically reliable experimental methods to establish such results for the individual principal elements of the ^{15}N CSA tensor, we assumed the above variation of ±6 ppm for all three principal elements. The variation of the $^{1}H-^{15}N$ dipolar coupling was estimated by investigating the structures for a small number of α-helical membrane proteins for which the structures were established by liquid-state NMR spectroscopy. These showed standard deviations

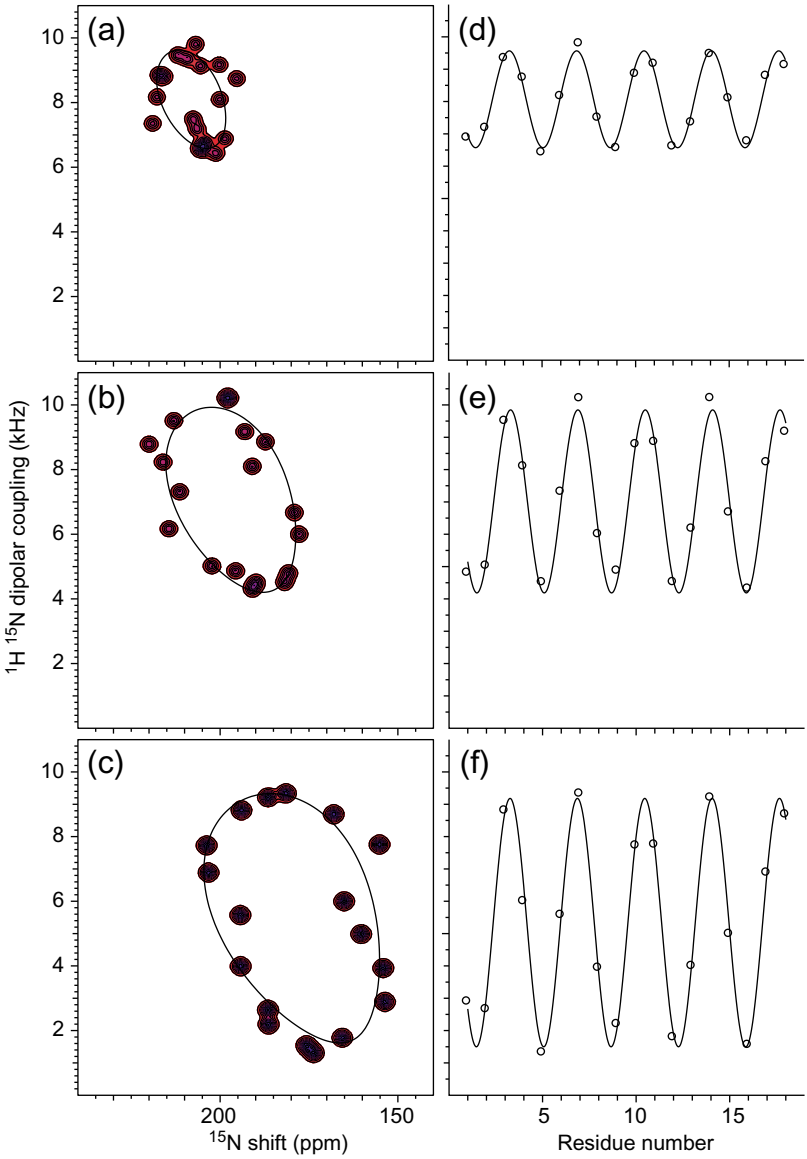

Fig. 6. (a–c) Simulated PISEMA spectra and (d–f) dipolar waves for an ideal 18-residue α-helix tilted by (a,d) 10°, (b,e) 20°, and (c,f) 30° with respect to the bilayer normal and B_0. Each of the resonances in the spectra (a–c) was calculated using a ^{1}H–^{15}N dipolar coupling of 9940 Hz with a random fluctuation within the range of ± 350 Hz, corresponding to a variation in the bond length of ∼ ± 0.015 Å and chemical shift principal elements of $\delta_{xx} = 60$ ppm, $\delta_{yy} = 79$ ppm, and $\delta_{zz} = 218$ ppm with a random fluctuation within ± 6 ppm on each principal element. The solid lines correspond to ideal PISA wheels. (d–f) Dipolar waves showing the effective dipolar coupling as function of the residue number. The solid lines correspond to the dipolar waves for an ideal α-helix with the corresponding tilt relative to the magnetic field.

of the N–H bond length of ± 0.015 Å corresponding to a fluctuation of ± 350 Hz in the $^{1}H-^{15}N$ dipolar coupling.

Despite the fact that the simulated PISEMA spectra in Fig. 6a–c display significant fluctuations in the resonance positions relative to the ideal patterns, it is evident that both the PISA wheels and dipolar waves (represented by solid lines in Fig. 6) allow accurate determination of the helix tilt angle. The dipolar wave representation only shows minor differences between the resonance points and the ideal waves, and when trying to fit a dipolar wave to the resonance points, it does not display any visible difference to the ideal curve.

5. EXPERIMENT DEVELOPMENT

So far, the vast majority of solid-state NMR experiments have been developed using appropriate combinations of intuition and analytical evaluations. Tools like effective (or average) Hamiltonian theory,[7] recently developed to high order[8] or even in exact form,[9,10] the product operator formalism,[6] and to some extent Floquet theory[11,12] have been used with great success to develop advanced solid-state NMR experiments for virtually all purposes. In particular, effective Hamiltonian theory has proven almost indispensable for design purposes since it allows the establishment of an ordered representation of the Hamiltonian along with simple recipes for manipulating (often eliminating) this Hamiltonian in a prioritized manner. For example, by the use of symmetry-based pulse sequences and combination of these in reflection symmetric[102] or phase-encoded supercyclic[8,85–88,103] arrangements, it is possible to systematically eliminate many of the ordered terms of the effective Hamiltonian simultaneously (e.g., all even order terms in the infinite expansion). Such features have proven useful in systematic design strategies, e.g., when incorporated[104,105] in analytical evaluation programs such Mathematica.[106] Effective Hamiltonian theory has also been used extensively in the post-design phase for explaining and evaluating the performance of the vast majority of re- and decoupling experiments presented in solid-state NMR spectroscopy so far. Due to its complexity (e.g., large matrix dimensions), Floquet theory has been far less used for design purposes, while it has found useful applications for experiment evaluation and for establishment of physical insight into the inner workings of advanced pulse sequences.

Considering the complexity of the solid-state NMR pulse sequences as well as the spin systems subject to investigation, it may appear surprising that an obvious alternative to the traditional methods – namely computer-based experiment design – has not found widespread application. One explanation may be the lack of general software facilitating such optimizations. Another, perhaps even more important, explanation may be that the time required for calculating a single spectrum until quite recently has been too long to render multiple-parameter optimization practically feasible. With the current availability of fast computers, the low prices for single or even clusters of Linux machines, and the development of numerical procedures for efficient handling of powder samples – such as REPULSION,[43] Lebedev,[44] and γ-COMPUTE[46–49] – the perspectives for computer-assisted experiment design have improved considerably in the past few years.

These perspectives are very exciting in the sense that computerized experiment design may help us alleviate some of the serious problems in biological solid-state NMR such as sample heating, insufficient ^{1}H decoupling, low coherence transfer efficiencies, off-resonance effects, and effects of instrumental imperfections such as rf inhomogeneity. In the following, we will describe two approaches for numerical experiment design.

5.1. Experiment design using non-linear optimization

The most obvious approach for numerical experiment design is to implement typical and intuitively rational pulse sequences with important flexibilities represented by few parameters into a simulation program such as SIMPSON, and then optimize the variables using incorporated[65] non-linear optimization procedures to obtain a pulse sequence optimally fulfilling a predefined quality criterion. The optimization procedures would typically be proven robust methods such as downhill SIMPLEX[107] or steepest descent, potentially combined with Monte Carlo approaches for establishment of different starting parameters.[66,108] The quality criterion could be as simple as the highest transfer efficiency for a pulse sequence mediating transfer of coherence from one spin species to another, or it could have multiple purposes like eliminating certain dipole–dipole couplings while simultaneously avoiding the chemical shifts to be truncated completely. The free variables could be the first few components in a Fourier series expansion of the amplitude or phase of continuous rf irradiation.

Typically, non-linear optimization and development of solid-state NMR pulse sequences have been closely linked to an analytical derivation of a first generation of pulse sequences through which the formalism with appropriate variables may readily be set up. One simple (and very early) example is the optimization of TOtal Suppression of Sidebands (TOSS) pulse sequences[109,110] for spinning sideband suppression under consideration of fast spinning and finite rf pulses. With specific formulae for the location of the four or six π-refocusing pulses (each of which has a finite length) relative to the rotor period, one aim may be to find the shortest possible TOSS sequence which, under given sample spinning and rf field conditions, is feasible without overlap of the π pulses. Indeed, non-linear optimization has been used as an easy tool to find such sequences enabling combination of TOSS with fast sample spinning.[111] We note that these sequences were based on four and six pulses, and that Levitt and co-workers later presented analytical solutions for even shorter five-pulse TOSS sequences with favorable pulse spacings facilitating fast sample spinning.[112]

In a more challenging study, Drobny and co-workers in 1990 presented pulse sequences for homonuclear decoupling developed using non-linear optimization.[113] By restricting their numerical search to a special class of semi-windowless, reflection-symmetric decoupling sequences, it proved possible to (i) obtain a sufficiently simple parameterization to render non-linear optimization feasible, (ii) exploit the advantage of reflection-symmetric sequences in eliminating all even-ordered bilinear terms of the effective Hamiltonian (independently on whether the analytical formulae were used for the optimization or not), and (iii) establish exact numerical as well as approximative analytical effective Hamiltonian parameterizations to be used as input in the numerical

optimization. Based on random parameters for the initial pulse sequence, it was possible to design a large number of well-behaved homonuclear decoupling sequences.

Despite these achievements, one more decade passed before homonuclear decoupling sequences derived by numerical means were to be considered reasonable alternatives to the broad array of experiments derived by analytical means such as Lee-Goldburg,[114] frequency-switched Lee-Goldburg (FSLG),[115] MREV-8,[116] BR24,[117] BLEW-12,[118] MSHOT-3[119,120] as well as high-order-truncation (HOT) versions of FSLG.[8,121] Based on a relatively simple analytical formalism, taking requests on cyclic propagators and pulse sequence reflection symmetry explicitly into account, Emsley and co-workers proposed BLEW-12 inspired windowless decoupling sequences, where the amplitude and the resonance offset were constant and the pulse phases were expressed in terms of a Fourier series. Using a least-squares steepest descent approach, it was possible to numerically establish optimal values for a modest range of Fourier coefficients to establish the so-called DUMBO-1 homonuclear decoupling sequence,[122] which has proven practically useful.[123] In order to derive the best decoupling sequences, the two-spin based optimizations were set up to achieve the best possible suppression of the bilinear homonuclear dipole–dipole coupling and simultaneously provide the highest possible scaling factor of the linear chemical shift terms while considering: (i) variations in the dipolar couplings to indirectly reflect variations in multiple-spin systems and (ii) variations in chemical shift offsets and rf inhomogeneities to provide experiments that are robust towards variations in these parameters.

Numerical methods have also found important applications in the design and optimization of pulse sequences for coherence/polarization transfer in MAS experiments. We note that we already in the preceeding section have discussed the evaluation of powerful pulse sequences for such purposes – all of which have been developed on analytical grounds. Considering heteronuclear coherence transfer by means of CP under MAS conditions, it is well known that the best match of rf amplitudes – depending on the homonuclear couplings between abundant spins – typically is found on the so-called Hartmann–Hahn sideband conditions where the rf field strengths on the two channels differ by one or two rotor frequencies. This is, for example, the basis for the DCP[89], *i*DCP[92], and GATE[93] experiments used for transfer of coherence between low-γ heteronuclei. Often, these sidebands are quite narrow, which have led to the proposal of more robust experiments, such as ramped[81] or variable amplitude CP.[124] Based on numerical optimization, Hediger *et al.* proposed an alternative method to broaden and intensify the Hartmann–Hahn centerband based on rotor-synchronized amplitude modulation of one of the rf fields active during the CP period.[125] These amplitude modulated CP (AM-CP) experiments were developed using GAMMA[53] in combination with MINUIT[66] non-linear optimization of six harmonic coefficients in a cosine-series modulation of the rf amplitude on one of the rf channels.

In an alternative approach, the coherence transfers may be achieved using adiabatic pulse sequences under MAS conditions as featured, in particular, by Meier and co-workers in the context of $^{1}H \rightarrow {}^{13}C$[126] as well as $^{15}N \rightarrow {}^{13}C$[84] and $^{13}C \rightarrow {}^{13}C$[127,128] transfers in a variety of applications. Combinations between the AM-CP sequences discussed above and adiabatic passage sequences have also been proposed.[129] These sequences have typically been developed on analytical basis, while numerical

simulations have played an important role in the evaluation of their performance in terms of transfer efficiency and robustness towards, e.g., resonance offsets and rf amplitude variations. From such analysis, it is evident that the adiabatic-passage has to be relatively slow to allow for efficient transfer of coherences from all crystallites in the sample – in which case it is possible to achieve up to 100% transfer efficiency for a powder sample. Considering specifically the $^{15}N \rightarrow {}^{13}C$ transfers – discussed extensively in the previous section using non-adiabatic pulse sequences – efficiencies exceeding 90% will typically require an excitation time of 8–10 ms. Using a tangential shape for the sweep of the rf field on the ^{13}C channel through the mth Hartmann–Hahn sideband condition, the rf fields (in angular units) should be adjusted according to

$$\omega_{\mathrm{rf}}^{\mathrm{C}}(T) = \omega_{\mathrm{rf}}^{N}(T) + m\omega_{\mathrm{r}} - \langle\omega_{D,0}^{(m)}\rangle \tan\left[\alpha\left(\frac{1}{2}\tau - T\right)\right], \tag{13}$$

where T is the time ranging from 0 to the total mixing time τ. The angular velocity is given by

$$\alpha = \frac{2\Delta}{\tau\langle\omega_{D,0}^{(m)}\rangle}, \tag{14}$$

where $\langle\omega_{D,0}^{(m)}\rangle$ in the present formulation optimally should be an averaged value of the mth Fourier component for the dipolar coupling interaction [see Eq. (6)], while $\pm\Delta$ is the amplitude span for the sweep.[126] Equipped with these formulae, it should be possible to establish good conditions for efficient coherence transfers, but it appears that very often the optimum for the parameters $\langle\omega_{D,0}^{(m)}\rangle$ and Δ have been found through experimental optimization – where we recall that the former variable will be optimized as a single value being representative of this otherwise crystallite-orientation dependent parameter.

Considering that full adiabadicity typically requires quite long mixing times and that the sweep condition in Eq. (13) actually spans all conditions from a simple DCP experiment (in which intense transient oscillations may provide very good transfer efficiencies for small spin systems with modest chemical shielding anisotropies) to the true adiabatic experiments, it may prove useful to use numerical optimization to determine the best conditions for the transfer efficiency. This will allow the establishment of the best experiment independently on whether this is considered a normal pulsed experiment (as will be the case for small mixing times) or adiabatic (as will be the case for long mixing times). This analysis is particularly interesting if we consider the role of typical rf inhomogeneities which are generally believed to be of no concern for adiabatic experiments.

Focusing on the $^{13}C^{\alpha}$–^{15}N two-spin system in glycine, it is a simple matter to establish a two-parameter MINUIT-based optimization within the framework of SIMPSON to provide optimal 'adiabatic' transfers as illustrated in Fig. 7. Using a constant amplitude of 37 kHz for the rf field on the ^{15}N rf channel and sweeping through the Hartmann–Hahn sideband at 47 kHz on the ^{13}C rf channel (the spinning frequency is 10 kHz), the filled squares, open circles, and filled circles in Fig. 7a reflect optimal transfer efficiencies for

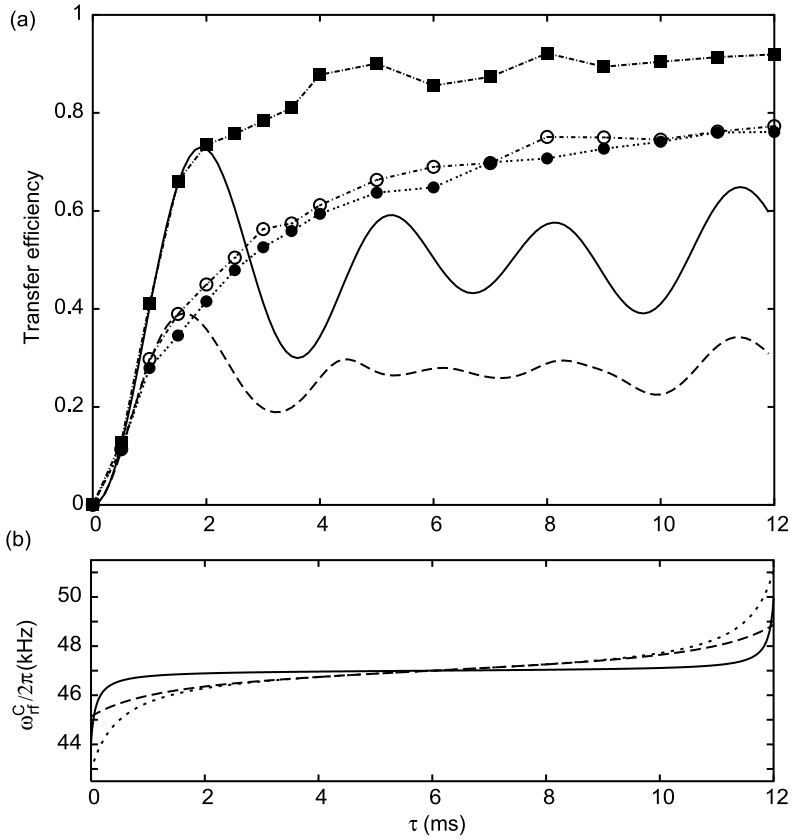

Fig. 7. (a) SIMPSON/MINUIT optimized $^{15}N \rightarrow {}^{13}C^{\alpha}$ transfer efficiencies obtained for the $^{13}C^{\alpha}{-}^{15}N$ two-spin system in glycine using an adiabatic CP pulse sequence with $\omega_{rf}^{N}/2\pi = 37$ kHz and a tangential adiabatic sweep on the ^{13}C channel centered around $\omega_{rf}^{C}/2\pi = 47$ kHz. The sweep was calculated using Eq. (13), the spinning frequency was $\omega_r/2\pi = 10$ kHz, the field strength 400 MHz for protons, the carriers were on-resonance for the two spins, while the spin system was characterized by the parameters $b_{NC}/2\pi = 890$ Hz, $J^{NC} = -11$ Hz, $\delta_N^{aniso} = 10.1$ ppm, $\eta_N = 0.17$, $\delta_C^{aniso} = 19.43$ ppm, $\eta_C = 0.98$, with the tensor orientations (in degrees) $\Omega_{PC}^{D} = \{0, 0, 0\}$, $\Omega_{PC}^{N} = \{-83.8, -79.0, 0.0\}$, and $\Omega_{PC}^{C} = \{64.9, 37.3, -28.8\}$. The symbols indicate adiabatic sequences without rf inhomogeneity (■), with 5% Lorentzian rf inhomogeneity (○), and with 9.2% Gaussian rf inhomogeneity (●), while the solid and dashed lines without symbols reflect DCP under ideal (solid line) and 5% Lorentzian (dashed line) rf field conditions. (b) Rf amplitudes on the ^{13}C rf channel for adiabatic sequences with 12 ms mixing time and homogeneous rf field conditions (solid line, $\langle\omega_{D,0}^{(m)}\rangle/2\pi = 66$ Hz, $\Delta/2\pi = 2960$ Hz), 5% Lorentzian rf inhomogeneity (dashed line, $\langle\omega_{D,0}^{(m)}\rangle/2\pi = 565$ Hz, $\Delta/2\pi = 1870$ Hz), and 9.2% Gaussian rf inhomogeneity (dotted line, $\langle\omega_{D,0}^{(m)}\rangle/2\pi = 495$ Hz, $\Delta/2\pi = 4080$ Hz).

cases without rf inhomogeneity, with 5% Lorentzian rf inhomogeneity, and with 9.2% Gaussian rf inhomogeneity (percentages reflect full width of the rf profile at half height relative to the nominal rf field strength; same inhomogeneity on both channels), respectively. For comparison, Fig. 7a contains transfer curves for DCP under

homogeneous (solid line) and 5% Lorentzian inhomogeneous (dashed line) rf conditions. It is clear that the tangential sweep expressed by Eq. (13) allows the optimization of sequences spanning the gap between efficient pulsed sequences with mixing times in the order of 2 ms and true adiabatic sequences at substantially longer mixing times – the intermediate regime is still influenced by weak transient oscillations. It is also evident that not only the short non-adiabatic sequences, such as DCP and some of the other sequences analyzed in Fig. 4 are influenced markedly by rf inhomogeneity (we should note that spin systems used for the calculations in Figs. 4 and 7 differ substantially in the anisotropic shielding parameters). This also applies for the adiabatic sequences which, even after 12 ms mixing time, display a loss of about 20% due to rf inhomogeneity.

To illustrate the substantial differences in the sweep profiles (and thereby the optimum values for the average $\langle\omega_{D,0}^{(m)}\rangle$ and Δ parameters) derived by numerical optimization, Fig. 7b shows representative $\omega_{\mathrm{rf}}^{\mathrm{C}}/2\pi$ rf field strengths for the 12 ms adiabatic sequences (last points in Fig. 7a) under ideal conditions (solid line), 5% Lorentzian rf inhomogeneity (dashed line), 9.2% Gaussian rf inhomogeneity (dotted line). As mentioned earlier, these rf profiles match the conditions for a typical 4 mm triple-resonance probe.

5.2. Automated design of experiments using optimal control theory

With increasing computer power and the availability of efficient numerical procedures for calculation of solid-state NMR powder spectra at hand, it is quite natural to ask the questions: Can we use computers as a primary tool for development of new experimental methods? If so, can this form the basis for automated experiment design? Design of methods that not necessarily need to be cast into 'historically' inspired pulse sequence elements with only a few free parameters. This would be highly desirable for several purposes. First, provided that automatic numerical procedures can be established, the group of researchers developing new experiments may be expanded to include the scientists actually doing the practical experiments. This is useful in the sense that they typically know exactly what they want access to – i.e., the most relevant nuclear spin parameters. Second, by eliminating the link to earlier experiments, as requested in the previous section due to problems with numerical handling of many free variables, it is possible that new experiments will be developed that challenge our current principles for experiment design. For example, it may prove important to abandon the fundamental principles of symmetrization to provide the best tailoring of the Hamiltonian. Symmetry principles have proven very useful, and have been a great help in handling complex experiments by principles of recursion, but at present, we do not have any guarantee that they may not form an important limitation, which may hinder us developing the best possible methods. Third, by increasing the number of free variables, i.e., the degree of freedom in our experiment design, it may be easier to develop methods that provide optimal performance under consideration of an increased number of additional parameters such as the available rf field strengths, rf inhomogeneities, specific offset ranges, or any kind of instrumental imperfections. A typical solid-state NMR approach for handling such effects is to use brute force methods often with the consequence of extremely high consumption of rf power (e.g., consider that C7[85] and POST-C7[86] may

be considered more robust variants of the HORROR experiment[83] achieved at the expense of a 14-fold increase in the required rf field strength). It may be envisaged that numerically derived methods with similar performance may require less rf power, and thereby alleviate one of the major problems in biological solid-state NMR, namely sample heating by intense rf irradiation.

To fulfill these needs, we recently undertook the task of developing and implementing optimal control design procedures into the SIMPSON software and described the first applications of this method to solid-state NMR spectroscopy by designing new dipolar recoupling experiments.[70] Optimal control theory[130,131] is an ideal vehicle for optimizing well-characterized analytical problems in terms of many parameters. Originating from economical sciences, the methods have later found many important applications in engineering, and recently for optimization of experiments in coherent optics,[132] imaging using magnetic resonance,[133,134] and optimization of liquid-state NMR experiments.[135–137] In all these contexts, optimal control theory has proven very useful in handling variable systems with many free parameters – giving a lot of promise for the method in solid-state NMR where the complexity of the formalism is high, due to the presence of anisotropic nuclear interactions with different performance for different crystallites in powder samples.

With reference to the description of dipolar recoupling in the previous sections and our first presentation of these data in Ref. 70, we here demonstrate the applicability of optimal control theory for the design of dipolar recoupling experiments for transfer of coherence from ^{15}N to ^{13}C, which could involve typical ^{15}N–^{13}C$'$ and ^{15}N–^{13}C$^{\alpha}$ spin pairs in the peptide backbone, or in this case, the ^{15}N–^{13}C$^{\alpha}$ spin pair in glycine. For this spin system, the procedure goes through the following steps: (i) We define the initial operator as x-phase coherence on the ^{15}N spins and the destination operator to be x-phase coherence on the ^{13}C spins. (ii) We choose our instrumental condition to be 10 kHz spinning, upper limits of 33 and 37 kHz for the available ^{15}N and ^{13}C rf field strengths, respectively, and an overall mixing time and the number of pulses this time should be divided into, e.g., 2.4 ms mixing time, taken in steps of 10 μs. (iii) We may enter specific information about rf inhomogeneity represented by an array of rf values along with a weighting factor for each of the two channels – the optimization adds the weighted response for these 'isochromats' to be evaluated in the optimization. (iv) We enter parameters for an arbitrary initial pulse sequence. (v) We define the quality criteria for the evaluation (e.g., maximation of the transfer efficiency). (vi) We start the optimization with a prespecified criterion for convergence. With this initialization, the optimal control procedure calculates the evolution of the density operator throughout the pulse sequence and the action of the pulse sequence on the target operator, out of which it determines the corrections to the rf pulse sequence – forming the basis for the next iteration. More details on the procedures will be deferred to a future paper – the program will later be released as part of the free SIMPSON software package.

An example of the application of optimal control theory for experiment design is described in Fig. 8, which in panel (a) shows the transfer efficiency achievable by optimal control sequences by the solid line, while corresponding efficiencies for the DCP experiment under ideal and inhomogeneous rf conditions as well as the performance of ramped versions of DCP are illustrated by the various dashed/dotted lines. We should

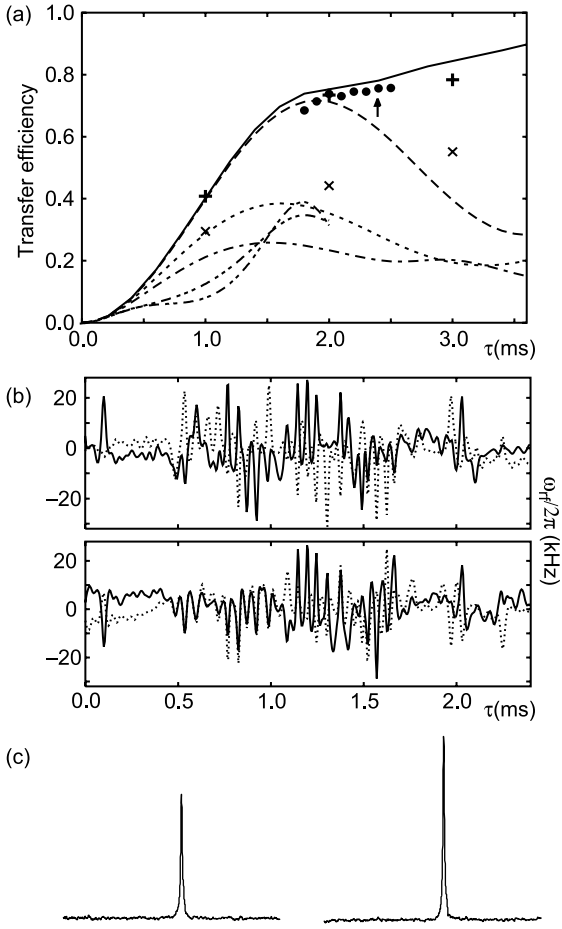

Fig. 8. (a) Comparison of $^{15}N \rightarrow {}^{13}C^{\alpha}$ coherence transfer in glycine calculated for various pulse sequences for a powder sample spinning of 10 kHz, using the parameters given in the caption to Fig. 7. The solid line and the • symbols reflect optimal control sequences under ideal conditions and 5% Lorentzian rf inhomogeneity, respectively. The + and × symbols reflect adiabatic sequences under ideal and 5% Lorentzian inhomogeneity conditions. The dashed curves correspond to DCP under conditions of (- - -) ideal rf, (···) 5% Lorentzian rf inhomogeneity, (---) 10% Lorentzian rf inhomogeneity, (-···) ramped DCP with ideal rf, and (-····) ramped DCP with 5% Lorentzian rf inhomogeneity. (b) *x*- (solid line) and *y*-phase (dotted line) rf amplitudes for the 2.4 ms optimal control sequence marked by an arrow in (a). Upper and lower panels correspond to the ^{15}N and ^{13}C rf channels, respectively. (c) Experimental DCP (left) and ^{OC}DCP (the sequence in b) – spectra of glycine. Reproduced from Ref. 70 with permission.

note that DCP is used for the present comparison, as this experiment is considered one of the most efficient method for $^{15}N \rightarrow {}^{13}C$ coherence transfer in the present case of small chemical shielding anisotropies. The solid-circles reflect optimal control sequences derived under assumption of a 5% Lorentzian rf field inhomogeneity. The + and × symbols illustrate the performance of computer-optimized tangential adiabatic-passage

sequences under ideal and 5% Lorentzian rf inhomogeneity conditions, respectively, as discussed in relation to Fig. 7. It is evident that the optimal control sequence for realistic cases of rf inhomogeneity may offer 50–100% better sensitivity than state-of-the-art recoupling sequences. An example of a 2.4 ms pulse sequence is given in Fig. 8b with the upper and lower panels showing the rf amplitudes (x phase: solid line, y phase: dashed line) for the ^{15}N and ^{13}C rf channels, respectively. The pulse sequence takes the appearance of an rf waveform digitized in steps of 10 μs, which can be implemented with good performance on most modern NMR spectrometers. We note the relatively low overall rf amplitudes, which is a great advantage for biological applications. The performance of the pulse sequence in Fig. 8b for $^{15}N \rightarrow {}^{13}C^{\alpha}$ coherence transfer in glycine is demonstrated experimentally in Fig. 8c by spectra recorded using DCP (to the left) and ^{OC}DCP (the optimum control variant DCP, to the right) – showing an improvement in sensitivity of 53% for the latter experiment.

6. DATA ANALYSIS

Considering the complexity of solid-state NMR spectra, and the potentials for many interactions as well as instrumental non-idealities to influence these, one of the most important roles of computer simulations and associated iterative fitting procedures is data interpretation. Correct interpretation is crucial for the accuracy of the determined nuclear spin interaction parameters and hence for all conclusions about structure and dynamics extracted from these. The applications range from numerically simple deconvolutions of overlapping Lorentzian or Gaussian lines over simulations of more complicated line shapes for powder samples containing nuclei influenced by several nuclear spin interactions, to advanced numerical calculations like simulation of spectral line shapes in multiple-dimensional NMR spectra under consideration of finite pulse effects. In this section, we will demonstrate the diversity of spectral analysis by a number of representative examples. The main focus will be biological solid-state NMR, realizing that some aspects, such as solid-state NMR spectroscopy of quadrupolar nuclei so far primarily have found applications in other areas. The quadrupolar methods, however, also have great potentials for the study of, e.g., metal-binding sites in proteins and for the study of molecular dynamics in biological systems.

6.1. Anisotropic ^{15}N chemical shifts from selectively labeled peptides

In order to establish structural constraints on proteins and peptides from solid-state NMR, it is important to consider all aspects from appropriate labeling of the sample, selection of the experiments providing the desired information, and to have appropriate reference data available to allow extraction of structural data from the (anisotropic interaction) parameters determined by the experiment. As an example, Cross and co-workers[138] investigated the conformation of the ion channel gramicidin A using selectively ^{15}N-labeled peptides in uniaxially oriented lipid bilayers (*c.f.*, Section 4.2). To translate the measured ^{15}N chemical shifts in the oriented samples into structural constraints, it is necessary to determine the magnitude and orientation of the ^{15}N chemical shift tensors

a priori. The magnitudes of the ^{15}N chemical shift tensors may be determined from ^{15}N powder spectra of singly labeled samples as illustrated in Fig. 9a–c. Subsequently, the orientation of the ^{15}N chemical shift tensor may be determined with respect to the C′–N internuclear axis from $^{13}C-^{15}N$ dipolar-coupled ^{15}N powder spectra. Such spectra prove to be quite sensitive to the relative orientation of the ^{15}N chemical shift tensor and the $^{13}C-^{15}N$ dipolar vector.

The positions of the singularities in the simple CSA spectra in Fig. 9a–c directly reflect the size of the three chemical shielding tensor principal components, and hence numerical simulations are not strictly necessary to determine the chemical shielding parameters from these spectra (*c.f.*, footnote to Table 2). However, it will often be more practical to determine the parameters from simulation of the line shape to compensate for the experimental line broadening and noise leading to less well-defined singularities. Numerical simulations also allow for a statistical evaluation of the precision of the parameters. While the simple CSA spectra could be interpreted analytically, this is not the case for the dipolar coupled spectra in Fig. 9d–f, where the combined effect of two interactions, depending on the size of the tensors as well as their mutual orientation, complicates the establishment of simple analytical expressions for the positions of the singularities. This implies that iterative numerical fitting is the most obvious way to determine the parameters describing the two nuclear spin interactions.

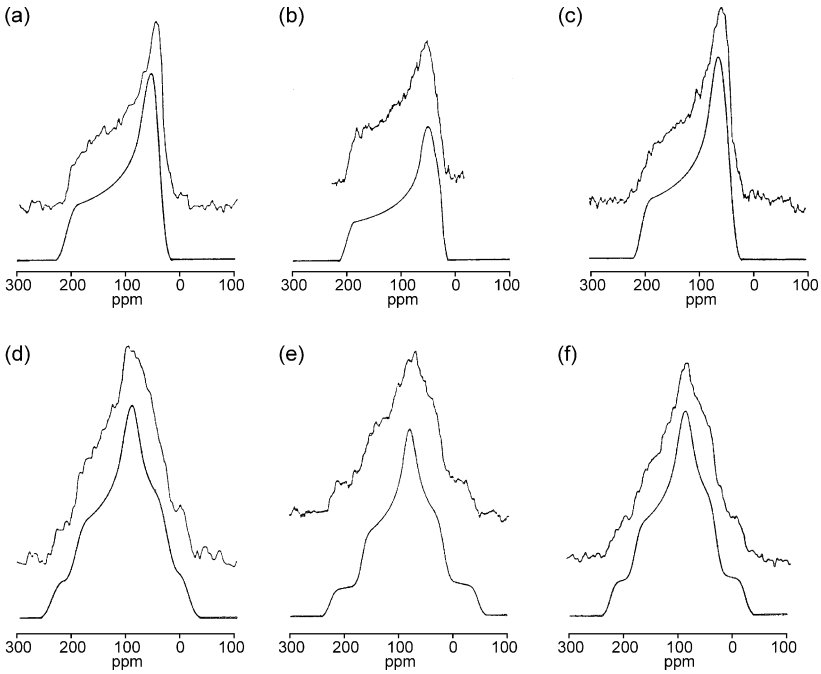

Fig. 9. ^{15}N solid-state NMR spectra obtained from dry powder samples of gramicidin A with selective ^{15}N labeling. The samples were [^{15}N]Val_1 (a,d), [^{15}N]Gly_2 (b,e), and [^{15}N]Trp_{11} (c,f), and the samples for (d–f) were additionally $^{13}C'$-labeled in the preceding residue, i.e., [^{13}C]formyl (d), [^{13}C]Val_1 (e), and [^{13}C]Leu_{10} (f). Reproduced from Ref. 138 with permission.

In the case of MAS, the spectra typically display a number of spinning sidebands spaced by the spinning frequency. The intensities of the spinning sidebands approximately represent the intensity of the static powder spectrum and hence the overall envelope of the sideband intensities represents the powder line shape. While analytical solutions have also been derived for the intensity of the sidebands as a function of the spinning frequency and anisotropic shielding parameters,[139] it is typically much easier to determine these interaction parameters from numerical simulations – again considering that this method directly takes the experimental errors and spectral noise into account.

6.2. Quadrupolar coupling and combinations with other effects

Like the anisotropic chemical shielding interaction, the first-order quadrupolar coupling interaction leads to simple powder patterns for the individual single-quantum central and satellite transitions for quadrupolar nuclei. The positions of the singularities are directly proportional to the size of the three principal components of the quadrupolar coupling tensor. Hence, the extraction of quadrupolar coupling parameters – and thereby information about the local electric field gradients at the site of the nucleus – from the satellite transitions from either static or MAS solid-state NMR spectra is a task very similar to extraction of chemical shielding parameters for spin-1/2 nuclei.[57,140]

In the case of large quadrupole coupling interactions, the spectra are not only influenced to first-order, but second-order effects appear for the central as well as the satellite transitions. Focusing on the central transition (i.e., $\left\{\frac{1}{2}, -\frac{1}{2}\right\}$) for half-integer spin quadrupolar nuclei, which is not influenced by the quadrupole coupling to first order, the second-order Hamiltonian [see Eq. (8)] will often result in a characteristic line shape that cannot be removed by MAS as illustrated by simulations in Fig. 10. It is possible to derive analytical expressions for the central-transition resonance frequency as a function of the powder Euler angles α and β for both static $(\alpha_{\mathrm{PL}}^{\mathrm{Q}}, \beta_{\mathrm{PL}}^{\mathrm{Q}})$ and rotating $(\alpha_{\mathrm{PR}}^{\mathrm{Q}}, \beta_{\mathrm{PR}}^{\mathrm{Q}})$ samples. By differentiating these frequency functions with respect to the two Euler angles, one obtains analytical expressions for the singularities in the powder spectrum. Figure 10a,b shows ideal second-order quadrupolar coupling line shapes under (a) static powder and (b) MAS conditions with labeling of the singularities referred to as peaks ('P') and shoulders ('S'). Table 4 summarizes the analytical expressions for these singularities.

Based on the expressions in Table 4, it is straightforward to determine the quadrupolar coupling parameters from the singularities in the experimental spectrum. Normally, however, it is safer to rely on numerical simulations since the experimental spectrum will often be subjected to line broadening or intensity distortions, which makes exact measurement of the singularities somewhat difficult. Also, as for the CSA example, the analytical expressions cannot be used in the presence of several interactions or if the infinite spinning frequency approximation is no longer valid.

Figure 10c shows a 2D multiple-quantum magic-angle spinning (MQMAS) experiment of $9Al_2O_3{\cdot}2B_2O_3$ (A9B2).[141] The MQMAS experiment[142] provides a high-resolution dimension – in which the second-order quadrupolar line broadening is removed – correlated to a second dimension where the second-order quadrupolar

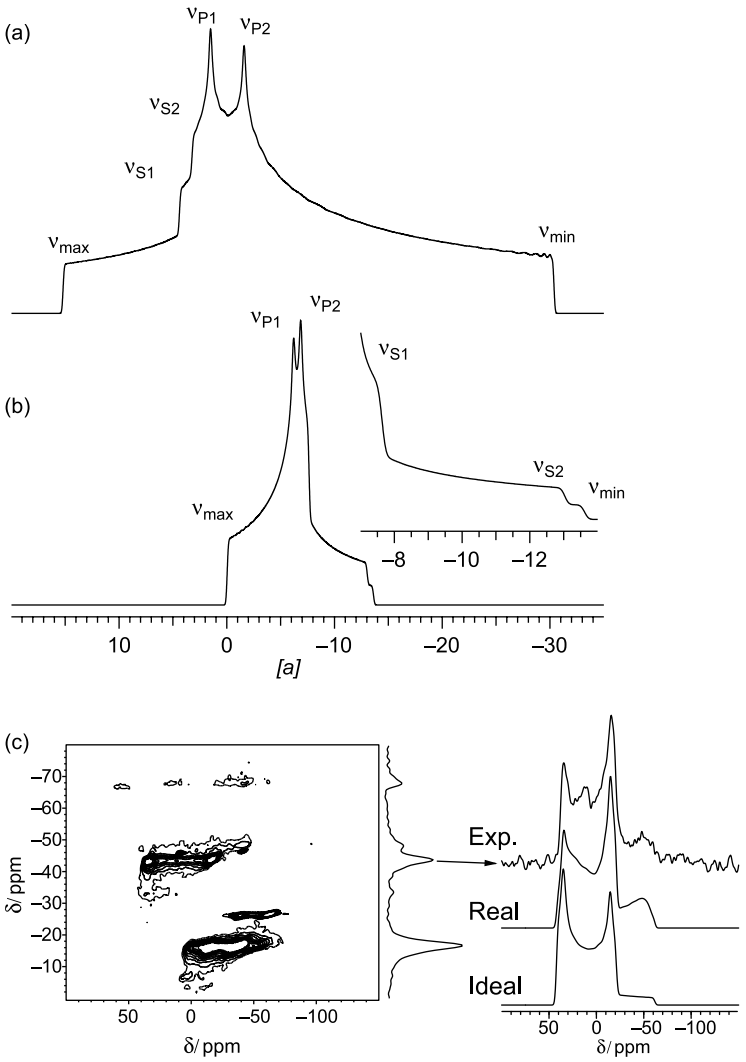

Fig. 10. Ideal second-order central-transition line shapes for half-integer quadrupolar nuclei in powder samples acquired under static (a) and MAS (b) conditions. The labels on the spectra display the singularities (shoulders S and peaks P) corresponding to the analytical resonance frequencies in Table 4. (c) 2D ^{27}Al MQMAS spectrum of $9Al_2O_3{\cdot}2B_2O_3$[141] on the left and a trace through one of the penta-coordinated Al sites on the right. The simulation labeled 'Real' includes effects of finite pulses, while the 'Ideal' simulation assumes no intensity distortions due to imperfect excitation. Spectra in (c) are reproduced from Ref. 65 with permission.

coupling information is present. Since the sample of A9B2 contains four different ^{27}Al sites with quadrupole couplings in the MHz range, it has recently been demonstrated that one should perform the experiments at around 40 T in order to provide resolution of all sites in a 1D experiment.[143] Hence, the MQMAS experiment is an obvious choice for this

Table 4. Characteristic central-transition frequencies for the second-order line shapes of half-integer quadrupolar nuclei in static or magic-angle spinning samples using frequency units of $a = 3\nu_Q^2/4\nu_0$[a]

	Static		MAS	
	$\eta_Q < \frac{1}{3}$	$\eta_Q > \frac{1}{3}$	$\eta_Q < \frac{3}{7}$	$\eta_Q > \frac{3}{7}$
ν_{max}	$(3+\eta_Q)^2 a$	$(3+\eta_Q)^2 a$	$-\frac{12}{7}(1-\eta_Q)^2 a$	$-\frac{12}{7}(1-\eta_Q)^2 a$
ν_{min}	$-16(1+\eta_Q)a$	$-16(1+\eta_Q)a$	$-2(6+\eta_Q^2)a$	$-2(6+\eta_Q^2)a$
ν_{P1}	$(3-\eta_Q)^2 a$	$8(1-\eta_Q^2)a$	$-\frac{12}{7}(1+\eta_Q)^2 a$	$-\frac{12}{7}(1+\eta_Q)^2 a$
ν_{P2}	$-16(1-\eta_Q)a$	$-16(1-\eta_Q)a$	$-\frac{1}{2}(15-6\eta_Q+7\eta_Q^2)a$	$-\frac{48}{7}a$
ν_{S1}		$(3-\eta_Q)^2 a$		$-\frac{1}{2}(15-6\eta_Q+7\eta_Q^2)a$
ν_{S2}	$4\eta_Q^2 a$	$4\eta_Q^2 a$	$-\frac{1}{2}(15+6\eta_Q+7\eta_Q^2)a$	$-\frac{1}{2}(15+6\eta_Q+7\eta_Q^2)a$

[a] ν_Q is defined as $\nu_Q = C_Q/(4I(2I-1))$ corresponding to $\omega_Q/2\pi$.

compound. The vertical projection in Fig. 10c shows four lines, and it has been possible to extract the trace displaying the anisotropic line shapes for the individual sites. As an example, the upper spectrum on the right (labeled Exp.) shows the trace through the isotropic shift for one of the pentacoordinated ^{27}Al sites. Indeed, this trace shows the characteristic line shape of a second-order quadrupolar broadened resonance (see Fig. 10a), but we also note that there are significant intensity distortions when comparing the line shape with the 'Ideal' spectrum shown at the bottom. Such intensity distortions are common in MQMAS NMR experiments since the experiment relies on evolution of multiple-quantum coherences in the indirect dimension. The excitation of multiple-quantum coherences and mixing into observable single-quantum coherences by finite rf pulses is highly dependent on the crystallite orientation, leading to non-uniform excitation and mixing. It is obvious that simulation of the experimental spectrum with an ideal line shape will easily lead to inaccurate determination of the quadrupole coupling parameters since the fit will be quite bad. However, with SIMPSON we are able to include the effects of the excitation and mixing and thereby produce 'Real' line shapes as shown in the middle spectrum in Fig. 10c.[65] We note that this line shape gives a much better agreement with the experimental one than is the case for the ideal line shape.

As a biologically relevant example of solid-state NMR on quadrupolar nuclei, Fig. 11 shows experimental and simulated ^{67}Zn solid-state NMR spectra of zinc diimidazole diacetate which may be considered a model compound for ^{67}Zn in metalloproteins.[144] The experimental spectrum was obtained by sampling the FID in between the refocusing pulses in a quadrupolar version of the Carr–Purcell–Meiboom–Gill experiment (QCPMG).[145] In this manner, the hundred kHz wide second-order quadrupolar powder pattern is split into a manifold of spin-echo sidebands with the consequence of highly

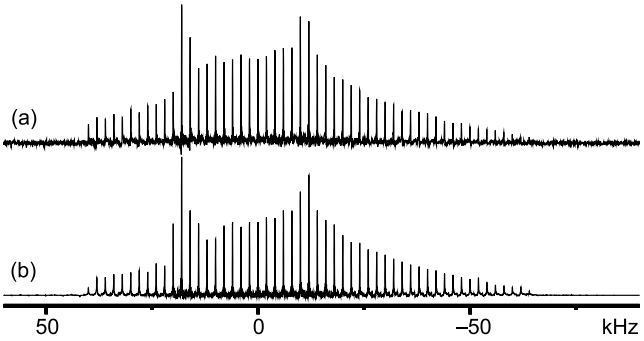

Fig. 11. (a) Experimental and (b) numerically simulated ^{67}Zn QCPMG spectra of zinc diimidazole diacetate. The experimental spectrum was recorded at 11.7 T using 24,000 transients with a recycle delay of 2 s. The simulated spectrum used $C_Q = 8.2$ MHz, $\eta_Q = 0.62$, and $\delta_{iso} = 155$ ppm (relative to a 0.9 M solution of $Zn(OOCCH_3)_2{\cdot}2H_2O$). Reproduced from Ref. 144 with permission.

improved sensitivity – which is of vital importance for the study of low-γ quadrupolar nuclei with the low molar amounts typically seen for biological macromolecule samples. In order to obtain information about the metal binding site from the spectrum in Fig. 11, numerical simulations that take effects from finite rf pulses and potentially the presence of several nuclear spin interactions into account are necessary. Also, the need for iterative fitting for determination of the many variables is quite evident. In the present case, the Zn^{2+} is coordinated to two N atoms (two imidazoles) and two O atoms (two monodentate acetates), representing a model for the coordination of Zn in thermolysin.[144] We note that the need for numerical simulations will be even higher for combinations of MQMAS and QCPMG, the so-called MQ-QCPMG-MAS experiment,[146,147] and for methods like FAM[148] and FASTER,[149] all with the aim of improving the sensitivity of the MQMAS experiment.

6.3. PISA wheels and dipolar waves for oriented proteins

Shifting the focus back to the direct extraction of structural parameters from experimental spectra supported by numerical simulations, it is clear from the discussion in the previous sections that the PISEMA experiment has a great potential for determination of the structure of proteins uniaxially oriented in planar membrane bilayers. In a recent study, Opella and co-workers[25] demonstrated the most important elements in such an analysis by determining the structure of a coat protein in fd filamentous bacteriophage particles. Figure 12a shows an experimental PISEMA spectrum of uniformly ^{15}N-labeled coat protein, where the letters indicate the assignment of the individual resonances to specific residues in the protein. While the spectrum clearly reveals a wheel-like pattern, it is not straightforward to assign all the resonances on the basis of this single spectrum. However, one may get the impression that there may be two overlapping wheel patterns of different sizes. To establish a complete assignment, the same experiment was performed on a series of residue-specific ^{15}N labeled samples of the proteins as shown in the middle and right columns of Fig. 12b. From these experiments, the assignments to the numerically

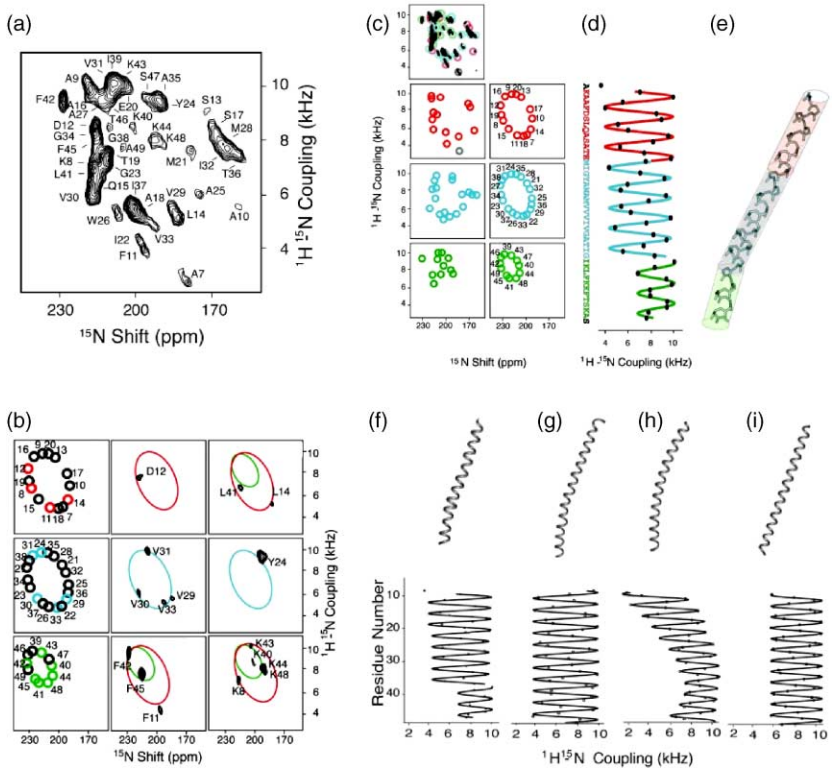

Fig. 12. (a) Experimental PISEMA spectrum of uniformly ^{15}N-labeled Y21M fd bacteriophage aligned in the magnetic field of the NMR spectrometer. (b) Experimental PISEMA spectra of residue-specific ^{15}N labeled samples (middle and right columns) accompanied by ideal wheels indicating the assignments (left column). (c) Representations of the experimental resonance positions (left column) and those of ideal PISA wheels (right column). (d) Dipolar waves fit to the experimental dipolar couplings obtained from the spectrum in (a). (e) 3D structure of the coat protein in bacteriophage particles determined from the dipolar waves in (d). (f–i) Ribbon renderings (top) and dipolar wave simulations (bottom) of (f) the NMR structure for the fd coat protein, (g) an X-ray fiber diffraction structure, (h) an ideal curved helix, and (i) an ideal straight helix. Reproduced from Ref. 25 with permission.

calculated ideal PISA wheels were made as illustrated in the left column of Fig. 12b. The experiments on the selectively labeled samples supported the assumption of the presence of at least two overlapping wheel patterns corresponding to the two ends of the α-helical protein. Figure 12c represents (left column) the experimentally measured resonance positions divided into three groups according to their location in the sequence of the protein and (right column) the corresponding ideal PISA wheels. An alternative representation, using the ^{1}H–^{15}N dipolar coupling only – the so-called dipolar waves (*vide supra*)[98–100] is shown in Fig. 12d and reveals more clearly the presence of individual domains of the structure.

From the data it was possible to establish the structure for the coat protein of the fd filamentous bacteriophage as shown in Fig. 12e. To qualitatively validate the structure,

Fig. 12f–i shows the dipolar waves for a number of different structures, supporting the solid-state NMR structure which corresponds to an α-helical structure with a kink near the C-terminal end.

6.4. Orientational constraints on bacteriorhodopsin in uniaxially oriented purple membranes

Based on a detailed numerical analysis of the perspectives for solid-state NMR investigations of uniaxially oriented membrane proteins in the 30–40 kDa regime,[68] we have recently explored experimental aspects of such studies with focus on PISEMA and $^{1}H-^{15}N$ chemical shift correlated (HETCOR) spectra for the seven-transmembrane (7 TM) protein bacteriorhodopsin (bR) in oriented purple membranes. Our initial numerical studies indicated that the spectra from the two types of 2D experiments on uniformly ^{15}N labeled bR would be too crowded to allow for assignment of all resonances.[68] For this reason, our first experiments focused on samples with more diluted labeling patterns, specifically bR with ^{15}N labeled methionines, i.e., ^{15N}Met-bR.[150] Figure 13a shows the sequence and the tentative location of the secondary structure elements of bR highlighting the nine Met residues of which six or seven are expected to be in the helix region (Fig. 13b). The experimental PISEMA and $^{1}H-^{15}N$ HETCOR spectra are shown in Fig. 13c,d, respectively. Despite large efforts in orienting the sample properly, we have not succeeded in getting sufficient resolution to resolve all resonances. We ascribe this to a mosaic spread in the alignment of the membrane, a phenomenon previously observed in studies of other large membrane proteins.[151] This motivated further development of numerical analysis methods to establish procedures for obtaining structural information from low-resolution spectra, on the basis of the philosophy that such spectra (i) despite their apparent low resolution still contain detailed structural information and (ii) they may be typical for proteins in native membranes. By focusing on the transmembrane helix region of the spectrum (between 150 and 230 ppm in the ^{15}N chemical shift dimension), it was indeed possible to deconvolute the line shape into seven well-defined regions corresponding to seven individual resonances. Based on this analysis, we could determine the conformation of the extracellular part of helix B, which has a tilt of $1-5^{\circ}$ relative to the membrane normal as described in more detail in Ref. 150.

It is always of interest to compare the performance of complementary experimental methods, such as liquid- and solid-state NMR spectroscopy, X-ray crystallography, and cryo-electron microscopy. This especially applies in novel, challenging areas such as that of membrane proteins, where a lot of debate concerns the physical state of the sample on which the structural analysis is performed. Considering that bR is one of the most well-characterized membrane proteins, it appeared obvious to compare the solid-state NMR data with the structures obtained by X-ray crystallography and cryo-electron diffraction. Such comparison may straightforwardly be conducted using SIMMOL[38] and SIMPSON,[36] which enable calculation of PISEMA and HETCOR spectra using the structural coordinates from any PDB file and fit these spectra to the experimental spectra. For the present purpose, we used the atomic coordinates of bR from recent X-ray[152,153] (PDB entries: 1C3W and 1KME) and cryo-electron[154] (PDB entry: 1FBB) diffraction studies to evaluate the compatibility of the different structures with our solid-state NMR

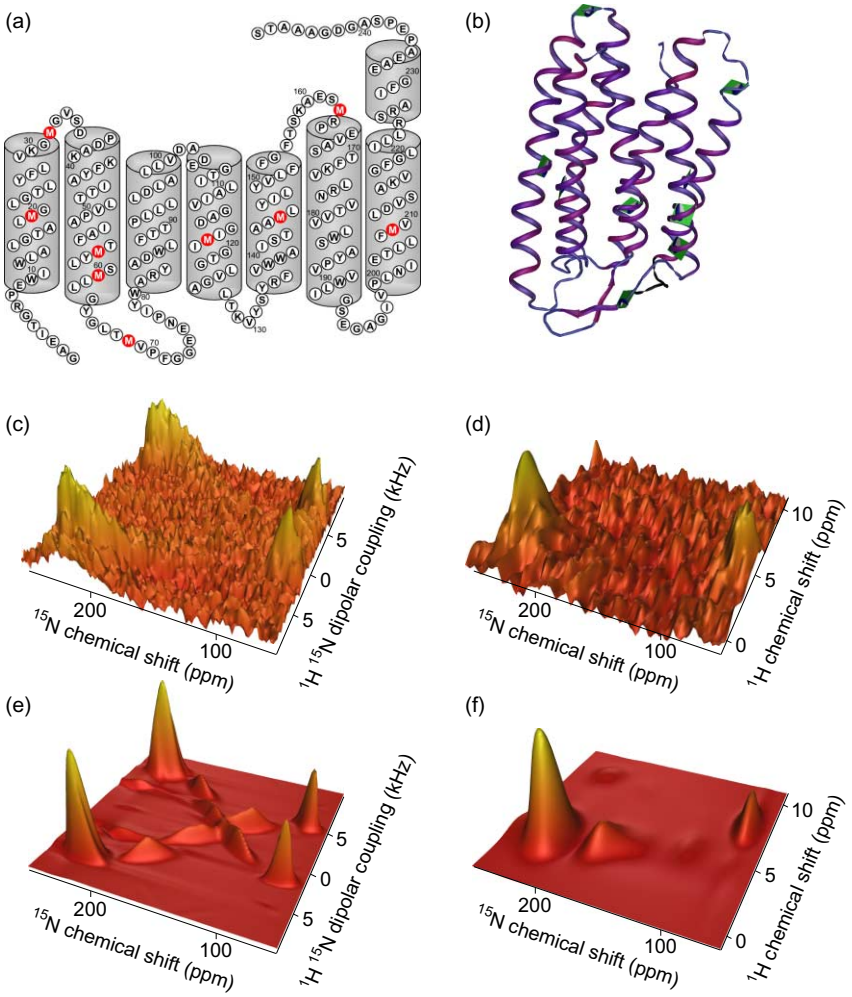

Fig. 13. (a) Primary sequence and schematic representation of the secondary structure of bR. (b) 3D structure of bR highlighting the nine [^{15}N]Met residues. Experimental (c,d) and simulated (e,f) PISEMA (c,e) and ^{1}H–^{15}N HETCOR (d,f) spectra of uniaxially oriented bR in purple membranes. The simulated spectra are calculated on the basis of the atomic coordinates from the 3.2 Å electron crystallography structure of Subramaniam and Henderson.[154] Reproduced from Ref. 31 with permission.

constraints.[150] These simulations revealed that although the resolution of our experiments is not sufficiently good to resolve all the individual resonances, the experiments are highly sensitive to the local structure of the individual amino acids. We found that the 3.2 Å cryo-electron diffraction structure[154] and the structure from bicelle crystallization[153] were most compatible with our data while the high-resolution (1.55 Å) XRD structure[152] of a crystal grown from a lipidic cubic phase was less compatible.[150]

For illustration, the simulated spectra from the cryo-electron diffraction structure (1FBB) are reproduced in Fig. 13e,f.

For the simulations in Fig. 13 showing a good agreement with the experimental solid-state NMR spectra, the imperfect alignment of the membranes was taken into account by including effects from mosaic spread in the simulations. This was done by using the normal REPULSION[43] or Alderman[155] crystallites characterized by their Euler angles and weight (α_i, β_i, w_i) and modifying the weight according to

$$w_i^{\text{gauss}} = N w_i \exp\left\{-\ln 2\left(\frac{\beta_i}{\Delta\beta}\right)^2\right\} \tag{15}$$

where $\Delta\beta$ represents the mosaic spread and N is a normalization factor ensuring that $\sum_i w_i^{\text{gauss}} = 1$. For the spectra in Fig. 13 a mosaic spread of $\Delta\beta = 2{-}5°$ was needed to account for the shape and width of the resonances.

6.5. Internuclear distances from REDOR experiments

One of the most widely used techniques to obtain structural constraints from solid-state NMR is rotational-echo double resonance (REDOR).[156] This method exploits recoupling of the heteronuclear dipolar coupling to provide internuclear distances with high precision. While there are numerous examples of the use of REDOR measurements in biological systems, we have chosen to focus on a recent example by Schaefer and co-workers.[157] Here, the authors characterized the binding of a shikimate-based bisubstrate inhibitor (SBBI) to 5-endolpyruvylshikimate-3-phosphate (EPSP) synthase using a trifluoromethyl labeled version of the SBBI and [$^{15}N_2$]Arg labeled EPSP-synthase. $^{15}N\{^{19}F\}$, $^{31}P\{^{15}N\}$, and $^{31}P\{^{19}F\}$ REDOR spectra were acquired, as shown in Fig. 14a. To obtain the internuclear distances, a series of experiments with different mixing time (dipolar recoupling time) need to be acquired. For each mixing time, a control experiment with no dipolar dephasing (S_0) and a dipolar dephasing (S) experiment are obtained, to calculate the effect of the dipolar dephasing ($\Delta S = S_0 - S$).

Figure 14b shows the dipolar dephasing curve for the $^{31}P\{^{19}F\}$ REDOR experiment which, through numerical analysis, allows for accurate determination of distances between the CF_3 group of the SBBI and ^{31}P of the phosphate in the shikimate ring and the closer non-ring phosphate. The resulting distances of 8.1 and 3.8 Å, respectively, along with less accurate distance restraints from the $^{15}N\{^{19}F\}$ and $^{31}P\{^{15}N\}$ REDOR experiments, were used as constraints for molecular modeling of the inhibitor–enzyme binding.[157]

6.6. Spider silk studied by $^{13}C'$–$^{13}C'$ double-quantum NMR

Another example of how numerical simulations of solid-state NMR spectra may contribute with important biological information is provided by a recent study of the secondary structure of *Samia cynthia ricini* silk.[158] van Beek *et al.*[158] produced a $^{13}C'$-labeled sample of silk by feeding silk worms with 1-^{13}C-alanine in aqueous solution.

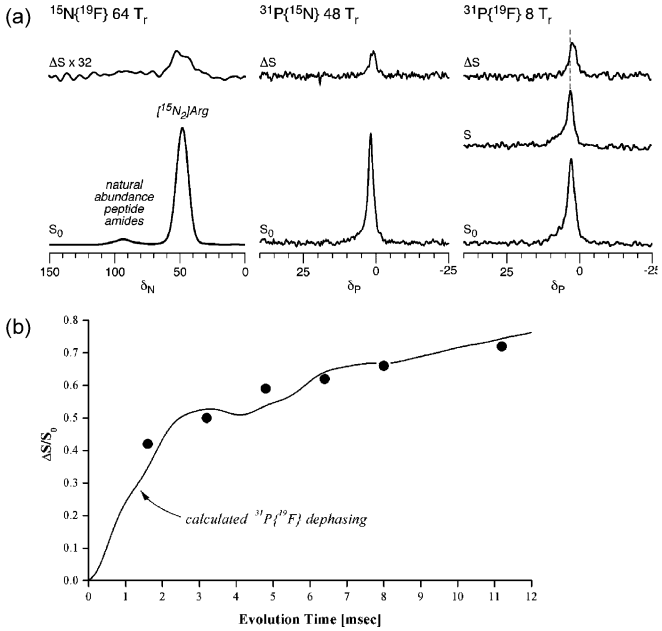

Fig. 14. (a) $^{15}N\{^{19}F\}$ (left), $^{31}P\{^{15}N\}$ (middle), and $^{31}P\{^{19}F\}$ (right) REDOR dephasing $(\Delta S/S_0)$ for a complex of CF_3-SBBI with $[^{15}N_2]$ Arg-EPSP synthase. (b) $^{31}P\{^{19}F\}$ REDOR dephasing $(\Delta S/S_0)$ for the SBBI–EPSP-synthase complex. The experimental dephasing for the sum of ring and non-ring phosphate ^{31}P is represented by filled circles. The solid line corresponds to a simulation using a CF_3 to non-ring phosphate distance of 3.8 Å while the corresponding distance to the ring phosphate was 8.1 Å. Reproduced from Ref. 157 with permission.

The silk produced by these worms displayed ~15% labeling of the poly-alanine chains, while the glycine-rich domains only reached a five times lower labeling fraction. For these samples, double-quantum correlation spectroscopy (DOQSY) experiments[159] were performed. The 2D $^{13}C'-^{13}C'$ DOQSY spectra prove to be highly sensitive to the peptide backbone torsion angles ϕ and ψ (Fig. 15a) as evident from the simulations in Fig. 15b.

The experimental $^{13}C'-^{13}C'$ DOQSY spectrum of the native silk fibers is reproduced in Fig. 15c. Since the polypeptide backbone of the silk structure is expected to show variations in the torsion angles, normal iterative fitting of the torsion angles to model the experimental spectrum will probably fail since it does not include a distribution of the parameters. To handle this problem, Meier and co-workers[158] used an alternative approach and modeled the experimental spectrum $S^{\exp}(\omega_1, \omega_2)$ as

$$S^{\exp}(\omega_1, \omega_2) = \int\int P(\phi, \psi) S(\phi, \psi, \omega_1, \omega_2) \mathrm{d}\phi \mathrm{d}\psi, \tag{16}$$

where $S(\phi, \psi, \omega_1, \omega_2)$ are the simulated spectra shown in Fig. 15b and $P(\phi, \psi)$ is the unknown probability distribution. Inversion of the integral is a so-called ill-posed problem, which gives many solutions of similar quality. Thus, the solutions need to be restricted, for example, by only accepting positive values for $P(\phi, \psi)$. While this is

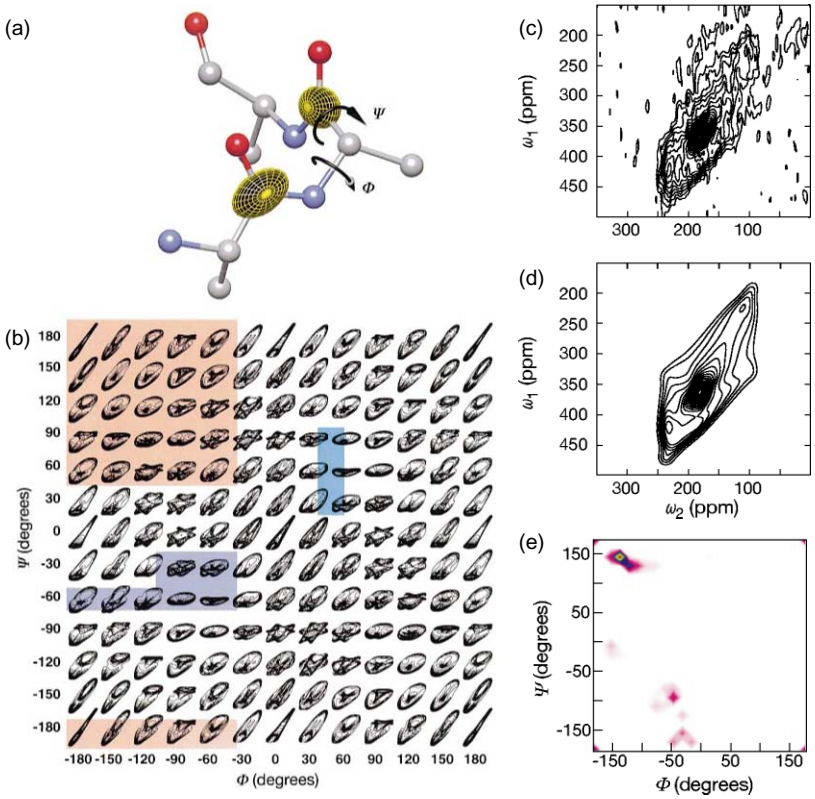

Fig. 15. (a) Geometry of a polypeptide showing the torsion angles (ϕ, ψ) and the orientation of the $^{13}C'$ chemical shift tensors. (b) Simulated double-quantum $^{13}C' - ^{13}C'$ spectra as a function of the ϕ and ψ torsion angles. The shaded backgrounds show typical α-helix and β-strand torsion angles. (c) Experimental and (d) simulated double-quantum spectra of silk fibers from *Samia cynthia ricini* silkworms. (e) Probability distribution determined from the experimental spectrum using Tikhonov regularization. Reproduced from Ref. 158 with permission.

normally not enough to provide meaningful results, Tikhonov regularization[160] is used to ensure that the probability function is smooth by adding a penalty proportional to the derivative of $P(\phi, \psi)$ to the RMS function. Using this method, the inversion of the experimental spectrum of the fibrillous silk leads to the modeled spectrum in Fig. 15d and the probability distribution for the dihedral angles shown in Fig. 15e. The major component corresponding to about 70% of $P(\phi, \psi)$ is found around $\phi, \psi = -135°, 150°$ corresponding to a β-sheet structure. The other components were attributed to interstrand contacts within the β-sheet.

6.7. Molecular motion from ^{2}H MAS and QCPMG spectra

Another area where advanced experimental methods typically have to be associated with efficient numerical simulation procedures is when solid-state NMR is used to extract information about molecular motion. Over the years, a large variety of different

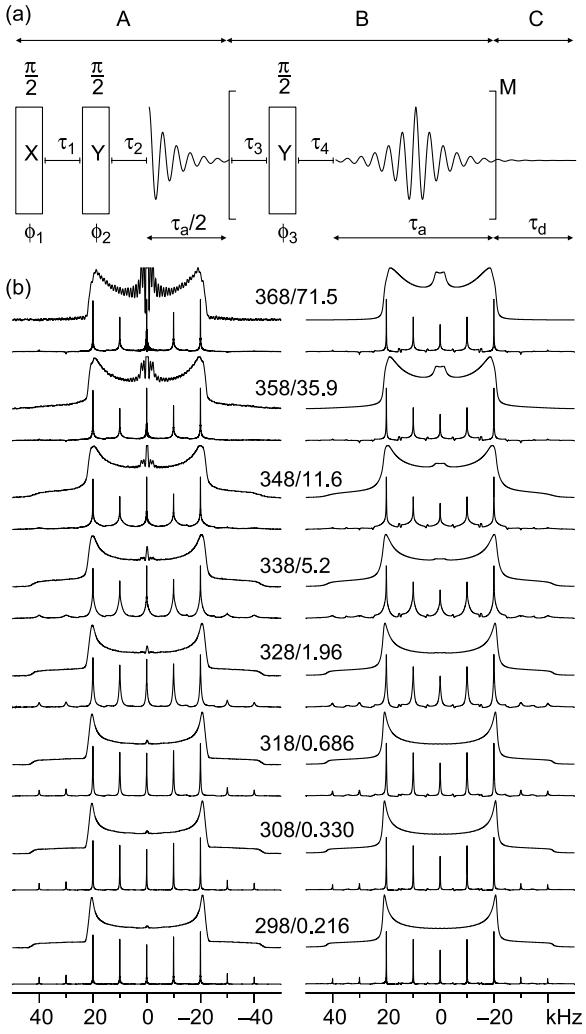

Fig. 16. (a) QCPMG pulse sequence consisting of an initial quadrupolar echo sequence (part A) followed by a train of $\pi/2$ refocusing pulses (part B) in between which the FID is sampled in the periods τ_a, with the last decay extended in part C to reduce truncation effects. (b) Experimental (left column) and simulated (right column) quadrupolar-echo (upper) and QCPMG (lower) spectra for DMS recorded at different temperatures. The temperature (in K)/kinetic constant (in ms) is written above each spectrum. More details can be found in Ref. 166 from where the spectra are reproduced with permission.

experiments has been proposed for determination of molecular motion on time scales ranging from picoseconds to hours. Many of these techniques have been developed for the study of polymers,[4] but they have also found many applications in biological systems such as biological membranes. Solid-state NMR on polymeric systems[161] and studies of

molecular motion[162] have been discussed extensively in this journal. Therefore, we will restrict ourselves to two simple complementary approaches for extraction of information about dynamics from ^{2}H solid-state NMR spectra. In different manners, the two methods exploit coherent averaging to produce spectra with high sensitivity and at the same time extend the regime over which precise information on molecular motion can be extracted through numerical simulations.

The first approach uses MAS spectra of deuterons to determine molecular motion. As illustrated by Kristensen *et al.*,[163,164] the range of applicability of the popular ^{2}H quadrupolar echo experiment for measurement of molecular motion may be extended considerably by using a simple MAS experiment which increases the experimental sensitivity by an order of magnitude. The overall envelope of the sideband patterns is similar to that observed for a static sample, while the line width/shape of the spinning sidebands contains additional important information about molecular dynamics, in particular in the intermediate motion regime (kinetic constants in the order of 10^3–10^6 Hz), where the motional effects and the sample rotation may interfere.

Focusing on static samples, similar effects – even with an increased flexibility to tune the interference between molecular motion and NMR manipulations – may be obtained by recording the quadrupolar-echo spectra in course of a train of refocusing pulses, i.e., using the QCPMG experiment[145] already addressed briefly in a prior example. In combination with numerical simulations, static and MAS versions of this experiment have, for example, found interesting applications for establishment of parameters for the orientation and magnitudes of chemical shielding and quadrupolar coupling tensors for quadrupolar nuclei of biological relevance.[144,165] An example of the application of static-sample QCPMG for determination of molecular dynamics[166] is given in Fig. 16. The figure shows the QCPMG pulse sequence in Fig. 16a along with experimental as well as computer simulated ^{2}H QCPMG spectra of dimethyl sulfone (DMS) at different temperatures in Fig. 16b. The temperature and the rate constant k in units of K and ms, respectively, are given above each set of spectra. For each set of spectra, the upper spectrum corresponds to a normal quadrupolar-echo experiment while the lower 'spin-echo sideband' spectra were obtained using the QCPMG pulse sequence which – in addition to providing higher accuracies on the rate constants – is governed by orders of magnitude of higher experimental sensitivity. We note that these results do not originate from biological samples, but we can refer to numerous quadrupolar echo dynamics studies of biological systems, e.g., Refs. 167–169 for which QCPMG experiments along with numerical simulations could prove very useful.

7. CONCLUDING REMARKS

In this chapter, we have discussed tools for numerical simulations in biological solid-state NMR spectroscopy along with a number of examples, which in different ways demonstrate the importance of computer methods in this rapidly developing research area. With a rapid increase in the performance and general availability of fast computers, along with increasing development of the solid-state NMR technology towards studies of increasingly complex molecular systems, we anticipate that computational methods

will have a substantially increasing impact on biological solid-state NMR in the years to come. Some of the grounds for this development have been formed by current powerful – and free and generally available – software packages allowing simulation of essentially all kinds of solid-state NMR experiments. We believe that this development will continue with increasing pace, and more and more features will be added for computer-aided experiment design, method evaluation, as well as precise extraction of highly accurate information about molecular structure and dynamics.

ACKNOWLEDGEMENTS

We acknowledge collaborations with the group of Prof. Steffen J. Glaser, Technische Universität München, and Prof. Navin Khaneja, Harvard University, on the new optimal control theory based automatic design of solid-state NMR pulse sequences and Dr. Miya Kamihira and the group of Prof. Anthony Watts, Oxford University, for collaboration on solid-state NMR analysis of bacteriorhodopsin. This work has been supported by the Danish Biotechnological Instrument Center (DABIC), Carlsberg Fondet, and the Danish Natural Science Foundation.

REFERENCES

1. K. Wüthrich, *NMR of Proteins and Nucleic Acids*, Wiley, New York, 1986.
2. R. R. Ernst, G. Bodenhausen and A. Wokaun, *Principles of Nuclear Magnetic Resonance in One and Two Dimensions*, Clarendon Press, Oxford, 1987.
3. M. Mehring, *Principles of High Resolution NMR in Solids*, Springer, New York, 1983.
4. K. Schmidt-Rohr and H. W. Spiess, *Multidimensional Solid-State NMR and Polymers*, Academic Press, London, 1996.
5. J. Cavanagh, W. J. Fairbrother, A. G. Palmer, III and N. J. Shelton, *Protein NMR Spectroscopy: Principles and Practice*, Academic Press, San Diego, 1996.
6. O. W. Sørensen, G. W. Eich, M. H. Levitt, G. Bodenhausen and R. R. Ernst, Product operator formalism for the description of NMR pulse experiments. *Progr. NMR Spectrosc.*, 1983, **16**, 163–192.
7. U. Haeberlen and J. S. Waugh, Coherent averaging effects in magnetic resonance. *Phys. Rev.*, 1968, **175**, 453–467.
8. M. Hohwy and N. C. Nielsen, Systematic design and evaluation of multiple-pulse experiments in nuclear magnetic resonance spectroscopy using a semi-continuous Baker-Campell-Hausdorff expansion. *J. Chem. Phys.*, 1998, **109**, 3780–3791.
9. T. S. Untidt and N. C. Nielsen, Closed solution to the Baker-Campbell-Hausdorff problem: exact effective Hamiltonian theory for analysis of nuclear-magnetic-resonance experiments. *Phys. Rev. E*, 2003, **65**, 021108-1–021108-17.
10. D. Siminovitch, T. S. Untidt and N. C. Nielsen, Exact effective Hamiltonian theory. II: Expansion of matrix functions and entangled unitary exponential operators. *J. Chem. Phys.*, 2004, **120**, 51–66.
11. Y. Zur, M. H. Levitt and S. Vega, Multiphoton NMR-spectroscopy on a spin system with $I = 1/2$. *J. Chem. Phys.*, 1983, **78**, 5293–5310.
12. G. J. Boender, S. Vega and H. J. M. de Groot, A physical interpretation of the Floquet description of magic angle spinning nuclear magnetic resonance spectroscopy. *Mol. Phys.*, 1998, **95**, 921–934.
13. S. J. Opella, NMR and membrane proteins. *Nat. Struct. Biol.*, 1997, **4**, 845–848.
14. R. G. Griffin, Dipolar recoupling in MAS spectra of biological solids. *Nat. Struct. Biol.*, 1998, **5**, 508–512.

15. S. J. Opella, F. M. Marassi, J. J. Gesell, A. P. Valente, Y. Kim, M. Oblatt-Montal and M. Montal, Structures of the M2 channel-lining segments from nicotinic acetylcholine and NMDA receptors by NMR spectroscopy. *Nat. Struct. Biol.*, 1999, **6**, 374–379.
16. A. McDermott, T. Polenova, A. Böckmann, K. W. Zilm, E. K. Paulsen, R. W. Martin and G. T. Montelione, Partial NMR assignment for uniformly (^{13}C,^{15}N)-enriched BPTI in the sold state. *J. Biomol. NMR*, 2000, **16**, 209–219.
17. R. Tycko, Solid-state NMR as a probe of amyloid fibril structure. *Curr. Opin. Chem. Biol.*, 2000, **4**, 500–506.
18. K. G. Valentine, S. F. Liu, F. M. Marassi, G. Veglia, S. J. Opella, F. X. Ding, S. H. Wang, J. M. Becker and F. Naider, Structure and topology of a peptide segment of the 6th transmembrane domain of the *Saccharomyces cerevisiae* alpha-factor receptor in phospholipid bilayers. *Biopolymer*, 2001, **59**, 243–256.
19. J. Wang, S. Kim, F. Kovacs and T. A. Cross, Structure of the transmembrane region of the M2 protein H^+ channel. *Prot. Sci.*, 2001, **10**, 2241–2250.
20. J. Castellani, B. van Rossum, A. Diehl, M. Schubert, K. Rehbein and H. Oschkinat, Structure of a protein determined by solid-state NMR spectroscopy. *Nature*, 2002, **420**, 98–102.
21. C. M. Rienstra, L. Tucker-Kellogg, C. P. Jaroniec, M. Hohwy, B. Reif, M. T. McMahon, B. Tidor, T. Lozano-Perez and R. G. Griffin, De novo determination of peptide structure with solid-state magic-angle spinning NMR spectroscopy. *Proc. Natl. Acad. Sci. USA*, 2002, **99**, 10260–10265.
22. A. T. Petkova, Y. Ishii, J. J. Balbach, O. N. Antzutkin, R. D. Leapman, F. Delaglio and R. Tycko, A structural model for Alzheimer's beta-amyloid fibrils based on experimental constraints from solid-state NMR. *Proc. Natl. Acad. Sci. USA*, 2003, **99**, 16742–16747.
23. J. D. van Beek, S. Hess, F. Vollrath and B. H. Meier, The molecular structure of spider dragline silk: folding and orientation of the protein backbone. *Proc. Natl. Acad. Sci. USA*, 2002, **99**, 10266–10271.
24. F. M. Marassi and S. J. Opella, Simultaneous assignment and structure determination of a membrane protein from NMR orientational restraints. *Prot. Sci.*, 2003, **12**, 403–411.
25. A. C. Zeri, M. F. Mesleh, A. A. Nevzorov and S. J. Opella, Structure of the coat protein in fd filamentous bacteriophage particles determined by solid-state NMR spectroscopy. *Proc. Natl. Acad. Sci. USA*, 2003, **100**, 6458–6463.
26. S. Luca, J. F. White, A. K. Sohal, D. V. Filiv, J. H. van Boom, R. Grisshammer and M. Baldus, The conformation of neutotensin bound to its G-protein coupled receptor investigated by 2D solid-state NMR. *Proc. Natl Acad. Sci. USA*, 2003, **100**, 10706–10711.
27. S. H. Park, A. A. Mrse, A. A. Nevzorov, M. F. Mesleh, M. Oblatt-Montal, M. Montal and S. J. Opella, Three-dimensional structure of the channel-forming trans-membrane domain of virus protein 'u' (Vpu) from HIV-1. *J. Mol. Biol.*, 2003, **333**, 409–424.
28. A. Böckmann, A. Lange, A. Galinier, S. Luca, N. Giraud, M. Juy, H. Heise, R. Monstserret, F. Penin and M. Baldus, Solid-state NMR sequential resonance assignments and conformational analysis of the 2×10.4 kDa dimeric form of the *Bactillus subtilus* protein Crh. *J. Biomol. NMR*, 2003, **27**, 323–339.
29. S. Luca, H. Heise and M. Balus, High-resolution solid-state NMR applied to polypeptides and membrane proteins. *Acc. Chem. Res.*, 2003, **36**, 858–865.
30. C. P. Jaroniec, C. E. MacPhee, V. S. Baja, M. T. McMahon, C. M. Dobson and R. G. Griffin, High-resolution molecular structure of a peptide in an amyloid fibril determined by magic angle spinning NMR spectroscopy. *Proc. Natl Acad. Sci. USA*, 2004, **101**, 711–716.
31. N. C. Nielsen, A. Malmendal and T. Vosegaard, Techniques and applications of NMR to membrane proteins. *Mol. Membr. Biol.*, 2004, **21**, 129–141. Taylor and Francis Ltd: http://www.tandf.co.uk/journals/.
32. U. Haeberlen, *High-Resolution NMR in Solids. Selective Averaging*, Academic Press, New York, 1976.
33. H. W. Spiess, Rotations of molecular and nuclear spin relaxation, NMR basic principles and progress, Vol. 15. Springer, Berlin, 1978.
34. B. C. Gerstein and C. R. Dybowski, *Transient Techniques in NMR of Solids. An Introduction to Theory and Practice*, Academic Press, Orlando, 1985.
35. M. H. Levitt, D. P. Raleigh, F. Creuzet and R. G. Griffin, Theory and simulations of homonuclear spin-pair systems in rotating solids. *J. Chem. Phys.*, 1990, **92**, 6347–6364.
36. M. Bak, J. T. Rasmussen and N. C. Nielsen, SIMPSON: a general simulation program for solid-state NMR spectroscopy. *J. Magn. Reson.*, 2000, **147**, 296–330.

37. M. H. Levitt, *Spin Dynamics. Basics of Nuclear Magnetic Resonance*, Wiley, Chichester, 2001.
38. M. Bak, R. Schultz, T. Vosegaard and N. C. Nielsen, Specification and visualization of anisotropic interaction tensors in polypeptides and numerical simulations in biological solid-state NMR. *J. Magn. Reson.*, 2002, **154**, 28–45.
39. Oak Ridge Thermal Ellipsoid Plot (ORTEP) program. Download site: http://www.ornl.gov/sci/ortep/ortep.html.
40. S. K. Zaremba, Good lattice points, discrepancy, and numerical integration. *Ann. Mat. Pure Appl.*, 1966, **293**, 4–73.
41. H. Conroy, Molecular Schrödinger equation. VIII. A new method for the evaluation of multidimensional integration. *J. Chem. Phys.*, 1967, **47**, 5307–5318.
42. V. B. Cheng, H. H. Suzukawa, Jr. and M. Wolfsberg, Investigations of a nonrandom numerical method for multidimensional integration. *J. Chem. Phys.*, 1973, **59**, 3992–3999.
43. M. Bak and N. C. Nielsen, REPULSION, a novel approach to efficient powder averaging in solid-state NMR. *J. Magn. Reson.*, 1997, **125**, 132–139.
44. M. Edén and M. H. Levitt, Computation of orientational averages in solid-state NMR by gaussian spherical quadrature. *J. Magn. Reson.*, 1998, **132**, 220–239.
45. M. Edén, Y. K. Lee and M. H. Levitt, Efficient simulation of periodic problems in NMR. Application to decoupling and rotational resonance. *J. Magn. Reson. A*, 1996, **120**, 56–71.
46. M. Hohwy, H. Bildsøe, H. J. Jakobsen and N. C. Nielsen, Efficient spectral simulations in NMR of rotating solids. The γ-COMPUTE algorithm. *J. Magn. Reson.*, 1999, **136**, 6–14.
47. T. Charpentier, C. Fermon and J. Virlet, Efficient time propagation technique for MAS NMR simulation: application to quadrupolar nuclei. *J. Magn. Reson.*, 1998, **132**, 181–190.
48. M. H. Levitt and M. Eden, Numerical simulation of periodic nuclear magnetic resonance problems: fast calculation of carousel averages. *Mol. Phys.*, 1998, **95**, 879–890.
49. W. B. Blanton, J. W. Logan and A. Pines, Rational reduction of periodic propagators for off-period observations. *J. Magn. Reson.*, 2004, **166**, 174–181.
50. W. B. Blanton, BlochLib: a fast NMR C++ tool kit. *J. Magn. Reson.*, 2003, **162**, 269–283.
51. M. Veshtort, and R.G. Griffin, Presentation at 45th Rocky Mountain NMR Conference, 2003.
52. F. S. de Bouregas and J. S. Waugh, ANTIOPE, a program for computer experiments on spin dynamics. *J. Magn. Reson.*, 1992, **96**, 280–289.
53. S. A. Smith, T. O. Levante, B. H. Meier and R. R. Ernst, Computer simulations in magnetic resonance. An object-oriented programming approach. *J. Magn. Reson.*, 1994, **106**, 75–105.
54. T. Karlsson, J. M. Popham, J. R. Long, N. Oyler and G. P. Drobny, A study of homonuclear dipolar recoupling pulse sequences in solid-state nuclear magnetic resonance. *J. Am. Chem. Soc.*, 2003, **125**, 7394–7407.
55. P. Hodgkinson and L. Emsley, Numerical simulation of solid-state NMR experiments. *Prog. NMR Spectrosc.*, 2000, **36**, 201–239.
56. (a) M. Edén, Computer simulations in solid-state NMR. Part I. Spin dynamics theory. *Concepts Magn. Reson.*, 2003, **17A**, 117–154; (b) M. Edén, Computer simulations in solid-state NMR II. Implementation for static and rotating samples. *Concepts Magn Reson*, 2003, **18A**, 1–23; (c) M. Edén, Computer simulations in solid-state NMR III. Powder averaging. *Concepts Magn. Reson.*, 2003, **18A**, 24–55.
57. J. Skibsted, N. C. Nielsen, H. Bildsøe and H. J. Jakobsen, Satellite transitions in MAS NMR spectra of quadrupolar nuclei. *J. Magn. Reson.*, 1991, **95**, 88–117.
58. H. Bildsøe, *STARS User's Guide. Spectrum Analysis for Rotating Solids*, Publ. No. 87-195233-00, Rev A0296, Varian Associates Inc, Palo Alto, 1996.
59. J.-P. Amoureux, Personal communication.
60. B. Stroustrup, *The C++ Programming Language*, Addison-Wesley, Reading, 1991.
61. MathWorks MABLAB, the language of technical computing. Website: http://www.mathworks.com/.
62. SIMPSON download site: http://bionmr.chem.au.dk/bionmr/software/simpson.php and discussion group: http://groups.yahoo.com/group/simpson-simmol.
63. B. B. Welch, *Practical Programming in Tcl and Tk*, Prentice Hall PTR, New Jersey, 1995.
64. J. K. Ousterhout, *Tcl and Tk Toolkit*, Addison-Wesley Publication Company, Reading, 1994.

65. T. Vosegaard, A. Malmendal and N. C. Nielsen, The flexibility of SIMPSON and SIMMOL for numerical simulations in solid and liquid-state NMR spectroscopy. *Chem. Monthly*, 2002, **133**, 1555–1574.
66. F. James and M. Ross, Minuit: a system for function minimization and analysis of the parameter errors and correlations. *Comput. Phys. Commun.*, 1975, **10**, 343–367, Manual available from the web site http://wwwinfo.cern.ch/asdoc/minuit/minmain.html.
67. J. H. Kristensen and I. Farnan, Efficient solid state NMR powder simulations using SMP and MPP parallel computation. *J. Magn. Reson.*, 2003, **161**, 183–190.
68. T. Vosegaard and N. C. Nielsen, Towards high-resolution solid-state NMR on large uniformly ^{15}N- and [^{13}C,^{15}N]-labeled membrane proteins in oriented lipid bilayers. *J. Biomol. NMR*, 2002, **22**, 225–247.
69. M. Bjerring, T. Vosegaard, A. Malmendal and N. C. Nielsen, Methodological development of solid-state NMR for characterization of membrane proteins. *Concepts Magn. Reson.*, 2003, **18A**, 111–129.
70. C. T. Kehlet, A. C. Sivertsen, M. Bjerring, T. O. Reiss, N. Khaneja, S. J. Glaser and N. C. Nielsen, Improving solid-state NMR dipolar recoupling by optimal control. *J. Am. Chem. Soc.*, 2004, **126**, 10202–10203.
71. F. M. Marassi and S. J. Opella, A solid-state NMR index of helical membrane protein structure and topology. *J. Magn. Reson.*, 2000, **144**, 150–155.
72. J. Wang, J. Denny, C. Tian, S. Kim, Y. Mo, F. Kovacs, Z. Song, K. Nishimura, Z. Gan, R. Fu, J. R. Quine and T. A. Cross, Imagining membrane protein helical wheels. *J. Magn. Reson.*, 2000, **144**, 162–167.
73. H. M. Berman, J. Westbrook, Z. Feng, G. Gilliland, T. N. Bhat, H. Weissig, I. N. Shindyalov and P. E. Bourne, The protein data bank. *Nucleic Acids Res.*, 2000, **28**, 235–242.
74. M. Phillips, S. Levy and T. Munzner, Geomview: an interactive geometry viewer. *Not. Am. Math. Soc.*, 1993, **40**, 985–988, Open source software at http://www.geomview.org.
75. C. Glaubitz and A. Watts, Magic angle-oriented sample spinning (MAOSS): a new approach toward biomembrane studies. *J. Magn. Reson.*, 1998, **130**, 305–316.
76. M. Bak, R. Schultz and N. C. Nielsen, *Numerical Simulations for Experiment Design and Extraction of Structural Parameters in Biological Solid-State NMR Spectroscopy. The Future of Solid-State NMR in Biology*, Kluwer, Dordrecht, 2001.
77. T. V. Vosegaard and N. C. Nielsen, Improved pulse sequences for pure exchange solid-state NMR spectroscopy. *Magn. Reson. Chem.*, 2004, **42**, 285–290.
78. S. Dusold and A. Sebald, Dipolar recoupling under magic-angle spinning conditions. *Ann. Rep. NMR Spectrosc.*, 2000, **41**, 185–264.
79. M. Baldus, Correlation experiments for assignment and structure elucidation of immobilized polypeptides under magic angle spinning. *Prog. NMR Spectrosc.*, 2002, **41**, 1–47.
80. A. Pines, M. G. Gibby and J. S. Waugh, Proton-enhanced nuclear induction spectroscopy. A method for high resolution NMR of dilute spins in solids. *J. Chem. Phys.*, 1972, **56**, 1776–1777.
81. G. Metz, W. Hu and S. O. Smith, Ramped-amplitude cross polarization in magic-angle-spinning NMR. *J. Magn. Reson. A*, 1994, **110**, 219–227.
82. E. H. Hardy, A. Detken and B. H. Meier, Fast-NMR total through-bond correlation spectroscopy using adiabatic pulses. *J. Magn. Reson.*, 2003, **165**, 208–218.
83. N. C. Nielsen, H. Bildsøe, H. J. Jakobsen and M. H. Levitt, Double-quantum homonuclear rotary resonance: efficient dipolar recovery in in magic-angle spinning nuclear magnetic resonance. *J. Chem. Phys.*, 1994, **101**, 1805–1812.
84. M. Baldus, D. G. Geurts, S. Hediger and B. H. Meier, Efficient ^{15}N-^{13}C polarization transfer by adiabatic-passage Hartmann–Hahn cross polarization. *J. Magn. Reson. A*, 1996, **118**, 140–144.
85. Y. K. Lee, N. D. Kurur, M. Helmle, O. G. Johannessen, N. C. Nielsen and M. H. Levitt, Efficient dipolar recoupling in the NMR of rotating solids. A sevenfold symmetric radiofrequency pulse sequence. *Chem. Phys. Lett.*, 1995, **242**, 304–309.
86. M. Hohwy, H. J. Jakobsen, M. Edén, M. H. Levitt and N. C. Nielsen, Broadband dipolar recoupling in the nuclear magnetic resonance of rotating solids: a compensated C7 pulse sequence. *J. Chem. Phys.*, 1998, **108**, 2686–2694.
87. M. Bjerring and N. C. Nielsen, Solid-state NMR heteronuclear dipolar recoupling using off-resonance symmetry-based pulse sequences. *Chem. Phys. Lett.*, 2003, **370**, 496–503.

88. M. Carravetta, M. Edén, X. Zhao, A. Brinkmann and M. H. Levitt, Symmetry principles for the design of radiofrequency pulse sequences in the nuclear magnetic resonance of rotating solids. *Chem. Phys. Lett.*, 2000, **321**, 205–215.
89. J. Schaefer, E. O. Stejskal, J. R. Garbow and R. A. McKay, Quantative determination of the concentrations of ^{13}C-^{15}N chemical bonds by double cross-polarization NMR. *J. Magn. Reson.*, 1984, **59**, 150–156.
90. X. Wu and K. W. Zilm, Cross polarization with high-speed magic-angle spinning. *J. Magn. Reson. A*, 1993, **104**, 154–165.
91. M. Baldus, A. T. Petkova, J. Herzfeld and R. G. Griffin, Cross polarization in the tilted frame: assignment and spectral simplification in the heteronuclear spin systems. *Mol. Phys.*, 1998, **95**, 1197–1207.
92. M. Bjerring and N. C. Nielsen, Solid-state NMR heteronuclear coherence transfer using phase and amplitude modulated rf irradiation at the Hartmann–Hahn sideband conditions. *Chem. Phys. Lett.*, 2003, **382**, 671–678.
93. M. Bjerring, J. T. Rasmussen, R. S. Krogshave and N. C. Nielsen, Heteronuclear coherence transfer in solid-state nuclear magnetic resonance using a γ-encoded transferred echo experiment. *J. Chem. Phys.*, 2003, **119**, 8916–8926.
94. K. Palczewski, T. Kumasaka, T. Hori, C. A. Behnke, H. Motoshima, B. A. Fox, I. L. Trong, D. C. Teller, T. Okada, R. E. Stenkamp, M. Yamamoto and M. Miyano, Crystal structure of rhodopsin: a G protein-coupled receptor. *Science*, 2000, **289**, 739–745.
95. F. M. Marassi, A simple approach to membrane protein secondary structure and topology based on NMR spectroscopy. *Biophys. J.*, 2001, **80**, 994–1003.
96. C. H. Wu, A. Ramamoorthy and S. J. Opella, High-resolution heteronuclear dipolar solid-state NMR spectroscopy. *J. Magn. Reson.*, 1994, **109A**, 270–272.
97. W. M. Tan, Z. Gu, A. C. Zeri and S. J. Opella, Solid-state NMR triple-resonance backbone assignments in a protein. *J. Biomol. NMR*, 1999, **13**, 337–342.
98. M. F. Mesleh, G. Veglia, T. M. DeSilva, F. M. Marassi and S. J. Opella, Dipolar waves as NMR maps of protein structure. *J. Am. Chem. Soc.*, 2002, **124**, 4206–4207.
99. M. F. Mesleh and S. J. Opella, Dipolar waves as NMR maps of helices in proteins. *J. Magn. Reson.*, 2003, **163**, 288–299.
100. M. F. Mesleh, S. Lee, G. Veglia, D. S. Thiriot, F. M. Marassi and S. J. Opella, Dipolar waves map the structure and topology of helices in membrane proteins. *J. Am. Chem. Soc.*, 2003, **125**, 8928–8935.
101. Web page for the BioMagResBank: http://www.bmrb.wisc.edu.
102. P. Mansfield, M. J. Orchard, D. C. Stalker and K. H. B. Richards, Symmetrized multipulse nuclear-magnetic-resonance experiments in solids: measurement of the chemical-shift shielding tensor in some compounds. *Phys. Rev.*, 1973, **B7**, 90–105.
103. M. H. Levitt, *Symmetry-Based Pulse Sequences in Magic-Angle Spinning Solid-State NMR*, Encyclopedia of NMR, Wiley, Chichester, 2002, pp. 165–196.
104. Mathematica routines for symmetry-based dipolar recoupling experiments at Southhampton University, UK: http://www.mhl.soton.ac.uk/.
105. Mathematica routines for Exact Effective Hamiltonian Theory (EEHT) at University of Aarhus, Denmark: http://bionmr.chem.au.dk/bionmr/software/index.php.
106. A. Wolfram, *MATHEMATICA. A System for Doing Mathematics by Computer*, Addison-Wesley, Redwood City, 1988.
107. J. A. Nelder and R. Mead, A simplex method for function minimization. *Comput. J.*, 1965, **7**, 308–313.
108. W. H. Press, S. A. Teukolsky and W. T. Vetterling, *Numerical Recipes in C: The Art of Scientific Computing*, Cambridge University Press, 1993.
109. W. T. Dixon, Spinning-sideband-free NMR spectra. *J. Magn. Reson.*, 1981, **44**, 220–223.
110. D. P. Raleigh, E. T. Olejniczak, S. Vega and R. G. Griffin, An analysis of sideband suppression techniques in magic-angle sample spinning NMR. *J. Magn. Reson.*, 1987, **72**, 238–250.
111. N. C. Nielsen, H. Bildsøe and H. J. Jakobsen, TOSS in high-speed MAS NMR. *J. Magn. Reson.*, 1988, **80**, 149–154.
112. Z. Song, O. N. Antzutkin, X. Feng and M. H. Levitt, Sideband suppression in magic-angle spinning NMR by a sequence of 5 π pulses. *Sol. Stat. Nucl. Magn. Reson.*, 1993, **2**, 143–146.

113. H. Liu, S. J. Glaser and G. P. Drobny, Development and optimization of multipulse propagators: Applications to homonuclear spin decoupling in solids. *J. Chem. Phys.*, 1990, **93**, 7543–7560.
114. M. Lee and W. I. Goldburg, Nuclear-magnetic-resonance line narrowing by a rotating rf field. *Phys. Rev.*, 1965, **140A**, 1261–1271.
115. A. Bielecki, A. C. Kolbert and M. H. Levitt, Frequency-switched pulse sequences – homonuclear decoupling and dilute spin NMR in solids. *Chem. Phys. Lett.*, 1989, **155**, 341–346.
116. W.-K. Rhim, D. D. Elleman and R. W. Vaughan, Analysis of multiple pulse NMR in solids. *J. Chem. Phys.*, 1973, **59**, 3740–3749.
117. D. P. Burum and W.-K. Rhim, Analysis of multiple pulse NMR in solids. 3. *J. Chem. Phys.*, 1979, **71**, 944–956.
118. D. P. Burum, M. Linder and R. R. Ernst, Low-power multipulse line narrowing in solid-state NMR. *J. Magn. Reson.*, 1981, **44**, 173–188.
119. M. Hohwy and N. C. Nielsen, Elimination of high order terms in multiple pulse nuclear magnetic resonance spectroscopy: Application to homonuclear decoupling in solids. *J. Chem. Phys.*, 1997, **106**, 7571–7586.
120. M. Hohwy, P. V. Bower, H. J. Jakobsen and N. C. Nielsen, A high-order and broadband CRAMPS experiment using z-rotational decoupling. *Chem. Phys. Lett.*, 1997, **273**, 297–303.
121. E. Vinogradov, P. K. Madhu and S. Vega, Proton spectroscopy in solid state nuclear magnetic resonance with windowed phase modulated Lee-Goldburg decoupling sequences. *Chem. Phys. Lett.*, 2002, **354**, 193–202.
122. D. Sakellariou, A. Lesage, P. Hodgkinson and L. Emsley, Homonuclear dipolar decoupling in solid-state NMR using continuous phase modulation. *Chem. Phys. Lett.*, 2000, **319**, 253–260.
123. A. Lesage, D. Sakellariou, S. Hediger, B. Elena, P. Charmont, S. Steuernagel and L. Emsley, Experimental aspects of proton NMR spectroscopy in solids using phase-modulated homonuclear dipolar decoupling. *J. Magn. Reson.*, 2003, **163**, 105–113.
124. O. B. Peersen, X. Wu, I. Kustanovich and S. O. Smith, Variable-amplitude cross-polarization MAS NMR. *J. Magn. Reson. A*, 1993, **104**, 334–339.
125. S. Hediger, B. H. Meier and R. R. Ernst, Rotor-synchronized amplitude-modulated nuclear magnetic resonance spin-lock sequences for improved cross polarization under fast magic angle sample spinning. *J. Chem. Phys.*, 1995, **102**, 4000–4011.
126. S. Hediger, B. H. Meier and R. R. Ernst, Adiabatic passage Hartmann–Hahn cross polarization in NMR under magic angle sample spinning. *Chem. Phys. Lett.*, 1995, **240**, 449–456.
127. R. Verel, M. Baldus, M. Nijman, J. W. M. van Os and B. H. Meier, Adiabatic homonuclear polarization transfer in magic-angle-spinning solid-state NMR. *Chem. Phys. Lett.*, 1997, **280**, 31–39.
128. R. Verel, M. Ernst and B. H. Meier, Adiabatic dipolar recoupling in solid-state NMR: the DREAM sequence. *J. Magn. Reson.*, 2001, **150**, 81–99.
129. S. Hediger, P. Signer, M. Tomaselli, R. R. Ernst and B. H. Beier, A combination of slow and fast RF field modulation for improved cross polarization in solid-state MAS NMR. *J. Magn. Reson.*, 1997, **125**, 291–301.
130. L. Pontryagin, B. Boltyanskii, R. Gamkredlidze and E. Mishchenko, *The Mathematical Theory of Optimal Processes*, Wiley-Interscience, New York, 1962.
131. A. Bryson, Jr. and Y. C. Ho, *Applied Optimal Control*, Hemisphere, Washington DC, 1975.
132. A. P. Peirce, M. Dahleh and H. Rabitz, Optimal control of quantum mechanical systems: existence, numerical approximations and applications. *Phys. Rev. A*, 1988, **37**, 4950–4964.
133. S. Conolly, D. Nishimura and A. Macovski, Optimal control solution to the magnetic resonance selective excitation problem. *IEEE Trans. Med. Imag.*, 1986, **MI-5**, 106–115.
134. D. Rosenfeld and Y. Zur, Design of adiabatic selective pulses using optimal control theory. *Magn. Reson. Med.*, 1996, **36**, 401–409.
135. T. O. Reiss, N. Khaneja and S. J. Glaser, Time optimal coherence-order-selective transfer of in-phase coherence in heteronuclear IS spin systems. *J. Magn. Reson.*, 2002, **154**, 192–195.
136. N. Khaneja, T. Reiss, B. Luy and S. J. Glaser, Optimal control of spin dynamics in the presence of relaxation. *J. Magn. Reson.*, 2003, **162**, 311–319.
137. T. E. Skinner, T. O. Reiss, B. Luy, N. Khaneja and S. J. Glaser, Application of optimal control theory to the design of broadband excitation pulses for high resolution NMR. *J. Magn. Reson.*, 2003, **163**, 8–15.

138. W. Mai, W. Hu, C. Wang and T. A. Cross, Orientational constraints as three-dimensional structural constraints from chemical shift anisotropy: The polypeptide backbone of gramicidin A in a lipid bilayer. *Protein Sci.*, 1993, **2**, 532–542.
139. J. Herzfeld and A. E. Berger, Sideband intensities in NMR spectra of samples spinning at the magic angle. *J. Chem. Phys.*, 1980, **73**, 6021–6030.
140. H. J. Jakobsen, J. Skibsted, H. Bildsøe and N. C. Nielsen, Magic-angle spinning NMR spectra of satellite transitions for quadrupolar nuclei in solids. *J. Magn. Reson.*, 1989, **85**, 173–180.
141. T. Vosegaard, D. Massiot and P. J. Grandinetti, Sensitivity enhancements in MQ-MAS NMR of spin-5/2 nuclei using modulated rf mixing pulses. *Chem. Phys. Lett.*, 2000, **326**, 454–460.
142. L. Frydman and J. S. Harwood, Isotropic spectra of half-integer quadrupolar spins from bidimensional magic-angle spinning NMR. *J. Am. Chem. Soc.*, 1995, **117**, 5367–5368.
143. Z. H. Gan, P. Gor'kov, T. A. Cross, A. Samoson and D. Massiot, Seeking higher resolution and sensitivity for NMR of quadrupolar nuclei at ultrahigh magnetic fields. *J. Am. Chem. Soc.*, 2002, **124**, 5634–5635.
144. F. H. Larsen, A. S. Lipton, H. J. Jakobsen, N. C. Nielsen and P. D. Ellis, ^{67}Zn QCPMG solid-state NMR studies of zinc complexes as models for metalloproteins. *J. Am. Chem. Soc.*, 1999, **121**, 3783–3784.
145. F. H. Larsen, H. J. Jakobsen, P. D. Ellis and N. C. Nielsen, Sensitivity-enhanced quadrupolar-echo NMR of half-integer quadrupolar nuclei. Magnitudes and relative orientation of chemical shielding and quadrupolar coupling tensors. *J. Phys. Chem. A*, 1997, **101**, 8597–8606.
146. T. Vosegaard, F. H. Larsen, H. J. Jakobsen, P. D. Ellis and N. C. Nielsen, Sensitivity-enhanced multiple-quantum MAS NMR of half-integer quadrupolar nuclei. *J. Am. Chem. Soc.*, 1997, **119**, 9055–9056.
147. F. H. Larsen and N. C. Nielsen, Effects of finite rf pulses and sample spinning speed in multiple-quantum magic-angle spinning (MQ-MAS) and multiple-quantum quadrupolar Carr-Purcell-Meiboom-Gill magic-angle spinning (MQ-QCPMG-MAS) nuclear magnetic resonance of half-integer quadrupolar nuclei. *J. Phys. Chem. A*, 1999, **103**, 10825–10832.
148. A. Goldbourt, P. K. Madhu and S. Vega, Enhanced conversion of triple to single-quantum coherence in the triple-quantum MAS NMR spectroscopy of spin-5/2 nuclei. *Chem. Phys. Lett.*, 2000, **320**, 448–456.
149. T. Vosegaard, P. Florian, D. Massiot and P. J. Grandinetti, Multiple quantum magic-angle spinning using rotary resonance excitation. *J. Chem. Phys.*, 2001, 4618–4624.
150. M. Kamihira, T. Vosegaard, A. J. Mason, S. Straus, N. C. Nielsen and A. Watts, *J. Struct. Biol.*, in press.
151. G. Gröbner, A. Taylor, P. T. F. Williamson, G. Choi, C. Glaubitz, J. A. Watts, W. J. de Grip and A. Watts, Macroscopic orientation of natural and model membranes for structural studies. *Anal. Biochem.*, 1997, **254**, 132–138.
152. H. Luecke, B. Schobert, H.-T. Richter, J.-P. Cartailler and J. K. Lanyi, Structure of bacteriorhodopsin at 1.55 Å resolution. *J. Mol. Biol.*, 1999, **291**, 899–911.
153. S. Faham and J. U. Bowie, Bicelle crystallization: a new method for crystallizing membrane proteins yields a monomeric bacteriorhodopsin structure. *J. Mol. Biol.*, 2002, **316**, 1–6.
154. S. Subramaniam and R. Henderson, Molecular mechanism of vectorial proton translocation by bacteriorhodopsin. *Nature*, 2000, **406**, 653–657.
155. D. W. Alderman, M. S. Solum and D. M. Grant, Methods for analyzing spectroscopic line shapes. NMR solid powder patterns. *J. Chem. Phys.*, 1986, **84**, 3717–3725.
156. T. Gullion and J. Schaefer, Rotational-echo double-resonance NMR. *J. Magn. Reson.*, 1989, **81**, 196–200.
157. L. M. McDowell, D. R. Studelska, B. Poliks, R. D. O'Connor and J. Schaefer, Characterization of the complex of a trifluoromethyl-substituted shikimate-based bisubstrate inhibitor and 5-enolpyruvylshikimate-3-phosphate synthase by REDOR NMR. *Biochemistry*, 2004, **43**, 6606–6611.
158. J. D. van Beek, L. Beaulieu, H. Schäfer, M. Demura, T. Asakura and B. H. Meier, Solid-state NMR determination of the secondary structure of *Samia cynthia ricini* silk. *Nature*, 2000, **405**, 1077–1079. http://www.nature.com/.
159. K. Schmidt-Rohr, A double-quantum solid-state NMR technique for determining torsion angles in polymers. *Macromolecules*, 1996, **29**, 3975–3981.
160. A. N. Tikhonov and V. Y. Arsenin, *Solutions of Ill-Posed Problems*, Wiley, New York, 1977.
161. K. Schmidt-Rohr and H. W. Spiess, Dynamics of polymers from one- and two-dimensional solid-state NMR spectroscopy. *Ann. Rep. NMR Spectrosc.*, 2002, **46**, 1–29.
162. M. J. Duer, Solid-state NMR studies of molecular motion. *Ann. Rep. NMR Spectrosc.*, 2000, **43**, 1–58.

163. J. H. Kristensen, H. Bildsøe, H. J. Jakobsen and N. C. Nielsen, Theory and simulations of molecular dynamics in ^{2}H MAS NMR. *J. Magn. Reson.*, 1992, **100**, 437–443.
164. J. H. Kristensen, G. L. Hoatson and R. L. Vold, Effects of restricted rotational diffusion on H-2 magic angle spinning nuclear magnetic resonance spectra. *J. Chem. Phys.*, 1999, **110**, 4533–4553.
165. F. H. Larsen, J. Skibsted, H. J. Jakobsen and N. C. Nielsen, Solid-state QCPMG NMR of low-γ quadrupolar metal nuclei in natural abundance. *J. Am. Chem. Soc.*, 2000, **122**, 7080–7086.
166. F. H. Larsen, H. J. Jakobsen, P. D. Ellis and N. C. Nielsen, Molecular dynamics from H-2 quadrupolar Carr-Purcell-Meiboom-Gill solid-state NMR spectroscopy. *Chem. Phys. Lett.*, 1998, **292**, 467–473.
167. R. G. Griffin, Solid state nuclear magnetic resonance of lipid bilayers. *Methods Enzymol.*, 1981, **72**, 108–174.
168. V. Copie, A. E. McDermott, K. Beshah, J. C. Williams, M. Spijker-Assingk, R. Gebhard, J. Lugtenburg, J. Herzfeld and R. G. Griffin, Deuterium solid-state nuclear magnetic resonance studies of methyl group dynamics in bacteriorhodopsin and retinal model compounds: evidence for a 6-s-trans chromophore in the protein. *Biochemistry*, 1994, **33**, 3280–3286.
169. D. J. Siminovitch, Solid-state NMR studies of proteins: the view from static ^{2}H NMR experiments. *Biochem. Cell Biol.*, 1998, **76**, 411–422.

Index